

# **Catalysis to produce solar fuels: From the production of hydrogen via water splitting, to hydrogen conversion to methanol by its reaction with CO<sub>2</sub>**

Thesis submitted in accordance with the requirement of Cardiff University for the degree of  
Doctor of Philosophy

**Jonathan Ruiz Esquius**



Cardiff  
Catalysis Institute  
Sefydliad Catalysis  
Caerdydd

School of Chemistry

Cardiff University

January 2019



## STATEMENTS AND DECLARATIONS

**STATEMENT 1** This thesis is being submitted in partial fulfilment of the requirements for the degree of Doctor of Philosophy

Signed

Date

### **STATEMENT 2**

This work has not been submitted in substance for any other degree or award at this or any other university or place of learning, nor is it being submitted concurrently for any other degree or award (outside of any formal collaboration agreement between the University and a partner organisation)

Signed

Date

### **STATEMENT 3**

I hereby give consent for my thesis, if accepted, to be available in the University's Open Access repository (or, where approved, to be available in the University's library and for inter-library loan), and for the title and summary to be made available to outside organisations, subject to the expiry of a University-approved bar on access if applicable.

Signed

Date

### **DECLARATION**

This thesis is the result of my own independent work, except where otherwise stated, and the views expressed are my own. Other sources are acknowledged by explicit references.

The thesis has not been edited by a third party beyond what is permitted by Cardiff University's Use of Third Party Editors by Research Degree Students Procedure.

Signed

Date

### **WORD COUNT: 57,330**

(Excluding summary, acknowledgements, declarations, contents pages, appendices, tables, diagrams and figures, references, bibliography, footnotes and endnotes)

# Summary

The development of a carbon-free emission energy system is needed to alleviate the increasing CO<sub>2</sub> concentration in the atmosphere. Current technology allows the production of energy from renewables (hydroelectric plants or solar and wind farms) however, due to the fluctuating nature of renewables, they do not provide a reliable alternative to polluting fossil fuels for a constant energy supply. To stabilise the energy supply, surpluses of electricity can be used to split water to hydrogen and oxygen. Hydrogen has one of the highest energy densities per mass and can be used as a green-fuel, not contributing to CO<sub>2</sub> emissions.

Water splitting involves the hydrogen evolution reaction (HER) at the cathode and the oxygen evolution reaction (OER) at the anode. Due to slow kinetics, OER accounts for large energy losses during water splitting, making OER the bottle-neck in the process. The most energy efficient route for water splitting is in a polymer membrane water electrolyser (PEM). IrO<sub>2</sub> is virtually the only feasible catalyst for this electrolyser. However, iridium is one of the rarest elements on earth. Hence it is vital to optimise the preparation of IrO<sub>2</sub> catalysts to reduce the metal loading on the anode for OER, while preserving catalytic activity and stability.

Green-hydrogen (produced from water splitting using renewables) can be incorporated into the current fossil fuel feed-stock by reaction with CO<sub>2</sub> to form hydrocarbons, such as methanol. Methanol at present is produced from syngas (CO + H<sub>2</sub>) over a copper catalyst. Syngas was originally produced from steam reforming of CH<sub>4</sub>, the overall process being highly CO<sub>2</sub>-emitting. Copper based catalysts are not stable against sintering during the direct CO<sub>2</sub> hydrogenation to methanol. PdZn alloy catalysts act as active sites for the CO<sub>2</sub> hydrogenation to methanol while being a stable alternative against sintering Cu-catalysts.

## Acknowledgements

First of all, I would like to thank Prof. Graham J. Hutchings and Prof. Michael Bowker for their supervision and for giving me the opportunity to carry out a PhD in heterogeneous catalysis, allowing for my professional development within the MaxNet energy consortium at the Cardiff Catalysis Institute, Cardiff University. I really appreciate Dr. Simon Freakley and Dr. Hasliza Bahruji's guidance throughout these three years and for the revision of the present Thesis. I would also like to thank Dr. Sankar Meenakshisundaram, Dr. James Hayward, Dr. Robert Armstrong, Dr. Grazia Malta, Simon Dawson and Anisa Tariq for their advice and comments and for helping with thesis corrections. I would like to acknowledge the professionals within Cardiff University who taught, helped and advised me throughout the process. Special thanks go to Dr. Thomas Davies for the TEM analysis, Dr. David J. Morgan for the XPS analysis, the technical CCI staff Dr. Chris Morgan, Dr. Greg Shaw and to Dr. Michal Perdjon for the teaching of the rest of the characterisation techniques. I would also like to thank the rest of the CCI students and especially those involved in the MaxNet team, Tanja Elisabeth, Margherita Macino, Stefano Cattaneo and Nishta Agarwal. I am grateful for the suggestions received from the external advisors panel and for the advice from fruitful collaboration with members of the diverse Max-Planck Institutes involved in the project, especially Dr. Ioannis Spanos for providing the flow cell, Dr. Gerardo Algara Siller for the low electron dose TEM and Dr. Olga Kasian for her advice on electrochemistry. I would like to thank Tanja and Simon for sharing seldom sunny lunches in the park.

Immeasurable thanks to Alba who followed me from Barcelona to the UK and who has always supported and encouraged me. Thank you for sharing your path with me for the last nine years. I would also like to thank my family and friends back home (I hope to see you all more often) as well as numberless friends made in Cardiff who shared my ups and downs (on the wall and inside the water); Lourdes, Felix, Christian, Pau, Oriol, Aaron, Tattiana, Martha, Celia, Ferdi, Rodri, Carlos, Pedro, Annegret, Auguste, Chris, Alec, Rob, Annie, Ian, Dayana, Alessandro (sincere apologies for the names not included, but I mentioned that they were innumerable).

I also want to declare my admiration for the tireless scientific community, which is always seeking to unravel nature's puzzles and finding solutions towards a more sustainable society. This Thesis aims to provide a grain of sand to aid in the energy challenge.

*“Give the ones you love wings to fly, roots to come back, and reasons to stay”*

*“It is under the greatest adversity that there exists the greatest potential for doing good, both for oneself and others”*

Dalai Lama

# Abstract

Increasing CO<sub>2</sub>-anthropogenic concentration in the atmosphere is surpassing sustainable levels and unambiguously jeopardising the global climate. The main share of CO<sub>2</sub> emissions corresponds to the production of energy, currently 17 TW per year. By analysing historical trends on population growth and energy consumption, it is expected that the global energy demand will reach 30 TW by 2050, which in turn will aggravate the stress on the environment. In order to alleviate adverse climate-change-related consequences, it was agreed to reduce global CO<sub>2</sub> emissions. This could be achieved by shifting the current energy system towards a carbon-free energy vector, hydrogen. Hydrogen can be obtained from the hydrolysis of water using surplus electricity generated from renewables, without contributing to CO<sub>2</sub> emissions. The main drawback to switching from a carbon to a hydrogen-based energy system is that H<sub>2</sub> is a gas and current technology has evolved around liquid fuels. In order to circumvent this energy transition, hydrogen can be further transformed to liquid fuels via its reaction with CO<sub>2</sub>.

In a polymer electrolyte membrane (PEM) electrolyser, water is oxidised at the anode to oxygen and protons, protons migrate through the membrane to the cathode where they recombine with electrons to form hydrogen. Due to the slow kinetics and multiple reaction steps on the anode compared to the cathode, the oxidation of water to oxygen (or oxygen evolution reaction, OER) is responsible for high overpotentials. Additionally, the anode needs to be made of iridium based catalysts, and because of its low natural abundance, it is essential to develop materials with an efficient Ir usage and to optimise its catalytic activity and stability.

This research is divided in two defined themes. The first (chapter 3 to chapter 6) focuses on the optimisation of IrO<sub>2</sub> catalysts for the oxygen evolution reaction, necessary half reaction in a PEM water electrolyser for the production of hydrogen. The second (chapter 7) comprises of the optimisation of PdZn catalysts supported on TiO<sub>2</sub> for the further transformation of H<sub>2</sub>, by its reaction with CO<sub>2</sub>, to solar fuels.

In chapters 3 and 4, the effect of the base on the hydrothermal synthesis of unsupported and supported amorphous iridium oxo-hydroxides is studied. The hydrothermal synthesis was chosen because it allowed the synthesis of amorphous IrO<sub>x</sub> materials without the need for heat treatment at high temperature, thus minimising the possible crystallisation and the concomitant decrease in activity towards OER. It was observed that the base plays an important role in tailoring the morphology, surface area and surface hydroxide concentration

of  $\text{IrO}_x$  catalysts, and thus it has a direct effect on the catalytic activity and stability. Specifically, the use of  $\text{Li}_2\text{CO}_3$  as a base led to a catalyst with porous morphology, higher surface area and higher hydroxide concentration, which this translated to an improved activity and stability towards OER compared to the state of the art catalyst  $\text{IrO}_2 \cdot 2\text{H}_2\text{O}$  (Premion, Alfa Aesar). In both chapters, heat treatment was proven to hinder the catalytic activity towards OER, presumably as a result of higher crystallinity, the loss of Ir(III) sites and the decrease in hydroxide concentration.

In chapter 5, two different  $\text{IrO}_2$  crystalline structures (rutile and hollandite) were synthesised, characterised and compared as OER catalysts. In accordance with the literature, the transformation of amorphous iridium oxo-hydroxide, containing Ir(III)/Ir(IV) sites, to crystalline rutile  $\text{IrO}_2$ , made only of Ir(IV) sites, led to a decrease in catalytic activity and stability. However, the presence of  $\text{Li}_2\text{CO}_3$  in the amorphous  $\text{IrO}_x$  catalyst led to the formation of hollandite  $\text{IrO}_2$  instead of rutile  $\text{IrO}_2$ , with lithium as the host cation within the hollandite channels. Apart from the difference in crystallinity, characterisation on hollandite  $\text{IrO}_2$  indicates that it was closer in nature to amorphous  $\text{IrO}_x$  than to rutile  $\text{IrO}_2$ . The presence of Ir(III) and Ir(IV) was confirmed by XPS, shorter Ir-Ir bond distances and longer Ir-O, compared to rutile  $\text{IrO}_2$ , were observed by EXAFS, and comparable OER activity to  $\text{IrO}_2 \cdot \text{Li}_2\text{CO}_3$  was detected by LSV. Additionally, the conversion of amorphous  $\text{IrO}_2 \cdot \text{Li}_2\text{CO}_3$  to hollandite  $\text{IrO}_2$  led to improved stability under OER reaction conditions.

In order to use iridium more efficiently and to reduce the iridium loading on the electrode, in chapter 6  $\text{IrO}_2$  was diluted with a more abundant and economic metal oxide, nickel or copper oxide. Catalysts with a homogeneous metal distribution and with a core-shell distribution, concentrating iridium at the surface and the non-noble metal oxide at the core, were prepared following a modification of the hydrothermal synthesis method. The synthesis of mixed oxide catalysts with a homogeneous metal distribution led to a decrease in the catalytic activity and the stability of the catalyst, which was proven to be an ineffective synthetic route for considerably decreasing the iridium loading on the electrode. The observed decline in the catalytic performance was attributed to the dissolution of the non-noble metal oxide in contact with the reaction media. However, through a core-shell distribution,  $\text{IrO}_x$  was concentrated on the surface of the catalyst, whilst the non-noble metal remained protected against dissolution inside the nanoparticle core. Following the core-shell synthetic approach, the iridium loading on the electrode was successfully halved without impairing the catalytic activity or stability, compared to pure  $\text{IrO}_2 \cdot \text{Li}_2\text{CO}_3$ .

The second part discussed in chapter 7, studied the optimisation of PdZn/TiO<sub>2</sub> catalysts prepared by chemical vapour impregnation (CVI) for the CO<sub>2</sub> hydrogenation (pre-reduction at 400 °C, 1 h, reaction at 250 °C, 20 bar, 30 ml·min<sup>-1</sup>, 60 % H<sub>2</sub>, 20 % CO<sub>2</sub>, 20 % N<sub>2</sub>) to methanol, as a stable alternative to copper catalysts. The first section of the chapter focused on the Pd to Zn molar ratio in the material, maintaining the palladium loading at 5 wt. %. Increasing the Pd:Zn molar ratio from (1:1) to (1:5) led to a greater formation of PdZn alloy, which improved CO<sub>2</sub> conversion, but without considerably affecting methanol selectivity. The further addition of zinc, as observed for the catalyst with a Pd:Zn molar ratio of (1:10), led to a decrease in the CO<sub>2</sub> conversion. This was presumably caused by zinc blocking active sites when in large excess.

The atomic proportion of zinc in the PdZn alloy can vary from 40 at. % to 60 at. %. Hence it could be hypothesised that increasing the pre-reduction temperature could lead to a higher proportion of zinc within the alloy, which in turn can improve methanol selectivity. In general, increasing the pre-reduction temperature from 400 °C to 650 °C led to an increase in the methanol productivity because of improved methanol selectivity, although lower CO<sub>2</sub> conversion was observed as a result of particle sintering. However, more interestingly, the CH<sub>4</sub> selectivity decreased by one order of magnitude after increasing the pre-reduction treatment from 400 °C to 650 °C, simultaneously with the transformation of ZnO and TiO<sub>2</sub> to rhombohedral ZnTiO<sub>3</sub>.

This lead to the hypothesis that the PdZn-TiO<sub>2</sub> interphase is responsible for methane production. To prove this hypothesis, PdZn/ZnTiO<sub>3</sub> and Pd/ZnTiO<sub>3</sub> catalysts were prepared by CVI, after pre-reduction at 400 °C. PdZn alloy formation was confirmed by XRD on both systems, indicating that Zn in the ZnTiO<sub>3</sub> phase can migrate out of the lattice to form PdZn. Thus, the PdZn-TiO<sub>2</sub> interface was generated in Pd/ZnTiO<sub>3</sub> but not in PdZn/ZnTiO<sub>3</sub>. When tested for CO<sub>2</sub> hydrogenation to methanol, the formation of methane on the former catalyst and its absence on the latter corroborated the formulated hypothesis that PdZn-TiO<sub>2</sub> acts as the active site for CH<sub>4</sub> formation.

# Glossary

(ad)	Adsorbed on a surface
at. %	Atomic percentage
atm	Atmospheres
ATO	Antimony doped tin oxide
ATR	Attenuated total reflection
a.u.	Arbitrary units
BET	Brunauer-Emmett-Teller surface area
CE	Counting electrode
cm	Centimetre
CVI	Chemical Vapour Impregnation
DFT	Density Functional Theory
e <sup>-</sup>	Electron
E°	Potential
Eq.	Equation
eV	Electron volts
FID	Flame ionisation detector
FTIR	Fourier-transform infrared
g	Gram
GC	Gas chromatography
GHG	Greenhouse gas
h	hours
H <sup>+</sup>	Proton
HER	Hydrogen evolution reaction
J	Current density ( $\text{mA}\cdot\text{cm}^{-2}$ )
K	Degrees Kelvin
kg	Kilo gram
kJ	Kilo joule ( $\text{kg}\cdot\text{m}^2\cdot\text{s}^{-2}$ )
L	litre
LED	Light-emitting diode
mA	Milliamp
mg	milligram
MFC	Mass flow controller
min	minute
ml	Millilitre ( $10^{-3} \text{ L}$ )

mmol	Millimoles ( $10^{-3}$ mol)
MPa	Megapascal (10 bar or 9.87 atm)
MS	Mass spectrometer
mV	millivolt
$\eta$	overpotential
NEXAFS	Near edge X-ray absorption fine structure
nm	Nanometre ( $10^{-9}$ m)
NOAA	National oceanic and atmospheric administration
OER	Oxygen evolution reaction
PEM	Polymer electrolyte membrane or proton exchange membrane
ppm	Parts per million (milligram per litre)
Ref. E	Reference electrode
RHE	Reversible hydrogen electrode
s	seconds
SEM	Scanning electron microscopy
SOE	Solid oxide water electrolyser
TCD	Thermal conductivity detector
TEM	Transmission electron microscopy
TGA	Thermogravimetric analysis
TPR	Temperature programmed reduction
TW	Tera watts ( $10^{12}$ W)
UV	Ultra violet
V	Volts ( $\text{kg}\cdot\text{m}^2\cdot\text{A}\cdot\text{s}^{-3}$ )
WE	Working electrode
WS	Water splitting
wt %	Weight percent
XPS	X-ray photoelectron spectroscopy
XRD	X-ray powder diffraction
$\Delta G$	Change in Gibbs energy
$\Delta H$	Change in enthalpy
$\Delta S$	Change in entropy
$^{\circ}\text{C}$	Degrees Celsius
$\mu\text{l}$	Microliter ( $10^{-6}$ L)
$\mu\text{m}$	Micrometre ( $10^{-6}$ m)

# Table of contents

	<b>Page</b>
Statements and declarations	i
Summary	ii
Acknowledgments	iii
Abstract	v
Glossary	viii
<b>Chapter 1. Introduction</b>	
<b>1.1 Greenhouse gasses and the climate change</b>	1
<b>1.2 The hydrogen economy</b>	2
1.2.1 Water electrolyzers	2
Alkaline water electrolyzers	3
Solid oxide water electrolyzers	4
Polymer membrane water electrolyzers	5
1.2.2 The kinetics of water splitting	6
1.2.3 OER mechanisms in PEM water electrolyzers	7
<b>1.3 OER catalyst in acid media</b>	10
1.3.1 Amorphous IrO <sub>x</sub> catalysts for OER	11
1.3.2 Hollandite IrO <sub>2</sub> catalysts for OER	12
1.3.3 Supported IrO <sub>2</sub> catalyst	14
1.3.4 Mixed oxide catalyst	16
<b>1.4 Hydrogen storage as conventional fuels</b>	18
1.4.1 Palladium-Zinc alloy catalyst for the direct carbon dioxide hydrogenation to methanol	21
<b>Research objectives</b>	24
<b>1.5 Bibliography</b>	25

## **Chapter 2. Experimental**

<b>2.1 Reagents used</b>	36
<b>2.2. Catalyst preparation</b>	38
2.2.1 Standard hydrothermal preparation of IrO <sub>2</sub> catalyst	38
2.2.2 Preparation of supported IrO <sub>2</sub> /ATO	38
2.2.3 Preparation of bimetallic metal oxides with core-shell structure	38
2.2.4 Standard preparation of PdZn catalyst by Chemical Vapour Impregnation (CVI)	39
2.2.5 Preparation of 5% Pd/ZnO catalyst by sol immobilisation	39
2.2.6 Preparation of ZnTiO <sub>3</sub> phase by Chemical Vapour Impregnation (CVI)	40
<b>2.3 Catalyst testing</b>	40
2.3.1 Oxygen Evolution Reaction (flow cell and standard cell in beaker)	40
2.3.2 CO <sub>2</sub> hydrogenation	41
<b>2.4 Characterisation techniques</b>	45
2.4.1 Absorption spectroscopy techniques	45
2.4.1.1 Ultraviolet - Visible Spectroscopy (UV-Vis)	45
2.4.1.2 Fourier transform Infra-Red attenuated total reflectance (FT-IR ATR)	46
2.4.1.3 Raman spectroscopy	47
2.4.1.4 X-ray photoelectron spectroscopy (XPS)	48
2.4.1.5 X-ray adsorption fine structure (XAFS)	49
2.4.2 Powder X-ray Diffraction (XRD)	50
2.4.3 Surface area analysis by the Brunauer-Emmett-Teller (BET) theory	52
2.4.4 Thermal analysis	53
2.4.4.1 Thermogravimetric analysis (TGA)	53
2.4.4.2 Temperature programed reduction (H <sub>2</sub> -TPR)	53

2.4.5 Electronic Microscopic techniques	54
2.4.5.1 Scanning Electron Microscopy (SEM)	55
2.4.5.2 Transmission Electron Microscopy (TEM)	56
<b>2.5 Bibliography</b>	57

## **Chapter 3. Effect of base on the preparation of IrO<sub>2</sub> catalysts**

### **towards OER through a hydrothermal synthesis**

<b>3.1 Introduction</b>	58
<b>3.2 Effect of the alkali metal base during the hydrothermal synthesis of IrO<sub>2</sub></b>	59
3.2.1 Catalysts preparation	59
3.2.2 Catalyst Characterisation	60
UV-Vis characterisation	60
Attenuated Total Reflectance - Fourier-Transform Infrared spectroscopy (ATR-FTIR)	64
X-ray powder diffraction (XRD)	65
Raman Spectroscopy	67
Thermal analysis	70
X-ray photoelectron spectroscopy (XPS)	76
Scanning electron microscopy (SEM)	80
Electron transmission microscopy (TEM)	82
3.2.3 Catalysts activity towards OER	84
<b>3.3. Conclusions</b>	92
<b>3.4 Bibliography</b>	94

**Chapter 4. Effect of base on the preparation of IrO<sub>2</sub> catalysts supported on ATO towards OER prepared via hydrothermal synthesis**

<b>4.1 Introduction</b>	98
<b>4.2 Effect of alkali metal bases on the synthesis of supported IrO<sub>2</sub> on ATO</b>	99
4.2.1. Catalysts Preparation	99
4.2.2 Catalysts Characterisation	99
X-Ray powder diffraction (XRD)	99
X-ray photoelectron spectroscopy (XPS)	100
Scanning Electron Microscopy coupled with Energy Dispersed X-ray (SEM-EDX)	101
Transmission electron microscopy (TEM)	104
4.2.3 Catalytic activity towards OER	106
<b>4.3 Heat treatment effect on the IrO<sub>2</sub>/ATO-Li<sub>2</sub>CO<sub>3</sub> catalyst</b>	111
4.3.1 Reduction and oxidation heat treatments on the IrO <sub>2</sub> /ATO-Li <sub>2</sub> CO <sub>3</sub> catalyst	111
4.3.2 Heat treated IrO <sub>2</sub> /ATO-Li <sub>2</sub> CO <sub>3</sub> catalysts characterisation	113
X-ray powder diffraction (XRD)	113
X-ray photoelectron spectroscopy (XPS)	114
Scanning electron microscopy (SEM)	120
High resolution transmission electron microscopy (HRTEM)	121
4.3.3 Catalytic activity towards OER	123
<b>4.4 Conclusions</b>	126
<b>4.5 Bibliography</b>	129

## **Chapter 5. Synthesis of crystalline $\text{Li}_x\text{IrO}_2$ hollandite as stable and active catalysts towards OER**

<b>5.1 Introduction</b>	132
<b>5.2 Single <math>\text{IrO}_2</math> hollandite and <math>\text{IrO}_2</math> rutile phase synthesis and characterisation</b>	133
5.2.1 Single $\text{IrO}_2$ hollandite and $\text{IrO}_2$ rutile phase electrochemistry towards OER	143
<b>5.3 Conclusions</b>	149
<b>5.4 Bibliography</b>	150

## **Chapter 6. Preparation of iridium mixed oxide catalysts. Rational design of catalysts for significantly lowering the iridium loading on the electrode**

<b>6.1 Introduction</b>	153
<b>6.2 Homogeneously dispersed iridium non-noble metal mixed oxide catalysts</b>	154
6.2.1 Catalyst synthesis	154
6.2.2 Catalyst characterisation	154
X-ray powder diffraction (XRD)	154
X-ray photoelectron spectroscopy (XPS)	157
6.2.3 Catalytic performance towards OER	163
<b>6.3 Core-shell IrNi and IrCu mixed oxide catalysts</b>	170
6.3.1 Core-shell catalysts preparation	170
6.3.2 Catalysts Characterisation	171
6.3.3 Catalysts electrochemistry	176
<b>6.4 Conclusion</b>	180
<b>6.5 Bibliography</b>	181

## **Chapter 7. CO<sub>2</sub> hydrogenation to methanol over PdZn/TiO<sub>2</sub> catalysts prepared by CVI**

<b>7.1 Introduction</b>	184
7.1.1 Chemical vapour impregnation (CVI) as a catalyst preparation technique	185
<b>7.2 Palladium to zinc molar ratio effect on supported TiO<sub>2</sub> catalysts by CVI</b>	186
7.2.1 Catalyst preparation	184
7.2.2 Catalyst characterisation	186
XRD characterisation	186
X-ray photoelectron spectroscopy (XPS)	194
Surface area measurement by BET	195
Transmission electron microscopy (TEM)	196
7.2.3 Catalyst activity	198
<b>7.3 Catalyst optimisation by high temperature pre-reduction</b>	200
7.3.1 Reduction at 400 °C, 550 °C and 650 °C for the 5 % PdZn(1:5)/TiO <sub>2</sub> catalyst	200
Catalyst characterisation	200
Catalyst activity	202
7.3.2 Different Palladium loading and ZnTiO <sub>3</sub> phase formation effect	203
Catalyst preparation and characterisation	203
Catalyst activity	212
<b>7.4 PdZn alloy catalysts supported on ZnTiO<sub>3</sub></b>	213
7.4.1 ZnTiO <sub>3</sub> preparation and characterisation	214
7.4.2 PdZn and Pd catalysts supported on ZnTiO <sub>3</sub>	215
Catalyst preparation	215
Catalyst characterisation	215

Catalytic activity	218
<b>7.5 Conclusions</b>	223
<b>7.6 Bibliography</b>	224
 <b>Chapter 8. Conclusions and future work</b>	
8.1 Chapter 3	228
8.2 Chapter 4	229
8.3 Chapter 5	230
8.4 Chapter 6	231
8.5 Chapter 7	232
<b>Appendix I</b>	234



# Chapter 1

## Introduction

### 1.1 Greenhouse gasses and the climate change.

The Earth's atmosphere is formed mainly of N<sub>2</sub> (78 %), O<sub>2</sub> (21 %) and Ar (0.9 %), while the remaining 0.1 % corresponds to greenhouse gases (GHGs).<sup>(1)</sup> GHGs are molecules that adsorb and emit in the infrared region (IR). These GHGs keep some of the solar radiation within the atmosphere, producing the so-called *green-house* effect. Without GHGs the average Earth's temperature would be 30 °C colder than at present.<sup>(2)</sup> Hence, although GHGs are present in the atmosphere in trace concentration, they are paramount in maintaining the global temperature within comfortable values, and variations in their concentration have a direct influence on the climate. The most common GHGs are: water (H<sub>2</sub>O), ozone (O<sub>3</sub>), carbon dioxide (CO<sub>2</sub>), methane (CH<sub>4</sub>) and nitrous oxide (N<sub>2</sub>O).

The climate, and the GHGs concentration, has remained considerably stable for the last 10,000 years. Without human intervention the climate was expected to remain stable for the next thousand years.<sup>(2)</sup> However, since the industrial revolution (1750s-1760s) the atmospheric CO<sub>2</sub> concentration has increased from 280 ppm to 414 ppm,<sup>(3)</sup> the highest CO<sub>2</sub> concentration recorded for the last 800,000 years<sup>(4)</sup> (figure 1.1). The increase in the CO<sub>2</sub> concentration is unambiguously related to anthropogenic emissions, human related activities, mainly associated with the production of energy from finite resources: coal, oil and natural gas.

It has been estimated that an increase in the CO<sub>2</sub> concentration above 350 ppm would correspond to an increase of 2 °C in the global temperature,<sup>(5)</sup> leading to irreversible consequences: sea level rises, extreme weather conditions, food and water insecurity, spread of tropical diseases to higher latitudes and mass migrations.<sup>(6, 7)</sup>

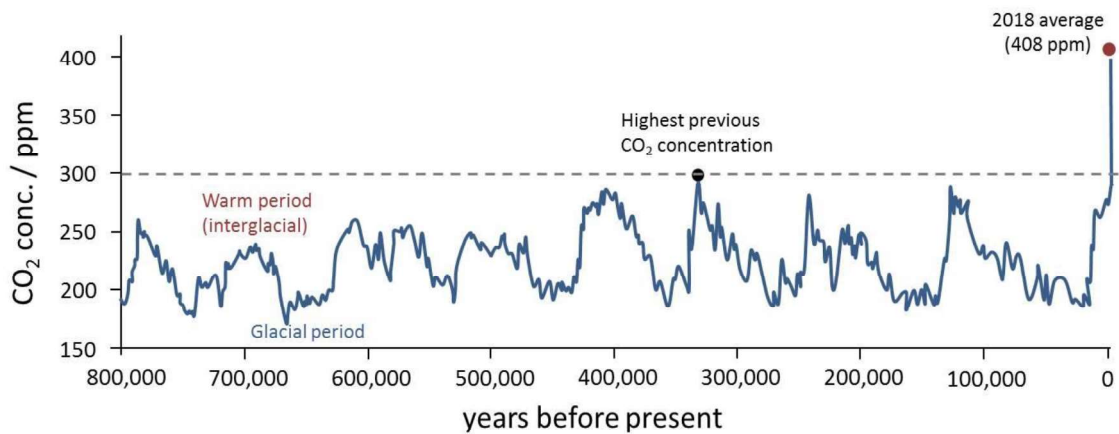


**Figure 1.1.** CO<sub>2</sub> concentration in the atmosphere for the past 800,000 years extracted from trapped air bubbles in Antarctica's ice.<sup>(3)</sup>

## 1.2 The hydrogen economy.

The production of energy from fossil fuels is the main cause for the increasing CO<sub>2</sub> concentration in the atmosphere, and thus, behind the climate change.<sup>(8)</sup> To reduce CO<sub>2</sub> emissions, the energy production is now increasingly shifting from fossil fuels to the so-called renewables: wind/solar farms and hydroelectric power stations.

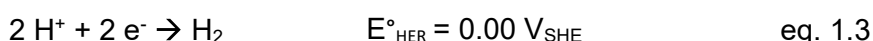
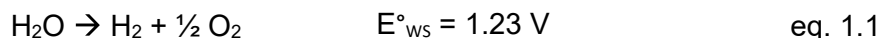
However, because of the intermittent nature of these renewable energies, when the electricity production exceeds the electricity demand, this surplus of energy needs to be stored, to make it available when the electricity demand exceeds its production. Several routes for storing energy surpluses are discussed in literature, the most efficient route is to use this electricity for splitting water (WS) into its elemental components, H<sub>2</sub> and O<sub>2</sub>, in a proton exchange membrane water electrolyser (PEM).<sup>(9)</sup> However, due to the wide inflammability range of hydrogen in air (4%-75%) and in oxygen (4%-95%), hydrogen will be further transformed to other molecules: ammonia, methanol or higher hydrocarbons.<sup>(9)</sup>

### 1.2.1 Water electrolyzers.

Thermodynamically, water is a stable molecule, under standard conditions 237.2 kJ·mol<sup>-1</sup> of energy needs to be applied to obtain its dissociation to hydrogen and oxygen<sup>(10, 11)</sup> (equation 1.1). In water electrolyzers, the necessary energy to split water is supplied in the form of electricity, by applying a potential between two electrodes: the cathode and the anode. The oxygen evolution reaction (OER) which consists in the oxidation of water to oxygen, protons and the release of electrons proceeds at the anode (equation 1.2). Whilst the hydrogen evolution reaction (HER), which consists in

the recombination of protons and electrons to hydrogen, occurs at the cathode (equation 1.3).

The minimum potential necessary to split water ( $E^\circ_{WS}$ ) can be obtained by subtracting the half reaction potential occurring at the cathode ( $E^\circ_{HER}$ ) to the half reaction potential at the anode ( $E^\circ_{OER}$ ):  $E^\circ_{WS} = E^\circ_{OER} - E^\circ_{HER} = 1.23 \text{ V}$ .



Water electrolysis was first observed by Troostwijk and Diemann in 1789.<sup>(12)</sup> Since then three different types of water electrolyzers have been developed: alkaline electrolyzers, solid oxide electrolyzers and polymer membrane electrolyzers.<sup>(10, 13, 14)</sup>

- Alkaline water electrolyzers.

Alkaline water electrolyzers (figure 1.2) have been widely developed over the last century<sup>(15)</sup> and is the most common water electrolysis technology, with over a thousand units installed worldwide.<sup>(16)</sup> Its commercial success over the other water electrolyzers is related to its low capital cost, because of the use of earth abundant elements (Ni, Co, Fe, Cu, Mn, Zn) deposited on the electrodes to perform both half reactions (OER and HER), and its high durability (over 15 years).<sup>(17)</sup>

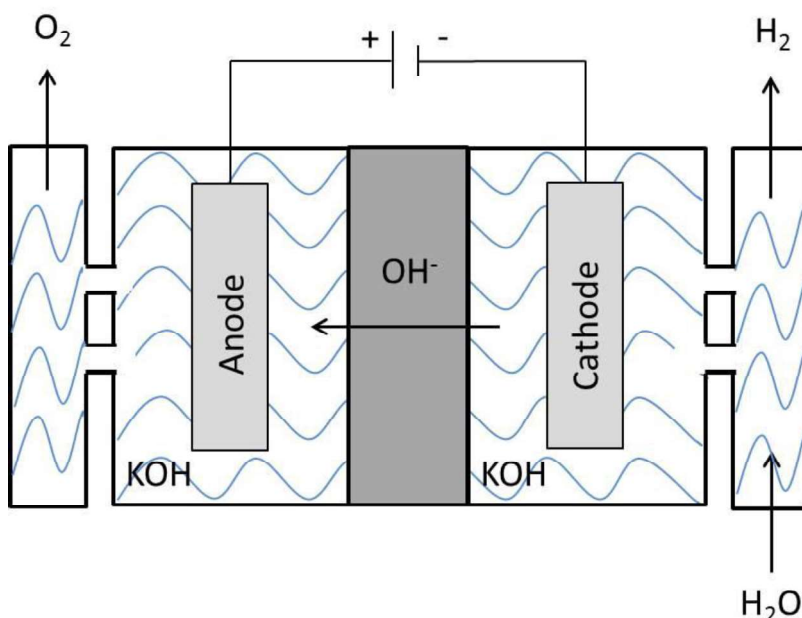


**Figure 1.2.** Schematic representation of an alkaline water electrolyser.

In alkaline electrolyzers, water is reduced at the cathode producing hydrogen and hydroxide anions (equation 1.4). Hydroxide anions travel through the diaphragm to the anode and recombine to form oxygen (equation 1.5). The diaphragm is made of fluorocarbons or hydrocarbons ion exchange polymers to physically separate the anode to the cathode, thus avoiding the formation of explosive H<sub>2</sub>/O<sub>2</sub> gas mixtures. Water electrolysis, in alkaline water electrolyzers, is performed under 25-35 wt. % KOH aqueous solution, this high concentration of base is required to provide good electrolyte conductivity between electrodes.



The main drawbacks of alkaline water electrolyzers is their operational low current density (0.4 A·cm<sup>-2</sup>) which limits the water splitting efficiency, and their low operational pressure (25-30 bar) to avoid the formation of explosive H<sub>2</sub>/O<sub>2</sub> mixtures, which constrains the formation of compact models. Additionally, hydrogen will need to be pressurised for an efficient transport or storage, adding an extra process for its production.

- Solid oxide water electrolyzers (SOE)

In a solid oxide electrolyser (SOE), illustrated in figure 1.3, steam is used instead of liquid water at temperatures between 600 °C and 900 °C. As a result of increasing the reaction temperature from 25 °C to 1000 °C, the necessary electric energy to split water is reduced from 237.2 kJ·mol<sup>-1</sup> to 177.5 kJ·mol<sup>-1</sup>. The first results on a SOE water electrolyser were reported by Dönitz and Erdle in the 1980s.<sup>(14)</sup> Even if the catalyst supported on the electrodes can be made of Earth abundant elements (Ni, Fe, Co) the availability of steam at elevated temperatures has limited its commercial application.<sup>(14)</sup>

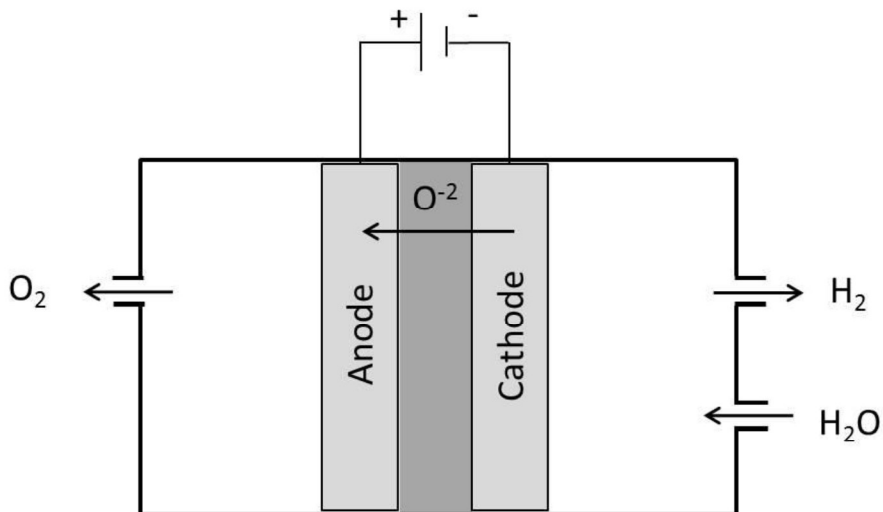


**Figure 1.3.** Schematic representation of a solid oxide electrolyser (SOE).

In a SOE electrolyser steam is reduced to hydrogen and oxide ions at the cathode (equation 1.6), oxide ions migrate through a ceramic membrane, made of  $Y_2O_3$ - $ZrO_2$ , to the anode where oxygen evolves (equation 1.7).<sup>(18)</sup>



- Polymer membrane water electrolyzers (PEM)

Polymer membrane water electrolyzers (PEM), also called proton exchange membrane electrolyzers (figure 1.4), were developed by General Electric in the 1960s.<sup>(14)</sup> The main difference between PEM and alkaline water electrolyzers is the thinner membrane (less than 0.2 mm compared to at least 1 mm) used to separate the cathode and the anode, which is made of sulfonated polystyrene, allowing only the migration of protons instead of hydroxides which allows the faster diffusion of ions. Several are the advantages of PEM water electrolyzers over alkaline water electrolyzers.<sup>(14)</sup> Firstly, PEM can operate at high pressure (up to 85 bar) without the formation of hazardous  $H_2/O_2$  gas mixtures, hydrogen is obtained at 35 bar, avoiding a pressuring step. Secondly, PEM can operate under variable electricity supply which is common in renewable energies. Thirdly, PEM can operate at higher current density (above  $1.6 A \cdot cm^{-2}$ ), which increase the overall process efficiency.<sup>(14)</sup>

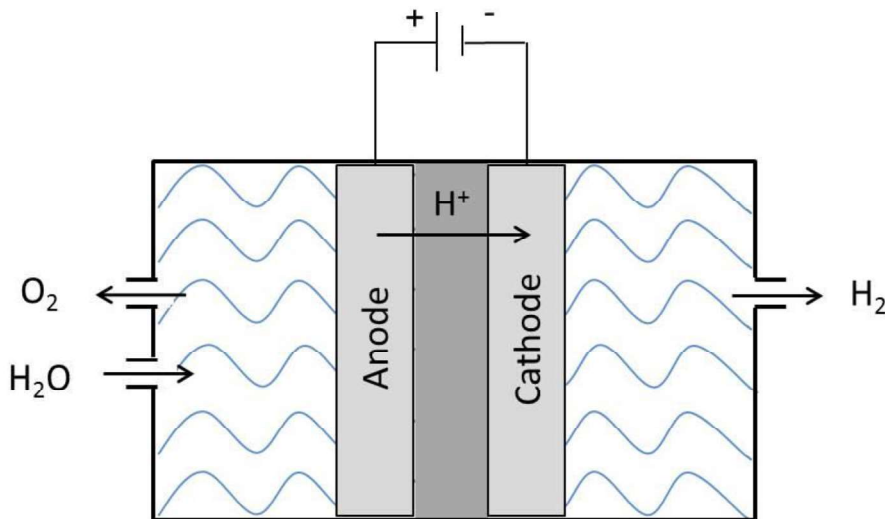


**Figure 1.4.** Schematic representation of a polymer membrane water electrolyser (PEM).

In a PEM, water is first oxidised to oxygen (equation 1.8) at the anode followed by the recombination of protons and electrons at the cathode (equation 1.9).



The main drawbacks of PEM water electrolyzers is their high investment cost, since noble metals (Pt, Ir and Ru) are used as catalyst on the electrodes, and their relative lower life time compared to alkaline water electrolyzers (10 years).

### 1.2.2 The kinetics of water splitting.

As briefly reported in the previous section, from the half reactions (OER and HER) involved in the water splitting reaction, the minimum potential to split water into hydrogen and oxygen was determined to be 1.23 V. However, on operational alkaline and PEM water electrolyzers, a minimum potential between 1.8-2.6 V<sub>RHE</sub> is generally reported before water splitting is observed.<sup>(19)</sup> As represented in equation 1.10, the difference in the potential between the thermodynamic ( $E^\circ$ ) and the experimental ( $E_{ap}$ ) value is defined as the overpotential ( $\eta$ ).

$$\eta = E_{ap} - E^\circ \quad \text{Eq. 1.10}$$

The detection of overpotential indicates the loss of electric energy during water splitting, normally as heat. From the total energy applied to split water, an overpotential of 0.57 V and 1.37 V ( $E_{ap}$  between 1.8 V<sub>RHE</sub> and 2.6 V<sub>RHE</sub>) would correspond to an energy loss of 31.7-53.0 %.<sup>(19)</sup> The overpotential associated to OER ( $\eta_{OER}$ ), to HER

( $\eta_{\text{HER}}$ ) and the electric resistance between the anode and the cathode (IR) contribute to the total overpotential (equation 1.11). The overpotential is sensitive to the cell design, experimental conditions and the catalyst used at the electrodes. Therefore, the overpotential is cell characteristic, thus comparison between reported data is non-trivial and needs to be done cautiously.

$$E_{\text{ap}} = (E^{\circ}_{\text{OER}} - E^{\circ}_{\text{HER}}) + (\eta_{\text{OER}} - \eta_{\text{HER}}) + \text{IR} \quad \text{Eq. 1.11}$$

In electrochemical reactions, only single electron transfer between the electrode and the reactant is allowed at a time. From equations 1.2 and 1.3, it can be noticed that for the formation of one molecule of hydrogen, two electron transfers occur, whilst for the formation of one molecule of oxygen, four electrons are transferred between the anode and water/reaction intermediates. Therefore, OER involve the formation of a higher number of reaction intermediates compared to HER, making the total overpotential associated mainly to the oxygen evolution reaction.

### 1.2.3 OER mechanisms in PEM water electrolyzers.

The reaction mechanism for OER is still under debate.<sup>(20)</sup> In 1986 Matsumoto and Sato reported four possible reaction mechanisms,<sup>(21)</sup> although the exact mechanism has not been experimentally confirmed. For all four mechanisms reported, the initial step consisted in the absorption of water onto the surface of the catalyst to form an OH<sub>(ad)</sub> intermediate.

In order to determine the rate determining step, and thus to confirm the reaction mechanism, the Tafel slope of a catalyst can be experimentally measured (equation 1.12). The Tafel slope can be defined as the current density changes with increasing overpotential during stationary-state reaction conditions.<sup>(20)</sup>

$$\frac{d \log(j)}{d \eta} = \frac{2.3 \cdot RT}{\alpha z F} \quad \text{Eq. 1.12}$$

Where  $j$  represents the current density,  $\eta$  the overpotential,  $F$  the faraday constant,  $R$  the ideal gas constant,  $T$  the temperature,  $z$  the number of electrons transferred in the rate determining step and  $\alpha$  the transfer coefficient.

From the Tafel slope measured on single-crystal RuO<sub>2</sub> (110) the mechanism described in equations 1.13 to 1.16 was proposed.<sup>(22)</sup> At low overpotential the Tafel slope was 60 mV·decade<sup>-1</sup>, however at high overpotential the measured Tafel slope was 120 mV·decade<sup>-1</sup>. Hence, it was proposed that the rate determining step is dependent on the potential applied. At low overpotential, the rate determining step was proposed to

be the water discharge to form a hydroxyl group (equation 1.13), whilst at high overpotential the rate determining step was proposed to be a hydroxyl recombination at the surface ( $\text{OH}_{(\text{ad})}$  formed in equation 1.13 to an activated form), before its discharge to form an oxide surface group.



Experimentally, the oxidation energy of a metal oxide to a higher oxidation state can be correlated with its activity for OER.<sup>(23)</sup> The energy to oxidise a metal oxide can be interpreted as the adsorption energy of oxygen at the metal oxide surface (equation 1.17).



Metal oxides which can be easily oxidised (e.g.,  $\text{Fe}_3\text{O}_4$ ,  $\text{Co}_3\text{O}_4$ ), adsorb oxygen strongly, making the evolution of oxygenated intermediates slow (rate determining step). Whereas, metal oxides difficult to oxidise (e.g.,  $\text{PbO}_2$ ,  $\text{Ni}_2\text{O}_3$ ), adsorb oxygen weakly, making the water discharge the rate determining step. Plotting the oxidation energy of metal oxides against their OER overpotential a volcano plot can be obtained, with  $\text{IrO}_2$  and  $\text{RuO}_2$  as the more active catalysts (figure 1.5).<sup>(23)</sup>

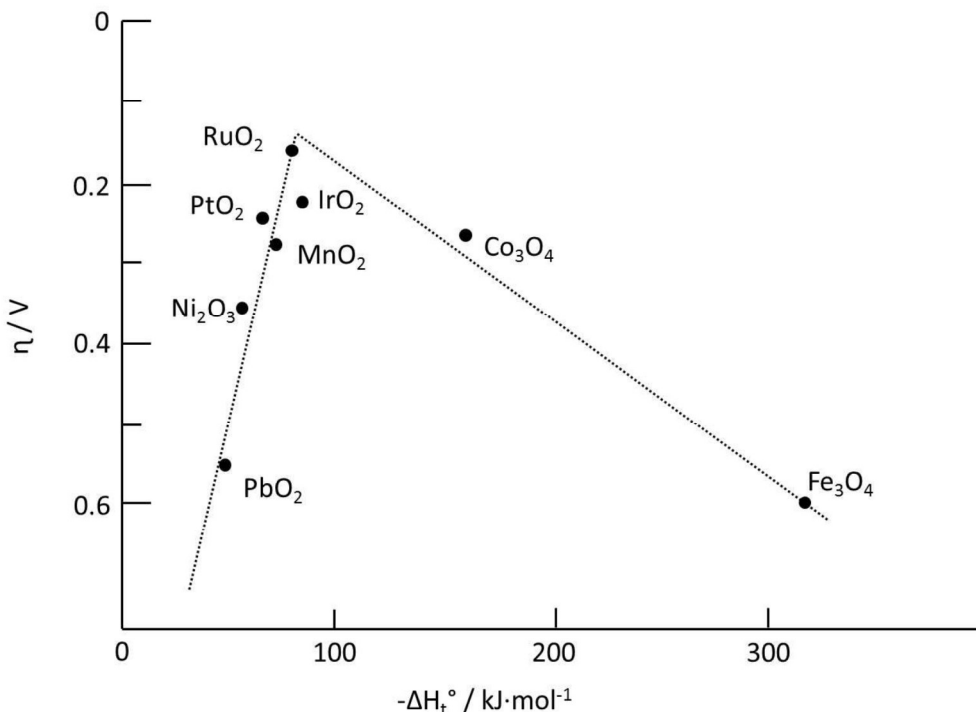


**Figure 1.5.** OER overpotential at different metal oxide electrodes as a function of the enthalpy change associated with the transition of a lower to a higher oxide state in acid media.<sup>(23)</sup>

More recently, Rossmeisl *et al.*<sup>(24)</sup> proposed a OER reaction mechanism based on the chemisorption energies of oxygenate intermediates at a metal oxide (equation 1.18 to equation 1.21).



In this work, based on DFT calculations, the nucleophilic attack of water to an adsorbed oxygen to form the peroxy intermediate ( $\text{OOH}_{(\text{ad})}$ ) (Eq. 1.23) was proposed as the rate determining step. By correlating the chemisorption energy of oxygenated intermediates on metal oxide surfaces to its theoretical OER overpotential, a volcano plot was obtained, with IrO<sub>2</sub> and RuO<sub>2</sub> as the best catalysts. In good agreement with trends observed by plotting the oxidation energy of metal oxides to their experimentally measured OER overpotential.<sup>(23)</sup>

Even if the proposed mechanisms represent a good way of predicting catalytic activity, they represent a simplified version of the overall process, since only changes in the oxygenate intermediates at the surface are considered. As reported by Fierro *et al.*,<sup>(25)</sup>

through isotopically labelled H<sub>2</sub>O and IrO<sub>2</sub>, the oxygen within the metal oxide lattice is directly involved in OER. Therefore, a thorough reaction mechanism should assess reactions occurring at the surface of the catalyst but also incorporate changes within the catalyst.

### **1.3 OER catalyst in acid media.**

As discussed in the previous section, IrO<sub>2</sub> and RuO<sub>2</sub> are the catalysts with lower overpotential (more active) for OER. RuO<sub>2</sub> presents higher activity compared to IrO<sub>2</sub>, however it dissolves as RuO<sub>4</sub> at OER reaction conditions.<sup>(26)</sup> Contrary, IrO<sub>2</sub> has lower activity but improved stability compared to RuO<sub>2</sub>.<sup>(27)</sup> As a result, to improve OER catalyst on PEM water electrolyzers research is focused on IrO<sub>2</sub>-based catalyst.

Various methods have been reported in the literature for the preparation of IrO<sub>2</sub> powders.

- *Adams fusion method*

This method was first reported for the preparation of PdO by R. Adams and R. L. Shriner,<sup>(28)</sup> it has since been adapted for the preparation of IrO<sub>2</sub>.<sup>(29-31)</sup> H<sub>2</sub>IrCl<sub>6</sub> is dissolved in the presence of NaNO<sub>3</sub> and heated to complete solvent evaporation. IrO<sub>2</sub> is then obtained by annealing in air. Materials made by this method presented better activity if annealed at milder temperature, as a result of lower crystallinity. For instance, Felix *et al*<sup>(29)</sup> prepared various IrO<sub>2</sub> catalysts through the Adam fusion method varying the annealing temperature, the IrO<sub>2</sub> catalyst annealed at 350 °C had a 50 mA·cm<sup>-2</sup> higher current density (indicating its higher activity) compared to catalysts annealed at 450 °C and 500 °C by chronoamperometry at 1.6 V.

- *Polyol synthesis method*

In this method, metallic nanoparticles are obtained from an iridium precursor through the addition of a reducing agent. A ligand, which can also act as the solvent, is used in order to stabilise the metallic-iridium nanoparticles. The oxide form is obtained by annealing in air at high temperature ( $\approx$ 500 °C).<sup>(32, 33)</sup>

- *Hydrothermal method*

This method consists of the hydrolysis of an iridium salt, IrCl<sub>3</sub> or H<sub>2</sub>IrCl<sub>6</sub>, under strong alkaline conditions to form a colloid suspension. The colloid suspension can be induced to precipitate by applying a source of energy such as heat<sup>(34)</sup> or UV-vis radiation.<sup>(35)</sup>

Massue *et al.*<sup>(36)</sup> prepared 30 wt % amorphous oxo-hydroxide  $\text{IrO}_2/\text{ATO}$  catalysts through a microwave assisted hydrothermal method. At 1.58 V<sub>RHE</sub> the fresh catalysts presented a current density of 0.7 A·mg<sub>Ir</sub><sup>-1</sup>. After annealing in air at 250 °C and at 350 °C the current density dropped to 0.5 A·mg<sub>Ir</sub><sup>-1</sup> and 0.2 A·mg<sub>Ir</sub><sup>-1</sup> respectively. This was attributed to a decrease in the concentration of hydroxyl groups and with the related transformation of amorphous iridium oxo-hydroxide into crystalline  $\text{IrO}_2$ .<sup>(36)</sup>

- Thermal decomposition method

This method involves the decomposition of an organic-iridium precursor by annealing at high temperature.<sup>(37-40)</sup> This methodology is commonly used for the preparation of  $\text{IrO}_2$  films. While the previously reported methods involve the use of chlorinated metal precursors, in this thermal decomposition method organometallic iridium precursors are normally used, avoiding chlorine contamination which can block OER active sites. Increasing the annealing temperature has a detrimental effect on the activity of  $\text{IrO}_2$  as a consequence of its higher crystallinity. For example, thermal decomposition of iridium acetate at 250 °C led to the formation of amorphous iridium oxo-hydroxide, whilst increasing the annealing temperature led to higher crystallinity and the concomitant decrease in catalytic activity towards OER.<sup>(41)</sup>

Generally, heat treatment at high temperature has proven to have a detrimental effect on the  $\text{IrO}_2$  catalytic performance,<sup>(29, 41, 42)</sup> possibly because of an increase in crystallinity<sup>(29)</sup> and the loss of surface OH groups.<sup>(37)</sup>

### **1.3.1 Amorphous $\text{IrO}_x$ catalysts for OER.**

Based on DFT calculations on rutile  $\text{IrO}_2$ , the nucleophilic attack of a water molecule to adsorbed  $\text{O}_{(\text{ad})}$  to form the peroxy intermediate,  $\text{OOH}_{(\text{ad})}$ , was proposed as the rate determining step.<sup>(24)</sup> Therefore, the presence of electrophilic oxygen species at the surface of the catalyst was speculated.

The formation of the O-O bond has been confirmed as the limiting step on other oxygen evolution systems, for example on  $\text{Co}_3\text{O}_4$  catalysts<sup>(43)</sup> and in the photosystem II, based on manganese.<sup>(44)</sup> On both systems, the catalytic cycle involve the metal centre in different oxidation states (Co(IV) and Co(III) or Mn(III), Mn(IV) and Mn(V) respectively). By comparison, Ir(III) and Ir(IV) sites would be expected on highly active  $\text{IrO}_2$  catalysts. Moreover, since lattice oxygen within the  $\text{IrO}_2$  is actively involved in OER,<sup>(25)</sup> catalyst with flexible structure, which would facilitate the migration of reagents and products in and out, are expected to outperform crystalline counterparts.

The presence of both, electrophilic oxygen species ( $\text{O}^-$ ) prone to nucleophilic attack by water molecules, and Ir(III)/Ir(IV) sites were confirmed by NEXAFS on active amorphous iridium oxo-hydroxides.<sup>(45, 46)</sup> In contrast, crystalline rutile  $\text{IrO}_2$ , which presents poor activity for OER, is formed entirely of Ir(IV) and  $\text{O}^{2-}$  sites. According to DFT calculations performed by Pfeifer *et al.*,<sup>(47)</sup> Ir(III) and  $\text{O}^-$  sites are formed simultaneously. As illustrated in figure 1.6, in a perfectly ordered rutile  $\text{IrO}_2$  structure, formed by Ir(IV) and  $\text{O}^{2-}$ , an iridium vacancy would produce the conversion of adjacent  $\text{O}^{2-}$  oxygen atoms to  $\text{O}^-$  and the transfer of two electrons to the cationic framework, leading to the reduction of two adjacent Ir(IV) centres to Ir(III).<sup>(47)</sup> The presence of Ir(III)/Ir(IV) and  $\text{O}^-$  sites are normally detected on amorphous  $\text{IrO}_x$  catalysts, and thus amorphous  $\text{IrO}_x$  are associated with improved catalytic activity for OER compared to rutile  $\text{IrO}_2$ .

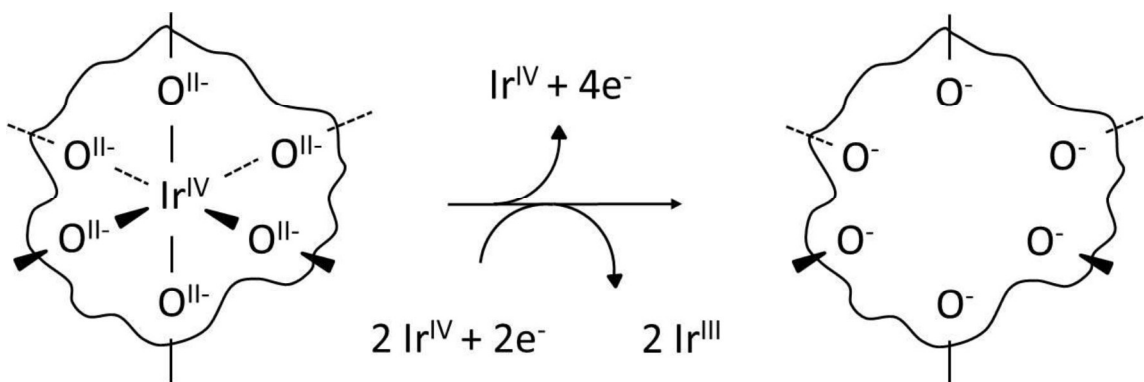


**Figure 1.6.** Schematic representation of  $\text{Ir}^{\text{III}}$  and  $\text{O}^-$  sites generated by an  $\text{Ir}^{\text{IV}}$  vacancy in the rutile  $\text{IrO}_2$  structure.<sup>(48)</sup>

### 1.3.2 Hollandite $\text{IrO}_2$ catalysts for OER.

As discussed in the previous section, crystalline rutile  $\text{IrO}_2$  performs poorly in terms of activity and stability compared to amorphous iridium oxo-hydroxides for the electrochemical OER reaction. For instance as reported by Pfeifer *et al.*,<sup>(47)</sup> at a current density of  $1 \text{ mA}\cdot\text{cm}^{-2}$ , commercial rutile  $\text{IrO}_2$  presented 240 mV higher overpotential compared to commercial amorphous  $\text{IrO}_2$ . A reason for the low activity of well-ordered rutile  $\text{IrO}_2$  catalysts is their thermodynamic stability, less prone to chemical or structural changes, necessary for the reaction to proceed.

Bestaoui *et al.*<sup>(49)</sup> reported that doping rutile  $\text{IrO}_2$  with potassium led to the crystalline phase transformation to hollandite  $\text{IrO}_2$ . The phase transformation from rutile to hollandite led to an increase in the catalytic activity for OER, as indicated by the rise in the current density from  $3.15 \text{ mA}\cdot\text{cm}^{-2}$  to  $10 \text{ mA}\cdot\text{cm}^{-2}$  at  $1.58 \text{ V}_{\text{RHE}}$ .<sup>(50)</sup> Both crystalline structures, rutile and hollandite, are made of  $\text{IrO}_6$  octahedral. Rutile  $\text{IrO}_2$  has a

tetragonal structure, where edge sharing  $\text{IrO}_6$  chains are connected to perpendicular-oriented  $\text{IrO}_6$  chains by sharing oxygen-corners positions (figure 1.7a); Hollandite  $\text{IrO}_2$  structure is monoclinic, where edge-sharing  $\text{IrO}_6$  pairs form chains connected by oxygen-corner-sharing positions, forming channels in which a dopant can be accommodated (figure 1.7b).

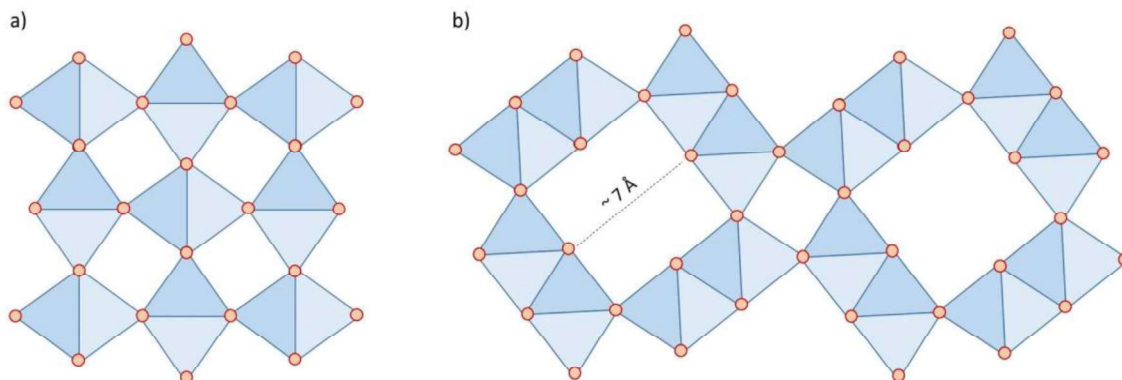


**Figure 1.7.** a) Rutile  $\text{IrO}_2$  and b) Hollandite  $\text{IrO}_2$  crystalline structures.<sup>(51)</sup>

The poor activity of rutile  $\text{IrO}_2$  compared to amorphous iridium oxo-hydroxide is associated with the absence of Ir(III) centres in the cationic framework. Improved activity observed for hollandite  $\text{IrO}_2$  compared to rutile  $\text{IrO}_2$  can be also associated to the formation of Ir(III) sites in the catalyst structure. The presence of Ir(III) centres were confirmed by XPS and XAS on  $\text{K}_{0.25}\text{IrO}_2$  hollandite.<sup>(50)</sup> XANES analysis revealed a distorted  $\text{IrO}_6$  octahedron with longer Ir-O and shorter Ir-Ir bond distances in the hollandite structure compared to rutile.<sup>(50)</sup> Compared to amorphous iridium oxo-hydroxides, were the Ir(III) and Ir(IV) sites are expected not to migrate within the catalyst, potassium can move throughout the hollandite channels, altering the cell parameters and modifying the oxidation state of iridium between Ir(III) and Ir(IV).<sup>(52)</sup> Channels of Iridium-based hollandite can accommodate other cations than potassium, as reported for  $\text{Rb}_{0.17}\text{IrO}_2$ .<sup>(53)</sup>  $\text{IrO}_2$  presents metal-like conductivity,<sup>(54)</sup> which is necessary to allow electron transfers between the electrode and the reaction media. The conductivity of  $\text{IrO}_2$  is not hampered by the incorporation of a cation to form the hollandite structure.<sup>(53)</sup>

More recently, two amorphous iridium oxo-hydroxides with different OER activity<sup>(34)</sup> were characterised by low electron dose HR-TEM.<sup>(51)</sup> On the catalyst with lower OER activity, only rigid rutile motifs were detected by HR-TEM; however, after doping with potassium the overpotential reduced by 60 mV at  $10 \text{ mA}\cdot\text{cm}^{-2}$ . On the K-doped catalyst, flexible hollandite motifs were detected by HR-TEM. Hence, the presence of hollandite motifs was related to the higher activity observed for the doped amorphous

$\text{IrO}_x$  catalyst. Hollandite  $\text{IrO}_2$  is not commonly employed as an OER catalyst, although it is reported to have activity comparable with amorphous iridium oxo-hydroxides. Cherevko *et al.*<sup>(55, 56)</sup> reported that amorphous  $\text{IrO}_x$  deactivates during the OER reaction by its progressive conversion to rutile  $\text{IrO}_2$ . Thus, as hollandite  $\text{IrO}_2$  is already crystalline, it could outperform amorphous  $\text{IrO}_x$  catalysts due to its greater stability.

### 1.3.3 Supported $\text{IrO}_2$ catalyst.

Iridium is one of the rarest and more expensive elements on Earth<sup>(57)</sup> and it is mainly obtained as a by-product from the mining of other precious metals such as Pt and Au. However,  $\text{IrO}_2$  is the only catalyst to perform OER under acid conditions. And therefore it is necessary to use it in the most efficient way possible. In literature, two routes for reducing the iridium loading on the electrode and increasing the iridium activity are proposed. The first approach is to synthesise  $\text{IrO}_2$  nanoparticles on a support. The second approach is to dilute  $\text{IrO}_2$  with a cheaper metal oxide (e.g., Ni or Cu).

Ideally the support for  $\text{IrO}_2$ -OER catalysts should have high surface area, to increase iridium dispersion; electrochemical stability against corrosion at potentials applied during OER in acid media; and also good conductivity to allow the flow of electrons from the electrode to the catalyst.

For example,  $\text{SnO}_2$ ,  $\text{TiO}_2$ ,  $\text{Ta}_2\text{O}_5$ ,  $\text{Nb}_2\text{O}_5$  or  $\text{Sb}_2\text{O}_5$  semiconductors were employed as support for  $\text{IrO}_2$  nanoparticles,<sup>(10)</sup> and although a good iridium dispersion with small  $\text{IrO}_2$  nanoparticles was achieved, the catalytic activity towards OER decreased as a result of the increase in the resistivity on the anode.<sup>(10)</sup> Moreover, high surface area carbon, commonly used in industrial catalytic processes (e.g., biomass conversion,<sup>(58)</sup> acetylene hydrochlorination,<sup>(59)</sup> purification of water, purification of oil in the petroleum refinery<sup>(60)</sup> and in fuel cells<sup>(61)</sup>) is excluded as a support for OER catalysts as a result of being unstable against anodic corrosion.<sup>(27, 32, 62)</sup>

Conductive titanium carbide ( $\text{TiC}$ ) has also been employed as support for  $\text{IrO}_2$  and tested for OER. The presence of  $\text{IrO}_2$  nanoparticles enhanced the electrocatalytic performance of an  $\text{IrO}_2/\text{TiC}$  catalyst compared to bulk  $\text{IrO}_2$ .<sup>(63, 64)</sup> However, a non-conductive  $\text{TiO}_2$  layer grew at the surface during reaction, leading to the catalyst passivation and eventually corrosion.<sup>(65)</sup> Tantalum carbide ( $\text{TaC}$ ) can be used as a support for  $\text{IrO}_2$  since it is stable against corrosion under OER reaction conditions,<sup>(66)</sup> however,  $\text{TaC}$  typically has very low surface area ( $\approx 3 \text{ m}^2 \cdot \text{g}^{-1}$ ). Other conductive

supports such as  $\text{Si}_3\text{N}_4$ , WB and  $\text{Mo}_2\text{B}_5$  have been employed to support  $\text{IrO}_2$  nanoparticles, however they lack stability under OER reaction conditions.<sup>(66)</sup>

Stoichiometric tin oxide ( $\text{SnO}_2$ ) is as an insulator with a band gap of 3.8 eV. However, when doped with low levels of antimony it behaves as a n-type semiconductor, with electric conductivity close to metals.<sup>(67)</sup> Antimony doped tin oxide (ATO) is the most employed support for  $\text{IrO}_2$  catalysts, due to its high stability towards corrosion during OER in acid media and its good electric conductivity.<sup>(68)</sup> Indium<sup>(69)</sup> and fluorine<sup>(70)</sup> have been used to increase the  $\text{SnO}_2$  conductivity; however, the use of antimony is preferred because of its higher stability against dissolution and its lower toxicity respectively.

Putiyapure *et al.*<sup>(68)</sup> compared bulk  $\text{IrO}_2$  with 60 wt. %  $\text{IrO}_2$ /ATO prepared by the Adams fusion method. At 1.8 V<sub>RHE</sub> the current density increased from 1341 mA·cm<sup>-2</sup> to 1625 mA·cm<sup>-2</sup> for the supported catalyst, which was associated to the synthesis of small  $\text{IrO}_2$  nanoparticles, with the concomitant increase in the  $\text{IrO}_2$  surface area. Liu *et al.*<sup>(71)</sup> with 50 wt. %  $\text{IrO}_2$  supported on nanowires or nanospheres ATO catalysts, prepared by the adams fusion method, showed an increase in the current density (at 1.7 V<sub>RHE</sub>) compared to bulk  $\text{IrO}_2$ , from 170 mA·cm<sup>-2</sup>·g<sub>Ir</sub><sup>-1</sup> to 270 mA·cm<sup>-2</sup> g<sub>Ir</sub><sup>-1</sup> and 410 mA·cm<sup>-2</sup> g<sub>Ir</sub><sup>-1</sup> respectively. In agreement with the Puthiyapura results, the increase in the catalytic activity towards OER was attributed to the higher  $\text{IrO}_2$  dispersion. Amorphous iridium oxo-hydroxides were prepared on ATO (30 wt.% Ir) by Massué *et al.*<sup>(36)</sup> following a hydrothermal synthesis, in agreement with previous reports, supporting  $\text{IrO}_2$  on ATO lead to enhanced activity compared to bulk  $\text{IrO}_2$ . In this study, the detrimental effect of annealing was also observed for the catalytic activity and stability for OER, which was correlated with the transformation of amorphous  $\text{IrO}_x$  to its crystalline oxide form.<sup>(36)</sup> For instance, at 350 mV overpotential, the current density for fresh  $\text{IrO}_2$ /ATO progressively decreased from 1.8 A·mg<sub>Ir</sub><sup>-1</sup> to 1.3 and 0.7 A·mg<sub>Ir</sub><sup>-1</sup> after annealing at 250 °C and at 350 °C respectively, indicating the degradation in the catalytic activity. The catalyst stability deteriorated as well with increasing the annealing temperature as observed by the degradation of the activity from 27 % to 80 % after chronopotentiometry (10 mA·cm<sup>-2</sup>, 2h).<sup>(36)</sup>

### 1.3.4 Mixed oxide catalyst.

As briefly mentioned before, RuO<sub>2</sub> is more active than IrO<sub>2</sub> towards OER, however, its use as catalyst is rare because of its high corrosion rate under reaction conditions. Nevertheless, RuO<sub>2</sub> is commonly used to enhance the IrO<sub>2</sub> catalytic activity.<sup>(72)</sup> Kötz and Stucki<sup>(73)</sup> prepared a series of IrO<sub>2</sub>-RuO<sub>2</sub> mixed oxide films covering the whole range of iridium concentration: from pure IrO<sub>2</sub> to pure RuO<sub>2</sub>. It was observed that doping RuO<sub>2</sub> with IrO<sub>2</sub> enhanced the catalyst stability against corrosion, whilst doping IrO<sub>2</sub> with RuO<sub>2</sub> enhanced the catalytic activity, this synergy effect was explained by the formation of a common electron band between IrO<sub>2</sub> and RuO<sub>2</sub>. However, Danilovic *et al.*<sup>(74)</sup> suggested that surface RuO<sub>2</sub> dissolves during OER reaction conditions, with the related formation of an IrO<sub>2</sub> shell that protected RuO<sub>2</sub> within the bulk against corrosion. Work undertaken by Kasian *et al.*<sup>(75)</sup> confirmed the hypothesis proposed by Danilovic. In this work, IrO<sub>2</sub>-RuO<sub>2</sub> were prepared and tested for OER, Ir and Ru dissolution were monitored by mass spectrometry (MS). Independently of the IrO<sub>2</sub>-RuO<sub>2</sub> mixed oxide composition, ruthenium dissolution was higher than iridium, hence it was assumed the dissolution of surface RuO<sub>2</sub> during reaction, leaving a more stable outer IrO<sub>2</sub> layer as proposed by Danilovic.<sup>(75)</sup> In general, it is agreed that the addition of RuO<sub>2</sub> into the IrO<sub>2</sub> lattice leads to an increase in the catalytic activity towards OER, but at the expense of the catalyst stability.<sup>(76-83)</sup>

The preparation of IrO<sub>2</sub>-SnO<sub>2</sub> mixed oxide catalysts has also been reported in the literature. De Pauli and Trasatti prepared IrO<sub>2</sub>-SnO<sub>2</sub> mixed oxide catalysts with a homogeneous metal distribution. A volcano plot was obtained when comparing the IrO<sub>2</sub> wt. % within the mixed oxide with the catalyst activity towards OER. The current density at 1.49 V<sub>RHE</sub> increased form 1.5 mA·cm<sup>-2</sup> for IrO<sub>2</sub> to 4.5 mA·cm<sup>-2</sup> for 40 wt. % IrO<sub>2</sub>-SnO<sub>2</sub>, the further addition of SnO<sub>2</sub> in the mixed oxide resulted in a decrease in the activity as a result of decreasing electric conductivity.<sup>(84)</sup> However, Marshall *et al.*<sup>(85)</sup> observed a different trend with increasing the SnO<sub>2</sub> concentration in the IrO<sub>2</sub>-SnO<sub>2</sub> mixed oxide catalyst, prepared with a homogeneous metal distribution by the polyol method. For example, at a current density of 1 mA·cm<sup>-2</sup>, the potential measured for IrO<sub>2</sub> was 1.49 V<sub>RHE</sub>, the potential increased progressively with increasing the SnO<sub>2</sub> composition to 1.57 V<sub>RHE</sub> for Ir<sub>0.2</sub>Sn<sub>0.8</sub>O<sub>2</sub>, which was attributed to the measured increased in the resistivity with increasing the SnO<sub>2</sub> concentration.<sup>(86)</sup> Thus, this indicated a linear decrease in activity with increasing the SnO<sub>2</sub> loading within the mixed oxide.

As discussed previously, the higher activity of amorphous  $\text{IrO}_x$  and hollandite  $\text{IrO}_2$  is assigned to the presence of both Ir(IV) and Ir(III) sites. On amorphous iridium oxohydroxides the formation of Ir(III) and electrophilic  $\text{O}^-$  sites are formed as a consequence of an Ir(IV) vacancy in the structure (48). On hollandite  $\text{IrO}_2$ , the presence of Ir(III) was assigned to the presence of a cationic dopant inside the hollandite channels.<sup>(52)</sup> To maintain the charge neutrality in the catalyst structure, substituting an Ir(IV) atom with a metal with a lower oxidation state (e.g.,  $\text{Ni}^{2+}$  or  $\text{Cu}^{2+}$ ) will induce the formation of Ir(III) site, electrophilic  $\text{O}^-$  species or oxygen vacancies in the structure.<sup>(87)</sup>

Additionally, as discussed previously a volcano plot was obtained after correlating the OER overpotential with the oxygen binding energy. According to this,  $\text{IrO}_2$  binds oxygen slightly too strongly, for the oxygenated intermediates to convert to molecular oxygen, accounting to the reaction overpotential.<sup>(23, 24)</sup> Thus, the reaction overpotential can be reduced by lowering  $\text{IrO}_2$  binding energy to oxygen. It has been reported that the binding energy of  $\text{IrO}_2$  weaken after doping with nickel<sup>(88, 89)</sup> or copper.<sup>(90)</sup> The weaker interaction of  $\text{IrO}_2$  after doping is explained by 5d orbital degeneration as shown in figure 1.8.

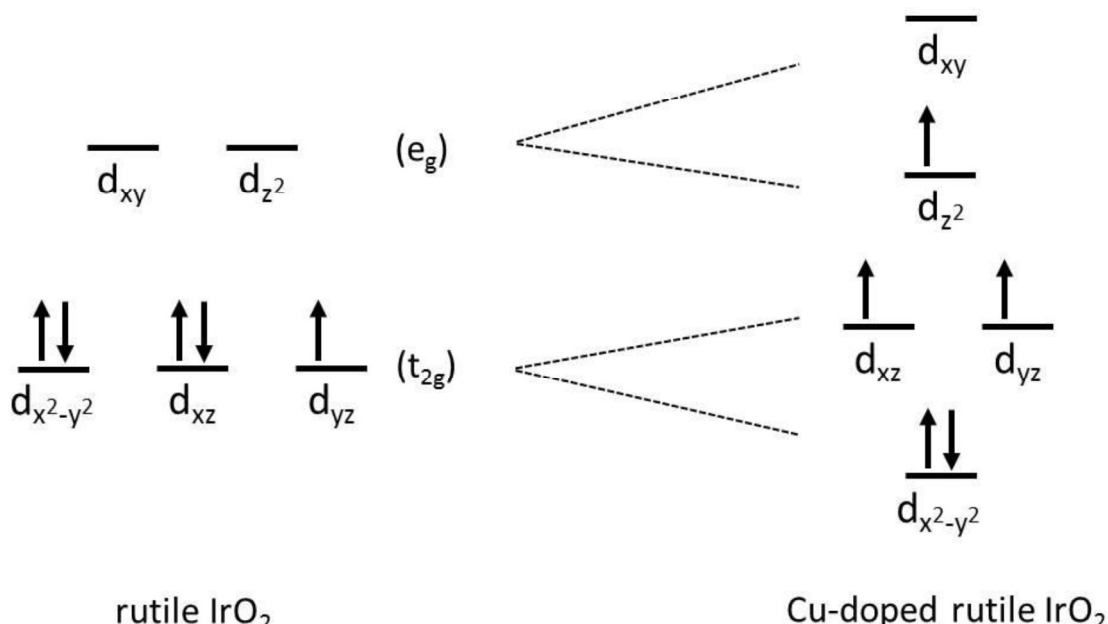


**Figure 1.8.** Rutile  $\text{IrO}_2$  bonding ( $t_{2g}$ ) and antibonding ( $e_g$ ) orbitals degeneration produced by Cu doping.<sup>(90)</sup>

$\text{Ir}_x\text{Ni}_{1-x}\text{O}_2$  mixed oxide catalysts were prepared by thermal decomposition by Xu *et al.*,<sup>(91)</sup> at low loading of nickel (up to 30 at %) a homogenous Ir and Ni distribution throughout the material was observed. The current density at 1.6 V<sub>RHE</sub> increased from

18 mA·cm<sup>-2</sup> for IrO<sub>2</sub> to 20 mA·cm<sup>-2</sup> for Ir<sub>0.7</sub>Ni<sub>0.3</sub>O<sub>2</sub>, showing improved activity. However, further increase in the Ni loading led to phase segregation, followed by a decrease in the catalytic activity.<sup>(91)</sup> Reier *et al.*<sup>(37)</sup> prepared Ir-Ni mixed oxide films by thermal decomposition, the current density of IrO<sub>2</sub> at 1.53 V<sub>RHE</sub> increased progressively from 1 mA·cm<sup>-2</sup> to 7 mA·cm<sup>-2</sup> for Ir<sub>0.21</sub>Ni<sub>0.79</sub>O<sub>2</sub>, indicating that catalytic activity of IrO<sub>2</sub> improved after doping with nickel. However, iridium dissolution increase linearly with increasing the concentration of nickel, thus compromising the catalyst stability.<sup>(37)</sup>

In general, nickel is not stable against dissolution during OER, hence nickel at the surface of the catalyst dissolves. As a result, more iridium sites are exposed to the reaction media, which translates in higher activity.<sup>(37, 92)</sup> However, high concentration of nickel compromises the overall catalyst stability.<sup>(37, 91-94)</sup>

Copper has also been used for the preparation of Ir<sub>x</sub>Cu<sub>1-x</sub>O<sub>2</sub> mixed oxide catalysts. Wang *et al.*<sup>(87)</sup> prepared Ir<sub>x</sub>Cu<sub>1-x</sub>O<sub>2</sub> colloids via hydrothermal treatment in aqueous alkaline media. The current density at 1.53 V<sub>RHE</sub> increased from 1.2 mA·cm<sup>-2</sup> from pure IrO<sub>2</sub> to 3.8 mA·cm<sup>-2</sup> for Ir<sub>0.89</sub>Cu<sub>0.11</sub>O<sub>2</sub> catalyst without impairing the catalytic stability, however, the further addition of Cu into the catalyst followed by a decrease in the activity and stability. Following a similar hydrothermal path, Sun *et al.*<sup>(90)</sup> prepared rutile Ir<sub>x</sub>Cu<sub>1-x</sub>O<sub>2</sub> catalysts. At 1.58 V<sub>RHE</sub> the current density of IrO<sub>2</sub> increased from 10 A·g<sub>cat</sub><sup>-1</sup> to 50 A·g<sub>cat</sub><sup>-1</sup> for Ir<sub>0.7</sub>Cu<sub>0.3</sub>O<sub>2</sub>. However, further addition of copper led to a decrease in the catalyst activity and stability.

Other transition metals, such as Sn,<sup>(84, 95)</sup> Ta,<sup>(95)</sup> Zn,<sup>(96)</sup> Fe<sup>(97)</sup> and Co,<sup>(88, 96)</sup> were employed for the synthesis of Ir-based mixed oxide catalysts with similar results to the reported for Ni and Cu. Generally, the dopant is not stable against dissolution, and thus, a high concentration of it can compromise the catalyst stability. However, at low concentration, its presence can improve the IrO<sub>2</sub> catalytic activity for OER. This can be explained by: The dopant dissolution at the surface of the catalyst which causes more Ir sites to be exposed to the reaction media;<sup>(37)</sup> an IrO<sub>2</sub> lattice strain caused by the difference in size between metal atoms;<sup>(88)</sup> and to the weaker binding between IrO<sub>2</sub> and the reaction oxygenated intermediates.<sup>(89)</sup>

#### **1.4 Hydrogen storage as conventional fuels.**

Hydrogen is an alternative energy vector to fossil fuels, its combustion leads to non-toxic exhaust emissions, it can be produced from water splitting using renewable energy and can be stored for long periods of time or transported in pipelines.<sup>(98)</sup> Hydrogen is also used in important chemical processes<sup>(99)</sup> and in the synthesis of

chemicals (ammonia and methanol) and polymers. Even though the use of hydrogen as the energy vector without further transformation seems ideal, it has some relevant drawbacks. The use of a gaseous energy carrier would require a technological transition from existent devices operating with liquid fuels. Moreover, hydrogen has a lower energy density per volume compared to conventional gasoline (8.4-10.4 kJ/L and 31.1 kJ/L respectively),<sup>(100)</sup> which would translate in to bulkier technology, limiting its application on mobile and small devices. Another concern about the direct use of hydrogen as a fuel relates to its safety when in contact with air. Once hydrogen is produced from renewable resources, through the use of non-carbon-related energy, such as solar or wind, it will need to be stored and or transported to the energy demand localisation.

Most of the current technology is based on liquid fuels, and hydrogen is difficult to liquefy from gas. To incorporate the H<sub>2</sub> produced from water splitting to the conventional fuel feed stock, it can be converted into liquid energy carriers such as NH<sub>3</sub> or CH<sub>3</sub>OH.<sup>(9)</sup> On one hand, the technology for synthesising ammonia from H<sub>2</sub> and N<sub>2</sub> at industrial scale, the Haber-Bosch process, has been extensively developed (400-450 °C, 200 atm, Fe-catalyst), with 500 million tons of NH<sub>3</sub> produced annually.<sup>(101)</sup> However, catalysts for the reverse reaction, NH<sub>3</sub> to H<sub>2</sub> and N<sub>2</sub>, still need to be developed to allow ammonia to be used as a fuel. The major controversy about using NH<sub>3</sub> as the energy carrier is its toxicity and its greater greenhouse effect compared to CO<sub>2</sub>.<sup>(9)</sup> On the other hand, methanol can be used as a fuel in current technology, and it can be synthesised via CO<sub>2</sub> hydrogenation. CO<sub>2</sub> is a non-toxic, non-flammable and non-corrosive gas. Ideally CO<sub>2</sub> would be obtained from the atmosphere, however, this process is challenging because of the low carbon dioxide concentration in air and the necessity to purify it from the other gases in the atmosphere. Nevertheless, CO<sub>2</sub> emissions from power stations and industrial process, such as in syngas or ammonia synthesis plants, can be easily captured. Thus, hydrogen in the form of methanol could be readily incorporated in the existing fuels feedstock.<sup>(9)</sup>

Methanol represents a commercial valuable commodity, with global productions of 57 million tons annually. It is used in the synthesis of relevant chemicals, such as in the synthesis of formaldehyde, acetic acid, methyl methacrylate, methylamines, ethylene and propylene or dimethyl carbonate.<sup>(102)</sup> Currently, the industrial production of methanol is performed over a CuO/ZnO/Al<sub>2</sub>O<sub>3</sub> catalyst (5-10 MPa, 250 °C - 300 °C). The primary feedstock is syngas, a mixture of CO and H<sub>2</sub>. CO is converted to CO<sub>2</sub> through the water gas shift (WGS) reaction (equation 1.22), and then CO<sub>2</sub> is transformed to methanol (equation 1.23). The overall reaction is illustrated in equation

1.24, although in order to favour the energy valance  $\text{CO}_2$  can be added up to 30 vol. % into the feedstock.<sup>(102, 103)</sup>



According to Le Chatelier's principle, methanol synthesis from CO or  $\text{CO}_2$  is favoured at low temperature and high pressure. Thermodynamically the direct  $\text{CO}_2$  hydrogenation to methanol (equation 1.23) is less favoured than the syngas route (equation 1.24). Thus, higher temperature is required for the direct  $\text{CO}_2$  hydrogenation to methanol. Counterproductively higher reaction temperature leads to the formation of CO via the reverse water was shift (RWGS) reaction (reverse reaction to WGS represented in equation 1.22).

Two possible  $\text{CO}_2$  hydrogenation mechanisms to  $\text{CH}_3\text{OH}$  over copper surfaces were elucidated by DFT calculations.<sup>(104)</sup> On both, the initial step is the dissociative adsorption of  $\text{H}_2$  and the non-dissociative adsorption of  $\text{CO}_2$  to form either a formate intermediate ( $\text{HCOO}$ ) or a hydrocarboxyl intermediate ( $\text{COOH}$ ) as it is shown in figure 1.9. Adsorbed formate or hydrocarboxyl are subsequently hydrogenated to adsorbed  $\text{HCOH}$  or  $\text{H}_2\text{CO}$  respectively and finally converted to adsorbed  $\text{H}_3\text{COH}$ .<sup>(104)</sup> Arguments supporting the formate and the hydrocarboxyl intermediate mechanism on copper catalysts are still under debate.<sup>(104)</sup> Behrens *et al.*<sup>(105)</sup> and Grabow *et al.*<sup>(106)</sup> suggested that the reaction proceeds through the most energetically favourable route, via the formate intermediate. Conversely, Zhao *et al.*<sup>(107)</sup> argued that the  $\text{HCOOH}$  intermediate proposed on the formate pathway would dissociate back to the formate, or desorb, suggesting that the reaction proceeds through the less energetically favoured hydrocarboxyl intermediate, which is stabilised by the presence of water formed during reaction. Even if the real reaction mechanism has not been verified, the activation energy barrier for the formate and the hydrocarboxyl route is lowered by the addition of Zn.<sup>(104)</sup>

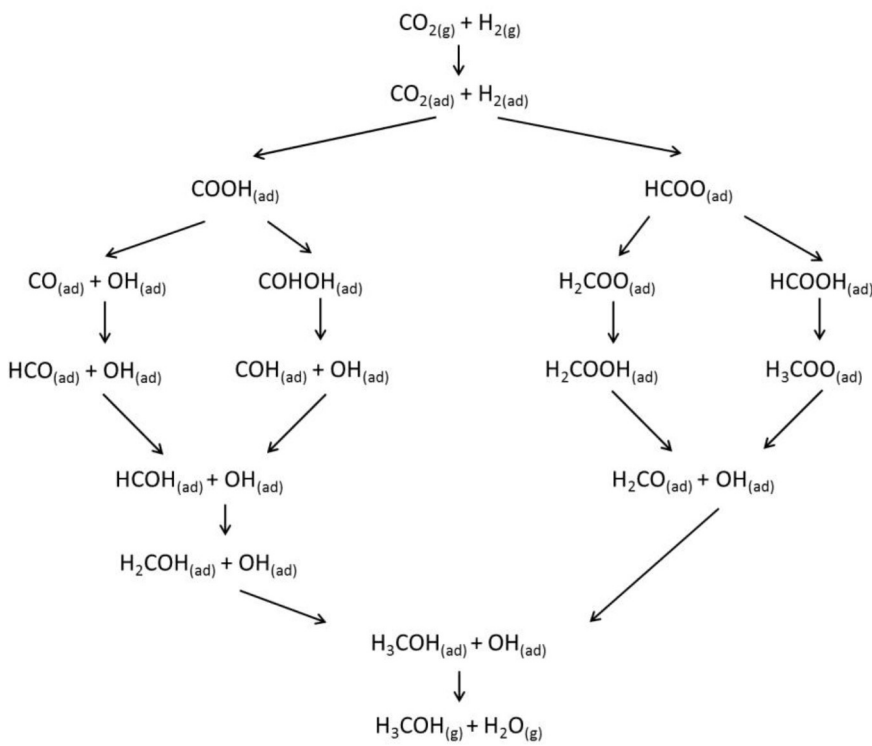


**Figure 1.9.** Schematic representation of the formate and hydrocarboxyl mechanisms for the direct  $\text{CO}_2$  hydrogenation to  $\text{CH}_3\text{OH}$ .<sup>(104)</sup>

Most of the research for the direct  $\text{CO}_2$  hydrogenation to  $\text{CH}_3\text{OH}$  is focused on Cu-based catalysts.<sup>(108-110)</sup> In general, the catalytic activity is directly proportional to the copper surface area, although the nature of active sites remains under discussion.  $\text{ZnO}$  is also active for the  $\text{CO}_2$  hydrogenation and synergy is observed with copper, the addition of  $\text{ZnO}$  improves Cu dispersion and Cu stability against sintering.

#### 1.4.1 Palladium-Zinc alloy catalysts for the direct carbon dioxide hydrogenation to methanol.

Although Cu-based catalysts remain the focus of research for the direct  $\text{CO}_2$  hydrogenation to  $\text{CH}_3\text{OH}$ , the presence of water produced during the reaction (equation 1.23) leads to copper sintering, and eventually to the concomitant catalyst deactivation.<sup>(102, 111)</sup> To minimise catalyst deactivation, noble metal-based catalysts were developed.

Palladium is the most studied noble metal for the hydrogenation of  $\text{CO}_2$  to methanol. The challenge remains in controlling the selectivity towards methanol, and not to over-reduce  $\text{CO}_2$  to  $\text{CH}_4$  or promoting the RWGS reaction to  $\text{CO}$  (reverse reaction to equation 1.22). The support plays an important role in controlling the selectivity. Shen *et al.*<sup>(112)</sup> prepared 3 wt. % Pd catalysts supported on  $\text{Al}_2\text{O}_3$ ,  $\text{SiO}_2$ ,  $\text{TiO}_2$  and  $\text{ZrO}_2$  via

deposition-precipitation method and assessed them towards the CO hydrogenation (20 bar, 250 °C). Over SiO<sub>2</sub> and ZrO<sub>2</sub> methanol was the main product, with 97 % and 84 % selectivity respectively, while DME and CH<sub>4</sub> selectivity reached 50 % over Al<sub>2</sub>O<sub>3</sub> and TiO<sub>2</sub> respectively.<sup>(112)</sup> Iwasa *et al.*<sup>(113)</sup> studied 10 wt. % Pd catalysts supported on ZnO, Ga<sub>2</sub>O<sub>3</sub>, In<sub>2</sub>O<sub>3</sub>, SiO<sub>2</sub>, MgO, CeO<sub>2</sub> and ZrO<sub>2</sub> and compared with a 45 wt. % Cu/ZnO towards the CO<sub>2</sub> hydrogenation (1 bar, 190 °C), catalytic data is summarised in table 1.1. Pd/SiO<sub>2</sub> and Pd/MgO showed no methanol productivity, with CO as the main product. Pd/CeO<sub>2</sub>, Pd/ZrO<sub>2</sub> and Pd/In<sub>2</sub>O<sub>3</sub> had low methanol selectivity, between 1-2 %, with CO remaining the main product. Pd/Ga<sub>2</sub>O<sub>3</sub> and Cu/ZnO showed 23 % and 30 % selectivity towards methanol, though the methanol productivity was one order of magnitude lower for the Pd/Ga<sub>2</sub>O<sub>3</sub> catalyst. The highest methanol selectivity (60 %), and with comparable methanol productivity to Cu/ZnO, was reported for the Pd/ZnO catalyst. An increase in methanol selectivity for the Pd/ZnO catalyst was observed with increasing pre-reduction temperature, which was attributed to the formation of PdZn alloy.<sup>(113)</sup>

**Table 1.1.** CO<sub>2</sub> hydrogenation over Pd-based catalysts (190 °C, 1 bar, CO<sub>2</sub>:H<sub>2</sub> 1:9). Catalyst were pre-reduced in 5% H<sub>2</sub>/N<sub>2</sub> (500 °C, 5 °C·min<sup>-1</sup>) prior to reaction.<sup>(113)</sup>

<b>Catalyst</b>	<b>Rate of formation / μmol·min<sup>-1</sup>·g<sup>-1</sup></b>			
	CH <sub>3</sub> OH	CO	CH <sub>4</sub>	CH <sub>3</sub> OH sel. / %
Pd/SiO <sub>2</sub>	0	0.52	0.09	0.00
Pd/MgO	0	2.05	0.07	0.00
Pd/CeO	0.11	9.90	0.16	1.08
Pd/ZrO <sub>2</sub>	0.22	13.2	0.06	1.65
Pd/In <sub>2</sub> O <sub>3</sub>	0.25	15.40	0.01	1.72
Pd/Ga <sub>2</sub> O <sub>3</sub>	0.17	0.61	0.01	23.3
Pd/ZnO	1.28	0.68	0.01	65.1
Cu/ZnO	1.74	3.96	0.00	30.4

Bahruji *et al.*<sup>(114)</sup> and Díez-Ramírez *et al.*<sup>(115)</sup> in separate studies of Pd/ZnO catalysts showed that the PdZn alloy acts as the active phase for methanol synthesis, whilst CO and CH<sub>4</sub> are formed over metallic Pd<sup>0</sup> sites.<sup>(116)</sup> Thus, pre-reduction prior to reaction is necessary to form the PdZn alloy phase. The PdZn alloy is formed by hydrogen spill over from metallic palladium to adjacent ZnO.<sup>(117, 118)</sup> Bahruji *et al.*<sup>(114)</sup> prepared a 5 wt % Pd/ZnO catalyst by sol immobilization. Increasing the pre-reduction temperature in hydrogen, from 150 °C to 400 °C, led to a progressive increase in the CO<sub>2</sub> conversion (20 bar, 250 °C) from 8.7 % to 10.7 % and enhanced methanol selectivity from 48 % to 60 %, attributed to the concomitant PdZn phase formation. Even though methanol selectivity increased with the pre-reduction temperature up to 700 °C, particle agglomeration observed above pre-reduction temperature at 400 °C had a detrimental effect on the catalytic activity.

The use of ZnO as a support for palladium favours formation of the active PdZn alloy phase. However, the poor surface area of ZnO (15 m<sup>2</sup>·g<sup>-1</sup>) compared to other supports could lead to particle agglomeration, reducing the number of surface active sites. One methodology to increase the surface area of the active phase is to form PdZn alloy nanoparticles on a high surface area support. Xu *et al.*<sup>(119)</sup> prepared Pd/ZnO/Al<sub>2</sub>O<sub>3</sub> and Pd/ZnO catalysts by co-precipitation and impregnation. When assessed for the direct CO<sub>2</sub> hydrogenation (180 °C, 30 bar, 69 vol % H<sub>2</sub>, 23 vol % CO<sub>2</sub>, 8 vol % N<sub>2</sub>), the addition of Al<sub>2</sub>O<sub>3</sub> led to an increase in the CO<sub>2</sub> conversion from 2.5 % to 2.9 % and the methanol selectivity from 72 % to 79 %. This was correlated with a better dispersion of the PdZn alloy. Xu *et al.*<sup>(119)</sup> also observed an increase in methanol selectivity with increasing pre-reduction temperature, which was correlated to a higher formation of PdZn alloy. Liang *et al.*<sup>(120)</sup> tested 16 wt. % Pd<sub>0.1</sub>Zn<sub>1</sub> supported on carbon nanotubes (CNTs), activated carbon (AC) and γ-Al<sub>2</sub>O<sub>3</sub> for the direct CO<sub>2</sub> hydrogenation (30 bar, 250 °C, 69 vol % H<sub>2</sub>, 23 vol % CO<sub>2</sub>, 8 vol % N<sub>2</sub>). All three catalysts presented methanol selectivity above 90 %. However, the higher CO<sub>2</sub> conversion observed when CNTs were used as the support (6.3 %) relative to AC or Al<sub>2</sub>O<sub>3</sub> (4.2 % and 3.6 % respectively) was attributed to the higher surface area, which led to smaller and better dispersed PdZn nanoparticles, and to the higher hydrogen adsorption capacity of the CNTs support.<sup>(120)</sup>

### **Research objectives.**

The present Thesis is divided in the development of two distinct catalytic systems, encompassing the overall process for producing fuels from renewable energy and water: from the production of hydrogen, to its conversion to methanol by reaction with CO<sub>2</sub>.

Chapter 3 to chapter 6 will focus on the optimisation of IrO<sub>2</sub> materials, for the preparation of electrodes used on OER in acid media, which can be used for the production of hydrogen in a PEM water electrolyser. The objectives of these chapters are as follow:

- Development of amorphous iridium oxo-hydroxide catalysts prepared through a hydrothermal synthesis method and an investigation into the role of various bases during this procedure.
- Study the effect of post-preparation heat treatment on the activity and stability of amorphous iridium oxo-hydroxide catalysts towards OER.
- Translation of the optimal preparation conditions (base and heat treatment) to develop a catalyst with lower iridium loading, by means of using a support or a secondary non-noble metal as a diluent.
- Study the metal arrangement in bimetallic systems for their activity and stability towards OER in acid media.

In chapter 7, PdZn alloy catalysts will be synthesised on TiO<sub>2</sub> and ZnTiO<sub>3</sub> following a chemical vapour impregnation and assessed towards the direct CO<sub>2</sub> hydrogenation to methanol, as a route to store hydrogen in the form of conventional liquid fuels. The aims of this chapter are presented below:

- To optimise the Pd to Zn metal ratio on PdZn alloy catalysts supported on TiO<sub>2</sub> prepared by chemical vapour impregnation, for the direct hydrogenation of CO<sub>2</sub> to methanol.
- To elucidate the temperature effect of pre-reduction treatment on the catalyst selectivity and activity.
- To correlate activity trends with the physicochemical properties of the catalyst.

## 1.5 Bibliography.

1. National Aeronautics and Space Administartion. [www.nasa.gov](http://www.nasa.gov), **2017**.
2. G. R. Bigg, *The Oceans and Climate*. Cambridge University Press, **2001**.
3. National Oceanic and Atmospheric Administartion. [www.research.noaa.gov](http://www.research.noaa.gov), **2019**.
4. D. Lüthi, M. Le Floch, B. Bereiter, T. Blunier, J. M. Barnola, U. Siegenthaler, D. Raynuad, J. Jouzel, H. Fischer, K. Kawamura, T. F. Stocker, High-resolution carbon dioxide concentration record 650,000-800,000 years before present, *Nature*, **2008**, 453, 379.
5. J. Rockstrom, W. Steffen, K Noone, A. Persson, F. S. Chapin, E. F. Lambin, T. M. Lenton, M. Scheffer, C. Folke, H.. J. Schellnhuber, B. Nykvist, C. A. Wit, T. Hughes, S. Leeuw, H. Rodhe, S. Sörlin, P. K. Snyder, R. Costanza, U. Svedin, M. Falkenmark, L. Karlberg, R. W. Corell, V. J. Fabry, J. Hansen, B. Walker, D. Liverman, K. Richardson, P. Crutzen, J. A. Foley, . A safe operating space for humanity, *Nature*, **2009**, 461 (7263), 472-475.
6. R. J. Nicholls, A. Cazenave, Sea-Level Rise and Its Impact on Coastal Zones, *Science*, **2010**, 328 (5985), 1517.
7. A. Costello, M. Abbas, A. Allen, S. Ball, S. Bell, R. Bellamy, S. Friel, N. Groce, A. Johnson, M. Kett, M. Lee, C. Levy, M. Maslin, D. McCoy, B. McGuire, H. Montgomery, D. Napier, C. Pagel, J. Patel, J. A. Puppim de Oliveira, N. Redclift, H. Rees, D. Rogger, J. Scott, J. Stephenson, J. Twigg, J. Wolff , C. Patterson, Managing the health effects of climate change: Lancet and University College London Institute for Global Health Commission, *The Lancet*, **2009**, 373 (9676), 1693-1733.
8. John Twidel TW. *Renewable Energy Resources*, Routledge, **2015**.
9. R. Schlögl, The Role of Chemistry in the Energy Challenge, *ChemSusChem*, **2010**, 3 (2), 209-222.
10. M. Carmo, D. L. Fritz, J. Mergel, D. Stolten, A comprehensive review on PEM water electrolysis, *International Journal of Hydrogen Energy*, **2013**, 38 (12), 4901-4934.
11. P. Millet, R. Ngameni, S. A. Grigoriev, N. Mbemba, F. Brisset, A. Ranjbari, C. Etiévant, PEM water electrolyzers: From electrocatalysis to stack development, *International Journal of Hydrogen Energy*, **2010**, 35 (10), 5043-5052.
12. R. De Levie, The electrolysis of water, *Journal of Electroanalytical Chemistry*, **1999**, 476 (1), 92-93.
13. U. Babic, M. Suermann, F. N. Büchi, L. Gubler, T. J. Schmidt, Critical Review-Identifying Critical Gaps for Polymer Electrolyte Water Electrolysis Development, *Journal of The Electrochemical Society*, **2017**, 164 (4), 387-399.

14. A. Ursua, L. M. Gandia, P. Sanchis, Hydrogen Production From Water Electrolysis: Current Status and Future Trends, *Proceedings of the IEEE*, **2012**, 100 (2), 410-426.
15. D. M. F. Santos, C. A. C. Sequeira, J. L. Figueiredo, Hydrogen production by alkaline water electrolysis, *Química Nova*, **2013**, 36, 1176-1193.
16. Ø. Ulleberg, T. Nakken, A. Eté, The wind/hydrogen demonstration system at Utsira in Norway: Evaluation of system performance using operational data and updated hydrogen energy system modelling tools, *International Journal of Hydrogen Energy*, **2010**, 35 (5), 1841-1852.
17. M. I. Jamesh, X. Sun, Recent progress on earth abundant electrocatalysts for oxygen evolution reaction (OER) in alkaline medium to achieve efficient water splitting - A review, *Journal of Power Sources*, **2018**, 400, 31-68.
18. M. A. Laguna-Bercero, S. J. Skinner, J. A. Kilner, Performance of solid oxide electrolysis cells based on scandia stabilised zirconia, *Journal of Power Sources*, **2009**, 192 (1), 126-131.
19. M. Wang, Z. Wang, X. Gong, Z. Guo, The intensification technologies to water electrolysis for hydrogen production - A review, *Renewable and Sustainable Energy Reviews*, **2014**, 29, 573-588.
20. E. Fabbri, A. Habererder, K. Waltar, R. Kotz, T. J. Schmidt, Developments and perspectives of oxide-based catalysts for the oxygen evolution reaction, *Catalysis Science & Technology*, **2014**, 4 (11), 3800-3821.
21. Y. Matsumoto, E. Sato, Electrocatalytic properties of transition metal oxides for oxygen evolution reaction, *Materials Chemistry and Physics*, **1986**, 14 (5), 397-426.
22. H. Dau, C. Limberg, T. Reier, M. Risch, S. Roggan, P. Strasser, The Mechanism of Water Oxidation: From Electrolysis via Homogeneous to Biological Catalysis, *ChemCatChem*, **2010**, 2 (7), 724-761.
23. S. Trasatti, Electrocatalysis by oxides - Attempt at a unifying approach, *Journal of Electroanalytical Chemistry and Interfacial Electrochemistry*, **1980**, 111 (1), 125-131.
24. I. C. Man, H. Y. Su, F. Calle-Vallejo, H. A. Hansen, J. I. Martínez, N. G. Inoglu, J. Kitchin, T. F. Jaramillo, J. K. Nørskov, J. Rossmeisl, Universality in Oxygen Evolution Electrocatalysis on Oxide Surfaces, *ChemCatChem*, **2011**, 3 (7), 1159-1165.
25. S. Fierro, T. Nagel, H. Baltruschat, C. Comninellis, Investigation of the oxygen evolution reaction on Ti/IrO<sub>2</sub> electrodes using isotope labelling and on-line mass spectrometry, *Electrochemistry Communications*, **2007**, 9 (8), 1969-1974.

26. R. Kötz, S. Stucki, D. Scherson, D. M. Kolb, In-situ identification of RuO<sub>4</sub> as the corrosion product during oxygen evolution on ruthenium in acid media, *Journal of Electroanalytical Chemistry and Interfacial Electrochemistry*, **1984**, 172 (1–2), 211-219.
27. T. Reier, M. Oezaslan, P. Strasser, Electrocatalytic Oxygen Evolution Reaction (OER) on Ru, Ir, and Pt Catalysts: A Comparative Study of Nanoparticles and Bulk Materials, *ACS Catalysis*, **2012**, 2 (8), 1765-1772.
28. R. Adams, R. L. Shriner, Platinum oxide as a catalyst in the reduction of organic compounds. Preparation and properties of the oxide of platinum obtained by the fusion of chloroplatinic acid with sodium nitrate, *Journal of the American Chemical Society*, **1923**, 45 (9), 2171-2179.
29. C. Felix, T. Maiyalagan, S. Pasapathi, B. Bladergroen, V. Linkov, Synthesis and optimization of IrO<sub>2</sub> electrocatalysts by Adams fusion method for solid polymer electrolyte electrolyzers., *Micro and nanosystems*, **2012**, 4, 186-191.
30. E. Rasten, G. Hagen, R. Tunold, Electrocatalysis in water electrolysis with solid polymer electrolyte, *Electrochimica Acta*, **2003**, 48 (25), 3945-3952.
31. E. Oakton, D. Lebedev, M. Povia, D. F. Abbott, E. Fabbri, A. Fedorov, M. Nachtegaal, C. Copéret, T. J. Schmidt, IrO<sub>2</sub>-TiO<sub>2</sub>: a High-Surface Area, Active and Stable Electrocatalyst for Oxygen Evolution Reaction, *ACS Catal*, **2017**, 7, 2346-2352.
32. Y. Lee, J. Suntivich, K. J. May, E. E. Perry, Y. Shao-Horn, Synthesis and Activities of Rutile IrO<sub>2</sub> and RuO<sub>2</sub> Nanoparticles for Oxygen Evolution in Acid and Alkaline Solutions, *The Journal of Physical Chemistry Letters*, **2012**, 3 (3), 399-404.
33. G. Li, H. Yu, W. Song, M. Dou, Y. Li, Z. Shao, B. Yi, A hard-template method for the preparation of IrO<sub>2</sub>, and its performance in a solid-polymer-electrolyte water electrolyzer, *ChemSusChem*, **2012**, 5 (5), 858-861.
34. C. Massué, X. Huang, A. Tarasov, C. Ranjan, S. Cap, R. Schlögl, Microwave Assisted Synthesis of Stable and Highly Active Ir-oxohydroxides for Electrochemical Oxidation of Water, *ChemSusChem*, **2017**, 10, 1958-1968.
35. Q. Wu, D. Xu, N. Xue, T. Liu, M. Xiang, P. Diao, Photo-catalyzed surface hydrolysis of iridium(III) ions on semiconductors: a facile method for the preparation of semiconductor/IrO<sub>x</sub> composite photoanodes toward oxygen evolution reaction, *Phys Chem Chem Phys*, **2017**, 19 (1), 145-154.
36. C. Massué, V. Pfeifer, X. Huang, J. Noack, A. Tarasov, S. Cap, R. Schlögl, High-performance supported Ir-oxohydroxide water oxidation electrocatalysts, *ChemSusChem*, **2017**, 10, 1943-1957.

37. T. Reier, Z. Pawolek, S. Cherevko, M. Bruns, T. Jones, D. Teschner, S. Selve, A. Bergmann, H. N. Nong, R. Schlögl, K. J. J. Mayrhofer, P. Strasser, Molecular Insight in Structure and Activity of Highly Efficient, Low-Ir Ir–Ni Oxide Catalysts for Electrochemical Water Splitting (OER), *Journal of the American Chemical Society*, **2015**, 137 (40), 13031-13040.
38. X. Yang, Y. Li, L. Deng, W. Li, Z. Ren, M. Yang, X. Yang, Y. Zhu, Synthesis and characterization of an  $\text{IrO}_2\text{-Fe}_2\text{O}_3$  electrocatalyst for the hydrogen evolution reaction in acidic water electrolysis, *RSC Adv*, **2017**, 7 (33), 20252-20258.
39. R. D. L. Smith, B. Sporinova, R. D. Fagan, S. Trudel, C. P. Berlinguet, Facile Photochemical Preparation of Amorphous Iridium Oxide Films for Water Oxidation Catalysis, *Chemistry of Materials*, **2014**, 26 (4), 1654-1659.
40. B. Johnson, F. Girgsdies, G. Weinberg, D. Rosenthal, A. Knop-Gericke, R. Schlögl, Suitability of Simplified  $(\text{Ir},\text{Ti})\text{O}_x$  Films for Characterization during Electrocatalytic Oxygen Evolution Reaction, *The Journal of Physical Chemistry C*, **2013**, 117 (48), 25443-25450.
41. T. Reier, D. Teschner, T. Lunkenbein, A. Bergmann, S. Selve, R. Krahnert, R. Schlögl, P. Strasser, Electrocatalytic Oxygen Evolution on Iridium Oxide: Uncovering Catalyst-Substrate Interactions and Active Iridium Oxide Species, *Journal of The Electrochemical Society*, **2014**, 161 (9), F876-F882.
42. M. Bernicke, E. Ortel, T. Reier, A. Bergmann, J. Ferreira de Araujo, P. Strasser, R. Krahnert, Iridium Oxide Coatings with Tempered Porosity as Highly Active Oxygen Evolution Catalysts: Structure-Activity Relationships, *ChemSusChem*, **2015**, 8 (11), 1908-1915.
43. M. Zhang, M. de Respinis, H. Frei, Time-resolved observations of water oxidation intermediates on a cobalt oxide nanoparticle catalyst, *Nature Chemistry*, **2014**, 6, 362.
44. Y. Gao, T. Åkermark, J. Liu, L. Sun, B. Åkermark, Nucleophilic Attack of Hydroxide on a Mn(V) Oxo Complex: A Model of the O-O Bond Formation in the Oxygen Evolving Complex of Photosystem II, *Journal of the American Chemical Society*, **2009**, 131 (25), 8726-8727.
45. V. Pfeifer, T. E. Jones, S. Wrabetz, C. Massué, J. J. Velasco Velez, R. Arrigo R, M. Scherzer, S. Piccinin, M. Hävecker, A. Knop-Gericke, R. Schlögl, Reactive oxygen species in iridium-based OER catalysts, *Chemical Science*, **2016**, 7 (11), 6791-6795.

46. V. Pfeifer, T. E. Jones, J. J. Velasco Velez, C. Massu  , M. T. Greiner, R. Arrigo, D. Teschner, F. Girgsdies, M. Scherzer, J. Allan, M. Hashagen, G. Weinberg, S. Piccinin, M. H  evecker, A. Knop-Gericke, R. Schl  gl, The electronic structure of iridium oxide electrodes active in water splitting, *Physical Chemistry Chemical Physics*, **2016**, 18 (4), 2292-2296.
47. V. Pfeifer, T. E. Jones, J. J. Velasco V  lez, C. Massu  , R. Arrigo, D. Teschner, F. Girgsdies, M. Scherzer, M. T. Greiner, J. Allan, M. Hashagen, G. Weinberg, S. Piccinin, M. H  evecker, A. Knop-Gericke, R. Schl  gla, The electronic structure of iridium and its oxides, *Surface and Interface Analysis*, **2016**, 48 (5), 261-273.
48. J. J. Velasco-V  lez, T. E. Jones, V. Streibel, M. H  evecker, C. H. Chuang, L. Frevel, M. Plodinec, A. Centeno, A. Zurutuza, R. Wang, R. Arrigo, R. Mom, S. Hofmann, R. Schl  gl, A. Knop-Gericke, Electrochemically active Ir NPs on graphene for OER in acidic aqueous electrolyte investigated by in situ and ex situ spectroscopies, *Surface Science*, **2019**, 681, 1-8.
49. N. Bestaoui, P. Deniard, R. Brec, Structural Study of a Hollandite-Type  $K_xIrO_2$ , *Journal of Solid State Chemistry*, **1995**, 118 (2), 372-377.
50. W. Sun, Y. Song, X. Q. Gong, L. Cao, J. Yang, Hollandite Structure  $K_{x=0.25}IrO_2$  Catalyst with Highly Efficient Oxygen Evolution Reaction, *ACS Applied Materials & Interfaces*, **2016**, 8 (1), 820-826.
51. E. Willinger, C. Massu  , R. Schl  gl, M. G. Willinger, Identifying Key Structural Features of  $IrO_x$  Water Splitting Catalysts, *Journal of the American Chemical Society*, **2017**, 139 (34), 12093-12101.
52. A. Talanov, W. A. Phelan, Z. A. Kelly, M. A. Siegler, T. M. McQueen, Control of the Iridium Oxidation State in the Hollandite Iridate Solid Solution  $K_{1-x}Ir_4O_8$ , *Inorganic Chemistry*, **2014**, 53 (9), 4500-4507
53. L. M. Schoop, J. W. Krizan, Q. D. Gibson, R. J. Cava, Structure and elementary properties of the new Ir hollandite  $Rb_{0.17}IrO_2$ , *Journal of Solid State Chemistry*, **2014**, 209, 37-41.
54. S. Trasatti, G. Buzzanca, Ruthenium dioxide: A new interesting electrode material. Solid state structure and electrochemical behaviour, *Journal of Electroanalytical Chemistry and Interfacial Electrochemistry*, **1971**, 29 (2), A1-A5.
55. S. Cherevko, S. Geiger, O. Kasian, A. Mingers, K. J. J. Mayrhofer, Oxygen evolution activity and stability of iridium in acidic media. Part 1. Metallic iridium, *Journal of Electroanalytical Chemistry*, **2016**, 773, 69-78.

56. S. Cherevko, S. Geiger, O. Kasian, A. Mingers, K. J. J. Mayrhofer, Oxygen evolution activity and stability of iridium in acidic media. Part 2. Electrochemically grown hydrous iridium oxide, *Journal of Electroanalytical Chemistry*, **2016**, 774, 102-110.
  57. P. C. K. Vesborg, T. F. Jaramillo, Addressing the terawatt challenge: scalability in the supply of chemical elements for renewable energy, *RSC Advances*, **2012**, 2 (21), 7933-7947.
  58. E. Lam, J. H. T. Luong, Carbon Materials as Catalyst Supports and Catalysts in the Transformation of Biomass to Fuels and Chemicals, *ACS Catalysis*, **2014**, 4 (10), 3393-3410.
  59. G. Malta, S. F. Freakley, S. A. Kondrat, G. J. Hutchings, Acetylene hydrochlorination using Au/carbon: a journey towards single site catalysis, *Chemical Communications*, **2017**, 53 (86), 11733-11746.
  60. Calgon carbon. [www.calgoncarbon.com](http://www.calgoncarbon.com), **2019**.
  61. A. L. Dicks, The role of carbon in fuel cells, *Journal of Power Sources*, **2006**, 156 (2), 128-141.
  62. F. Maillard, A. Bonnefont, F. Micoud, An EC-FTIR study on the catalytic role of Pt in carbon corrosion, *Electrochemistry Communications*, **2011**, 13 (10), 1109-1111.
  63. L. Ma, S. Sui, Y. Zhai, Preparation and characterization of Ir/TiC catalyst for oxygen evolution, *Journal of Power Sources*, **2008**, 177 (2), 470-477.
  64. S. Sheng, M. Lirong, Z. Yuchun, Investigation on the proton exchange membrane water electrolyzer using supported anode catalyst, *Asia-Pacific Journal of Chemical Engineering*, **2009**, 4 (1), 8-11.
  65. R. D. Cowling, H. E. Hintermann, The Corrosion of Titanium Carbide, *Journal of The Electrochemical Society*, **1970**, 117 (11), 1447-1449.
  66. J. Polonský, I. M. Petrushina, E. Christensen, K. Bouzek, C. B. Prag, J. E. T. Andersen, N. J. Bjerrum, Tantalum carbide as a novel support material for anode electrocatalysts in polymer electrolyte membrane water electrolyzers, *International Journal of Hydrogen Energy*, **2012**, 37 (3), 2173-2181.
  67. T. Nütz, U. Felde, M. Haase, Wet-chemical synthesis of doped nanoparticles: Blue-colored colloids of n-doped SnO<sub>2</sub>:Sb, *The Journal of Chemical Physics*, **1999**, 110 (24), 12142-12150.
  68. V. K. Puthiyapura, M. Mamlouk, S. Pasupathi, B. G. Pollet, K. Scott, Physical and electrochemical evaluation of ATO supported IrO<sub>2</sub> catalyst for proton exchange membrane water electrolyser, *Journal of Power Sources*, **2014**, 269, 451-460.
-

69. S. Geiger, O. Kasian, A. M. Mingers, K. J. J. Mayrhofer, S. Cherevko, Stability limits of tin-based electrocatalyst supports, *Scientific Reports*, **2017**, 7 (1), 4595-4601.
70. A. N. Banerjee, S. Kundoo, P. Saha, K. K. Chattopadhyay, Synthesis and Characterization of Nano-Crystalline Fluorine-Doped Tin Oxide Thin Films by Sol-Gel Method, *Journal of Sol-Gel Science and Technology*, **2003**, 28 (1), 105-110.
71. G. Liu, J. Xu, Y. Wang, X. Wang, An oxygen evolution catalyst on an antimony doped tin oxide nanowire structured support for proton exchange membrane liquid water electrolysis, *Journal of Materials Chemistry A*, **2015**, 3 (41), 20791-20800.
72. F. I. Mattos-Costa, P. de Lima-Neto, S. A. S. Machado, L. A. Avaca, Characterisation of surfaces modified by sol-gel derived  $\text{Ru}_x\text{Ir}_{1-x}\text{O}_2$  coatings for oxygen evolution in acid medium, *Electrochimica Acta*, **1998**, 44 (8–9), 1515-1523.
73. R. Kötz, S. Stucki, Stabilization of  $\text{RuO}_2$  by  $\text{IrO}_2$  for anodic oxygen evolution in acid media, *Electrochimica Acta*, **1986**, 31 (10), 1311-1316.
74. N. Danilovic, R. Subbaraman, K. C. Chang, S. H. Chang, Y. Kang, J. Snyder, A. P. Paulikas, D. Strmcnik, Y. T. Kim, D. Myers, V. R. Stamenkovic, N. M. Markovic, Using Surface Segregation To Design Stable Ru-Ir Oxides for the Oxygen Evolution Reaction in Acidic Environments, *Angewandte Chemie*, **2014**, 126 (51), 14240-14245.
75. O. Kasian, S. Geiger, P. Stock, G. Polymeros, B. Breitbach, A. Savan, A. Ludwig, S. Cherevko, K. J. J. Mayrhofera, On the Origin of the Improved Ruthenium Stability in  $\text{RuO}_2\text{-IrO}_2$  Mixed Oxides, *Journal of The Electrochemical Society*, **2016**, 163 (11), 5.
76. J. Cheng, H. Zhang, G. Chen, Y. Zhang, Study of  $\text{Ir}_x\text{Ru}_{1-x}\text{O}_2$  oxides as anodic electrocatalysts for solid polymer electrolyte water electrolysis, *Electrochimica Acta*, **2009**, 54 (26), 6250-6256.
77. C. Angelinetta, S. Trasatti, L. D. Atanososka, R. T. Atanasoski, Surface properties of  $\text{RuO}_2 + \text{IrO}_2$  mixed oxide electrodes, *Journal of Electroanalytical Chemistry and Interfacial Electrochemistry*, **1986**, 214 (1-2), 535-546.
78. G. Li, H. Yu, W. Song, X. Wang, Y. Li, Z. Shao, B. Yi, Zeolite-templated  $\text{Ir}_x\text{Ru}_{1-x}\text{O}_2$  electrocatalysts for oxygen evolution reaction in solid polymer electrolyte water electrolyzers, *International Journal of Hydrogen Energy*, **2012**, 37 (22), 16786-16794.
79. E. Mayousse, F. Maillard, F. Fouada-Onana, O. Sicardy, N. Guillet, Synthesis and characterization of electrocatalysts for the oxygen evolution in PEM water electrolysis, *International Journal of Hydrogen Energy*, **2011**, 36 (17), 10474-10481.

80. N. Mamaca, E. Mayousse, S. Arrii-Clacens, T. W. Napporn, K. Servat, N. Guillet, K. B. Kokoh, Electrochemical activity of ruthenium and iridium based catalysts for oxygen evolution reaction, *Applied Catalysis B: Environmental*, **2012**, 111–112, 376-380.
81. T. Audichon, E. Mayousse, S. Morisset, C. Morais, C. Comminges, T. W. Napporn, K. B. Kokoh, Electroactivity of RuO<sub>2</sub>-IrO<sub>2</sub> mixed nanocatalysts toward the oxygen evolution reaction in a water electrolyzer supplied by a solar profile, *International Journal of Hydrogen Energy*, **2014**, 39 (30), 16785-16796.
82. T. Audichon, B. Guenot, S. Baranton, M. Cretin, C. Lamy, C. Coutanceau, Preparation and characterization of supported Ru<sub>x</sub>Ir<sub>(1-x)</sub>O<sub>2</sub> nano-oxides using a modified polyol synthesis assisted by microwave activation for energy storage applications, *Applied Catalysis B: Environmental*, **2017**, 200, 493-502.
83. M. Escudero-Escribano, A. F. Pedersen, E. A. Paoli, R. Frydendal, D. Friebel, P. Malacrida, J. Rossmeisl, I. E. L. Stephens, I. Chorkendorff, Importance of Surface IrO<sub>x</sub> in Stabilizing RuO<sub>2</sub> for Oxygen Evolution, *J Phys Chem B*, **2017**, 122, 947–955.
84. C. P. De Pauli, S. Trasatti, Composite materials for electrocatalysis of O<sub>2</sub> evolution: IrO<sub>2</sub>+SnO<sub>2</sub> in acid solution, *Journal of Electroanalytical Chemistry*, **2002**, 538-539, 145-151.
85. A. Marshall, B. Børresen, G. Hagen, M. Tsypkin, R. Tunold, Preparation and characterisation of nanocrystalline Ir<sub>x</sub>Sn<sub>1-x</sub>O<sub>2</sub> electrocatalytic powders, *Materials Chemistry and Physics*, **2005**, 94 (2), 226-232.
86. A. Marshall, B. Børresen, G. Hagen, M. Tsypkin, R. Tunold, Electrochemical characterisation of Ir<sub>x</sub>Sn<sub>1-x</sub>O<sub>2</sub> powders as oxygen evolution electrocatalysts, *Electrochimica Acta*, **2006**, 51 (15), 3161-3167.
87. C. Wang, R. B. Moghaddam, S. H. Bergens, Active, Simple Iridium-Copper Hydrous Oxide Electrocatalysts for Water Oxidation, *The Journal of Physical Chemistry C*, **2017**, 121 (10), 5480-5486.
88. W. Q. Zaman, Z. Wang, W. Sun, Z. Zhou, M. Tariq, L. Cao, X. Q. Gong, J. Yang, Ni-Co Codoping Breaks the Limitation of Single-Metal-Doped IrO<sub>2</sub> with Higher Oxygen Evolution Reaction Performance and Less Iridium, *ACS Energy Lett*, **2017**, Ahead of Print.
89. H. N. Nong, T. Reier, H. S. Oh, M. Gliech, P. Paciok, T. H. Thi Vu, D. Teschner, M. Heggen, V. Petkov, R. Schlögl, T. Jones, P. Strasser, A unique oxygen ligand environment facilitates water oxidation in hole-doped IrNiO<sub>x</sub> core-shell electrocatalysts, *Nature Catalysis*, **2018**, 1 (11), 841-851.

90. W. Sun, Y. Song, X. Q. Gong, L. M. Cao, J. Yang, An efficiently tuned d-orbital occupation of  $\text{IrO}_2$  by doping with Cu for enhancing the oxygen evolution reaction activity, *Chemical Science*, **2015**, 6 (8), 4993-4999.
  91. S. Xu, Y. Liu, J. Tong, W. Hu, Q. Xia, Iridium-nickel composite oxide catalysts for oxygen evolution reaction in acidic water electrolysis, *Russ J Electrochem*, **2016**, 52 (11), 1021-1031.
  92. A. Papaderakis, N. Pliatsikas, C. Prochaska, G. Vourlias, P. Patsalas, D. Tsiplakides, S. Balomenou, S. Sotiropoulos, Oxygen Evolution at  $\text{IrO}_2$  Shell-Ir-Ni Core Electrodes Prepared by Galvanic Replacement, *The Journal of Physical Chemistry C*, **2016**, 120 (36), 19995-20005.
  93. R. B. Moghaddam, C. Wang, J. B. Sorge, M. J. Brett, S. H. Bergens, Easily prepared, high activity Ir-Ni oxide catalysts for water oxidation, *Electrochemistry Communications*, **2015**, 60, 109-112.
  94. H. N. Nong, L. Gan, E. Willinger, D. Teschner, P. Strasser,  $\text{IrO}_x$  core-shell nanocatalysts for cost-and energy-efficient electrochemical water splitting, *Chemical Science*, **2014**, 5 (8), 2955-2963.
  95. C. Felix, T. Maiyalagan, S. Pasupathi, B. Bladergroen, V. Linkov, Synthesis, characterisation and evaluation of  $\text{IrO}_2$  based binary metal oxide electrocatalysts for oxygen evolution reaction, *Int J Electrochem Sci*, **2012**, 7 (12), 12064-12077.
  96. E. Kuznetsova, V. Petrykin, S. Sunde, P. Krtil, Selectivity of Nanocrystalline  $\text{IrO}_2$ -Based Catalysts in Parallel Chlorine and Oxygen Evolution, *Electrocatalysis*, **2015**, 6 (2), 198-210.
  97. L. Fu, P. Cai, G. Cheng, W. Luo, Colloidal synthesis of iridium-iron nanoparticles for electrocatalytic oxygen evolution, *Sustainable Energy & Fuels*, **2017**, 1 (5), 1199-1203.
  98. A. Midilli, M. Ay, I. Dincer, M. A. Rosen, On hydrogen and hydrogen energy strategies I: current status and needs, *Renewable and Sustainable Energy Reviews*, **2005**, 9 (3), 255-271.
  99. R. Ramachandran, R. K. Menon, An overview of industrial uses of hydrogen, *International Journal of Hydrogen Energy*, **1998**, 23 (7), 593-598.
  100. Energy efficiency and renewable energy. [www.energy.com](http://www.energy.com)
  101. J. W. Erisman, M. A. Sutton, J. Galloway, Z. Klimont, W. Winiwarter, How a century of ammonia synthesis changed the world, *Nature Geoscience*, **2008**, 1, 636.
-

102. S. G. Jadhav, P. D. Vaidya, B. M. Bhanage, J. B. Joshi, Catalytic carbon dioxide hydrogenation to methanol: A review of recent studies, *Chemical Engineering Research and Design*, **2014**, 92 (11), 2557-2567.
103. M. Aresta, A. Dibenedetto, Utilisation of CO<sub>2</sub> as a chemical feedstock: opportunities and challenges, *Dalton Transactions*, **2007**, (28), 2975-2992.
104. E. V. Kondratenko, G. Mul, J. Baltrusaitis, G. O. Larrazabal, J. Perez-Ramirez, Status and perspectives of CO<sub>2</sub> conversion into fuels and chemicals by catalytic, photocatalytic and electrocatalytic processes, *Energy & Environmental Science*, **2013**, 6 (11), 3112-3135.
105. M. Behrens, F. Studt, I. Kasatkin, S. Kühl, M. Hävecker, F. Abild-Pedersen, S. Zander, F. Girgsdies, P. Kurr, B. L. Kniep, M. Tovar, R. W. Fisher, J. N. Nørskov, R. Schlögl, The Active Site of Methanol Synthesis over Cu/ZnO/Al<sub>2</sub>O<sub>3</sub> Industrial Catalysts, *Science*, **2012**, 336 (6083), 893.
106. L. C. Grabow, M. Mavrikakis, Mechanism of Methanol Synthesis on Cu through CO<sub>2</sub> and CO Hydrogenation, *ACS Catalysis*, **2011**, 1 (4), 365-384.
107. Y. F. Zhao, Y. Yang, C. Mims, C. H. F. Peden, J. Li, D. Mei, Insight into methanol synthesis from CO<sub>2</sub> hydrogenation on Cu(111): Complex reaction network and the effects of H<sub>2</sub>O, *Journal of Catalysis*, **2011**, 281 (2), 199-211.
108. X. M. Liu, G. Q. Lu, Z. F. Yan, J. Beltramini, Recent Advances in Catalysts for Methanol Synthesis via Hydrogenation of CO and CO<sub>2</sub>, *Industrial & Engineering Chemistry Research*, **2003**, 42 (25), 6518-6530.
109. H. Yang, C. Zhang, P. Gao, H. Wang, X. Li, L. Zhong, W. Wie, Y. Sun, A review of the catalytic hydrogenation of carbon dioxide into value-added hydrocarbons, *Catalysis Science & Technology*, **2017**, 7 (20), 4580-4598.
110. S. Dang, H. Yang, P. Gao, H. Wang, X. Li, W. Wei, Y. Sun, A review of research progress on heterogeneous catalysts for methanol synthesis from carbon dioxide hydrogenation, *Catalysis Today*, **2019**, 330, 61-75.
111. J. Ma, N. Sun, X. Zhang, N. Zhao, F. Xiao, W. Wie, Y. Sun, A short review of catalysis for CO<sub>2</sub> conversion, *Catalysis Today*, **2009**, 148 (3), 221-231.
112. W. J. Shen, M. Okumura, Y. Matsumura, M. Haruta, The influence of the support on the activity and selectivity of Pd in CO hydrogenation, *Applied Catalysis A: General*, **2001**, 213 (2), 225-232.
113. N. Iwasa, H. Suzuki, M. Terashita, M. Arai, N. Takezawa, Methanol synthesis from CO<sub>2</sub> under atmospheric pressure over supported Pd catalysts, *Catalysis letters*, **2004**, 96 (1-2), 75-78.

114. H. Bahruji, M. Bowker, G. J. Hutchings, N. Dimitratos, P. Wells, E. Gibson, W. Jones, C. Brookes, D. J. Morgan, G. Lalev, Pd/ZnO catalysts for direct CO<sub>2</sub> hydrogenation to methanol, *Journal of Catalysis*, **2016**, 343, 133-146.
115. J. Díez-Ramírez, P. Sánchez, A. Rodríguez-Gómez, J. L. Valverde, F. Dorado, Carbon Nanofiber-Based Palladium/Zinc Catalysts for the Hydrogenation of Carbon Dioxide to Methanol at Atmospheric Pressure, *Industrial & Engineering Chemistry Research*, **2016**, 55 (12), 3556-3567.
116. X. Wang, H. Shi, J. H. Kwak, J. Szanyi, Mechanism of CO<sub>2</sub> Hydrogenation on Pd/Al<sub>2</sub>O<sub>3</sub> Catalysts: Kinetics and Transient DRIFTS-MS Studies, *ACS Catal*, **2015**, 5, 6337–6349.
117. C. T. Hong, C. T. Yeh, F. H. Yu, Effect of Reduction and Oxidation Treatments on Pd/ZnO Catalysts, *Applied Catalysis*, **1989**, 48 (2), 385-396.
118. P. Kast, M. Friedrich, F. Girgsdies, J. Kröhnert, D. Teschner, Lunkenbein T, M. Behren, R. Schlögl, Strong metal-support interaction and alloying in Pd/ZnO catalysts for CO oxidation, *Catalysis Today*, **2016**, 260, 21-31.
119. J. Xu, X. Su, X. Liu, X. Pan, G. Pei, Y. Huang, X. Wang, T. Zhang, H. Geng, Methanol synthesis from CO<sub>2</sub> and H<sub>2</sub> over Pd/ZnO/Al<sub>2</sub>O<sub>3</sub>: Catalyst structure dependence of methanol selectivity, *Appl Catal, A*, **2016**, 514, 51-59.
120. X. L. Liang, X. Dong, G. D. Lin, H. B. Zhang, Carbon nanotube-supported Pd-ZnO catalyst for hydrogenation of CO<sub>2</sub> to methanol, *Applied Catalysis B: Environmental*, **2009**, 88 (3–4), 315-322.

# Chapter 2

## Experimental

### 2.1 Reagents used.

The materials listed were used as received in the course of this research.

#### *Metal precursors*

Iridium chloride hydrate, IrCl<sub>3</sub> (99.9 %, Alfa Aesar)

Nickel chloride hexahydrate, NiCl<sub>2</sub>·6H<sub>2</sub>O (99.9 %, Sigma Aldrich)

Copper chloride, CuCl<sub>2</sub> (99.9 %, Sigma Aldrich)

Palladium acetylacetonate, Pd(acac)<sub>2</sub> (99 %, Sigma Aldrich)

Zinc acetylacetonate hydrate, Zn(acac)<sub>2</sub> (99 %, Sigma Aldrich)

Rutile IrO<sub>2</sub> (99.9 % metal basis, Sigma Aldrich)

IrO<sub>2</sub>·2H<sub>2</sub>O (99.99 % metal basis, Premion®, AlfaAesar)

#### *Bases*

Lithium carbonate, Li<sub>2</sub>CO<sub>3</sub> (> 99 %, Fisher Chemicals)

Lithium hydroxide, LiOH (> 98 %, Sigma Aldrich)

Sodium carbonate, Na<sub>2</sub>CO<sub>3</sub> (>99.5 %, Fisher Chemicals)

Sodium hydroxide, NaOH (99.59 %, Fisher Chemicals)

Potassium carbonate, K<sub>2</sub>CO<sub>3</sub> (> 99 %, Fisher Chemicals)

Potassium hydroxide, KOH (> 95 %, Fisher Chemicals)

Magnesium carbonate, MgCO<sub>3</sub> (> 40 % based on MgO, Sigma Aldrich)

Magnesium hydroxide, Mg(OH)<sub>2</sub> (> 98 %, Sigma Aldrich)

Calcium carbonate, CaCO<sub>3</sub> (99 %, Sigma Aldrich)

Calcium hydroxide, Ca(OH)<sub>2</sub> (> 98 %, Acros Organics)

*Supports*

Titanium (IV) oxide, TiO<sub>2</sub> (> 99.5 %, < 20 nm, P25 Aeroxide®, Sigma Aldrich)

Antimony doped tin oxide, Sb<sub>2</sub>O<sub>3</sub>-SnO (99.5 %, < 50 nm, Sigma Aldrich)

Zinc oxide, ZnO (80 % based on Zn, < 100 nm, Sigma Aldrich)

*Gases*

20 % CO<sub>2</sub> / 60 % H<sub>2</sub>/ 20 % N<sub>2</sub> (BOC gases)

5% H<sub>2</sub> / Ar (99.99 % BOC gases)

Carbon monoxide, CO (2900 ppm, 5550 ppm, 7200 ppm, 9500 ppm, 19050 ppm,  
99.99 % BOC gases)

Methane, CH<sub>4</sub> (99.99 % BOC gases)

Helium, He (99.99 % BOC gases)

*Other chemicals*

Perchloric acid, HClO<sub>4</sub> (70 % in water, Honeywell Fluka)

5% Perfluorinated resin solution (Nafion® solution, Sigma Aldrich)

Methanol, CH<sub>3</sub>OH (100 %, VWR Chemicals)

Ethanol, CH<sub>3</sub>CH<sub>2</sub>OH (100 %, VWR Chemicals)

## 2.2 Catalyst preparation.

### 2.2.1 Standard hydrothermal preparation of IrO<sub>2</sub> catalyst.

1 mmol of IrCl<sub>3</sub> hydrate (299 mg) and 8 mmol of base (591 mg of Li<sub>2</sub>CO<sub>3</sub>, 192 mg of LiOH, 848 mg of Na<sub>2</sub>CO<sub>3</sub>, 320 mg of NaOH, 1106 mg of K<sub>2</sub>CO<sub>3</sub> or 500 mg of KOH) were dissolved in 10 ml of deionised water and stirred for 16 h at room temperature in a 50 ml round bottom flask. A further 10 ml of deionised water was then added to the solution after this initial period followed by heating to reflux for 3 hours. A blue precipitate was observed which was recovered by filtration and washed with 2 L of hot deionised water.<sup>(1)</sup> Finally, the material was dried at room temperature inside a fumehood overnight.

For the preparation of homogeneously dispersed Ir<sub>x</sub>M<sub>1-x</sub>O<sub>2</sub> mixed oxide catalysts (M = Ni or Cu) the synthetic procedure is the same as described above. However, the desired amount of the metal precursors was added at the beginning maintaining the total metal precursor (IrCl<sub>3</sub> + MCl<sub>2</sub>) to 1 mmol / 10 ml.

### 2.2.2 Preparation of supported IrO<sub>2</sub>/ATO.

In order to prepare 670 mg of 27 wt. % Ir on ATO a modification of the previous methodology was followed. 1 mmol of IrCl<sub>3</sub> hydrate (299 mg) and 8 mmol of base (591 mg of Li<sub>2</sub>CO<sub>3</sub>, 848 mg of Na<sub>2</sub>CO<sub>3</sub> or 1106 mg of K<sub>2</sub>CO<sub>3</sub>) were dissolved in 10 ml of deionised water and stirred for 16 h at room temperature in a 50 ml round bottom flask. A further 10 ml of deionised water were added to the solution after this initial period. The ATO support (448 mg) was added slowly over the slurry for a period of 10 minutes. The solution was then heated to reflux for 3 hours. The material was recovered by filtration and washed with 2 L of hot deionised water. Finally, the material was dried at room temperature inside a fumehood overnight.

### 2.2.3 Preparation of bimetallic metal oxides with core-shell structure.

For the preparation of core shell Ir<sub>x</sub>M<sub>1-x</sub>O<sub>2</sub> mixed oxide catalysts (M = Ni or Cu) two precursors solutions were prepared separately before mixing. The total amount of metal precursors (IrCl<sub>3</sub> + MCl<sub>2</sub>) after the solutions were combined was 1 mmol. As an example, the preparation of Ir<sub>0.5</sub>Cu<sub>0.5</sub>O<sub>2</sub> core shell catalysts is described as follows. 0.5 mmol of IrCl<sub>3</sub> hydrate (149 mg) and 4 mmol of Li<sub>2</sub>CO<sub>3</sub> (295 mg) were dissolved in 10 ml of deionised water and stirred at room temperature for 16 hours. 0.5 mmol of CuCl<sub>2</sub> hydrate (84 mg) and 4 mmol of LiOH (96 mg) was dissolved in 10 ml of deionised water and stirred overnight at room temperature for 16 h in a second flask. The latter solution

was heated to 95 °C for 30 min before the  $\text{IrCl}_3$  solution was added drop-wise to the  $\text{CuCl}_2$  solution. After the addition, the  $\text{IrCl}_3$  flask was cleaned with 10 ml of deionised water and this was added to the reaction mixture drop-wise. The solution was heated to reflux for 1.5 h. A precipitate formed which was recovered by filtration and washed with 1 L of cold water and 1 L of hot water. Finally, it was dried in a fumehood overnight.

#### **2.2.4 Standard preparation of PdZn catalyst by Chemical Vapour Impregnation (CVI).**

In chapter 7, PdZn alloy catalysts prepared by CVI on  $\text{TiO}_2$  and  $\text{ZnTiO}_3$  with different palladium loadings and Pd:Zn molar ratios are described.<sup>(2,3)</sup>

The same preparation procedure was followed for the preparation of all catalysts, as an example the preparation of 3 g of 5 wt. % palladium, PdZn(1:5)/ $\text{TiO}_2$  catalyst is described as follows: 0.43 g of  $\text{Pd}(\text{acac})_2$  and 2.06 g of  $\text{Zn}(\text{acac})_2$  were weighed into a 8 cm high glass vial. The precursors were mixed by physical shaking until a homogeneous powder was observed. Then 2.39 g of  $\text{TiO}_2$  (P25) was added to the glass vial, the mixture was shaken until a homogeneous dispersion was observed. The blend was then transferred to a schlenk flask and heated to 145 °C under vacuum for 1 h. After impregnation, the material was annealed in static air (500 °C, 10 °C·min<sup>-1</sup>, 16 h) in a Carbolite Gero muffle furnace.

#### **2.2.5 Preparation of 5% Pd/ZnO catalyst by sol immobilisation.**

The following procedure for the preparation of 2 g of 5% Pd/ZnO catalyst by sol immobilisation was adapted from the literature.<sup>(4)</sup> 0.1673 g of  $\text{PdCl}_2$  was dissolved in 25 ml of water with two drops of concentrated HCl in a 50 ml beaker. Once the  $\text{PdCl}_2$  was fully dissolved it was transferred to a 2 L beaker and 1 L of deionised water was added to the beaker. A fresh solution of PVA (0.1 g in 10 ml of water) was prepared and under continuous stirring, 6.5 ml of the fresh PVA solution was added and stirred for 15 min. A fresh solution of  $\text{NaBH}_4$  (0.1134 g in 15 ml of water) was prepared. 12.69 ml of the fresh  $\text{NaBH}_4$  solution were added to the preparation beaker and the solution was stirred for a further 30 min. Then, the  $\text{ZnO}$  support (1.9 g) was added into the beaker followed by the addition of 2 drops of concentrated  $\text{H}_2\text{SO}_4$ . The solution was stirred for 2 hours before recovering the catalysts by filtration. The catalysts was washed with 2 L of deionised water and dried in static air (110 °C, 16 h).

## 2.2.6 Preparation of ZnTiO<sub>3</sub> phase by Chemical Vapour Impregnation (CVI).

For the preparation of 3 g of ZnTiO<sub>3</sub> 1.5 g of TiO<sub>2</sub> (P25) and 5.40 g of Zn(acac)<sub>2</sub> were weighed into a vial and mixed by physically shaking until a homogenous material was observed. Then it was transferred to a schlenk flask and heated to 145 °C under vacuum for 1 h. After impregnation, the material was annealed in static air (500 °C, 16 h) in a Carbolite Gero muffle furnace followed by reduction in 5% H<sub>2</sub>/Ar (650 °C, 5 °C·min<sup>-1</sup>, 3 h) in a carbolite tubular furnace.

## 2.3 Catalyst Testing.

### 2.3.1 Oxygen Evolution Reaction (flow cell and standard cell in beaker).

In order to prepare the catalyst ink, 5 mg of catalyst were re-dispersed in 1.23 mL of water, 1.23 mL of ethanol and 40 µl of nafion solution. The mixture was sonicated for 30 min in order to ensure the complete re-dispersion of the material. 10 µl of the catalyst ink was drop-casted onto the working electrode and dried under a N<sub>2</sub> flow for 30 min. The catalysts loading on the working electrode was 100 µg·cm<sup>-2</sup> in all cases unless otherwise stated.

IrO<sub>2</sub> catalysts described in chapter 3, chapter 4 and chapter 5 were tested in a flow cell reactor made of polyether ether ketone (PEEK) provided by the Max Planck Institute for Chemical Energy Conversion in Mülheim, Germany.<sup>(5)</sup> Mixed oxide catalysts described in chapter 6 were tested in a conventional 3-electrode set up inside a 50 mL beaker. In both cases, the counter electrode and the reference electrode was a coiled platinum wire (127 µm diameter, 99.99 %, Sigma Aldrich) and a calomel electrode [Cl<sup>-</sup>/Hg<sub>2</sub>Cl<sub>2</sub>/Hg/Pt] from IJ Cambria Scientific Ltd (model CHI-150). The glassy carbon working electrode used in the flow system was made by the workshop in the Max Planck Institute for Chemical Energy Conversion in Mülheim. It consisted of a glassy carbon tip of 0.196 cm<sup>2</sup> area, a copper spring coated with Au to connect the carbon tip with the potentiostat and coated first with a 0.2 mm silicon gasket to avoid electrolyte leaks and protected with an external PEEK case. The glassy carbon used in the conventional set-up in a beaker was commercially available from IJ Cambria Scientific Ltd (5 mm internal diameter). All measurements were performed on a Biologic SP-150 potentiostat. Potential values were presented against the reversible hydrogen electrode (RHE) and IR corrected. A 0.1 M aqueous solution of HClO<sub>4</sub> was used as the electrolyte at pH 1 during reaction.

A diagram of the flow cell used is shown in figure 2.1a. The electrolyte was degased with N<sub>2</sub> for 30 min prior to reaction. The electrolyte was pumped through the flow cell

using a Cole-Parmer Masterflex C/L single channel pump at  $1.2 \text{ ml}\cdot\text{min}^{-1}$ . Figure 2.1b shows the conventional 3-electrode set up. The solution was stirred using a X-shape stirrer bar at 750 rpm. In this set-up, no differences in the electrocatalytic measurements were observed with or without purging the electrolyte solution prior to reaction with  $\text{N}_2$  for 30 min. However, due to the different reactor design LSV and CP results in the conventional set-up were shifted approximately 100 mV towards higher overpotentials compared to the flow cell. Therefore, data comparison between reactors is not possible unless compared to a standard catalyst.

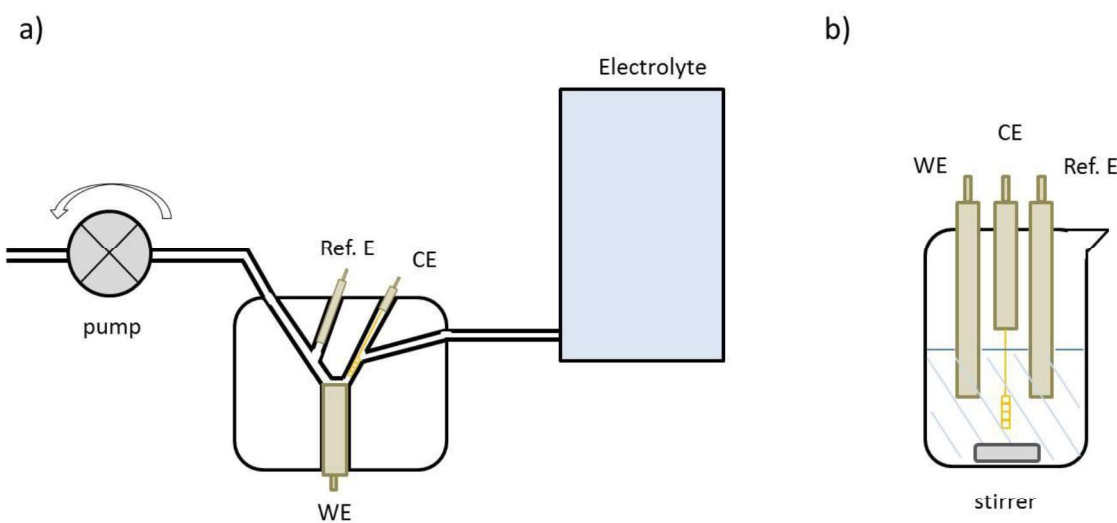


**Figure 2.1.** Schematic representation of the a) flow cell and b) conventional 3-electrode setup used for the electrochemical testing of  $\text{IrO}_2$  catalysts towards OER.

After reaction, the counter electrode and the reaction vessel (the flow cell or the beaker) were cleaned in boiling deionised water for 2 h. The working electrode was thoroughly polished with  $1.0 \mu\text{m}$  alumina powder on a nylon pad and then cleaned with excess water and then further washed twice in an ultrasonic bath with water to remove the remaining alumina. Then it was polished with  $0.05 \mu\text{m}$  alumina powder on a microcloth pad and washed again with excess deionised water. The remaining alumina was removed from the working electrode with water in the ultrasonic bath.

### 2.3.2 $\text{CO}_2$ hydrogenation.

A custom-built six-bed flow reactor was used for the analysis of the PdZn alloy catalysts towards the  $\text{CO}_2$  hydrogenation ( $250^\circ\text{C}$ , 20 bar,  $30 \text{ ml}\cdot\text{min}^{-1}$ , 60 %  $\text{H}_2$ , 20 %  $\text{CO}_2$ , 20 %  $\text{N}_2$ ). A representation of the reactor is shown in figure 2.2. Exhaust gas products were analysed online using a GC Agilent 7890 system fitted with a TCD and a FID detector, and an Agilent CP7557 column with He as the carrier gas. In order to avoid product condensation, post reactor lines and valves prior to the GC were

wrapped with heating tape and kept at 130 °C. A thermocouple introduced inside a thermowell placed inside the reactor tube allowed control of the temperature inside the catalyst bed. Simultaneously a reactor tube was always kept empty to measure the reaction blank activity.

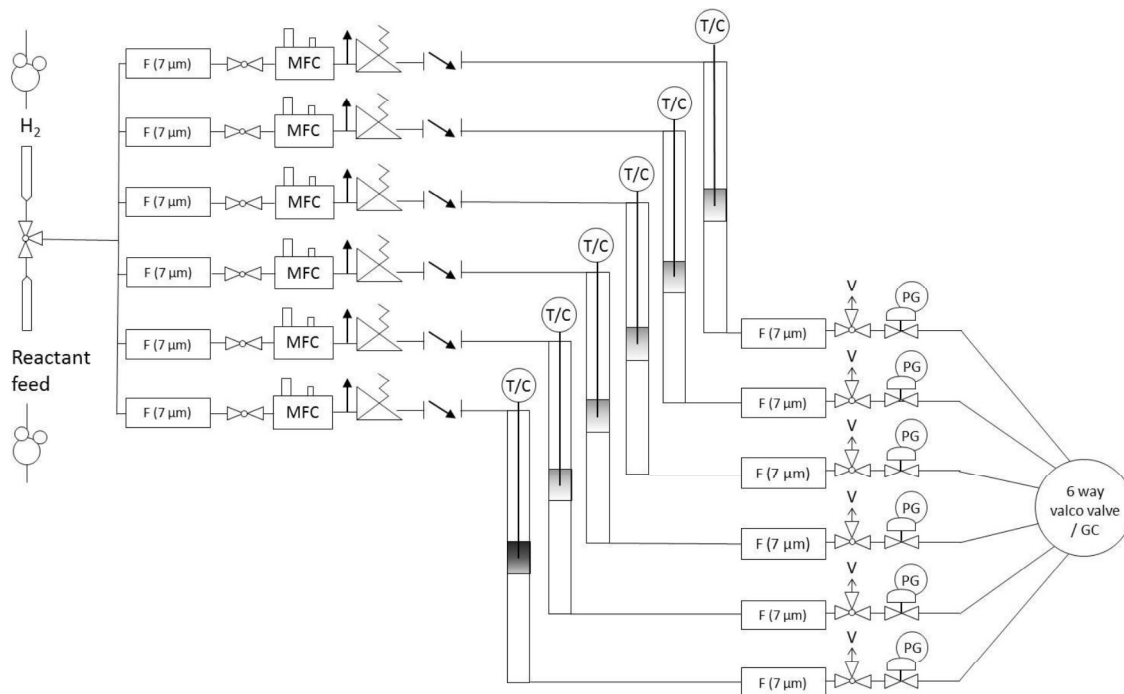


**Figure 2.2.** Schematic representation of the six-bed reactor used for the analysis of PdZn alloy catalysts towards the CO<sub>2</sub> hydrogenation. Diagram produced by Dr. Robert D. Armstrong, professional staff within Cardiff Catalysis Institute.

Prior to reaction, catalysts were pelleted (10 ton, 600–425 μm) and pre-reduced *in situ* in pure H<sub>2</sub> (400 °C, 30 ml·min<sup>-1</sup>, 1 h, 5 C·min<sup>-1</sup>). Catalysts were placed in the middle of the reactor tube (stainless steel, 0.5 cm x 50 cm), which coincided with the position of the thermowell, and held in place using quartz wool. Hydrocarbons produced during the reaction such as methanol or methane were detected using a flame ionisation detector (FID), while, non-hydrocarbon gases like CO, CO<sub>2</sub> and N<sub>2</sub> were analysed using a thermal conductivity detector (TCD). The GC program used to separate the different products was as follows. An initial temperature of 50 °C was maintained for 4 min followed by heating to 150 °C (10 °C·min<sup>-1</sup>, 10 min). After the run, the inlet was purged with helium for 2 min to avoid cross reactor contamination.

The methanol calibration was done by preparing standard dissolution of methanol in water. CO calibration was performed using standard CO/He cylinders with a known concentration from BOC. CO<sub>2</sub> and CH<sub>4</sub> calibrations were performed in an autoclave by mixing the desired gas with helium through the ideal gas law. Fresh methanol solutions

in water were prepared prior to calibration. Obtained calibrations with its respective response factors (rF) for CO<sub>2</sub>, CO, CH<sub>4</sub> and CH<sub>3</sub>OH are presented in figure 2.3.

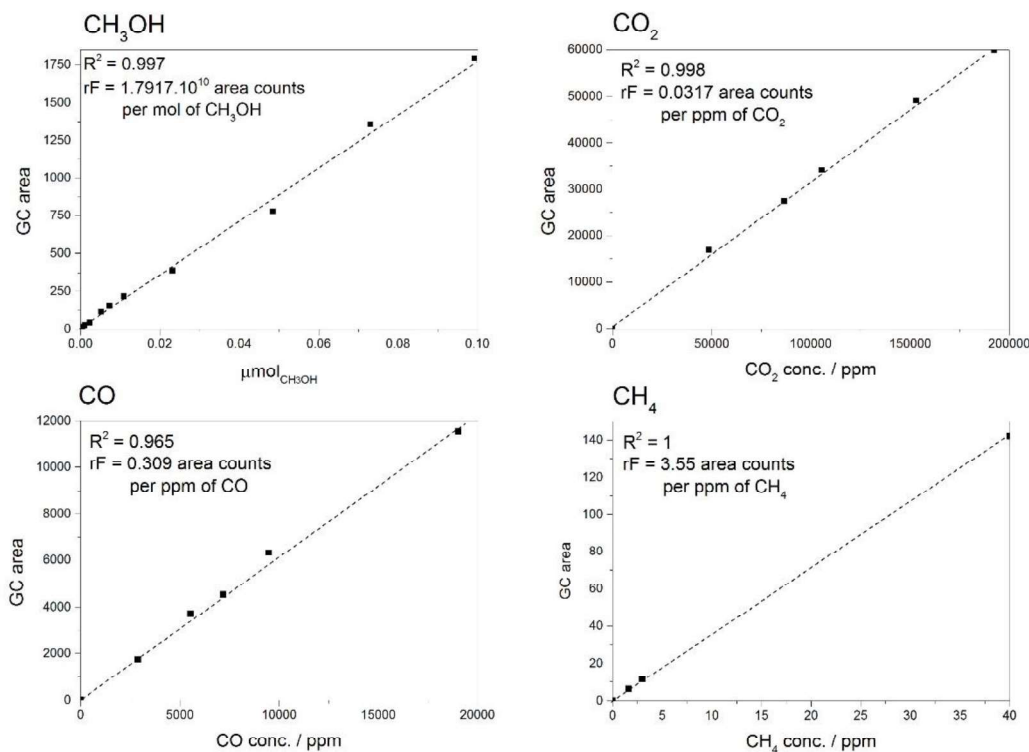


**Figure 2.3.** Calibrations performed by GC on the CO<sub>2</sub> hydrogenation products with its respective linear fitting and response factors.

The following calculations were used to determine the CO<sub>2</sub> conversion, the product selectivity and its productivities.

Through the ideal gas law (equation 2.1) were  $P$  is the pressure of the reaction mixture at the MFC (1 bar),  $R$  is the gas constant ( $83.15 \cdot 10^{-3} \text{ dm}^3 \cdot \text{bar} \cdot \text{K}^{-1} \cdot \text{mol}^{-1}$ ),  $T$  is the temperature (298.15 K) and  $V$  is the volume ( $0.03 \text{ dm}^3 \cdot \text{min}^{-1}$  obtained from the flow gas used during the reaction of  $30 \text{ ml} \cdot \text{min}^{-1}$ ) the total molar gas ( $n$ ) flow was calculated.

$$PV = nRT \quad n = 1.21 \cdot 10^{-3} \text{ CO}_2 \text{ mol} \cdot \text{min}^{-1} \quad \text{Eq. 2.1}$$

Nitrogen gas was used as internal standard at a concentration of 20 vol. %. The CO<sub>2</sub> conversion was calculated according to equation 2.2.

$$\text{CO}_2 \text{ conv. \%} = \frac{\left( \frac{(\text{Blank } \int \text{ CO}_2 / \text{area count}) - (\int \text{ CO}_2 / \text{area count})}{\text{Blank } \int \text{ N}_2 / \text{area counts}} \right)}{\left( \frac{\text{Blank } \int \text{ CO}_2 / \text{area count}}{\text{Blank } \int \text{ N}_2 / \text{area counts}} \right)} \times 100 \quad \text{Eq 2.2}$$

Because the number of moles in the gas phase change during the reaction, a compression factor (CF) is needed. This was obtained from equation 2.3.

$$CF = \frac{\int N_2 / \text{area counts}}{\text{Blank} \int N_2 / \text{area counts}} \quad \text{Eq 2.3}$$

The CO, CH<sub>4</sub> and CH<sub>3</sub>OH productivity were calculated according to the following equations 2.4 - 2.6, were *rF* is the response factor obtained from the respective calibrations. The moles of unreacted CO<sub>2</sub> were calculated through equation 2.7.

$$\text{CH}_3\text{OH mol}\cdot\text{min}^{-1} = \frac{\left( \left( \frac{\int \text{CH}_3\text{OH} / \text{area counts}}{rF \text{CH}_3\text{OH}} \right) \times \left( \frac{\text{total gas flow}/\text{ml min}^{-1}}{0.25 \text{ ml loop volume}} \right) \right)}{CF} \quad \text{Eq. 2.4}$$

$$\text{CH}_4 \text{ mol}\cdot\text{min}^{-1} = \frac{\frac{\int \text{CH}_4 / \text{area counts}}{rF \text{CH}_4} \times (\text{total gas flow} / \text{mol}\cdot\text{min}^{-1})}{CF} \quad \text{Eq. 2.5}$$

$$\text{CO mol}\cdot\text{min}^{-1} = \frac{\frac{\int \text{CO} / \text{area counts}}{rF \text{CO}} \times (\text{total gas flow} / \text{mol}\cdot\text{min}^{-1})}{CF} \quad \text{Eq. 2.6}$$

$$\text{Non-reacted CO}_2 \text{ mol}\cdot\text{min}^{-1} = \frac{\frac{\int \text{CO}_2 / \text{area counts}}{rF \text{CO}_2} \times (\text{total gas flow} / \text{mol}\cdot\text{min}^{-1})}{CF} \quad \text{Eq. 2.7}$$

The carbon balance (CB) can then be calculated from the sum of the productivities and the unreacted CO<sub>2</sub> divided by the molar flow concentration of CO<sub>2</sub> entering the reactor, which is 20 % from the total molar gas flow, according to the CO<sub>2</sub> concentration in the reaction mixture (equation 2.8).

$$CB \% = \left( \frac{(\text{productivities CH}_4 + \text{CH}_3\text{OH} + \text{CO}) + \text{unreacted CO}_2 / \text{mol min}^{-1}}{\text{molar flow rate CO}_2 / \text{mol min}^{-1}} \right) \times 100 \quad \text{Eq. 2.8}$$

The product selectivity was determined by dividing its productivity by the productivities of all the products. For instance, methanol selectivity was calculated following equation 2.9.

$$\text{CH}_3\text{OH sel. \%} = \left( \frac{\text{CH}_3\text{OH productivity} / \text{mol min}^{-1}}{\text{productivities CH}_4 + \text{CH}_3\text{OH} + 2\text{CH}_3\text{OCH}_3 + \text{CO}} \right) \times 100 \quad \text{Eq. 2.9}$$

Molar productivities obtained in mol·min<sup>-1</sup> could be normalised to the mass of catalysts used during the reaction (0.5 g) and expressed as mol·kg<sub>cat</sub><sup>-1</sup>·h<sup>-1</sup> according to equation 2.10 as shown for methanol.

$$\text{CH}_3\text{OH prod mol}\cdot\text{kg}_{\text{cat}}^{-1}\cdot\text{h}^{-1} = \left( \frac{\text{CH}_3\text{OH productivity} / \text{mol min}^{-1}}{(\text{catalyst mass g} / 1000)} \right) \times 60 \quad \text{Eq. 2.10}$$

## 2.4 Characterisation techniques.

### 2.4.1 Absorption spectroscopy techniques.

The study of the interaction of electromagnetic radiation with molecules or materials producing an energy transition between vibrational or electronic energy levels is known as absorption spectroscopy. As discussed below, the wavelength of radiation dictates its energy (figure 2.4), determining its interaction with matter.<sup>(6)</sup>

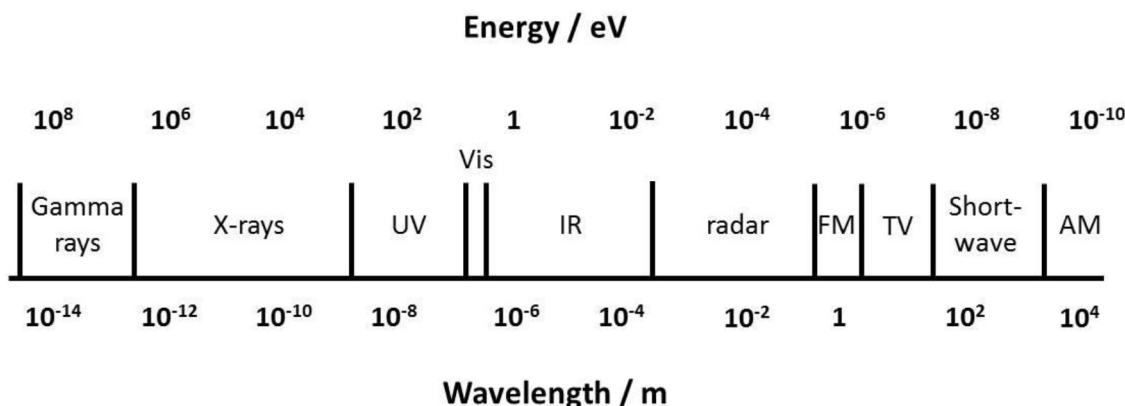


Figure 2.4. Energy and wavelength relationship of electromagnetic radiation.

#### 2.4.1.1 Ultraviolet - Visible Spectroscopy (UV-Vis).

This technique utilizes the interaction between electromagnetic radiation in the ultraviolet and visible region with matter. The absorption of radiation in this energy region is related to the molecular excitation of electronic states. Since a determined electronic transition is limited by the difference in energy between the different electronic states, it will occur only at determined wavelengths. All spectrophotometers are composed of a source of continuous radiation over the UV-Vis wavelength, the radiation wavelength is swept through the energy range using a monochromator (prisms, optical filters, diffraction gratings) and a detector.

To measure the UV-Vis spectra of a molecule in solution, the sample is placed in a cuvette made of a transparent material to UV-Vis radiation, glass or silica. Radiation going through the sample  $I$  is compared with a blank cuvette filled with the solvent  $I_0$  to determine its absorption  $A$  at a determined wavelength (equation 2.11).

$$A = -\log (I/I_0) \quad \text{Eq. 2.11}$$

According to the Beer-Lambert law (equation 2.12), the adsorption of radiation is proportional to the concentration of the active molecules in the UV-Vis region in

solution. Where  $\varepsilon$  is the extinction co-efficient or the molar absorption coefficient ( $\text{mol}^{-1}\cdot\text{cm}^{-1}$ ),  $l$  is the optical path length (cm) and  $c$  is the molar concentration ( $\text{mol}\cdot\text{L}^{-1}$ ).

$$A = \varepsilon \cdot c \cdot l \quad \text{Eq. 2.12}$$

UV-Vis spectroscopy was used to monitor the hydrothermal conversion of  $\text{IrCl}_3\cdot(\text{H}_2\text{O})_3$  precursor to  $\text{IrO}_x$  colloid synthesised with different bases. Reactions were carried out in a 50 mL 3-neck bottom flask with a reflux condenser attached at the top neck. The other two necks were sealed using a silicon septum to avoid solvent evaporation. Measurements were recorded on a Cary UV 60 Agilent Technologies Spectrophotometer by sampling a 0.1 mL aliquot with a needle and diluting it with 2 ml of deionised water.

#### 2.4.1.2 Fourier transform Infra-Red attenuated total reflectance (FT-IR ATR).

Atoms in a molecule are not in a static position but vibrate at determined frequencies. Specific functional groups vibrate at determined frequencies, these can be excited by IR radiation. This makes IR spectroscopy a useful technique in identifying specific functional groups in a material. In early spectrometers, the transmission was measured as the IR radiation was swept between two values, as it is done for UV-Vis measurements. However, modern spectrometers use a light source encompassing the full spectrum of wavelength instead of using monochromatic radiation, which enables spectra to be recorded faster. Since multiple wavelengths are analysed simultaneously, raw data needs to be processed using a Fourier Transform (FT). Attenuated total reflectance (ATR) is used to study the FT-IR absorption of solid materials.<sup>(7)</sup> An ATR crystal consists of a trapezoidal block made of IR transparent material (silver chloride, thallium halides or germanium). If the incident IR radiation angle is properly chosen, radiation will undergo total reflection (figure 2.5) several times before emerging at the other end of the ATR crystal. Sample information is obtained because radiation penetrates  $10^{-4}$  cm to  $10^{-3}$  cm into the sample at each reflection on the ATR crystal. This limits the radiation path length through the sample reducing strong signal attenuation commonly caused by solids.

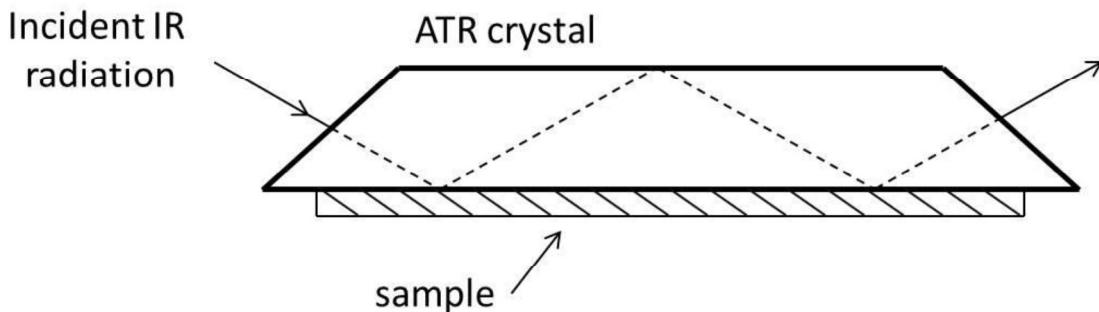


**Figure 2.5.** Schematic representation of an ATR crystal.

Only vibrational modes that cause a change in the electric dipole moment are active in IR, hence non-polar molecules such as N<sub>2</sub> are not active in IR.

FT-IR ATR was used to characterise the IrO<sub>2</sub>-base catalysts prepared through a hydrothermal process using different bases. Ir-OH vibration modes, O-H stretching and the presence of impurities such as carbonates were detected by this technique. Measurements were recorded on a Cary 6330 FTIR Agilent Technologies.

#### 2.4.1.3 Raman spectroscopy.

The use of an intense laser radiation in the visible light region can excite a molecule to a virtual vibrational state, with undefined energy, that leads to a transition state otherwise forbidden. As a result of relaxation, a photon is emitted, with a different wavelength than the incident photon by amounts equivalent to vibrational frequencies of the molecule. Only vibrational modes that correspond to a change in the polarizability of the molecule are active in Raman spectroscopy, and hence normally Raman is an IR complementary technique for molecules with a centre of symmetry, since modes active in one region are not in the other.

Due to the nature of Raman spectroscopy, the vibrational excitation to a virtual state corresponds to a forbidden transition, and hence, it is a rare transition giving a limited signal. To increase the frequency at what the transition occurs a high intensity laser is used, however, in order to collect the produced signal, the laser frequency needs to be filtered.

Raman spectroscopy was used to confirm the absence of rutile related adsorptions on amorphous iridium oxo-hydroxides, prepared through the hydrothermal methodology using different bases. Measurements were performed on a Renishaw InVia Raman Spectrometer using a 514 nm laser with 25 mW power and a beam diameter of 0.65

nm. Data acquisition was performed at 5 % laser intensity, 500 accumulations and 5 s of exposure time.

#### **2.4.1.4 X-ray photoelectron spectroscopy (XPS).**

Each element has a characteristic electron configuration. The strength of the bond between an electron and an atom is known as binding energy. Electrons can be excited by interaction with incident radiation to higher energy states. Excited electrons eventually return to the ground state. However, if the incident radiation has high enough energy, electrons can be exited into the continuum and leave the atom at a certain kinetic energy (equation 2.13). When an electron from an inner shell is ionised (primary electron), it leaves a hole behind. An electron from an outer shell relaxes to fill the hole, emitting energy equal to the difference between the energy states transition. If this released energy is greater than the ionisation energy of an outer shell electron, this secondary electron can leave the atom, known as Auger electron (figure 2.6).

$$E_K = h\nu - I \quad \text{Eq. 2.13}$$

Where  $E_K$  is the kinetic energy of the emitted electrons,  $I$  is the ionisation energy (or the binding energy) and  $h\nu$  is the energy of the incident radiation ( $h$  is the Planck's constant and  $\nu$  frequency of the incident radiation).

A monochromatic radiation source with known frequency, and hence known energy, is used in XPS to obtain the binding energy of materials.<sup>(8)</sup> Specific binding energies are characteristic of elements and vary depending on the atomic environment of the element. Hence, XPS is a powerful technique for determining elemental composition of a sample, including the presence of impurities, and gain information about the chemical environment. Ejected electrons need to leave the material to the vacuum chamber in order to be detected, electrons produced beyond a few nanometres are reabsorbed by adjacent atoms. Hence, XPS is a surface sensitive technique.

XPS measurements were performed on a Kratos Axis Ultra DLD XPS spectrometer equipped with an Al Ka X-ray source (300 W, 1486.3 eV). Data treatment was carried out using Casa XPS software.

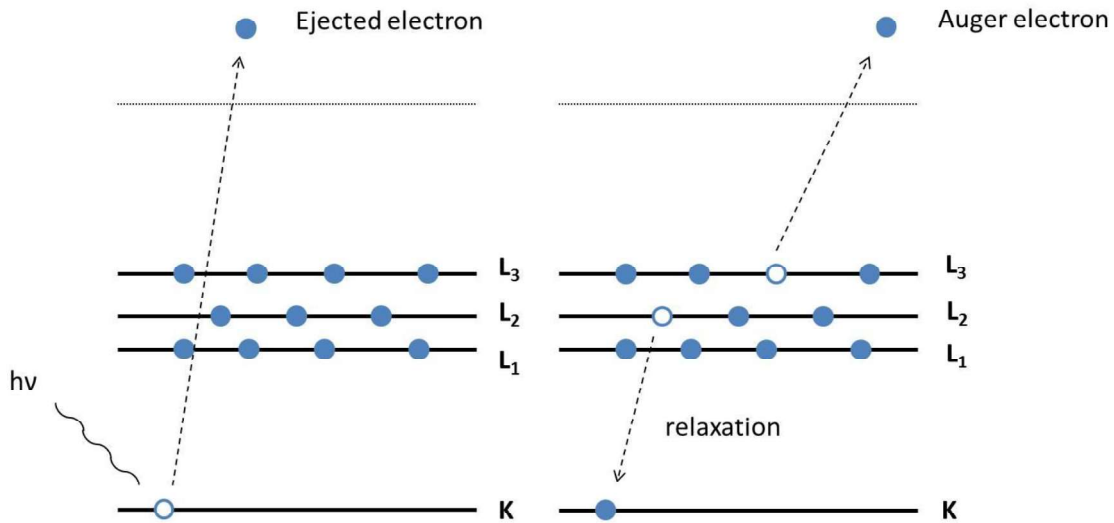


**Figure 2.6.** Schematic representation of the photoelectric effect and the relaxation process that lead to the ejection of an Auger electron.

#### 2.4.1.5 X-ray adsorption fine structure (XAFS).

X-ray adsorption fine structure (XAFS) consists on studying the absorption of monochromatic X-ray radiation with matter. The adsorption phenomenon is divided in two regions, each leading to different chemical information. On one hand, the region close to the absorption is known as x-ray near-edge spectroscopy (XANES). When an X-ray photon, with higher energy than the binding energy of a core-electron, collides with this core-electron it can be ejected into the continuum, with energy equal to the difference between the incident photon and the binding energy of the ejected electron. The binding energy of electrons is element specific and highly sensitive to its chemical environment. Hence, XANES is strongly sensitive in determining the oxidation state of a desired element. On the other hand, extended x-ray absorption fine-structure spectroscopy (EXAFS) focused on the interaction of the ejected electron with the neighbouring atoms. The ejected electron could be viewed as a spherical wave that scatters with surrounding atoms, altering its frequency, before returning to the origin of the adsorption (figure 2.7). Information from the number of neighbouring atoms, the distance between atoms and the disorder in the surrounding environment can be obtained from the complex data obtained from the diverse scattering processes taking place.<sup>(9)</sup>

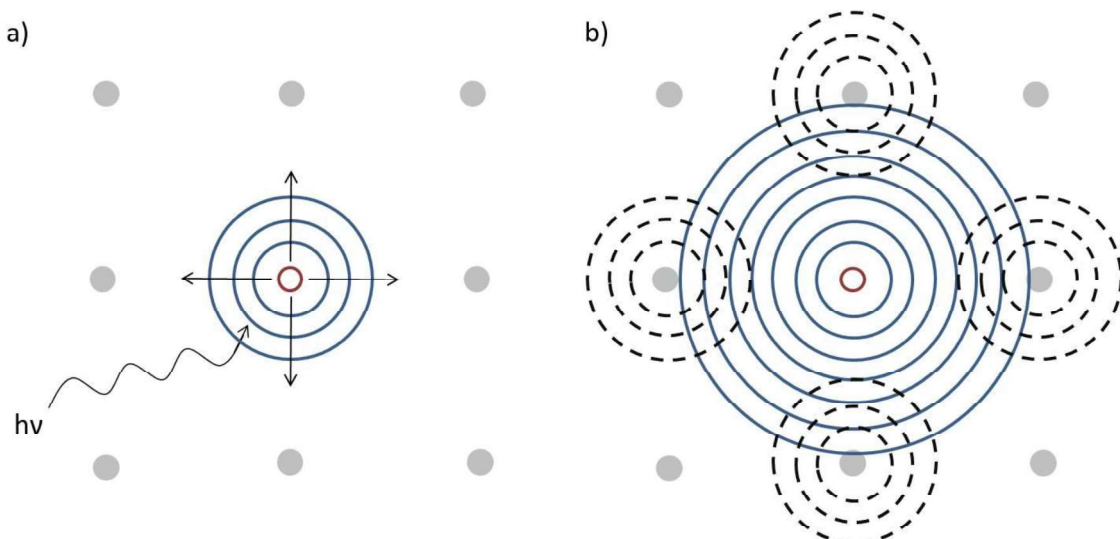


**Figure 2.7.** Schematic representation of EXAFS principles a) core-electron being ejected as a wave by an incident photon b) wave reflected by interaction with surrounding atoms.

Commercial standards (rutile  $\text{IrO}_2$  and amorphous  $\text{IrO}_2$ ) and synthesised amorphous  $\text{IrO}_2\text{-Li}_2\text{CO}_3$  and hollandite  $\text{IrO}_2$  were analysed at Diamond Light Source, B18 beam line. 9 mg of  $\text{IrO}_2$  catalyst (or 11 mg of  $\text{IrCl}_3$ ) were diluted with 100 mg of cellulose. The mixture was grinded thoroughly in a mortar until a uniform powder was obtained. After pressing the mixture with 15 ton, a 3 cm diameter pellet was obtained. Pellets were attached to the grid using a polyimide tape to reduce X-ray radiation adsorption. Because samples were concentrated, XAFS analyses were measured in transmittance.

#### 2.4.2 Powder X-ray Diffraction (XRD).

X-ray radiation can be scattered by electrons surrounding atoms. A periodic array of atoms, or scattering centres, separated by a distance similar to the wavelength of the incident radiation (around 100 pm) can produce diffraction. Hence, XRD is a useful technique to understand the crystallinity, ordered spatial arrangement of atoms in a material. Diffraction by atomic planes can be thought of as the reflection of light on two parallel adjacent surfaces separated by a distance  $d$  (figure 2.8), the angle  $\theta$  at which constructive interference occurs between waves of a  $\lambda$  wavelength is given by the Bragg equation (equation 2.14).

$$\lambda = 2 \cdot d \cdot \sin\theta \quad \text{Eq. 2.14}$$

Detected intensities depend on the crystal structure and the elemental composition of the material, localisation in the unit cell and electron density around the atom. Hence, a recorded diffraction pattern (angles and intensities) is representative of the structure of a material.<sup>(8)</sup> When X-ray radiation interacts with multiple crystallites with random

orientation the beam is diffracted in all possible directions, giving rise to a diffraction cone. In order to determine the  $\theta$  angle for each diffraction cone an X-ray detector moves around the sample, the intensity is then recorded as a function of the detector angle.

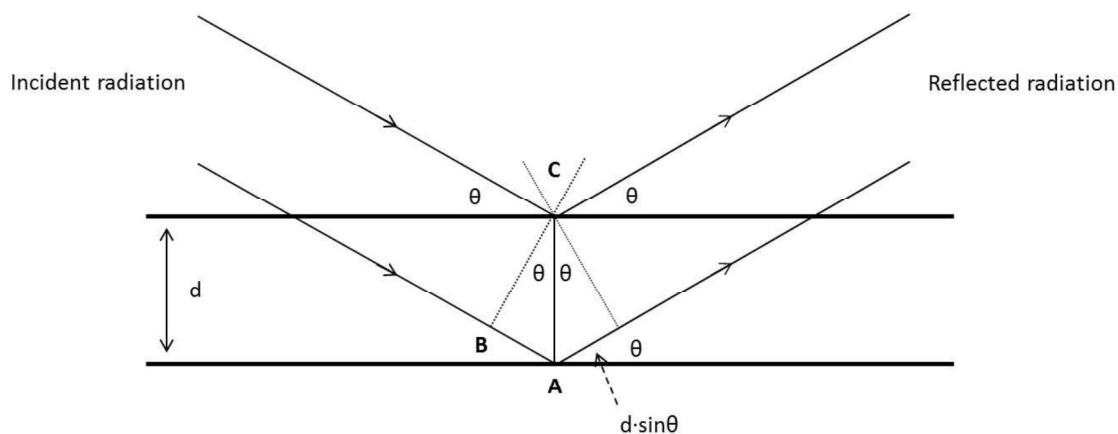


**Figure 2.8.** Schematic representation of the diffraction phenomenon that sets the basis for XRD.

Apart from obtaining an insight in the spatial rearrangement of atoms in a material, the crystallite size can be related with the reflections broadening through the Scherrer equation 2.15.

$$\tau = \frac{K\lambda}{\beta \cos\theta} \quad \text{Eq. 2.15}$$

Where  $\tau$  is the crystallite size,  $\beta$  the reflection broadening at half maximum intensity,  $\theta$  is the reflection position,  $\lambda$  is the X-ray radiation wavelength used and  $K$  is a constant that depends on the crystallite shape.

XRD patterns were recorded at room temperature on an X'PertPro Panalytical instrument fitted with a hemispherical analyser. The source of X-ray is a Cu K $\alpha$  (1.54 Å, 40 eV) with a Ni filter, calibrated against a Si standard. Data was treated using the X'pert HighScore software. *In situ* XRD were recorded on an X'PertPro Panalytical fitted with an Anton Parr heated stage. Annealing experiments were recorded on artificial air (70 % N<sub>2</sub>, 30 % O<sub>2</sub>), reduction treatments were performed on 5 % H<sub>2</sub>/N<sub>2</sub> by mixing both gases. Characteristic sets of  $d$  spacing obtained by XRD were used as a fingerprint to determine the crystalline structure of materials. The absence of diffractions is also useful information as indicates that materials are disordered. Due to the disordered nature of synthesised IrO<sub>x</sub> catalyst and the broad reflections of PdZn catalysts, as a results of small particle size, the Scherrer equation was used to

determine the catalyst support degradation and phase transformation. On chapter 7, for PdZn(1:5)/TiO<sub>2</sub> catalysts, the Scherrer equation was used to observe the rutile TiO<sub>2</sub> particle growth after reduction treatment at 650 °C and the phase transformation from TiO<sub>2</sub> to ZnTiO<sub>3</sub>.

#### 2.4.3 Surface area analysis by the Brunauer-Emmett-Teller (BET) theory.

According to Langmuir theorem, assuming that an adsorbate molecule does not alter the adsorption at neighbouring sites and that all adsorbing sites are equivalent, molecules adsorb on a surface forming a monolayer. Analogously studying the N<sub>2</sub> adsorption via weak Van der Waals bonds on a material it is possible to determine the materials surface area. A linear adsorption isotherm according to equation 2.16 can be obtained by admitting stepwise known amounts of nitrogen gas into the sample tube and measuring the pressure difference at equilibrium.

$$\frac{1}{V\left[\left(\frac{P_o}{P}\right) - 1\right]} = \frac{1}{V_m \cdot C} + \frac{(C - 1)}{V_m \cdot C} \cdot \frac{P}{P_o} \quad \text{Eq. 2.16}$$

Where  $P$  is the equilibrium pressure,  $P_o$  is the saturation pressure,  $V$  is the volume,  $V_m$  is the volume required to cover the surface in a monolayer and  $C$  is a constant. From the linear representation, calculating the slope and the y-axis intercept,  $V_m$  and  $C$  values can be obtained.

The total surface area,  $S_{tot}$ , and the specific surface area,  $S_{BET}$ , could be obtained through equations 2.17 and 2.18. Where  $N_A$  is the Avogadro's number,  $S$  is the N<sub>2</sub> cross section area,  $V$  is the molar volume of the adsorbate and  $m$  is the mass of the material.

$$S_{tot} = \frac{N_A \cdot S \cdot V_m}{V} \quad \text{Eq. 2.17}$$

$$S_{BET} = \frac{S_{tot}}{m} \quad \text{Eq. 2.18}$$

Specific surface area of IrO<sub>2</sub> catalysts were measured on a Micromeritics 3-flex. Prior to analysis the materials were annealed in static air in a furnace (130 °C, 20 h). Then were transferred to the BET bulb and dried under vacuum (130 °C, 16 h). Specific surface area of PdZn alloy catalysts were measured on a Quantachrome Nova 2200e, prior to analysis samples were dried under vacuum at 120 °C for 4 h. The BET analysis consisted of five data points at relative pressures ( $P/P_o$ ) of  $5 \cdot 10^{-2}$ ,  $1.125 \cdot 10^{-1}$ ,  $1.750 \cdot 10^{-1}$ ,  $2.375 \cdot 10^{-1}$ ,  $3.0 \cdot 10^{-1}$  respectively.

## 2.4.4 Thermal analysis.

### 2.4.4.1 Thermogravimetric analysis (TGA).

TGA consists of monitoring the weight change of a sample as the temperature is increased. Materials undergo chemical reactions such as decomposition, loss of water, crystallisation or oxidation upon heating processes. TGA could be coupled with different techniques to gain a deeper understanding of the reactions taking place. TGA-MS could be used to determine the products leaving a material on a specific reaction, for instance  $\text{H}_2\text{O}$  and  $\text{CO}_2$ . Analysed compounds by MS in conjunction with the variation in weight could be used for quantitative analysis and to determine the chemical composition. Another commonly coupled technique with TGA is Differential Scanning Calorimetry (TGA-DSC). In DSC the sample and an inert reference material are heated separately at the same rate. The difference in the power supply for keeping a constant temperature ramp would indicate if changes occurring in the sample are exothermic or endothermic reactions.<sup>(6)</sup>

TGA-MS-DSC measurements on  $\text{IrO}_2$  samples prepared through the hydrothermal process using different bases were performed on a Netzsch STA 449 thermoanalyser coupled to a QMS200 Omnistar mass spectrometer by Dr. Andrey Tarasov at the Fritz Haber Institute in Berlin, Germany. 25 mg of sample were analysed from 30 °C to 800 °C ( $10 \text{ }^{\circ}\text{C} \cdot \text{min}^{-1}$ ) in 21 %  $\text{O}_2/\text{Ar}$  ( $100 \text{ ml} \cdot \text{min}^{-1}$ ).

### 2.4.4.2 Temperature programed reduction ( $\text{H}_2\text{-TPR}$ ).

TPR is a useful technique for determining the reducibility of a material. Moreover, the quantity of reducing gas reacted could be quantified if the proper calibration of the signal is performed. Reducing profiles could be used as a fingerprint and to determine intermetallic interactions. For instance, amorphous iridium oxo-hydroxides are reported to reduce under  $\text{H}_2$  below 100 °C, while crystalline rutile  $\text{IrO}_2$  reduces at 250 °C.

$\text{H}_2\text{-TPR}$  results reported on chapter 3 were performed by Dr. Andrey Tarasov at the Fritz Haber Institute in Berlin, Germany. The remaining  $\text{H}_2\text{-TPR}$  reported in the following chapters were performed on a CHEMBET TPR/TPD, Quantachrome Industries fitted with a TCD detector. 60 mg of sample were degased under helium at 110 °C for 2 hours, the analysis was performed under 10 %  $\text{H}_2 / \text{Ar}$ , 100 ml / min from room temperature to 800 °C at 5 °C / min.

### 2.4.5 Electronic Microscopic techniques.

A microscope is an instrument that allows the magnification of small specimens. Classically, resolution refers to the minimum distance that can be resolved,  $\delta$ . According to the Rayleigh theorem for optic microscopes, represented in equation 2.19, the resolution is roughly half of the wavelength of the radiation used for imaging.<sup>(10)</sup>

$$\delta = \frac{0.61 \cdot \lambda}{\mu \cdot \sin\beta} \quad \text{Eq. 2.19}$$

Where  $\lambda$  is wavelength of radiation,  $\mu$  is the refractive index of the viewing medium and  $\beta$  the semi-angle of collection of the magnifying lens.  $\mu \cdot \sin\beta$  could be approximated to 1.

Classical microscopes use visible light as the probe radiation with wavelength ranging from 400 nm to 700 nm, from the Rayleigh equation it could be assumed that the maximum resolution would be 244 nm and that no images could be obtained beyond this point. Nanomaterials such as catalysts are in the nanoscale regime, normally from 1 nm to 100 nm, and hence it is not possible to obtain atomic information using conventional microscopes. This limitation could be overtaken using electrons as the source of radiation. In an electronic microscope, electrons are accelerated to a certain kinetic energy and irradiated to the sample. The energy of electrons,  $E$ , determines its wavelength through the Broglie equation (equation 2.20).

$$\lambda = \frac{1.22}{E^{1/2}} \quad \text{Eq. 2.20}$$

A wavelength of 0.004 nm could be obtained using electrons with energy of 100 KeV. This should lower the resolution limit to 0.002 nm, which is much smaller than the hydrogen atom, 0.1 nm, the smallest atom of all. Currently, this degree of resolution has not been obtained due to technical limitations. Nevertheless atomic resolution could be obtained using state of the art equipment.<sup>(10)</sup>

The different interactions of electron radiation with matter are represented in figure 2.9 and are the origin of the different signals processed to obtain information about the specimen.

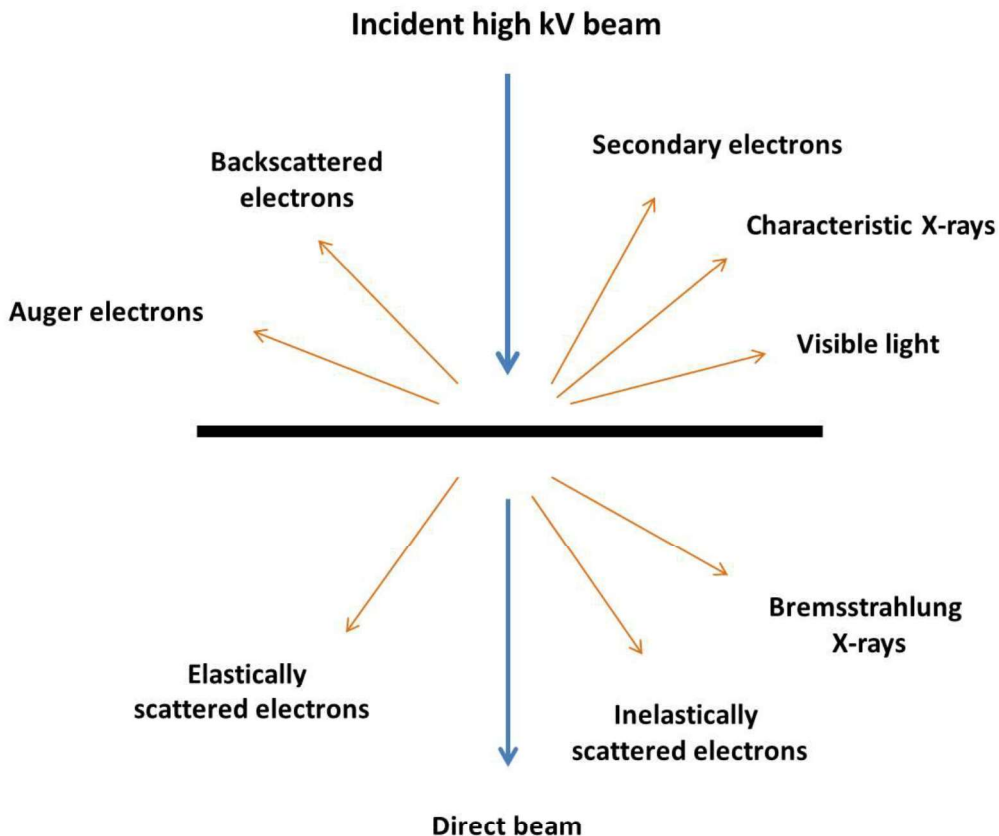


**Figure 2.9.** Schematic representation of the different signals generated when a high energy beam of electrons interact with a thin specimen.<sup>(10)</sup>

#### 2.4.5.1 Scanning Electron Microscopy (SEM).

SEM is commonly used to obtain the macroscopic morphology and the composition of a material. The electron beam interacts within a few microns in depth with the material. Contrary to TEM, thick materials could be analysed since the specimen is generally placed on to a carbon tape, as a result just electrons escaping the sample in the opposite direction than the incident beam could be analysed (e.g., secondary electrons, backscattered electrons and characteristic X-ray).

Backscattered electrons arise from the interaction of the incident beam electrons with the sample. The trajectory of the incident electrons is modified by its interaction with atoms in the material without altering the energy of the incident electrons. Backscattered electrons are sensitive to the atomic mass of the nuclei they scatter from. Heavier atoms produce more scattering and as a consequence are seen brighter than lighter atoms.

The interaction of the incident beam could excite some of the sample electrons producing secondary electrons. Only secondary electrons produced from atoms near

the surface of the sample would escape and be detected; the analysis of those atoms is normally used when high surface resolution is desired.

The elemental composition of a sample could be obtained by X-ray energy dispersive spectroscopy (EDX). The incident high energy electron beam could interact with a core electron from the sample producing its excitation to the continuum. In order to stabilise the ionised atom, the electron hole is filled with an electron from the outer shell emitting X-ray radiation characteristic for each element.

The macroscopic morphology of as prepared  $\text{IrO}_2$  and  $\text{Ir}_x\text{M}_{1-x}\text{O}_2$  mixed oxide catalysts ( $\text{M} = \text{Ni}$  or  $\text{Cu}$ ) were determined by SEM on a Hitachi TM3030 Plus. High magnification SEM images performed on  $\text{IrO}_2/\text{ATO}$  samples to study the formation of a support shell over the catalysts after heat treatment were obtained using a Tescan Maia 3 microscope. However, samples were not stable under the electron beam.

#### **2.4.5.2 Transmission Electron Microscopy (TEM).**

As illustrated in figure 2.7, the interactions of the incident beam with the sample produce numerous signals. SEM focuses on scattered electrons from the sample in the opposite direction than the incident beam. However, the primary signals analysed by TEM are transmitted electrons, electrons that go through the sample. Since electrons need to pass through the sample it needs to be thin, hence, secondary and backscattered electrons become less frequent.

Incident electrons are uniform when emitted to the sample. However, through its interaction with the atoms in the sample its trajectory is altered. Structural and chemical information could be obtained from this non-uniform electron distribution obtained after its interaction with the sample.<sup>(10)</sup>

On beam sensitive  $\text{IrO}_x$  samples, TEM images were recorded by Dr. Gerardo Algara-Siller on a low electron dose Titan 80-300 HRTEM operated at 200 kV in the Fritz Haber Institute in Berlin, Germany. The use of this specific TEM was needed to confirm the non-crystalline rearrangement of the synthesised materials. PdZn catalyst's particle size and size distribution were obtained by TEM on a JEOL 2100 microscope with a  $\text{LaB}_6$  filament operating at 200 kV in Cardiff. Samples analysed in Cardiff were dispersed in ethanol and allowing a drop to evaporate on a lacey carbon film supported over a 300 mesh copper TEM grid.

## 2.5 Bibliography.

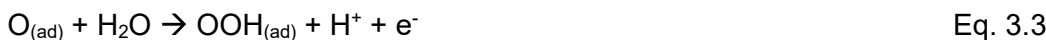
1. F. Berkermann, *Preparation and Application of Aqueous Iridium Oxide Colloids* (Doctoral Thesis). Ruhr University Bochum, Germany, **2010**.
2. M. M. Forde, R. D. Armstrong, R. McVicker, P. P. Wells, N. Dimitratos, Q. He, L. Lu, R. L. Jenkins, C. Hammond, J. A. Lopez-Sanchez, C. J. Kielyc, G. J. Hutchings, Light alkane oxidation using catalysts prepared by chemical vapour impregnation: tuning alcohol selectivity through catalyst pre-treatment, *Chemical Science*, **2014**, 5 (9), 3603-3616.
3. H. Bahruji, M. Bowker, W. Jones, J. Hayward, J. Ruiz Esquius, D. J. Morgan, G. J. Hutchings, PdZn catalysts for CO<sub>2</sub> hydrogenation to methanol using chemical vapour impregnation (CVI), *Faraday Discussions*, **2016**, 197, 309-324.
4. H. Bahruji, M. Bowker, G. Hutchings, N. Dimitratos, P. Wells, E. Gibson, W. Jones, C. Brookes, D. Morgan, G. Lalev, Pd/ZnO catalysts for direct CO<sub>2</sub> hydrogenation to methanol, *Journal of Catalysis*, **2016**, 343, 133-146.
5. I. Spanos, A. A. Auer, S. Neugebauer, X. Deng, H. Tueysuez, R. Schlöegl, Standardized Benchmarking of Water Splitting Catalysts in a Combined Electrochemical Flow Cell/Inductively Coupled Plasma-Optical Emission Spectrometry (ICP-OES) Setup, *ACS Catal*, **2017**, 7, 3768-3778.
6. F. W. Fifield, D. Kealey, *Principles and practice of analytical chemistry*, Blackie academic & professional, **1995**.
7. C. N. Banwell, E. M. McCash, *Fundamentals of Molecular Spectroscopy*, The McGraw-Hill Companies, **1994**.
8. P. Atkins T. Overton, J. Rourke, M. Weller, F. Armstrong, *Inorganic Chemistry*. 4<sup>th</sup> edition, Oxford University Press, Shriver & Atkins, **2006**.
9. M. Newville, *Fundamentals of XAFS*, Chicago University, **2004**.
10. D. B. Williams, C. B. Carter, *Transmission Electron Microscopy. Part 1: Basics*, Springer, **2009**.

# Chapter 3

## Effect of base on the preparation of IrO<sub>2</sub> catalysts towards OER through a hydrothermal synthesis

### 3.1 Introduction.

In a proton exchange membrane water electrolyser (PEM), the oxygen evolution reaction (OER) occurs at the anode. OER consists of four single electron transfers (equation 3.1 to 3.4), <sup>(1)</sup> the first step is the water discharge at the surface of the catalyst to produce a hydroxyl group, OH<sub>(ad)</sub>, followed for a proton-coupled electron transfer to form a metal-oxo intermediate, O<sub>(ad)</sub>. (Eq. 3.1 and Eq. 3.2 respectively). The subsequent nucleophilic attack of a water molecule to form the peroxy intermediate, OOH<sub>(ad)</sub>, is considered the rate determining step (Eq. 3.3), accounts to high overpotential. The peroxy intermediate finally evolves to the formation of molecular oxygen (Eq. 3.4) via another proton-coupled electron transfer and the regeneration of the catalyst surface active site.



In acid media, PEM operating conditions, IrO<sub>2</sub> is virtually the only feasible catalyst for OER due to its higher resistance against corrosion and considerable high catalytic activity.<sup>(2-4)</sup> Amorphous iridium oxo-hydroxides (IrO<sub>x</sub>) have better catalytic performance towards OER compared to crystalline rutile IrO<sub>2</sub>,<sup>(5)</sup> possibly because of the presence of Ir(III)/Ir(IV) and electrophilic O<sup>-</sup> sites<sup>(6-8)</sup> and the higher concentration of surface hydroxide groups<sup>(9)</sup> on amorphous IrO<sub>x</sub>, whilst rutile IrO<sub>2</sub> is composed only of Ir(IV) and O<sup>2-</sup>.

From the preparation methodologies described previously in the introductory chapter, the hydrothermal preparation is preferred for the preparation of IrO<sub>x</sub> because it avoids high temperature heat treatment after drying to form the active phase, thus minimising the crystallisation and the loss of surface hydroxide groups.<sup>(10)</sup> As reported by Reetz and Schulenburg, stable IrO<sub>x</sub> colloidal solutions can be obtained from iridium chloride salts (IrCl<sub>3</sub> or H<sub>2</sub>IrCl<sub>6</sub>) under strong aqueous alkaline conditions, without the need for organic stabilisers.<sup>(11)</sup> IrO<sub>x</sub> colloids can be precipitated as amorphous IrO<sub>x</sub> powders by heating the solution. Several examples in literature show the hydrothermal preparation of colloidal IrO<sub>x</sub>

under alkaline conditions,<sup>(12-18)</sup> typically using NaOH or KOH as base. However, limited studies have been performed on the effect of the base used during the synthesis of IrO<sub>2</sub> powders through a hydrothermal method. A brief study was undertaken on the preparation of colloidal IrO<sub>x</sub> in the PhD thesis of Dr. Frederic Berkerman,<sup>(19)</sup> where no differences in the stability of IrO<sub>2</sub> colloidal solutions were observed when using NaOH, KOH or Li<sub>2</sub>CO<sub>3</sub> as base, nevertheless, they were not tested towards OER.

In this chapter, the role of the base (Li<sub>2</sub>CO<sub>3</sub>, LiOH, Na<sub>2</sub>CO<sub>3</sub>, NaOH, K<sub>2</sub>CO<sub>3</sub> or KOH) on the hydrothermal preparation of amorphous iridium oxo-hydroxides has been studied. Synthesised IrO<sub>x</sub> catalysts were thoroughly characterised by means of XRD, XPS, BET, SEM and Raman spectroscopy and tested for the oxygen evolution reaction (OER) in acid media. The aim of it is to identify catalytic trends with structural or chemical features.

### **3.2 Effect of the alkali metal base during the hydrothermal synthesis of IrO<sub>2</sub>.**

#### **3.2.1 Catalysts preparation.**

A modification of the hydrothermal method reported by Reetz and Feigel was followed.<sup>(19)</sup> 1 mmol of IrCl<sub>3</sub> hydrate and 8 mmol of base (Li<sub>2</sub>CO<sub>3</sub>, LiOH, Na<sub>2</sub>CO<sub>3</sub>, NaOH, K<sub>2</sub>CO<sub>3</sub> or KOH) were dissolved in 10 ml of deionised water and stirred for 16 h at room temperature in a 50 ml round bottom flask. The pH of the solution remained at 11-12 during this process. The solution remained yellow when carbonate bases (Li<sub>2</sub>CO<sub>3</sub>, Na<sub>2</sub>CO<sub>3</sub> or K<sub>2</sub>CO<sub>3</sub>) were used, while blue solutions were observed for hydroxide bases (LiOH, NaOH or KOH). A further 10 ml of deionised water were added to the solution after this initial period. The solution was then heated to reflux for 3 hours. A blue precipitate was observed, which was recovered by filtration and washed with 2 L of hot deionised water. Finally, the material was dried at room temperature inside a fumehood overnight. Samples are denoted as IrO<sub>2</sub>-(base), for instance, the sample prepared using Li<sub>2</sub>CO<sub>3</sub> as a base would be referred as IrO<sub>2</sub>-Li<sub>2</sub>CO<sub>3</sub>.

The molar ratio between the iridium precursor and base was kept constant at 1:8 for all catalysts. From the blue coloration of the solution after 3 h reflux, when using LiOH, NaOH and KOH, it could be deduced that iridium colloidal species remained in solution due to incomplete precipitation, which is also observed as lower solid catalyst yield (table 3.1) which suggests that the strong hydroxide media can electrostatically stabilise the iridium oxide colloids in solution.<sup>(18)</sup>

**Table 3.1.** Catalyst yield for IrO<sub>2</sub> samples prepared with different alkali metal bases. \*Yield was calculated assuming that all IrCl<sub>3</sub> precursor should convert to IrO<sub>2</sub> and without taking into account the level of hydration of the final material.

Catalyst	*Yield / %	Catalyst	*Yield / %
IrO <sub>2</sub> -Li <sub>2</sub> CO <sub>3</sub>	93	IrO <sub>2</sub> -LiOH	50
IrO <sub>2</sub> -Na <sub>2</sub> CO <sub>3</sub>	78	IrO <sub>2</sub> -NaOH	36
IrO <sub>2</sub> -K <sub>2</sub> CO <sub>3</sub>	57	IrO <sub>2</sub> -KOH	61

### 3.2.2 Catalyst Characterisation.

#### *UV-Vis characterisation*

The IrCl<sub>3</sub> conversion to IrO<sub>2</sub> can be monitored using UV-Vis spectroscopy since the precursor, intermediates and IrO<sub>x</sub> colloids present absorption in different UV-Vis regions. In order to facilitate the sampling, a 100 ml 3-neck round bottom flask was used to allow 0.1 ml aliquots to be sampled using a syringe during the preparation. The IrCl<sub>3</sub> and base added were kept constant; however, instead of 10 + 10 mL of deionised water used during normal preparation conditions, 40 ml of water were added from the beginning of the preparation. Reaction aliquots were sampled every hour for five hours at 25 °C; following this, the solution was stirred for 16 h at 25 °C. Starting from 25 °C, the solution was heated in intervals of 10 °C to reflux. The temperature was stabilised for 5 minutes at each temperature before sampling.

IrO<sub>2</sub> samples prepared with carbonate bases followed the same evolution of UV-Vis bands during preparation. However, the behaviour for samples prepared using hydroxide bases differed, indicating that the overall reaction rate differs depending on the nature of the base used. IrCl<sub>3</sub> in aqueous solution is first solvated to Ir(H<sub>2</sub>O)<sub>3</sub>Cl<sub>3</sub> which was observed by the small low intense absorption close to 400 nm.<sup>(20)</sup> When Li<sub>2</sub>CO<sub>3</sub> (figure 3.1a), Na<sub>2</sub>CO<sub>3</sub> or K<sub>2</sub>CO<sub>3</sub> were used as a base it was observed that the hydrolysis of Ir(H<sub>2</sub>O)<sub>3</sub>Cl<sub>3</sub> to Ir(OH)<sub>6</sub><sup>2-/3-</sup> occurred after stirring for 16 h at 25 °C. Absorbance values for Ir(OH)<sub>6</sub><sup>2-</sup> and Ir(OH)<sub>6</sub><sup>3-</sup> are reported in literature at 313 nm and 320 nm respectively.<sup>(14, 20)</sup> However, from the obtained data, the oxidation state of iridium on the Ir(OH)<sub>6</sub><sup>x-</sup> intermediate cannot be determined and possibly both, Ir(OH)<sub>6</sub><sup>2-</sup> and Ir(OH)<sub>6</sub><sup>3-</sup>, were present in solution. The band at 580 nm that indicates the formation of Ir-O-Ir linkages<sup>(14)</sup> was not observed until the solution was heated

to around 85–95 °C. At that point  $\text{Ir}(\text{OH})_6^{2-3-}$  started to condense forming first a  $\text{IrO}_2$  colloidal solution which upon continuous heating to reflux agglomerated leading to  $\text{IrO}_x$  precipitation.

In the case of hydroxide bases,  $\text{LiOH}$  (figure 3.1b),  $\text{NaOH}$  or  $\text{KOH}$ , used during the synthesis, the reaction mechanism for the formation of  $\text{IrO}_x$  colloids followed the same transformations,  $\text{Ir}(\text{H}_2\text{O})_3\text{Cl}_3$  was hydrolysed to  $\text{Ir}(\text{OH})_6^{2-3-}$ , then the hydroxide condensed forming Ir-O-Ir linkages until a precipitate was formed. However, in comparison with carbonate bases,  $\text{IrO}_x$  colloidal solution was formed after stirring at room temperature without the need of heating up to 85–95 °C. Both  $\text{Ir}(\text{OH})_6^{2-}$  and Ir-O-Ir chains coexisted in solution after stirring for 16 h at room temperature as indicated by the bands at 314 nm and 580 nm respectively. The dark blue coloration of the solution indicated that iridium was present as  $\text{Ir}(\text{IV})$ .<sup>(21)</sup> Both bands, 314 nm and 580 nm, remain steady up to 75 °C, when the  $\text{Ir}(\text{OH})_6^{2-}$  started to drop in intensity while the Ir-O-Ir linkages band raised. After reflux for 3 h  $\text{Ir}(\text{OH})_6^{2-3-}$  was still detected, indicating that iridium species remained in solution stabilised by the strong hydroxide environment, in agreement with the lower obtained catalysts yield for hydroxide bases.

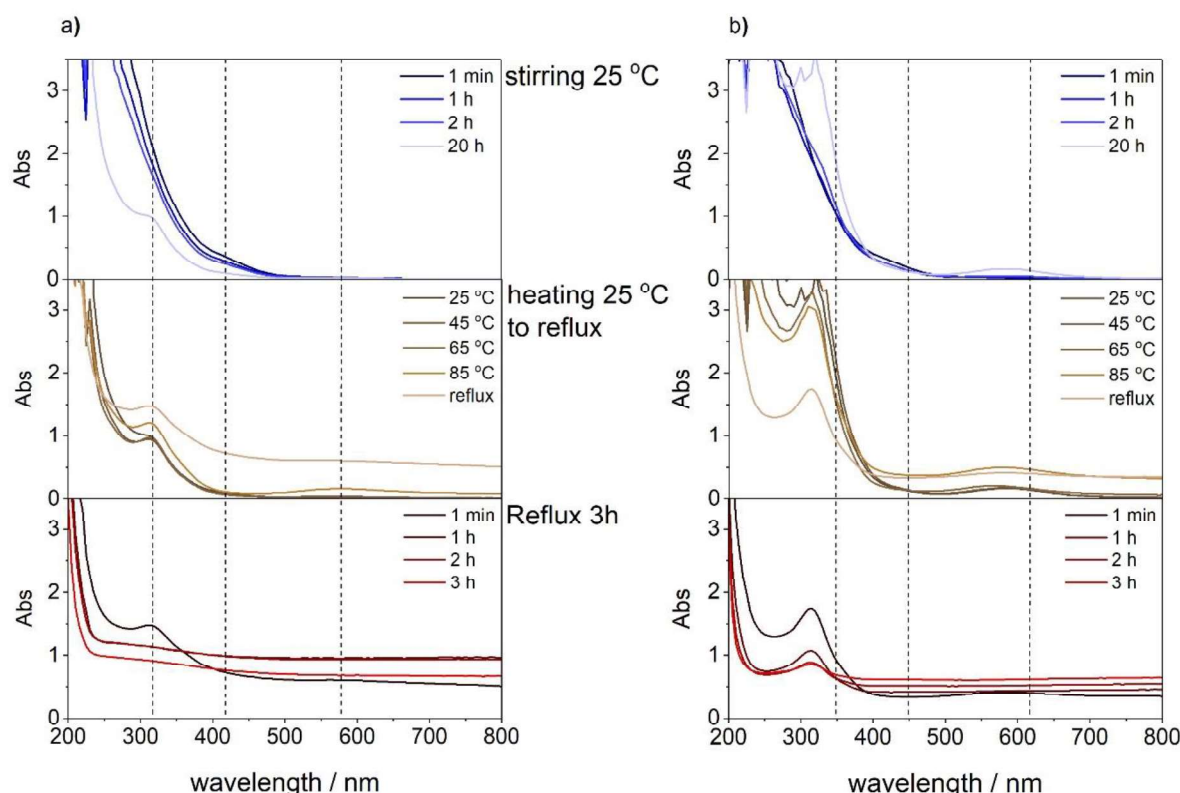


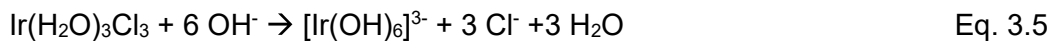
**Figure 3.1.** From top to bottom  $\text{IrCl}_3$  transformation to  $\text{IrO}_x$  UV monitoring for, 16 hours stirring at room temperature, heat from 25 °C up to reflux and finally reflux for 3 hours. a)  $\text{Li}_2\text{CO}_3$  and b)  $\text{LiOH}$  base were used during the synthesis.

The higher solubility of hydroxide alkaline metal bases (12.8 g, 111 g and 112 g per 100 ml in water at 20 °C for LiOH, NaOH and KOH respectively) compared to carbonate alkaline metal bases (1.3, 30.7 and 110.5 g per 100 ml in water at 20 °C for  $\text{Li}_2\text{CO}_3$ ,  $\text{Na}_2\text{CO}_3$  and  $\text{K}_2\text{CO}_3$  respectively) in addition with the stronger basicity of hydroxide bases, classified as strong bases, compared to the carbonate counterparts, classified as weak bases, could explain the faster kinetics observed for the formation of Ir-O-Ir linkages.

During the transformation from  $\text{IrCl}_3$  to  $\text{Ir}(\text{OH})_6^{2-}$ , the oxidation state of iridium has to change from Ir(III) to Ir(IV). In order to understand if oxygen was responsible for this oxidation,  $\text{IrO}_2$ -KOH was prepared under  $\text{N}_2$ . Prior to the addition of the iridium salt and the base, the reflux system and the solvent needed were purged with  $\text{N}_2$  for 40 minutes. Once the two precursors were added, the system was purged with  $\text{N}_2$  again for 10 further minutes. The top of the reflux condenser was sealed with a septum to avoid air entering the system. Moreover, in order to avoid air contamination in to the system during the overnight stirring, a balloon filled with argon was attached at the top of the reflux.

In the case that oxygen was oxidising Ir(III) to Ir(IV), the hydrolysis of  $\text{Ir}(\text{H}_2\text{O})_3\text{Cl}_3$  to  $\text{Ir}(\text{OH})_6^{3-}$  would be expected to occur in the absence of oxygen, but not the further formation of Ir-O-Ir linkages. However, it has been observed that anhydrous and hydrated  $\text{RuCl}_3$  precursors present the same ruthenium to chlorine ratio and that probably both contains a mixture of Ru(III) and Ru(IV).<sup>(22)</sup> The same behaviour could be expected for  $\text{IrCl}_3$ , a mixture of Ir(III) and Ir(IV) could co-exist in the material.<sup>(23)</sup> As observed by the UV-Vis monitoring of  $\text{IrO}_2$ -KOH catalyst under  $\text{N}_2$ , the solution turned blue after stirring for 16 h at room temperature indicating the presence of Ir(IV). The presence of the band at 580 nm correlated with the formation of Ir-O-Ir linkages, suggesting the presence of Ir(IV) in solution (figure 3.2). One possibility for the Ir-O-Ir linkages formation under  $\text{N}_2$  could be the presence of Ir(IV) in the starting material, since  $\text{IrO}_x$  colloids present an intense dark blue coloration compared to the pale yellow of  $\text{Ir}(\text{OH})_6^{2/3-}$ . Alternatively, some Ir(III) oxidation to Ir(IV) could have been formed from  $\text{O}_2$  contamination inside the reflux system, or that water was acting as the oxidant. However, it was observed that no precipitate was formed upon reflux for three hours (image 3.1). Hence, even though the presence of oxygen could not be attributed to the oxidation of  $\text{IrCl}_3$  or  $\text{Ir}(\text{OH})_6^{3-}$  to  $\text{Ir}(\text{OH})_6^{2-}$ , its presence is necessary in order to form the Ir-O-Ir bridge bonds between colloids to induce aggregation and precipitation.

Alternatively, Xu *et al.*<sup>(20)</sup> proposed the mechanism illustrated in equations 3.5 to 3.7 for the hydrothermal formation of  $\text{IrO}_2$  in aqueous alkaline media.



If the proposed alternative mechanism is accepted, the Ir-O-Ir band observed at 580 nm could be associated with the  $\text{Ir}_2\text{O}_3$  intermediate, in which iridium remains as Ir(III). Therefore, the solution's blue coloration would not be related to the presence of Ir(IV) as previously believed, but to Ir-O-Ir linkages present in the  $\text{Ir}_2\text{O}_3$  intermediate. This would explain the trend observed by UV-Vis for the  $\text{IrO}_2$ -KOH catalyst carried out under nitrogen atmosphere, in which no  $\text{IrO}_2$  precipitation was observed.

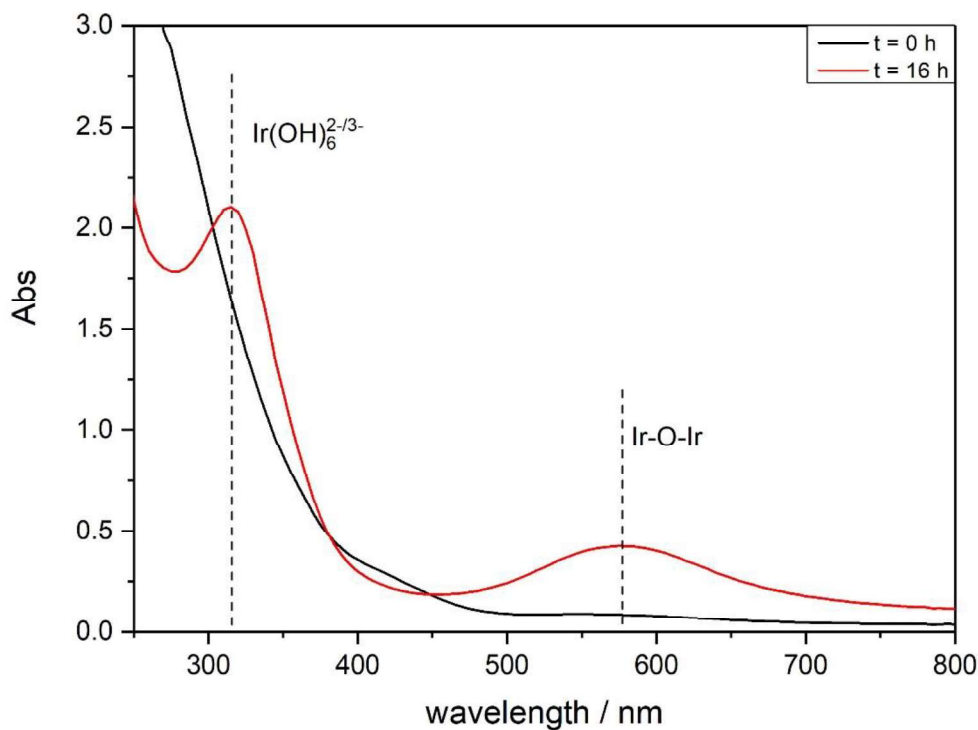


**Figure 3.2.** UV-Vis spectra for  $\text{IrCl}_3$  in alkaline KOH aqueous solution under  $\text{N}_2$  atmosphere after stirring at room temperature for 16 hours.

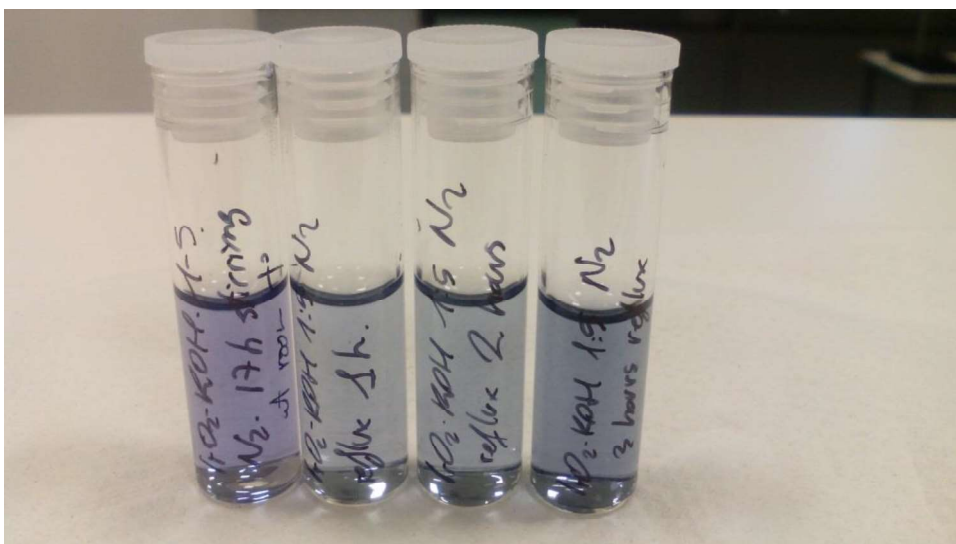


**Image 3.1.** IrCl<sub>3</sub> in aqueous KOH under N<sub>2</sub> atmosphere, reaction aliquots analysed by UV-Vis. From left to right, aliquot stirred at room temperature after for 16 h, reflux for 1 h, reflux for 2 h and reflux for 3 h.

#### *Attenuated Total Reflectance - Fourier-Transform Infrared spectroscopy (ATR-FTIR)*

ATR-FTIR spectroscopy is a useful technique for determining the presence of functional groups in a material since specific vibrational modes adsorb at different infrared frequencies. This spectroscopic technique was used to qualitatively compare water and impurities, such as the presence of carbonates from the base, present between samples (figure 3.3). According to literature, O-H stretching appears at around 3400 cm<sup>-1</sup>.<sup>(24)</sup> However the presence of a band in that region could not specify if it is due to the presence of physisorbed water or to the presence of surface hydroxide groups, since materials were not dried in a furnace. Previous reports on these materials show that Ir-OH stretching appear at 460 cm<sup>-1</sup>.<sup>(24)</sup> The analysis of the Ir-O stretching at 460 cm<sup>-1</sup> allows differentiation between physisorbed water and surface hydroxide groups. Commercial anhydrous IrO<sub>2</sub> from Sigma-Aldrich and IrO<sub>2</sub>·2H<sub>2</sub>O from Premion (Alfa Aesar) were used as received as standards for comparison. Anhydrous IrO<sub>2</sub> did not show any intensity at 3400 cm<sup>-1</sup>, while commercial IrO<sub>2</sub>·2H<sub>2</sub>O showed a broad band around 3400 cm<sup>-1</sup> due to O-H stretching and a band at 460 cm<sup>-1</sup> corresponding to Ir-OH vibrations. When using potassium bases, KOH or K<sub>2</sub>CO<sub>3</sub>, the spectra was comparable to the one obtained for commercial IrO<sub>2</sub>·2H<sub>2</sub>O. On the other hand, when using sodium or lithium bases, bands associated with OH stretching and Ir-OH vibration increased significantly in intensity, thus indicating a higher presence of surface hydroxyl groups on those materials. Carbonate impurities were observed as a triplet band centred at 1500 cm<sup>-1</sup> for IrO<sub>2</sub> catalysts prepared with Li<sub>2</sub>CO<sub>3</sub>, Na<sub>2</sub>CO<sub>3</sub> and K<sub>2</sub>CO<sub>3</sub>.

Though only qualitative data could be obtained from the ATR-FTIR analysis, it indicated substantial differences between materials. Absorption on the O-H stretching region at  $3400\text{ cm}^{-1}$ , which could indicate either the presence of physisorbed water or the presence of surface hydroxyl groups, seemed to be related with the Ir-OH vibration absorption at  $460\text{ cm}^{-1}$ . The use of potassium bases, KOH and  $\text{K}_2\text{CO}_3$ , reduced the amount of hydroxide groups on the material compared to the use of NaOH,  $\text{Na}_2\text{CO}_3$ , LiOH or  $\text{Li}_2\text{CO}_3$  bases which in turn can indicate a more-oxide like nature.

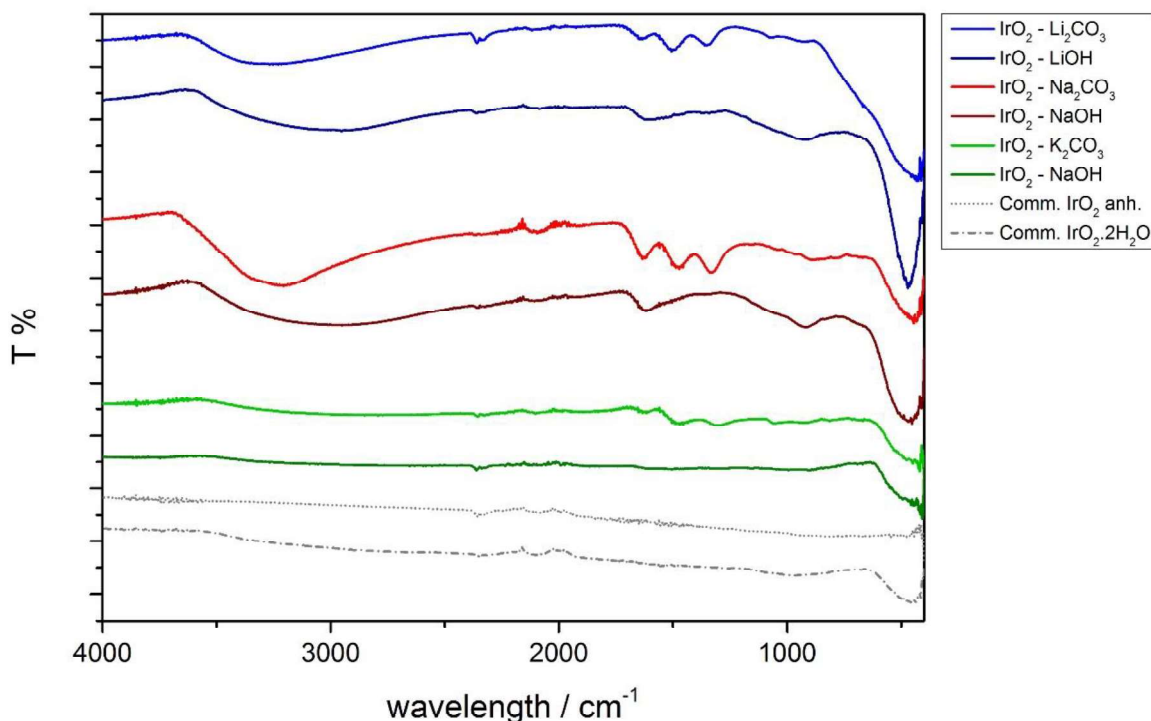


**Figure 3.3.** FTIR-ATR characterisation for prepared  $\text{IrO}_2$  catalysts through the hydrothermal synthesis using different alkali metal bases.

#### X-ray powder diffraction (XRD)

Previous reports made on  $\text{IrO}_2$  materials used for OER have shown that amorphous  $\text{IrO}_x$  presents higher activity compared to crystalline-rutile  $\text{IrO}_2$ .<sup>(7, 10)</sup> Thus, the synthesis of amorphous iridium oxo-hydroxides seems to be a requirement to obtain high active catalysts. XRD characterisation was performed in order to determine the crystalline phase or the amorphous nature of the synthesised catalysts. Commercial crystalline  $\text{IrO}_2$  and hydrous  $\text{IrO}_2\cdot 2\text{H}_2\text{O}$  were analysed as standards for comparison. Rutile is a common crystalline tetragonal phase for  $\text{IrO}_2$ . Commercial anhydrous  $\text{IrO}_2$  showed rutile reflections by XRD at

$28.0^\circ$ ,  $34.6^\circ$ ,  $40.0^\circ$ ,  $54.0^\circ$ ,  $58.1^\circ$ ,  $65.7^\circ$ ,  $69.1^\circ$  and  $73.0^\circ$  for (110), (101) (200), (211), (220), (221), (301) and (202) crystallographic planes respectively (JCPDS-015-0876). Commercial  $\text{IrO}_2 \cdot 2\text{H}_2\text{O}$  did not present rutile reflections but contained metallic iridium impurities at  $40.8^\circ$ ,  $47.4^\circ$  and  $69.3^\circ$  for (111), (200) and (220) crystallographic planes respectively (JCPDS-006-0598). Low intensity broad reflections were observed for the  $\text{IrO}_2 \cdot 2\text{H}_2\text{O}$  sample at  $19.0^\circ$ ,  $34.3^\circ$  and  $59.1^\circ$  indicating its amorphous nature (figure 3.4). XRD patterns for commercial anhydrous and hydrated  $\text{IrO}_2$  were in accordance with previous reports done on these standard catalysts, where it was concluded by XPS quasi *in-situ* XPS and near edge – X-ray absorption spectroscopy that commercial  $\text{IrO}_2 \cdot 2\text{H}_2\text{O}$  consisted predominantly of amorphous  $\text{IrO}_2$  with a core of metallic iridium while commercial crystalline  $\text{IrO}_2$  was made entirely of crystalline rutile  $\text{IrO}_2$ .<sup>(5)</sup>

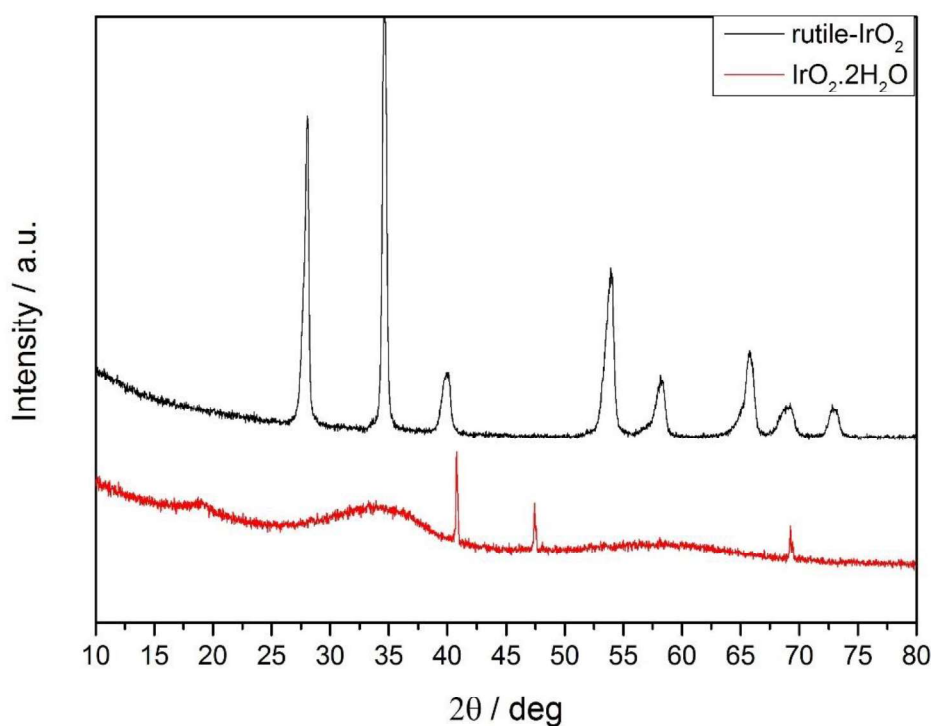


**Figure 3.4.** XRD patterns for as received commercial  $\text{IrO}_2$  catalysts. In black anhydrous rutile  $\text{IrO}_2$  from Sigma Aldrich, and in red amorphous  $\text{IrO}_2 \cdot 2\text{H}_2\text{O}$  from Alfa Aesar.

$\text{IrO}_x$  samples prepared with different bases did not show reflections corresponding to either rutile  $\text{IrO}_2$  or metallic Ir. Instead, two broad and low intense reflections at  $34^\circ$  and  $58^\circ$   $2\theta$  degrees were observed (figure 3.5) which indicated that synthesised catalysts were not crystalline but amorphous  $\text{IrO}_2$ .

The XRD reflections broaden and decrease in intensity with smaller nanoparticles size.<sup>(25)</sup> The commercial  $\text{IrO}_2 \cdot 2\text{H}_2\text{O}$  has been described as amorphous, and by having diffraction patterns similar to the commercial standard, broad reflections at  $34^\circ$  and  $58^\circ$ , it is then intuitive to assume that prepared samples are amorphous as well.

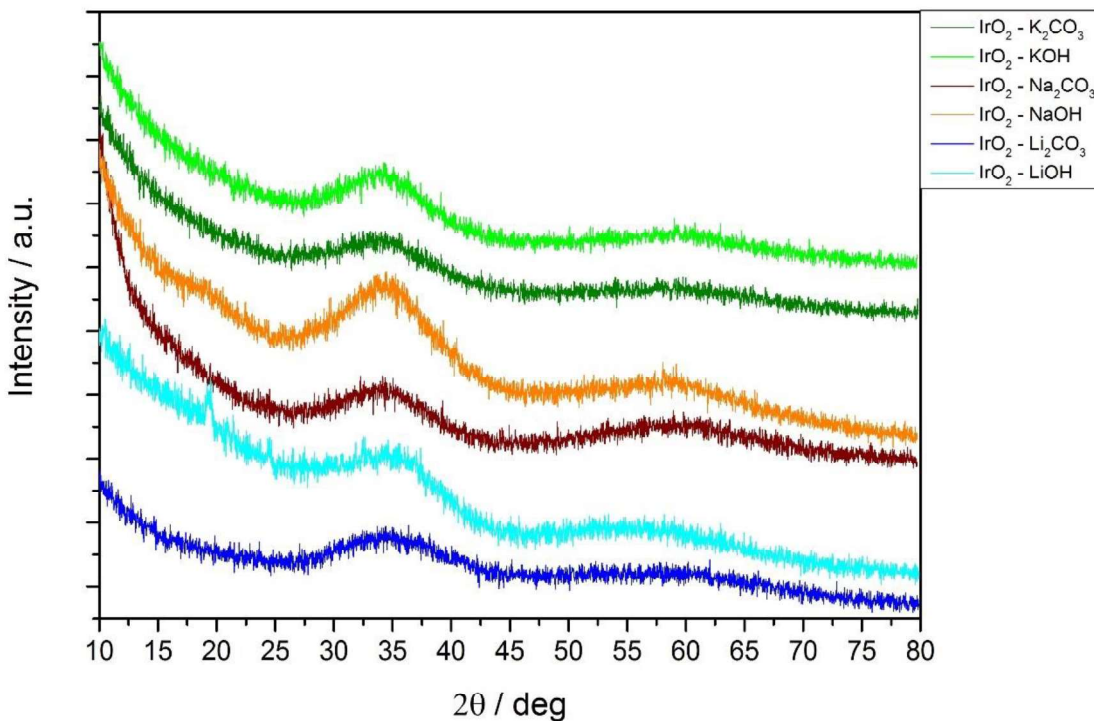


**Figure 3.5.** XRD pattern for as prepared  $\text{IrO}_2$  catalysts using different alkali metal bases.

#### Raman Spectroscopy

Raman spectroscopy is commonly used in the detection of vibrational modes that produce no change in the dipolar moment. Iridium, within the  $\text{IrO}_2$  structure, has octahedral coordination and hence does not have a net dipole moment. Nevertheless, some vibrational modes lead to the polarisability of the rutile structure, giving active modes. Thus Raman spectroscopy was used to confirm the amorphous structure of prepared  $\text{IrO}_2$  samples as a complementary technique to XRD.

As it will be shown later and in accordance with literature.<sup>(26)</sup> Performing electron microscopy analysis is difficult as amorphous iridium oxo-hydroxide tends to crystallise under electron beam irradiation. Hence, there is the possibility that amorphous  $\text{IrO}_2$  might also be sensitive to changes under other forms of excitation such as laser irradiation.<sup>(27)</sup> Raman bands for

single crystal rutile- $\text{IrO}_2$  are centred at  $752\text{ cm}^{-1}$  and  $561\text{ cm}^{-1}$  corresponding to the  $A_{1g}$  and  $E_g$  vibrational modes respectively.<sup>(24, 28)</sup> The minimum necessary laser intensity for obtaining the characteristic rutile Raman bands was determined for the commercial-crystalline  $\text{IrO}_2$ . Using 0.5 % or 1% laser intensity, (500 accumulations and 5 s of exposure time) no rutile bands were observed. However, when using 5% of laser intensity, bands at  $556\text{ cm}^{-1}$  and  $740\text{ cm}^{-1}$  were detected for the commercial rutile  $\text{IrO}_2$ . At this laser intensity, amorphous commercial  $\text{IrO}_2 \cdot 2\text{H}_2\text{O}$  did not show rutile related bands, as expected in correlation with XRD results (figure 3.6).

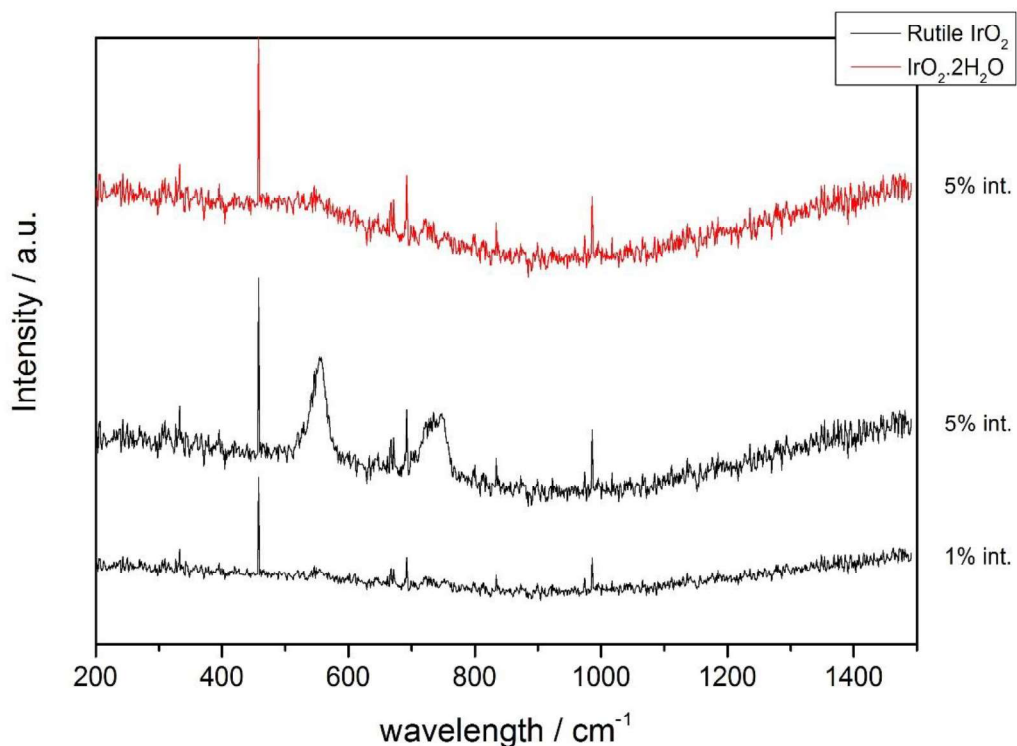


**Figure 3.6.** Raman spectroscopy for as received commercial  $\text{IrO}_2$  (rutile and amorphous) analysed at different laser intensities.

In order to ensure that using 5 % laser intensity, 500 accumulations and 5 s of exposure time are suitable for analysing the prepared  $\text{IrO}_x$ -base samples, the  $\text{IrO}_2\text{-Li}_2\text{CO}_3$  catalyst was analysed at different Raman laser intensities, 0.5 %, 1%, 5%, 10 % and 50 % maintaining a constant number of accumulations and exposure time. To avoid cumulative changes due to prolonged exposure to the laser, each analysis was performed on a fresh spot of the sample. At the lower laser intensities, 0.5% and 1%, the spectrum was completely featureless. In correlation with what was observed for the commercial crystalline  $\text{IrO}_2$  catalyst, the use of low laser intensity did not produce detectable signal. At medium laser intensities, 5% and

10%, a broad low intense band at  $480\text{ cm}^{-1}$  started to appear. This indicates that signal can be detected using medium laser intensities, since the difference in the signal observed at 5% and at 10% did not improve significantly, the milder 5% laser intensity will be used in the analysis of the synthesised samples. The recorded Raman spectra for  $\text{IrO}_2\text{-Li}_2\text{CO}_3$  was similar to the spectra measured for amorphous  $\text{IrO}_2\cdot 2\text{H}_2\text{O}$ , thus supporting the amorphous nature observed by XRD characterisation. At the highest laser intensity, 50%, the typical bands associated with  $\text{IrO}_2$  rutile appeared indicating that prepared  $\text{IrO}_2$  samples are prone to structural changes under high intensity laser irradiation (figure 3.7).

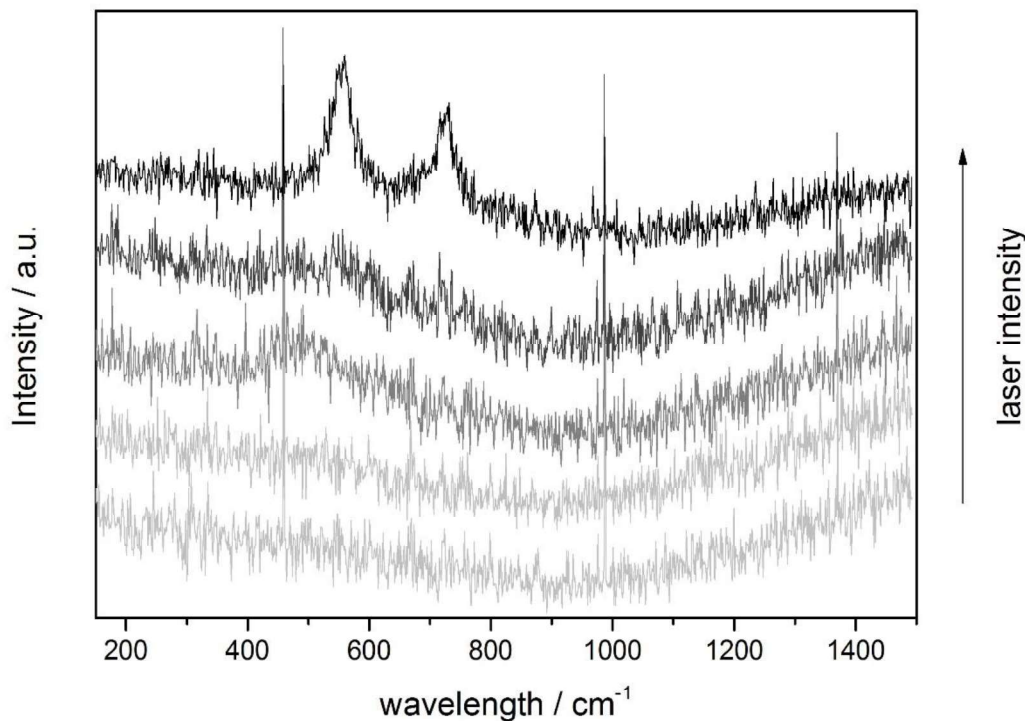


**Figure 3.7.** From bottom to top, increasing laser intensity in the analysis of  $\text{IrO}_2\text{-Li}_2\text{CO}_3$  catalyst (0.5%, 1%, 5%, 10% and 50%; 500 accumulations, 5 s laser exposure time).

Synthesised samples were dried in a fumehood and then analysed at 5% laser intensity, 500 accumulations and 5 s of laser exposure. The as-prepared samples did not show vibrations corresponding to rutile bands after analysis at three different locations, indicating that amorphous phase was obtained through the hydrothermal synthesis of  $\text{IrO}_2$  regardless of the base used during the synthesis. However, rutile-related bands were observed by Raman spectroscopy for  $\text{IrO}_2\text{-NaOH}$ ,  $\text{IrO}_2\text{-Na}_2\text{CO}_3$  and  $\text{IrO}_2\text{-K}_2\text{CO}_3$  samples at certain spots. This observation could mean that samples were not homogeneous, with some crystalline domains, or that those samples were more beam sensitive than  $\text{IrO}_2\text{-LiOH}$ ,  $\text{IrO}_2\text{-Li}_2\text{CO}_3$  and

$\text{IrO}_2\text{-KOH}$  catalysts (figure 3.8). Since no crystalline phase was detected by XRD, crystallite domains were small in size and low in population.

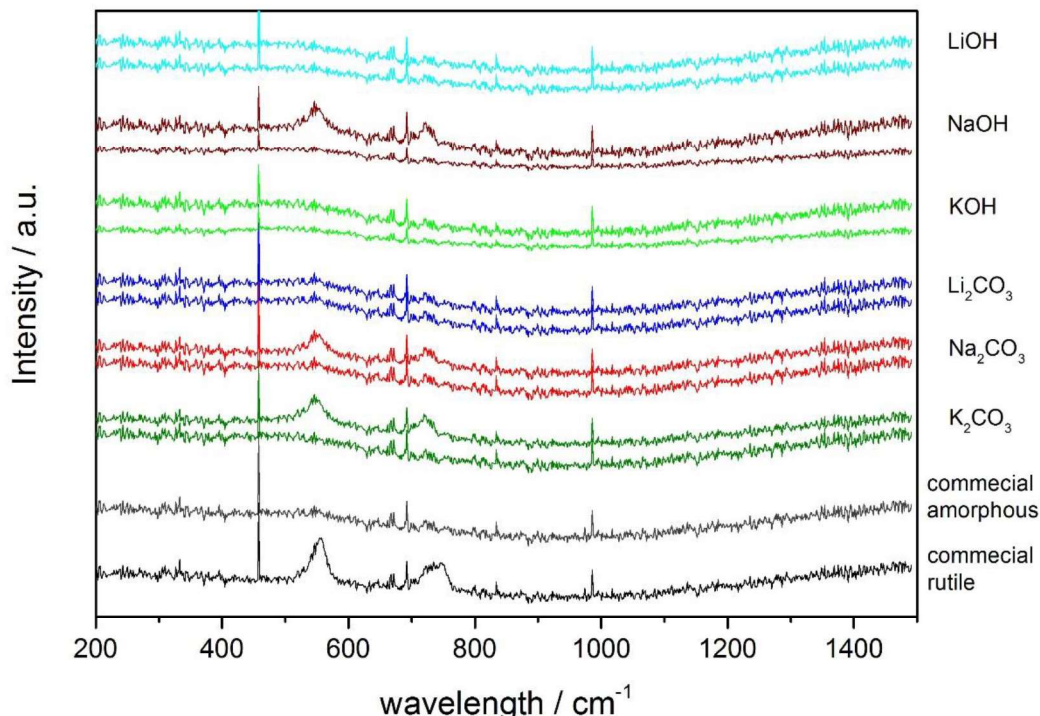


**Figure 3.8.** Raman spectroscopy measured at 5% laser intensity, 500 accumulations and 5 s of laser exposure time for hydrothermally prepared  $\text{IrO}_2$ -samples using different alkali metal bases.

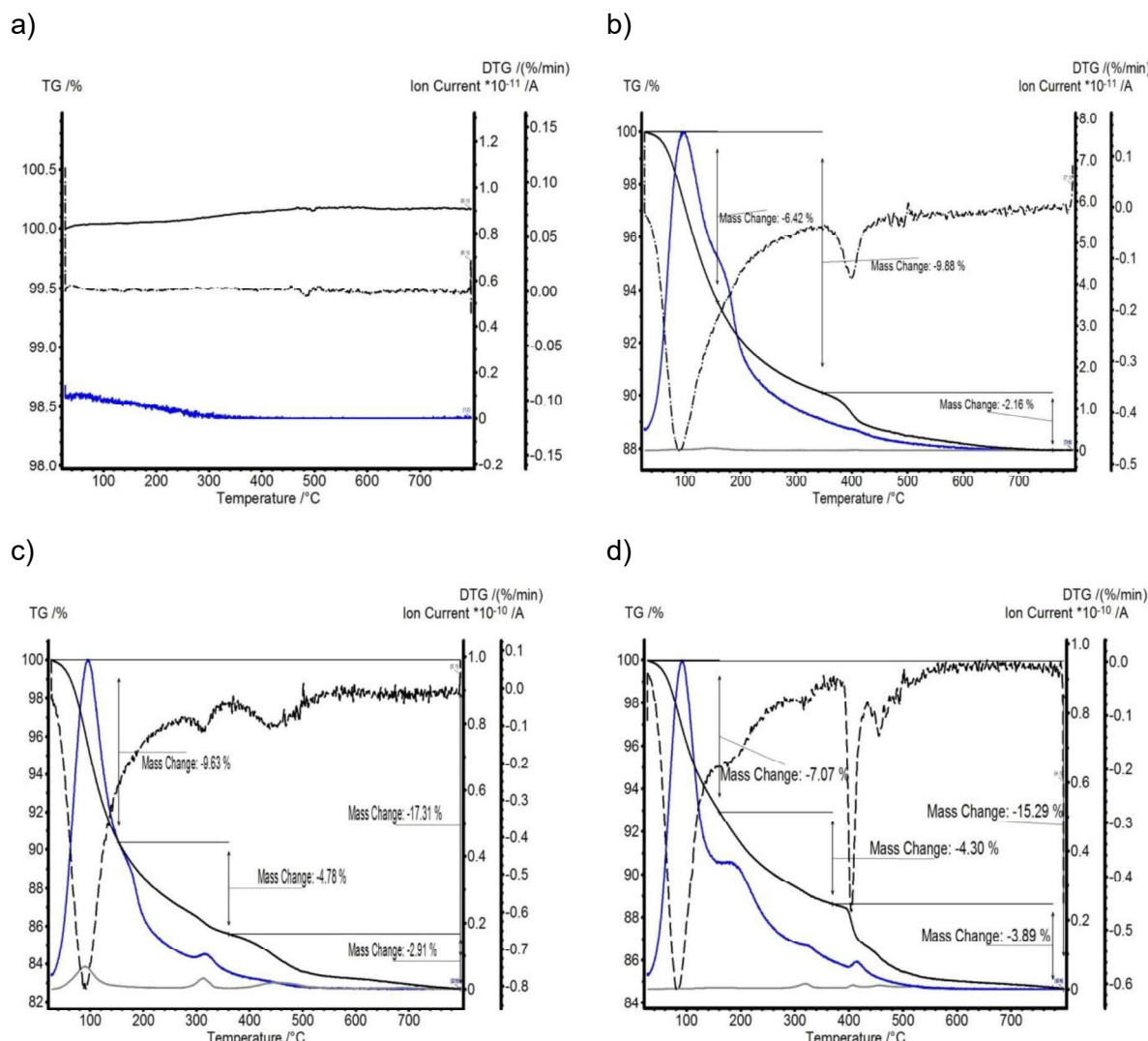
#### *Thermal analysis*

Thermal analysis, thermogravimetry (TG), differential scanning calorimetry (DSC), temperature programmed reduction (TPR) and transient hydrogen adsorption ( $\text{H}_2\text{-TA}$ ), were performed at the Fritz-Haber Institute as part of the MaxNet energy consortium by Dr. Andrey Tarasov.

##### *- Thermogravimetry and differential scanning calorimetry (TGA-DSC)*

TGA-DSC was performed under 21 %  $\text{O}_2$  / Ar with a 100 ml / min gas flow. 25 mg of sample was heated from room temperature to 800 °C at a ramp rate of 5 °C / min. The exhaust gas stream was analysed on-line by mass spectrometry (MS) in order to identify the associated elements with the observed mass lost. Individual TGA-DSC-MS analysis performed for each  $\text{IrO}_2$  catalysts, prepared through the hydrothermal synthesis using different alkali metal bases or purchased standards, are presented in figure 3.9.

Apart from the crystalline rutile sample, which did not lose mass through the heating process, all materials presented multiple exothermic mass loses as indicated by DSC. A first mass loss was present in all materials and observed at around  $150\text{ }^\circ\text{C}$ , MS confirmed that it was related to water and hence it is thought to be associated with the loose of physisorbed water. A second mass loss associated with water was detected between  $200\text{ }^\circ\text{C}$  and  $400\text{ }^\circ\text{C}$  and it is hypothesise that might correlate with chemisorbed water in the form of surface hydroxyls. Above  $400\text{ }^\circ\text{C}$ , samples kept losing weight related to the loss of strongly bonded chemisorbed water, although, for samples prepared with carbonate bases the release of  $\text{CO}_2$  was detected to be the major contribution to the mass loss, presumably as a result of carbonate decomposition. Samples prepared with hydroxide bases showed a small weight loss associated with  $\text{CO}_2$ , which could be related to  $\text{CO}_2$  adsorption from the atmosphere. The mass loss above  $400\text{ }^\circ\text{C}$  could relate to chemisorbed water within the lattice and to the crystallisation of materials to rutile  $\text{IrO}_2$ .



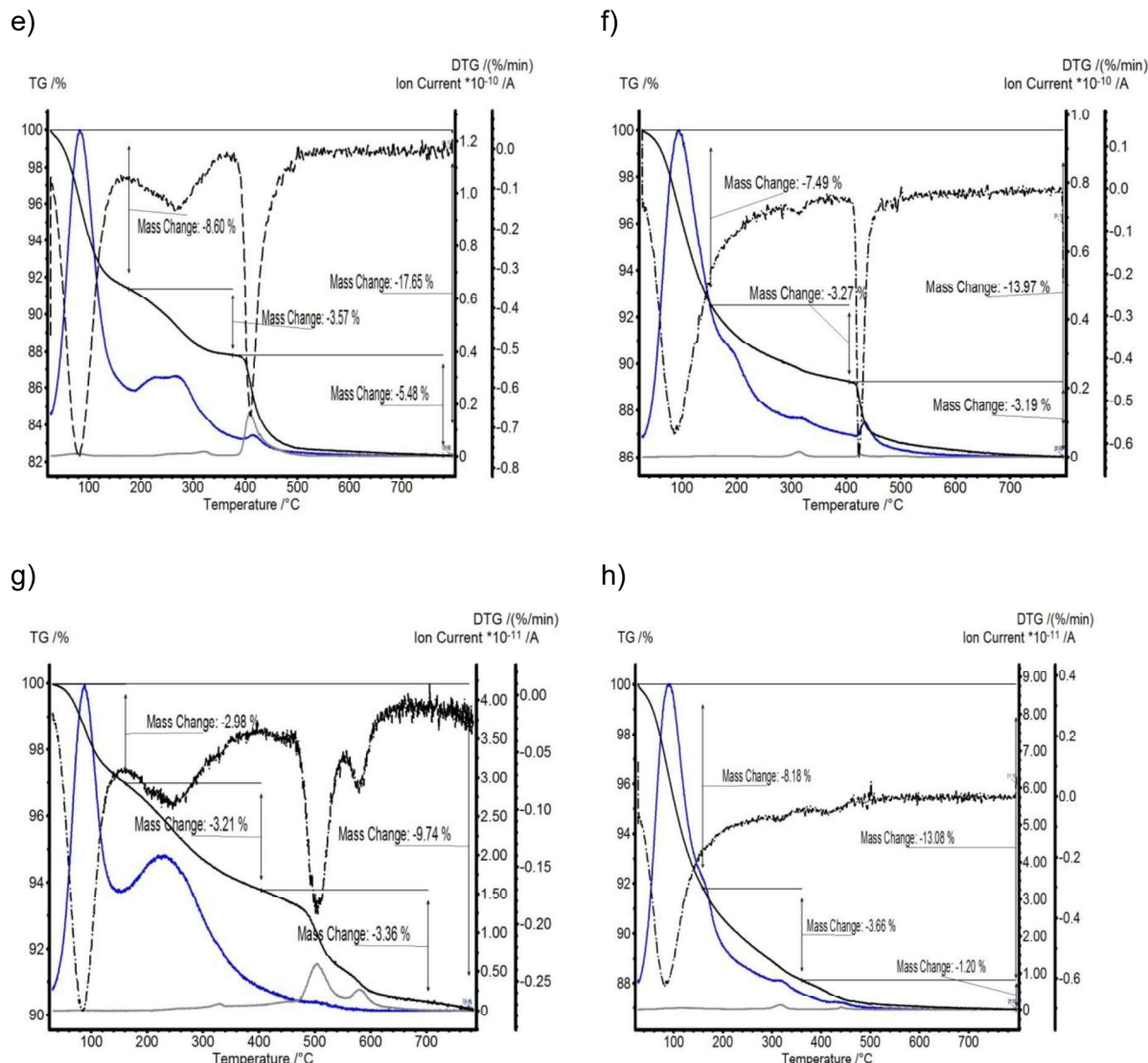


**Figure 3.9.** TGA-DSC-MS analysis performed under 21 %  $\text{O}_2$  / Ar at the Fritz Haber Institute in Berlin, Germany for a) commercial rutile  $\text{IrO}_2$  b) commercial  $\text{IrO}_2\text{-}2\text{H}_2\text{O}$  c)  $\text{IrO}_2\text{-Li}_2\text{CO}_3$  d)  $\text{IrO}_2\text{-LiOH}$  e)  $\text{IrO}_2\text{-Na}_2\text{CO}_3$  f)  $\text{IrO}_2\text{-NaOH}$  g)  $\text{IrO}_2\text{-K}_2\text{CO}_3$  h)  $\text{IrO}_2\text{-KOH}$ . Solid-black line corresponds to TGA measurements, dashed-black line correspond to DSC. Grey and blue lines correspond to  $\text{CO}_2$  and  $\text{H}_2\text{O}$  detected by MS respectively.

TGA analysis unveiled that synthesised materials have a chemical formulation more complex than mere  $\text{IrO}_2$ , as opposed to commercial crystalline  $\text{IrO}_2$ , which presented no mass loss. Hydrous iridium oxo-hydroxides can be more realistically represented by the generic formula  $\text{IrO}_x(\text{OH})_y\text{-nH}_2\text{O}$ .

- *Transient hydrogen adsorption (H<sub>2</sub>-TA)*

This technique allows the detection of hydrogen consumption by the catalyst at room temperature. Crystalline rutile IrO<sub>2</sub> is thermodynamically stable and hence it does not reduce at room temperature, normally, reduction at elevated temperatures is necessary to reduce crystalline IrO<sub>2</sub> to metallic Ir. Conversely, amorphous hydrous iridium oxo-hydroxides are less thermodynamically stable compared to well-structured rutile and a characteristic feature is its hydrogen adsorption at room temperature.<sup>(8)</sup> Samples were first degased with a 100 ml·min<sup>-1</sup> He flow for 3 hours. The blank H<sub>2</sub>-TA was performed over a reactor tube filled with 250 mg of SiC and then it was compared with the reactor tube containing 25 mg of catalyst mixed with 250 mg of SiC. For the analysis 5% H<sub>2</sub> / Ar at 80 ml·min<sup>-1</sup> gas flow was used. Three different interactions with hydrogen were observed between catalysts. Commercial rutile IrO<sub>2</sub>, IrO<sub>2</sub>-LiOH and IrO<sub>2</sub>-K<sub>2</sub>CO<sub>3</sub> catalysts showed no hydrogen adsorption at room temperature. Commercial amorphous IrO<sub>2</sub>·2H<sub>2</sub>O and IrO<sub>2</sub>-KOH presented hydrogen adsorption during the first 10 minutes of reaction and hydrogen adsorption appeared as a sharp peak. IrO<sub>2</sub>-NaOH, IrO<sub>2</sub>-Na<sub>2</sub>CO<sub>3</sub> and IrO<sub>2</sub>-Li<sub>2</sub>CO<sub>3</sub> presented slower hydrogen adsorption kinetics at room temperature than the previous group of catalysts, hydrogen adsorption was observed as a broad peak that extended up to 60 minutes (figure 3.10). By comparison, no absorption would refer to a more ordered structure or to the lack of active functionalities, and fast or slow hydrogen adsorption would refer to different reducible functional groups at the surface. However, extra studies would be needed to understand the nature of the different hydrogen adsorption kinetics between catalysts.

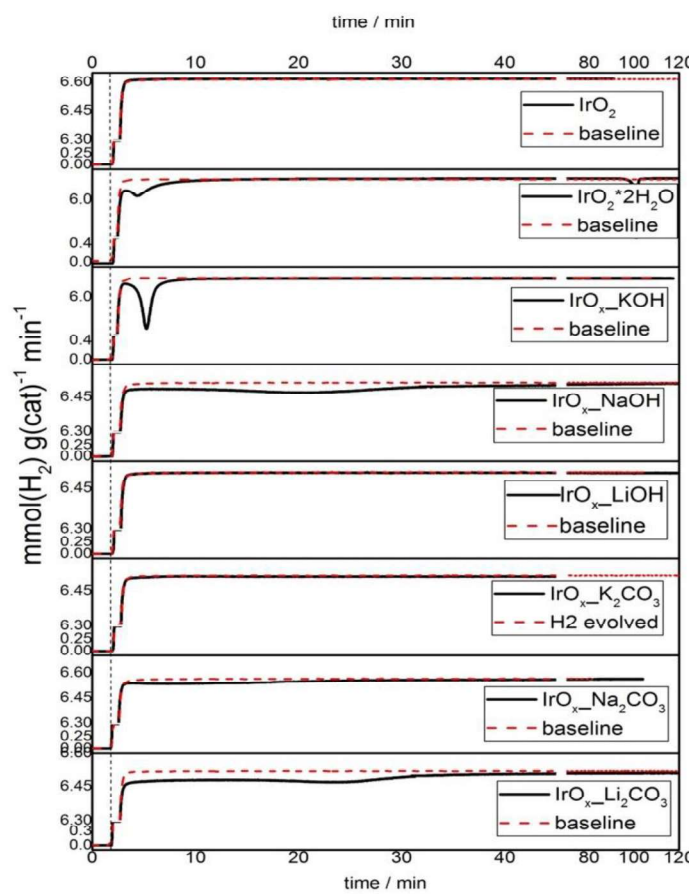


**Figure 3.10.** Transient hydrogen adsorption for  $\text{IrO}_2$  catalysts prepared with different metal alkali bases. Dotted red-line represents the blank measurement done with SiC. Solid black line represents the hydrogen adsorption for the different catalysts. Top graph represents the commercial rutile-type  $\text{IrO}_2$ .

#### - Temperature programed reduction ( $\text{H}_2\text{-TPR}$ )

After measuring the hydrogen adsorption at room temperature, the reduction behaviour of prepared  $\text{IrO}_x$  catalysts under heating were analysed by  $\text{H}_2\text{-TPR}$ . Ordered-crystalline  $\text{IrO}_2$  is thermodynamically more favourable than non-ordered amorphous  $\text{IrO}_2$ , therefore rutile- $\text{IrO}_2$  reduction occurs at higher temperatures compared to amorphous iridium oxo-hydroxide  $\text{IrO}_2$ .<sup>(18)</sup>  $\text{H}_2\text{-TPR}$  was performed from room temperature to 280 °C after the  $\text{H}_2\text{-TA}$  using the same analysis conditions, 5%  $\text{H}_2/\text{Ar}$  at  $80 \text{ ml}\cdot\text{min}^{-1}$  gas flow. In agreement with the literature, crystalline-rutile  $\text{IrO}_2$  presented a characteristic reduction peak near 250 °C. The remaining  $\text{IrO}_2$  samples, including the commercial  $\text{IrO}_2\cdot2\text{H}_2\text{O}$ , reduced between 60 °C and 110 °C according to a less ordered arrangement (figure 3.11a). When hydroxide base was used for the synthesis, reduction temperature increased from  $\text{IrO}_2\text{-KOH}$ ,  $\text{IrO}_2\text{-NaOH}$  and  $\text{IrO}_2\text{-LiOH}$ .

However the reverse trend was observed for carbonates, reduction temperature increased from  $\text{IrO}_2\text{-Li}_2\text{CO}_3$ ,  $\text{IrO}_2\text{-Na}_2\text{CO}_3$  and  $\text{IrO}_2\text{-K}_2\text{CO}_3$ .

Exhaust gases were analysed simultaneously by MS. As expected, the main product observed for all catalysts was water. However,  $\text{CO}_2$  and  $\text{CH}_4$  were also detected, being more abundant on samples prepared with carbonate bases (figure 3.11b). This observation is also in agreement with the ATR-FTIR results, which showed the presence of carbonates remaining in these samples. The minor presence of  $\text{CH}_4$ , for samples prepared with hydroxide bases, could be explained by  $\text{CO}_2$  adsorption, and consecutive hydrogenation, on the surface of the material.

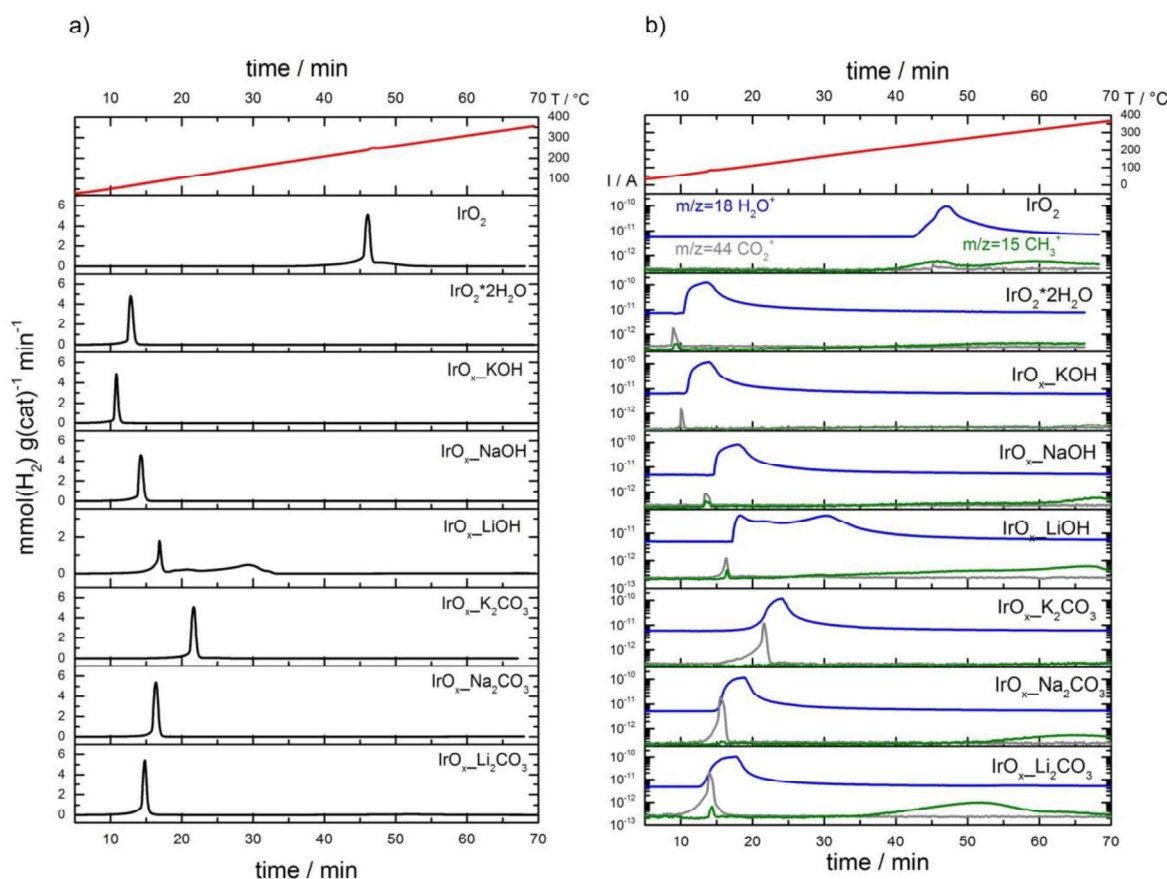


**Figure 3.11.** a)  $\text{H}_2\text{-TPR}$  and b) online MS gas composition analysis for hydrothermally prepared samples using different metal alkali bases.

A characteristic feature of amorphous iridium oxo-hydroxides is its reduction at lower temperature compared to crystalline rutile  $\text{IrO}_2$ . Hence it allowed the confirmation of the amorphous nature of the  $\text{IrO}_2$  materials, as suggested by XRD and Raman spectroscopy.

### X-ray photoelectron spectroscopy (XPS)

In order to gain a deeper understanding in the nature of iridium species present at the surface of the synthesised IrO<sub>2</sub> catalysts, XPS characterisation was carried out. XRD and Raman spectroscopy characterisation has shown that materials presented an amorphous structure. In addition, TGA and H<sub>2</sub> adsorption at room temperature and H<sub>2</sub>-TPR indicated that synthesised samples have a hydrous iridium oxo-hydroxide complex structure. High active amorphous IrO<sub>2</sub> have been widely associated with the presence of Ir(III) and Ir(IV) sites. XPS is a key characterisation technique to determine the presence of different oxidation states and element speciation and hence it was used to determine variations from commercial rutile IrO<sub>2</sub>.

Ir(4f) and O(1s) core-levels for single crystal IrO<sub>2</sub> have been shown to be asymmetric as a result of its conductive metallic-like properties. However, normal fitting curves used for metallic samples are not suitable for IrO<sub>2</sub><sup>(29)</sup> making the Ir(4f) orbital speciation challenging due to combined influence of band structure (4f and 5p),<sup>(23)</sup> electron correlation and spin-orbit coupling on the electronic structure.<sup>(29, 30)</sup>

Recent studies on commercial rutile IrO<sub>2</sub> and amorphous IrO<sub>2</sub>, from Sigma Aldrich and Alfa Aesar respectively, were thoroughly characterised by Pfeifer *et al.*<sup>(10)</sup> by synchrotron-based XPS. It was concluded that rutile-type IrO<sub>2</sub> was composed entirely of Ir(IV), while amorphous IrO<sub>2</sub> consisted of a mixture of Ir(IV) and Ir(III). To simplify comparison between samples, standard materials were purchased from the same commercial suppliers, crystalline IrO<sub>2</sub> from Sigma Aldrich and amorphous IrO<sub>2</sub> from Alfa Aesar. Amorphous IrO<sub>2</sub> presented a shift towards higher binding energy and a much broader Ir(4f) (figure 3.12a) and O(1s) orbital envelope compared to rutile-like IrO<sub>2</sub>, in agreement with results obtained by Pfeifer. Since commercial rutile IrO<sub>2</sub> is considered to be composed entirely of Ir(IV) sites, the Ir(4f) line shape obtained from the commercial rutile IrO<sub>2</sub> in our XPS system (represented with a red line in the Ir(4f) orbital) would be considered as the lattice Ir(IV) contribution for the following analysed samples. When compared with other samples, envelope broadening (represented with a blue line in the Ir(4f) orbital) would be assumed to be responsible from either the presence of Ir(III) sites or the hydration of IrO<sub>2</sub>. In accordance with complete Ir(IV) presence for the commercial rutile IrO<sub>2</sub>, O(1s) was composed entirely of the oxide form, the presence of the shoulder on the O(1s) orbital corresponded to a satellite contribution. whilst, commercial amorphous IrO<sub>2</sub> presented a broader and shifted towards higher binding energy O(1s) peak, which can be deconvoluted into: oxide, hydroxide and water (fitting parameters

reported previously by Morgan *et. al.*,<sup>(23)</sup>). Hydroxide was the main form of oxygen in the amorphous commercial sample (figure 3.12b).

It is worth remarking that XPS is a surface sensitive technique, and hence, the bulk of the material could still be in the form of oxide, but a major hydroxide presence at the surface would enhance the oxide to hydroxide speciation ratio.<sup>(23)</sup>

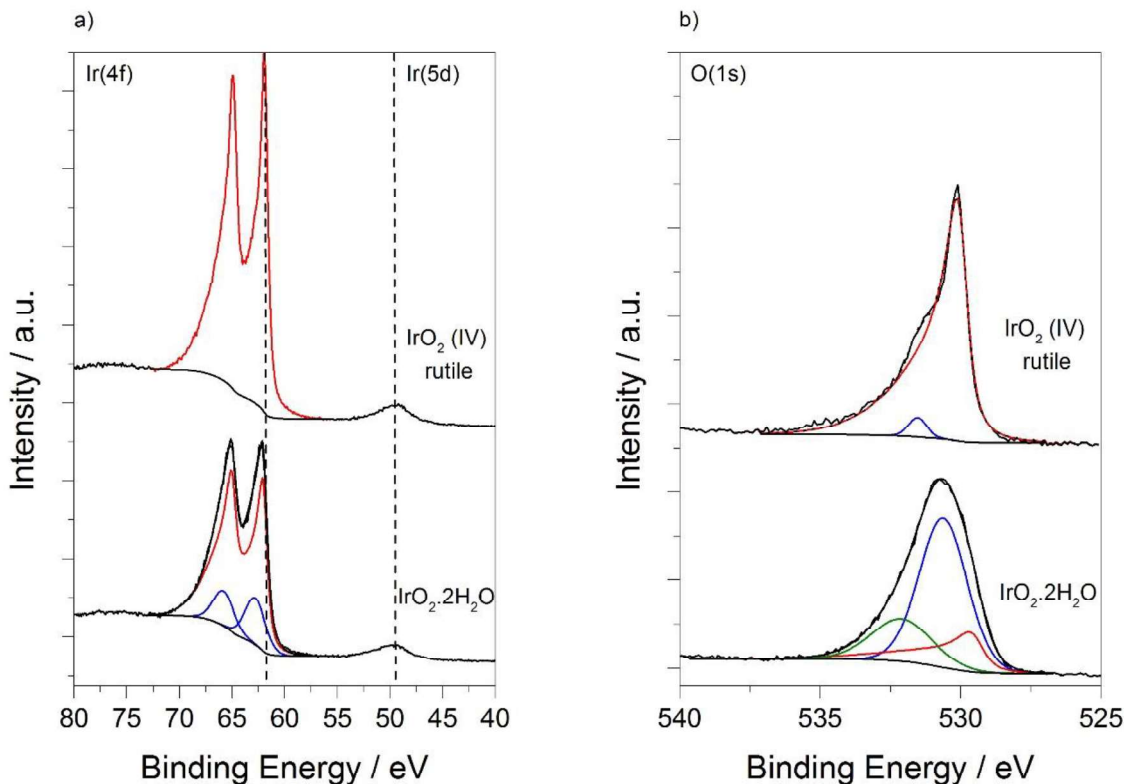


**Figure 3.12.** a) Ir(4f) and b) O(1s) XPS analysis for commercial rutile and amorphous  $\text{IrO}_2$  catalysts. The red line for amorphous  $\text{IrO}_2 \cdot 2\text{H}_2\text{O}$  on the Ir(4f) orbital corresponds to the line shape of  $\text{IrO}_2$  (IV) rutile. Lattice oxygen, hydroxide and water in the O(1s) are represented with a red, blue and green line respectively.

$\text{IrO}_2$  catalysts synthesised using different bases were compared against the  $\text{IrO}_2$ -rutile commercial standard using the same approach. The line shape of rutile  $\text{IrO}_2$  was transferred to the Ir(4f) orbital for determining the presence of Ir(IV), the extra necessary fitting for filling the shape would be considered to correspond to the presence of Ir(III) sites and/or surface hydroxide contributions.

Regardless of the base used during the synthesis, the Ir(4f) peak was shifted towards higher binding energy and presented a broader line shape compared to the crystalline standard

sample (figure 3.13). This, as elucidated previously, apart from the presence of lattice Ir(IV) sites can be associated with the presence of Ir(III) or to the presence of hydroxide groups at the surface, but without implying a change in the oxidation state. TGA analysis showed that all analysed materials, with the exception of rutile  $\text{IrO}_2$ , have a considerably amount of physisorbed water, which in correlation with the Ir-O vibration observed by IR, lead to the conclusion that surface hydroxide groups do exist in the prepared materials. Thus, most probably the Ir(4f) peak broadening would be attributed to both contributions, the presence of Ir(III) sites as suggested by Pfeifer and to surface hydroxide groups as observed by TGA.

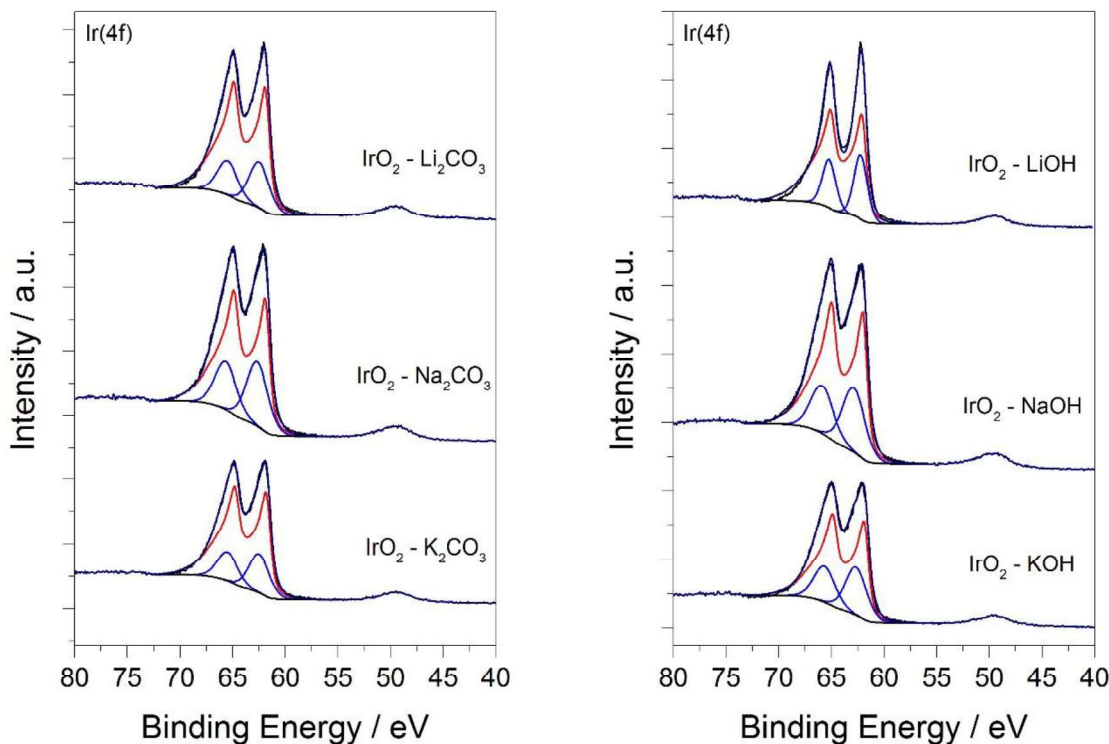


**Figure 3.13.** Ir(4f) XPS scan for  $\text{IrO}_2$  catalysts synthesised with different bases. Red line corresponds to the line shape of rutile  $\text{IrO}_2$ .

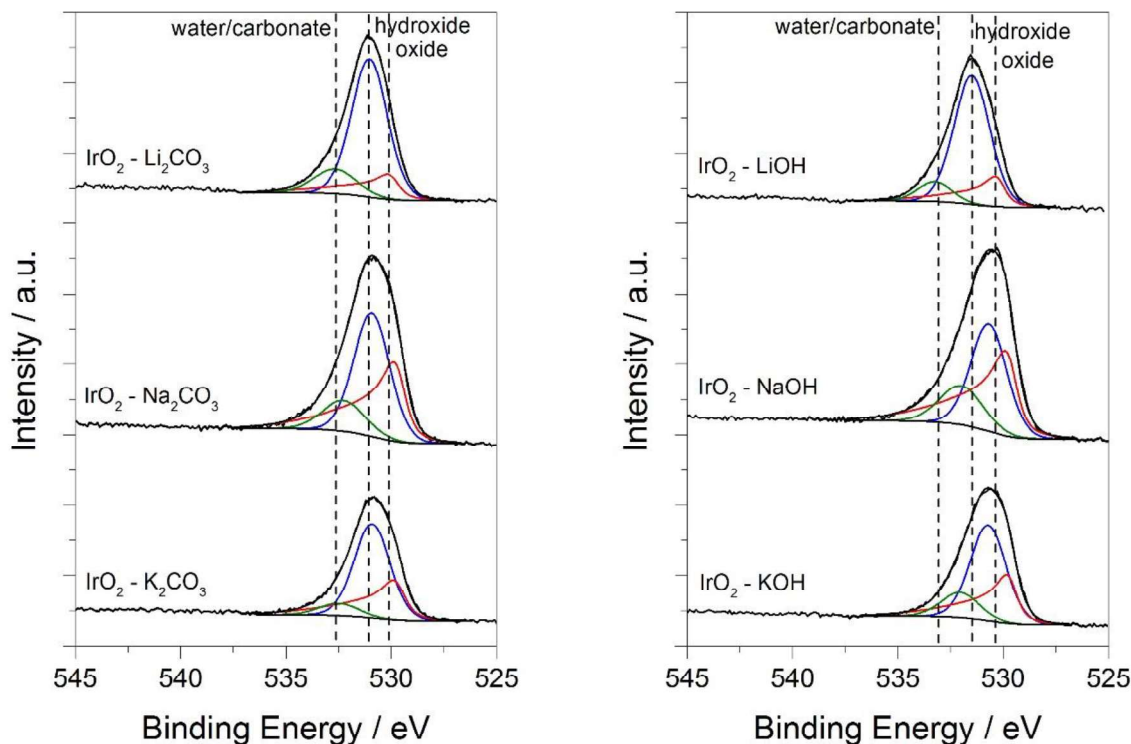
The O(1s) orbital for synthesised samples (figure 3.14), broader and shifted approximately by 1 eV towards higher binding energy compared to rutile  $\text{IrO}_2$ , also indicated the presence of diverse oxygen species. According to published literature,<sup>(23, 31)</sup> oxygen from iridium oxide appears as an asymmetric peak at 530.5 eV, iridium hydroxides are present at 531.6 eV and a small contribution of water and/or carbonates is present at 532.9 eV.

Table 3.2 shows an approximation of the surface composition obtained from the quantification of the different oxygen components assigned in the O(1s) peak. As observed,

the amount of water, physisorbed and/or chemisorbed, do not significantly change among catalysts regardless of the base:  $30 \pm 10\%$ . Catalysts prepared with lithium-containing bases presented the lowest oxide concentration and the highest hydroxide proportion compared to materials prepared with potassium and sodium bases. No differences in the surface chemical composition were observed depending on the nature of the base, hydroxide or carbonate, with the same cation.

**Table 3.2.** Empirical formula for prepared  $\text{IrO}_x$  catalysts obtained from the oxide, hydroxide and water proportion calculated from the O(1s) peak.

catalyst	empirical formula	catalyst	Empirical formula
*Rutile $\text{IrO}_2$	$\text{IrO}_2$	$^*\text{IrO}_{2.4}\cdot 2\text{H}_2\text{O}$	$\text{IrO}_{0.4}(\text{OH})_{1.2}\cdot 0.4\text{H}_2\text{O}$
$\text{IrO}_2\text{-LiOH}$	$\text{IrO}_{0.4}(\text{OH})_{1.4}\cdot 0.2\text{H}_2\text{O}$	$\text{IrO}_2\text{-Li}_2\text{CO}_3$	$\text{IrO}_{0.3}(\text{OH})_{1.4}\cdot 0.3\text{H}_2\text{O}$
$\text{IrO}_2\text{-NaOH}$	$\text{IrO}_{0.8}(\text{OH})_{0.8}\cdot 0.4\text{H}_2\text{O}$	$\text{IrO}_2\text{-Na}_2\text{CO}_3$	$\text{IrO}_{0.8}(\text{OH})_{0.9}\cdot 0.3\text{H}_2\text{O}$
$\text{IrO}_2\text{-KOH}$	$\text{IrO}_{0.6}(\text{OH})_{1.0}\cdot 0.3\text{H}_2\text{O}$	$\text{IrO}_2\text{-K}_2\text{CO}_3$	$\text{IrO}_{0.7}(\text{OH})_{1.2}\cdot 0.2\text{H}_2\text{O}$

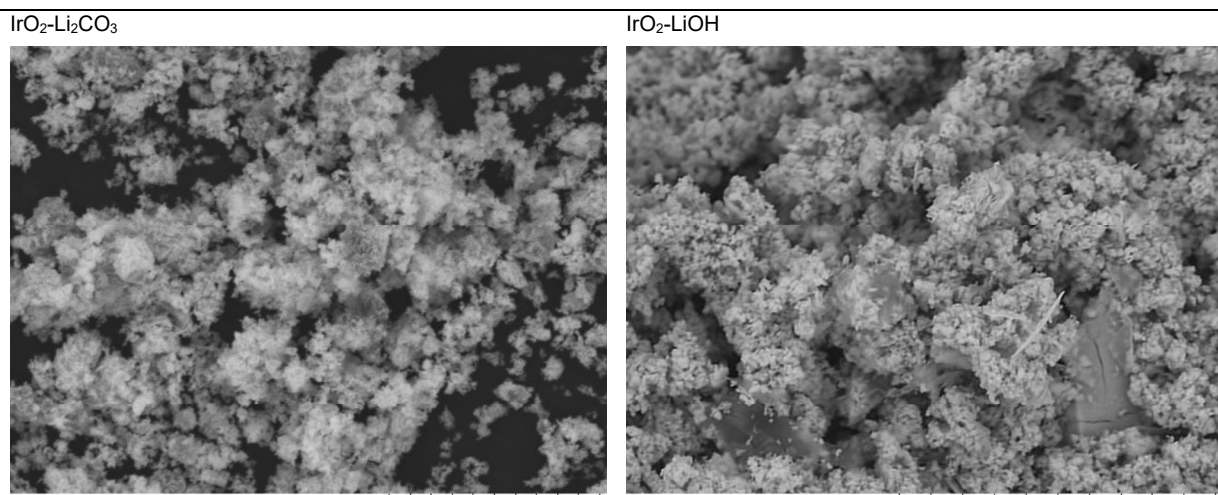


**Figure 3.14.** O(1s) XPS characterisation for  $\text{IrO}_2$  catalysts synthesised with different bases. Oxide, hydroxide and water/carbonates represented in red, blue and green respectively.

*Scanning electron microscopy (SEM)*

TGA and XPS characterisation indicated that prepared IrO<sub>2</sub> have a more complex formulation, IrO<sub>2-1/2x</sub>(OH)<sub>x</sub>·nH<sub>2</sub>O, with the presence of physisorbed and chemisorbed water. XRD and Raman spectroscopy unveiled the catalysts amorphous arrangement. However, the uses of different bases have not lead to significant changes among materials apart from the different H<sub>2</sub> adsorption kinetics.

SEM allowed the macroscopic differences in the morphology of catalysts to be determined (image 3.2). From the images obtained, it was clear that the cation from the base present during the synthesis has an effect on controlling the final morphology of IrO<sub>2</sub>, this independently of the hydroxide or carbonate nature of the base. When potassium was present during the synthesis, large flat surfaces were observed on IrO<sub>2</sub>. For bases containing lithium, sponge-like morphology was observed. The use of sodium bases led to an intermediate morphology, flat surfaces and sponge-like regions were observed. Differences in the morphology were also observed between commercial IrO<sub>2</sub> samples, rutile IrO<sub>2</sub> was more similar to potassium based catalysts whereas amorphous IrO<sub>2</sub> was closer to lithium based catalysts with the presence of small aggregates. SEM-EDX analyses showed an atomic concentration close to 2 % of K and Na impurities. Li was too light to be detected by EDX, however, it could be assumed that it would be present in the same proportion as K<sup>+</sup> and Na<sup>+</sup>.



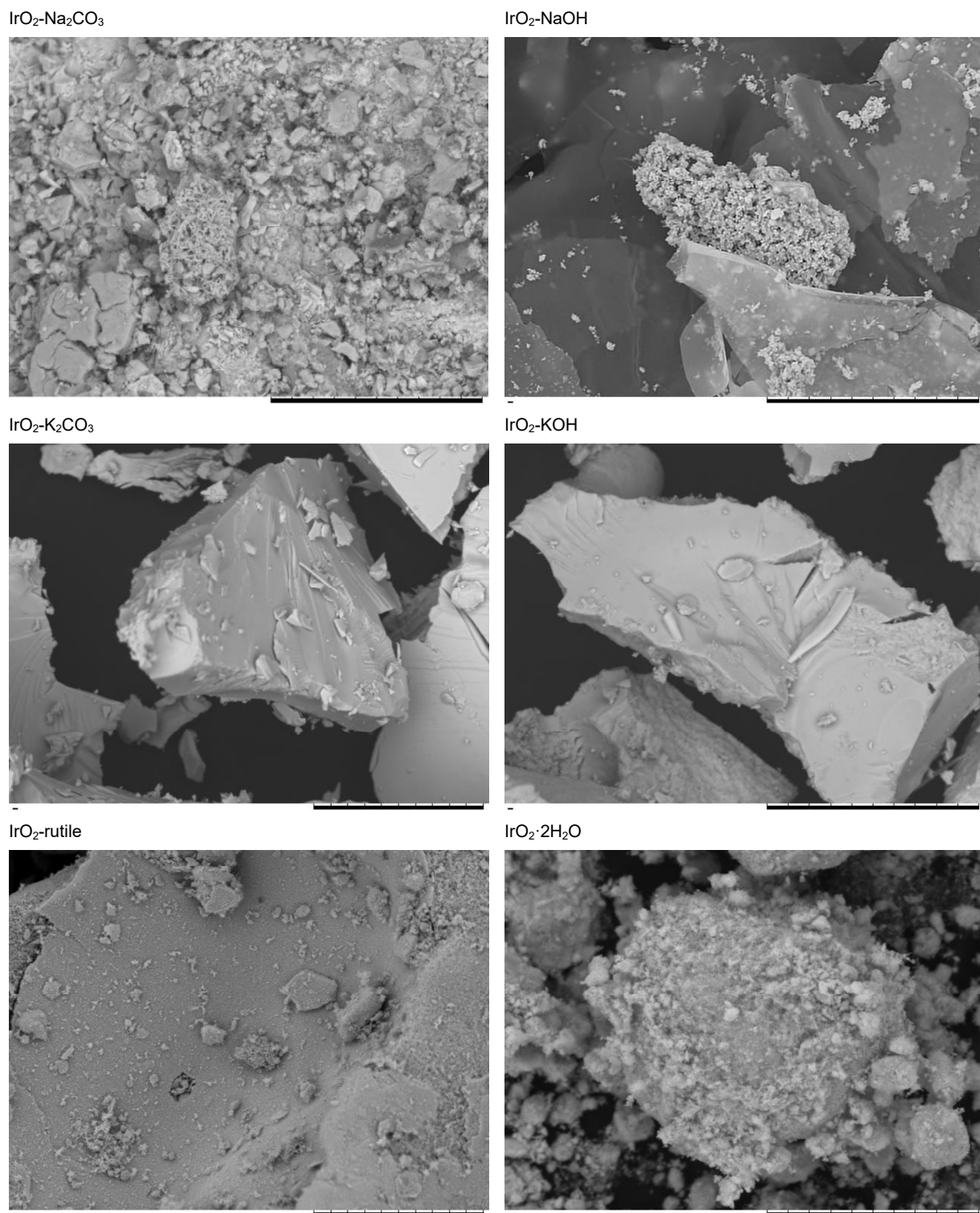


**Image 3.2.** SEM images for  $\text{IrO}_2$ -base prepared samples. The scale bar for Li and Na prepared samples correspond to 30  $\mu\text{m}$ , scale bar for commercial samples and K prepared samples correspond to 50  $\mu\text{m}$ .

The different morphology observed by SEM could have an effect on the surface area of the  $\text{IrO}_2$  catalysts. Because large particles with flat surfaces were observed for  $\text{IrO}_2\text{-KOH}$  and

$\text{IrO}_2\text{-K}_2\text{CO}_3$  catalysts, it would be expected that they would have lower surface area compared to the rest of the materials, and  $\text{IrO}_2\text{-LiOH}$  and  $\text{IrO}_2\text{-Li}_2\text{CO}_3$  would be expected to have higher surface area as a result of the sponge like morphology. Due to the considerably amount of physisorbed and chemisorbed water within the prepared catalysts, as indicated by TGA and XPS characterisation, prior to the BET surface area analysis catalyst were dried in a muffle for 20 h at 130 °C, and an additional heating step at 130 °C for 16 h under vacuum in the instrument was performed. As presented in table 3.3,  $\text{IrO}_2\text{-Li}_2\text{CO}_3$  and  $\text{IrO}_2\cdot 2\text{H}_2\text{O}$  had comparable high surface area compared to the rest of the materials. The measured surface area for  $\text{IrO}_2\text{-Li}_2\text{CO}_3$  dramatically dropped when sodium or potassium bases were used during the synthesis, approaching the low surface area for commercial crystalline  $\text{IrO}_2$ .

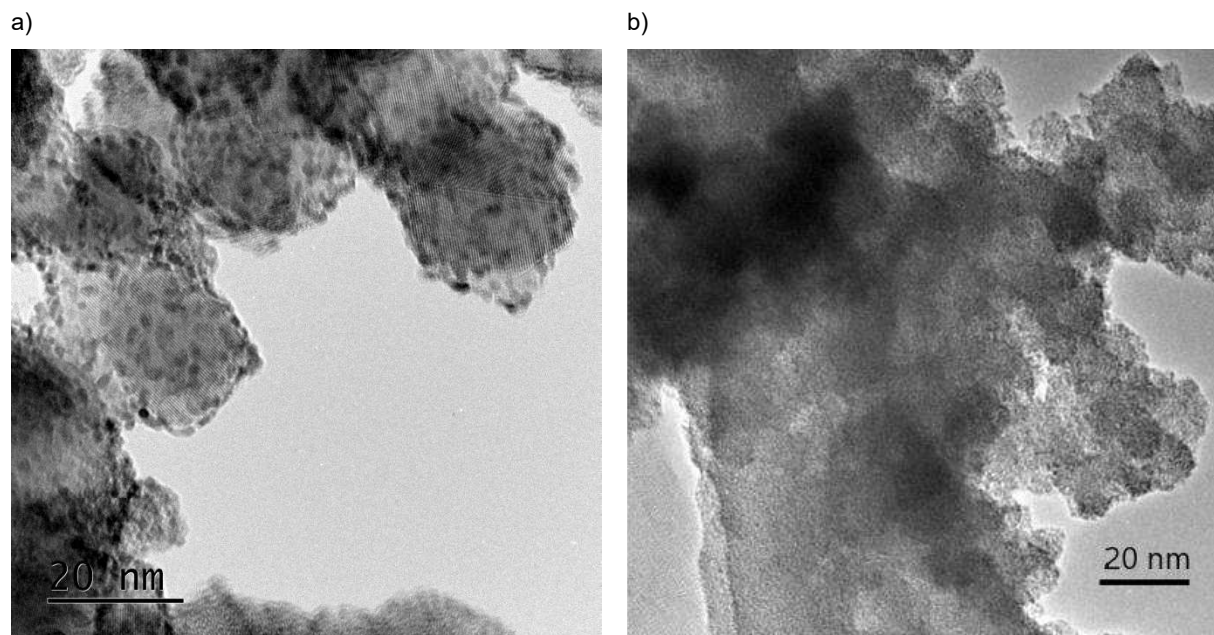
**Table 3.3.** BET surface area analysis for prepared  $\text{IrO}_2$  with different alkali metal bases.

catalyst	BET surface area $\text{m}^2/\text{g}_{\text{cat}}$	catalyst	BET surface area $\text{m}^2/\text{g}_{\text{cat}}$
Rutile $\text{IrO}_2$	2	$\text{IrO}_2\cdot 2\text{H}_2\text{O}$	33
$\text{IrO}_2\text{-LiOH}$	10	$\text{IrO}_2\text{-Li}_2\text{CO}_3$	35
$\text{IrO}_2\text{-NaOH}$	3	$\text{IrO}_2\text{-Na}_2\text{CO}_3$	3
$\text{IrO}_2\text{-KOH}$	1	$\text{IrO}_2\text{-K}_2\text{CO}_3$	1

#### *Electron transmission microscopy (TEM)*

In materials science, electron microscopy is a useful technique in order to understand in depth a catalytic system, as it can be used to correlate catalytic activity with the catalyst structure. As a drawback, it requires expensive equipment and cannot be used as a standard technique for characterising materials. In a TEM microscope, a uniform beam of electrons is transmitted through the sample. By different interactions with the atoms in the sample, the electron beam is altered, which allows to form an image of the material. In order to confirm the amorphous nature of prepared samples, as indicated by XRD, Raman spectroscopy and H<sub>2</sub>-TPR,  $\text{IrO}_2\text{-Li}_2\text{CO}_3$  catalyst was analysed by TEM. The more accessible TEM placed in Cardiff University (JEM 2100 LaB6) was first used for the analysis. The material seemed to be composed of 20 nm domains of crystalline-rutile  $\text{IrO}_2$  covered with 1-2 nm small particles (image 3.3a). This information contradicts the characterisation undertaken previously. As observed during the Raman spectroscopy measurements, amorphous  $\text{IrO}_2\text{-Li}_2\text{CO}_3$  was prone to structural changes depending on the laser intensity used during the

acquisition, with the crystallisation of the amorphous materials as a consequence of Raman spectroscopy damage also reported before for carbons.<sup>(32)</sup> Likewise, but through another excitation pathway, the interaction of high energy electrons, necessary for TEM imaging, with materials has been widely reported to produce structural changes on sensitive specimens, commonly known as beam damage.<sup>(33)</sup> As shown in image 3.3a, prepared  $\text{IrO}_2\text{-Li}_2\text{CO}_3$  catalyst was prone to beam damage under the TEM measuring conditions. Recently, it was published by Willinger *et al.* that using low dose imaging TEM is a suitable alternative for imaging amorphous  $\text{IrO}_2$  without being beam damaged.<sup>(26)</sup> From the valuable networking opportunity provided by the MaxNet energy consortium, Dr. Gerardo Algara Siller from the Fritz Haber Institute analysed the  $\text{IrO}_2\text{-Li}_2\text{CO}_3$  catalyst on a TITAN 80-300 HR-TEM operated at 200 kV. Under low dose TEM no crystalline planes could be observed on the analysed areas (image 3.3b). Similarly, nano-beam electron diffraction does not show any crystalline reflections (image 3.3c and 3.3d). Thus, confirming that the  $\text{IrO}_2\text{-Li}_2\text{CO}_3$  catalyst was completely amorphous. Unfortunately, the other synthesised materials could not be analysed by low-dose TEM. However, in correlation with XRD and Raman characterisation, an amorphous arrangement could be expected for the other synthesised catalysts.



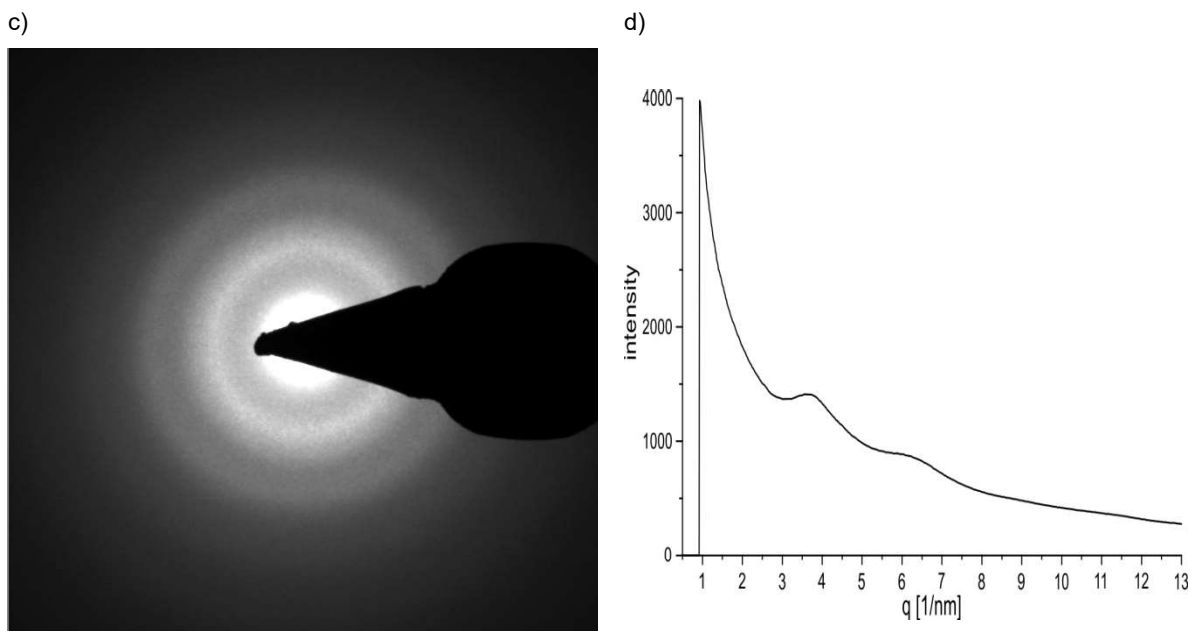


**Image 3.3.** a)  $\text{IrO}_2\text{-Li}_2\text{CO}_3$  sample analysed in a JEM 2100 TEM. b)  $\text{IrO}_2\text{-Li}_2\text{CO}_3$  image, c) electron diffraction pattern and d) radial profile of the electron diffraction pattern analysed in a low dose TITAN 80-300 HRTEM.

### 3.2.3 Catalysts activity towards OER.

$\text{IrO}_2$  prepared with different bases were tested on a flow cell provided by collaborators from the Max Planck Institute for Chemical Energy Conversion in Mülheim, Germany. Commercial  $\text{IrO}_2$ , crystalline and amorphous, were tested previously in Mülheim using a similar replica of the reactor.<sup>(34)</sup> The electrochemical flow cell and the electrode preparation protocol to obtain a  $\text{IrO}_x$  concentration of  $100 \mu\text{g}_{\text{cat}}\cdot\text{cm}^{-2}$  were described in detail in the experimental section.

The electrochemistry protocol performed on  $\text{IrO}_2$  materials for assessing catalysts activity and stability towards OER was as follows: LSV from  $1.2 \text{ V}_{\text{RHE}}$  to  $1.8 \text{ V}_{\text{RHE}}$  at  $5 \text{ mV}\cdot\text{s}^{-1}$ , 50 CV cycles between  $0.7 \text{ V}_{\text{RHE}}$  and  $1.4 \text{ V}_{\text{RHE}}$  at  $50 \text{ mV}\cdot\text{s}^{-1}$ , LSV from  $1.2 \text{ V}_{\text{RHE}}$  to  $1.8 \text{ V}_{\text{RHE}}$  at  $5 \text{ mV}\cdot\text{s}^{-1}$ , CP for 2 hours at  $10 \text{ mA}\cdot\text{cm}^{-2}$  and LSV from  $1.2 \text{ V}_{\text{RHE}}$  to  $1.8 \text{ V}_{\text{RHE}}$  at  $5 \text{ mV}\cdot\text{s}^{-1}$ . All measurements were performed on  $1.2 \text{ mL} / \text{min}$  flow of  $0.1 \text{ M HClO}_4$  electrolyte.

Intrinsic catalyst activity was determined by LSV at the beginning of the experiment, the potential at what current density is observed corresponds to the on-set potential, or the potential at what OER takes place. LSV was also performed after CV and after CP in order to observe any degradation of the material after measurements, indicated by a shift in the on-set potential.

The initial activity determined by LSV for standard catalysts was in agreement with previous published data comparing commercial amorphous oxo-hydroxide and crystalline rutile  $\text{IrO}_2$  towards OER.<sup>(5, 34)</sup> Rutile  $\text{IrO}_2$  showed almost no current density for the whole LSV scan range, as a consequence of the absence of hydroxide groups and the lack of  $\text{Ir}^{\text{III}}/\text{Ir}^{\text{IV}}$  sites. Oxygen evolution was detected at  $1.48 \text{ V}_{\text{RHE}}$  for commercial  $\text{IrO}_2\cdot 2\text{H}_2\text{O}$  (figure 3.14).

$\text{IrO}_2\text{-K}_2\text{CO}_3$ ,  $\text{IrO}_2\text{-KOH}$ ,  $\text{IrO}_2\text{-Na}_2\text{CO}_3$  and  $\text{NaOH}$  catalysts presented lower activity than commercial  $\text{IrO}_2\cdot 2\text{H}_2\text{O}$ , which might account from its low surface area, comparable to rutile  $\text{IrO}_2$ , and its more surface oxide nature as elucidated by XPS. Interestingly, lithium-base prepared catalysts,  $\text{IrO}_2\text{-Li}_2\text{CO}_3$  and  $\text{IrO}_2\text{-LiOH}$ , presented enhanced activity compared to the rest of the bases used. The initial OER activity measured for  $\text{IrO}_2\text{-LiOH}$  overlapped with the activity of commercial amorphous  $\text{IrO}_2$  ( $5 \text{ mA}\cdot\text{cm}^2$  at  $1.52 \text{ V}_{\text{RHE}}$ ), albeit having a third of the surface area, while  $\text{IrO}_2\text{-Li}_2\text{CO}_3$  outperformed the commercial catalyst by  $25 \text{ mV}$  at  $5 \text{ mA}\cdot\text{cm}^{-2}$  (figure 3.15). Therefore, the surface area of a catalyst is not directly related to its activity towards OER. Thus, other factors, such as the concentration of  $\text{Ir}(\text{III})$  sites or surface hydroxide groups, would have a greater contribution in the activity. From prepared catalysts, considering the differences in surface area and morphology that also affects the activity, the least proportion of oxide and the higher concentration of hydroxide, obtained by XPS, seems to account positively in the activity towards OER.

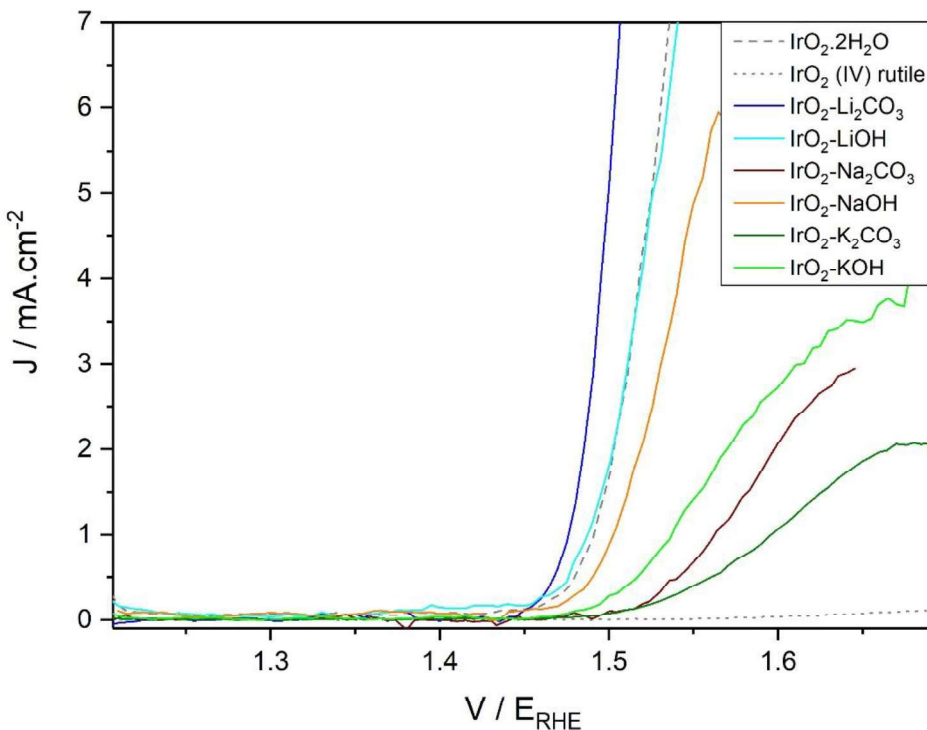


**Figure 3.15.** Initial LSV from 1.2  $V_{\text{RHE}}$  to 1.8  $V_{\text{RHE}}$  at 5 mV/s scan rate performed on prepared  $\text{IrO}_2$  using different alkali metal bases and compared with commercial  $\text{IrO}_2$  standards.

In order to determine the stability of the catalysts, chronopotentiometry for 2 hours at 10  $\text{mA}\cdot\text{cm}^{-2}$  was performed. The potential required in order to keep a constant current density at 10  $\text{mA}\cdot\text{cm}^{-2}$  is an indication of the stability of the catalysts. Stable catalyst would show steady potential while unstable catalyst would present a rise in the potential during reaction. As for commercial standards, rutile  $\text{IrO}_2$  presented a sharp increase in the potential up to 2.2  $V_{\text{RHE}}$ , which corresponded with the glassy carbon corrosion. Amorphous  $\text{IrO}_2\cdot2\text{H}_2\text{O}$  presented a slight but steady increase through time in the observed potential. This indicated that the catalyst was deactivating as the reaction proceeded. All synthesised catalyst, apart from  $\text{IrO}_2\text{-LiOH}$  and  $\text{IrO}_2\text{-Li}_2\text{CO}_3$ , presented poor stability (figure 3.16) and the glassy carbon corrosion potential was observed after just 2 minutes for  $\text{IrO}_2\text{-Na}_2\text{CO}_3$ ,  $\text{IrO}_2\text{-NaOH}$ ,  $\text{IrO}_2\text{-K}_2\text{CO}_3$  and  $\text{IrO}_2\text{-KOH}$  catalysts.  $\text{IrO}_2\text{-LiOH}$  showed the same performance as commercial  $\text{IrO}_2\cdot2\text{H}_2\text{O}$  with a 170 mV increase in the potential within the experiment duration, whereas  $\text{IrO}_2\text{-Li}_2\text{CO}_3$  presented higher stability with the measured potential almost constant (12 mV potential increase in two hours of reaction).

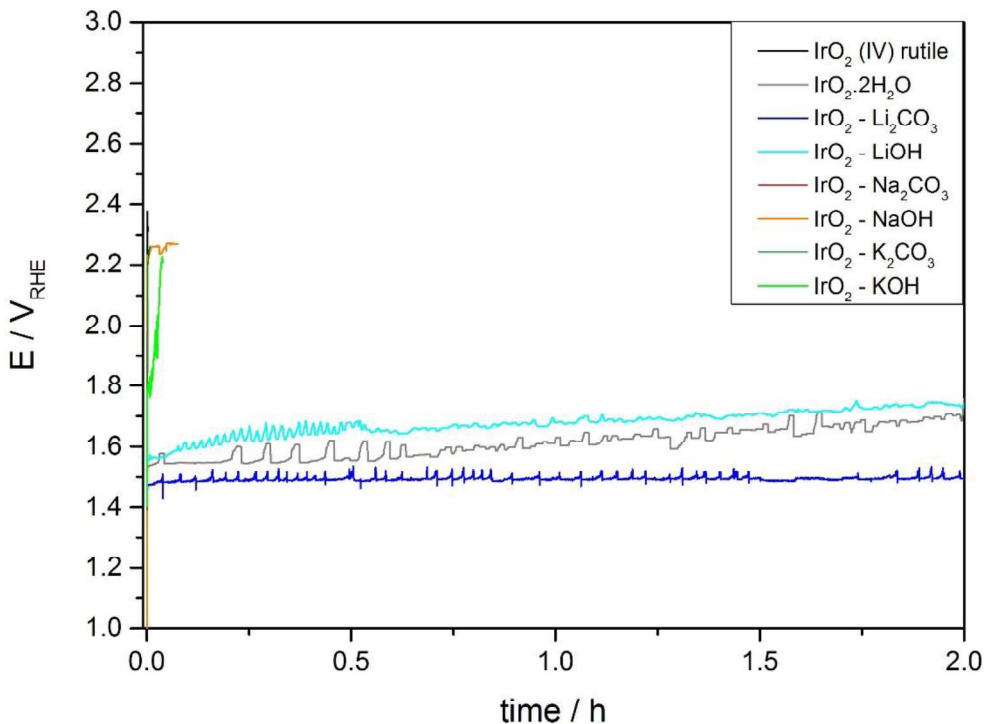
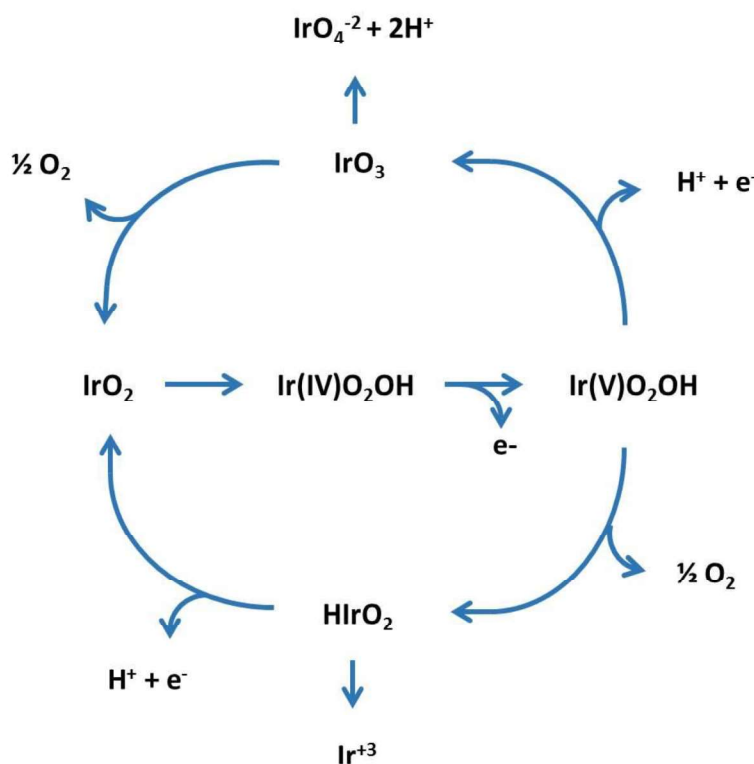


**Figure 3.16.** Chronopotentiometry at  $10 \text{ mA.cm}^{-2}$  current density for 2 hours for synthesised  $\text{IrO}_2$ -base materials and compared against commercial standards.

One explanation for the increase in potential through time could be due to iridium leaching out of the electrode. It has been suggested that the oxygen evolution reaction and iridium dissolution share common intermediates.<sup>(35)</sup> A simplified version of the proposed mechanism in acidic media is as follows, water discharge is believed to form OH radicals at the surface of the  $\text{IrO}_2$ , then  $\text{Ir(IV)}$  converts to  $\text{Ir(V)}$  by the loss of one electron to form  $\text{Ir(V)}\text{O}_2\text{OH}$ . On one hand this intermediate can decompose to  $\text{Hlr(III)}\text{O}_2$  releasing  $\text{O}_2$ , in order to close the cycle  $\text{Hlr(III)}\text{O}_2$  can be transformed back to  $\text{IrO}_2$  or alternatively it can dissolve as  $\text{Ir(III)}$ . On the other hand,  $\text{Ir(V)}\text{O}_2\text{OH}$  intermediate can be further oxidised to unstable  $\text{IrO}_3$ , which in turn can decompose to  $\text{IrO}_2$  and  $\text{O}_2$  or alternatively dissolve as  $\text{IrO}_4^{2-}$  (scheme 3.1). Another factor contributing to the instability of  $\text{IrO}_2$  is the oxygen formation. During OER,  $\text{O}_2$  is produced at the surface of the electrode; if it is not detached from the electrode efficiently it agglomerates with other oxygen molecules forming a bubble and blocking the contact between active sites and the electrolyte. This causes an increase in the overpotential which could lead to catalyst detachment from the electrode<sup>(36)</sup> as indicated by the potential fluctuation observed for  $\text{IrO}_2\text{-Li}_2\text{CO}_3$ ,  $\text{IrO}_2\text{-LiOH}$  and commercial  $\text{IrO}_2\cdot 2\text{H}_2\text{O}$ .



**Scheme 3.1.** Proposed mechanism for OER and  $\text{IrO}_2$  dissolution, both pathways share common intermediates.<sup>(35)</sup>

In order to facilitate catalyst stability comparison, two easy calculations were made. Firstly, the increase in the potential to reach a current density of  $5 \text{ mA}\cdot\text{cm}^{-2}$  between the initial LSV measurement and the LSV recorded after the CP test were compared in figure 3.16, black columns. Dashed columns indicate that the catalyst was unable to reach the established current density of  $5 \text{ mA}\cdot\text{cm}^{-2}$  after the stability test. Secondly, the red columns in figure 3.17 represent the increase in the potential to maintain a constant current density of  $10 \text{ mA}\cdot\text{cm}^{-2}$  during the CP stability test. Dashed lines indicate that the glassy carbon corrosion potential was reached during the stability test.

It was observed that  $\text{IrO}_2\text{-LiOH}$  showed an increase of 170 mV in the potential similar to the commercial  $\text{IrO}_2\cdot 2\text{H}_2\text{O}$ , although the synthesised catalyst showed greater deactivation, since after the stability test the current density threshold of  $5 \text{ mA}\cdot\text{cm}^{-2}$  was not reached in the LSV measured at the end of the experiment. It is also highlighted the enhancement in activity and stability of the synthesised  $\text{IrO}_2\text{-Li}_2\text{CO}_3$  compared to the commercially available  $\text{IrO}_2\cdot 2\text{H}_2\text{O}$ .

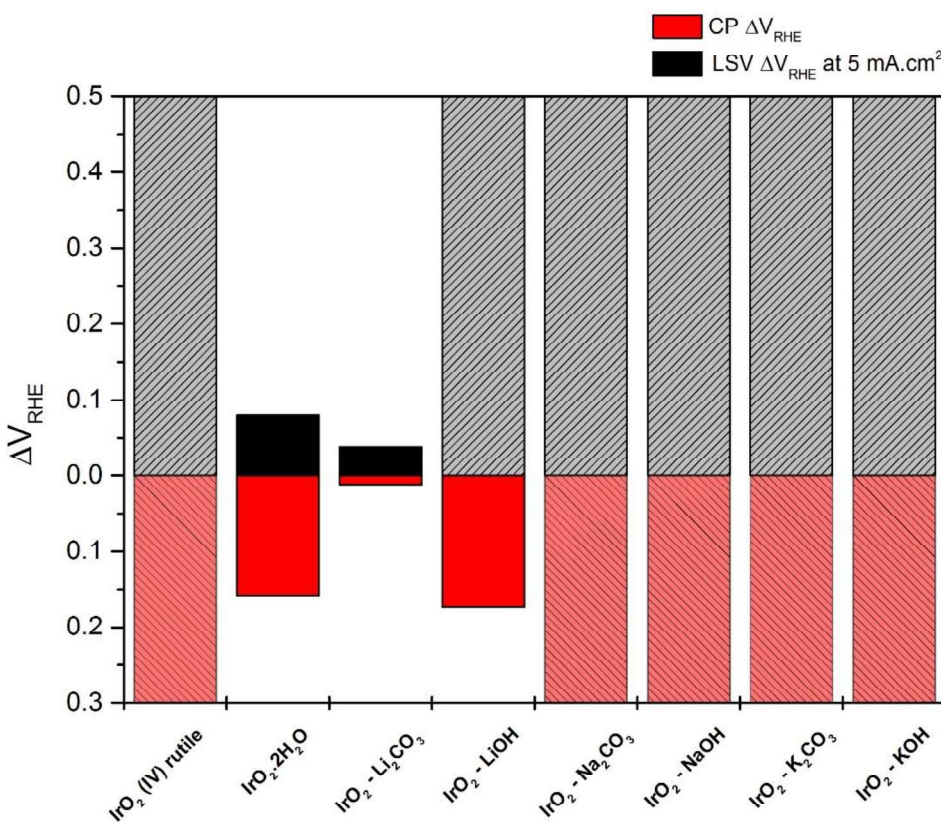


**Figure 3.17.** Catalysts stability and activity markers comparison determined by the increase in the potential measured in the LSV experiment to reach a current density of  $5 \text{ mA} \cdot \text{cm}^{-2}$  at the beginning and at the end of the experiment (black columns) and the increase in the potential during the CP at  $10 \text{ mA} \cdot \text{cm}^{-2}$  for 2 h (red columns).

Unambiguously, the base used in the hydrothermal synthesis of  $\text{IrO}_2$  catalysts has an effect on its final morphology. It also has an important effect on tailoring the activity and stability of the catalysts towards the OER reaction.  $\text{Li}_2\text{CO}_3$  seemed to enhance the electrochemical properties of  $\text{IrO}_2$  compared to other alkali metal bases studied in this work. In the catalysts preparation procedure, annealing, even at low temperature, was not conducted. The reason is that previous reports showed that increasing the annealing temperature has a detrimental effect on the performance of the catalyst.<sup>(2, 10, 37)</sup> Moreover, it has been confirmed that hydrous iridium oxo-hydroxides are more active than crystalline  $\text{IrO}_2$ .<sup>(6)</sup> Heat treatment could reduce the amount of hydroxides at the surface of the catalysts, leading to a more oxide-like speciation, which in theory would reduce the activity of the materials.

In order to confirm this assumption,  $\text{IrO}_2\text{-Li}_2\text{CO}_3$  was heat treated at  $200^\circ\text{C}$ ,  $400^\circ\text{C}$  and  $500^\circ\text{C}$  for 3 hours in static air. The LSV measured at the beginning of the experiment showed a decrease in the activity with increasing annealing temperature (figure 3.18a). Interestingly, as prepared  $\text{IrO}_2\text{-Li}_2\text{CO}_3$  was stable during the CP stability test, showing little increase in the

potential. Heat treatment at 200 °C and at 400 °C led to catalyst instability as observed by the sudden rise in the monitored potential up to 2.2 V<sub>RHE</sub>, indicative of glassy carbon corrosion. However, the catalyst stability was recovered after heat treatment at 500 °C (figure 3.18b), this is discussed in further detail in chapter 5.

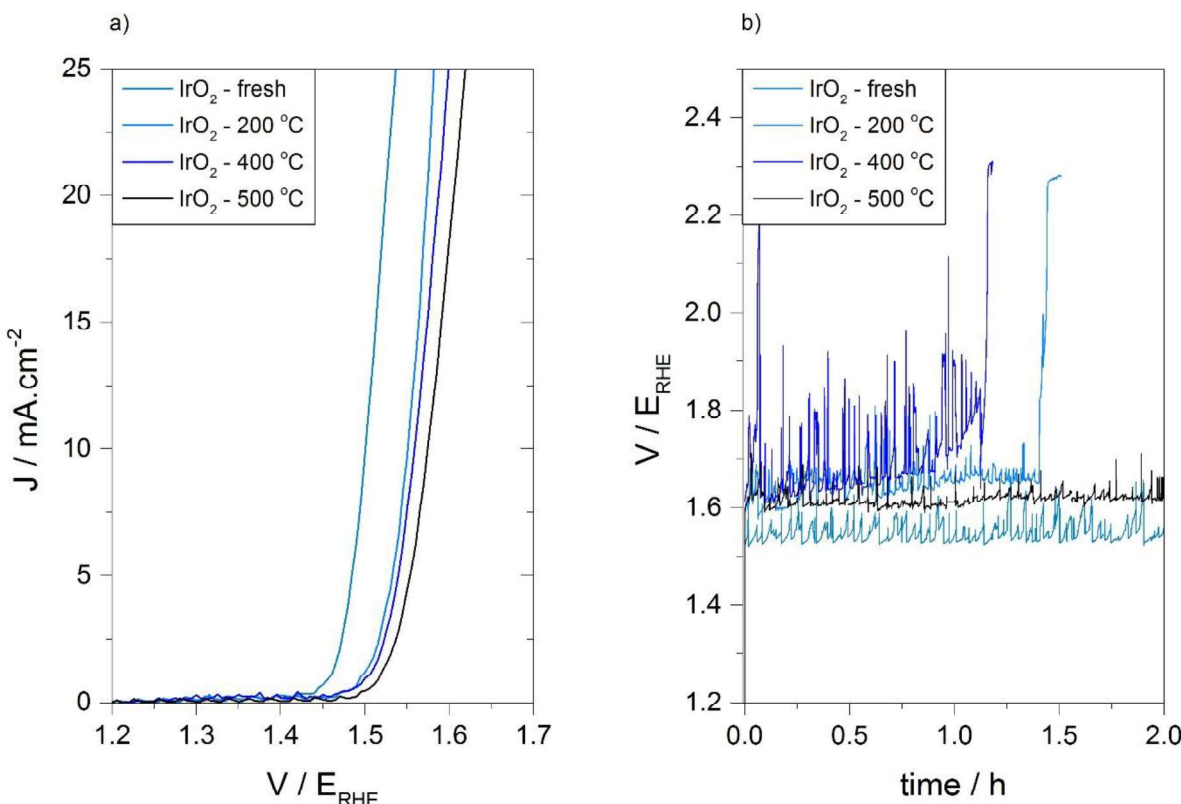
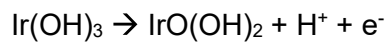
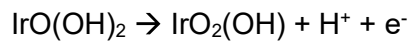


**Figure 3.18.** a) LSV and b) CP at 10  $\text{mA} \cdot \text{cm}^{-2}$  for  $\text{IrO}_2\text{-Li}_2\text{CO}_3$  as prepared and heat treated at 200 °C, 400 °C and 500 °C.

Heat treatment, at a temperature as mild as 130 °C for 2 hours, has also a detrimental effect on the as prepared  $\text{IrO}_2\text{-Li}_2\text{CO}_3$ . A part from the LSV shift towards higher potential the shape of the CV abruptly changed (figure 3.19). Fresh  $\text{IrO}_2\text{-Li}_2\text{CO}_3$  presented an asymmetric CV shape along the potential axis. The oxidation of Ir(III) to Ir(IV) (equation 3.8) was observed as a broad irreversible peak at 0.95 V<sub>RHE</sub>.<sup>(38, 39)</sup> Moreover, a small-broad peak at 1.2 V<sub>RHE</sub> which could be associated with the Ir(IV) to Ir(V) transition (equation 3.9) was also present.<sup>(39)</sup> On the other hand,  $\text{IrO}_2\text{-Li}_2\text{CO}_3$  dried at 130 °C presents a much more symmetric CV shape along the potential axis with higher charging contribution at lower potentials, charging can be caused by the accumulation of charges (electrons or ions) on the electrode, in which the observed current density do not correlate with an electronic transition. The Ir(III)/Ir(IV) transition peak at 0.95 V<sub>RHE</sub> and the Ir(IV)/Ir(V) transition peak at 1.2 V<sub>RHE</sub> were not observed.



Eq. 3.8



Eq. 3.9

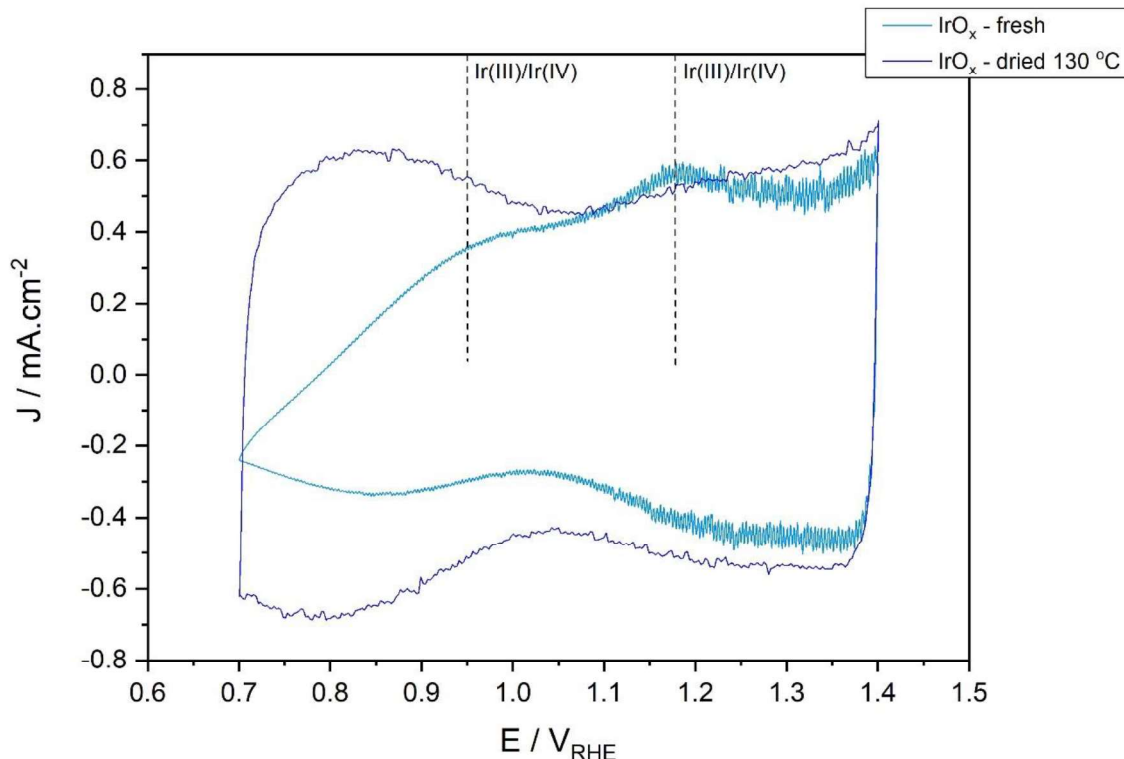


**Figure 3.19.** CV for  $\text{IrO}_2\text{-Li}_2\text{CO}_3$  fresh (light blue) and heat treated in air at 130 °C for 2 hours (dark blue) catalysts.

### 3.3. Conclusions.

The hydrothermal synthesis is commonly employed in the preparation of IrO<sub>2</sub> materials. In the literature NaOH and KOH are commonly used to provide the alkaline media. Chapter 3 aimed to determine the effect of the base used during the hydrothermal synthesis of IrO<sub>2</sub> and to identify if it is a key variable in the optimisation process.

In conclusion, IrO<sub>2</sub> materials were synthesised through the hydrothermal method using diverse alkali metal bases (Li<sub>2</sub>CO<sub>3</sub>, LiOH, Na<sub>2</sub>CO<sub>3</sub>, NaOH, K<sub>2</sub>CO<sub>3</sub> and KOH). The amorphous structure of the IrO<sub>2</sub> prepared materials was proposed by XRD, Raman spectroscopy and H<sub>2</sub>-TPR in conjunction with low dose electron TEM for IrO<sub>2</sub>-Li<sub>2</sub>CO<sub>3</sub>.

XPS characterisation indicated the presence of three different oxygen species: oxide, hydroxide and water. The use of IrO<sub>2</sub>-LiOH and IrO<sub>2</sub>-Li<sub>2</sub>CO<sub>3</sub> as base led to catalysts with the lowest proportion of the oxide form and the highest hydroxide concentration. However, no differences on the Ir(4f) orbital were observed between catalysts. Ir(4f) suggested the presence of different iridium sites. Presumably a lattice formed of Ir(IV) sites with a mixture of Ir(III) and hydroxide species. XPS, TGA and IR characterisation suggested that the surface of the IrO<sub>2</sub> was highly hydroxylated and that the chemical structure of the catalysts resembles more to IrO<sub>x</sub>(OH)<sub>y</sub>·nH<sub>2</sub>O instead of the nominal IrO<sub>2</sub> formula for rutile. The cation from the base has an important role in directing the morphology of IrO<sub>2</sub>, independently of the hydroxide or carbonate nature of the base. Lithium bases, Li<sub>2</sub>CO<sub>3</sub> and LiOH, led to sponge-like structures with improved surface area, flat surfaces were observed when K<sub>2</sub>CO<sub>3</sub> and KOH were used and a morphology halfway between potassium-like and lithium-like morphology was observed when sodium bases were used.

The catalysts activity and stability towards OER was evaluated and compared with commercial IrO<sub>2</sub> samples in a 3-electrode flow cell set up provided by our MaxNet collaborators. Apart from lithium-based IrO<sub>2</sub> catalysts, materials showed lower performance than the commercially available IrO<sub>2</sub>·2H<sub>2</sub>O, which can be related to their higher oxide nature and lower surface area. Although the two catalysts with higher surface area, IrO<sub>2</sub>-Li<sub>2</sub>CO<sub>3</sub> and commercial IrO<sub>2</sub>·2H<sub>2</sub>O, had the best electrocatalytic performance towards OER, the surface area cannot be directly correlated to the catalyst activity. IrO<sub>2</sub>-LiOH has a third of the surface area of IrO<sub>2</sub>·2H<sub>2</sub>O but showed similar activity by LSV. Instead the oxide/hydroxide concentration at the surface of the catalysts is thought to have a more pronounced effect on the activity towards OER.

Between IrO<sub>2</sub>-LiOH and IrO<sub>2</sub>-Li<sub>2</sub>CO<sub>3</sub>, the latter had improved activity and stability compared to the commercial standard. The cation from the base used during the synthesis (Li<sup>+</sup>, Na<sup>+</sup> or K<sup>+</sup>) remained in the IrO<sub>2</sub> materials. The concentration of lithium was not quantified since it could not be detected by XPS or SEM-EDX, therefore lithium doping could be responsible for the improved activity and stability of IrO<sub>2</sub>-Li<sub>2</sub>CO<sub>3</sub> compared to IrO<sub>2</sub>-LiOH. The presence of lithium is expected to be higher in the former material as a result of the comparably lower solubility of Li<sub>2</sub>CO<sub>3</sub> compared to LiOH; nevertheless, the exact role of lithium will be an exciting topic of discussion for future research.

### 3.4 Bibliography.

1. I. C. Man, H. Y. Su, F. Calle-Vallejo, H. A. Hansen, J. I. Martínez, N. G. Inoglu, J. Kitchin, T. F. Jaramillo, J. K. Nørskov, J. Rossmeisl, Universality in Oxygen Evolution Electrocatalysis on Oxide Surfaces, *ChemCatChem*, **2011**, 3 (7), 1159-1165.
2. S. Trasatti, Electrocatalysis in the anodic evolution of oxygen and chlorine, *Electrochimica Acta*, **1984**, 29 (11), 1503-1512.
3. J. Rossmeisl, Z. W. Qu, H. Zhu, G. J. Kroes, J. K. Nørskov, Electrolysis of water on oxide surfaces, *Journal of Electroanalytical Chemistry*, **2007**, 607, 83.
4. C. C. L. McCrory, S. Jung, I. M. Ferrer, S. M. Chatman, J. C. Peters, T. F. Jaramillo, Benchmarking Hydrogen Evolving Reaction and Oxygen Evolving Reaction Electrocatalysts for Solar Water Splitting Devices, *Journal of the American Chemical Society*, **2015**, 137 (13), 4347-4357.
5. V. Pfeifer, T. E. Jones, J. J. Velasco Vélez, C. Massué, R. Arrigo, D. Teschner, F. Girgsdies, M. Scherzer, M. T. Greiner, J. Allan, M. Hashagen, G. Weinberg, S. Piccinin, M. Hävecker, A. Knop-Gericke, R. Schlögl, The electronic structure of iridium and its oxides, *Surface and Interface Analysis*, **2016**, 48 (5), 261-273.
6. V. Pfeifer, T. E. Jones, J. J. Velasco Velez, C. Massué, M. T. Greiner, R. Arrigo, D. Teschner, F. Girgsdies, M. Scherzer, J. Allan, M. Hashagen, G. Weinberg, S. Piccinin, M. Hävecker, A. Knop-Gericke, R. Schlögl, The electronic structure of iridium oxide electrodes active in water splitting, *Physical Chemistry Chemical Physics*, **2016**, 18 (4), 2292-2296.
7. V. Pfeifer, T. E. Jones, S. Wrabetz, C. Massué, J. J. Velasco Velez, R. Arrigo R, M. Scherzer, S. Piccinin, M. Hävecker, A. Knop-Gericke, R. Schlögl, Reactive oxygen species in iridium-based OER catalysts, *Chemical Science*, **2016**, 7 (11), 6791-6795.
8. C. Massué, V. Pfeifer, X. Huang, J. Noack, A. Tarasov, S. Cap, R. Schlögl, High-performance supported Ir-oxohydroxide water oxidation electrocatalysts, *ChemSusChem*, **2017**, 10, 1943-1957.
9. T. Reier, Z. Pawolek, S. Cherevko, M. Bruns, T. Jones, D. Teschner, S. Selve, A. Bergmann, H. N. Nong, R. Schlögl, K. J. J. Mayrhofer, P. Strasser, Molecular Insight in Structure and Activity of Highly Efficient, Low-Ir Ir-Ni Oxide Catalysts for Electrochemical Water Splitting (OER), *Journal of the American Chemical Society*, **2015**, 137 (40), 13031-13040.

10. T. Reier, D. Teschner, T. Lunkenbein, A. Bergmann, S. Selve, R. Krahnert, R. Schlögl, P. Strasser, Electrocatalytic Oxygen Evolution on Iridium Oxide: Uncovering Catalyst-Substrate Interactions and Active Iridium Oxide Species, *Journal of The Electrochemical Society*, **2014**, 161 (9), F876-F882.
11. D. Astruc, *Nanoparticles and Catalysis*, Wiley-VCH Verlag GmbH & Co, **2008**.
12. T. Nakagawa, C. A. Beasley, R. W. Murray, Efficient Electro-Oxidation of Water near Its Reversible Potential by a Mesoporous IrO<sub>x</sub> Nanoparticle Film, *The Journal of Physical Chemistry C*, **2009**, 113 (30), 12958-12961.
13. T. Reier, M. Oezaslan, P. Strasser, Electrocatalytic Oxygen Evolution Reaction (OER) on Ru, Ir, and Pt Catalysts: A Comparative Study of Nanoparticles and Bulk Materials, *ACS Catalysis*, **2012**, 2 (8), 1765-1772.
14. Y. Zhao, E. A. Hernandez-Pagan, N. M. Vargas-Barbosa, J. L. Dysart, T. E. Mallouk, A High Yield Synthesis of Ligand-Free Iridium Oxide Nanoparticles with High Electrocatalytic Activity, *The Journal of Physical Chemistry Letters*, **2011**, 2 (5), 402-406.
15. T. Nakagawa, N. S. Bjorge, R. W. Murray, Electrogenerated IrO<sub>x</sub> Nanoparticles as Dissolved Redox Catalysts for Water Oxidation, *Journal of the American Chemical Society*, **2009**, 131 (43), 15578-15579.
16. S. H. A. Lee, Y. Zhao, E. A. Hernandez-Pagan, L. Blasdel, W. J. Youngblood, T. E. Mallouk, Electron transfer kinetics in water splitting dye-sensitized solar cells based on core-shell oxide electrodes, *Faraday Discussions*, **2012**, 155, 165-176.
17. Y. Zhao, N. M. Vargas-Barbosa, M. E. Strayer, N. S. McCool, M. E. Pandelia, T. P. Saunders, J. R. Swierk, J. F. Callejas, L. Jensen, T. E. Mallouk, Understanding the Effect of Monomeric Iridium(III/IV) Aquo Complexes on the Photoelectrochemistry of IrO<sub>x</sub>·nH<sub>2</sub>O-Catalyzed Water-Splitting Systems, *Journal of the American Chemical Society*, **2015**, 137 (27), 8749-8757.
18. C. Massué, X. Huang, A. Tarasov, C. Ranjan, S. Cap, R. Schlögl, Microwave Assisted Synthesis of Stable and Highly Active Ir-oxohydroxides for Electrochemical Oxidation of Water, *ChemSusChem*, **2017**, 10, 1958-1968.
19. F. Berkermann, *Preparation and Application of Aqueous Iridium Oxide Colloids* (Doctoral Thesis). Ruhr University Bochum, Germany, **2010**.
20. D. Xu, P. Diao, T. Jin, Q. Wu, X. Liu, X. Guo, H. Gong, F. Li, M. Xiang, Y. Ronghai, Iridium Oxide Nanoparticles and Iridium/Iridium Oxide Nanocomposites: Photochemical Fabrication and Application in Catalytic Reduction of 4-Nitrophenol, *ACS Applied Materials & Interfaces*, **2015**, 7 (30), 16738-16749.

21. Z. Pavlovic, C. Ranjan, Q. Gao, M. van Gastel, R. Schlögl, Probing the Structure of a Water-Oxidizing Anodic Iridium Oxide Catalyst using Raman Spectroscopy, *ACS Catalysis*, **2016**, 6 (12), 8098-8105.
22. D. J. Morgan, Resolving ruthenium: XPS studies of common ruthenium materials, *Surface and Interface Analysis*, **2015**, 47 (11), 1072-1079.
23. S. J. Freakley, J. Ruiz Esquius, D. J. Morgan, The X-ray photoelectron spectra of Ir, IrO<sub>2</sub> and IrCl<sub>3</sub> revisited, *Surface and Interface Analysis*, **2017**, 49 (8), 794-799.
24. S. Musić, S. Popović, M. Maljković, Z. Skoko, K. Furić, A. Gajović, Thermochemical formation of IrO<sub>2</sub> and Ir, *Materials Letters*, **2003**, 57 (29), 4509-4514.
25. J. Singh, N. Kaurav, N. P. Lalla, G. S. Okram, Naturally self-assembled nickel nanolattice, *Journal of Materials Chemistry C*, **2014**, 2 (42), 8918-8924.
26. E. Willinger, C. Massué, R. Schlögl, M. G. Willinger, Identifying Key Structural Features of IrO<sub>x</sub> Water Splitting Catalysts, *Journal of the American Chemical Society*, **2017**, 139 (34), 12093-12101.
27. T. Audichon, B. Guenot, S. Baranton, M. Cretin, C. Lamy, C. Coutanceau, Preparation and characterization of supported Ru<sub>x</sub>Ir<sub>(1-x)</sub>O<sub>2</sub> nano-oxides using a modified polyol synthesis assisted by microwave activation for energy storage applications, *Applied Catalysis B: Environmental*, **2017**, 200, 493-502.
28. P. C. Liao, C. S. Chen, W. S. Ho, Y. S. Huang, K. K. Tiong, Characterization of IrO<sub>2</sub> thin films by Raman spectroscopy, *Thin Solid Films*, **1997**, 301 (1), 7-11.
29. J. M. Kahk, C. G. Poll, F. E. Oropeza, J. M. Ablett, D. Céolin, J. P. Rueff, S. Agrestini, Y. Utsumi, K. D. Tsuei, Y. F. Liao, F. Borgatti, G. Panaccione, A. Regoutz, R. G. Egddell, B. J. Morgan, D. O. Scanlon, D. J. Payne, Understanding the Electronic Structure of IrO<sub>2</sub> Using Hard-X-ray Photoelectron Spectroscopy and Density-Functional Theory, *Physical Review Letters*, **2014**, 112 (11), 117601.
30. S. K. Panda, S. Bhowal, A. Delin, O. Eriksson, I. Dasgupta, Effect of spin orbit coupling and Hubbard *U* on the electronic structure of IrO<sub>2</sub>, *Physical Review B*, **2014**, 89 (15), 155102-155107.
31. A. M. Cruz, L. Abad, N. M. Carretero, J. Moral-Vico, J. Fraxedas, P. Lozano, G. Subías, V. Padial, M. Carballo, J. E. Collazos-Castro, N. Casañ-Pastor, Iridium Oxohydroxide, a Significant Member in the Family of Iridium Oxides. Stoichiometry, Characterization, and Implications in Bioelectrodes, *The Journal of Physical Chemistry C*, **2012**, 116 (8), 5155-5168.

32. A. C. Ferrari, J. Robertson, Resonant Raman spectroscopy of disordered, amorphous, and diamondlike carbon, *Physical Review B*, **2001**, *64* (7), 075414.
33. D. B. Williams, C. B. Carter, *Transmission Electron Microscopy. Part 1: Basics*. Springer, **2009**.
34. I. Spanos, A. A. Auer, S. Neugebauer, X. Deng, H. Tüysüz, R. Schlöegl, Standardized Benchmarking of Water Splitting Catalysts in a Combined Electrochemical Flow Cell/Inductively Coupled Plasma-Optical Emission Spectrometry (ICP-OES) Setup, *ACS Catal*, **2017**, *7*, 3768-3778.
35. O. Kasian, J. P. Grote, S. Geiger, S. Cherevko, K. J. J. Mayrhofer, The Common Intermediates of Oxygen Evolution and Dissolution Reactions during Water Electrolysis on Iridium, *Angewandte Chemie International Edition*, **2018**, *57* (9), 2488-2491.
36. A. R. Zeradjanin, A. A. Topalov, Q. Van Overmeere, S. Cherevko, X. Chen, E. Ventosa, W. Schuhmann, K. J. J. Mayrhofer, Rational design of the electrode morphology for oxygen evolution - enhancing the performance for catalytic water oxidation, *RSC Advances*, **2014**, *4* (19), 9579-9587.
37. C. Felix, T. Maiyalagan, S. Pasapathi, B. Bladergroen, V. Linkov, Synthesis and optimization of IrO<sub>2</sub> electrocatalysts by Adams fusion method for solid polymer electrolyte electrolyzers., *Micro and nanosystems*, **2012**, *4*, 186-191.
38. L. Ouattara, S. Fierro, O. Frey, M. Koudelka, Comninellis C, Electrochemical comparison of IrO<sub>2</sub> prepared by anodic oxidation of pure iridium and IrO<sub>2</sub> prepared by thermal decomposition of H<sub>2</sub>IrCl<sub>6</sub> precursor solution, *Journal of Applied Electrochemistry*, **2009**, *39* (8), 1361-1367.
39. J. Juodkazyte, B. Sebeka, I. Valsiunas, K. Juodkazis, Iridium Anodic Oxidation to Ir(III) and Ir(IV) Hydrous Oxides, *Electroanalysis*, **2005**, *17* (11), 947-952.

# Chapter 4

## Effect of base on the preparation of IrO<sub>2</sub> catalysts supported on ATO towards OER prepared via hydrothermal synthesis

### 4.1 Introduction.

The formation of amorphous iridium oxo-hydroxide, with Ir(III)/Ir(IV) and electrophilic O<sup>-</sup> sites, are preferred compared to rutile IrO<sub>2</sub> because of its better catalytic performance towards OER.<sup>(1, 2)</sup> In the previous chapter it was demonstrated that amorphous iridium oxo-hydroxides can be synthesised following a hydrothermal preparation under strong aqueous alkaline conditions. Amorphous IrO<sub>x</sub> catalysts were obtained for all employed bases (Li<sub>2</sub>CO<sub>3</sub>, LiOH, Na<sub>2</sub>CO<sub>3</sub>, NaOH, K<sub>2</sub>CO<sub>3</sub> or KOH), although chemical and physical properties changed from base to base. Sponge-like morphology with higher concentration of hydroxides was obtained when using Li-bases, whilst large agglomerates with higher proportion of oxide were observed for K-base materials. The catalytic activity and stability for OER was found to be base-dependent, with IrO<sub>2</sub>-Li<sub>2</sub>CO<sub>3</sub> outperforming the rest of the prepared catalysts.

The use of a support can improve the IrO<sub>2</sub> dispersion, increasing the IrO<sub>2</sub> surface area, consequently improving the IrO<sub>2</sub> activity towards OER.<sup>(3-5)</sup> Antimony doped tin dioxide (ATO) is normally used as support because of its metal-like conductivity and electrochemical stability in acid media under OER operation conditions. In this chapter, supported IrO<sub>x</sub> on ATO was prepared following a hydrothermal synthesis; Li<sub>2</sub>CO<sub>3</sub>, Na<sub>2</sub>CO<sub>3</sub> or K<sub>2</sub>CO<sub>3</sub> were employed as a base during the synthesis.

The aim of the chapter was to determine if the catalytic properties of supported IrO<sub>2</sub>/ATO were affected by the base used, as observed for no-supported IrO<sub>x</sub> in chapter 3. Furthermore, the effect of heat treatment under oxidative or reductive atmosphere in the activity and stability towards OER was systematically studied.

## 4.2 Effect of alkali metal bases on the synthesis of supported IrO<sub>2</sub> on ATO.

### 4.2.1. Catalysts Preparation.

A modification of the hydrothermal synthesis reported by Reetz *et al.*<sup>(6)</sup> used in chapter 3 was followed. In a 50 mL bottom flask, 1 mmol of IrCl<sub>3</sub> and 8 mmol of base (Li<sub>2</sub>CO<sub>3</sub>, Na<sub>2</sub>CO<sub>3</sub> or K<sub>2</sub>CO<sub>3</sub>) were dissolved in 10 mL of deionised water and stirred for 16 h at room temperature. A further 10 mL of deionised water were added to the slurry, followed by 448 mg of ATO (Sigma Aldrich), added slowly throughout a period of 30 minutes, in order to obtain an iridium loading of 26.6 wt. %. Afterwards, the mixture was heated to reflux for 3 h. Once the solution cooled, the catalyst was recovered by filtration and washed with 2 L of deionised water. The supernatant solutions before filtration were colourless for the three bases used, indicating the absence of soluble iridium species in solution. Finally, the material was dried inside a fume hood at room temperature overnight.

### 4.2.2 Catalysts Characterisation.

#### X-Ray powder diffraction (XRD)

Amorphous iridium oxo-hydroxides have been related to high active catalysts towards OER, in contrast to crystalline rutile IrO<sub>2</sub>.<sup>(1)</sup> In order to determine crystal structures present in the prepared materials XRD patterns were recorded. ATO (JCPDS-041-1445) and IrO<sub>2</sub> (JCPDS-015-0876) have the same crystal structure, however, due to the different atomic size of Sn and Ir, reflections are shifted and both phases can be individually identified by XRD. The recorded XRD reflections for commercial ATO did not change after the adsorption of IrO<sub>2</sub> when using Li<sub>2</sub>CO<sub>3</sub> or Na<sub>2</sub>CO<sub>3</sub>. However, a reduction in the ATO reflection intensity was observed when K<sub>2</sub>CO<sub>3</sub> was used as a base, suggesting lower crystallinity (figure 4.1). In order to confirm the crystallographic reduction of ATO under the presence of K<sub>2</sub>CO<sub>3</sub> base, the crystallite size of ATO was calculated using the Scherrer equation. According to it, the crystallite size of the as received ATO was 25 nm. However, no changes on the crystallite size were observed for prepared IrO<sub>2</sub>/ATO samples, regardless of the base used.

Previously in chapter 3, the hydrothermal process was shown to be appropriate for the synthesis of amorphous IrO<sub>2</sub>. In agreement, no reflections related to crystalline rutile IrO<sub>2</sub> (28.0°, 34.7°, 54.1°) or metallic Ir (40.9°, 47.6° 2θ degree) were detected for supported IrO<sub>2</sub>/ATO catalysts, confirming its amorphous nature.

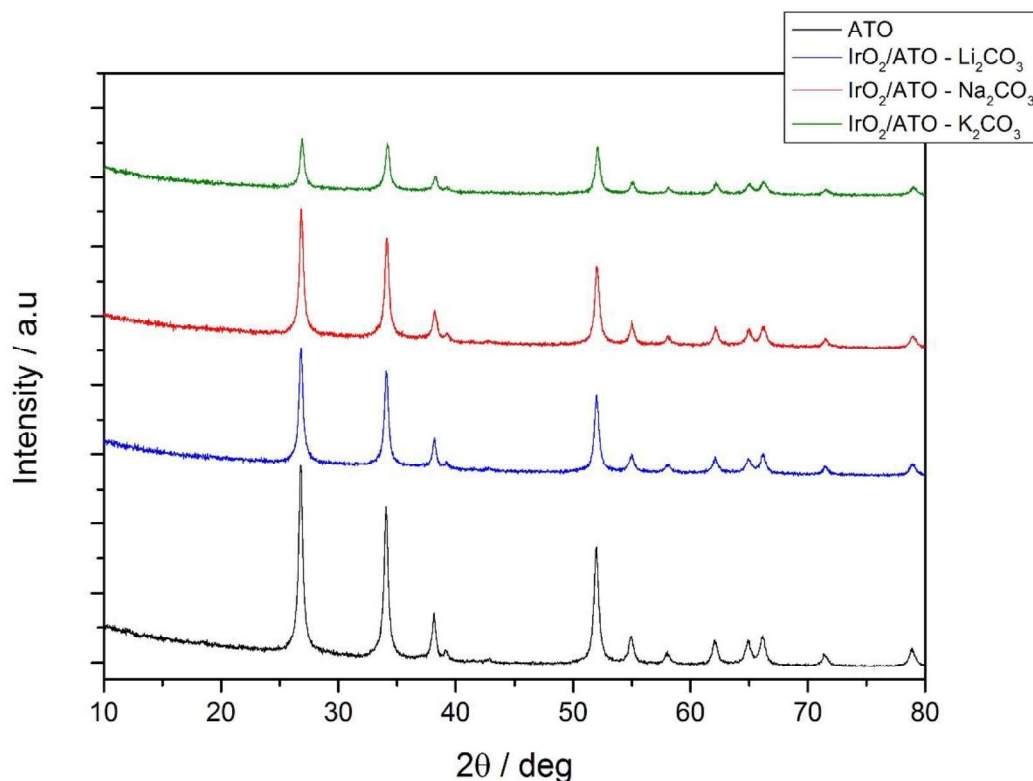


**Figure 4.1.** XRD pattern for supported  $\text{IrO}_2$  on ATO prepared through hydrothermal synthesis with  $\text{Li}_2\text{CO}_3$ ,  $\text{Na}_2\text{CO}_3$  or  $\text{K}_2\text{CO}_3$  as a base.

#### X-ray photoelectron spectroscopy (XPS)

Impurities at the surface of the catalyst can be detected by XPS. The presence of residual carbonates was detected at a binding energy of 284.8 eV, C(1s), for all prepared catalysts as a small peak on the Ir(4d) region. In order to ensure reliable data comparison, the remaining elements present were calibrated against the C(1s) signal. The presence of  $\text{K}^+$  was clearly detected at 293.3 eV as a shoulder in the Ir(4d) binding energy for  $\text{IrO}_2/\text{ATO}-\text{K}_2\text{CO}_3$  catalyst (figure 4.3a). However, the presence of  $\text{Na}^+$  or  $\text{Li}^+$  was not detected on  $\text{IrO}_2/\text{ATO}-\text{Na}_2\text{CO}_3$  or  $\text{IrO}_2/\text{ATO}-\text{Li}_2\text{CO}_3$  respectively on the survey scan. The presence of residual chlorine was not detected for any catalysts by XPS.

XPS is not only a useful technique in the detection of impurities present on materials, but it can also give useful information about oxidation state and chemical environment. No appreciable differences were observed between  $\text{IrO}_2/\text{ATO}-\text{Li}_2\text{CO}_3$  and  $\text{IrO}_2/\text{ATO}-\text{Na}_2\text{CO}_3$  catalysts on the O(1s), Ir(4d), Ir(4f), Sn(3d) and Sb(3d) binding energies. However, the binding energies for  $\text{IrO}_2/\text{ATO}-\text{K}_2\text{CO}_3$  catalyst were shifted towards slightly lower values compared to  $\text{IrO}_2/\text{ATO}-\text{Li}_2\text{CO}_3$  and  $\text{IrO}_2/\text{ATO}-\text{Na}_2\text{CO}_3$  (figure 4.2). In order to avoid

interferences from the O(1s) into the Sb(3d) orbital, just the Sb( $3\text{d}_{3/2}$ ) was analysed.<sup>(7)</sup> A shift towards lower binding energy on the Sb(3d) region could indicate a major presence of Sb(III) sites. In ATO, Sb(III) concentrates at the surface of the materials while Sb(V) is localised at the bulk.<sup>(8)</sup> This could indicate that under basic  $\text{K}_2\text{CO}_3$  treatment, Sb segregation occurs at the surface of ATO. More studies would be needed to verify this phenomenon but it is outside of the objectives of this research.

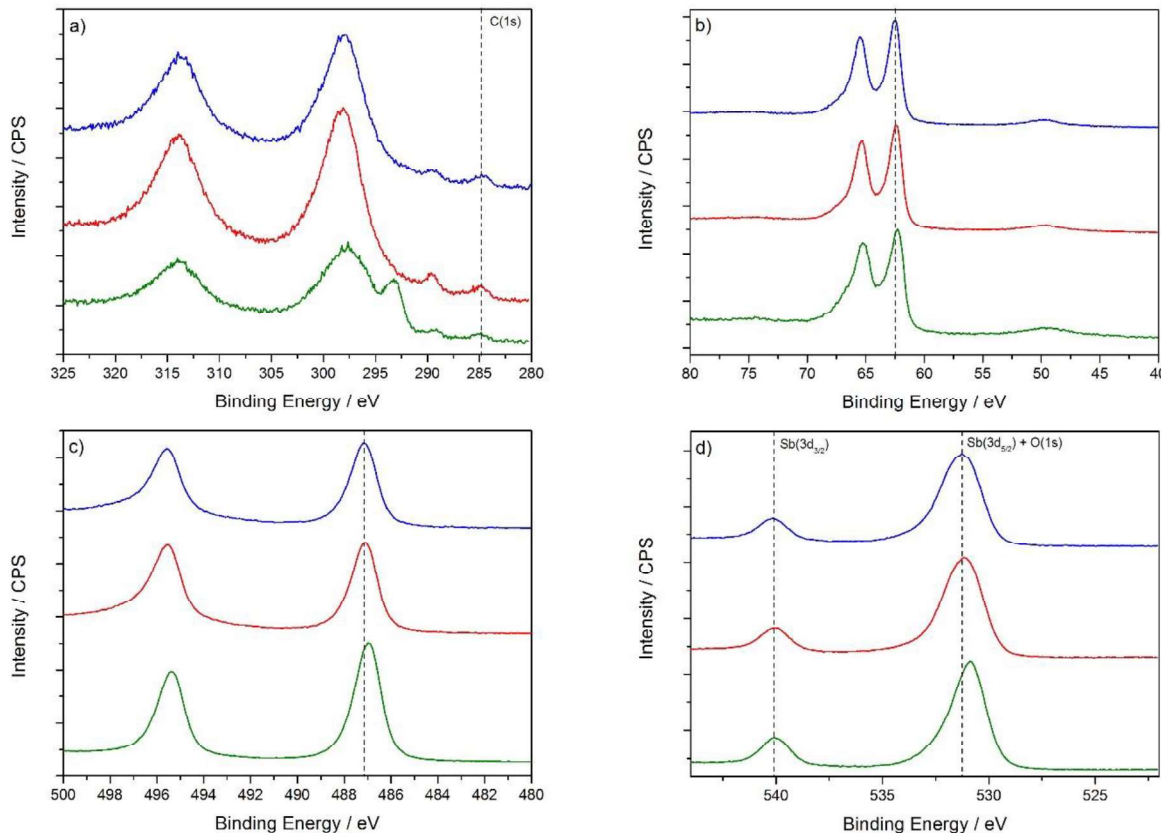


**Figure 4.2.** a) Ir(4d), b) Ir(4f), c) Sn(3d) and d) Sb(3d) and O(1s) XPS analysis for synthesised  $\text{IrO}_2$ /ATO catalysts through the hydrothermal process. Catalysts prepared with  $\text{Li}_2\text{CO}_3$ ,  $\text{Na}_2\text{CO}_3$  and  $\text{K}_2\text{CO}_3$  are represented in blue, red and green respectively.

#### *Scanning Electron Microscopy coupled with Energy Dispersed X-ray (SEM-EDX)*

In order to detect macroscopic changes in the morphology, ATO supported catalysts were analysed by SEM imaging. As received commercial ATO from Sigma Aldrich was present as a fine powder (image 4.1a). After supporting  $\text{IrO}_2$ , agglomeration was observed, which could be expected because as received ATO was dry but it has been in contact with water during the synthesis and dried inside a fume hood. Nevertheless,  $\text{IrO}_2$ /ATO- $\text{Li}_2\text{CO}_3$  and  $\text{IrO}_2$ /ATO- $\text{Na}_2\text{CO}_3$  showed a similar degree of agglomeration (image 4.1b and 4.1c respectively),

whereas the use of  $\text{K}_2\text{CO}_3$  led to the presence of considerably larger aggregates (image 4.1d).

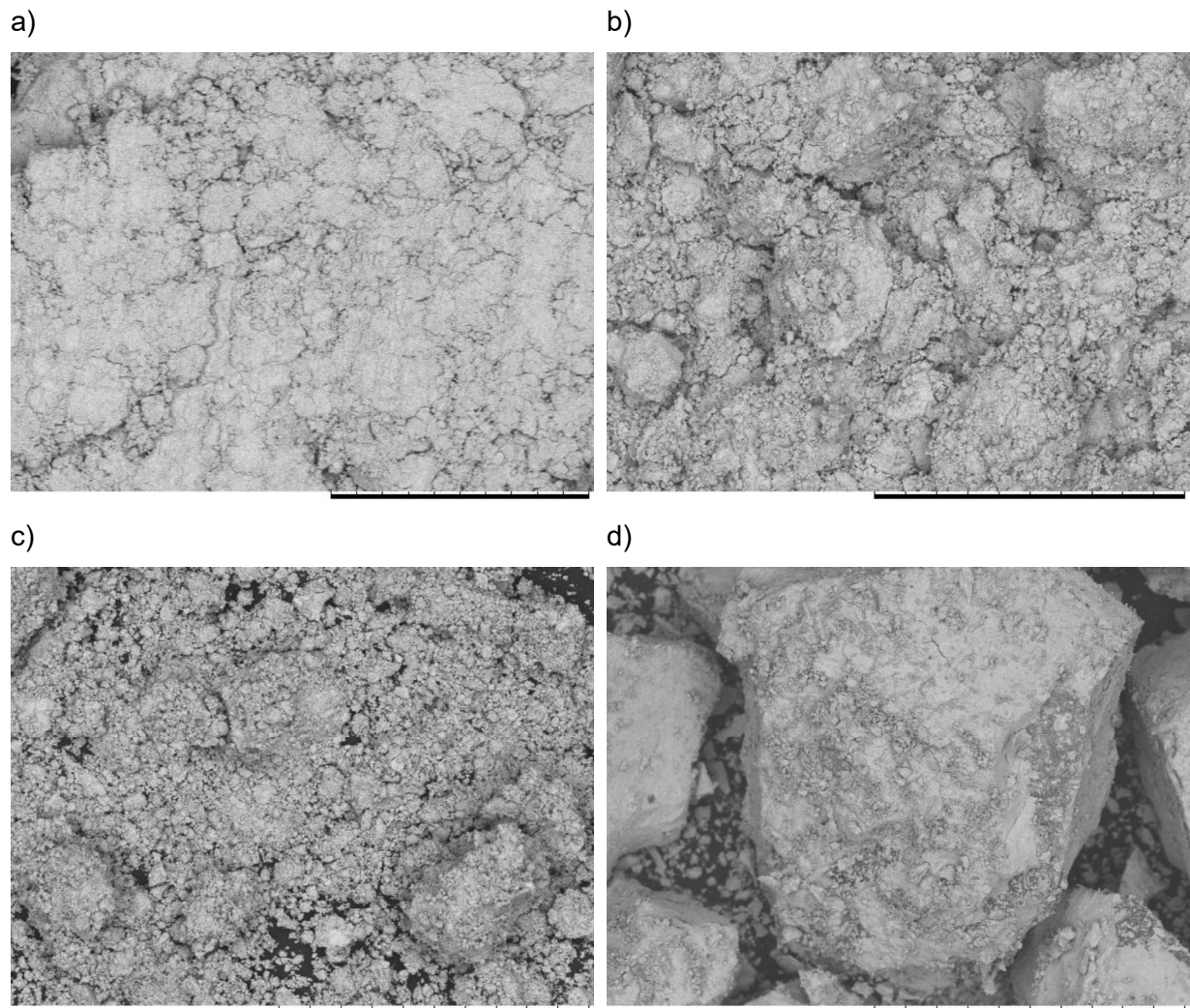


**Image 4.1.** SEM images for a) as received commercial ATO.  $\text{IrO}_2$  supported on ATO prepared through a hydrothermal synthesis using b)  $\text{Li}_2\text{CO}_3$ , c)  $\text{Na}_2\text{CO}_3$  and d)  $\text{K}_2\text{CO}_3$  as a base. The scale bar corresponds to 300  $\mu\text{m}$ .

Apart from the difference in morphology, more meaningful information could be obtained from elemental quantification by EDX. From the commercial ATO supplier a  $\text{Sb}_2\text{O}_5$  concentration between 7 wt. % and 11 wt. % was specified, this corresponds to a Sn/Sb molar ratio of 8.7 and 14.3 respectively. The measurement of Sb concentration against Sn was necessary because both  $\text{Sb}_2\text{O}_5$  and  $\text{SnO}_2$  contain oxygen in their chemical formula.

The elemental quantification for commercial ATO and for prepared  $\text{IrO}_2$ /ATO catalysts is presented in table 4.1. EDX analysis on the commercial ATO was able to verify the Sn/Sb

molar ratio to  $9.2 \pm 0.4$ , as stipulated from the supplier. The Sn/Sb molar ratio in IrO<sub>2</sub>/ATO-Li<sub>2</sub>CO<sub>3</sub> and IrO<sub>2</sub>/ATO-Na<sub>2</sub>CO<sub>3</sub> catalysts was consistent with the ratio detected for commercial ATO. Nevertheless, when K<sub>2</sub>CO<sub>3</sub> was used as a base during the synthesis, the concentration of antimony slightly decreased. Elemental quantification was required to confirm the iridium loading on to the catalysts, EDX analysis showed that the iridium loading was in good agreement with the theoretical value of 26.6 wt. % for all prepared catalysts.

From the XPS results, potassium impurities were detected on IrO<sub>2</sub>/ATO-K<sub>2</sub>CO<sub>3</sub> catalyst, however, Na<sup>+</sup> or Li<sup>+</sup> were not quantified on the respective catalysts. Since XPS is a surface technique, impurities trapped in the bulk during the precipitation of the iridium oxo-hydroxide would be difficult to detect. EDX quantification was used in order to confirm that no impurities were present in the bulk of IrO<sub>2</sub>/ATO catalysts. In accordance with the XPS characterisation, no chlorine was detected by EDX for any of the prepared IrO<sub>2</sub>/ATO samples. However, impurities of sodium and potassium were detected for IrO<sub>2</sub>/ATO-Na<sub>2</sub>CO<sub>3</sub> and IrO<sub>2</sub>/ATO-K<sub>2</sub>CO<sub>3</sub> respectively. The presence of lithium cannot be detected by EDX as it is too light, but because K<sup>+</sup> and Na<sup>+</sup> were detected for IrO<sub>2</sub>/ATO-Na<sub>2</sub>CO<sub>3</sub> and IrO<sub>2</sub>/ATO-K<sub>2</sub>CO<sub>3</sub>, lithium would be expected to be present in IrO<sub>2</sub>/ATO-Li<sub>2</sub>CO<sub>3</sub> in similar concentration.

**Table 4.1.** Elemental EDX quantification for commercial ATO and synthesised IrO<sub>2</sub>/ATO catalysts with different alkali metal bases. The iridium weight percent was obtained by its comparison against tin and antimony. The amount of oxygen was not taken into account.

Catalyst	Sn/Sb molar ratio	Ir % weight	Cation % weight (K <sup>+</sup> or Na <sup>+</sup> )
ATO commercial	$9.2 \pm 0.4$	-	-
IrO <sub>2</sub> /ATO-Li <sub>2</sub> CO <sub>3</sub>	$8.5 \pm 0.3$	$25.6 \pm 0.4$	Not detectable
IrO <sub>2</sub> /ATO-Na <sub>2</sub> CO <sub>3</sub>	$8.9 \pm 0.9$	$25.6 \pm 0.9$	$1.0 \pm 0.9$
IrO <sub>2</sub> /ATO-K <sub>2</sub> CO <sub>3</sub>	$10.4 \pm 0.6$	$26.7 \pm 2.1$	$2.2 \pm 0.5$

### *Transmission electron microscopy (TEM)*

At the end of the synthesis of supported  $\text{IrO}_2/\text{ATO}$ , colourless supernatant solutions were observed indicating that no iridium species remained in solution. Iridium was detected by XPS and EDX, indicating that it was in the material. However, as observed in chapter 3,  $\text{IrO}_2$  precipitated as a powder after reflux through the hydrothermal synthesis; this powder was obtained by filtration and washed with water. Thus, the presence of Ir by XPS and its detection by EDX did not provide any evidence that iridium was adsorbed onto the surface of the support. In order to confirm that  $\text{IrO}_2$  has been attached to the surface, ATO catalysts were analysed by TEM.

As shown in the previous chapter,  $\text{IrO}_2$  can suffer from beam damage under TEM conditions unless it is performed using low dose imaging.<sup>(9)</sup> Unsupported amorphous  $\text{IrO}_2\text{-Li}_2\text{CO}_3$  was observed as rutile  $\text{IrO}_2$  under normal TEM imaging conditions but confirmed as amorphous under low electron dose TEM. Therefore, it is important to bear in mind that images obtained using the more accessible TEM in Cardiff (JEM 2100 LaB6) would be indicative of the  $\text{IrO}_2$  dispersion on the support but not representative of the true nature of iridium.

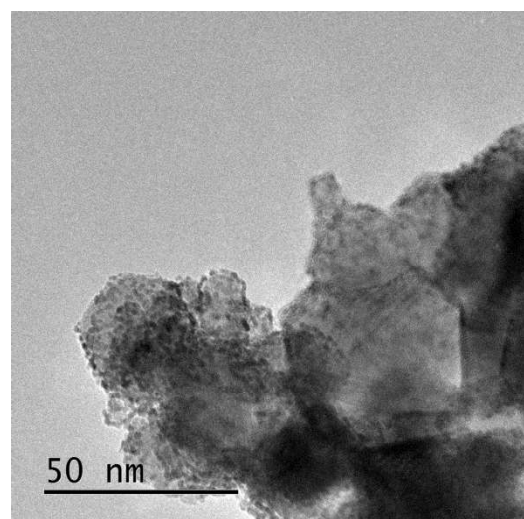
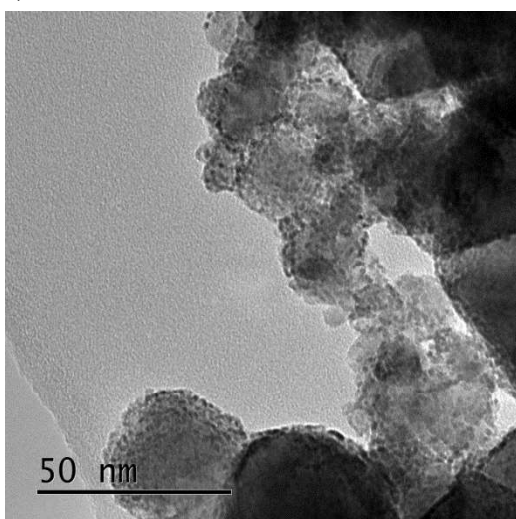
As presented in image 4.2a for  $\text{IrO}_2/\text{ATO-Li}_2\text{CO}_3$ ,  $\text{IrO}_2$  was well dispersed throughout the material. The support was covered by small  $\text{IrO}_2$  aggregates. However, TEM imaging of amorphous iridium oxo-hydroxide is challenging due to its susceptibility towards being beam damaged. Therefore, contrary to the observed small  $\text{IrO}_2$  aggregates, the formation of an amorphous iridium oxo-hydroxide film covering the surface of the ATO would be considered a more realistic representation. As observed with other characterisation techniques, such as XRD, XPS and SEM, the use of  $\text{Li}_2\text{CO}_3$  or  $\text{Na}_2\text{CO}_3$  resulted in no appreciable changes between the prepared materials by TEM. On  $\text{IrO}_2/\text{ATO-Na}_2\text{CO}_3$ , iridium was homogenously dispersed on the ATO as small aggregates, likewise, this is thought to be a consequence of the iridium oxo-hydroxide film being beam damaged during TEM image acquisition (image 4.2b). Conversely,  $\text{IrO}_2/\text{ATO-K}_2\text{CO}_3$  presented two distinct regions: On one hand, there were regions where  $\text{IrO}_2$  was absent and the support presented as smaller-spherical particles; On the other hand, large  $\text{IrO}_2$  agglomerates were present but without being attached to the ATO surface (image 4.2c).

In accordance with the other characterisation techniques,  $\text{IrO}_2/\text{ATO}$  prepared with  $\text{K}_2\text{CO}_3$  as a base differed from catalysts prepared with  $\text{Li}_2\text{CO}_3$  and  $\text{Na}_2\text{CO}_3$ . The ATO reflections decreased in intensity by XRD indicating a possible loss of crystallinity even though the crystallite size calculated from the Scherrer equation was similar to those catalysts prepared

with  $\text{Li}_2\text{CO}_3$  or  $\text{Na}_2\text{CO}_3$  as a base. It could be hypothesised that for  $\text{IrO}_2/\text{ATO-K}_2\text{CO}_3$ , regions with small spherical aggregates corresponded to non-crystalline ATO, while the crystallinity of the ATO regions surrounded by  $\text{IrO}_2$  aggregates was not affected. Larger agglomerates were detected by SEM on  $\text{IrO}_2/\text{ATO}$  prepared with  $\text{K}_2\text{CO}_3$  as a base compared to the other catalysts. Moreover, XPS peaks were shifted towards lower binding energy. It remains unclear what causes the presence of potassium during the synthesis of  $\text{IrO}_2/\text{ATO}$  catalysts to modify the support compared to lithium or sodium and further research should be conducted to draw a conclusive hypothesis.

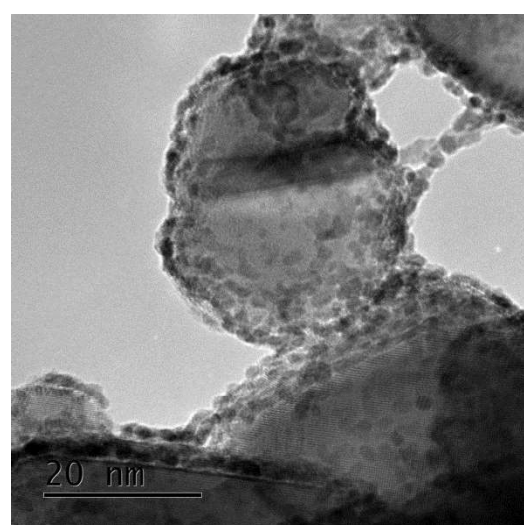
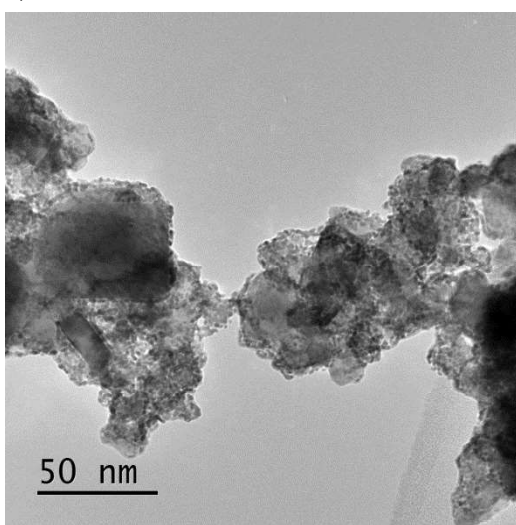
---

a)



---

b)



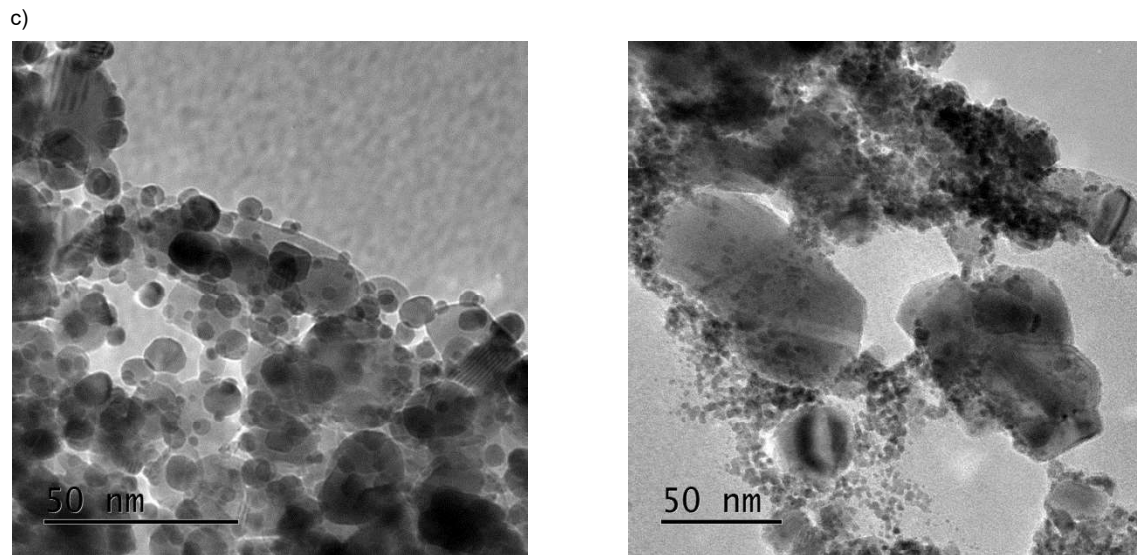


**Image 4.2.** TEM images undertaken on a JEM 2100 LaB6 for IrO<sub>2</sub>/ATO catalysts prepared through a hydrothermal synthesis using a) Li<sub>2</sub>CO<sub>3</sub> b) Na<sub>2</sub>CO<sub>3</sub> c) K<sub>2</sub>CO<sub>3</sub> as a base.

#### 4.2.3 Catalytic activity towards OER.

Catalysts were tested on a 3-electrode flow cell<sup>(10)</sup> provided by our collaborators in the Max Plank Institute for chemical energy conversion in Mülheim, Germany. A detailed flow-cell description and the working electrode preparation protocol are described in chapter 2. Catalyst activity and stability was assessed as follows: initial LSV (from 1.2 V<sub>RHE</sub> to 1.8 V<sub>RHE</sub> at 5 mV·s<sup>-1</sup>), CV (50 CV cycles between 0.7 V<sub>RHE</sub> and 1.4 V<sub>RHE</sub> at 50 mV·s<sup>-1</sup>), LSV (1.2 V<sub>RHE</sub> to 1.8 V<sub>RHE</sub> at 5 mV·s<sup>-1</sup>), CP (2 hours at 10 mA·cm<sup>-2</sup>) and a final LSV (1.2 V<sub>RHE</sub> to 1.8 V<sub>RHE</sub> at 5 mV·s<sup>-1</sup>).

Supported IrO<sub>2</sub>/ATO catalysts were compared to unsupported IrO<sub>2</sub>-Li<sub>2</sub>CO<sub>3</sub> catalyst discussed in chapter 3. This catalyst was selected as standard due to the higher activity and stability compared to commercial IrO<sub>2</sub>·2H<sub>2</sub>O and also because it was prepared using the same synthetic procedure. Whilst the total catalyst loading on supported materials was 100 µg·cm<sup>-2</sup>, the iridium loading on the electrode was 35 µg·cm<sup>-2</sup>. Since ATO is known to not present activity towards OER, the standard unsupported IrO<sub>2</sub>-Li<sub>2</sub>CO<sub>3</sub> was compared at the same precious metal loading.

The activity of prepared IrO<sub>2</sub>/ATO was determined by LSV. The initial LSV performed at the beginning of the experiment revealed that IrO<sub>2</sub>/ATO-K<sub>2</sub>CO<sub>3</sub> had lower intrinsic activity towards OER compared to IrO<sub>2</sub>/ATO-Na<sub>2</sub>CO<sub>3</sub> and IrO<sub>2</sub>/ATO-Li<sub>2</sub>CO<sub>3</sub>. At 5 mA·cm<sup>-2</sup> the measured potential was 1.49 V<sub>RHE</sub>, 1.51 V<sub>RHE</sub> and 1.63 V<sub>RHE</sub> for IrO<sub>2</sub>/ATO catalysts prepared

with  $\text{Na}_2\text{CO}_3$ ,  $\text{Li}_2\text{CO}_3$  and  $\text{K}_2\text{CO}_3$  respectively. Compared to unsupported  $\text{IrO}_2$  ( $1.54 \text{ V}_{\text{RHE}}$  at  $5 \text{ mA}\cdot\text{cm}^{-2}$ ) supported  $\text{IrO}_2/\text{ATO-Na}_2\text{CO}_3$  and  $\text{IrO}_2/\text{ATO-Li}_2\text{CO}_3$  presented improved activity (figure 4.3).

In order to detect catalyst degradation, LSV was recorded after CV and after CP (figure 4.4).  $\text{IrO}_2/\text{ATO-Na}_2\text{CO}_3$  catalyst had better initial activity than  $\text{IrO}_2/\text{ATO-Li}_2\text{CO}_3$ . Both catalysts,  $\text{IrO}_2/\text{ATO-Li}_2\text{CO}_3$  and  $\text{IrO}_2/\text{ATO-Na}_2\text{CO}_3$ , were stable after the CV cycles giving almost identical LSV profiles before and after the CV. In comparison,  $\text{IrO}_2/\text{ATO-K}_2\text{CO}_3$ , showed deactivation after the CV cycles as observed by the shift by 68 mV towards higher potentials of the LSV at  $5 \text{ mV}\cdot\text{cm}^{-2}$ . Both supported,  $\text{IrO}_2/\text{ATO-Li}_2\text{CO}_3$ , and unsupported,  $\text{IrO}_2\text{-Li}_2\text{CO}_3$ , catalysts presented a comparable potential increase during the CP stability test. However, LSV performed after the stability test indicated that unsupported catalyst has undergone three times higher deactivation than supported  $\text{IrO}_2$ .

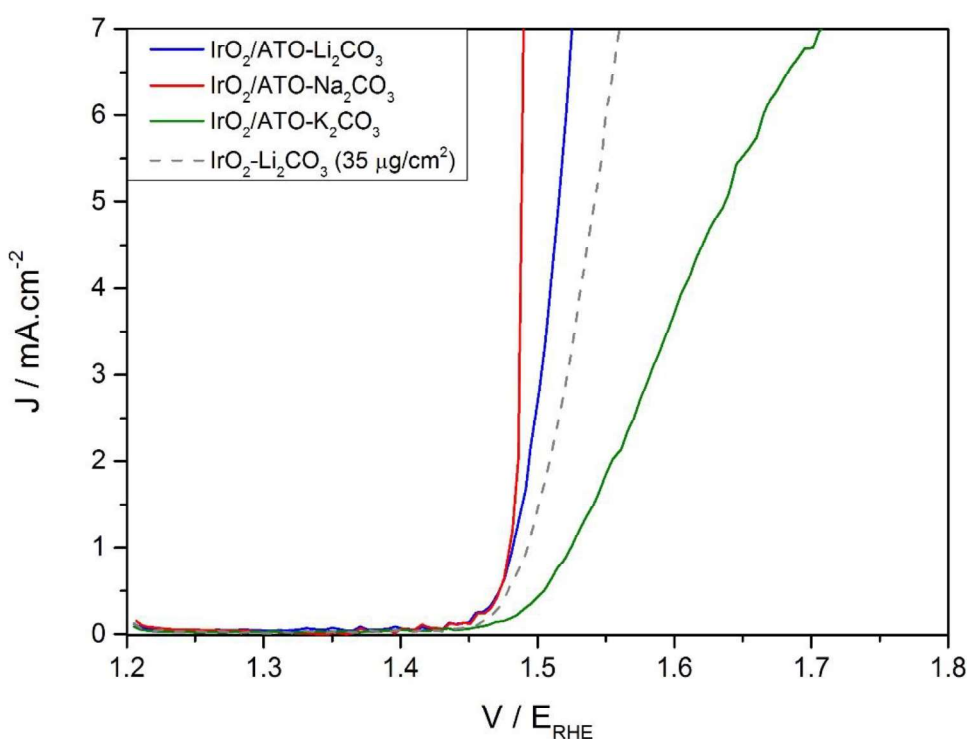


**Figure 4.3.** Initial LSV performed for supported  $\text{IrO}_2/\text{ATO}$  prepared through a hydrothermal synthesis using  $\text{Li}_2\text{CO}_3$ ,  $\text{Na}_2\text{CO}_3$  or  $\text{K}_2\text{CO}_3$  as a base. Dashed-grey line represents the unsupported  $\text{IrO}_2\text{-Li}_2\text{CO}_3$  catalyst. Iridium loading for all catalysts is  $35 \mu\text{g}\cdot\text{cm}^{-2}$ .

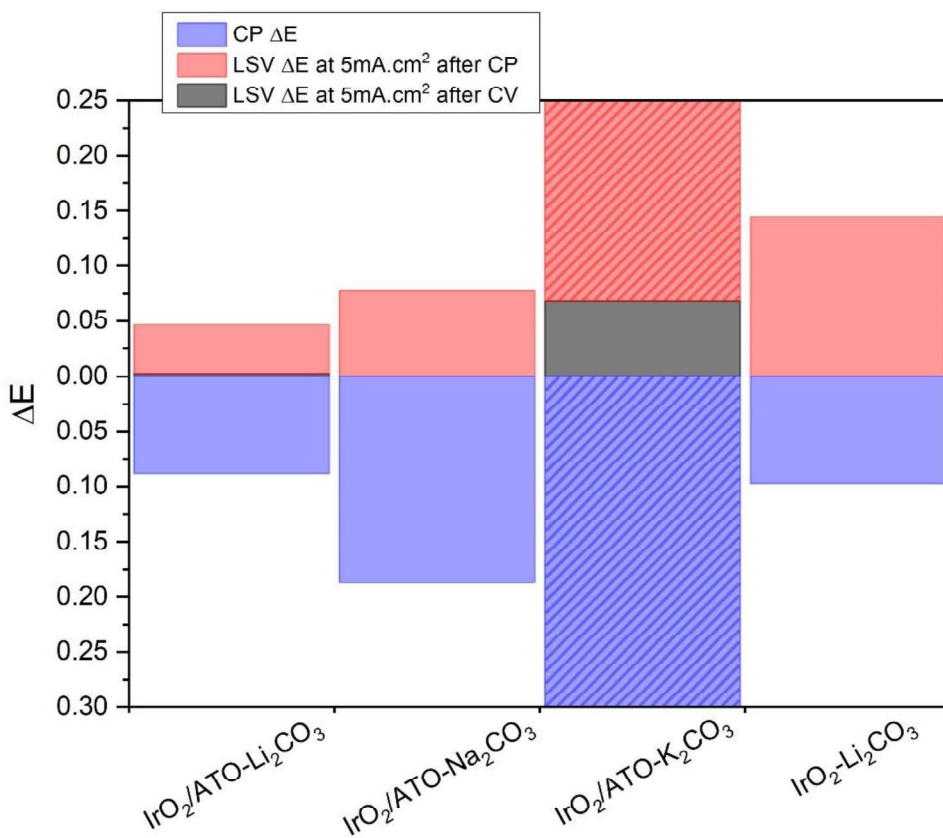


**Figure 4.4.** Stability indicators for  $\text{IrO}_2/\text{ATO}$  catalysts prepared through a hydrothermal process using different alkali metal bases. The black bars represent the increase in potential to reach a current density of  $5 \text{ mA}\cdot\text{cm}^{-2}$  after CV. Red bars represents the increase in potential to reach a current density of  $5 \text{ mA}\cdot\text{cm}^{-2}$  after CP. Blue bars indicate the increase in potential during the CP (dashed lines indicate that no  $5 \text{ mA}\cdot\text{cm}^{-2}$  were reached or that the glassy carbon corrosion potential was observed).

Chronopotentiometry (CP) was used to determine the stability of the catalysts. The potential needed to maintain a constant current density of  $10 \text{ mA}\cdot\text{cm}^{-2}$  for 2 h was monitored. Stable catalysts would present a steady potential, nevertheless, deactivation of the catalysts would be observed as an increase of the potential as the reaction proceeds. A measured potential close to the glassy carbon corrosion,  $2.2 \text{ V}_{\text{RHE}}$ , would indicate the complete deactivation of the catalyst.  $\text{IrO}_2/\text{ATO}-\text{K}_2\text{CO}_3$  presented a sharp rise in the potential, which reached the glassy carbon corrosion after 1 h, indicating its complete degradation. The poor stability of  $\text{IrO}_2/\text{ATO}-\text{K}_2\text{CO}_3$  was expected from the TEM characterisation, where agglomeration of  $\text{IrO}_2$  without intimate interaction with the support was observed. On the other hand, supported  $\text{IrO}_2/\text{ATO}-\text{Li}_2\text{CO}_3$ ,  $\text{IrO}_2/\text{ATO}-\text{Na}_2\text{CO}_3$  and unsupported  $\text{IrO}_2-\text{Li}_2\text{CO}_3$  showed a more steady potential through time (figure 4.5). The signal measured during the CP test was noisy, potential spikes were detected through the experiment due to the formation of oxygen bubbles. The growth of bubbles at the surface of the electrode blocked active sites inducing

an extra overpotential, if the bubble is not detached from the electrode, its progressive growth would result in the loss of contact between the electrodes, producing the observed potential spike, until the bubble is released from the electrode.<sup>(10, 11)</sup> Because of the signal noise, monitored potentials overlapped with each other (light coloured lines in figure 4.5), hence, in order to allow catalysts comparison signals were smoothed applying a filter available within the origin software used for data processing (dark coloured lines in figure 4.5).

The percentile filter is recommended against other widely used data smoothing filters, such Savitzky-Golay or FFT (Fast Fourier Transform), on data that presents noise localised as spikes and when the overall shape of the curve is not desired. The basic schematic idea behind the percentile filter is to determine the median value in a window of data points. Each raw data point is substituted with the median value of neighbouring data points. The necessary data points, or window width, to measure the median value in order to obtain a clear signal depends on the magnitude of the noise. The wider the window the more raw data points are discriminated and hence it is preferable to narrow as much as possible the window used. The number of data points applied on  $\text{IrO}_2$ ,  $\text{IrO}_2/\text{ATO-Li}_2\text{CO}_3$ ,  $\text{IrO}_2/\text{ATO-Na}_2\text{CO}_3$  and  $\text{IrO}_2/\text{ATO-K}_2\text{CO}_3$  to smooth the data were 480, 100, 750 and 750 respectively.

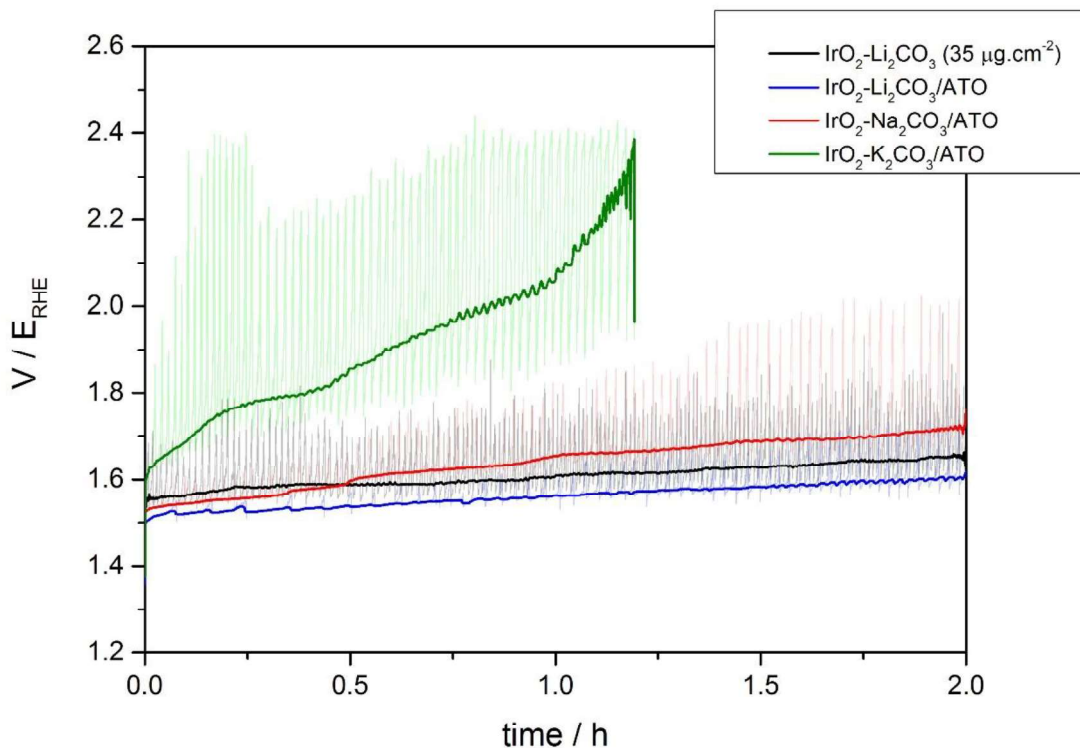


**Figure 4.5.** Supported  $\text{IrO}_2/\text{ATO}$  catalysts stability determination by CP ( $10 \text{ mA} \cdot \text{cm}^{-2}$  during 2 h). The Iridium loading on the electrode was  $35 \mu\text{g} \cdot \text{cm}^{-2}$  for supported and unsupported  $\text{IrO}_2$  catalysts.

To summarise, high dispersion of the scarce  $\text{IrO}_2$  on ATO was obtained through a hydrothermal process in alkaline conditions.  $\text{Li}_2\text{CO}_3$ ,  $\text{Na}_2\text{CO}_3$  or  $\text{K}_2\text{CO}_3$  was used as a base during the synthesis. No differences were observed between  $\text{IrO}_2/\text{ATO}-\text{Li}_2\text{CO}_3$  and  $\text{IrO}_2/\text{ATO}-\text{Na}_2\text{CO}_3$  on the performed characterisation. It is believed that a film of iridium oxohydroxide was formed on the support surface. However,  $\text{IrO}_2$  agglomerates without support interaction were observed for  $\text{IrO}_2/\text{ATO}-\text{K}_2\text{CO}_3$ , which in turn presented poor activity and stability towards OER. As observed for un-supported  $\text{IrO}_2$  in chapter 3, the use of  $\text{Li}_2\text{CO}_3$  as a base during the synthesis enhanced the catalytic performance towards OER.

Supporting  $\text{IrO}_2$  presented multiple benefits. It represents a more efficient iridium usage since the active phase was concentrated at the surface of the ATO. The iridium mass activity increased since more active sites would be available. Therefore, it allows the reduction of iridium loading on the electrode, in a total catalysts loading of  $100 \mu\text{g}_{\text{cat}} \cdot \text{cm}^{-2}$  on to the electrode, the iridium loading was reduced from  $85 \mu\text{g} \cdot \text{cm}^{-2}$  for  $\text{IrO}_2$  to  $27 \mu\text{g} \cdot \text{cm}^{-2}$  for supported  $\text{IrO}_2/\text{ATO}$ . Moreover, supported catalyst activity and stability towards OER was enhanced compared to un-supported  $\text{IrO}_2$ .

### 4.3 Heat treatment effect on the IrO<sub>2</sub>/ATO-Li<sub>2</sub>CO<sub>3</sub> catalyst.

It was observed that the base used during the hydrothermal synthesis of supported amorphous iridium oxo-hydroxides has a considerably influence in the activity and stability of the catalyst towards OER. The use of Li<sub>2</sub>CO<sub>3</sub> in the preparation of IrO<sub>2</sub>/ATO produced a catalyst that outperformed in activity and stability IrO<sub>2</sub>/ATO catalysts prepared with Na<sub>2</sub>CO<sub>3</sub> or K<sub>2</sub>CO<sub>3</sub> bases. However, the activity of the IrO<sub>2</sub>/ATO-Li<sub>2</sub>CO<sub>3</sub> catalyst degraded through reaction, as observed by the steady increase in the potential during CP and to the increase in the overpotential by LSV before and after the stability test. Therefore, there is still room for improvement. It has been reported by Olga *et al.* that the formation of O<sub>2</sub> and the dissolution of IrO<sub>2</sub> share common intermediates, IrO<sub>3</sub> or IrO<sub>2</sub>OH depending of the reaction pathway.<sup>(12)</sup> Since SnO<sub>2</sub> is a reducible support, heat treatment in a reducing environment followed by oxidation, both at mild temperatures, could lead to a thin growth of the support over the IrO<sub>2</sub>.<sup>(13, 14)</sup> Metal-support interactions could lead to the stabilisation of the iridium intermediates, balancing the equilibrium towards the oxygen evolution instead of to the iridium dissolution.

#### 4.3.1 Reduction and oxidation heat treatments on the IrO<sub>2</sub>/ATO-Li<sub>2</sub>CO<sub>3</sub> catalyst.

Reduction and oxidation heat treatments performed on IrO<sub>2</sub>/ATO-Li<sub>2</sub>CO<sub>3</sub> catalyst are listed in table 4.2. The reduction treatment would lead to the reduction of IrO<sub>2</sub> to metallic iridium and to the growth of the support over it. A subsequent oxidation treatment would be necessary in order to regenerate the IrO<sub>2</sub> phase since metallic iridium is active but unstable against dissolution under OER reaction conditions.<sup>(15)</sup> Relatively mild oxidation treatment is desired, as it has been observed previously in the literature that amorphous iridium oxo-hydroxides are more active than bulk oxides. In chapter 3, it was observed a decrease in the activity and stability of the IrO<sub>2</sub>-Li<sub>2</sub>CO<sub>3</sub> catalyst after annealing at mild conditions. Additionally, numerous reports on the preparation of IrO<sub>2</sub> indicate a decrease in the activity with increasing heat treatment temperature.<sup>(16-18)</sup>

Before starting with the reducing and oxidising heat treatments, it was necessary to determine the minimum temperature to reduce the support, and hence to induce its growth over the iridium. From chapter 3, it was observed by H<sub>2</sub>-TPR that amorphous iridium oxo-hydroxides reduced below 100 °C. Nevertheless, as illustrated in figure 4.6, the reduction of commercial ATO started at 450 °C. H<sub>2</sub>-TPR for IrO<sub>2</sub>/ATO-Li<sub>2</sub>CO<sub>3</sub> catalyst presented three differentiated reduction peaks. The first peak close to 100 °C was related with the reduction of amorphous iridium oxo-hydroxide to metallic iridium, the two following peaks were

associated with the support.<sup>(5)</sup> The former reduction peak starting at 300 °C was most probably related to the reduction of superficial  $\text{SnO}_2$  in contact with iridium. As observed for other precious metals,  $\text{H}_2$  dissociates on metal surfaces and then H atoms migrate to the metal/support interphase.<sup>(19)</sup> In this case, and as it will be confirmed by TEM, hydrogen spill-over induce the support to grow over the metallic Ir particles. Another possible scenario for reducible supports would be the formation of an alloy with the precious metal as observed for Pd and Zn.<sup>(20)</sup> The complete encapsulation of metallic iridium by the support stopped the hydrogen spill over mechanism, explaining the latter reduction peak, correlated with the reduction of bulk  $\text{SnO}_2$  at 450 °C as observed for as received commercial ATO.

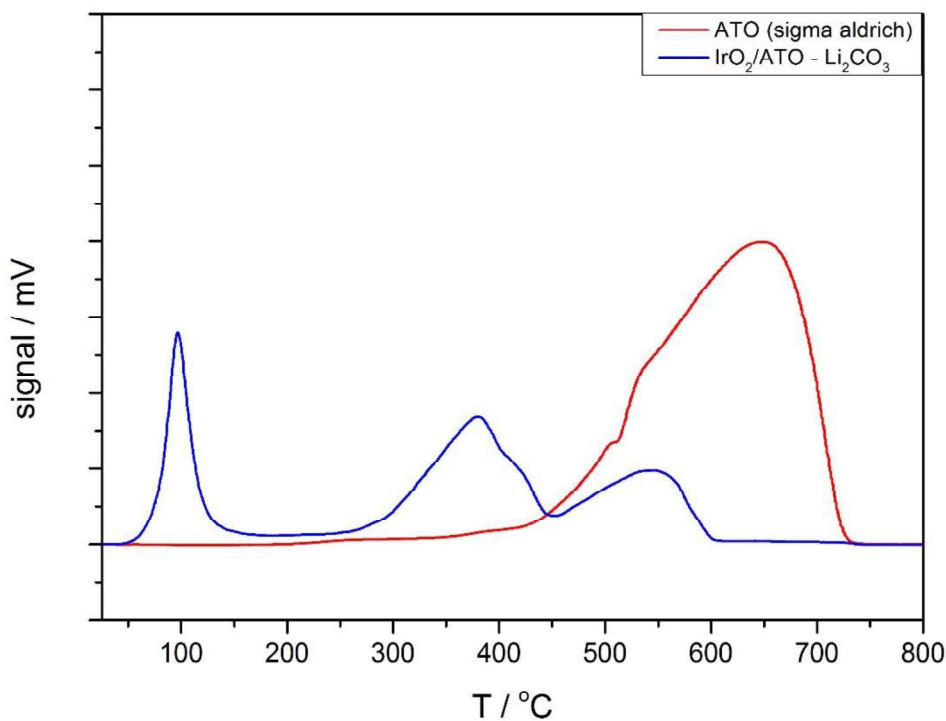


**Figure 4.6.** The reduction profile for as received commercial ATO (Sigma Aldrich) and hydrothermally prepared  $\text{IrO}_2/\text{ATO}-\text{Li}_2\text{CO}_3$  by  $\text{H}_2$ -TPR (60 mg of material were degased under a helium stream for 2 hours, the TPR was undertaken under 10 %  $\text{H}_2/\text{Ar}$  with a  $100 \text{ ml}\cdot\text{min}^{-1}$  flow,  $5 \text{ }^\circ\text{C}\cdot\text{min}^{-1}$  to 800 °C).

From the  $\text{H}_2$ -TPR profile it was observed that the support started to reduce at 300 °C on  $\text{IrO}_2/\text{ATO}-\text{Li}_2\text{CO}_3$  catalyst. Reductions were performed under 5 %  $\text{H}_2/\text{Ar}$  flow and oxidation treatments were done in static air. Heat treatment conditions, reduction and oxidation, were carried out at 300 °C for 3 h and at a  $10 \text{ }^\circ\text{C}\cdot\text{min}^{-1}$  ramp rate.

**Table 4.2.** Reduction and oxidation heat treatments performed on  $\text{IrO}_2/\text{ATO-Li}_2\text{CO}_3$  catalyst.

Oxidation / °C	Reduction / °C	Oxidation / °C
300	-	-
300	300	
300	300	300

#### 4.3.2 Heat treated $\text{IrO}_2/\text{ATO-Li}_2\text{CO}_3$ catalysts characterisation.

##### *X-ray powder diffraction (XRD)*

The crystalline phase changes of  $\text{IrO}_2/\text{ATO-Li}_2\text{CO}_3$  catalyst after the different reduction and oxidation heat treatments were followed by XRD. Heat treatment at 300 °C in air was not sufficiently high to produce the crystallisation of hydrous iridium oxo-hydroxide to rutile as observed by XRD, since no  $\text{IrO}_2$  rutile (JCPDS-015-0876) reflections were observed. Conversely, a broad reflection appeared at 40.8° after the reduction treatment at 300 °C indicating the formation of metallic iridium (JCPDS-006-0598). The reflection attributed to metallic iridium observed after the reduction treatment remained visible in the XRD pattern after the consecutive oxidation at 300 °C, indicating the no complete re-oxidation of metallic iridium to an oxide form (figure 4.7). Since metallic iridium is not stable against anodic dissolution during the reaction, the catalyst after reduction was annealed in air at 500 °C for 3 h; nevertheless, the metallic iridium reflection persisted. In accordance with published results on the commercial  $\text{IrO}_2 \cdot 2\text{H}_2\text{O}$  catalyst, where the presence of metallic iridium was detected by XRD even after annealing in pure  $\text{O}_2$  at 800 °C for 50 hours, it is though that a metallic-iridium-core remained inaccessible to oxygen and that it is being protected by a shell of  $\text{IrO}_2$ .<sup>(1)</sup>

Heat treatment, either oxidation or reduction, produced a decrease in the intensity of the support reflections as if crystallinity of  $\text{SnO}_2$  was being reduced; however, no decrease on the ATO crystallite size was detected using the Scherrer equation. In fact, the calculation of the crystallite size indicated a subtle increase as presented in table 4.3, probably produced by sintering.

**Table 4.3.** Determination of the ATO crystallite size through the Scherrer equation for the  $\text{IrO}_2/\text{ATO-Li}_2\text{CO}_3$  catalyst after heat treatment at 300 °C under reducing or oxidising conditions.

<b><math>\text{IrO}_2/\text{ATO-Li}_2\text{CO}_3</math> heat treatment</b>	<b>Crystallite size / nm</b>
fresh	27
Oxidation	27
Oxidation + Reduction	30
Oxidation + Reduction + Oxidation	32

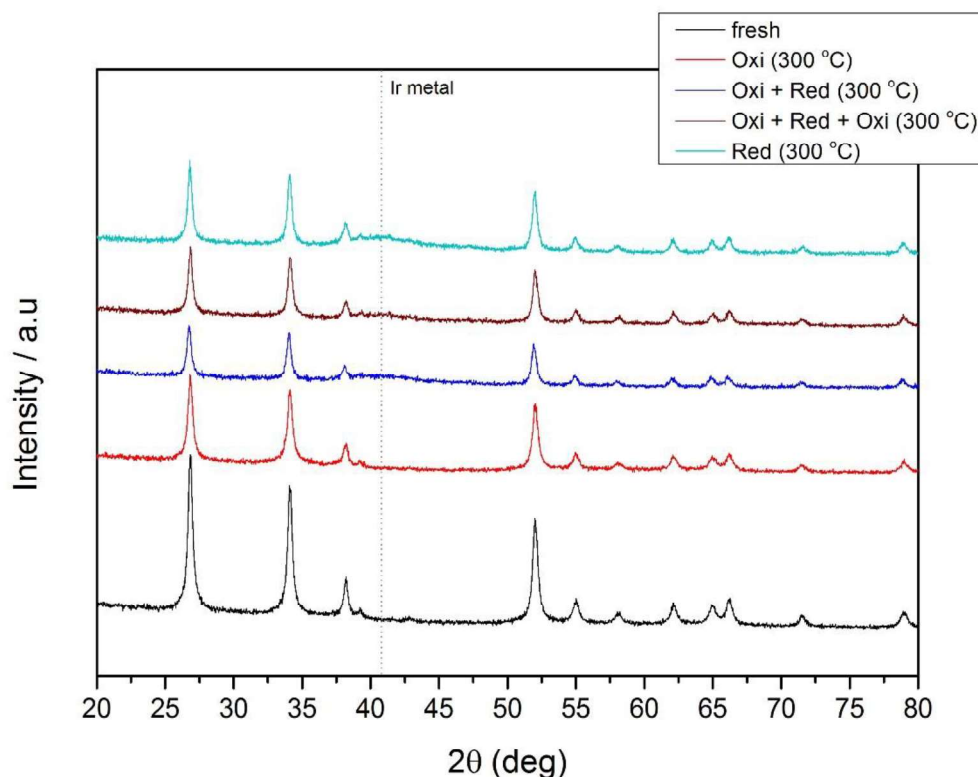


**Figure 4.7.** XRD pattern for heat treated (reduction and oxidation)  $\text{IrO}_2/\text{ATO-Li}_2\text{CO}_3$  catalysts. Reduction and oxidation treatment was performed at 300 °C,  $10 \text{ °C}\cdot\text{min}^{-1}$  for 3 h.

#### X-ray photoelectron spectroscopy (XPS)

XRD characterisation indicated that once the  $\text{IrO}_2/\text{ATO-Li}_2\text{CO}_3$  catalyst has gone through a reducing treatment, and metallic iridium was formed, it could not be completely re-oxidised to  $\text{IrO}_2$ , even if treatment in air at 500 °C. Annealing in air at 300 °C followed by a shift of the Ir(4f) peak towards lower binding energy which can be attributed to the oxidation of Ir(III) sites to Ir(IV), as reported by Pfeifer.<sup>(21)</sup> In accordance with the results obtained by XRD, reduction treatment at 300 °C shifted the Ir(4f) orbital binding energy downwards, from 62.5

eV for the fresh catalyst or 62.0 eV for the annealed catalyst to 60.5 eV (figure 4.8), indicating the transformation of iridium oxo-hydroxide to metallic iridium.<sup>(22)</sup>

The heat treatment in air at 300 °C of the catalyst containing metallic iridium led to a shift towards higher binding energy on the Ir(4f) peak; however, it shifted to an intermediate binding energy between the metallic and the oxide state, indicating the partial oxidation of metallic iridium to  $\text{IrO}_2$ , as indicated by XRD.

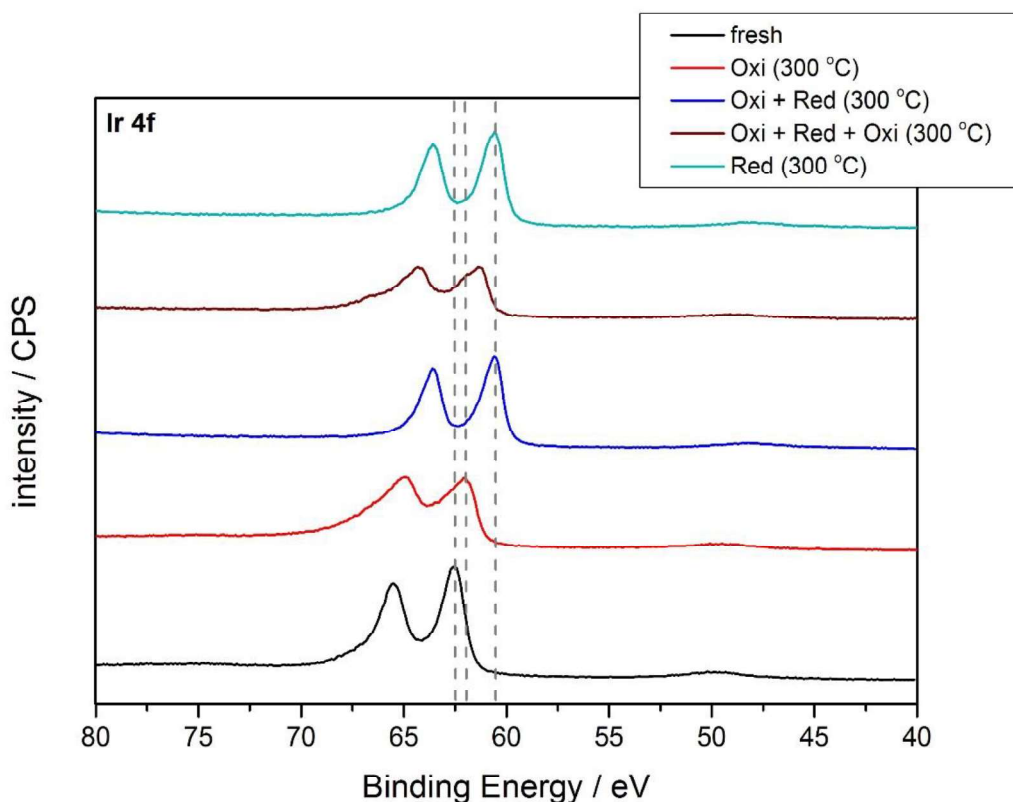


**Figure 4.8.** Ir(4f) XPS orbital recorded for  $\text{IrO}_2/\text{ATO}-\text{Li}_2\text{CO}_3$  catalyst after heat treatment under reducing in 5 % /  $\text{H}_2/\text{Ar}$  or oxidising in static air for 3 h.

Conversely, reversible reduction and oxidation of tin was observed by XPS. The oxidation treatment at 300 °C produced little changes in the chemical shift of the Sn(3d) orbital at 486.9 eV. Nevertheless, a new peak at 485.7 eV appeared upon reduction at 300 °C, indicating the partial reduction of  $\text{Sn}^{+4}$  to  $\text{Sn}^{+2}$ .<sup>(23)</sup> The Sn(3d) signal intensity increased after reduction, which might indicate tin migration towards the surface and through the iridium layer. As observed by H<sub>2</sub>-TPR, the support presented two distinct reduction peaks, the one at 300 °C was assigned to  $\text{SnO}_2$  in contact with the metallic iridium and the second at 450 °C to bulk  $\text{SnO}_2$ . Hence, the peak contribution at 486.9 eV which was not affected by reducing conditions can be assigned to bulk  $\text{SnO}_2$ . Consecutive annealing in air at 300 °C followed by

the disappearance of the Sn<sup>+2</sup> peak, indicating its re-oxidation to Sn<sup>+4</sup> (figure 4.9). The analysis of the Sb(3d) orbital was more complex since O(1s) overlaps with the Sb(3d<sub>5/2</sub>) orbital.<sup>(7, 14)</sup> Additionally, Sb<sub>2</sub>O<sub>3</sub> and Sb<sub>2</sub>O<sub>5</sub> coexist in the SnO<sub>2</sub> lattice. Previous reports suggested that Sb<sub>2</sub>O<sub>3</sub> is predominantly present near the surface while Sb<sub>2</sub>O<sub>5</sub> resides deeper in the ATO bulk.<sup>(8)</sup> The Sb(3d<sub>3/2</sub>) and Sb(3d<sub>5/2</sub>) contributions were assigned at 540.6 eV and 531.2 eV for Sb<sub>2</sub>O<sub>5</sub> respectively. The lower oxidation state corresponding to Sb<sub>2</sub>O<sub>3</sub> were assigned at 539.6 eV and 530.7 eV for Sb(3d<sub>3/2</sub>) and Sb(3d<sub>5/2</sub>) respectively. Oxygen contributions were assigned at 530.6 eV. It is important to stress that due to the complexity of the antimony peak, determined speciation for Sb<sub>2</sub>O<sub>5</sub>, Sb<sub>2</sub>O<sub>3</sub> and oxygen is indicative of the chemical changes during the reduction and oxidation treatment but they might be subject to discrepancies. For instance, the oxygen peak has been given an asymmetric shape. However, it is well known that conductive metal oxides, as in IrO<sub>2</sub>, presents an asymmetric peak.<sup>(22)</sup> Additionally, a single oxygen peak has been assigned, but different oxygen species coexist in the sample, IrO<sub>2</sub>, SnO<sub>2</sub> and Sb<sub>2</sub>O<sub>x</sub>.

Analogous to the behaviour observed for the Sn(3d) orbital, a shoulder at lower binding energy, 538.3 eV and 528.9 eV in the Sb(3d<sub>3/2</sub>) and Sb(3d<sub>5/2</sub>) respectively, appeared after reduction at 300 °C. Since the shoulder was present on both Sb(3d) orbitals, it cannot be assigned merely to an oxygen change as it only overlaps with the Sb(3d<sub>5/2</sub>) orbital. The appearance of this new peak at 528.9 eV can be assigned to the reduction of surface Sb<sub>2</sub>O<sub>3</sub> to metallic Sb<sup>(24)</sup> (figure 4.10). The shoulder assigned to metallic Sb disappeared after consecutive annealing in air at 300 °C indicating its complete re-oxidation to Sb<sub>2</sub>O<sub>3</sub>. Parameters used for fitting the Sn(3d), Sb(3d) and O(1s) are presented in table 4.4.

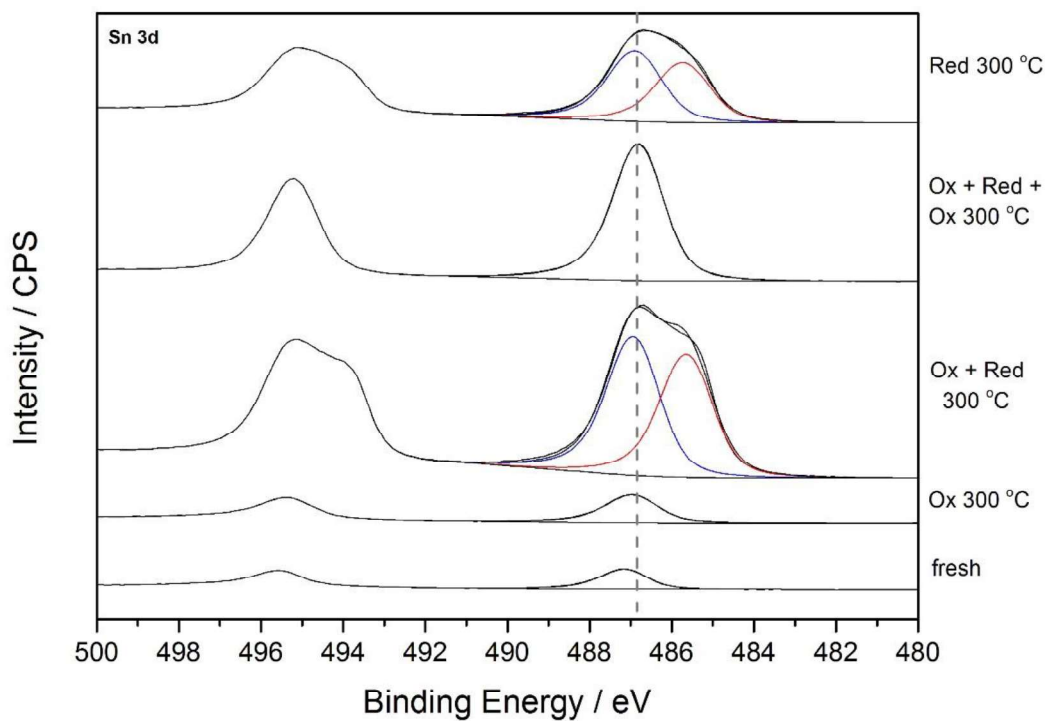


**Figure 4.9.** XPS Sn(3d) spectra for hydrothermally prepared  $\text{IrO}_2/\text{ATO}-\text{Li}_2\text{CO}_3$  catalyst being heat treated under reducing and oxidising conditions. Peak fitting was done just on the  $\text{Sn}(3d_{5/2})$  orbital, lower binding energy, blue and red fitting relates to Sn(IV) and Sn(II) respectively.

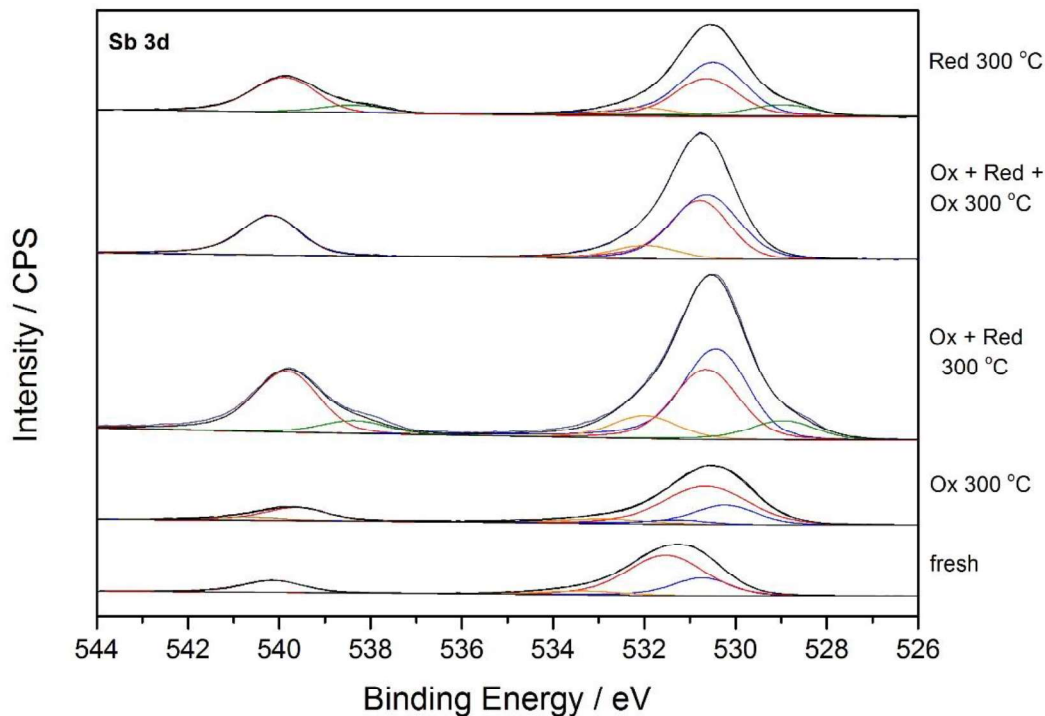


**Figure 4.10.** XPS Sb(3d) and O(1s) spectra for hydrothermally prepared  $\text{IrO}_2/\text{ATO}-\text{Li}_2\text{CO}_3$  catalysts heat treated under reducing and oxidising conditions. Higher binding energy peak corresponds to  $\text{Sb}(3\text{d}_{3/2})$  orbital and the peak at lower binding energy correspond to  $\text{Sb}(3\text{d}_{5/2})$  peak overlapping with O(1s) peak.  $\text{Sb}_2\text{O}_5$ ,  $\text{Sb}_2\text{O}_3$  and metallic Sb are assigned to orange, red and green peak fitting respectively. Oxygen is represented in blue fitting.

**Table 4.4.** Peak parameters used for fitting the Sn(3d5/2), Sb(3d5/2) and the O(1s) orbitals. Sn, Sb and O components were fitted using a LF(0.7, 0.9, 45, 380), LF(0.7, 1.255, 280, 6) and LF(0.9, 1.255, 280, 3) line shape respectively.

	$\text{Sn}_2\text{O}_5$	$\text{Sn}^0$	$\text{Sb}_2\text{O}_3$	$\text{Sb}_2\text{O}_5$	$\text{Sb}^0$	O
Position / eV	486.9	485.7	530.4	532.0	528.9	530.6
FWHM / eV	1.5	1.5	1.6	1.7	1.6	1.7

The XPS orbital shape and binding energy shift from a determined element is representative of changes in the oxidation state and chemical environment. Moreover, since it is a surface

sensitive technique, valuable information about the surface composition could be obtained from the elements quantification. It was suggested that a layer of ATO would grow on supported IrO<sub>2</sub> after heat treatment in a reducing atmosphere.<sup>(14)</sup> In order to study the growth of the support over the iridium oxo-hydroxide layer, upon consecutive reduction and oxidation heat treatments, the element quantification was calculated by XPS. Because of Sb(3d) overlapping with O(1s) peak, the Sb(4d) orbital was used instead for its quantification; Ir (4d) and Sn (3d) were used for the quantification of the respective elements.

As illustrated in table 4.5, annealing at 300 °C in air induced no composition changes in the surface element quantification compared to the fresh IrO<sub>2</sub>/ATO-Li<sub>2</sub>CO<sub>3</sub> sample. However, a rise in the Sn quantification simultaneously with a shrink on the Ir quantification was detected after reducing at 300 °C, suggesting tin migration towards the surface of the catalyst and the concomitant iridium encapsulation. The consecutive oxidation treatment in air produced no changes on the surface element quantification, thus indicating that the chemical rearrangement obtained under reducing conditions is not reversible.

**Table 4.5.** IrO<sub>2</sub>/ATO-Li<sub>2</sub>CO<sub>3</sub> catalysts surface element quantification obtained from the analysis of Sn(3d), Sb(4d) and Ir(4d) orbital by XPS after oxidation and reduction heat treatments.

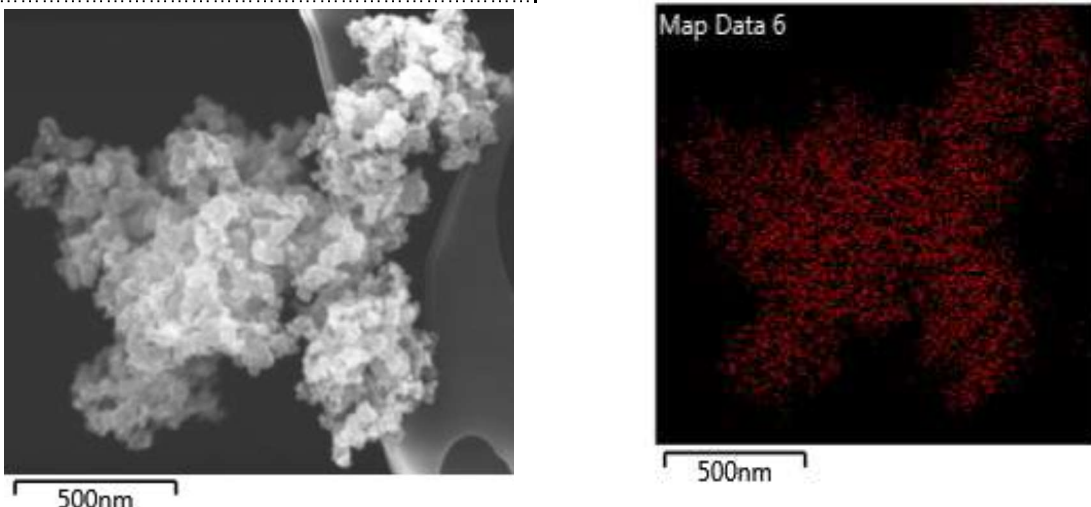
Heat treatment	At. Quant. / %		
	Ir (4d)	Sb (4d)	Sn (3d)
fresh	66	20	15
Ox. 300 °C	67	17	16
Ox + Red 300 °C	28	22	51
Ox + Red + Ox 300 °C	23	23	54
Red 300 °C	27	24	46

*Scanning electron microscopy (SEM)*

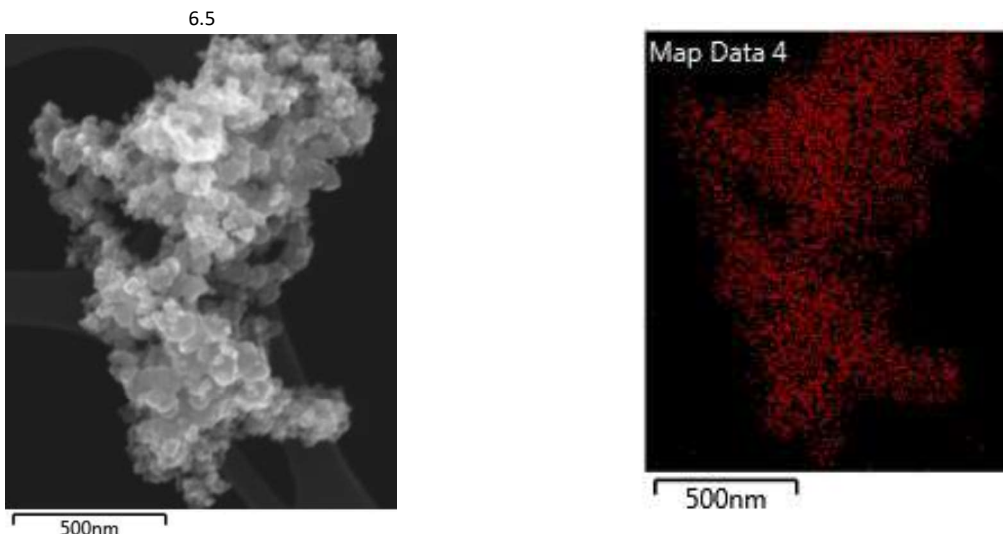
SEM-EDX imaging, undertaken on a TESCAN-MAIA3 SEM with a resolution on the nanoscale range, was performed in order to gain an insight in the morphological changes during the heat treatment under reducing or oxidising conditions. Even though the loading of iridium was slightly under 30 wt. %, samples were not stable under analysing conditions and suffered from electron beam damage, as observed previously during TEM imaging on IrO<sub>2</sub>-Li<sub>2</sub>CO<sub>3</sub> and supported IrO<sub>2</sub>/ATO prepared with different bases. This limited the use of this instrument for the analysis of the catalysts, resolution on the nanoscale range was desired in order to observe changes at the surface of the material and to detect the SnO layer growth over the IrO<sub>2</sub>. However, high magnification images could not be recorded as a result of the sample evolving under the electron beam. However, qualitative characterisation was obtained. As observed previously for fresh IrO<sub>2</sub>/ATO-Li<sub>2</sub>CO<sub>3</sub> by TEM (image 4.2a), iridium was homogeneously dispersed throughout the surface of the support. Likewise, SEM-EDX imaging showed that iridium dispersion through the materials seemed not to be affected after heat treatment at 300 °C, either under reducing or oxidising atmosphere (image 4.3). No big iridium agglomerates were observed; Nevertheless, the formation of the tin oxide layer could not be confirmed using this microscopic technique.

---

a).....



b).....



c).....

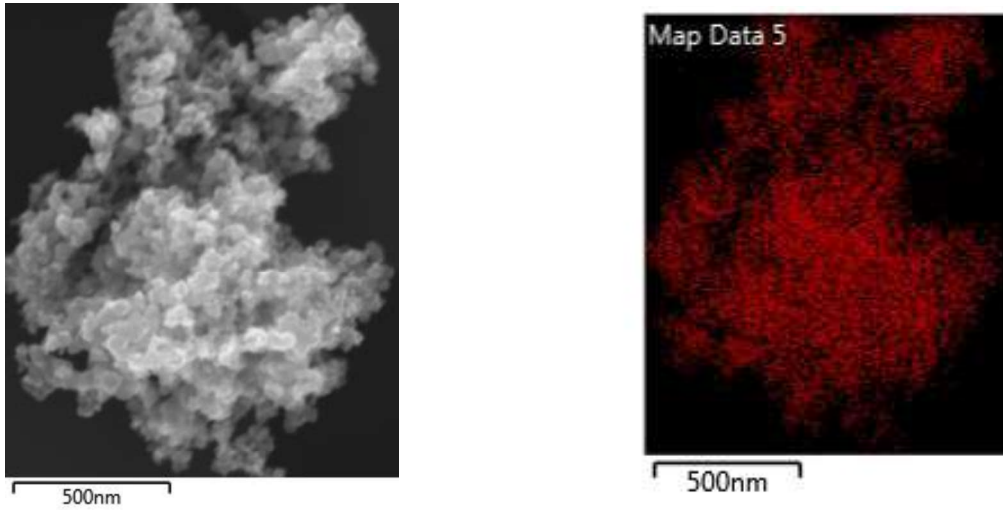


**Image 4.3.** Left side IrO<sub>2</sub>/ATO-Li<sub>2</sub>CO<sub>3</sub> catalyst images for a) fresh, b) annealed at 300 °C in air for 3 h and c) reduced at 300 °C under 5% H<sub>2</sub> / Ar for 3 h. Right side represents the respective iridium distribution obtained by EDX.

#### *High resolution transmission electron microscopy (HRTEM)*

As discussed previously, microscopy analysis on amorphous iridium oxo-hydroxide samples is challenging, even for supported samples. TEM characterisation for supported IrO<sub>2</sub>/ATO catalysts prepared with different bases suggests that a layer of IrO<sub>2</sub> was deposited onto the support surface forming a film; however, beam damage occurred during the acquisition, and hence the real image of the catalyst was not unveiled. As shown in chapter 3, and thanks to the characterisation expertise in the Fritz Haber Institute, amorphous hydrous iridium oxo-hydroxide could be analysed using low electron dose imaging without inducing beam damage on the sample.<sup>(9)</sup> It was suggested that for as prepared samples a film of

amorphous IrO<sub>2</sub> was formed on the ATO support through the hydrothermal synthesis. XPS characterisation indicated that no changes on the element quantification at the surfaces of the catalyst took place during annealing in air, hence, it could be assumed that the IrO<sub>2</sub> film remained unchanged. Conversely, an increase in the tin quantification by XPS from 15 % to 50 % with the concomitant iridium reduction from 66 % to 25 % was detected after reduction, indicating the growth of the support over metallic iridium. Low dose HRTEM is a non-conventional technique and access to it is limited. Thus, just the IrO<sub>2</sub>/ATO-Li<sub>2</sub>CO<sub>3</sub> reduced at 300 °C in 5 % H<sub>2</sub>/Ar was analysed.

Low electron dose imaging for IrO<sub>2</sub>/ATO-Li<sub>2</sub>CO<sub>3</sub> catalyst reduced at 300 °C was performed by Dr. Gerardo Algara Siller at the Fritz Haber Institute in Berlin as part of the MaxNet consortium. This imaging technique is desired as it avoids iridium rearrangement under the electron beam, allowing the accurate disclosure of the catalyst's morphology (image 4.4). HRTEM imaging for the sample after the reduction treatment showed metallic iridium agglomeration, the metallic iridium, however, was not forming a layer over the support but it was observed as small nanoparticles with an approximate particle size of 3-4 nm. As suggested from the H<sub>2</sub>-TPR profile, a support layer has grown over the metallic iridium covering it completely.

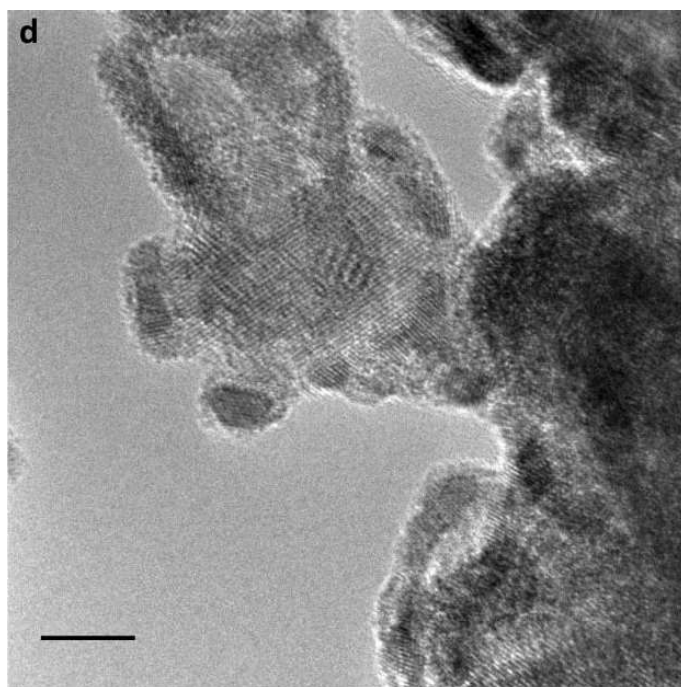


**Image 4.4.** Low electron dose HRTEM image for IrO<sub>2</sub>/ATO-Li<sub>2</sub>CO<sub>3</sub> after reduction at 300 C in 5% H<sub>2</sub>/Ar. The scale bar at the bottom-left corresponds to 5 nm.

#### 4.3.3 Catalytic activity towards OER.

Catalysts were tested in a three-electrode flow cell provided by the Max Planck Institute for chemical energy conversion in Mülheim, Germany<sup>(10)</sup> to determine its catalytic activity and stability. The testing protocol consisted of LSV, CV, LSV, CP, LSV. Linear sweep voltammetry was performed from  $1.2 \text{ V}_{\text{RHE}}$  to  $1.8 \text{ V}_{\text{RHE}}$  at  $5 \text{ mV}\cdot\text{s}^{-1}$ , cyclic voltammetry was done between  $0.7 \text{ V}_{\text{RHE}}$  and  $1.4 \text{ V}_{\text{RHE}}$  at  $50 \text{ mV}\cdot\text{s}^{-1}$  for 50 cycles. The stability was tested through a chronopotentiometry by maintaining  $10 \text{ mA}\cdot\text{cm}^{-2}$  during 2 hours. Details about the catalyst ink preparation and the working electrode preparation can be found in the experimental section.

LSV, performed at the beginning of the experiment in order to determine the intrinsic catalyst activity, showed that, after the heat oxidation treatment in air at  $300 \text{ }^\circ\text{C}$ , the potential increased by 22 mV compared to the fresh catalyst (figure 4.11). Similar deactivation behaviour was observed previously for unsupported  $\text{IrO}_2\text{-Li}_2\text{CO}_3$  catalyst. Comparable published results in the literature showed that heat treatment normally have a detrimental effect on the activity of  $\text{IrO}_2$  towards OER,<sup>(17)</sup> usually associated with a decrease in the hydration and loss of surface hydroxides in the conversion of amorphous iridium oxohydroxides to its crystalline counterpart.<sup>(1, 2, 25)</sup> After the reduction heat treatment at  $300 \text{ }^\circ\text{C}$ , the catalyst activity plummeted. It has been reported that metallic iridium presented higher activity than its oxide, however its dissolution during OER reaction is three orders of magnitude higher.<sup>(15, 26)</sup> Hence, the sharp decrease in activity was more likely to be associated with iridium encapsulation by the non-active support growth, induced by the reducing environment as observed by low electron dose HRTEM and XPS quantification. The consecutive oxidation treatment in air at  $300 \text{ }^\circ\text{C}$  led to no recovery in the catalyst activity since the iridium encapsulation was not disrupted as indicated by XPS quantification. Therefore, water access to the OER active sites was restricted and iridium migration towards the surface did not occur after annealing.

In order to induce iridium migration towards the surface, the catalyst reduced at  $300 \text{ }^\circ\text{C}$  was annealed in air at  $500 \text{ }^\circ\text{C}$  for 3 h. Nevertheless, no improvement on the catalyst activity was observed. Under the reducing conditions applied, the layer of  $\text{IrO}_2$  assumed to be formed on the as prepared catalyst agglomerated to metallic iridium particles; presumably this occurred around  $100 \text{ }^\circ\text{C}$  as observed by the  $\text{H}_2\text{-TPR}$  reduction profile. Higher reduction temperatures led to the reduction of ATO in contact with the metallic Ir nanoparticles, followed by its migration over the iridium particles forming a layer. The formed structure could not be altered

by consecutive oxidation treatment. Thus, a protective layer of the support was successfully grown after the reduction treatment, although it blocked reagents access to the active sites.

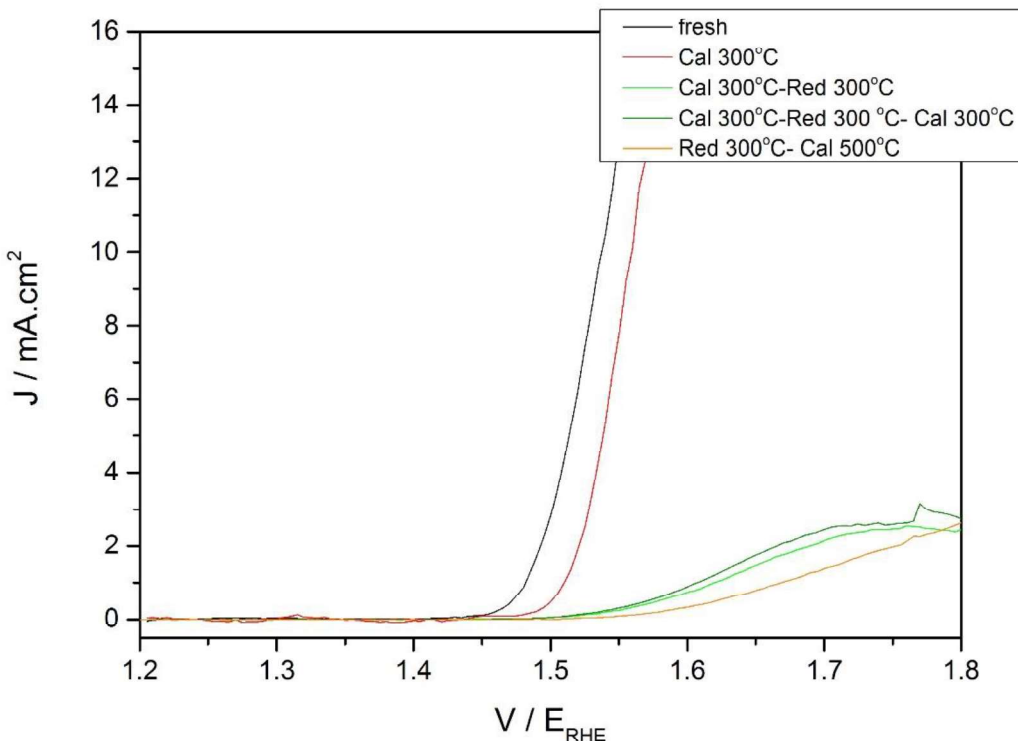


**Figure 4.11.** Initial LSV in order to determine the intrinsic catalyst activity of heat treated  $\text{IrO}_2/\text{ATO}-\text{Li}_2\text{CO}_3$  samples under reducing (5 %  $\text{H}_2/\text{Ar}$ ) and oxidising conditions (static air).

Information about the active sites involved during OER could be unveiled by CV. On one hand, the area under the CV curve is indicative of the concentration of active sites, on the other, its shape reveals the oxidation state of the iridium sites. An asymmetric CV curve with charging at high potential with the low intense  $\text{Ir}(\text{III})/\text{Ir}(\text{IV})$  and  $\text{Ir}(\text{IV})/\text{Ir}(\text{V})$  transitions was observed for fresh  $\text{IrO}_2\text{-Li}_2\text{CO}_3$  catalyst,<sup>(27, 28)</sup> a comparable CV curve was observed for as prepared  $\text{IrO}_2/\text{ATO-Li}_2\text{CO}_3$  (figure 4.12a). After annealing at 300 °C in air for 3 h, a high symmetric peak distinctive of rutile  $\text{IrO}_2$  without any iridium transitions was observed (figure 4.12b) which agrees with the observed deterioration in activity by LSV.

The current density measured during CV dropped one order of magnitude after the reduction treatment (figure 4.12c) in accordance with ATO growing over the iridium, as observed by HRTEM and XPS, hampering the access of the reaction media to the active phase. Following the trend observed on the LSV measurements, subsequent annealing did not translate in an increase in the measured current density or change in the CV shape (figure

4.12d). As discussed previously, annealing treatment did not alter the surface composition and, even though partial metallic iridium oxidation to  $\text{IrO}_2$  was observed, the active sites remained inaccessibly covered by a support layer.

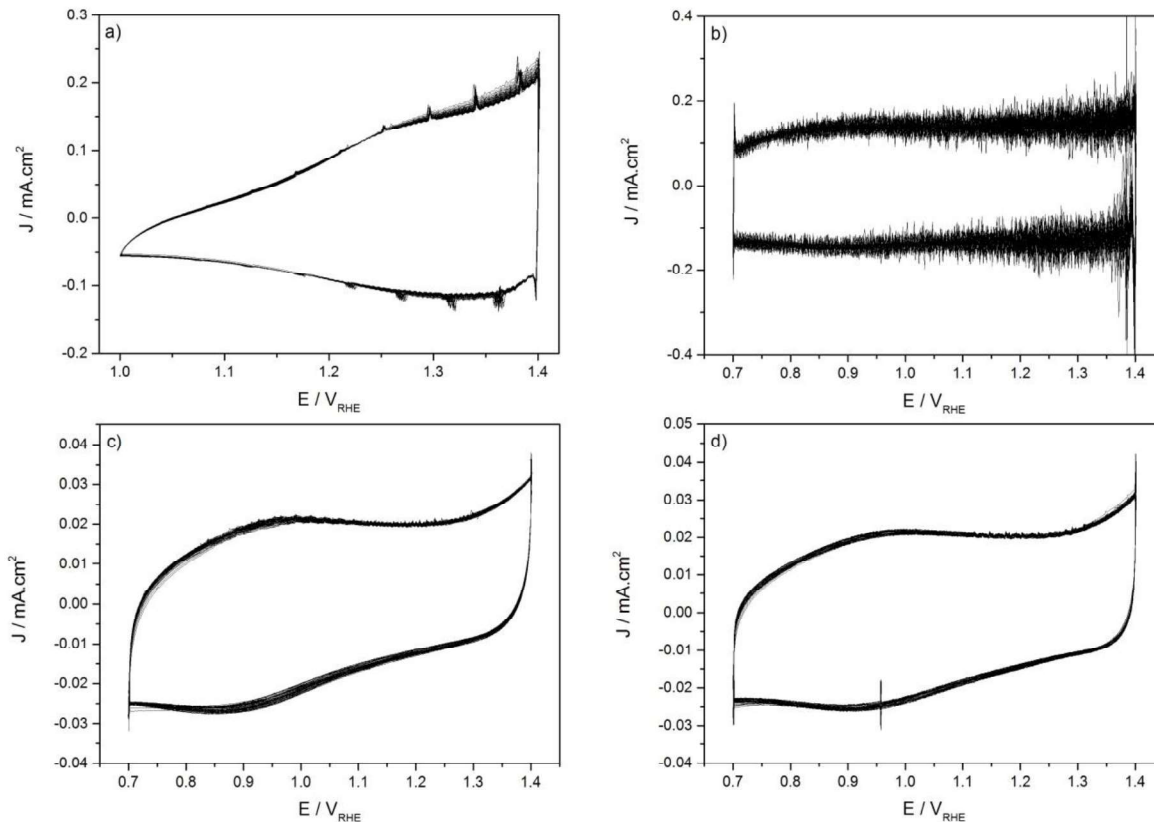


**Figure 4.12.** CV (50 cycles,  $0.7 \text{ V}_{\text{RHE}}$  to  $1.4 \text{ V}_{\text{RHE}}$  at  $50 \text{ mV/s}$ ) curves performed after the initial LSV measurement for  $\text{IrO}_2/\text{ATO}-\text{Li}_2\text{CO}_3$  catalysts a) fresh and b) after annealing at  $300 \text{ }^\circ\text{C}$ , c) annealing and reduction at  $300 \text{ }^\circ\text{C}$ , d) annealing, reduction and annealing at  $300 \text{ }^\circ\text{C}$ .

In order to assess the catalyst stability, chronopotentiometry at  $10 \text{ mA}\cdot\text{cm}^{-2}$  for 2 h was carried out (figure 4.13). As observed previously, the  $\text{IrO}_2/\text{ATO}-\text{Li}_2\text{CO}_3$  fresh catalyst presented a 90 mV rise in the potential through the 2 h of the CP stability test, indicating that degradation occurred.  $\text{IrO}_2/\text{ATO}-\text{Li}_2\text{CO}_3$  annealed at  $300 \text{ }^\circ\text{C}$  in air for 3 h presented a slightly higher potential rise of 122 mV during the CP experiment. In order to reduce the noise produced from oxygen bubbles detachment from the electrode, which present as sharp spikes in the potential, a percentile filter was applied.

After the reduction treatment and the growth of the support over the iridium nanoparticles, the catalyst lost its activity as observed by LSV and CV. Consecutive annealing led to no improvement of the catalytic properties. As expected from the previous LSV and CV results,

the potential related to the glassy carbon electrode corrosion was detected almost instantaneously after the beginning of the CP test, demonstrating its poor stability.

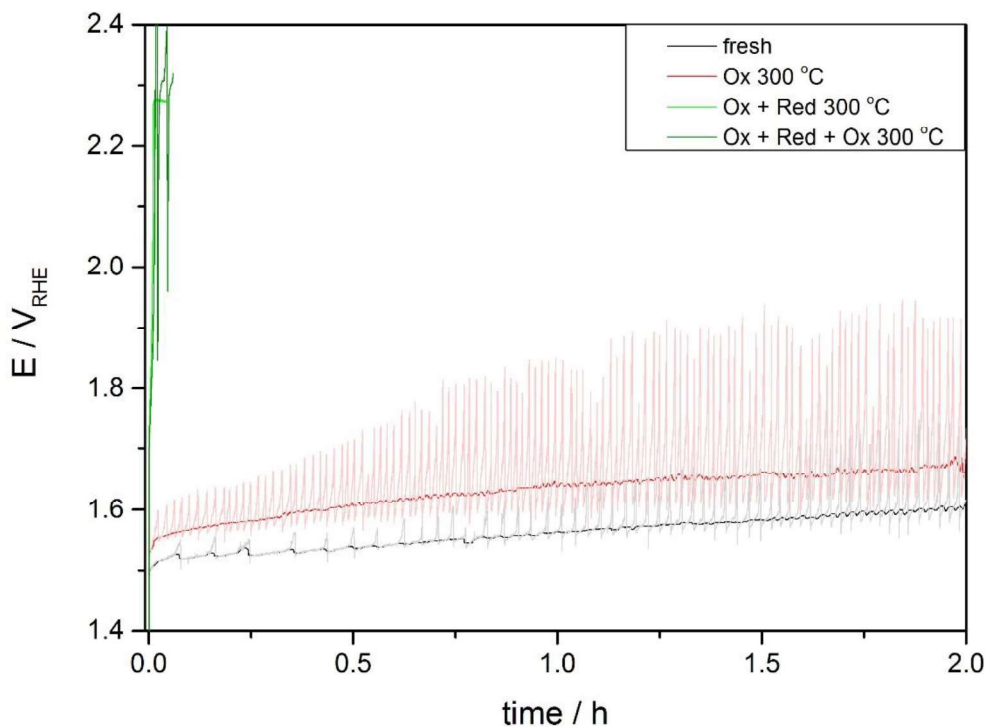


**Figure 4.13.** Stability of  $\text{IrO}_2/\text{ATO}-\text{Li}_2\text{CO}_3$  catalysts after heat treatment under reducing and oxidising conditions by chronoapotentiometry at  $10 \text{ mA}\cdot\text{cm}^{-2}$  for 2 h. Light lines represents the raw data, dark lines represents the data after being applied a percentile filter for reducing the noise.

#### 4.4 Conclusions.

Amorphous iridium oxo-hydroxide catalysts supported on commercial antimony doped tin oxide (ATO) were synthesised through a hydrothermal method. The base used during the synthesis was probed to be an important variable on optimising the catalytic activity and stability towards OER. The  $\text{IrO}_2/\text{ATO}-\text{Li}_2\text{CO}_3$  outperformed catalysts prepared with  $\text{Na}_2\text{CO}_3$  and  $\text{K}_2\text{CO}_3$  as base.

The poor performance of  $\text{IrO}_2/\text{ATO}-\text{K}_2\text{CO}_3$  was attributed to the poor  $\text{IrO}_2/\text{support}$  interaction observed by TEM. An iridium oxo-hydroxide film was formed throughout the support when  $\text{Li}_2\text{CO}_3$  or  $\text{Na}_2\text{CO}_3$  was used as a base, which resulted in an improved OER performance compared to  $\text{IrO}_2/\text{ATO}-\text{K}_2\text{CO}_3$ .

$\text{IrO}_2/\text{ATO}-\text{Li}_2\text{CO}_3$  presented advantages to the unsupported counterpart,  $\text{IrO}_2-\text{Li}_2\text{CO}_3$ . On one hand, iridium was used more efficiently since the active phase was concentrated at the surface of the material. On the other hand, at a current density of  $5 \text{ mA}\cdot\text{cm}^{-2}$ , the overpotential normalised to the iridium loading reduced by 25 mV for the supported catalysts whilst improving its stability under reaction conditions. Therefore, reduction of the iridium loading on the electrode without impairing the catalytic performance can be achieved by supporting amorphous iridium oxo-hydroxides on ATO *via* a hydrothermal synthesis.

However, a potential rise was observed during the CP stability test which was correlated to catalyst degradation. In order to improve the iridium catalyst stability and reduce its leaching during OER, it was proposed that growing a layer of the support over the  $\text{IrO}_2$ , upon reducing conditions, could lead to iridium stabilisation via metal-support interactions.

The  $\text{H}_2\text{-TPR}$  profile showed that for the  $\text{IrO}_2/\text{ATO}-\text{Li}_2\text{CO}_3$  catalyst reduction at  $300^\circ\text{C}$  was necessary to reduce the support, reduction of iridium oxo-hydroxide to metallic iridium was observed at  $100^\circ\text{C}$ . The  $\text{IrO}_2/\text{ATO}$  catalyst after the reduction treatment was analysed by low dose electron HRTEM to avoid beam damage, microscopy showed the presence of 3-4 nm metallic iridium nanoparticles encapsulated inside an ATO layer. It was proposed that the initial  $\text{IrO}_x$  film aggregated under reducing conditions, forming metallic iridium nanoparticles, upon continuous heating;  $\text{SnO}$  in contact with the metallic nanoparticles reduced by hydrogen spill over encapsulating them. This hampered the re-oxidation from metallic iridium to  $\text{IrO}_2$  after annealing in air.

In line with TEM and XPS characterisation, the overgrown support layer prevented the access of any reagent molecules to the active sites and hence no activity towards OER was observed. In conclusion, improved stability sought by growing a protective layer of the support over the formed  $\text{IrO}_x$  layer was unsuccessful. Moreover, as demonstrated in chapter 3, heat treatment is accompanied by an increase in the overpotential towards OER.

From this work further research on the optimisation of supported  $\text{IrO}_2/\text{ATO}$  should focus on the preparation protocol and on the support rather than the posterior heat treatments.

#### 4.5 Bibliography.

1. V. Pfeifer, T. E. Jones, J. J. Velasco Vélez, C. Massué, R. Arrigo, D. Teschner, F. Girgsdies, M. Scherzer, M. T. Greiner, J. Allan, M. Hashagen, G. Weinberg, S. Piccinin, M. Hävecker, A. Knop-Gericke, R. Schlögl, The electronic structure of iridium and its oxides, *Surface and Interface Analysis*, **2016**, 48 (5), 261-273.
2. V. Pfeifer, T. E. Jones, S. Wrabetz, C. Massué, J. J. Velasco Velez, R. Arrigo R, M. Scherzer, S. Piccinin, M. Hävecker, A. Knop-Gericke, R. Schlögl, Reactive oxygen species in iridium-based OER catalysts, *Chemical Science*, **2016**, 7 (11), 6791-6795.
3. V. K. Puthiyapura, M. Mamlouk, S. Pasupathi, B. G. Pollet, K. Scott, Physical and electrochemical evaluation of ATO supported IrO<sub>2</sub> catalyst for proton exchange membrane water electrolyser, *Journal of Power Sources*, **2014**, 269, 451-460.
4. G. Liu, J. Xu, Y. Wang, X. Wang, An oxygen evolution catalyst on an antimony doped tin oxide nanowire structured support for proton exchange membrane liquid water electrolysis, *Journal of Materials Chemistry A*, **2015**, 3 (41), 20791-20800.
5. C. Massué, V. Pfeifer, X. Huang, J. Noack, A. Tarasov, S. Cap, R. Schlögl, High-performance supported Ir-oxohydroxide water oxidation electrocatalysts, *ChemSusChem*, **2017**, 10, 1943-1957.
6. F. Berkermann, *Preparation and Application of Aqueous Iridium Oxide Colloids* (Doctoral Thesis). Ruhr University Bochum, Germany, **2010**.
7. S. Sladkevich, A. A. Mikhaylov, P. V. Prikhodchenko, T. A. Tripol'skaya, O. Lev, Antimony Tin Oxide (ATO) Nanoparticle Formation from H<sub>2</sub>O<sub>2</sub> Solutions: a New Generic Film Coating from Basic Solutions, *Inorganic Chemistry*, **2010**, 49 (20), 9110-9112.
8. S. Geiger, O. Kasian, A. M. Mingers, K. J. J. Mayrhofer, S. Cherevko, Stability limits of tin-based electrocatalyst supports, *Scientific Reports*, **2017**, 7 (1), 4595-4601.
9. E. Willinger, C. Massué, R. Schlögl, M. G. Willinger, Identifying Key Structural Features of IrO<sub>x</sub> Water Splitting Catalysts, *Journal of the American Chemical Society*, **2017**, 139 (34), 12093-12101.
10. I. Spanos, A. A. Auer, S. Neugebauer, X. Deng, H. Tüysüz, R. Schlöegl, Standardized Benchmarking of Water Splitting Catalysts in a Combined Electrochemical Flow Cell/Inductively Coupled Plasma-Optical Emission Spectrometry (ICP-OES) Setup, *ACS Catal.*, **2017**, 7, 3768-3778.

11. A. R. Zeradjanin, A. A. Topalov, Q. Van Overmeere, S. Cherevko, X. Chen, E. Ventosa, W. Schuhmannc, K. J. J. Mayrhofer, Rational design of the electrode morphology for oxygen evolution - enhancing the performance for catalytic water oxidation, *RSC Advances*, **2014**, 4 (19), 9579-9587.
12. O. Kasian, J. P. Grote, S. Geiger, S. Cherevko, K. J. J. Mayrhofer, The Common Intermediates of Oxygen Evolution and Dissolution Reactions during Water Electrolysis on Iridium, *Angewandte Chemie International Edition*, **2018**, 57 (9), 2488-2491.
13. S. J. Freakley, Q. He, J. H. Harrhy, L. Lu, D. A. Crole, D. J. Morgan, E. N. Ntanjua, J. K. Edwards, A. F. Carley, A. Y. Borisevich, C. J. Kiely, G. J. Hutchings, Palladium-tin catalysts for the direct synthesis of H<sub>2</sub>O<sub>2</sub> with high selectivity, *Science*, **2016**, 351 (6276), 965-968.
14. R. G. Haverkamp, A. T. Marshall, B. C. C. Cowie, Energy resolved XPS depth profile of (IrO<sub>2</sub>, RuO<sub>2</sub>, Sb<sub>2</sub>O<sub>5</sub>, SnO<sub>2</sub>) electrocatalyst powder to reveal core-shell nanoparticle structure, *Surface and Interface Analysis*, **2011**, 43 (5), 847-855.
15. S. Cherevko, S. Geiger, O. Kasian, A. Mingers, K. J. J. Mayrhofer, Oxygen evolution activity and stability of iridium in acidic media. Part 1. - Metallic iridium, *Journal of Electroanalytical Chemistry*, **2016**, 773, 69-78.
16. C. Felix, T. Maiyalagan, S. Pasapathi, B. Bladergroen, V. Linkov, Synthesis and optimization of IrO<sub>2</sub> electrocatalysts by Adams fusion method for solid polymer electrolyte electrolyzers., *Micro and nanosystems*, **2012**, 4, 186-191.
17. T. Reier, D. Teschner, T. Lunkenbein, A. Bergmann, S. Selve, R. Krahnert, R. Schlögl, P. Strasser, Electrocatalytic Oxygen Evolution on Iridium Oxide: Uncovering Catalyst-Substrate Interactions and Active Iridium Oxide Species, *Journal of The Electrochemical Society*, **2014**, 161 (9), F876-F882.
18. M. Bernicke, E. Ortel, T. Reier, A. Bergmann, J. Ferreira de Araujo, P. Strasser, R. Krahnert, Iridium Oxide Coatings with Templatized Porosity as Highly Active Oxygen Evolution Catalysts: Structure-Activity Relationships, *ChemSusChem*, **2015**, 8 (11), 1908-1915.
19. R. Prins, Hydrogen Spillover. Facts and Fiction, *Chemical Reviews*, **2012**, 112 (5), 2714-2738.
20. H. Bahruji, M. Bowker, Hutchings G, Dimitratos N, Wells P, Gibson E, W. Jones, C. Brookes, D. J. Morgan, G. Lalev, Pd/ZnO catalysts for direct CO<sub>2</sub> hydrogenation to methanol, *Journal of Catalysis*, **2016**, 343, 133-146.

21. V. Pfeifer, T. E. Jones, J. J. Velasco Velez, C. Massué, M. T. Greiner, R. Arrigo, D. Teschner, F. Girgsdies, M. Scherzer, J. Allan, M. Hashagen, G. Weinberg, S. Piccinin, M. Hävecker, A. Knop-Gericke, R. Schlögl, The electronic structure of iridium oxide electrodes active in water splitting, *Physical Chemistry Chemical Physics*, **2016**, 18 (4), 2292-2296.
22. S. J. Freakley, J. Ruiz Esquius, D. J. Morgan, The X-ray photoelectron spectra of Ir, IrO<sub>2</sub> and IrCl<sub>3</sub> revisited, *Surface and Interface Analysis*, **2017**, 49 (8), 794-799.
23. X. T. Chen, K. X. Wang, Y. B. Zhai, H. J. Zhang, X. Y. Wu, X. Wei, J. S. Chen, A facile one-pot reduction method for the preparation of a SnO/SnO<sub>2</sub>/GNS composite for high performance lithium ion batteries, *Dalton Transactions*, **2014**, 43 (8), 3137-3143.
24. D. J. Morgan, Metallic antimony (Sb) by XPS, *Surface Science Spectra*, **2017**, 24 (2), 24004.
25. S. Trasatti, Electrocatalysis in the anodic evolution of oxygen and chlorine, *Electrochimica Acta*, **1984**, 29 (11), 1503-1512.
26. S. Cherevko, S. Geiger, O. Kasian, N. Kulyk, J. P. Grote, A. Savan, B. R. Shrestha, S. Merzlikin, B. Breitbach, A. Ludwig, K. J. J. Mayrhofer, Oxygen and hydrogen evolution reactions on Ru, RuO<sub>2</sub>, Ir, and IrO<sub>2</sub> thin film electrodes in acidic and alkaline electrolytes: A comparative study on activity and stability, *Catalysis Today*, **2016**, 262, 170-180.
27. L. Ouattara, S. Fierro, O. Frey, M. Koudelka, Comninellis C, Electrochemical comparison of IrO<sub>2</sub> prepared by anodic oxidation of pure iridium and IrO<sub>2</sub> prepared by thermal decomposition of H<sub>2</sub>IrCl<sub>6</sub> precursor solution, *Journal of Applied Electrochemistry*, **2009**, 39 (8), 1361-1367.
28. J. Juodkazyte, B. Sebeka, I. Valsiunas, K. Juodkazis, Iridium Anodic Oxidation to Ir(III) and Ir(IV) Hydrous Oxides, *Electroanalysis*, **2005**, 17 (11), 947-952.

# Chapter 5

## Synthesis of crystalline $\text{Li}_x\text{IrO}_2$ hollandite as stable and active catalysts towards OER

### 5.1 Introduction.

As discussed previously, the higher catalytic activity of amorphous iridium oxo-hydroxides compared to rutile  $\text{IrO}_2$  was assigned to the presence of Ir(III)/Ir(IV) sites, electrophilic O<sup>-</sup> sites and a higher concentration of surface hydroxide groups.<sup>(1-4)</sup> Furthermore, Fierro *et al.*<sup>(5)</sup> through isotopically labelled  $\text{H}_2\text{O}$  and  $\text{IrO}_2$  for OER, showed that oxygen within the catalyst's lattice is directly involved in the reaction. This suggested that flexible structures, as in amorphous iridium oxo-hydroxides, should facilitate oxygen evolution compared to rigid structures, as in rutile  $\text{IrO}_2$ . Willinger *et al.*<sup>(6)</sup> compared by low dose electron HRTEM (High-resolution transmission electron microscopy) two amorphous  $\text{IrO}_x$  catalysts with comparable different catalytic activity towards OER. In a HRTEM, scattered and transmitted electrons are collected to form a image with higher resolution than a standard TEM. On one catalyst the presence of flexible hollandite motifs, formed as a consequence of potassium doping, were observed, whilst on the other, only rigid rutile motifs were detected. Hence, the improved catalytic activity for the former catalyst over the latter was assigned to the presence of hollandite motifs.<sup>(6)</sup> The presence of Ir(III)/Ir(IV) sites were confirmed for crystalline hollandite  $\text{IrO}_2$  materials.<sup>(7-10)</sup> Analogously to rutile  $\text{IrO}_2$ , both crystalline structures are composed of  $\text{IrO}_6$  octahedral units. In hollandite, the  $\text{IrO}_6$  edge-sharing pair form chains connected between them by oxygen-corner-sharing positions forming channels, whilst on rutile, edge sharing  $\text{IrO}_6$  chains are connected to perpendicular-oriented  $\text{IrO}_6$  chains by sharing oxygen-corners positions. Sun *et al.*<sup>(7)</sup> synthesised hollandite  $\text{K}_{0.25}\text{IrO}_2$  and compared it to rutile  $\text{IrO}_2$  towards OER. The former presented a current density of  $10 \text{ mA}\cdot\text{cm}^{-2}$  at  $0.35 \text{ V}$  overpotential, while rutile  $\text{IrO}_2$ , at the same overpotential, showed a current density of  $3.15 \text{ mA}\cdot\text{cm}^{-2}$ .<sup>(7)</sup> Literature on  $\text{IrO}_2$  hollandites is scarce, and only K and Rb as host cations have been reported.

On a comparable system,  $\text{MnO}_2$  can crystallise as hollandite, channels within the structure can accommodate monovalent or divalent cations<sup>(11-13)</sup> with different sizes, including lithium. As discussed in chapter 3 and chapter 4, the use of  $\text{Li}_2\text{CO}_3$  as base during the hydrothermal synthesis of  $\text{IrO}_x$  led to catalysts with reduced overpotential and improved stability compared to the state of the art  $\text{IrO}_2\cdot2\text{H}_2\text{O}$  (Premion). Therefore, the objective of this chapter is to report for the first time the synthesis of a hollandite  $\text{IrO}_2$  phase with  $\text{Li}^+$  as the host cation and to compare it towards OER against a rutile  $\text{IrO}_2$  catalyst.

## 5.2 Single $\text{IrO}_2$ hollandite and $\text{IrO}_2$ rutile phase synthesis and characterisation.

In chapter 3 it was reported the detrimental effect of annealing on the catalytic activity of  $\text{IrO}_2\text{-Li}_2\text{CO}_3$  catalyst towards OER, as observed by the successive LSV potential shift towards higher values with increasing the calcination temperature.

In order to study the structural changes in the material through the annealing process, *in situ* XRD in air was performed (figure 5.1). A new  $\text{IrO}_2\text{-Li}_2\text{CO}_3$  sample was prepared using the hydrothermal method described in chapter 3. The initial XRD scan was recorded at 25 °C. The temperature was then raised at 5 °C·min<sup>-1</sup> to 600 °C. A XRD scan was recorded every 25 °C; however, to reduce the signal to noise ratio due to phase transitions during heating, the temperature was hold constant for 5 minutes before recording the XRD pattern.

As observed by the initial XRD pattern recorded at 25 °C, the broad and low intensity reflections assigned to amorphous iridium oxo-hydroxide were observed, although the new  $\text{IrO}_2\text{-Li}_2\text{CO}_3$  batch clearly had  $\text{Li}_2\text{CO}_3$  impurities (JCPDS-036-0787) after the washing step. Heat treatment up to 400 °C led to the disappearance of the  $\text{Li}_2\text{CO}_3$  related reflections, without affecting the amorphous  $\text{IrO}_2$  reflections. At 450 °C broad  $\text{IrO}_2$  rutile-related reflections (JCPDS-015-0876) started to appear. At 475 °C rutile reflections became sharper indicating higher crystallinity and bigger crystalline domains. However,  $\text{IrO}_2$  rutile was not the only phase detected by XRD. Intense reflections related to hollandite (JCPDS-044-0141) were detected as well.<sup>(8)</sup>

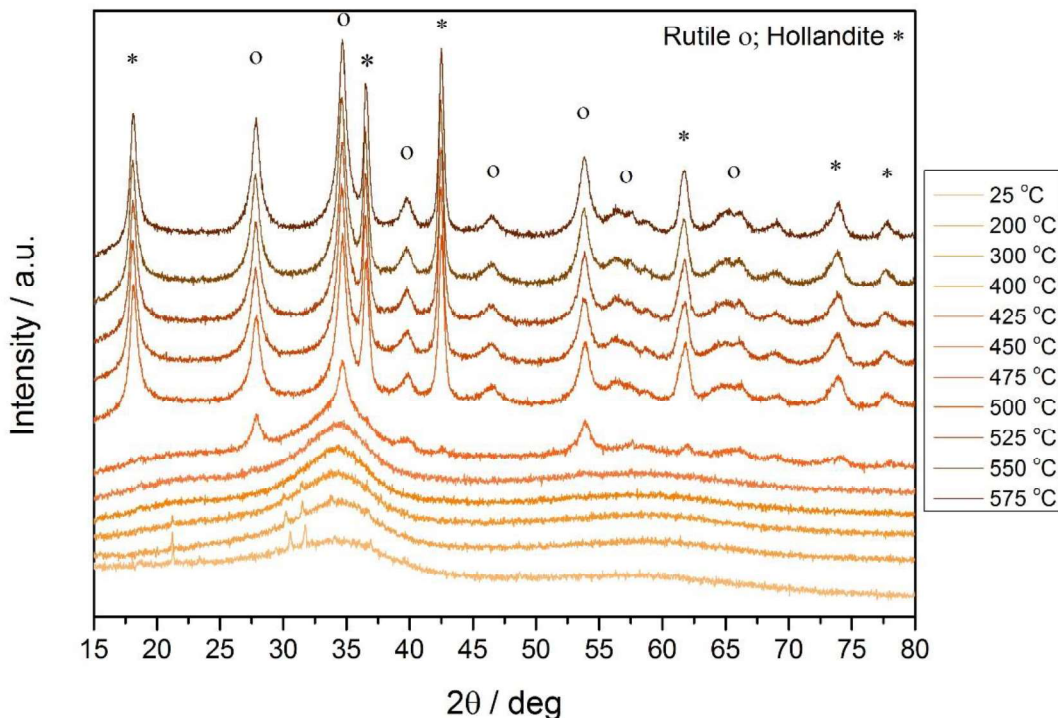


**Figure 5.1.** *In situ* XRD patterns for as prepared  $\text{IrO}_2\text{-Li}_2\text{CO}_3$  from 25 °C to 600 °C in air.  $\text{IrO}_2$ -rutile reflections are represented as an open circle and  $\text{IrO}_2$ -hollandite reflections are represented with a star.

Since  $\text{Li}_2\text{CO}_3$  was present in the as prepared iridium oxo-hydroxide material, it was assumed that  $\text{Li}^+$  could be incorporated inside the  $\text{IrO}_2$ -rutile lattice to form the hollandite phase, in an analogous way to the previous reported potassium containing examples. Further annealing increased the intensity of  $\text{IrO}_2$ -rutile related reflections indicating the growth of rutile domains, as would be expected as a result of sintering (figure 5.2a). Nevertheless, no intensity increase was observed for the hollandite-related reflections (figure 5.2b).

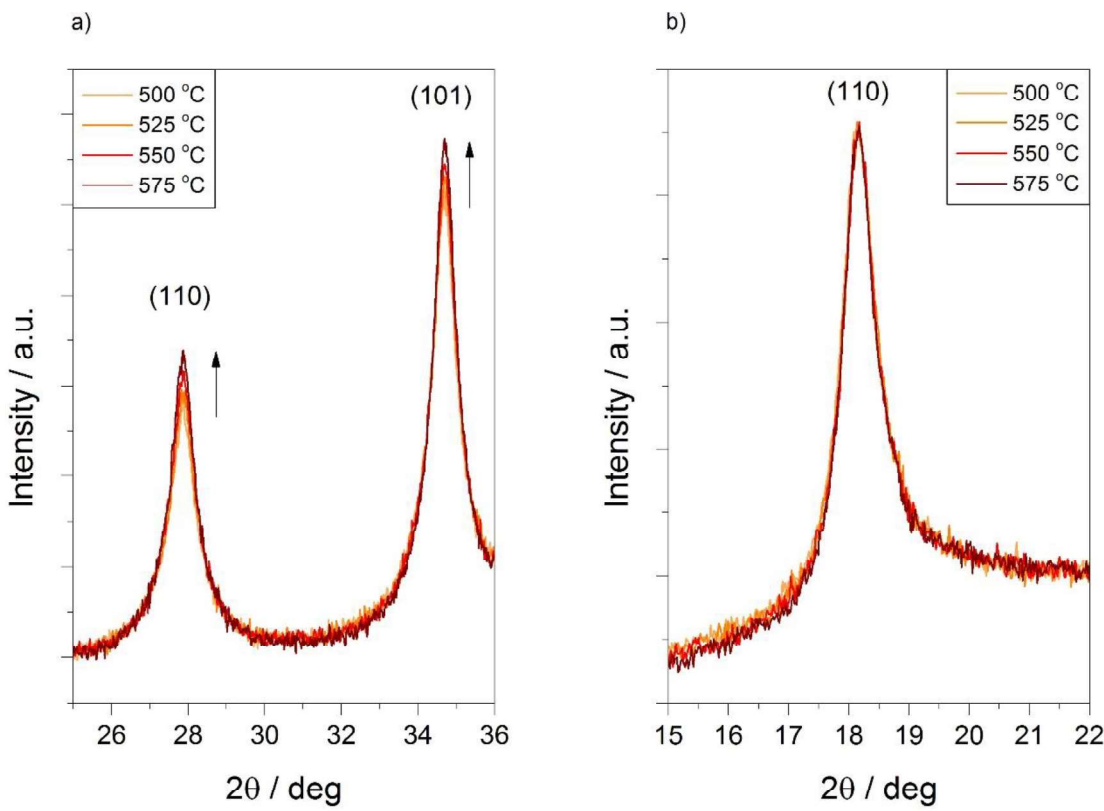


**Figure 5.2.** *In situ* XRD reflections measured above 500 °C for a) (101) and (101) rutile planes and b) (110) hollandite plane.

*In situ* XRD characterisation suggested that remaining lithium in the material was incorporated into the crystalline lattice structure of  $\text{IrO}_2$  rutile upon annealing at 500 °C, forming the  $\text{IrO}_2$  hollandite phase. Hollandite domains did no grow in size with higher annealing temperature, presumably because of a lack of lithium availability. Therefore, it would be possible to form hollandite as the major crystalline phase if excess of lithium is available. In order to probe this,  $\text{IrO}_2\text{-Li}_2\text{CO}_3$  was prepared using the standard protocol described in chapter 3.  $\text{IrCl}_3$  and  $\text{Li}_2\text{CO}_3$  were dissolved in water and stirred for 16 h at room temperature. The mixture was then heated to reflux for 3 hours. The formed precipitate was then recovered by filtration, but in this case it was not washed with water in order to remove the  $\text{Li}_2\text{CO}_3$  from the material. Finally, the dried unwashed mixture was annealed at 500 °C for 3 hours in order to induce the formation of crystalline hollandite. As observed by XRD (figure 5.3), no  $\text{IrO}_2$  rutile-related reflections were detected and only reflections assigned to  $\text{IrO}_2$  hollandite, and remaining  $\text{Li}_2\text{CO}_3$ , were observed. In order to remove the excess of  $\text{Li}_2\text{CO}_3$  remaining in the material, the catalyst was washed with 2 L of deionised water after calcination.

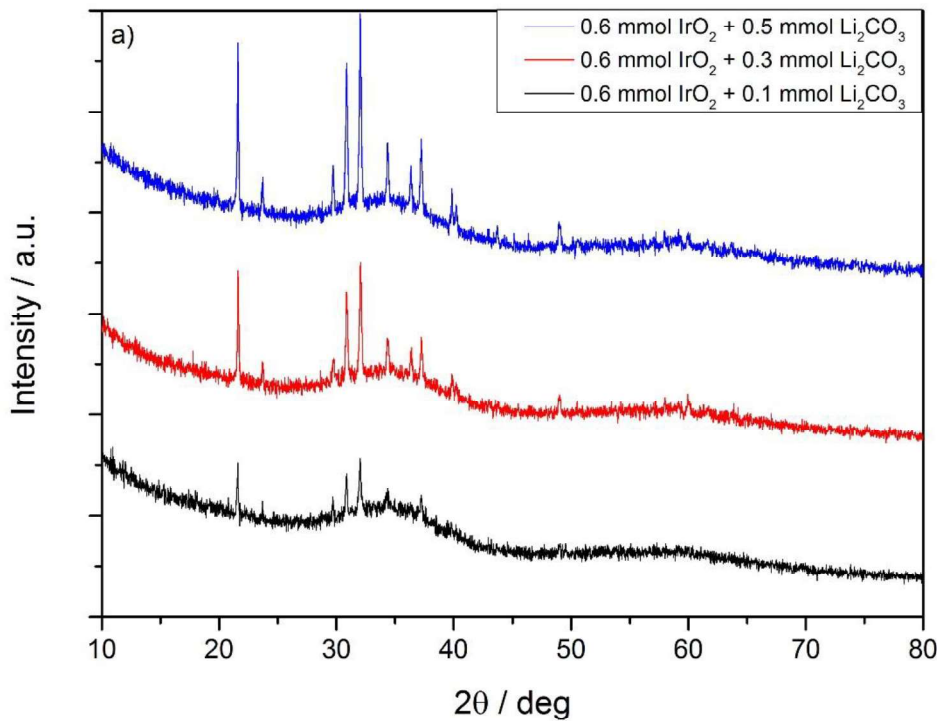


**Figure 5.3.** XRD pattern for single phase  $\text{IrO}_2$  hollandite preparation. From bottom to top, fresh unwashed  $\text{IrO}_2\text{-Li}_2\text{CO}_3$ , unwashed  $\text{IrO}_2\text{-Li}_2\text{CO}_3$  catalyst after annealing at 500 °C in air and  $\text{IrO}_2$ -hollandite after washing out the remaining  $\text{Li}_2\text{CO}_3$  base.

On the other hand, if the synthesis of pure rutile phase is the desired crystalline phase, the presence of lithium in the material should be avoided. In chapter 3, materials were washed with 2 L of hot deionised water. This proved to be efficient for avoiding chlorine contamination, however,  $\text{Na}^+$  and  $\text{K}^+$  were detected by SEM-EDX and so it is expected that  $\text{Li}^+$  would be also present in the material after washing. Additionally, the solubility of  $\text{Li}_2\text{CO}_3$  in water is reported to increase with lowering the aqueous solution temperature.<sup>(14)</sup> Therefore, to completely remove  $\text{Li}_2\text{CO}_3$  the catalyst was washed first with 1.5 L of cold deionised water, and then with 1.5 L of hot deionised water to remove chlorine contamination. This ensured a material free of chlorine and lithium contamination. Consecutive annealing at 500 °C for 3 hours led to the synthesis of rutile  $\text{IrO}_2$  single phase as observed by XRD (figure 5.4).

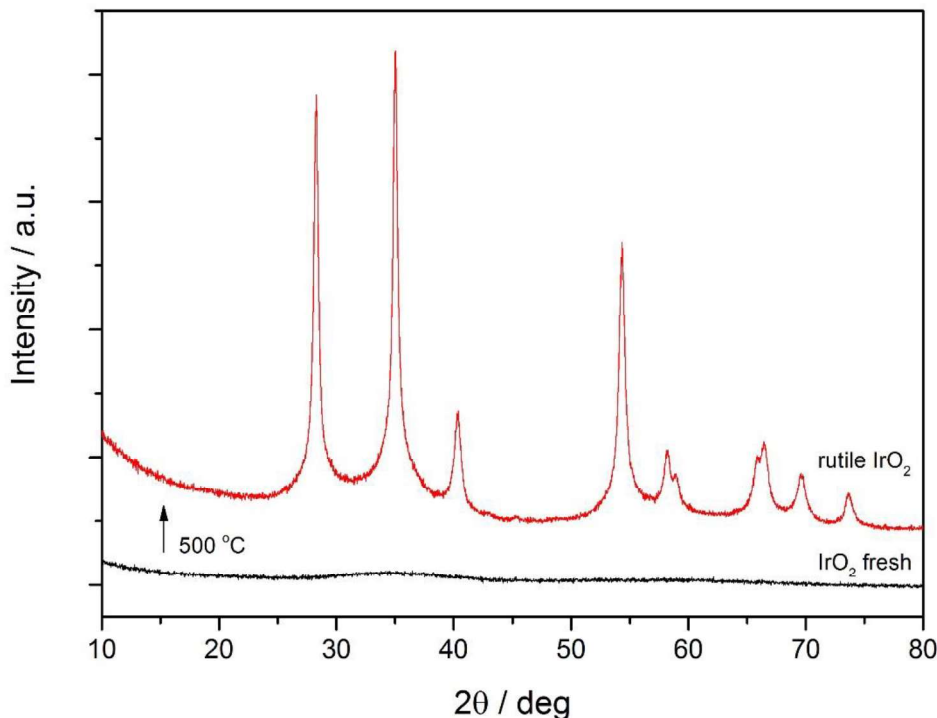


**Figure 5.4.** XRD pattern for single phase synthesis of rutile  $\text{IrO}_2$ . From bottom to top,  $\text{Li}^+$ -contamination-free  $\text{IrO}_2$  prepared through a hydrothermal synthesis using  $\text{Li}_2\text{CO}_3$  as a base and single phase  $\text{IrO}_2$ -rutile after annealing at  $500^\circ\text{C}$  for 3 h in air.

XRD characterisation confirmed that it is feasible to synthesise single phase  $\text{IrO}_2$ -hollandite and single phase  $\text{IrO}_2$ -rutile (figure 5.5) through a hydrothermal synthesis using  $\text{Li}_2\text{CO}_3$  as a base. In the absence of  $\text{Li}^+$ , amorphous iridium oxo-hydroxide crystallised to the  $\text{IrO}_2$ -rutile phase. However, if there is enough  $\text{Li}^+$  available  $\text{IrO}_2$ -hollandite phase was formed preferably instead of  $\text{IrO}_2$ -rutile after annealing at  $500^\circ\text{C}$ .

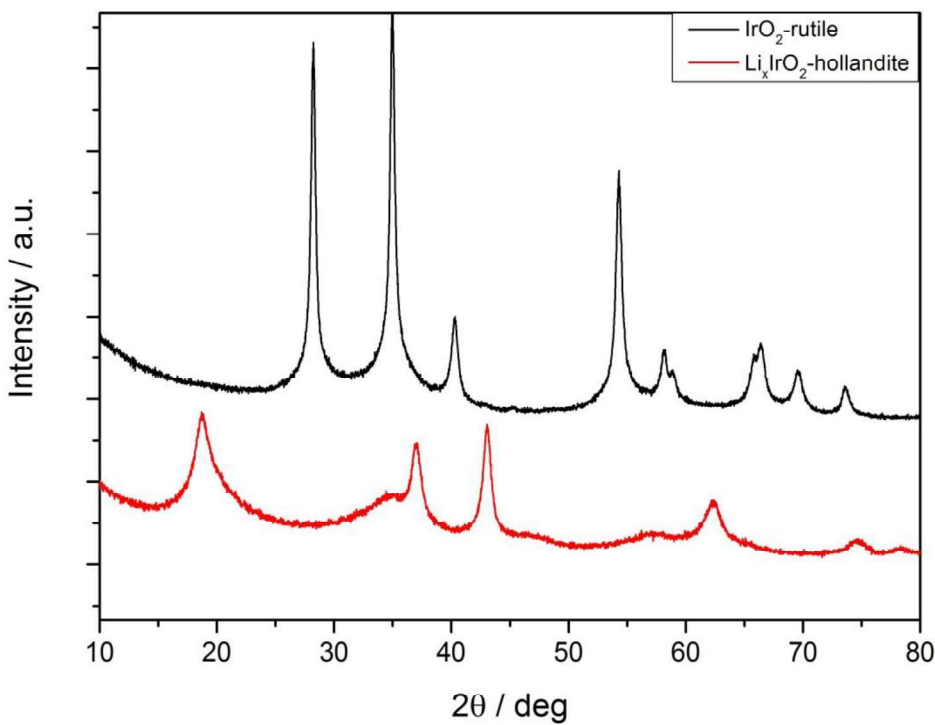


**Figure 5.5.** XRD pattern for synthesised single phase  $\text{IrO}_2$ - rutile and  $\text{IrO}_2$ -hollandite.

The XPS for synthesised single phase  $\text{IrO}_2$  rutile was first compared with commercial rutile  $\text{IrO}_2$ . Commercial rutile  $\text{IrO}_2$  has been fully characterised previously in the literature,<sup>(2)</sup> it was concluded that only Ir(IV) sites were present in the material. Characterisation done in chapter 3 for the commercial rutile  $\text{IrO}_2$  was in agreement with published results. The binding energy for both, commercial and synthesised,  $\text{IrO}_2$ -rutile catalysts was at 62.0 eV and 65.0 eV for  $\text{Ir}(4f_{7/2})$  and  $\text{Ir}(4f_{5/2})$  orbitals respectively.<sup>(15)</sup> The  $\text{Ir}(4f)$  peak envelope for the prepared rutile  $\text{IrO}_2$  overlapped almost perfectly with the commercial standard, however, the peak fitting is slightly broader for the prepared rutile sample compared to the commercial  $\text{IrO}_2$  (figure 5.6a).

The analysis of the O(1s) orbital for the commercial rutile  $\text{IrO}_2$  was in agreement with the  $\text{Ir}(4f)$  characterisation, iridium was present as Ir(IV) in the material concomitantly the oxygen peak at 530.1 eV with a small satellite contribution at 531.5 eV corresponded with oxide lattice oxygen.<sup>(16)</sup> The O(1s) peak has shown to have a small satellite contribution which differs slightly from water and hydroxide oxygen chemical shift. Synthesised rutile  $\text{IrO}_2$  presented a considerably more intense peak contribution at slightly lower binding energy compared to the satellite of commercial rutile  $\text{IrO}_2$ . The broadening observed on the synthesised rutile  $\text{IrO}_2$   $\text{Ir}(4f)$  peak, compared to the commercial standard, indicated that not all iridium was present as lattice Ir(IV) and might suggest the presence of surface hydroxide groups. In accordance, the O(1s) line shape for the prepared rutile catalyst indicated the

presence of lattice oxygen and the presence of hydroxide groups (figure 5.6b). Even though both materials presented the same crystal structure, as observed by XRD, chemical differences in the iridium environment were detected by XPS.

Carbon was detected on synthesised single phase catalysts, IrO<sub>2</sub> rutile and IrO<sub>2</sub> hollandite, presumably due to contamination from the Li<sub>2</sub>CO<sub>3</sub> used during the synthesis. In order to ensure reliable data comparison, the Ir(4f) and the O(1s) peaks were calibrated against the C(1s) signal at 284.8 eV. In chapter 3, the Ir(4f) XPS line shape for the commercial rutile IrO<sub>2</sub> was used as a fitting in the hydrothermally synthesised materials in order to quantify the lattice Ir(IV) contributions. Likewise, the envelope shape from the standard IrO<sub>2</sub> rutile was used as a fitting in the prepared single phase IrO<sub>2</sub> hollandite and rutile in order to determine the proportion of lattice Ir(IV) sites. In the case of IrO<sub>2</sub> hollandite, additional fitting to fill the Ir(4f) orbital would be assumed to correspond to the presence of Ir(III) sites, in accordance with previous reports on K<sub>x</sub>IrO<sub>2</sub> hollandite, which suggested the presence of Ir(III) and Ir(IV) in hollandite materials.<sup>(8)</sup> The Ir(4f) peak for prepared IrO<sub>2</sub> hollandite was broader and shifted towards higher binding energy compared to commercial IrO<sub>2</sub> rutile (figure 5.7a), suggesting that Ir(III) and Ir(IV) centres were present in the material.

Oxygen within the rutile structure appeared at 530.1 eV, as observed for commercial and synthesised IrO<sub>2</sub> rutile catalysts. The oxide oxygen in the rutile lattice is surrounded by Ir(IV) centres. Oxide oxygen at 530.1 eV was detected in the O(1s) peak on the IrO<sub>2</sub> hollandite catalyst, however its contribution was not the predominant one as it was for rutile catalysts. The major contribution on the O(1s) for the IrO<sub>2</sub> hollandite material was centred at a lower binding energy than the satellite observed on the standard catalyst. The presence of hydroxide and water in IrO<sub>2</sub> materials are assigned at 531.6 eV and 532.9 eV respectively,<sup>(17, 18)</sup> which are at a higher binding energy than the satellite contribution on rutile IrO<sub>2</sub>. This suggests that both assigned oxygen peaks in the O(1s) orbital could correspond to two lattice oxygen with different chemical environment as a result of Ir(III) sites in the structure (figure 5.6b). Because Li<sub>2</sub>CO<sub>3</sub> was used as a base during the synthesis of the hollandite single phase, lithium was assumed to be the cation hosted in the hollandite structure. The Li(1s) orbital appears at 55 eV, between the Ir(4f) and Ir(5p<sub>3/2</sub>) orbital. However, its presence was not clearly detected by XPS as observed in figure 5.7a. This did not exclude the presence of lithium into the structure. On one hand the response factor of lithium is three orders of magnitude smaller than the one for iridium. On the other hand, it has been reported that even a complete channel occupation would correspond to only a quarter of host cations per mole of iridium.<sup>(19)</sup> Therefore, a complete channel occupation by lithium would refer to a chemical formula of Li<sub>0.25</sub>IrO<sub>2</sub>. We are reluctant to specify the exact

chemical formula due to a lack of lithium quantification and also because it is known that other ions such as  $\text{H}_3\text{O}^+$ ,  $\text{OH}^-$  or even  $\text{H}_2\text{O}$  can be present within the hollandite cavities.<sup>(12)</sup>

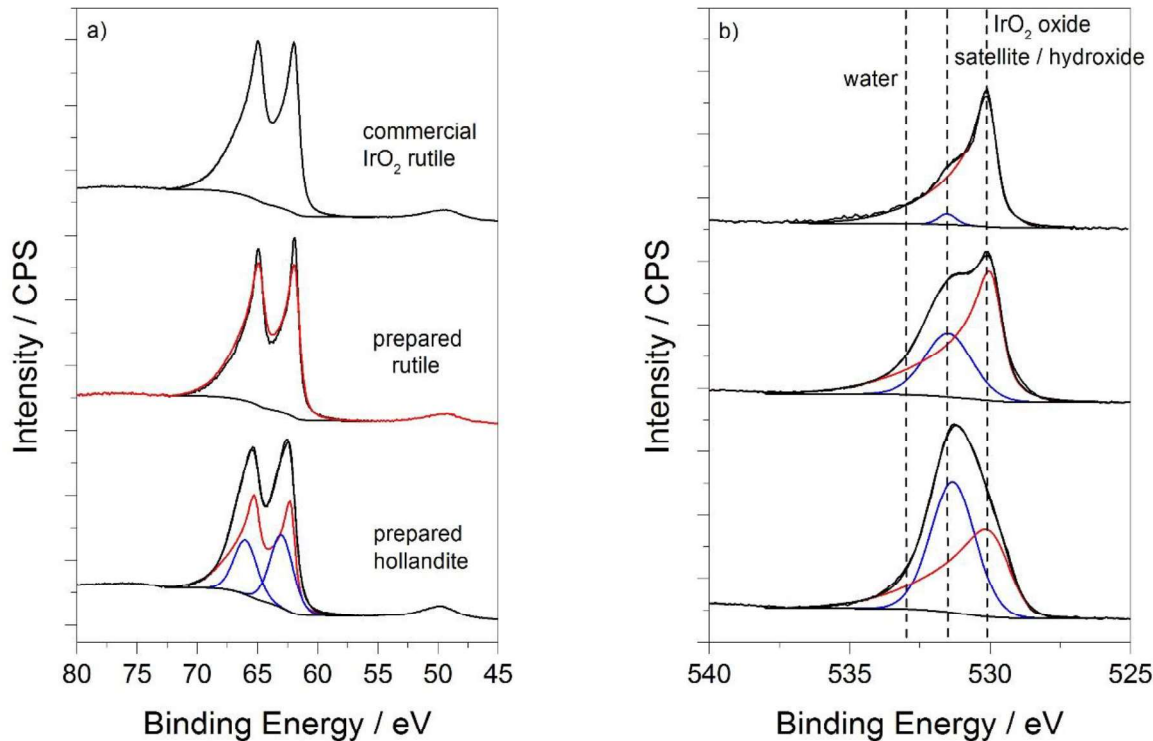


**Figure 5.6.** XPS characterisation for single phase prepared  $\text{IrO}_2$  rutile and  $\text{IrO}_2$  hollandite and commercial rutile  $\text{IrO}_2$  (Sigma Aldrich) a) Ir(4f) and b) O(1s) orbital.

Differences in the crystalline structure between the prepared  $\text{IrO}_2$  rutile and  $\text{IrO}_2$  hollandite were evidenced by XRD characterisation.  $\text{IrO}_2$  rutile has a tetragonal structure whilst  $\text{IrO}_2$  hollandite has a monoclinic unit cell. Moreover, rutile is formed from  $\text{IrO}_6$  corner sharing octahedra while in the hollandite structure it the  $\text{IrO}_6$  octahedral shares corner and edges. Additionally, differences in the oxidation state of iridium on  $\text{IrO}_2$  rutile and  $\text{IrO}_2$  hollandite were observed by XPS characterisation. Rutile was formed almost entirely of Ir(IV) while in the hollandite structure a mixture of Ir(III) and Ir(IV) sites were proposed.

In order to gain a deeper understanding in the structural and electronic differences between rutile and hollandite  $\text{IrO}_2$ , both synthesised materials were analysed by X-ray adsorption fine structure (XAFS)<sup>(20)</sup> at Diamond Light Source in the B18 beam line. In a XAFS experiment, X-ray radiation is used to eject a core-electron from a desired element, in our case iridium, to the continuum. A XAFS signal is generally divided in two regions, X-ray near-edge spectroscopy (XANES) and X-ray absorption fine-structure spectroscopy (EXAFS). The energy at what adsorption occurs, which indicates that a core-electron has been ejected,

gives information about the oxidation state of the element (XANES). The nature and number of neighbouring atoms can be elucidated by analysing the relaxation process of the ejected electron (EXAFS).

For better comparison,  $\text{IrCl}_3$ , amorphous prepared  $\text{IrO}_2\text{-Li}_2\text{CO}_3$  and commercial  $\text{IrO}_2$  rutile were used as standards. Analysis of the Ir L<sub>3</sub> edge, electronic transition 2p to 5d, can reveal important structural properties between the different materials. Firstly, the white line position obtained from the XANES measurement would indicate the average oxidation state of iridium in the material. Commercial rutile  $\text{IrO}_2$  is known to have an oxidation state of +4, a shift of the adsorption towards lower energy would indicate an oxidation state lower than +4 as a result of weaker electron-core binding energy. Secondly, it has been reported that well-structured rutile  $\text{IrO}_2$  has an Ir-O average bond distance of 1.97 Å, four Ir-O distances of 1.998 Å and two Ir-O bonds of 1.96 Å. Nevertheless, according to the literature, amorphous  $\text{IrO}_x$  and  $\text{K}_{0.25}\text{IrO}_2$  hollandite has longer Ir-O bond distance and shorter Ir-Ir bond distance than rutile  $\text{IrO}_2$ , this attributed to an octahedron distortion.<sup>(7, 18, 21, 22)</sup> Comparing the commercial rutile  $\text{IrO}_2$  bond distances with the prepared materials,  $\text{IrO}_2$  hollandite and amorphous oxo-hydroxide  $\text{IrO}_2\text{-Li}_2\text{CO}_3$ , differences in the bond distances could be detected.

For comparison purposes, the white line of commercial  $\text{IrCl}_3$  and commercial rutile  $\text{IrO}_2$  were used as standards and assigned to oxidation states of Ir(III) and Ir(IV) respectively. XANES characterisation showed that the white line position for synthesised  $\text{IrO}_2$  rutile overlapped with the white line position measured for the commercial rutile standard, indicating that the oxidation state was Ir(IV) as expected. Previous XAFS characterisation in literature suggested the presence of Ir(III) and Ir(IV) sites in highly active amorphous iridium oxo-hydroxides and  $\text{IrO}_2$  hollandites.<sup>(2, 4, 7, 23)</sup> Conversely, no significant shift on the white line position towards lower energy indicating the presence of Ir(III) sites was detected for  $\text{Li}_x\text{IrO}_2$  hollandite or amorphous  $\text{IrO}_2\text{-Li}_2\text{CO}_3$  catalysts. Thus it can be assumed that the majority of the iridium sites have an oxidation state of Ir(IV), however the presence of few Ir(III) sites as discussed by XPS could not be ruled out (figure 5.7).

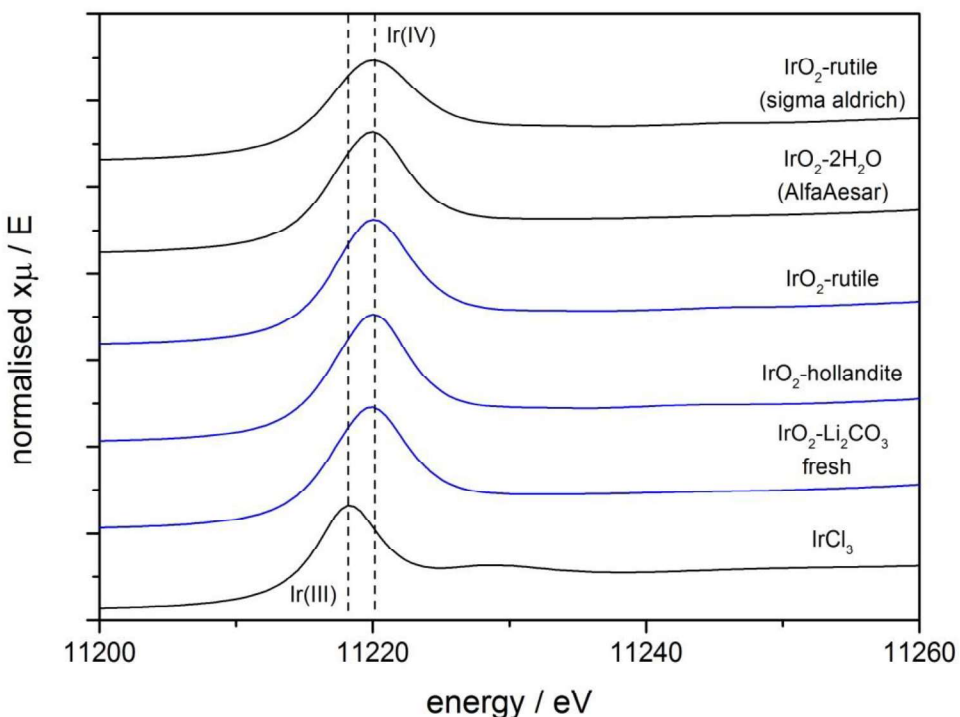


**Figure 5.7.** XANES Ir  $L_3$  edge spectra for synthesised  $\text{IrO}_2$ -rutile,  $\text{IrO}_2$ -hollandite and  $\text{IrO}_2\text{-Li}_2\text{CO}_3$  catalysts. Commercial  $\text{IrO}_2$  rutile,  $\text{IrO}_2\cdot 2\text{H}_2\text{O}$  and  $\text{IrCl}_3$  were used as standards.

A comprehensive structure refinement was not undertaken in this research and the exact bond distances were not calculated. Nevertheless, comparison between the well-defined commercial rutile  $\text{IrO}_2$  with the prepared samples would allow the identification of structural changes. No differences in the Ir-O or Ir-Ir bond distances were observed between commercial and synthesised rutile  $\text{IrO}_2$ . Therefore, the rutile prepared sample has the same tetragonal structure as the commercial catalyst in accordance with the XRD characterisation.

Synthesised samples, amorphous  $\text{IrO}_2\text{-Li}_2\text{CO}_3$  and  $\text{IrO}_2$  hollandite, presented similar structure to commercial amorphous  $\text{IrO}_2\cdot 2\text{H}_2\text{O}$  catalyst. The Ir-O bond distances were slightly longer, while the Ir-Ir bond distances were considerably shorter, compared to the standard rutile  $\text{IrO}_2$  (figure 5.8). The longer Ir-O and shorter Ir-Ir bond distances have been reported on other amorphous iridium oxo-hydroxides and in  $\text{IrO}_2$  hollandite structures and associated with a distortion in the  $\text{IrO}_6$  octahedron.<sup>(7)</sup>

Cruz *et al.*<sup>(18)</sup> reported that the oxidation state of iridium is quasi-linearly correlated with the Ir-O bond distance and that the presence of Ir(III) sites is not necessarily perceived in the white line position, since the presence of Ir(III) sites can translate in a decrease in the transition intensity. Longer Ir-O bond distances compared to rutile  $\text{IrO}_2$  were assigned to the presence of Ir(III) sites. Therefore, in agreement with XPS characterisation, and in line with

previous reports that suggested the presence of Ir(III) and Ir(IV) centres on commercial amorphous  $\text{IrO}_2 \cdot 2\text{H}_2\text{O}$ ,<sup>1, 2</sup> it can be confirmed the presence of Ir(III) sites on hollandite  $\text{Li}_x\text{IrO}_2$  and on amorphous  $\text{IrO}_2\text{-Li}_2\text{CO}_3$  reported in chapter 3.

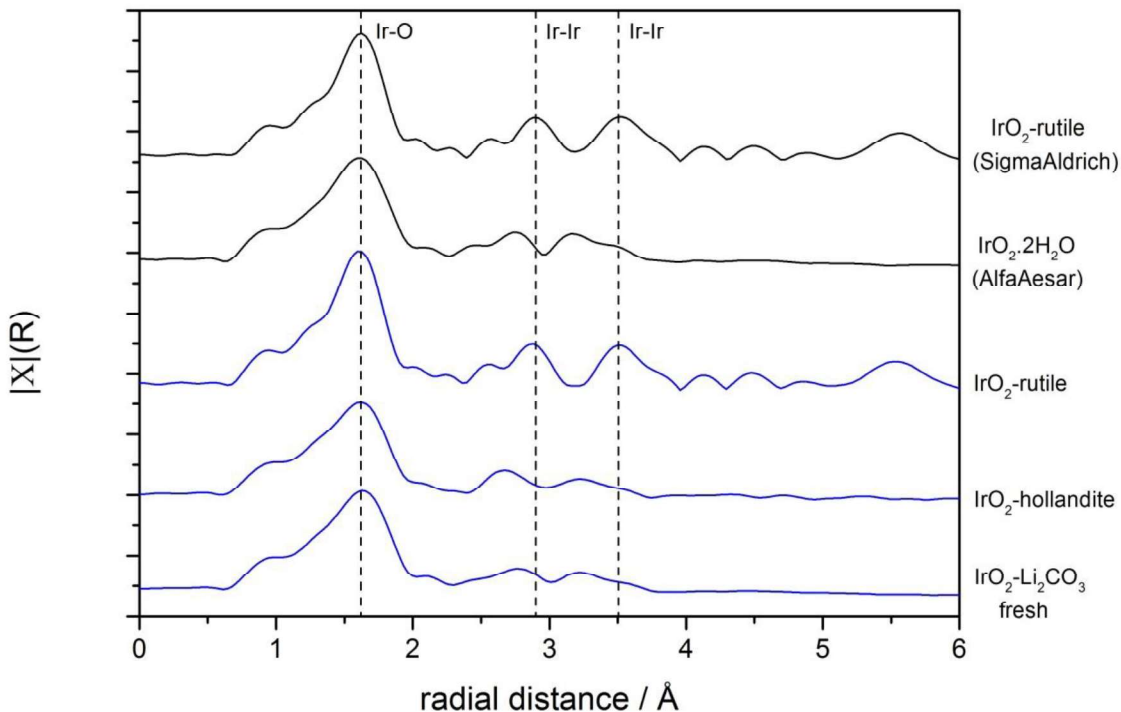


**Figure 5.8.** EXAFS structural determination for synthesised  $\text{IrO}_2$  rutile,  $\text{IrO}_2$  hollandite and  $\text{IrO}_2\text{-Li}_2\text{CO}_3$ , samples were compared to commercial  $\text{IrO}_2$  rutile and amorphous  $\text{IrO}_2 \cdot 2\text{H}_2\text{O}$ .

### 5.2.1 Single $\text{IrO}_2$ hollandite and $\text{IrO}_2$ rutile phase electrochemistry towards OER.

From the hydrothermal synthesis optimisation described in chapter 3, the use of  $\text{Li}_2\text{CO}_3$  as a base, led to  $\text{IrO}_2$  with improved catalytic activity and stability towards OER compared to the standard state of the art  $\text{IrO}_2 \cdot 2\text{H}_2\text{O}$ . Annealing of the synthesised  $\text{IrO}_2\text{-Li}_2\text{CO}_3$  catalyst had a detrimental effect on its activity and stability. A shift towards higher overpotential was observed by LSV with increasing the annealing temperature. The decrease in activity with increasing annealing temperatures was observed for various reported  $\text{IrO}_2$  materials, and normally assigned to the loss of structural flexibility of amorphous materials compared to rigid crystalline structures.<sup>24, 25</sup> The presence of Ir(III) and Ir(IV) were detected on highly active amorphous iridium oxo-hydroxides, in contrast, the low activity of rutile  $\text{IrO}_2$  is associated with iridium being all in the Ir(IV) oxidation state. However, after annealing the  $\text{IrO}_2\text{-Li}_2\text{CO}_3$  catalyst at 500 °C, a stable material under OER reaction conditions was obtained, which was hypothesise to be related to the presence of hollandite motifs. To prove

this hypothesis, single phase  $\text{IrO}_2$  rutile and single phase  $\text{Li}_x\text{IrO}_2$  were prepared from a common iridium oxo-hydroxide starting material obtained through a hydrothermal synthesis.

Single phase  $\text{Li}_x\text{IrO}_2$  hollandite, single phase  $\text{IrO}_2$  rutile and as prepared  $\text{IrO}_2\text{-Li}_2\text{CO}_3$  catalysts were tested towards OER in a 3-electrode flow cell reactor provided by our collaborators from the Max Planck Institute for Chemical Energy Conversion in Mülheim, Germany.<sup>(26)</sup> A detailed flow cell description and the working electrode preparation were described previously in the experimental chapter.

The intrinsic catalyst activity was determined by LSV (1.2 V<sub>RHE</sub> to 1.8 V<sub>RHE</sub> at 5 mV·s<sup>-1</sup>) at the beginning of the reaction and the catalyst stability was obtained by measuring the increase in the potential observed during the LSV after CV (50 CV cycles between 0.7 V<sub>RHE</sub> and 1.4 V<sub>RHE</sub> at 50 mV·s<sup>-1</sup>) and after CP (2 hours at 10 mA·cm<sup>-2</sup>) as well as from the increase in the potential during the chronopotentiometry at 10 mA·cm<sup>-2</sup> for 2 h. Reactions were carried out in a 0.1 M HClO<sub>4</sub> solution.

As expected, annealing at 500 °C, in order to induce the crystallisation of the amorphous iridium oxo-hydroxide to its rutile form, led to a decrease in the intrinsic activity of the catalyst, as observed by the 100 mV shift towards higher potentials in the initial LSV measurement at a current density of 10 mA·cm<sup>-2</sup>. Nevertheless, annealing at 500 °C in the presence of lithium carbonate to induce the hollandite phase formation led to no decrease in the intrinsic  $\text{IrO}_2\text{-Li}_2\text{CO}_3$  catalyst activity towards OER (figure 5.9). The  $\text{IrO}_2\text{-Li}_2\text{CO}_3$  synthesised in chapter 3 presented higher activity compared to the commercial state of the art  $\text{IrO}_2\cdot 2\text{H}_2\text{O}$ ; likewise,  $\text{Li}_x\text{IrO}_2$  hollandite presents improved activity compared to the commercial catalyst.

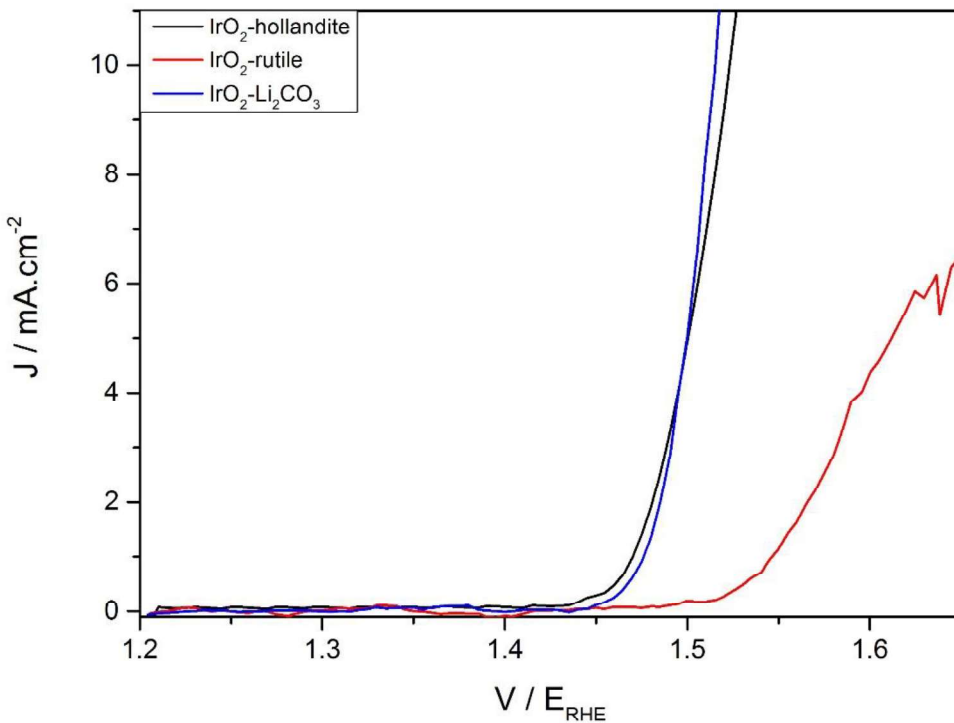


**Figure 5.9.** LSV (1.2  $\text{V}_{\text{RHE}}$  to 1.8  $\text{V}_{\text{RHE}}$  at  $5 \text{ mV}\cdot\text{s}^{-1}$ ) performed at the beginning of the experiment for synthesised single phase  $\text{IrO}_2$ -rutile,  $\text{IrO}_2$ -hollandite and compared to the as prepared  $\text{IrO}_2\text{-Li}_2\text{CO}_3$  catalyst.

In order to determine the stability of the catalysts, a LSV measurement was recorded after CV (50 CV cycles between 0.7  $\text{V}_{\text{RHE}}$  and 1.4  $\text{V}_{\text{RHE}}$  at  $50 \text{ mV}\cdot\text{s}^{-1}$ ) and after CP (2 hours at  $10 \text{ mA}\cdot\text{cm}^{-2}$ ) tests. If the catalysts undergo deactivation during CV or CP, the potential observed in the LSV to reach the same current density would be shifted towards higher values compared to the initial LSV measurement. The rise in the monitored potential during the CP is also indicative of the catalyst stability. A steady potential to maintain a constant current density would be expected for stable catalysts, however, under deactivation a potential rise would be observed until 2.2  $\text{V}_{\text{RHE}}$ , which correspond to the corrosion of the glassy carbon electrode. Figure 5.10 illustrates the increase in the potential on the LSV experiment to reach a current density of  $5 \text{ mA}\cdot\text{cm}^{-2}$  after CV (represented with black columns) and after CP (represented as red columns) test compared to the initial LSV measurement. The potential rise during the chronopotentiometry at  $10 \text{ mA}\cdot\text{cm}^{-2}$  for 2 h is represented by blue columns.

As expected, prepared  $\text{IrO}_2$  rutile showed poor performance in terms of activity and stability towards OER. It presented the highest deactivation, as observed by the increase of 56 mV and 150 mV in the potential, by LSV, after CV and after CP measurements respectively. In line, rutile  $\text{IrO}_2$  showed a 95 mV potential rise during the CP test compared to 17 mV and 11 mV for hollandite and amorphous  $\text{IrO}_2$ , respectively. Conversely,  $\text{IrO}_2$  hollandite presented a slightly increase of 7 mV in the potential after the CV test, by LSV, which was not observed for  $\text{IrO}_2\text{-Li}_2\text{CO}_3$  catalyst. However, even though the potential during the CP stability test rose slightly more for  $\text{IrO}_2$ -hollandite than for  $\text{IrO}_2\text{-Li}_2\text{CO}_3$ , the LSV measurement after the CP showed an increase of 5mV and 38 mV, respectively, in comparison with the initial LSV, indicating its improved stability against corrosion.

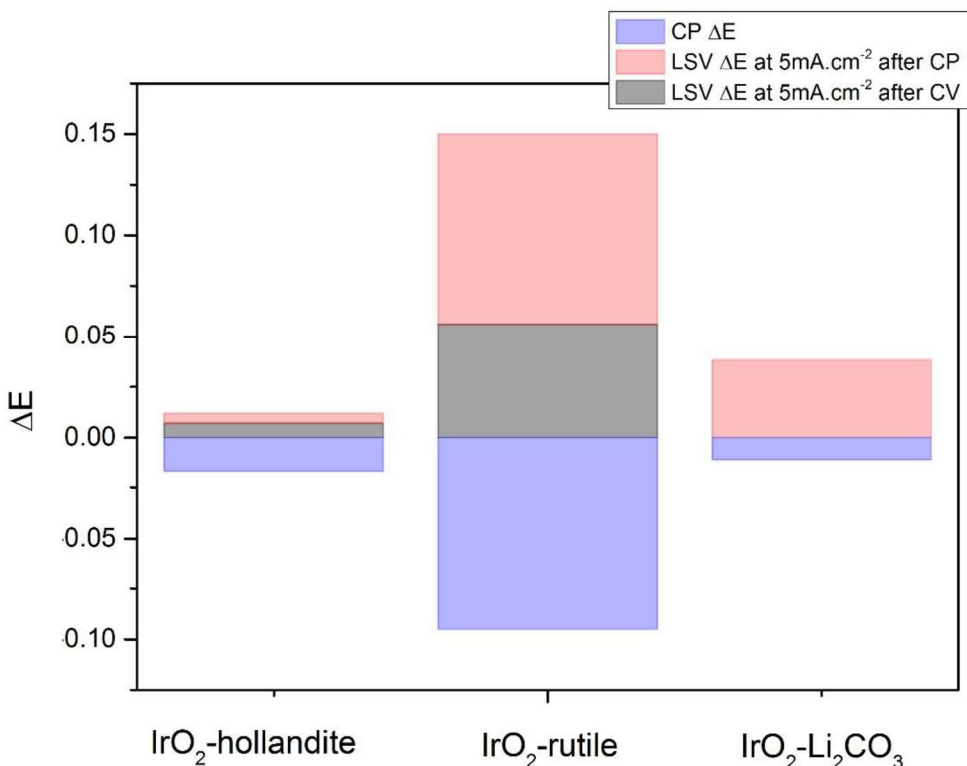


**Figure 5.10.** Stability indicators for single phase  $\text{IrO}_2$  rutile and  $\text{IrO}_2$  hollandite catalysts compared to  $\text{IrO}_2\text{-Li}_2\text{CO}_3$  catalyst. The black bars represent the increase in potential to reach a current density of 5  $\text{mA}\cdot\text{cm}^{-2}$  after CV (50 CV cycles between 0.7 VRHE and 1.4 VRHE at 50  $\text{mV}\cdot\text{s}^{-1}$ ). Red bars represents the increase in potential to reach a current density of 5  $\text{mA}\cdot\text{cm}^{-2}$  after CP (2 hours at 10  $\text{mA}\cdot\text{cm}^{-2}$ ). Blue bars indicate the increase in potential during the CP stability test.

During the CP experiment, oxygen bubbles were formed continuously on the anode; because the use of a stationary working electrode oxygen could remain adsorbed on the electrode surface producing an increase in the potential.<sup>(26-28)</sup> The bubble rate formation and its detachment could have an influence in the potential rise observed during CP, which could vary between catalysts as a result of different electrode surface properties (surface roughness, the presence of crags and its size or the surface hydrophobicity), hence small changes in the potential are difficult to be assigned to slightly more stable or less stable catalysts. However, LSV measurements at the beginning of the experiment and after the CP test were indicative of the improved stability of  $\text{IrO}_2$  hollandite compared to the as prepared  $\text{IrO}_2\text{-Li}_2\text{CO}_3$  catalyst.

Useful information about synthesised  $\text{IrO}_2$  materials could be obtained from its CV shape and area under its curve (figure 5.11). On one hand, the detection of Ir(III)/Ir(IV) and Ir(IV)/Ir(V) electronic transitions assigned at 0.9  $V_{\text{RHE}}$  and 1.2  $V_{\text{RHE}}$  respectively would indicate the presence of Ir(III) and Ir(IV) sites.<sup>(29)</sup> The common symmetric peak reported for  $\text{IrO}_2$  rutile without the presence of any electronic transitions<sup>(30, 31)</sup> was observed for prepared single phase  $\text{IrO}_2$  rutile.  $\text{IrO}_2\text{-Li}_2\text{CO}_3$  showed a Ir(III)/Ir(IV) reversible broad and low intense peak at 0.9  $V_{\text{RHE}}$ , the Ir(IV)/Ir(V) pair was observed as an irreversible peak in the anodic potential at 1.2  $V_{\text{RHE}}$ .  $\text{IrO}_2$  hollandite catalyst presented a more intense reversible Ir(III)/Ir(IV) transition. XANES analysis showed that  $\text{IrO}_2\text{-Li}_2\text{CO}_3$  and hollandite  $\text{IrO}_2$  have very close oxidation state, indicating a similar proportion of Ir(III) and Ir(IV) sites. Thus, higher intensity in  $\text{IrO}_2$ -hollandite catalyst during the CV would indicate a higher transition of Ir(III) to Ir(IV) sites compared to  $\text{IrO}_2\text{-Li}_2\text{CO}_3$ . On the other hand, the area on the CV curve is indicative of the active surface area of the catalyst. Rutile  $\text{IrO}_2$  catalyst presented the lowest area and this correlates with being the less active catalyst. Comparing  $\text{IrO}_2\text{-Li}_2\text{CO}_3$  and hollandite  $\text{IrO}_2$ , the latter had enhanced area which suggested a higher concentration of active sites. However, as observed by LSV, hollandite  $\text{IrO}_2$  showed no improved activity which might indicate that the reaction was limited by mass transfer.

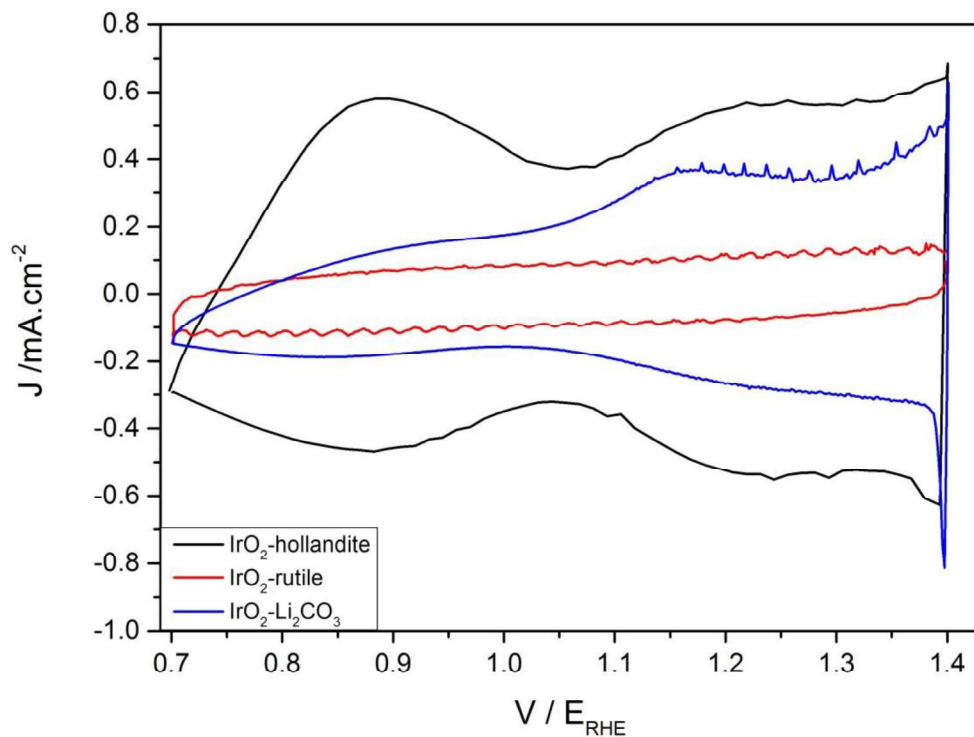


**Figure 5.11.** CV curves ( $0.7 \text{ V}_{\text{RHE}}$  and  $1.4 \text{ V}_{\text{RHE}}$  at  $50 \text{ mV}\cdot\text{s}^{-1}$ ) in  $\text{HClO}_4$  ( $0.1 \text{ M}$ ) for prepared crystalline single phase rutile and hollandite  $\text{IrO}_2$  and compared with amorphous  $\text{IrO}_2\text{-Li}_2\text{CO}_3$ .

### 5.3 Conclusions.

The synthesis of single phase  $\text{Li}_x\text{IrO}_2$  hollandite and  $\text{IrO}_2$  rutile was achieved through a hydrothermal synthesis and confirmed by XRD. To our best knowledge, this is the first time that hollandite  $\text{IrO}_2$  with lithium as the host cation has been reported. When a lithium free amorphous iridium oxo-hydroxide is annealed in air, it crystallises to rutile. However, the synthesis of single phase hollandite  $\text{IrO}_2$  indicates that, in the presence of lithium, amorphous iridium oxo-hydroxide preferably crystallises to hollandite instead of rutile. Commercial rutile  $\text{IrO}_2$  is made entirely of Ir(IV) and  $\text{O}^{2-}$  sites as observed by XPS. Synthesised rutile  $\text{IrO}_2$ , however, has a higher concentration of hydroxides at the surface compared to commercial rutile, which could be related to its higher OER activity.

Apart from the difference in structure between rutile and hollandite observed by XRD, the presence of Ir(III) and Ir(IV) sites in the hollandite  $\text{Li}_x\text{IrO}_2$  were confirmed by XPS and XANES characterisation, in accordance with previous reports on hollandite materials. EXAFS showed a  $\text{IrO}_6$  octahedron distortion in the hollandite structure with longer Ir-O associated with the presence of Ir(III) and shorter Ir-Ir bond distances. Amorphous  $\text{IrO}_2\text{-Li}_2\text{CO}_3$  synthesised and discussed in chapter 3 presented a comparable  $\text{IrO}_6$  octahedron to hollandite  $\text{Li}_x\text{IrO}_2$  by EXAFS, with longer Ir-O and shorter Ir-Ir bond distances.

Synthesised single phase catalysts were tested towards OER in a three-electrode flow cell. The intrinsic activity of the catalysts was determined by performing a LSV at the beginning of the experiment. As expected, rutile  $\text{IrO}_2$  showed poor catalytic activity and stability. Nevertheless, hollandite  $\text{Li}_x\text{IrO}_2$  and amorphous  $\text{IrO}_2\text{-Li}_2\text{CO}_3$  catalysts presented comparable intrinsic activity, with improved activity compared to the commercial state of the art  $\text{IrO}_2\text{-}2\text{H}_2\text{O}$  catalyst.

Moreover, the catalyst stability was tested by measuring a LSV after a CP ( $10 \text{ mA}\cdot\text{cm}^{-2}$  for 2h) test and also by monitoring the potential rise during the CP. Hollandite  $\text{Li}_x\text{IrO}_2$  showed improved stability against corrosion compared to amorphous  $\text{IrO}_2\text{-Li}_2\text{CO}_3$ , as observed by the smaller increase of 5 mV compared to 38 mV respectively at  $5 \text{ mA}\cdot\text{cm}^{-2}$  by LSV.

To conclude, it seems that the presence of Ir(III) and Ir(IV) sites on the catalysts are responsible for the improved activity compared to rutile  $\text{IrO}_2$ , composed entirely of Ir(IV) centres. Additionally, the stability of amorphous  $\text{IrO}_2\text{-Li}_2\text{CO}_3$  catalyst under OER reaction conditions in acid media was improved by its transformation into the crystalline hollandite  $\text{Li}_x\text{IrO}_2$  phase without impairing its catalytic activity.

#### 5.4 Bibliography.

1. V. Pfeifer, T. E. Jones, J. J. Velasco Velez, C. Massué, M. T. Greiner, R. Arrigo, D. Teschner, F. Girgsdies, M. Scherzer, J. Allan, M. Hashagen, G. Weinberg, S. Piccinin, M. Hävecker, A. Knop-Gericke, R. Schlögl, The electronic structure of iridium oxide electrodes active in water splitting, *Physical Chemistry Chemical Physics*, **2016**, 18 (4), 2292-2296.
2. V. Pfeifer, T. E. Jones, J. J. Velasco Vélez, C. Massué, R. Arrigo, D. Teschner, F. Girgsdies, M. Scherzer, M. T. Greiner, J. Allan, M. Hashagen, G. Weinberg, S. Piccinin, M. Hävecker, A. Knop-Gericke, R. Schlögla, The electronic structure of iridium and its oxides, *Surface and Interface Analysis*, **2016**, 48 (5), 261-273.
3. V. Pfeifer, T. E. Jones, S. Wrabetz, C. Massué, J. J. Velasco Velez, R. Arrigo R, M. Scherzer, S. Piccinin, M. Hävecker, A. Knop-Gericke, R. Schlögl, Reactive oxygen species in iridium-based OER catalysts, *Chemical Science*, **2016**, 7 (11), 6791-6795.
4. V. Pfeifer, T. E. Jones, J. J. Velasco Velez, R. Arrigo, S. Piccinin, M. Hävecker, A. Knop-Gericke, R. Schlögl, In situ observation of reactive oxygen species forming on oxygen-evolving iridium surfaces, *Chem Sci*, **2016**, 8, 2143-2149.
5. S. Fierro, T. Nagel, H. Baltruschat, C. Comninellis, Investigation of the oxygen evolution reaction on  $\text{Ti}/\text{IrO}_2$  electrodes using isotope labelling and on-line mass spectrometry, *Electrochemistry Communications*, **2007**, 9 (8), 1969-1974.
6. E. Willinger, C. Massué, R. Schlögl, M. G. Willinger, Identifying Key Structural Features of  $\text{IrO}_x$  Water Splitting Catalysts, *Journal of the American Chemical Society*, **2017**, 139 (34), 12093-12101.
7. W. Sun, Y. Song, X. Q. Gong, L. Cao, J. Yang, Hollandite Structure  $\text{K}_{x=0.25}\text{IrO}_2$  Catalyst with Highly Efficient Oxygen Evolution Reaction, *ACS Applied Materials & Interfaces*, **2016**, 8 (1), 820-826.
8. A. Talanov, W. A. Phelan, Z. A. Kelly, M. A. Siegler, T. M. McQueen, Control of the Iridium Oxidation State in the Hollandite Iridate Solid Solution  $\text{K}_{1-x}\text{Ir}_4\text{O}_8$ , *Inorganic Chemistry*, **2014**, 53 (9), 4500-4507.
9. L. M. Schoop, J. W. Krizan, Q. D. Gibson, R. J. Cava, Structure and elementary properties of the new Ir hollandite  $\text{Rb}_{0.17}\text{IrO}_2$ , *Journal of Solid State Chemistry*, **2014**, 209, 37-41.
10. N. Bestaoui, P. Deniard, R. Brec, Structural Study of a Hollandite-Type  $\text{K}_x\text{IrO}_2$ , *Journal of Solid State Chemistry*, **1995**, 118 (2), 372-377.

11. J. Dai, S. F. Y. Li, K. S. Siow, Z. Gao, Synthesis and characterization of the hollandite-type  $\text{MnO}_2$  as a cathode material in lithium batteries, *Electrochimica Acta*, **2000**, 45 (14), 2211-2217.
12. L. T. Tseng, Y. Lu, H. M. Fan, Y. Wang, X. Luo, T. Liu T, P. Munroe, S. Li, J. Yi, Magnetic properties in  $\alpha\text{-MnO}_2$  doped with alkaline elements, *Scientific Reports*, **2015**, 5, 9094-9100.
13. J. E. Post, Manganese Oxide Minerals: Crystal Structures and Economic and Environmental Significance, *Proc. Natl. Acad. Sci.*, **1999**, 96, 3447-3454.
14. A. Pfennig, O. Kirk, *Chemie Ingenieur Technik*, **1995**, 67 (3), 352-353.
15. R. G. Haverkamp, A. T. Marshall, B. C. C. Cowie, Energy resolved XPS depth profile of ( $\text{IrO}_2$ ,  $\text{RuO}_2$ ,  $\text{Sb}_2\text{O}_5$ ,  $\text{SnO}_2$ ) electrocatalyst powder to reveal core-shell nanoparticle structure, *Surface and Interface Analysis*, **2011**, 43 (5), 847-855
16. S. J. Freakley, J. Ruiz Esquius, D. J. Morgan, The X-ray photoelectron spectra of Ir,  $\text{IrO}_2$  and  $\text{IrCl}_3$  revisited, *Surface and Interface Analysis*, **2017**, 49 (8), 794-799.
17. T. Reier, Z. Pawolek, S. Cherevko, M. Bruns, T. Jones, D. Teschner, S. Selve, A. Bergmann, H. N. Nong, R. Schlögl, K. J. J. Mayrhofer, P. Strasser, Molecular Insight in Structure and Activity of Highly Efficient, Low-Ir Ir–Ni Oxide Catalysts for Electrochemical Water Splitting (OER), *Journal of the American Chemical Society*, **2015**, 137 (40), 13031-13040.
18. A. M. Cruz, L. Abad, N. M. Carretero, J. Moral-Vico, J. Fraxedas, P. Lozano, G. Subías, V. Padial, M. Carballo, J. E. Collazos-Castro, N. Casañ-Pastor, Iridium Oxohydroxide, a Significant Member in the Family of Iridium Oxides. Stoichiometry, Characterization, and Implications in Bioelectrodes, *The Journal of Physical Chemistry C*, **2012**, 116 (8), 5155-5168.
19. L. M. Schoop, J. W. Krizan, Q. D. Gibson, R. J. Cava, Structure and elementary properties of the new Ir hollandite  $\text{Rb}_{0.17}\text{IrO}_2$ , *Journal of Solid State Chemistry*, **2014**, 209, 37-41.
20. M. Newville, *Fundamentals of XAFS*, Chicago University, **2004**.
21. Y. Mo, I. C. Stefan, W. B. Cai, J. Dong, P. Carey, D. A. Scherson, In Situ Iridium  $\text{L}_{\text{III}}$ -Edge X-ray Absorption and Surface Enhanced Raman Spectroscopy of Electrodeposited Iridium Oxide Films in Aqueous Electrolytes, *The Journal of Physical Chemistry B*, **2002**, 106 (14), 3681-3686.
22. E. Oakton, D. Lebedev, M. Povia, D. F. Abbott, E. Fabbri, A. Fedorov, M. Nachtegaal, C. Copéret, T. J. Schmidt,  $\text{IrO}_2\text{-TiO}_2$ : a High-Surface Area, Active and Stable Electrocatalyst for Oxygen Evolution Reaction, *ACS Catal*, **2017**, 7, 2346-2352.
23. C. Massué, V. Pfeifer, X. Huang, J. Noack, A. Tarasov, S. Cap, R. Schlögl, High-performance supported Ir-oxohydroxide water oxidation electrocatalysts, *ChemSusChem*, **2017**, 10, 1943-1957.

24. M. Bernicke, E. Ortel, T. Reier, A. Bergmann, J. Ferreira de Araujo, P. Strasser, R. Krahnert, Iridium Oxide Coatings with Templated Porosity as Highly Active Oxygen Evolution Catalysts: Structure-Activity Relationships, *ChemSusChem*, **2015**, 8 (11), 1908-1915.
25. T. Reier, D. Teschner, T. Lunkenbein, A. Bergmann, S. Selve, R. Krahnert, R. Schlögl, P. Strasser, Electrocatalytic Oxygen Evolution on Iridium Oxide: Uncovering Catalyst-Substrate Interactions and Active Iridium Oxide Species, *Journal of The Electrochemical Society*, **2014**, 161 (9), F876-F882.
26. I. Spanos, A. A. Auer, S. Neugebauer, X. Deng, H. Tüysüz, R. Schlöegl, Standardized Benchmarking of Water Splitting Catalysts in a Combined Electrochemical Flow Cell/Inductively Coupled Plasma-Optical Emission Spectrometry (ICP-OES) Setup, *ACS Catal*, **2017**, 7, 3768-3778.
27. C. Felix, T. Maiyalagan, S. Pasapathi, B. Bladergroen, V. Linkov, Synthesis and optimization of  $\text{IrO}_2$  electrocatalysts by Adams fusion method for solid polymer electrolyte electrolyzers., *Micro and nanosystems*, **2012**, 4, 186-191.
28. C. Spöri, J. T. H. Kwan, A. Bonakdarpour, D. P. Wilkinson, P. Strasser, The Stability Challenges of Oxygen Evolving Catalysts: Towards a Common Fundamental Understanding and Mitigation of Catalyst Degradation, *Angewandte Chemie International Edition*, **2017**, 56 (22), 5994-6021.
29. L. Ouattara, S. Fierro, O. Frey, M. Koudelka, Comninellis C, Electrochemical comparison of  $\text{IrO}_2$  prepared by anodic oxidation of pure iridium and  $\text{IrO}_2$  prepared by thermal decomposition of  $\text{H}_2\text{IrCl}_6$  precursor solution, *Journal of Applied Electrochemistry*, **2009**, 39 (8), 1361-1367.
30. Y. Lee, J. Suntivich, K. J. May, E. E. Perry, Y. Shao-Horn, Synthesis and Activities of Rutile  $\text{IrO}_2$  and  $\text{RuO}_2$  Nanoparticles for Oxygen Evolution in Acid and Alkaline Solutions, *J Phys Chem Lett*, **2012**, 3 (3), 399-404.
31. X. Yang, Y. Li, L. Deng, W. Li, Z. Ren, M. Yang, X. Yang, Y. Zhu, Synthesis and characterization of an  $\text{IrO}_2\text{-Fe}_2\text{O}_3$  electrocatalyst for the hydrogen evolution reaction in acidic water electrolysis, *RSC Adv*, **2017**, 7 (33), 20252-20258.

# Chapter 6

## Preparation of iridium mixed oxide catalysts. Rational design of catalysts for significantly lowering the iridium loading on the electrode

### 6.1 Introduction.

Iridium is one of the rarest elements on Earth.<sup>(1)</sup> It is used in diverse applications, such as alloying agent in piping, alloying to harden platinum, to produce cardiovascular stents<sup>(2)</sup> and in the manufacture of LED<sup>(3)</sup> for smartphones, tablets, televisions and automobiles, apart than on PEM electrolyzers. Therefore, it is paramount to be as efficient as possible with its usage. Iridium can be used most efficiently on PEM electrolyzers by improving its dispersion on the electrode. This can be achieved by diluting IrO<sub>2</sub> with a cheaper non-noble metal oxide, as discussed in this chapter, or by dispersing IrO<sub>2</sub> nanoparticles on a conductive support,<sup>(4, 5)</sup> as shown in chapter 4.

The non-noble metal introduced in the IrO<sub>2</sub> lattice to form the mixed oxide catalyst is not stable towards OER and dissolves during reaction.<sup>(6-8)</sup> Ir-Ni mixed oxide catalysts are the most reported on the literature. Reier *et al.*<sup>(6)</sup> prepared Ir-Ni films by thermal decomposition at 450 °C on Ti cylinders. Increasing the nickel concentration on the mixed oxide catalyst to 67-79 at. % led to an eight-fold increase in the catalytic activity compared to IrO<sub>2</sub>, however, at the expenses of the catalyst stability. Improved activity was attributed to surface nickel leaching, leading to an increase in the concentration of surface iridium and hydroxide groups.<sup>(6)</sup> Similar results were also reported by Nong *et al.*<sup>(9, 10)</sup> for Ir-Ni mixed oxide catalysts. The catalyst with a Ir:Ni molar ratio of 1:3.3 showed improved catalytic activity towards OER compared to IrO<sub>2</sub>, which was attributed to surface nickel dissolution; this led to the formation of iridium vacancies and electrophilic O<sup>-</sup> sites.<sup>(9, 10)</sup> Improved activity was not only assigned to Ni-leaching, and the concomitant higher number of IrO<sub>2</sub> sites exposed to reaction, but also to the weaker bonding of OER reaction intermediates with the catalyst compared to IrO<sub>2</sub>, as a result of the intermetallic interactions.<sup>(11)</sup>

In this chapter, Ir<sub>x</sub>Ni<sub>1-x</sub>O<sub>2</sub> and Ir<sub>x</sub>Cu<sub>1-x</sub>O<sub>2</sub> mixed oxide catalyst were hydrothermally prepared with a homogeneous elemental distribution or with a core-shell arrangement. The aim of this chapter is to halve the iridium loading on the electrode, without impairing the catalytic activity or stability towards OER, in order to optimise the iridium efficiency compared to IrO<sub>2</sub>-Li<sub>2</sub>CO<sub>3</sub> catalyst synthesised in chapter 3.

## 6.2 Homogeneously dispersed iridium non-noble metal mixed oxide catalysts.

### 6.2.1 Catalyst synthesis.

Homogeneously dispersed  $\text{Ir}_{0.8}\text{Ni}_{0.2}\text{O}_2$ ,  $\text{Ir}_{0.5}\text{Ni}_{0.5}\text{O}_2$ ,  $\text{Ir}_{0.8}\text{Cu}_{0.2}\text{O}_2$  and  $\text{Ir}_{0.5}\text{Cu}_{0.5}\text{O}_2$  catalysts were prepared following a modification of the hydrothermal method described by Reetz and Feigel for the synthesis of  $\text{IrO}_2$  materials.<sup>(12)</sup> To prepare the catalysts, the desired amount of the chloride precursors ( $\text{IrCl}_3$ ,  $\text{NiCl}_2$  or  $\text{CuCl}_2$ ) to obtain a total of 1 mmol of metal were mixed with  $\text{Li}_2\text{CO}_3$  (8 mmol) in a 50 ml bottom flask and dissolved in 10 ml of deionised water. The slurry was stirred for 16 h at room temperature, a further 10 ml of deionised water were added, and the slurry was heated to reflux for 3 hours. A brown precipitate was formed in all cases, which was recovered by filtration and washed with 2 L of deionised water. Materials were dried in a fumehood overnight. Half the amount of the material obtained was annealed in air at 500 °C for 3 h to investigate the effect of heat treatment on mixed oxide catalysts.

### 6.2.2 Catalyst characterisation.

#### *X-ray powder diffraction (XRD)*

As prepared mixed oxide  $\text{Ir}_x\text{M}_{1-x}\text{O}_2$  catalysts, formed through the hydrothermal synthesis, showed a XRD pattern typical of amorphous  $\text{IrO}_x$  with broad reflections at 35° and 60° as shown in figure 6.1 and figure 6.2 for  $\text{Ir}_x\text{Ni}_{1-x}\text{O}_2$  and  $\text{Ir}_x\text{Ni}_{1-x}\text{O}_2$  respectively. Information on the atomic distribution within the material could not be obtained from the XRD patterns for the as prepared catalysts. However, rutile  $\text{IrO}_2$  (JCPDS 015-0876) reflection without the presence of  $\text{NiO}$  (JCPDS 004-0835),  $\text{Ni}_2\text{O}_3$  (JCPDS 14-0481) or  $\text{CuO}$  (JCPDS 001-1117),  $\text{Cu}_2\text{O}$  (JCPDS 5-0667) phase were observed after annealing in air at 500 °C for 3 h. Although the elemental distribution could change during calcination, the observation of no phase segregation suggested that a solid solution, homogeneous distribution of iridium and nickel atoms throughout the material, was obtained on fresh samples.

Figure 6.1 shows the XRD pattern for as prepared and annealed  $\text{Ir}_x\text{Ni}_{1-x}\text{O}_2$  mixed oxide catalysts. After annealing at 500 °C, no distinct  $\text{NiO}$  or  $\text{Ni}_2\text{O}_3$  reflections were detected in the material, suggesting the formation of a solid solution with  $\text{IrO}_2$ . Nickel is smaller than iridium, and its substitution into the lattice has been reported to produce a shift of the rutile- $\text{IrO}_2$  reflections towards higher 2θ degrees by XRD as a result of a lattice contraction.<sup>(13)</sup> Nevertheless, no apparent reflection shift was observed for annealed  $\text{Ir}_x\text{Ni}_{1-x}\text{O}_2$  mixed oxide catalysts with increasing the nickel loading compared to  $\text{IrO}_x$ . Additionally, the addition of Ni into the  $\text{IrO}_2$  lattice reduced the crystallinity of the mixed oxide catalysts even after high

temperature calcination, as observed by the decrease in intensity and broadening of the  $\text{IrO}_2$ -rutile related reflections.

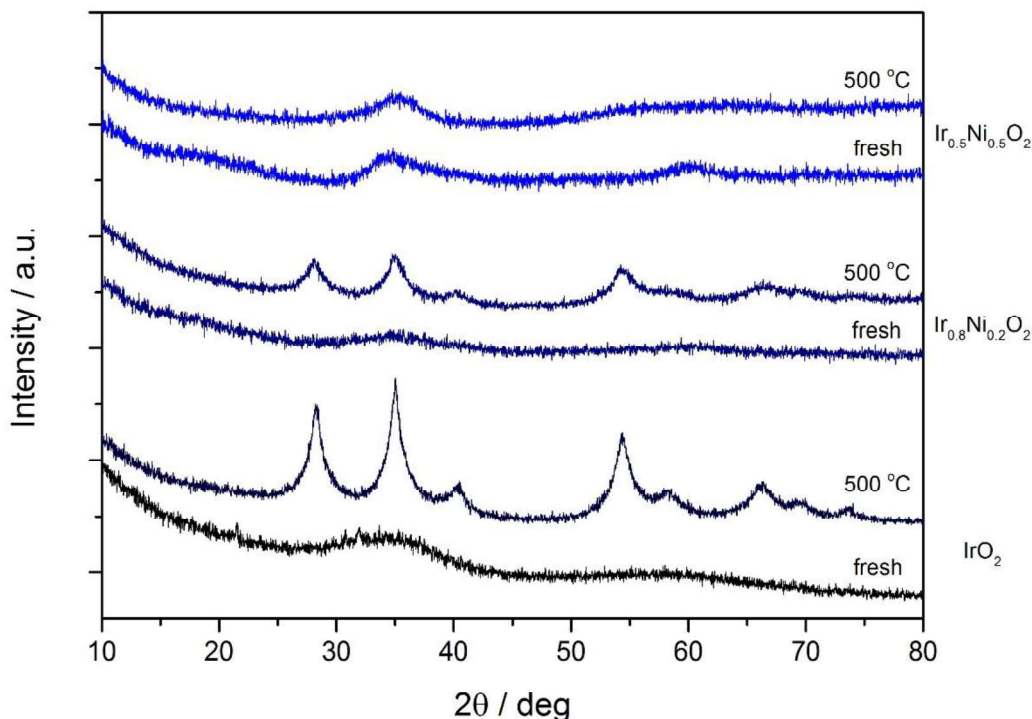


**Figure 6.1.** XRD patterns for  $\text{Ir}_x\text{Ni}_{1-x}\text{O}_2$  mixed oxide catalysts ( $x = 1, 0.8$  and  $0.5$ ) prepared through the hydrothermal synthesis. XRD patterns are grouped by nickel content, the annealed material is presented above its respective fresh catalyst.

In the case of Cu-doped  $\text{IrO}_2$  catalysts, the behaviour differed from that observed for Ni doped catalysts (figure 6.2). Rutile- $\text{IrO}_2$  reflections were observed after annealing in air at 500 °C without the presence of  $\text{CuO}$  or  $\text{Cu}_2\text{O}$  reflections, indicating the formation of a solid solution within the studied composition range.<sup>(11)</sup> Contrary to what observed for  $\text{Ir}_{0.5}\text{Ni}_{0.5}\text{O}_2$  catalysts, the catalyst crystallinity was not altered at high dopant concentration. Moreover, lattice contractions was observed by a shift towards higher angles in the (101), (211) and (112) crystalline planes indexed at 34.8°, 54.1° and 66.2° respectively (figure 6.3).

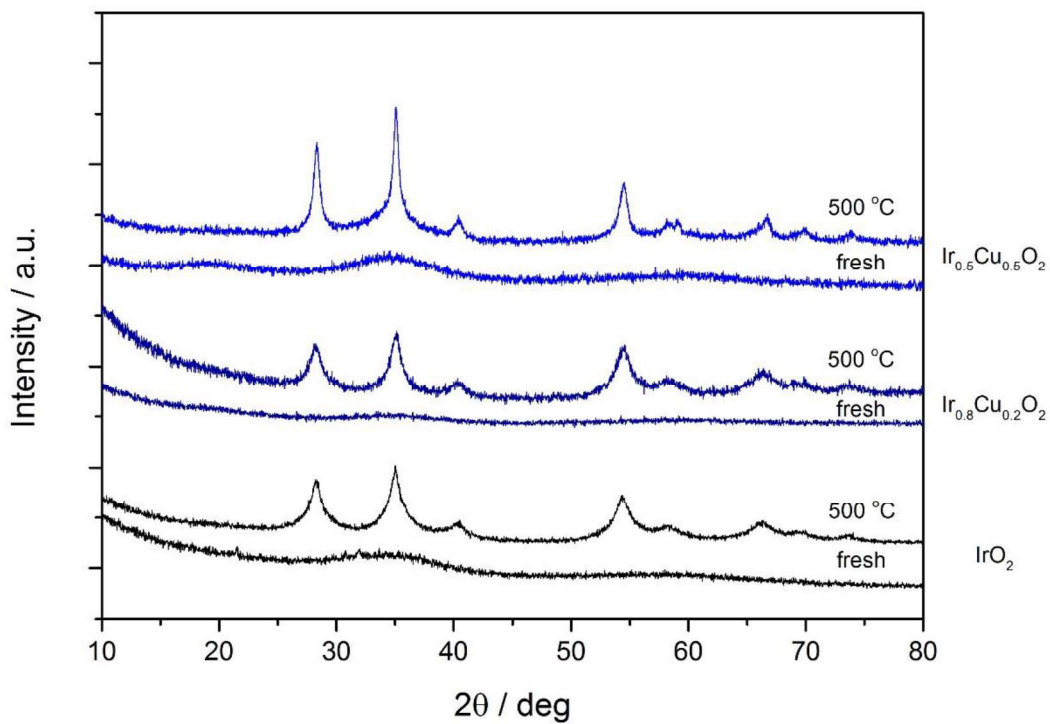


**Figure 6.2.** XRD patterns for  $\text{Ir}_x\text{Cu}_{1-x}\text{O}_2$  mixed oxide catalysts ( $X = 1, 0.8$  and  $0.5$ ) prepared through the hydrothermal synthesis. XRD patterns are grouped by copper content, the annealed sample is presented above its fresh counterpart.

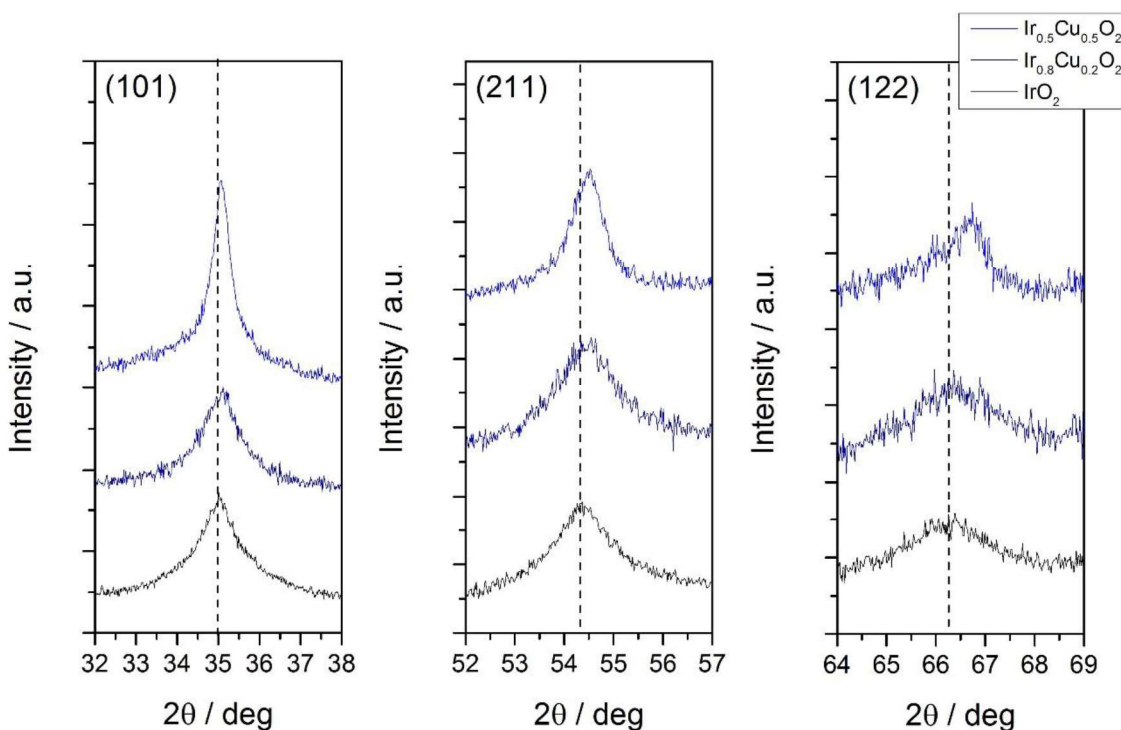


**Figure 6.3.** XRD reflections corresponding to (101), (211) and (122) planes for  $\text{Ir}_x\text{Cu}_{1-x}\text{O}_2$  mixed oxide catalysts ( $X = 1, 0.8$  and  $0.5$ ) prepared through the hydrothermal synthesis after annealing in static air at  $500^\circ\text{C}$  for 3 h.

#### X-ray photoelectron spectroscopy (XPS)

Since for as prepared mixed oxide catalysts elemental distribution was thought to be homogeneous through the material, XPS quantification, although a surface technique, should be representative of the bulk composition. Element's distribution can change after annealing in air at  $500^\circ\text{C}$ , hence XPS quantification was used to determine metal migration towards the surface after heat treatment. The non-noble metal added for diluting the amount of  $\text{IrO}_2$  on the electrode are not active towards OER nor stable against corrosion during reaction. Therefore, the formation of a protective iridium shell upon annealing to deter the dissolution of the dopant element during the harsh reaction conditions would be desired, as reported by Ji Yang *et al.*<sup>(14)</sup> for Ni-doped catalysts prepared through a hydrothermal synthesis followed by annealing in air at  $400^\circ\text{C}$ .

Measured metal quantification for prepared  $\text{Ir}_x\text{M}_{1-x}\text{O}_2$  catalysts ( $M = \text{Ni}$  or  $\text{Cu}$ ) before and after annealing in air at  $500^\circ\text{C}$  for 3 h are presented in table 6.1. Because the  $\text{Ir}(4f)$  orbital overlaps with the  $\text{Ni}(3p)$  orbital the  $\text{Ir}(4d)$ ,  $\text{Ni}(2p_{3/2})$  and  $\text{Cu}(2p_{3/2})$  orbitals were used for

determining catalyst's composition. The measured metal quantification for the as prepared catalysts was in agreement with the theoretical values, indicating the complete precipitation of both metals during the hydrothermal synthesis to form the mixed oxide phase. After annealing in air at 500 °C no significant changes in the composition were observed for Ni-doped  $\text{IrO}_2$  catalysts. Conversely, the metal composition for the  $\text{Ir}_{0.5}\text{Cu}_{0.5}\text{O}_2$  catalyst remained unchanged after annealing, whilst a pronounced copper enrichment was observed on the  $\text{Ir}_{0.8}\text{Cu}_{0.2}\text{O}_2$  sample.

**Table 6.1.** Elemental XPS quantification for fresh and annealed in static air at 500 °C for 3 h  $\text{Ir}_x\text{M}_{1-x}\text{O}_2$  catalysts ( $\text{M} = \text{Ni}, \text{Cu}$ ) prepared through the hydrothermal method. Ir(4d), Ni(2p<sub>3/2</sub>) and Cu(2p<sub>3/2</sub>) orbitals were used for the quantification.

Catalyst	As prepared metal composition		500 °C metal composition	
	Ir at %	Dopant at %	Ir at %	Dopant at %
$\text{Ir}_{0.8}\text{Ni}_{0.2}\text{O}_2$	80.9	19.1	78.5	21.5
$\text{Ir}_{0.5}\text{Ni}_{0.5}\text{O}_2$	47.1	52.9	50.5	49.5
$\text{Ir}_{0.8}\text{Cu}_{0.2}\text{O}_2$	82.6	17.4	75.3	24.7
$\text{Ir}_{0.5}\text{Cu}_{0.5}\text{O}_2$	51.8	48.2	50.6	49.4

As discussed in more detail in chapter 3,  $\text{IrO}_2$  catalyst prepared through the hydrothermal synthesis, using  $\text{Li}_2\text{CO}_3$  as a base, showed a wider Ir(4f) orbital envelope compared to rutile  $\text{IrO}_2$ , based on previous reports<sup>(4, 15)</sup> where the presence of Ir(IV) and Ir(III) sites was proposed. Moreover, the O(1s) peak was mainly composed of hydroxide, albeit lattice oxide oxygen and water were detected.<sup>(2, 16)</sup>

For prepared mixed oxide samples, the presence of carbonates was detected by XPS, therefore the rest of elements were referenced against the C(1s) peak at 284.8 eV. Moreover, chloride contamination at a concentration in the order of 0.4 at % was detected in all catalysts. The Ni(3p) orbital at 67.3 eV<sup>(17)</sup> overlaps with the Ir(4f<sub>5/2</sub>) orbital at 61.9 eV; in a situation without intermetallic interactions, the Ni(3p) orbital would appear as a shoulder on the Ir(4f) peak, with increasing intensity at higher nickel loading and with the concomitant iridium related peak reduction. However, the Ir(4f) peak shifted and broadened<sup>(6)</sup> for the as prepared  $\text{Ir}_x\text{Ni}_{1-x}\text{O}_2$  samples, unequivocally indicating a perturbation of the iridium chemical environment caused by its interaction with nickel (figure 6.4a). As discussed in chapter 3, the broad Ir(4f) orbital shape indicates the presence of various Ir(III) and Ir(IV) species. As expected, the interaction of nickel with iridium was also reflected on the Ni(2p) orbital (figure

6.4b). From the nickel point of view, the addition of iridium was followed by a Ni(2p) shift towards lower binding energies.

The same Ir(4f) peak fitting used for  $\text{IrO}_x$  in chapter 3 was used to fit the Ir(4f) orbital of  $\text{Ir}_x\text{Ni}_{1-x}\text{O}_2$  catalysts. Hence, no extra peak was included to represent the Ni(3d) contributions. As can be observed in figure 6.4a, the curve fitting overlapped almost perfectly with the recorded peak envelope, indicating the close interaction between iridium and nickel. In a similar way, the Ni(2p) orbital was fitted using peak shapes obtained for NiO and  $\text{Ni}(\text{OH})_2$  standards, without including any peak for representing the Ni-O-Ir contribution. The nickel chemical environment has been unambiguously disturbed by the close proximity of iridium, since the Ni(2p) peak cannot be fitted with only NiO and  $\text{Ni}(\text{OH})_2$  as observed in figure 6.4b.

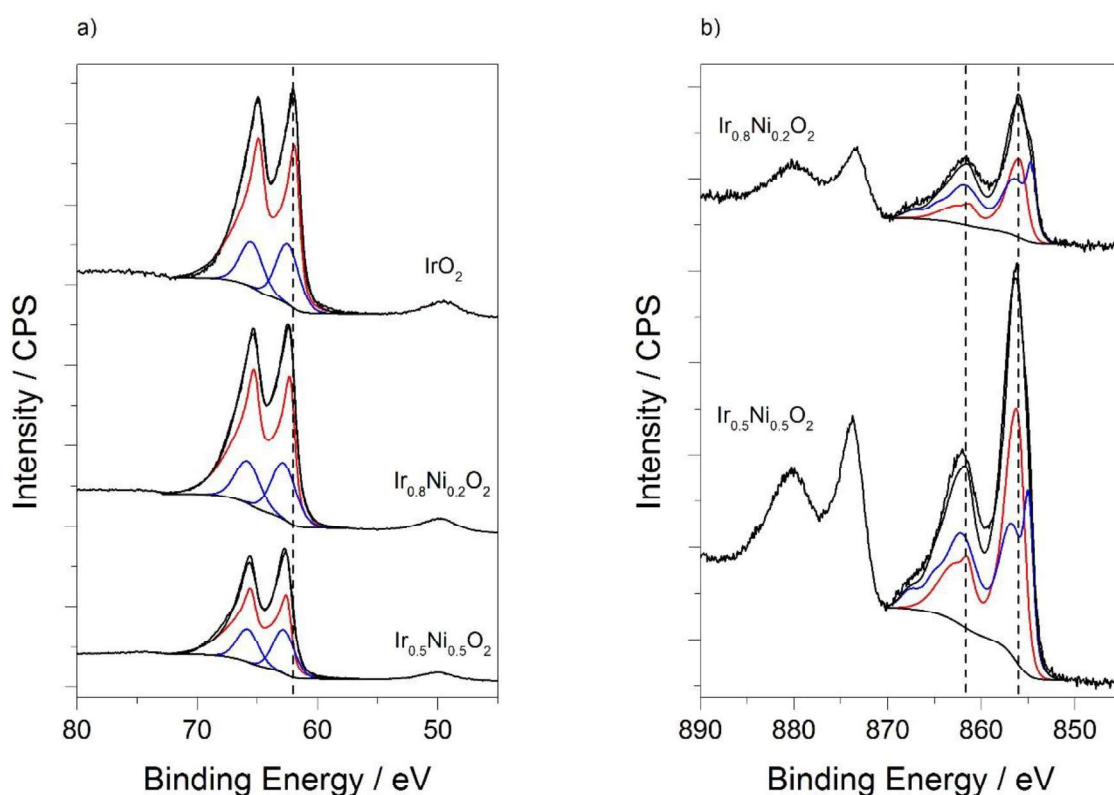


**Figure 6.4.** XPS characterisation for as prepared  $\text{Ir}_x\text{Ni}_{1-x}\text{O}_2$  mixed oxide catalysts. a) Ir(4f) orbital, blue fitting and red fitting approximately correspond to  $\text{IrO}_2$  and  $\text{Ir}(\text{OH})_x$  contributions, b) Ni(2p) orbital, blue and red curve fitting correspond roughly to NiO and  $\text{Ni}(\text{OH})_x$  respectively.

The O(1s) orbital of  $\text{IrO}_2\text{-Li}_2\text{CO}_3$  catalyst presented oxygen contributions related to oxide, hydroxide and water at 530.5 eV, 531.6 eV and 532.9 eV respectively. Reier *et al.*<sup>(6)</sup> reported that oxygen bridging iridium and nickel centres can be observed at 529.2 eV by XPS; in their case, increasing the amount of nickel into the  $\text{Ir}_x\text{Ni}_{1-x}\text{O}_2$  mixed oxide led to the appearance of

a contribution at a lower binding energy than lattice  $\text{IrO}_2$ . The oxygen from  $\text{NiO}$  has been reported at 529.6 eV<sup>(17)</sup> also, it appears at lower binding energy than lattice oxygen from  $\text{IrO}_2$ . Nevertheless, for the as prepared samples no evidence of  $\text{NiO}$  or Ir-O-Ni bridges were observed, conversely, the O(1s) peak shifted towards higher binding energy with increasing nickel content, following the same trend observed on the Ir(4f) and Ni(2p) orbitals. Therefore, the O(1s) peak was fitted using the components employed previously for  $\text{IrO}_2$  samples described in chapter 3: oxide, hydroxide and water, without differentiating between iridium or nickel species. For the  $\text{Ir}_{0.5}\text{Ni}_{0.5}\text{O}_2$  catalyst no evidence of lattice-oxygen from  $\text{IrO}_2$  or  $\text{NiO}$  was detected, suggesting that all the oxygen present at the surface was in the form of hydroxide (figure 6.5).

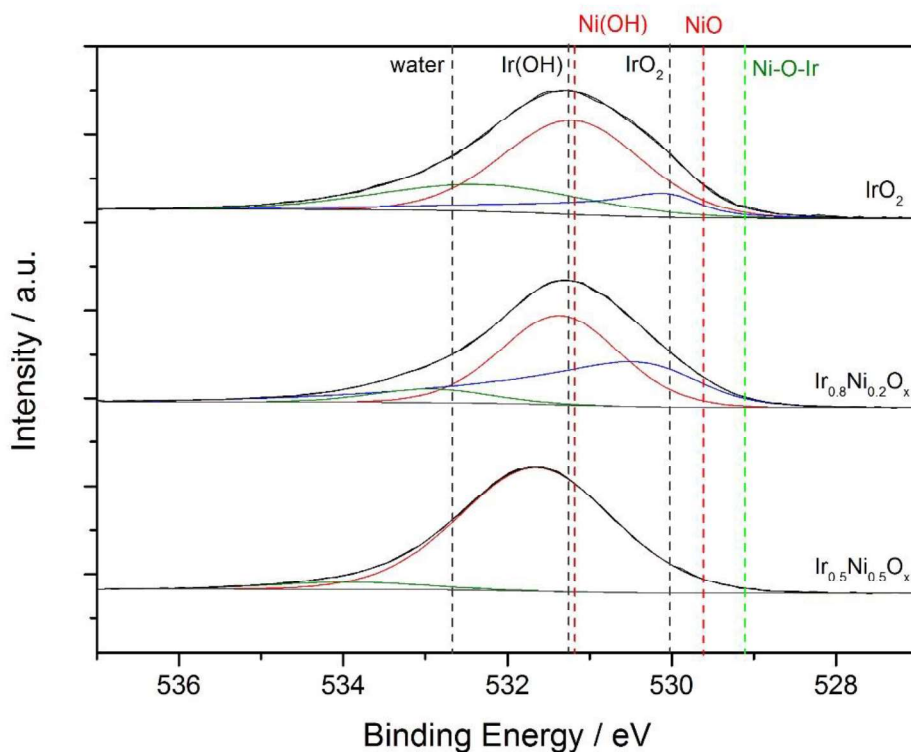


**Figure 6.5.** O(1s) orbital characterisation by XPS for as prepared  $\text{Ir}_x\text{Ni}_{1-x}\text{O}_2$  mixed oxide catalysts.

The iridium nickel interaction remained after annealing in air at 500 °C for 3 h, as observed in the Ir(4f) (figure 6.6a) and Ni(2p) orbitals; both orbitals shifted towards higher binding energy with increasing the amount of nickel into the mixed oxide catalyst. The Ir(4f) peak sharpened and shifted towards lower binding energy after annealing, indicating the presence of mainly lattice Ir(IV) centres and assigned to the formation of rutile  $\text{IrO}_2$ . The absence of a distinct shoulder peak at 67.3 eV, associated with the formation of  $\text{NiO}$ , indicated that no phase segregation occurred in accordance with the XPS elemental quantification. Moreover,

the Ir(4f) orbital envelope broadened with increasing nickel loading in the  $\text{Ir}_x\text{Ni}_{1-x}\text{O}_2$  mixed oxide catalyst as a result of iridium-nickel interaction. As expected, after annealing at 500 °C, the O(1s) peak shifted to 530 eV, corresponding to the presence of lattice oxygen (figure 6.6b). The oxygen bridge between iridium and nickel atoms have been reported at 529.2 eV, however, this value falls really close to NiO and  $\text{IrO}_2$  at 529.6 eV and 530.5 eV respectively. Therefore, a distinct peak for  $\text{IrO}_2$ , NiO and Ir-O-Ni bridge could not be assigned in the fitting, thus the peak at 530.1 eV represents an agglomeration of oxygen oxide species ( $\text{IrO}_2$ , NiO and Ir-O-Ni). In line, a shoulder at 531.5 eV on the O(1s) was observed; its position was between the values reported for  $\text{Ir}(\text{OH})$  and  $\text{Ni}(\text{OH})$  at 531.6 eV and 531.2 eV, hence this peak was associated to hydroxide species in the material.

Although simplified peak fitting was used, with one peak for oxide species and another for hydroxides, reliable comparison between samples can be carried out. It can be observed that increasing the proportion of nickel in the mixed oxide leads to an increase in the hydroxide proportion, compared to the oxide, from 31 % for  $\text{IrO}_x$  to 45 % and 57 % for  $\text{Ir}_{0.8}\text{Ni}_{0.2}\text{O}_2$  and  $\text{Ir}_{0.5}\text{Ni}_{0.5}\text{O}_2$  respectively.

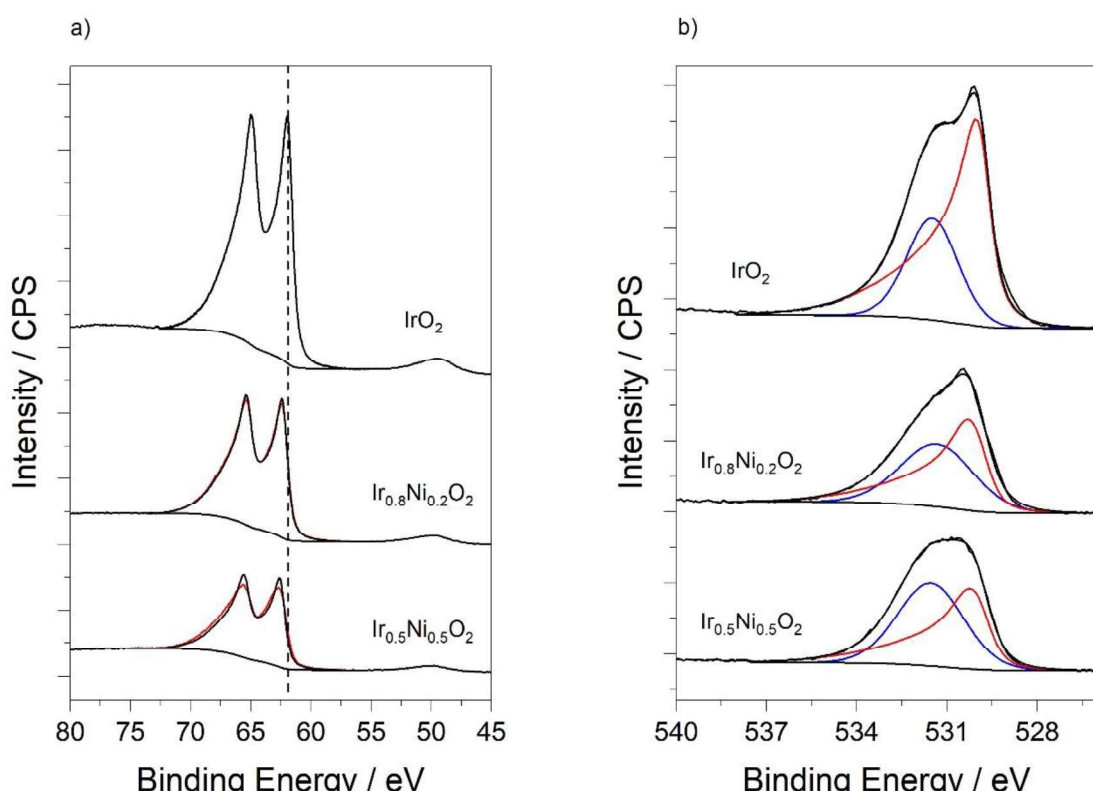


**Figure 6.6.** a) Ir(4f) and b) O(1s) orbital for  $\text{Ir}_x\text{Ni}_{1-x}\text{O}_2$  mixed oxide catalysts synthesised by the hydrothermal method followed by annealing in static air at 500 °C for 3 h. Red fitting in Ir(4f) and O(1s) represents the peak shape obtained for  $\text{IrO}_2$ , blue fitting in O(1s) represents hydroxide contributions.

Likewise, the interaction between iridium and copper was observed for fresh  $\text{Ir}_x\text{Cu}_{1-x}\text{O}_2$  mixed oxide catalysts in the Ir(4f) peak (figure 6.7a). Increasing the amount of copper in the  $\text{IrO}_2$  lattice resulted in a shift in the Ir(4f) orbital towards higher binding energy. Contrary to what was observed for  $\text{Ir}_x\text{Ni}_{1-x}\text{O}_2$  catalysts, the Cu(3p) orbital at 77.7 eV does not overlap with the Ir(4f) orbital. Therefore, the observed shift could be only associated with the change in the chemical environment of iridium, induced by the introduction of copper into the lattice.<sup>(18)</sup> As prepared samples suggested the presence of multiple iridium species, as indicated by the similar fitting compared to fresh  $\text{IrO}_2\text{-Li}_2\text{CO}_3$  catalyst. After annealing at 500 °C, it was observed by XPS quantification that an increase in the copper proportion in the  $\text{Ir}_{0.8}\text{Cu}_{0.2}\text{O}_2$  catalyst indicates copper migration towards the surface. This translated into phase segregation, and the loss of the Ir-Cu intermetallic interaction, as observed by the Ir(4f) peak at 61.9 eV (figure 6.7b). As expected, the Ir(4f) orbital sharpened after the heat treatment corresponding to the presence of crystalline rutile  $\text{IrO}_2$ .

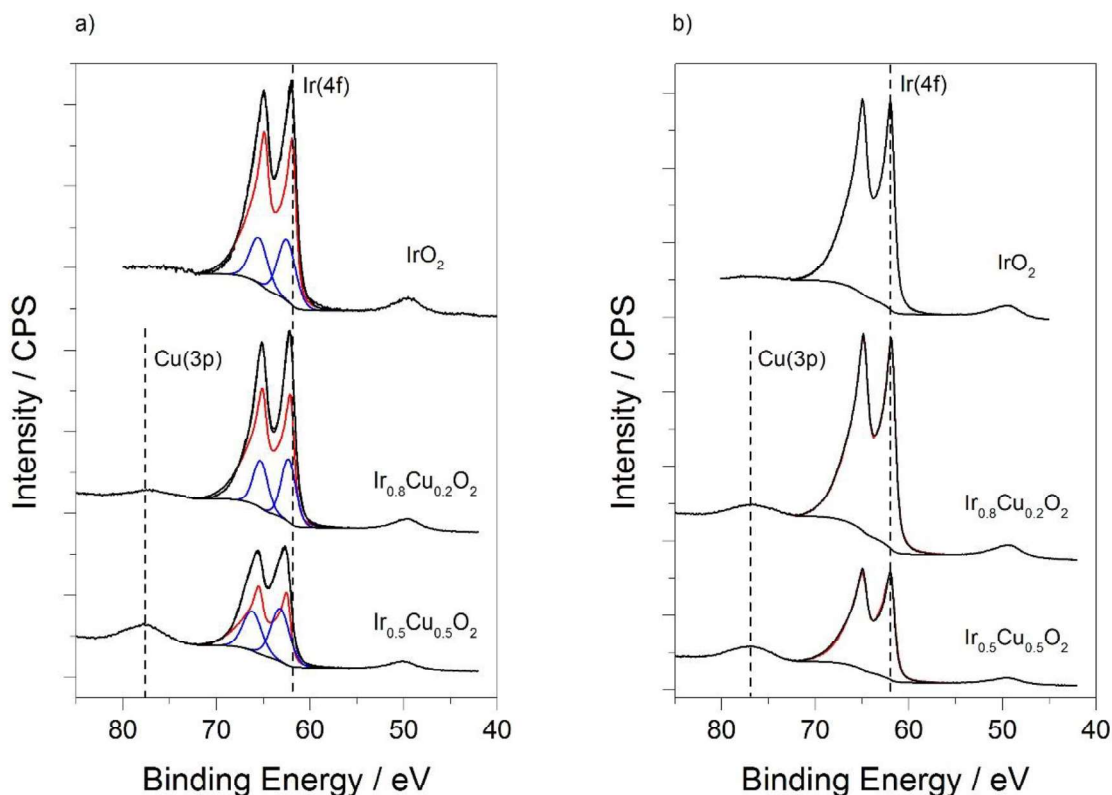


**Figure 6.7.** Ir(4f) orbital analysed by XPS a) as prepared and b) annealing in static air at 500 °C for 3h for  $\text{Ir}_x\text{Cu}_{1-x}\text{O}_2$  mixed oxide catalysts prepared through the hydrothermal synthesis.

The Cu(LM<sub>2</sub>) orbital for as prepared  $\text{Ir}_{0.8}\text{Cu}_{0.2}\text{O}_2$  and  $\text{Ir}_{0.5}\text{Cu}_{0.5}\text{O}_2$  shifted from a kinetic energy of 916.6 eV to 917.8 eV after annealing in air at 500 °C, indicating its oxidation to CuO (figure 6.8a). The Cu(2p) peak position for as prepared catalysts at 934.4 eV suggested that

$\text{Cu}(\text{OH})_2$  was the main form on the fresh catalysts<sup>(17)</sup> and that heat treatment induced the loss of surface hydroxide to form the  $\text{CuO}$ .

Some reports have assigned the presence of oxygen bridging between iridium and copper atoms in the O(1s) peak to a contribution at 529.5 eV;<sup>(18)</sup> however, due to the close presence of the  $\text{CuO}$ ,  $\text{CuO}_2$  and  $\text{IrO}_2$  assigned at 529.6 eV, 530.5 eV and 530.5 eV respectively, its detection was not conclusive. The O(1s) for as prepared  $\text{Ir}_x\text{Cu}_{1-x}\text{O}_2$  catalysts could be fitted with two peaks, following the same reasoning used for  $\text{Ir}_x\text{Ni}_{1-x}\text{O}_2$  mixed oxide catalysts, one peak assigned to lattice oxygen ( $\text{IrO}_2$ ,  $\text{CuO}_x$  and Ir-O-Cu) at approximately 530 eV and a second peak at 531.3 eV assigned to hydroxides (figure 6.8b). After annealing, the peak associated with hydroxides disappeared, indicating the presence of only lattice oxide oxygen.

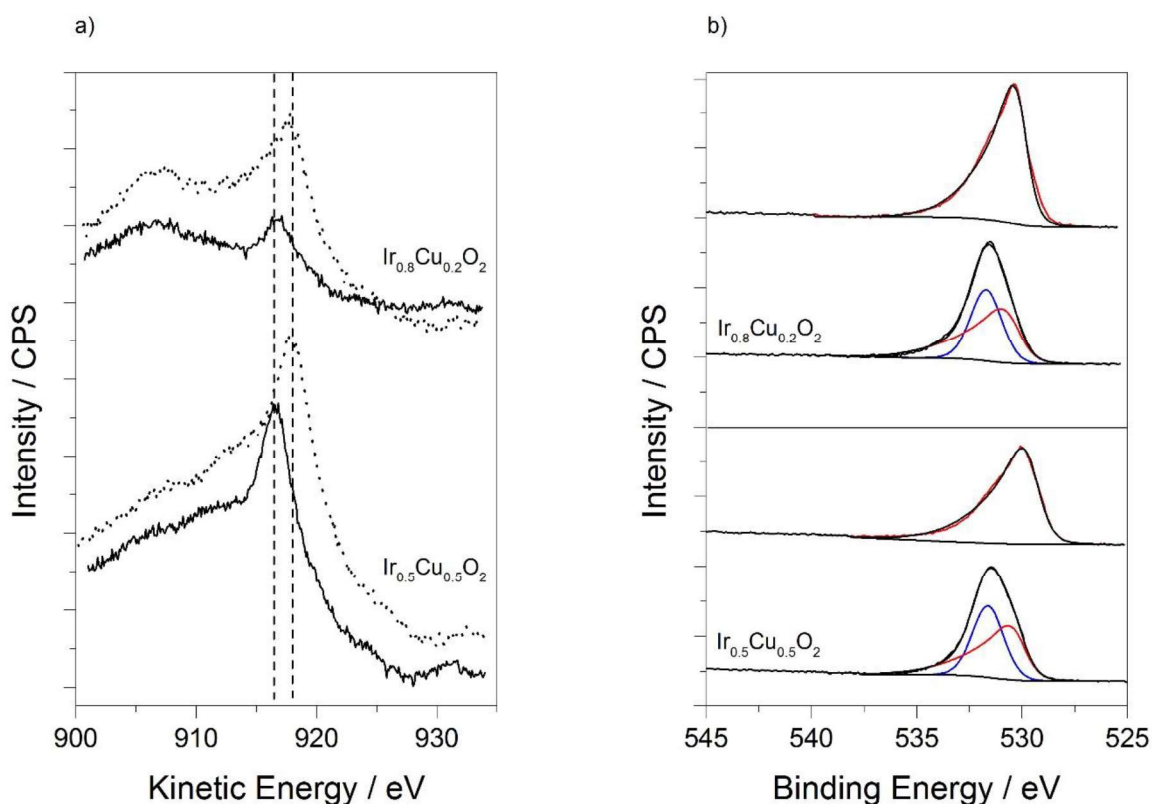


**Figure 6.8.** a)  $\text{Cu}(\text{LM}_2)$  orbital analysed by XPS for  $\text{Ir}_x\text{Cu}_{1-x}\text{O}_2$  mixed oxide catalysts. Solid line represents fresh materials and dotted lines represent annealed in air at 500 °C for h materials. b) O(1s) orbital analysed by XPS for  $\text{Ir}_x\text{Cu}_{1-x}\text{O}_2$  mixed oxide catalysts. The annealed catalyst is placed above its respective fresh counterpart. Oxide and hydroxide contributions are represented in red and blue respectively.

### 6.2.3 Catalytic performance towards OER.

In order to determine the effect of doping  $\text{IrO}_2$  with Ni or Cu, the prepared mixed oxide catalysts were tested towards OER in a conventional three electrode system. Catalyst ink was drop casted in a glassy carbon electrode to obtain a  $100 \mu\text{g}_{\text{cat}} \cdot \text{cm}^{-2}$ , a platinum wire and a calomel electrode [ $\text{Cl}^-/\text{Hg}_2\text{Cl}_2/\text{Hg}/\text{Pt}$ ] were used as the counter electrode and reference electrode respectively. Reactions were undertaken in  $\text{HClO}_4$  0.1 M electrolyte solution. The preparation of the catalyst ink has been discussed in detail previously in chapter 2.

In order to assess the activity and stability of the catalysts the following protocol, which comprised LSV (1.2  $V_{\text{RHE}}$  to 1.8  $V_{\text{RHE}}$  at  $5 \text{ mV} \cdot \text{s}^{-1}$ ), CV (50 CV cycles between 0.7  $V_{\text{RHE}}$  and 1.4  $V_{\text{RHE}}$  at  $50 \text{ mV} \cdot \text{s}^{-1}$ ) and CP (2 hours at  $10 \text{ mA} \cdot \text{cm}^{-2}$ ) measurements, was used: LSV, CV, LSV, CP, LSV and CV.

The intrinsic activity of the materials was determined by measuring a LSV at the start of the experiment. Possible deactivation, as a consequence of CV or CP test, was measured by subsequent LSV measurements. The instability of the catalysts can be observed by the increase in the potential during the CP experiment or by the current density decline by LSV after the CV and the CP measurements. Presented results were IR corrected and were not normalised against the iridium mass or iridium surface area but to the working electrode surface area. For instance, when comparing  $\text{IrO}_2$  and  $\text{Ir}_{0.5}\text{Ni}_{0.5}\text{O}_2$  the concentration on the electrode was kept at  $100 \mu\text{g}_{\text{cat}} \cdot \text{cm}^{-2}$ .

The main issue when testing the  $\text{Ir}_x\text{M}_{1-x}\text{O}_2$  mixed oxide catalysts was the preparation of the catalysts ink, as indicated by the SEM characterisation (image 6.1), agglomeration occurred after the addition of the dopant element. Catalysts needed to be thoroughly ground before re-dispersion. Despite grinding, as prepared and annealed  $\text{Ir}_{0.5}\text{Cu}_{0.5}\text{O}_2$  and annealed  $\text{Ir}_{0.2}\text{Cu}_{0.8}\text{O}_2$  catalysts were unable to be tested due to a lack of re-dispersion during the preparation of the catalyst ink. Mixed oxide catalysts were compared to  $\text{IrO}_2\text{-Li}_2\text{CO}_3$  described previously in chapter 3; it is used as standard since its activity and stability outperformed the commercial  $\text{IrO}_2\text{:2H}_2\text{O}$  from Alfa Aesar, note that no grinding was necessary prior to testing on  $\text{IrO}_2\text{-Li}_2\text{CO}_3$  due to its lower agglomeration compared to the mixed oxide catalysts.

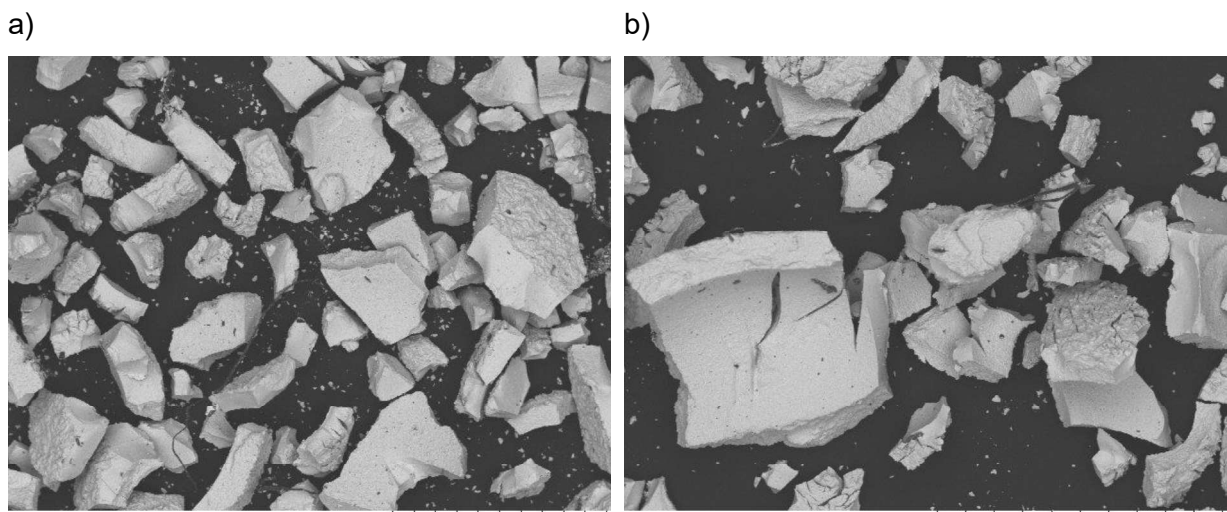


**Image 6.1.** SEM for as prepared mixed oxide catalysts synthesised through the hydrothermal process. a)  $\text{Ir}_{0.8}\text{Ni}_{0.2}\text{O}_2$  and b)  $\text{Ir}_{0.8}\text{Cu}_{0.2}\text{O}_2$ . Scale bar corresponds to 1 mm.

As observed for as prepared  $\text{Ir}_x\text{Ni}_{1-x}\text{O}_2$  catalysts in figure 6.9, the intrinsic activity measured by LSV at the start of the experiment considerably declined with the addition of nickel into the material. Heat treatment at 500 °C led to  $\text{Ir}_x\text{Ni}_{1-x}\text{O}_2$  catalysts deactivation, as observed by the poor current density in the initial LSV experiment. Iridium and nickel were thought to be homogeneously distributed, as suggested by the XRD and XPS characterisation, hence, in the  $\text{Ir}_{0.8}\text{Ni}_{0.2}\text{O}_2$  catalyst it would be expected that approximately the 20 % of surface metallic atoms would correspond to nickel and 80 % to iridium. A study conducted by Reier *et al.*<sup>(6)</sup> on the stability of IrNi mixed oxide catalysts concluded that surface nickel was not stable against dissolution during the OER reaction, and albeit the activity of  $\text{IrO}_2$  increased due to a higher Ir surface area, the iridium dissolution increased at a higher rate than the catalytic activity. The higher activity, normalised to the iridium surface area in mixed oxide catalysts, was assigned to Ir-Ni interactions in the sub-surface layer, which produced a lattice constrain, and to the formation of surface hydroxide groups as a results of nickel leaching.

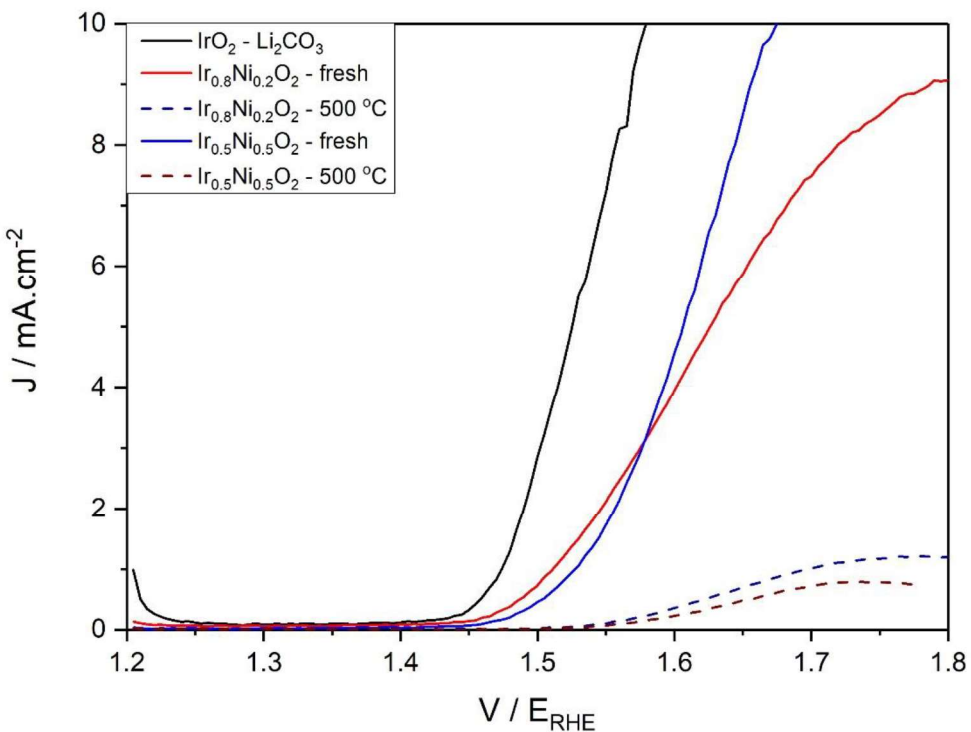


**Figure 6.9.** Intrinsic activity of  $\text{Ir}_x\text{Ni}_{1-x}\text{O}_2$  mixed oxide catalysts determined by LSV.

Chemical information can be obtained from the shape and the area under the curve of a CV. Therefore, after the initial LSV to determine the intrinsic activity of the  $\text{Ir}_x\text{Ni}_{1-x}\text{O}_2$  materials, a CV measurement was performed (figure 6.10a). On one hand, characteristic redox pair chemical transitions would indicate the presence of certain species. For instance, the  $\text{Ir}(\text{III})/\text{Ir}(\text{IV})$  and the  $\text{Ir}(\text{IV})/\text{Ir}(\text{V})$  redox pair have been reported at  $0.9 \text{ V}_{\text{RHE}}$  and  $1.2 \text{ V}_{\text{RHE}}$  respectively.<sup>(19, 20)</sup> On the other hand, the current density associated with each transition is indicative of the number of active sites being involved in the reaction. The higher the area under a CV curve the higher the active site concentration on a catalyst. As illustrated in figure 6.11a for fresh samples, the  $\text{IrO}_2\text{-Li}_2\text{CO}_3$  CV area was quantitatively larger than that of  $\text{Ir}_x\text{Ni}_{1-x}\text{O}_2$  catalysts. It is known that nickel oxide is not active towards OER in acid conditions and a progressive reduction of the CV area would be expected as the amount of iridium on the catalysts surface was reduced. Nevertheless,  $\text{Ir}_{0.8}\text{Ni}_{0.2}\text{O}_2$  and  $\text{Ir}_{0.5}\text{Ni}_{0.5}\text{O}_2$  catalysts presented comparable CV areas, indicating that the introduction of small amounts of nickel considerably reduced the concentration of active sites and hampered the redox properties of iridium. Regarding to the shape observed on the CV, a broad band at  $0.94 \text{ V}_{\text{RHE}}$  related to the  $\text{Ir}(\text{III})/\text{Ir}(\text{IV})$  transition pair was observed. The presence of  $\text{Ir}(\text{III})$  and  $\text{Ir}(\text{IV})$  sites have been widely associated with active amorphous iridium oxo-hydroxide catalysts.<sup>(15)</sup> The  $\text{Ir}(\text{III})/\text{Ir}(\text{IV})$

transition could not be clearly observed for the fresh Ni-doped  $\text{Ir}_x\text{Ni}_{1-x}\text{O}_2$  materials. The CV area further reduced after annealing and no distinct electronic transitions were observed indicating that only Ir(IV) was present.

Catalysts stability was determined by CP, monitoring the necessary potential to maintain a constant current density at  $10 \text{ mA}\cdot\text{cm}^{-2}$  for 2 h. Steady potential during the CP test, as observed in the case of  $\text{IrO}_2\text{-Li}_2\text{CO}_3$  catalyst, indicated a stable material towards OER. However, the addition of nickel into the mixed oxide catalysts resulted in severe corrosion, as observed by the increase in the potential during the CP experiment (figure 6.10b). As expected from the low activity observed by LSV, and the small CV area for the  $\text{Ir}_x\text{Ni}_{1-x}\text{O}_2$  catalysts after annealing, the potential observed during the CP corresponded to the glassy carbon corrosion, indicating that the material was not involved in the reaction.

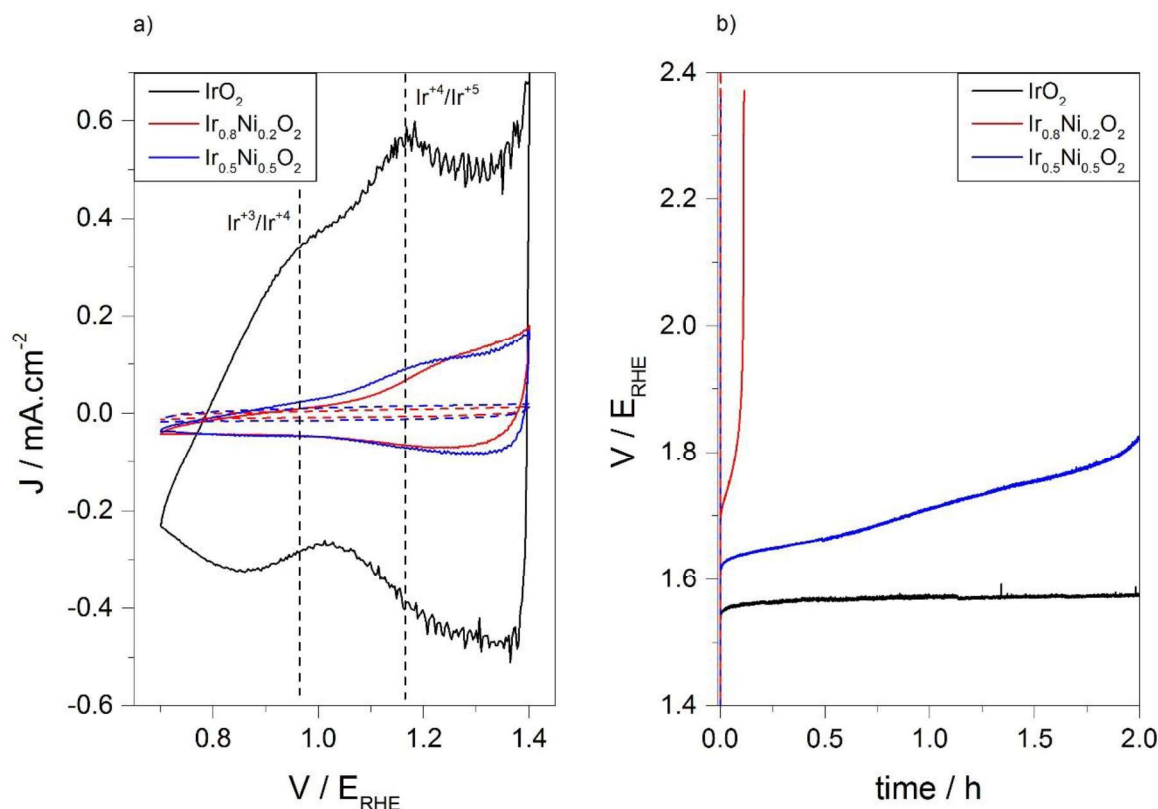


**Figure 6.10.** a) CV ( $0.7 \text{ E}_{\text{RHE}} 1.4 \text{ E}_{\text{RHE}}$  at  $50 \text{ mV}\cdot\text{s}^{-1}$ ) and b) CP ( $10 \text{ mA}\cdot\text{cm}^{-2}$  for 2 h) for  $\text{Ir}_x\text{Ni}_{1-x}\text{O}_2$  mixed oxide catalysts prepared through the hydrothermal synthesis. Solid lines represent fresh catalysts while dashed lines correspond to catalyst after annealing in static air at  $500 \text{ }^{\circ}\text{C}$  for 3 h. The catalyst loading on the electrode was  $100 \text{ }\mu\text{g}_{\text{cat}}\cdot\text{cm}^{-2}$ .

In the case of catalysts doped with copper, a similar behaviour to  $\text{Ir}_x\text{Ni}_{1-x}\text{O}_2$  catalysts was observed. The fresh  $\text{Ir}_{0.8}\text{Cu}_{0.2}\text{O}_2$  catalyst presented lower intrinsic activity compared to  $\text{IrO}_2$ -

$\text{Li}_2\text{CO}_3$ , as illustrated by the LSV taken at the start of the experiment (figure 6.11). The homogeneous distribution of the mixed oxide catalysts, suggested by elemental XPS quantification, indicated that approximately 20 % of surface atoms corresponded to inactive and unstable Cu atoms. The overpotential measured by LSV at  $5 \text{ mA}\cdot\text{cm}^{-2}$  increased after the CV and after the CP by 35 mV and 206 mV respectively, indicating that deactivation occurred during those measurements. Contrary to what was observed for the stable  $\text{IrO}_2\text{-Li}_2\text{CO}_3$  catalyst, in which the LSV potential recorded at the beginning of the experiment and after the CP test increased by only 7 mV.

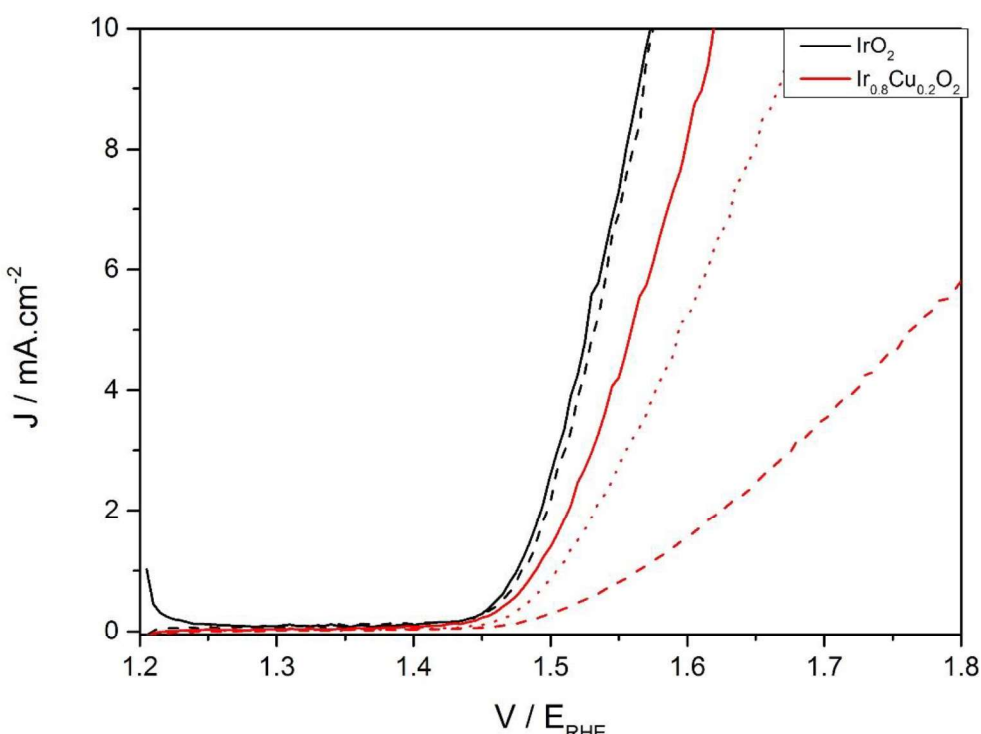


**Figure 6.11.** LSV measurements for as prepared  $\text{Ir}_{0.8}\text{Cu}_{0.2}\text{O}_2$  mixed oxide catalyst and compared to  $\text{IrO}_2\text{-Li}_2\text{CO}_3$ . Solid line represents the intrinsic activity of the catalysts determined by the LSV measurement recorded at the start of the experiment. Dotted and dashed lines correspond to the LSV measurements after the CV and CP test respectively, and its shift compared to the LSV for as prepared samples is indicative of catalyst degradation.

Moreover, the deactivation of the  $\text{Ir}_{0.8}\text{Cu}_{0.2}\text{O}_2$  catalyst was evidenced by the steady increase in the measured potential during the CP stability test (figure 6.12b). Chemical changes during the CP test were observed by CV measurements recorded before and after the stability test (figure 6.12a). The addition of Cu into the  $\text{IrO}_2$  lattice resulted in a decrease in the CV area, indicating the lower concentration of active sites. Apart from the rise in the

monitored potential during the CP, and the shift towards higher overpotential on the LSV, the deactivation of a catalyst could be followed by the area and shape change in the CV. As observed,  $\text{IrO}_2\text{-Li}_2\text{CO}_3$  catalysts presented a steady potential during the CP at  $10 \text{ mA}\cdot\text{cm}^{-2}$ , indicating that it was stable under OER reaction conditions for at least 2 hours. No considerable differences in the CV before and after the CP stability test were detected. However, the broad transition associated to  $\text{Ir}(\text{III})/\text{Ir}(\text{IV})$  and the clear  $\text{Ir}(\text{IV})/\text{Ir}(\text{V})$  reduction pair at  $0.9 \text{ V}_{\text{RHE}}$  and  $1.22 \text{ V}_{\text{RHE}}$  respectively, in the  $\text{Ir}_{0.8}\text{Cu}_{0.2}\text{O}_2$  catalyst significantly decreased in intensity after the CP stress test, thus, indicating the loss of active sites during OER. As mentioned, the  $\text{Ir}_{0.8}\text{Cu}_{0.2}\text{O}_2$  annealed at  $500 \text{ }^\circ\text{C}$  and the  $\text{Ir}_{0.5}\text{Cu}_{0.5}\text{O}_2$  catalysts were not tested due to not being possible to prepare the catalyst ink. Nevertheless, most probably due to the homogeneous distribution of the mixed oxide catalysts, the  $\text{Ir}_{0.5}\text{Cu}_{0.5}\text{O}_2$  catalyst was expected to present poor catalytic activity and stability towards OER as a consequence of having a high concentration of Cu atoms at the surface. Moreover, phase segregation was observed after annealing in air at  $500 \text{ }^\circ\text{C}$ , with copper migration towards the surface of the catalysts. Therefore, poor performance was expected for annealed  $\text{Ir}_x\text{Cu}_{1-x}\text{O}_2$  materials.

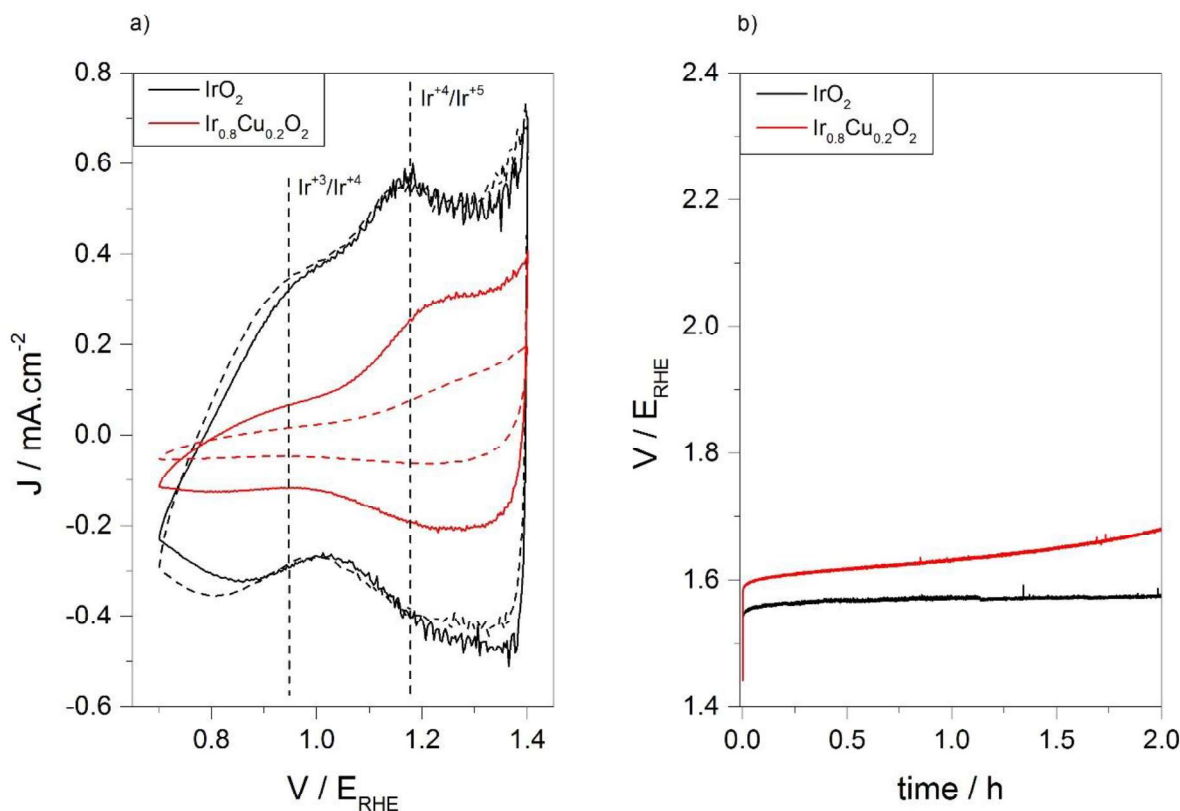


**Figure 6.12.** a) CV test measured before (solid line) and after (dashed line) the stability test, b) chronopotentiometry ( $10 \text{ mA}\cdot\text{cm}^{-2}$  for 2 h) for  $\text{Ir}_{0.8}\text{Cu}_{0.2}\text{O}_2$  prepared through the hydrothermal synthesis.

Diverse  $\text{Ir}_x\text{M}_{1-x}\text{O}_2$  mixed oxide catalysts were prepared through hydrothermal synthesis. From XRD and XPS characterisation the metallic distribution through the materials was thought to be homogeneous. The shift in the Ir(4f) orbital for as prepared materials towards higher binding energy indicated intermetallic interactions between the iridium and the non-noble metal. However, a decrease in activity and stability was detected for all tested mixed oxide catalysts compared to  $\text{IrO}_2$ . It is widely accepted that Ni and Cu are not active towards OER or stable against its dissolution during the reaction conditions in acid media. Therefore, the homogeneous distribution of iridium and the non-noble metal at the surface it is believed to be the cause of the lower performance. In order to overcome this strain, the formation of a protective  $\text{IrO}_2$  layer is desired.

### **6.3 Core-shell IrNi and IrCu mixed oxide catalysts.**

The non-noble metal used to dilute the  $\text{IrO}_2$  is not active towards OER or stable against dissolution during the harsh reaction conditions. Hence, only small quantities of doping have proved effective in enhancing the  $\text{IrO}_2$  activity without compromising its stability in homogenously dispersed catalysts.<sup>(6, 18, 21)</sup> The objective of the following section is to develop core-shell materials, concentrating iridium at the surface and using a cheaper material in the core, in order to employ iridium more efficiently, reducing its loading on the electrode.

In order to probe the efficiency of the core-shell structure on considerably reducing the amount of precious metal in the catalysts, equimolar  $\text{Ir}_{0.5}\text{Ni}_{0.5}\text{O}_2$  and  $\text{Ir}_{0.5}\text{Cu}_{0.5}\text{O}_2$  core-shell catalysts were prepared.

#### **6.3.1 Core-shell catalysts preparation.**

Previous groups have published the synthesis of core-shell structures with a mixture of Ir-Ni at the core and a protective and active layer of  $\text{IrO}_2$  at the shell.<sup>(8, 9, 22)</sup> Normally, a metallic IrNi alloy was first formed and the nickel present at the surface was leached, leaving behind an outer layer of  $\text{IrO}_2$ . Although it was an effective approach for forming an  $\text{IrO}_2$ -shell, iridium utilisation was not optimised, since non accessible iridium remained inside the bulk of the material. In order to concentrate  $\text{IrO}_2$  just at the shell, a modification of the hydrothermal preparation proposed by Reetz and Feigel<sup>(23)</sup> was followed. For the synthesis of  $\text{Ir}_{0.5}\text{Ni}_{0.5}\text{O}_2$  and  $\text{Ir}_{0.5}\text{Cu}_{0.5}\text{O}_2$  core-shell catalysts, two different solutions were prepared in two separate 50 ml bottom flasks. The first solution contained  $\text{IrCl}_3$  and  $\text{Li}_2\text{CO}_3$  in 10 ml of deionised water, it was stirred at room temperature for 16 h in order to convert the  $\text{IrCl}_3$  to  $\text{Ir}(\text{OH})_6^{2-3-}$ .<sup>(24)</sup> The second solution consisted of  $\text{NiCl}_3$  (or  $\text{CuCl}_2$ ),  $\text{LiOH}$  and 10 ml of deionised water, it was stirred at room temperature for 16 h in order to obtain a  $\text{NiO}_x$  (or  $\text{CuO}_x$ ) colloid solution.<sup>(25)</sup> No

precipitate was observed for any of the prepared solutions after 16 h of stirring at room temperature. The  $\text{NiO}_x$  (or  $\text{CuO}_x$ ) colloid solution was heated to 95 °C and stirred for 30 min to form a colloidal dispersion. Then, the  $\text{Ir(OH)}_6^{2-3-}$  solution was added dropwise into the 95 °C  $\text{NiO}_x$  (or  $\text{CuO}_x$ ) solution. The mixture was then heated to reflux for 90 min. A black precipitate formed which was recovered by filtration, washed with 2 L of deionised water and dried in a fumehood overnight. In order to differentiate the core shell structure with the homogeneous dispersion, the new prepared catalysts were named as  $\text{Ir}_{0.5}\text{M}_{0.5}\text{O}_2\text{-CS}$  ( $\text{M} = \text{Ni}$  or  $\text{Cu}$ ).

### **6.3.2 Catalysts Characterisation.**

As prepared homogeneously dispersed  $\text{Ir}_{0.5}\text{Ni}_{0.5}\text{O}_2$  and  $\text{Ir}_{0.5}\text{Cu}_{0.5}\text{O}_2$  catalysts had amorphous structure as suggested by XPS quantification. By XRD no nickel oxide, copper oxide or  $\text{IrO}_2$  crystalline phases were observed, after annealing at 500 °C,  $\text{IrO}_2$  rutile reflections were observed without evidence of phase segregation.

For the preparation of core-shell structures, the  $\text{NiO}_x$  and  $\text{CuO}_x$  colloid core was synthesised beforehand and used as scaffold for growing the  $\text{IrO}_2$  shell. On as prepared  $\text{Ir}_{0.5}\text{Ni}_{0.5}\text{O}_2\text{-CS}$  and  $\text{Ir}_{0.5}\text{Cu}_{0.5}\text{O}_2\text{-CS}$  catalysts the presence of  $\text{Ni(OH)}_2$  (JCPDS 014-0117) and  $\text{CuO}$  (JCPDS 001-1117) crystalline phases were detected by XRD at 18.8°, 33.5° and 38.7° or 35.7° and 38.9° respectively, confirming the successful synthesis of the non-noble metal core. After annealing in air at 500 °C for 3 h, additionally to the  $\text{NiO}$  (JCPDS 004-0835) and  $\text{CuO}$  core-related reflections, rutile  $\text{IrO}_2$  was detected by XRD (figure 6.13).

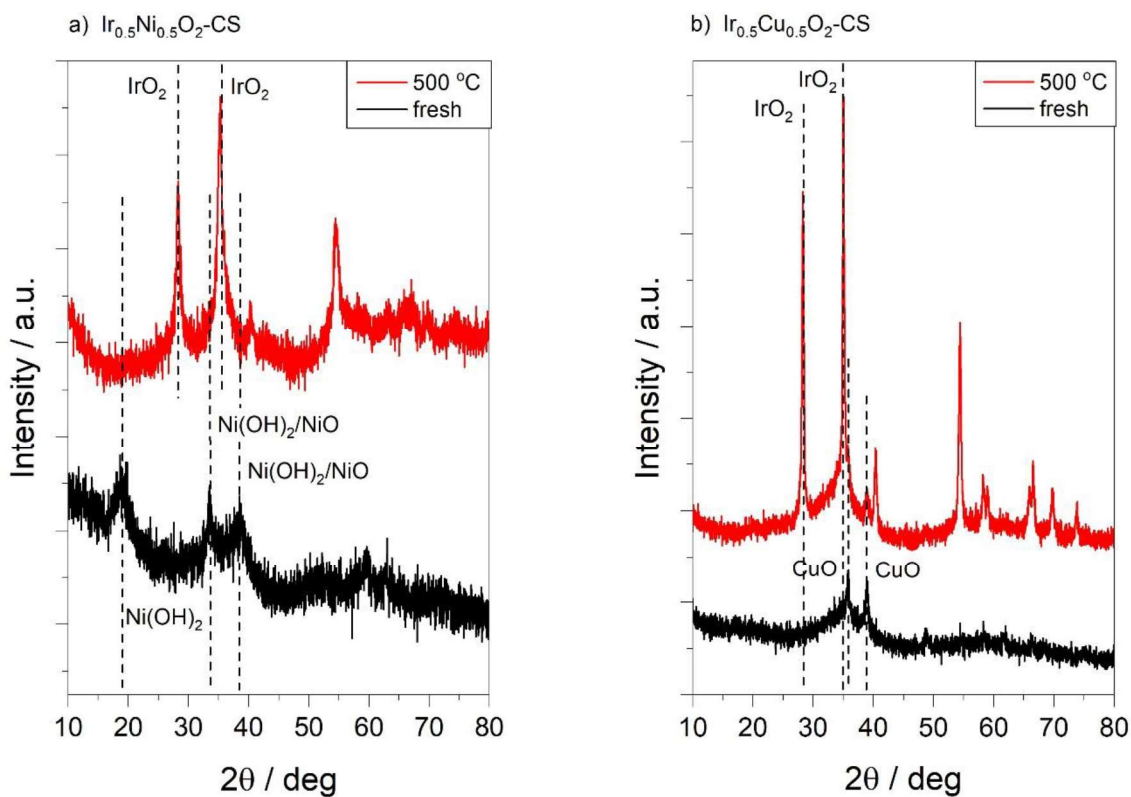


**Figure 6.13.** XRD pattern for as prepared and annealed at  $500^\circ\text{C}$  core shell a)  $\text{Ir}_{0.5}\text{Ni}_{0.5}\text{O}_2\text{-CS}$  and b)  $\text{Ir}_{0.5}\text{Cu}_{0.5}\text{O}_2\text{-CS}$  catalysts.

In homogeneously dispersed  $\text{Ir}_x\text{M}_{1-x}\text{O}_2$  ( $\text{M} = \text{Ni}, \text{Cu}$ ) mixed oxide catalysts, the  $\text{Ir}(4f)$  orbital shifted towards higher binding energy as a results of the close interaction with the dopant. Moreover, in the case of Ni-doped catalysts, the  $\text{Ni}(3p)$  orbital, which overlaps with the  $\text{Ir}(4f)$ , was not observed as a distinct shoulder-peak indicating a homogenous distribution of both metals within the material.

Conversely, and in accordance with XRD characterisation, for  $\text{Ir}_{0.5}\text{Ni}_{0.5}\text{O}_2\text{-CS}$  and  $\text{Ir}_{0.5}\text{Cu}_{0.5}\text{O}_2\text{-CS}$  catalysts, the XPS quantification suggested the formation of a core-shell structure (table 6.2), as indicated by the higher iridium concentration compared to the nominal value. Because XPS is a surface sensitive technique, the higher concentration of iridium compared to Ni or Cu indicates that it is concentrated at the surface of the material, hence, forming a shell.

After annealing at  $500^\circ\text{C}$ , the non-noble metal migrated from the core towards the surface as indicated by the increase in the concentration of Ni or Cu by XPS quantification. On  $\text{Ir}_{0.5}\text{Ni}_{0.5}\text{O}_2\text{-CS}$  and  $\text{Ir}_{0.5}\text{Cu}_{0.5}\text{O}_2\text{-CS}$  catalysts the iridium elemental quantification reduced from 60 % and 70 % respectively to 53 %, close to the nominal value.

**Table 1.2.** Elemental XPS quantification for core-shell  $\text{Ir}_{0.5}\text{Ni}_{0.5}\text{O}_2\text{-CS}$  and  $\text{Ir}_{0.5}\text{Cu}_{0.5}\text{O}_2\text{-CS}$  catalysts. The Ni(2p), Cu(2p) and Ir(4f) were used for quantification

Catalyst	Fresh		500 °C / air	
	Ir %	Ni / Cu %	Ir %	Ni / Cu %
$\text{Ir}_{0.5}\text{Ni}_{0.5}\text{O}_2\text{-CS}$	60.1	39.9	46.7	53.3
$\text{Ir}_{0.5}\text{Cu}_{0.5}\text{O}_2\text{-CS}$	70.0	30.0	46.9	53.1

As a consequence of  $\text{IrO}_x$  being in the outerlayer, and  $\text{NiO}_x$  or  $\text{CuO}_x$  in the core, no electronic perturbation on the Ir(4f) orbital was observed, indicating the absence of intermetallic interactions. The Ir(4f) orbital for  $\text{Ir}_{0.5}\text{Ni}_{0.5}\text{O}_2\text{-CS}$  and  $\text{Ir}_{0.5}\text{Cu}_{0.5}\text{O}_2\text{-CS}$  mixed oxide catalysts was centred at 61.9 eV

In the  $\text{Ir}_{0.5}\text{Ni}_{0.5}\text{O}_2\text{-CS}$  catalyst, a distinct shoulder at 67.3 eV, related to Ni(3p), was observed on the Ir(4f) orbital (figure 6.14), emphasising the lack of interaction between metal centres. After annealing at 500 °C for 3 h in air, the Ir(4f) orbital sharpened and shifted towards lower binding energy indicating the formation of rutile- $\text{IrO}_2$ . A low intense shoulder related with the presence of NiO was observed at 67.3 eV. Although the nickel migrated towards the surface after annealing, as observed by XPS quantification, no significant shift in the Ir(4f) peak was observed, suggesting no intermetallic interactions.

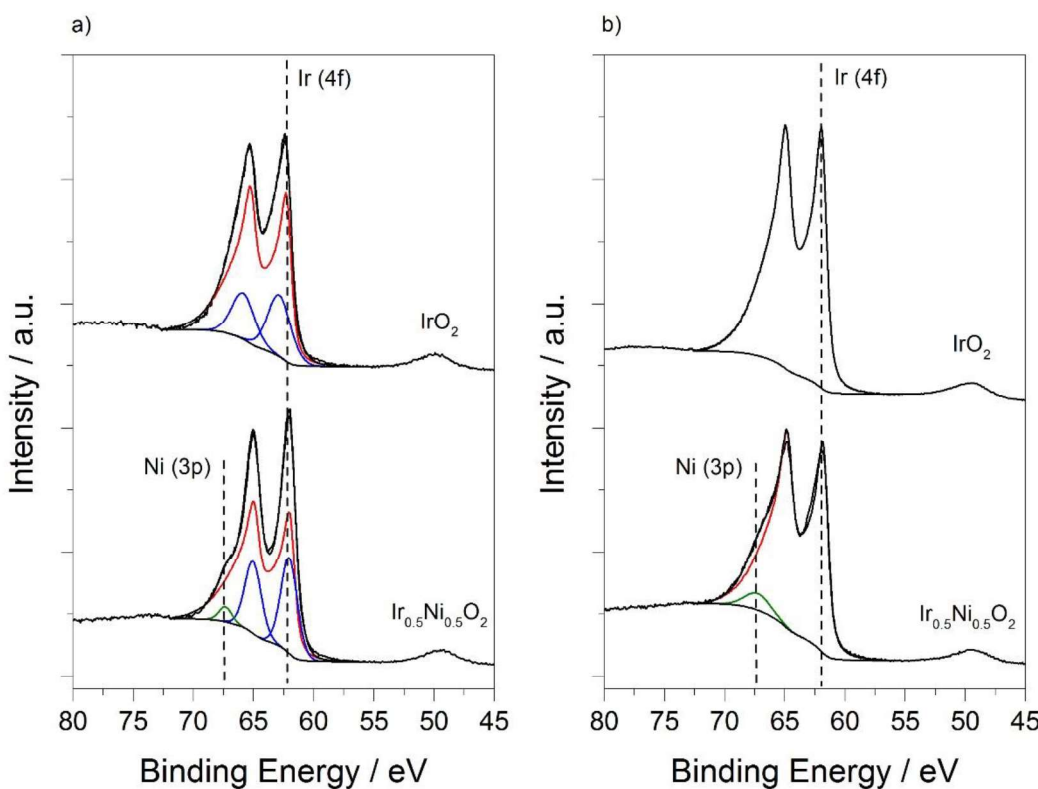


**Figure 6.14.** Ir(4f) orbital characterisation by XPS for a) fresh and b) annealed in air at 500 °C for 3 h  $\text{Ir}_{0.5}\text{Ni}_{0.5}\text{O}_2\text{-CS}$  catalyst. The Ir(4f) orbital shape translated from rutile  $\text{IrO}_2$  is represented in red, blue fitting represents the necessary contribution to fit the Ir(4f) peak for amorphous  $\text{IrO}_x$ , Ni(3p) is represented in green.

As observed for  $\text{Ir}_{0.5}\text{Cu}_{0.5}\text{O}_2\text{-CS}$  catalysts in table 6.2, copper migration towards the surface was observed on the  $\text{Ir}_{0.5}\text{Cu}_{0.5}\text{O}_2\text{-CS}$  catalysts after annealing at 500 °C in air for 3 h.

A comparable XPS trend was observed on the  $\text{Ir}_{0.5}\text{Cu}_{0.5}\text{O}_2\text{-CS}$  catalyst. Homogeneously dispersed  $\text{Ir}_{0.8}\text{Cu}_{0.2}\text{O}_2$  and  $\text{Ir}_{0.5}\text{Cu}_{0.5}\text{O}_2$  mixed oxide catalysts showed a progressive shift towards higher binding energy on the Ir(4f) orbital with increasing the copper concentration. However, on the  $\text{Ir}_{0.5}\text{Cu}_{0.5}\text{O}_2\text{-CS}$  catalyst, with a core shell distribution, the Ir(4f) peak was centred at 61.9 eV, showing no shift compared to  $\text{IrO}_2$  (figure 6.15).

After annealing, the Ir(4f) peak shifted towards lower binding energy, from 62.4 eV to 62.0 eV, closer to the reported value to rutile  $\text{IrO}_2$  at 61.9 eV.<sup>(2)</sup> Nevertheless, the peak envelope was broader than that assigned to rutile Ir(IV), indicating that not all iridium was present as lattice Ir(IV) sites in a rutile structure. As observed by XPS quantification copper migrated towards the surface after annealing. The nature of the iridium species contributing to the

Ir(4f) broadening were determined, it could be related to the presence of Ir(III) sites, the interaction with copper, structural defects or the presence of hydroxide groups.

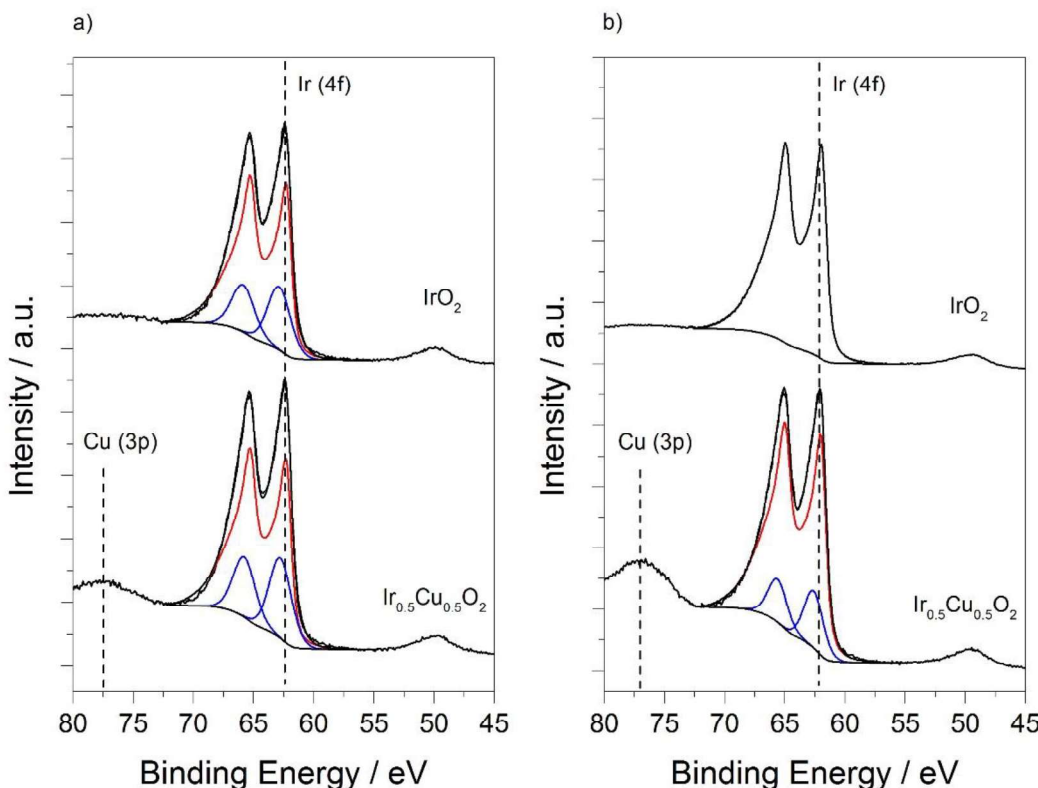


**Figure 6.15.** Ir(4f) orbital characterisation by XPS for a) fresh and b) annealed in air at 500 °C for 3 h  $\text{Ir}_{0.5}\text{Cu}_{0.5}\text{O}_2$ -CS catalyst. The Ir(4f) orbital shape translated from rutile  $\text{IrO}_2$  is represented in red, blue fitting represents the necessary contribution to fit the Ir(4f) peak for amorphous  $\text{IrO}_x$ .

Apart from the deterioration of the catalytic activity and stability observed for the homogeneously dispersed  $\text{Ir}_x\text{M}_{1-x}\text{O}_2$  ( $\text{M} = \text{Ni}$  and  $\text{Cu}$ ) mixed oxide catalysts, an additional issue was the material's agglomeration, which made challenging the catalyst ink preparation and hence limiting its testing. It can be expected that smaller agglomerates will re-disperse easier than larger ones.

In order to observe differences in the macroscopic morphology of  $\text{Ir}_{0.5}\text{Ni}_{0.5}\text{O}_2$  and  $\text{Ir}_{0.5}\text{Cu}_{0.5}\text{O}_2$  prepared materials with core-shell or solid solution distribution, SEM imaging was undertaken (image 6.2).

Compared to SEM images presented in chapter 3 for  $\text{IrO}_2\text{-Li}_2\text{CO}_3$  or  $\text{IrO}_2\text{-LiOH}$ , with small sponge-like morphologies, particle agglomeration was observed after the incorporation of nickel or copper in the formation of  $\text{Ir}_{0.5}\text{Ni}_{0.5}\text{O}_2$  and  $\text{Ir}_{0.5}\text{Cu}_{0.5}\text{O}_2$  homogeneously dispersed

catalysts. Nevertheless, the preparation of core-shell structures considerably reduced the size of the particle aggregates, which should facilitate the catalyst ink preparation.

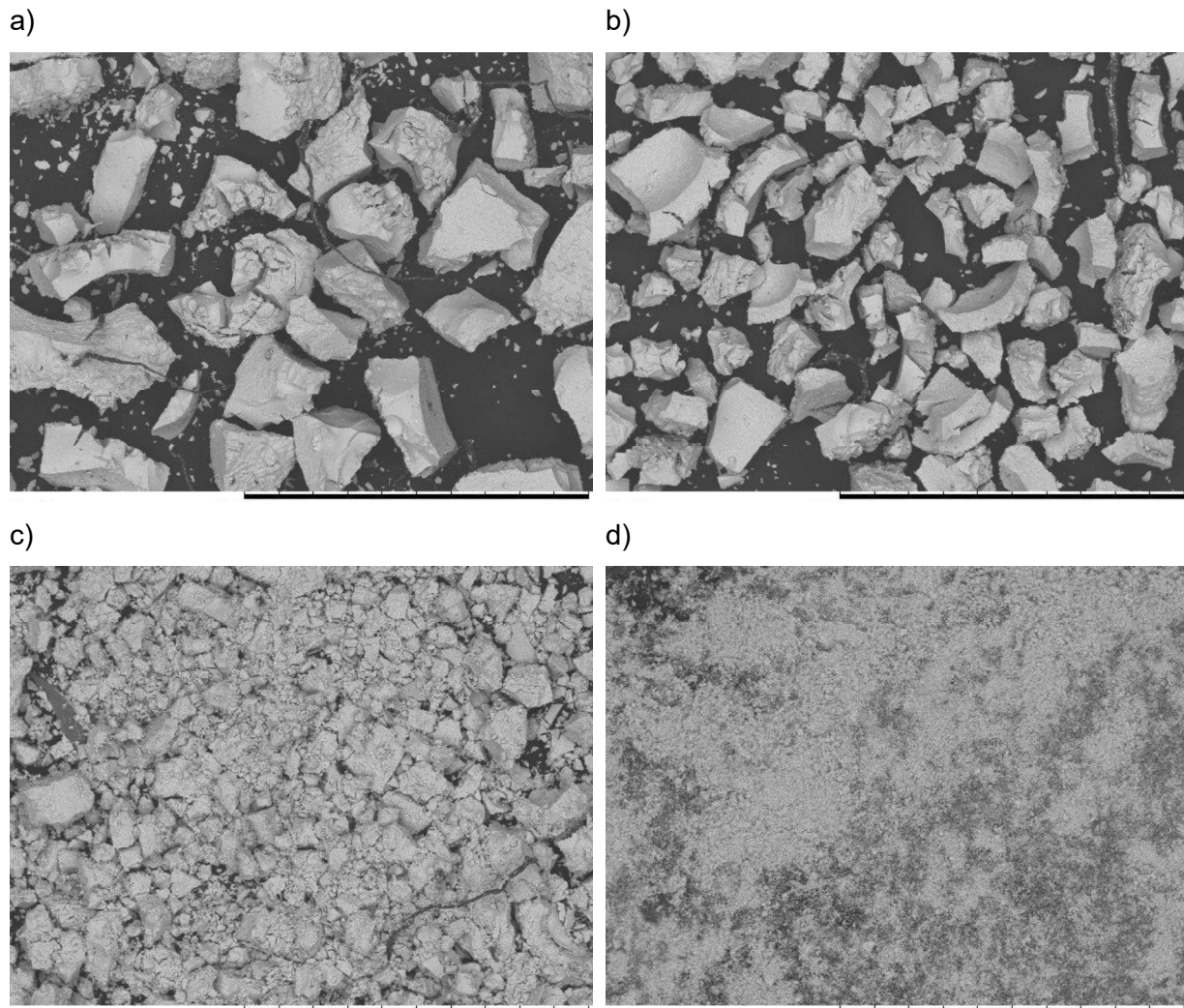


**Image 6.2.** SEM image for a) Ir<sub>0.5</sub>Ni<sub>0.5</sub>O<sub>2</sub> fresh b) Ir<sub>0.5</sub>Cu<sub>0.5</sub>O<sub>2</sub> fresh c) Ir<sub>0.5</sub>Ni<sub>0.5</sub>O<sub>2</sub>-CS d) Ir<sub>0.5</sub>Cu<sub>0.5</sub>O<sub>2</sub>-CS. Scale bar corresponded to 1 mm.

### 6.3.3 Catalysts electrochemistry.

Ir<sub>0.5</sub>Ni<sub>0.5</sub>O<sub>2</sub>-CS and Ir<sub>0.5</sub>Cu<sub>0.5</sub>O<sub>2</sub>-CS prepared with a non-noble metal core and an iridium shell were tested as OER catalysts in a conventional 3-electrode system. The electrocatalytic setup, the catalyst ink preparation, the reaction conditions and the testing protocol used were explained in detail previously.

The intrinsic activity towards OER of as prepared materials was determined by a LSV, performed at the beginning of the experiment (figure 6.16). Even though the molar iridium loading on to the electrode was halved for Ir<sub>0.5</sub>Ni<sub>0.5</sub>O<sub>2</sub>-CS catalyst compared to IrO<sub>2</sub>-Li<sub>2</sub>CO<sub>3</sub>,

the intrinsic activity prevailed almost unchanged with just a 4 mV potential rise at  $5 \text{ mA}\cdot\text{cm}^{-2}$ . Slightly lower intrinsic activity was observed for  $\text{Ir}_{0.5}\text{Cu}_{0.5}\text{O}_2\text{-CS}$  catalyst, 16 mV overpotential compared to  $\text{IrO}_2$  at  $5 \text{ mA}\cdot\text{cm}^{-2}$ . After annealing at  $500^\circ\text{C}$ , a decrease of 80 mV and 52 mV in the catalytic activity compared to fresh  $\text{Ir}_{0.5}\text{Ni}_{0.5}\text{O}_2\text{-CS}$  and  $\text{Ir}_{0.5}\text{Cu}_{0.5}\text{O}_2\text{-CS}$  catalyst was observed, albeit the deterioration of activity was improved compared to homogeneously dispersed catalysts. The hampering in the intrinsic catalytic activity after annealing can be attributed to the migration of the non-noble metal, concentrated at the core on fresh samples, towards the surface as indicated by XPS elemental quantification. Additionally, annealing induced the crystallisation of the amorphous iridium oxo-hydroxide to rutile, which is known to perform poorly, as a consequence of the lower concentration of Ir(III) sites and hydroxide groups.

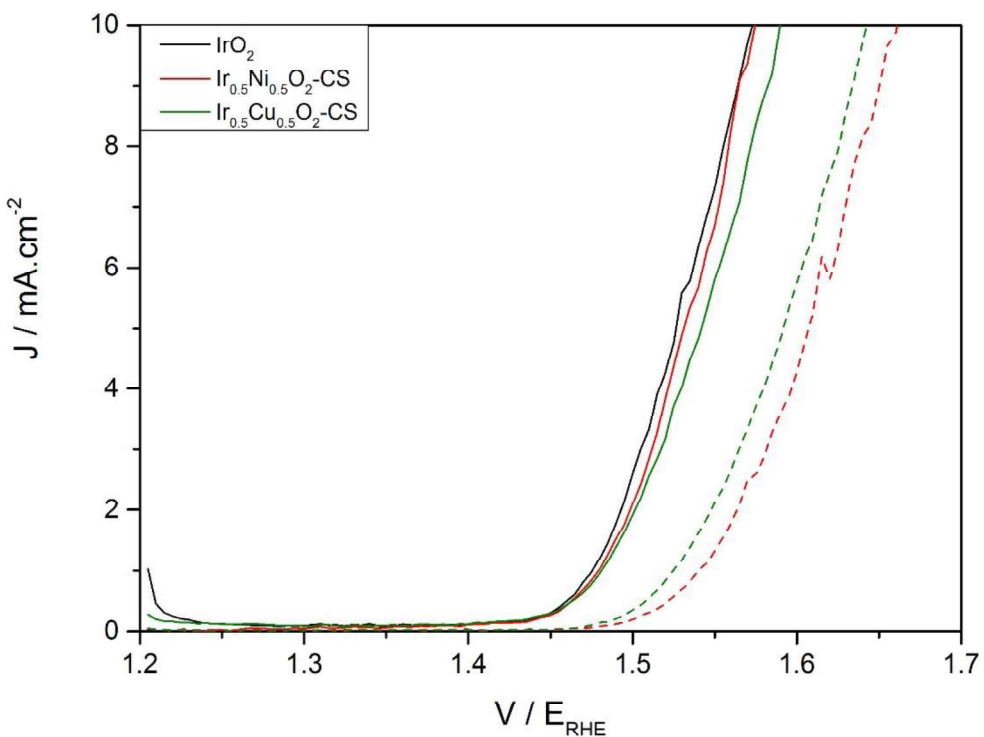


**Figure 6.16.** Intrinsic activity determined by LSV at the beginning of the experiment for  $\text{Ir}_{0.5}\text{Ni}_{0.5}\text{O}_2\text{-CS}$  and  $\text{Ir}_{0.5}\text{Cu}_{0.5}\text{O}_2\text{-CS}$  fresh (solid lines) and after annealing in air at  $500^\circ\text{C}$  for 3 h (dashed lines).

Cyclic voltammetry is a useful technique to compare the amount of active sites in a catalyst by comparing the area under the curve and its shape. As prepared  $\text{IrO}_2$  and  $\text{Ir}_{0.5}\text{Ni}_{0.5}\text{O}_2\text{-CS}$  catalysts had similar CV curves, the CV corresponding to the core shell mixed oxide catalysts presented slightly smaller area than  $\text{IrO}_2$ , but preserving the same Ir(III)/Ir(IV) and Ir(IV)/Ir(V) electronic transitions (figure 6.17a) at  $0.95 \text{ V}_{\text{RHE}}$  and  $1.25 \text{ V}_{\text{RHE}}$  respectively.<sup>(19)</sup>

However, the Ir(III)/Ir(IV) transition was not observed on the  $\text{Ir}_{0.5}\text{Cu}_{0.5}\text{O}_2\text{-CS}$  catalyst, this was not expected from the Ir(4f) orbital, which indicated the presence of Ir(III) sites, and it would need further investigation.

The change in the iridium speciation after annealing was clearly observed by CV (figure 6.17b). Apart from the drop in the CV area, the symmetric CV curve commonly reported for rutile  $\text{IrO}_2$ , without the presence of distinct redox transitions, was observed in agreement with changes observed on the Ir(4f) orbital by XPS.

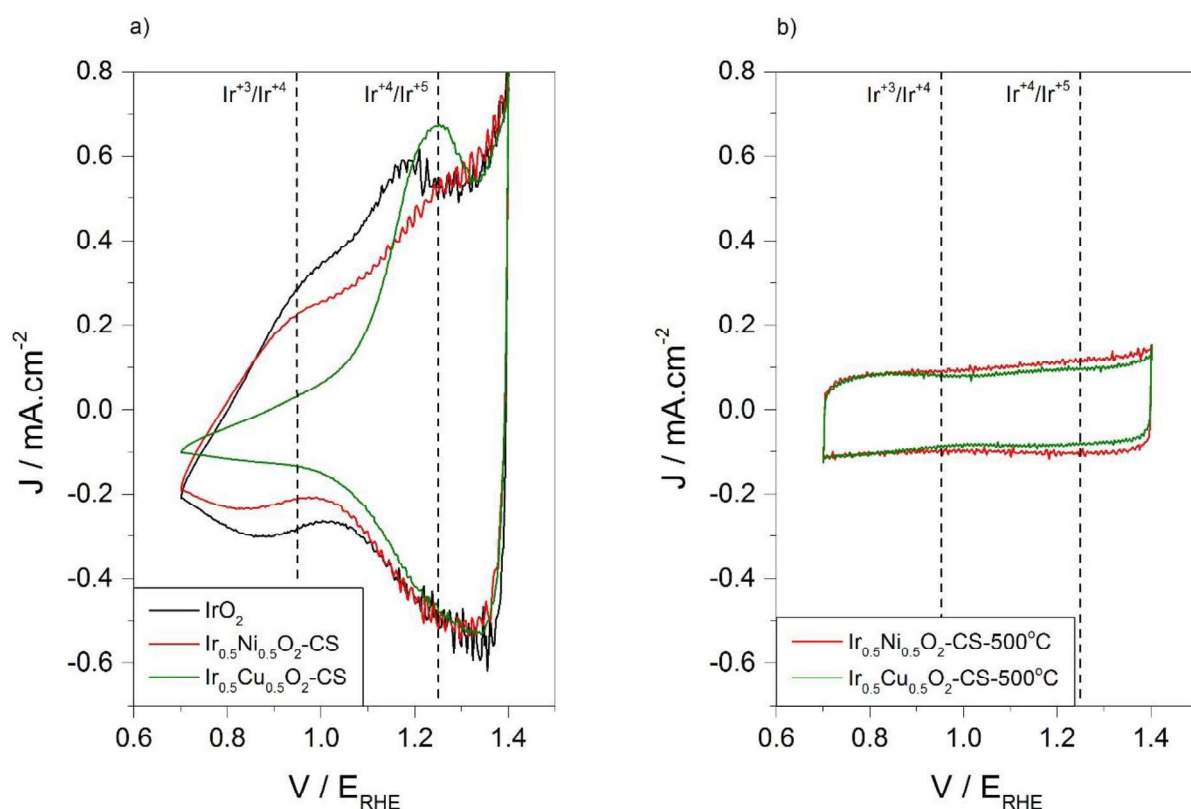


**Figure 6.17.** CV ( $0.7 \text{ E}_{\text{RHE}}$  to  $1.4 \text{ E}_{\text{RHE}}$  at  $50 \text{ mV} \cdot \text{s}^{-1}$ ) for a) as prepared and b) annealed in air at  $500 \text{ }^{\circ}\text{C}$  for 3 h  $\text{Ir}_{0.5}\text{Ni}_{0.5}\text{O}_2\text{-CS}$  and  $\text{Ir}_{0.5}\text{Cu}_{0.5}\text{O}_2\text{-CS}$  catalysts.

During the analysis of homogeneously dispersed  $\text{Ir}_x\text{M}_{1-x}\text{O}_2$  ( $\text{M} = \text{Ni}$  or  $\text{Cu}$ ), it was noted the poor catalytic stability of the mixed oxide catalysts during the CP stability test (2 h at  $10 \text{ mA} \cdot \text{cm}^{-2}$ ), even for the catalysts with the lowest no-noble metal concentration (figure 6.18a). Conversely, a stable potential was observed for the 2 h duration of the stability test for the prepared core-shell catalysts (figure 6.18b). The as prepared  $\text{Ir}_{0.5}\text{Ni}_{0.5}\text{O}_2\text{-CS}$  and  $\text{Ir}_{0.5}\text{Cu}_{0.5}\text{O}_2\text{-CS}$  catalysts have the same potential through time as  $\text{IrO}_2\text{-Li}_2\text{CO}_3$  catalyst albeit the molar concentration of iridium on the catalysts was halved. OER occurs at the surface of the catalyst, due to the dynamic nature of materials several can be involved in the reaction,

however, the non-active and non-stable  $\text{NiO}$  and  $\text{CuO}$  remained protected against corrosion by an iridium shell. Whilst the active phase, iridium oxo-hydroxide, is concentrated at the outer layer of the catalyst. After annealing, a steady potential though time was observed during the CP stability test, albeit 50 mV higher compared to fresh counterparts. This in agreement with the poorer OER activity and lower CV area, which can be explained by Cu and Ni migration towards the surface, the higher crystallinity, the reduction of hydroxide groups and the loss of Ir(III) sites.

Therefore, the rational design of core-shell catalysts, compared to a solid solution distribution, allows the concentration of the active phase at the surface and it is proved to be an effective approach for reducing considerably the amount of iridium on the electrode without hampering the catalytic activity or stability.

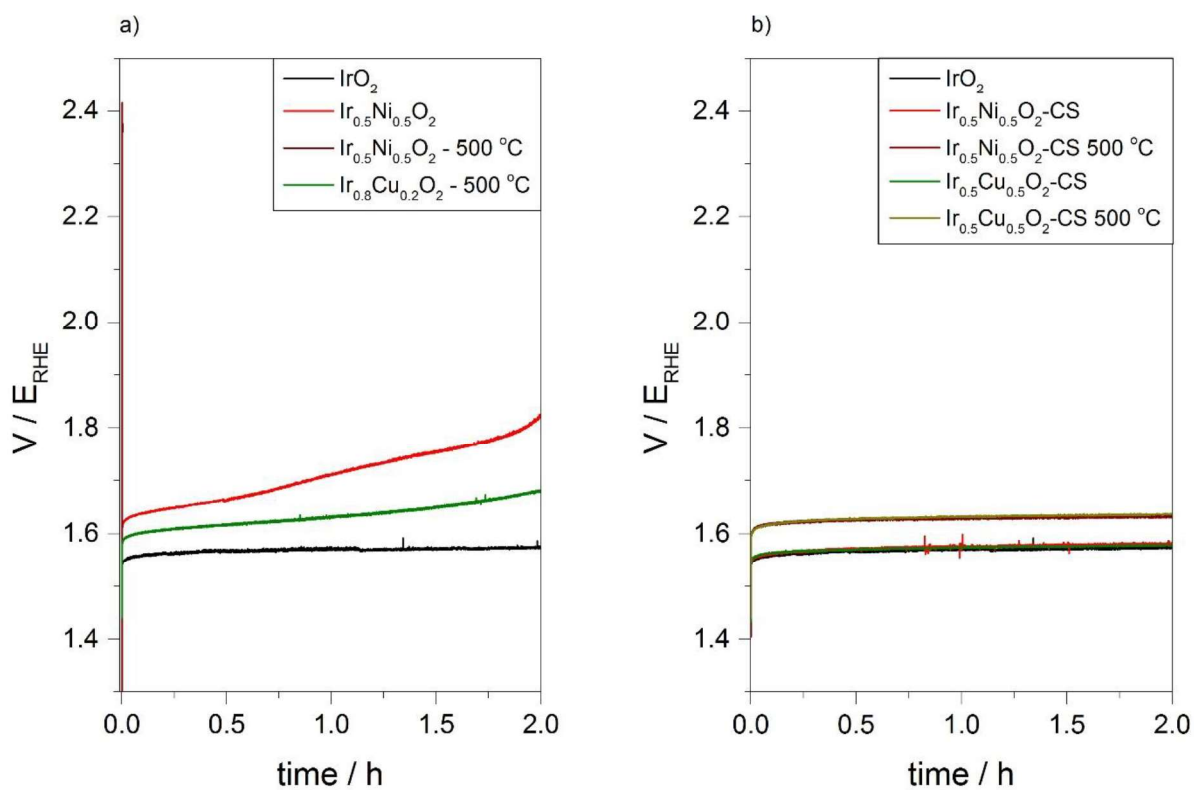


**Figure 6.18.** Stability test comparison by chronopotentiometry ( $10 \text{ mA} \cdot \text{cm}^{-2}$ ) of  $\text{Ir}_{0.5}\text{Ni}_{0.5}\text{O}_2$  and  $\text{Ir}_{0.5}\text{Cu}_{0.5}\text{O}_2$  catalysts with a) a homogeneous distribution or b) with a core-shell arrangement.

#### 6.4 Conclusion.

When a non-active and non-stable material, such as Ni or Cu, was introduced into the  $\text{IrO}_2$  lattice, forming a solid solution, the catalytic activity and stability towards OER was compromised. Metals were distributed homogenously throughout the catalyst as indicated by XPS elemental quantification. Hence the concentration of iridium and the non-noble metal, nickel or copper, at the surface would be the nominal value leading to the dopant's dissolution during reaction. The introduction of an inactive secondary element could be used for manipulating the structural and electronic properties of  $\text{IrO}_2$ , as observed by XRD and XPS, however it is an inefficient approach for decreasing significantly the amount of iridium on the electrode.

Therefore, it is desirable to avoid the presence of a non-active and non-stable element at the surface of the catalyst, and hence, in contact with the reaction mixture. This was achieved by synthesising core-shell catalysts, with iridium at the outer-layer and the cheaper element forming the core.

Through a simple modification of the hydrothermal treatment, a core made of  $\text{NiO}_x$  or  $\text{CuO}_x$  was prepared and used as a scaffold for growing a protective and active layer of  $\text{IrO}_x$ . The intermetallic interaction observed in the Ir(4f) orbital by XPS on homogeneously dispersed catalysts was absent on the core-shell approach. This was due to two metal oxides being physically separated.

$\text{Ir}_{0.5}\text{Ni}_{0.5}\text{O}_2\text{-CS}$  and  $\text{Ir}_{0.5}\text{Cu}_{0.5}\text{O}_2\text{-CS}$  catalysts with a core-shell distribution showed comparable mass normalised catalytic activity and stability towards OER compared to synthesised  $\text{IrO}_2\text{-Li}_2\text{CO}_3$ , albeit the concentration of iridium on the electrode was halved. Thus, it can be hypothesised that only the outer layers of the catalyst were involved in the reaction.

In line with previous chapters, it is again highlighted the detrimental effect of heat treatment on the catalyst activity towards OER. Annealing induced the non-noble metal migration towards the surface of the catalyst as indicated by XPS elemental quantification. Additionally, the more active iridium oxo-hydroxide phase was transformed to the less active crystalline rutile  $\text{IrO}_2$  with the concomitant loss of Ir(III) and hydroxide groups commonly associated with active OER catalysts.

## 6.5 Bibliography.

1. P. C. K. Vesborg, T. F. Jaramillo, Addressing the terawatt challenge: scalability in the supply of chemical elements for renewable energy, *RSC Advances*, **2012**, 2 (21), 7933-7947.
2. S. J. Freakley, J. Ruiz Esquius, D. J. Morgan, The X-ray photoelectron spectra of Ir,  $\text{IrO}_2$  and  $\text{IrCl}_3$  revisited, *Surface and Interface Analysis*, **2017**, 49 (8), 794-799.
3. M. Carmo, D. L. Fritz, J. Mergel, D. Stolten, A comprehensive review on PEM water electrolysis, *International Journal of Hydrogen Energy*, **2013**, 38 (12), 4901-4934.
4. C. Massué, V. Pfeifer, X. Huang, J. Noack, A. Tarasov, S. Cap, R. Schlögl, High-performance supported Ir-oxohydroxide water oxidation electrocatalysts, *ChemSusChem*, **2017**, 10, 1943-1957.
5. V. K. Puthiyapura, M. Mamlouk, S. Pasupathi, B. G. Pollet, K. Scott, Physical and electrochemical evaluation of ATO supported  $\text{IrO}_2$  catalyst for proton exchange membrane water electrolyser, *Journal of Power Sources*, **2014**, 269, 451-460.
6. T. Reier, Z. Pawolek, S. Cherevko, M. Bruns, T. Jones, D. Teschner, S. Selve, A. Bergmann, H. N. Nong, R. Schlögl, K. J. J. Mayrhofer, P. Strasser, Molecular Insight in Structure and Activity of Highly Efficient, Low-Ir Ir–Ni Oxide Catalysts for Electrochemical Water Splitting (OER), *Journal of the American Chemical Society*, **2015**, 137 (40), 13031-13040.
7. O. Kasian, S. Geiger, P. Stock, G. Polymeros, B. Breitbach, A. Savan, A. Ludwig, S. Cherevko, K. J. J. Mayrhofer, On the Origin of the Improved Ruthenium Stability in  $\text{RuO}_2\text{-IrO}_2$  Mixed Oxides, *Journal of The Electrochemical Society*, **2016**, 163 (11), 5.
8. A. Papaderakis, N. Pliatsikas, C. Prochaska, G. Vourlias, P. Patsalas, D. Tsipakides, S. Balomenou, S. Sotiropoulos, Oxygen Evolution at  $\text{IrO}_2$  Shell-Ir-Ni Core Electrodes Prepared by Galvanic Replacement, *The Journal of Physical Chemistry C*, **2016**, 120 (36), 19995-20005.
9. H. N. Nong, H. S. Oh, T. Reier, E. Willinger, M. G. Willinger, V. Petkov, D. Teschner, P. Strasser, Oxide-Supported  $\text{IrNiO}_x$  Core-Shell Particles as Efficient, Cost-Effective, and Stable Catalysts for Electrochemical Water Splitting, *Angewandte Chemie International Edition*, **2015**, 54 (10), 2975-2979.
10. H. N. Nong, T. Reier, H. S. Oh, M. Gliech, P. Paciok, T. H. Thi Vu, D. Teschner, M. Heggen, V. Petkov, R. Schlögl, T. Jones, P. Strasser, A unique oxygen ligand environment facilitates water oxidation in hole-doped  $\text{IrNiO}_x$  core-shell electrocatalysts, *Nature Catalysis*, **2018**, 1 (11), 841-851.

11. W. Sun, Y. Song, X. Q. Gong, L. M. Cao, J. Yang, An efficiently tuned d-orbital occupation of  $\text{IrO}_2$  by doping with Cu for enhancing the oxygen evolution reaction activity, *Chemical Science*, **2015**, 6 (8), 4993-4999.
12. Y. Zhao, K. R. Yang, Z. Wang, X. Yan, S. Cao, Y. Ye, Q. Dong, X. Zhang, J. E. Thorne, L. Jin, K. L. Materna, A. Trimpalis, H. Bai, S. C. Fakra, X. Zhong, P. Wang, X. Pan, J. Guo, M. Flytzani-Stephanopoulos, G. W. Brudvig, V. S. Batista, D. Wang, Stable iridium dinuclear heterogeneous catalysts supported on metal-oxide substrate for solar water oxidation, *Proceedings of the National Academy of Sciences*, **2018**, 115 (12), 2902-2907.
13. S. Xu, Y. Liu, J. Tong, W. Hu, Q. Xia, Iridium-nickel composite oxide catalysts for oxygen evolution reaction in acidic water electrolysis, *Russ J Electrochem*, **2016**, 52 (11), 1021-1031.
14. W. Q. Zaman, Z. Wang, W. Sun, Z. Zhou, M. Tariq, L. Cao, X. Q. Gong, J. Yang, Ni-Co Codoping Breaks the Limitation of Single-Metal-Doped  $\text{IrO}_2$  with Higher Oxygen Evolution Reaction Performance and Less Iridium, *ACS Energy Lett*, **2017**, Ahead of Print.
15. V. Pfeifer, T. E. Jones, J. J. Velasco Vélez, C. Massué, R. Arrigo, D. Teschner, F. Girgsdies, M. Scherzer, M. T. Greiner, J. Allan, M. Hashagen, G. Weinberg, S. Piccinin, M. Hävecker, A. Knop-Gericke, R. Schlögl, The electronic structure of iridium and its oxides, *Surface and Interface Analysis*, **2016**, 48 (5), 261-273.
16. A. M. Cruz, L. Abad, N. M. Carretero, J. Moral-Vico, J. Fraxedas, P. Lozano, G. Subías, V. Padial, M. Carballo, J. E. Collazos-Castro, N. Casañ-Pastor, Iridium Oxohydroxide, a Significant Member in the Family of Iridium Oxides. Stoichiometry, Characterization, and Implications in Bioelectrodes, *The Journal of Physical Chemistry C*, **2012**, 116 (8), 5155-5168.
17. N. S. McIntyre, M. G. Cook, X-ray photoelectron studies on some oxides and hydroxides of cobalt, nickel, and copper, *Analytical Chemistry*, **1975**, 47 (13), 2208-2213.
18. C. Wang, R. B. Moghaddam, S. H. Bergens, Active, Simple Iridium-Copper Hydrous Oxide Electrocatalysts for Water Oxidation, *The Journal of Physical Chemistry C*, **2017**, 121 (10), 5480-5486.
19. L. Ouattara, S. Fierro, O. Frey, M. Koudelka, Comninellis C, Electrochemical comparison of  $\text{IrO}_2$  prepared by anodic oxidation of pure iridium and  $\text{IrO}_2$  prepared by thermal decomposition of  $\text{H}_2\text{IrCl}_6$  precursor solution, *Journal of Applied Electrochemistry*, **2009**, 39 (8), 1361-1367.

20. J. Juodkazyte, B. Sebeka, I. Valsiunas, K. Juodkazis, Iridium Anodic Oxidation to Ir(III) and Ir(IV) Hydrous Oxides, *Electroanalysis*, **2005**, 17 (11), 947-952.
21. R. B. Moghaddam, C. Wang, J. B. Sorge, M. J. Brett, S. H. Bergens, Easily prepared, high activity Ir-Ni oxide catalysts for water oxidation, *Electrochemistry Communications*, **2015**, 60, 109-112.
22. H. N. Nong, L. Gan, E. Willinger, D. Teschner, P. Strasser,  $\text{IrO}_x$  core-shell nanocatalysts for cost-and energy-efficient electrochemical water splitting, *Chemical Science*, **2014**, 5 (8), 2955-2963.
23. F. Berkermann, *Preparation and Application of Aqueous Iridium Oxide Colloids* (Doctoral Thesis). Ruhr University Bochum, Germany, **2010**.
24. Y. Zhao, E. A. Hernandez-Pagan, N. M. Vargas-Barbosa, J. L. Dysart, T. E. Mallouk, A High Yield Synthesis of Ligand-Free Iridium Oxide Nanoparticles with High Electrocatalytic Activity, *The Journal of Physical Chemistry Letters*, **2011**, 2 (5), 402-406.
25. C. L. Carnes, J. Stipp, K. J. Klabunde, J. Bonevich, Synthesis, Characterization, and Adsorption Studies of Nanocrystalline Copper Oxide and Nickel Oxide, *Langmuir*, **2002**, 18 (4), 1352-1359.

# Chapter 7

## CO<sub>2</sub> hydrogenation to methanol over PdZn/TiO<sub>2</sub> catalysts prepared by CVI

### 7.1 Introduction.

Hydrogen, produced from renewables as a route for storing surplus energy, is the best alternative to polluting carbon based fuels. Hydrogen gas is difficult to incorporate directly in the current energy system, since most of the technology uses conventional liquid fuels; To bridge the hydrogen economy with current technology, H<sub>2</sub> can be further converted to CH<sub>3</sub>OH by its reaction with CO<sub>2</sub>.<sup>(1)</sup> This would alleviate greenhouse emissions while providing a drop-in fuel for current technology.

Apart from copper, palladium is the second most studied metal for the selective hydrogenation of CO<sub>2</sub> to methanol.<sup>(2)</sup> Over metallic palladium, CO<sub>2</sub> is reduced to CO via the reverse water gas shift reaction (equation 7.1) or to CH<sub>4</sub> (equation 7.2) depending on the support,<sup>(3-5)</sup> whilst after the addition of zinc into palladium, to form PdZn alloy, results in CO<sub>2</sub> hydrogenation to methanol (equation 7.3).<sup>(6, 7)</sup>



Use of ZnO as a support for palladium favours formation of the active PdZn alloy phase. However, the poor surface area of ZnO (15 m<sup>2</sup>·g<sup>-1</sup>) compared to other supports could lead to particle agglomeration, reducing the number of surface active sites. One methodology to increase the surface area of the active phase is to form the PdZn alloy on a high surface area support. Xu *et al.*<sup>(8)</sup> prepared Pd/ZnO/Al<sub>2</sub>O<sub>3</sub> and Pd/ZnO catalysts by co-precipitation and impregnation. When assessed at 180 °C and 30 bar (69 vol % H<sub>2</sub>, 23 vol % CO<sub>2</sub>, 8 vol % N<sub>2</sub>), addition of a half equivalent of Al<sub>2</sub>O<sub>3</sub> to Pd/ZnO led CO<sub>2</sub> conversion to increase from 2.5 % to 2.9 % and methanol selectivity from 72 % to 79 %. This correlated well with an observed increase in PdZn dispersion. Xu *et al.*<sup>(8)</sup> also observed an increase in methanol selectivity with increasing pre-reduction temperature. This correlates well with studies by Bahruji *et al.*<sup>(7)</sup> who reported higher methanol selectivity with increasing the pre-reduction temperature simultaneously with a higher formation of PdZn alloy. Liang *et al.*<sup>(9)</sup> assessed a catalyst containing 16 wt. % Pd<sub>0.1</sub>Zn<sub>1</sub> supported on carbon nanotubes (CNTs), activated carbon (AC) and γ-Al<sub>2</sub>O<sub>3</sub> for CO<sub>2</sub> hydrogenation at 30 bar (69 vol % H<sub>2</sub>, 23 vol % CO<sub>2</sub>, 8 vol

% N<sub>2</sub>) and 250 °C. Catalysts presented methanol selectivity above 90 %. However, the higher CO<sub>2</sub> conversion observed when CNTs were used as the support (6.3 %) relative to AC or Al<sub>2</sub>O<sub>3</sub> (4.2 % and 3.6 % respectively), was attributed to the higher surface area, which led to smaller and better dispersed PdZn nanoparticles, and to the higher hydrogen adsorption capacity of the CNT support.<sup>(9)</sup> Bahruji *et al.*<sup>(10)</sup> prepared PdZn alloy catalysts supported on ZnO, Al<sub>2</sub>O<sub>3</sub> and TiO<sub>2</sub> (P25) by chemical vapour impregnation (CVI), with a constant palladium loading of 5 wt.% and a Pd to Zn molar ratio of 1:10, TiO<sub>2</sub>, Al<sub>2</sub>O<sub>3</sub> and ZnO-supported catalysts gave methanol productivities of 1510, 635 and 1070 mmol<sub>MeOH</sub>·kg<sub>cat</sub><sup>-1</sup>·h<sup>-1</sup> respectively (250 °C, 20 bar, 60 % H<sub>2</sub>, 20 % CO<sub>2</sub>, 20 % N<sub>2</sub>).

### 7.1.1 Chemical vapour impregnation (CVI) as a catalyst preparation technique.

Preparation of highly-dispersed, small particle is desirable in catalysis since it leads to an increase in metal surface area. This increases the number of active sites at the surface. It is therefore preferable to synthesise highly dispersed PdZn alloy nanoparticles on a higher surface area support than ZnO, for instance TiO<sub>2</sub>-P25 (50 m<sup>2</sup>·g<sup>-1</sup>).

Chemical Vapour Impregnation (CVI) has been used in the preparation of various catalysts affording highly dispersed small nanoparticles. It also has the benefit of avoiding use of solvents, stabilising ligands or chloride metal precursors which could poison the final catalyst. Additionally, CVI can be used with a range of metal acetylacetonate precursors and supports. This technique consists of sublimation of the organometallic precursor by heating under vacuum, with simultaneous deposition of the organometallic onto the support material in one step. Temperature has to be carefully controlled to achieve sublimation of the organometallic precursor but avoid its thermal decomposition. Forde *et al.*<sup>(11, 12)</sup> prepared highly-dispersed Fe and Cu nanoparticles on ZSM-5(30) with a mean particle size smaller than 3 nm by CVI. Small precious metal nanoparticles such as Pd and Pt could be successfully deposited onto titania with high dispersion by CVI, being the preparation of Pd-Pt bimetallic compounds also feasible.<sup>(13)</sup>

Bahruji *et al.*<sup>(14)</sup> previously reported methanol productivities of 635 mmol·kg<sub>cat</sub><sup>-1</sup>·h<sup>-1</sup>, 1070 mmol·kg<sub>cat</sub><sup>-1</sup>·h<sup>-1</sup> and 1510 mmol·kg<sub>cat</sub><sup>-1</sup>·h<sup>-1</sup> for 5 wt % Pd 15 wt % Zn supported on Al<sub>2</sub>O<sub>3</sub>, ZnO and TiO<sub>2</sub> (P25) respectively (250 °C, 20 bar, prepared by CVI, Pd:Zn = 1 : 10 mol/mol). As a continuation from previous results, this chapter focuses on optimisation of TiO<sub>2</sub> supported PdZn alloy catalysts prepared by CVI for the CO<sub>2</sub> hydrogenation to methanol. With an aim to maximise methanol yields, the Pd to Zn ratio is systematically studied, as are the effect of palladium loading and pre-reduction temperature.

## 7.2 Palladium to zinc molar ratio effect on supported TiO<sub>2</sub> catalysts by CVI.

### 7.2.1 Catalyst preparation.

Catalysts with a palladium to zinc molar ratio of between 1:1 and 1:10 were prepared by CVI with total Pd loading maintained at 5 wt. %. The standard procedure goes as follows: the calculated amount of Pd(acac)<sub>2</sub> and Zn(acac)<sub>2</sub> were physically mixed thoroughly with the support, TiO<sub>2</sub> (P25). The mixture was then transferred to a schlenk flask and heated at 145 °C under vacuum for one hour. After impregnation, the sample was annealed in static air (500 °C, 16 h). Prior to testing catalysts were pelleted (600 µm - 425 µm mesh) and reduced *in situ* (400 °C, 1h, 1 atm, 30 ml·min<sup>-1</sup> 5 % H<sub>2</sub> in Ar). Following this methodology, 5 % Pd:Zn(1:1)/TiO<sub>2</sub>; 5 % Pd:Zn(1:2)/TiO<sub>2</sub>; 5 % Pd:Zn(1:5)/TiO<sub>2</sub> and 5 % Pd:Zn(1:10)/TiO<sub>2</sub> were prepared.

### 7.2.2 Catalyst characterisation.

#### XRD characterisation

##### Standard catalyst XRD characterisation

The tetragonal β-PdZn phase alloy reflections can be observed at 41° and 44° 2θ degrees for (111) and (200) planes respectively.<sup>(15-17)</sup> Unfortunately, when using TiO<sub>2</sub> (P25) as the support, which consists of a mixture of anatase and rutile crystalline phases, the PdZn alloy peaks overlap with the TiO<sub>2</sub>-rutile (111) and (201) reflections, making the PdZn alloy phase formation challenging to analyse by XRD. Therefore, 5% Pd/ZnO prepared by sol immobilisation (SIM) and 5% Pd:Zn(1:1)/TiO<sub>2</sub> anatase prepared by CVI were used as standards and analysed previously by XRD.

Firstly, *in situ* XRD on the 5% Pd/ZnO standard was performed to monitor the PdZn alloy formation. Without prior thermal treatment, 5% Pd/ZnO SIM was annealed in flowing air (10 ml·min<sup>-1</sup>) with XRD patterns collected between 25 °C and 500 °C (figure 7.1). The temperature was maintained constant for 5 minutes at each interval before recording any XRD pattern. At 230 °C, PdO appeared as a broad shoulder at 33.3° (JCPDS-041-1107) which increased in intensity as the temperature increased. Simultaneously, the broad peak at 40°, assigned to metallic Pd, disappeared. This is consistent with oxidation to PdO. No changes in the ZnO peaks were observed during the annealing process.

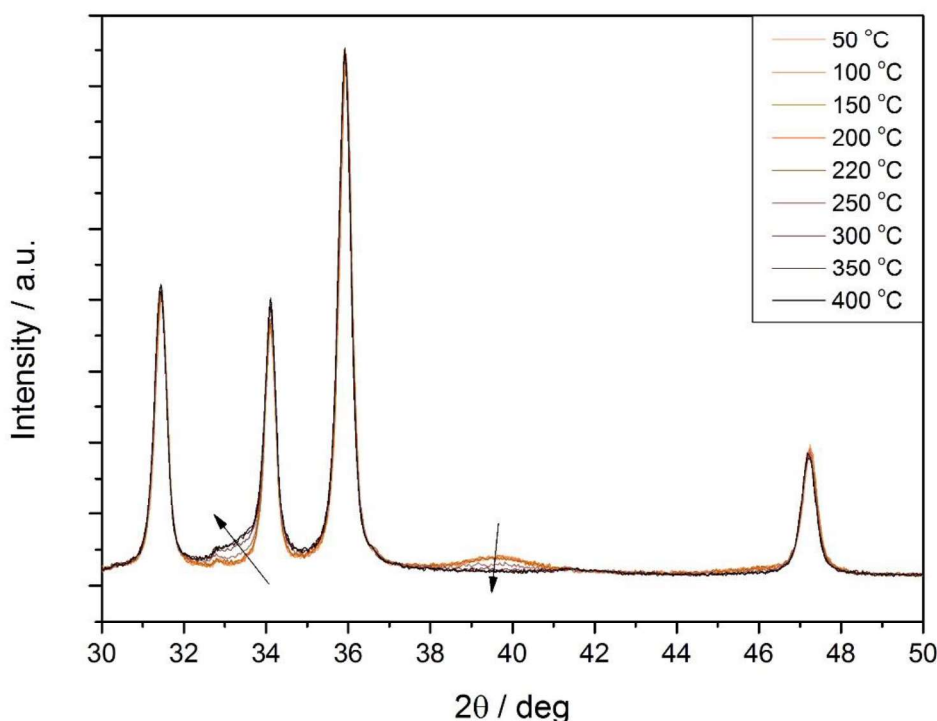


**Figure 7.1.** Selected *In situ* XRD patterns recorded for 5% Pd/ZnO prepared by sol immobilization during annealing in air from 25 °C to 500 °C.

Once the *in situ* XRD cell cooled to room temperature, the gas feed was changed to 5% H<sub>2</sub>/Ar (10 ml·min<sup>-1</sup>) and XRD patterns were collected across a 25 °C - 500 °C temperature range. The *in situ* reduction is illustrated in figure 7.2. Between 50 °C and 75 °C, an appreciable decrease in intensity of the (100), (002) and (101) ZnO peaks was observed at 31.8°, 34.4° and 36.3° respectively (JCPDS-036-1451). At the same time, the shoulder peak assigned to PdO at 33.3° decreased in intensity. However, it is not possible to assign this to reduction of the PdO due to overlap with the ZnO peak at 34.1°. It should be noted though that no peaks for Pd<sup>0</sup> or PdZn were observed at this temperature. At 125 °C, the PdO peak decreased in intensity and no further changes on the PdO region were detected with higher reduction temperatures. A peak at 39.9°, corresponding to the (111) plane (JCPDS-046-1043) in metallic Pd, was detected at 280 °C. At 350 °C, this peak shifted from 39.9° to 40.8°, indicating its transformation to PdZn alloy. Further increase in the reduction temperature to 400 °C led to growth in the PdZn alloy crystallite size. Formation of metallic Pd from PdO, leading to reduction of the ZnO support by hydrogen spill-over is in agreement with the previous mechanism proposed for PdZn formation.<sup>(16)</sup>

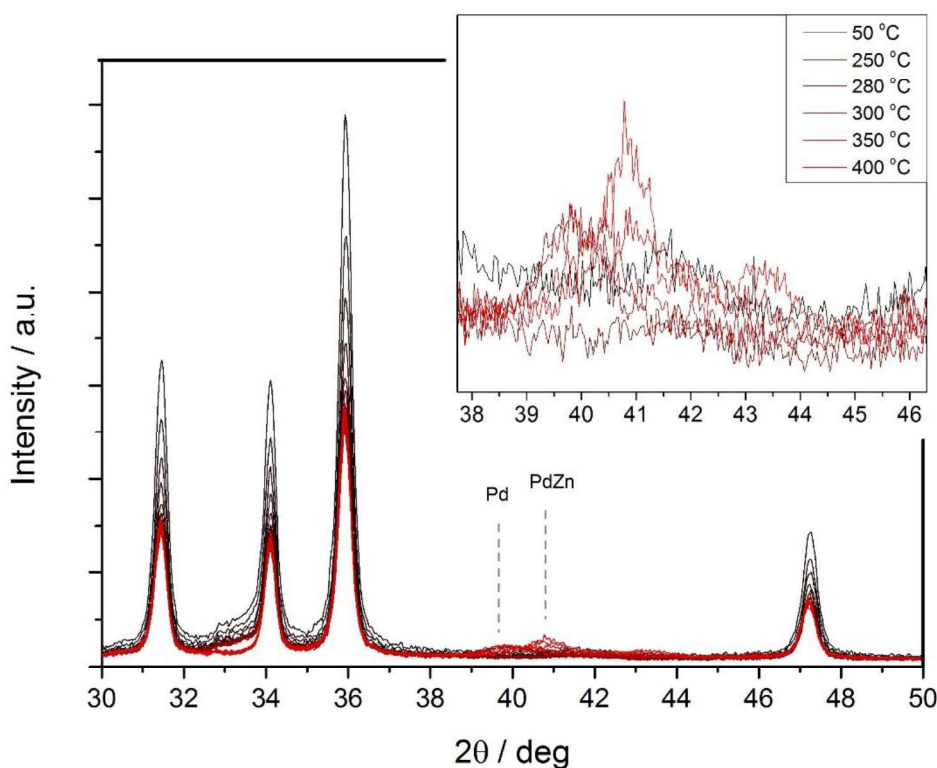


**Figure 7.2.** *In situ* XRD patterns for 5 % Pd/ZnO catalyst prepared by sol immobilization during reduction in 5 % H<sub>2</sub>/Ar.

The formation of  $\beta$ -PdZn alloy was observed by XRD in Fig. 7.2 upon reductive heat treatment of Pd/ZnO. However, in order to confirm that the PdZn alloy forms on TiO<sub>2</sub>, a PdZn catalyst was prepared using anatase TiO<sub>2</sub> to avoid potential overlaps between PdZn and the rutile TiO<sub>2</sub> peaks in P25. The 5% Pd:Zn(1:1)/TiO<sub>2</sub> anatase TiO<sub>2</sub> was synthesised by CVI.

As observed by XRD in figure 7.3, before heat treatment 5% Pd:Zn(1:1)/ anatase TiO<sub>2</sub>, showed no peaks for Pd-species (PdO, Pd<sup>0</sup> or PdZn). This indicates that the Pd(acac)<sub>2</sub> precursor remains intact, as indicated by the peaks between 10° to 20°.<sup>(18)</sup> Same applies for the absence of zinc related reflections on the fresh material. The catalyst was then annealed in air at 500 °C for 16 h to remove the organic part from the metallic precursors. After annealing, the PdO main peak at 34.1° appeared. However, no peaks corresponding to zinc oxide were observed, presumably due to its small crystallite size and high distribution on the support. After reductive treatment in a flow of 5 % H<sub>2</sub>/Ar (400 °C, 1 h), the main PdO peak at 34.1° disappeared leading to the formation of PdZn at 41.4° and 44.1° and metallic Pd at 40.2°. This indicated that not all palladium was incorporated into the alloy since zinc was present in stoichiometric loading to form the  $\beta$ -PdZn phase. As proposed previously in Fig

7.2, PdZn alloy is formed from the palladium spill-over on neighbouring zinc oxide particles. Hence, possibly metallic palladium remained in the core of the alloy nanoparticle.

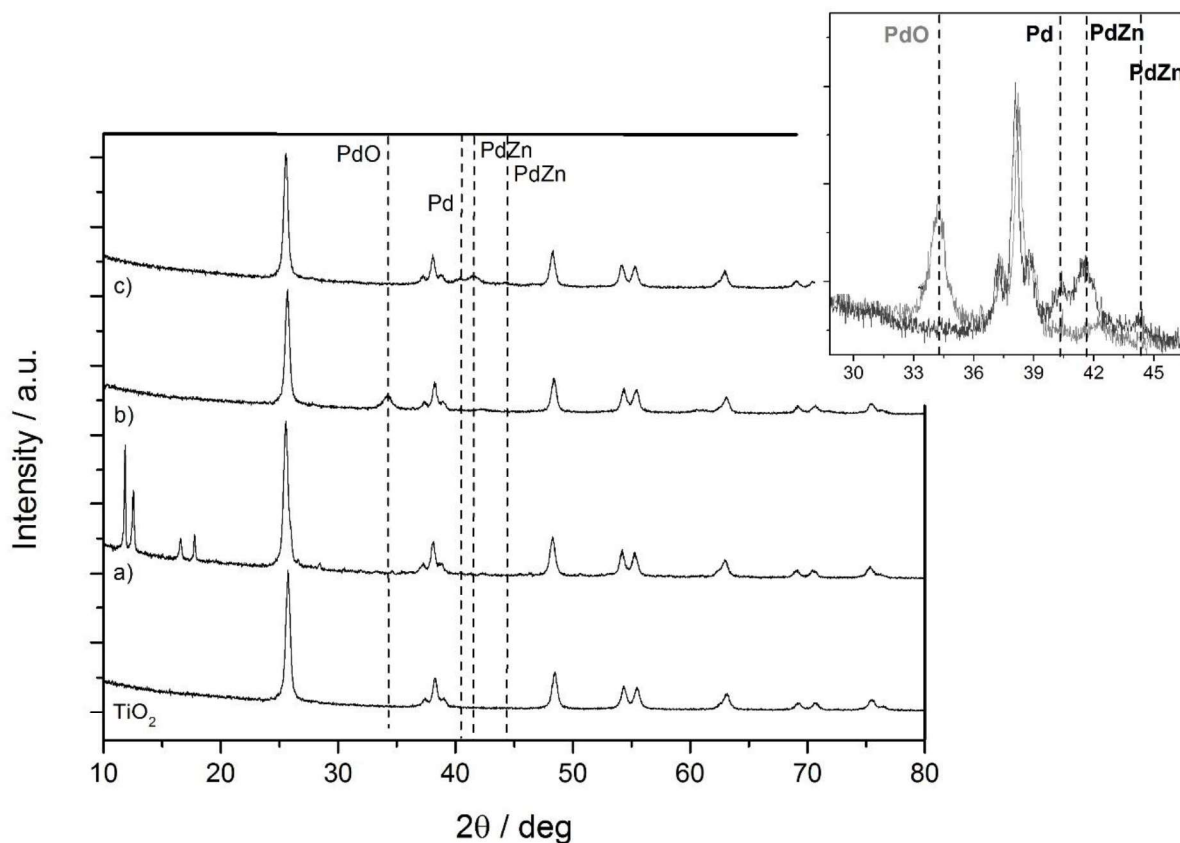


**Figure 7.3.** XRD patterns for as received TiO<sub>2</sub> anatase (Sigma Aldrich) and a) fresh 5% PdZn (1:1)/TiO<sub>2</sub> anatase prepared by CVI b) annealed in air (500 °C, 16 h) and c) reduced in 5% H<sub>2</sub>/Ar (400 °C, 1 h).

#### Palladium to zinc metal ratio XRD characterisation

Palladium loading was kept constant at 5 wt. % while changing the Pd to Zn molar ratio. Four catalysts were prepared by CVI, Pd:Zn(1:1)/TiO<sub>2</sub>, Pd:Zn(1:2)/TiO<sub>2</sub>, Pd:Zn(1:5)/TiO<sub>2</sub> and Pd:Zn(1:10)/TiO<sub>2</sub>. These catalysts were annealed in air (500 C, 16 h) followed by a reductive heat treatment in 5% H<sub>2</sub>/Ar (400 °C, 1 h).

XRD patterns for 5% PdZn(1:2)/TiO<sub>2</sub>, following annealing and reduction, are presented in figure 7.4. As observed in Fig. 7.3 for PdZn/anatase TiO<sub>2</sub>, synthesised catalysts showed the presence of PdO at 34.1° after annealing in air. Subsequent reduction in hydrogen led to decreased intensity of the PdO reflection at 34.1° and increased intensity of the PdZn peaks at 41.4° and 44.1°.

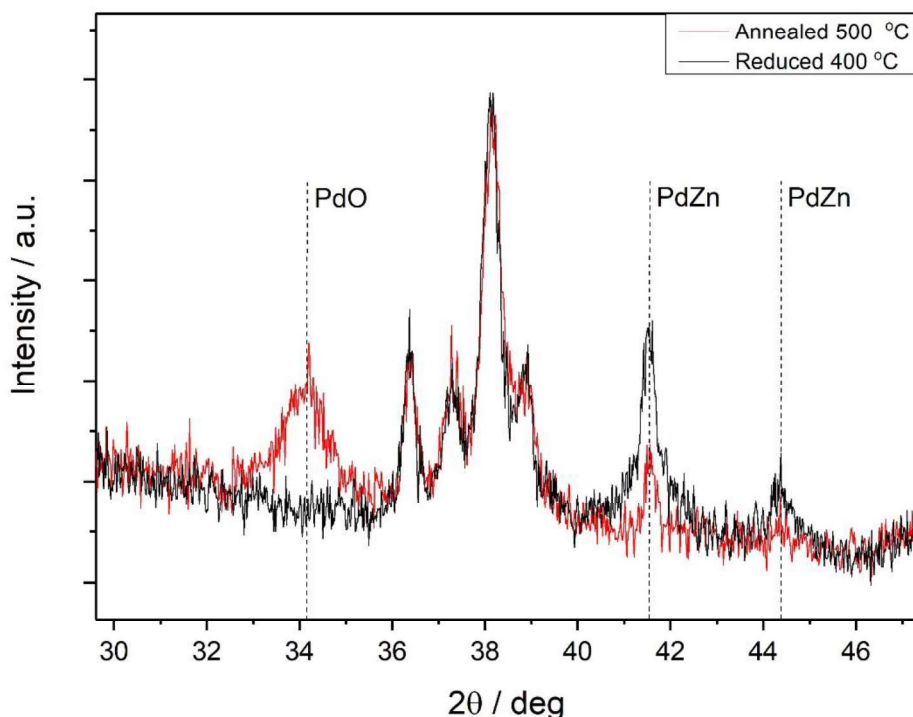


**Figure 7.4.** XRD patterns for 5% PdZn(1:2)/TiO<sub>2</sub> after annealing in air (500 °C, 16 h) and subsequent reduction in 5% H<sub>2</sub>/Ar (400 °C, 1 h).

Although the rutile TiO<sub>2</sub> peaks overlapped with those of the β-PdZn alloy at 41° and 44°, a gradual increase in the intensity of the peak at 41° was observed with increasing zinc concentration (figure 7.5a). Thus, indicating the formation of larger alloy nanoparticles a larger quantity of alloy present in the material. After the reductive heat treatment in 5% H<sub>2</sub>/Ar (400 °C, 1 h), non-alloyed Zn was observed as ZnO at 32° and 34° in the catalysts with higher zinc loadings: 5% Pd:Zn(1:5)/TiO<sub>2</sub> and 5% Pd:Zn(1:10)/TiO<sub>2</sub>. Presumably the PdZn alloy was saturated with zinc and no further zinc incorporation was possible. 5% Pd:Zn(1:1)/TiO<sub>2</sub> and 5% PdZn(1:2)/TiO<sub>2</sub> showed no ZnO peaks after reduction, indicating its absence or that its crystallite size was beyond the XRD detection limit (figure 7.5b).

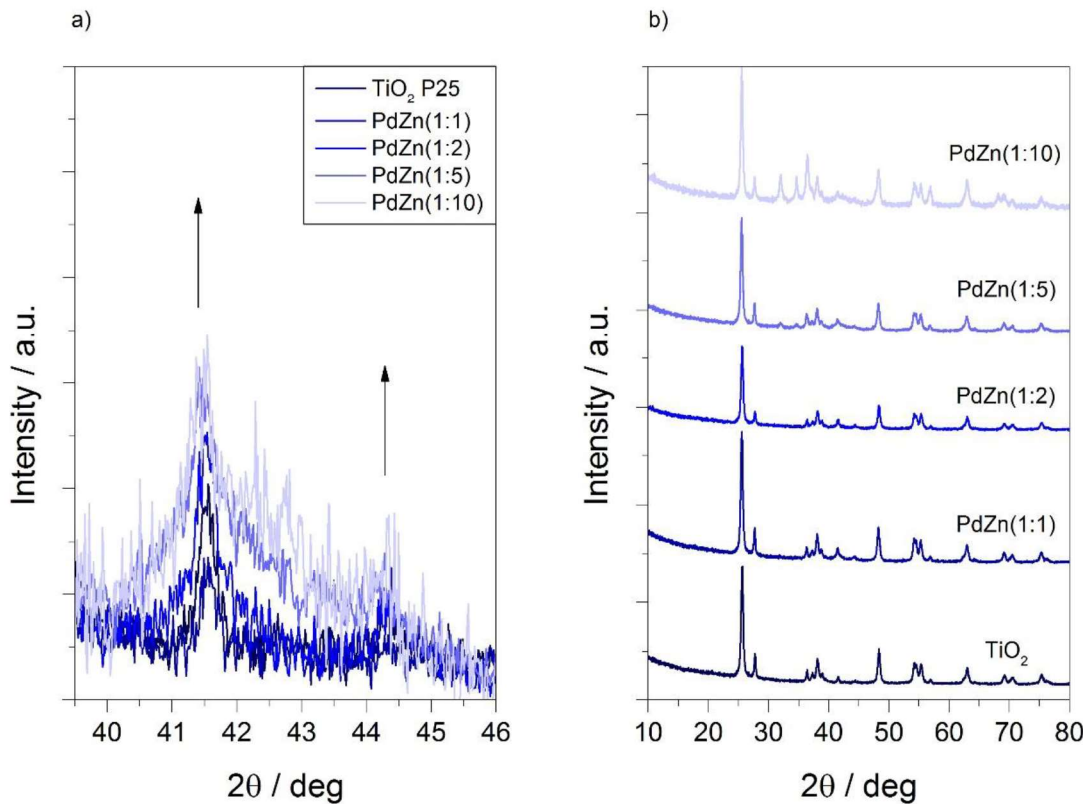


**Figure 7.5.** XRD patterns for 5% PdZn(1:1 to 1:10)/TiO<sub>2</sub> P25 after both annealing in air (500 °C, 16 h) and subsequent reduction in 5% H<sub>2</sub>/Ar (400 °C, 1 h). a) zoom between 40° and 46° to focus on the PdZn alloy reflections region and b) complete XRD region.

#### X-ray photoelectron spectroscopy (XPS)

*In situ* XRD in Fig. 7.2 for 5% Pd/ZnO SIM showed that the β-PdZn alloy started to form at 350 °C under reducing conditions. This in agreement with previous literature on 5% Pd/ZnO SIM, where PdZn alloy formation was detected by XPS between 250 °C and 400 °C.<sup>(7)</sup> Similarly, Zsoldos *et al.* reported that the transition from metallic palladium to PdZn alloy can be observed by XPS on a 8 % Pd/ZnO catalyst prepared by mechanical mixing after reducing from 147 °C to 607 °C.<sup>(19)</sup> The Pd(3d) peak at 335.0 eV observed after reduction at 147 °C was assigned to Pd<sup>0</sup>, however, after reduction at 607 °C a shoulder corresponding to PdZn formation appeared at 336.0 eV.<sup>(19)</sup> Hydrogen dissociation on metallic palladium and consecutive hydrogen spill-over to the support produce the reduction of neighbouring ZnO to Zn, which then are incorporated into the Pd<sup>0</sup> lattice forming the PdZn alloy.<sup>(20)</sup> The shift in the core and valence orbitals of metallic Pd towards higher binding energy can be explained by the hybridisation of d-d orbitals from the palladium electron-rich 4d (almost fully occupied) band with the 4p and 4s zinc electron-poor orbitals. The electron density of the Pd(4d) is also distributed with the Pd(5s) and Pd(5p) orbitals. Hence a decrease in the electron

population of Pd(4d) is observed with a gain in the electron population for Pd(5s, 5p) orbitals. Since electrons are moving from inner and localised orbitals, 4d orbitals, to more external and less defined orbitals, 5s and 5p, electron-electron repulsion decreased and the core orbitals are shifted towards higher binding energy.<sup>(21)</sup>

As Pd, PdZn alloy and PdO are reported to be well distinguished by XPS, palladium speciation through the Pd(3d) orbital was performed for 5% PdZn/(1:1 to 1:10)/TiO<sub>2</sub> catalysts (figure 7.6). According to the proposed PdZn growth mechanism revealed by *in situ* XRD characterisation, metallic palladium is formed first and then zinc is reduced by hydrogen spill-over and incorporated into the palladium lattice to form the alloy. Therefore, the presence of metallic Pd in all PdZn catalysts after pre-reduction (400 °C, 1 h) was expected. At the lowest zinc concentration: PdZn(1:1)/TiO<sub>2</sub>, palladium was predominantly in its metallic form as indicated by the Pd(3d) peak centred at 334.9 eV. Increasing the zinc concentration to (1:10) led to a shift of the Pd(3d) peak from 334.9 eV to 336.2 eV indicating that palladium speciation evolved from metallic Pd to PdZn alloy.

The β-PdZn alloy phase is not equimolar, one atom of zinc per atom of palladium, and the zinc proportion in the alloy can range from 40 at. % to 60 at. %.<sup>(22)</sup> This variation on the atomic composition of the PdZn alloy can explain the increase in the PdZn alloy phase observed by XRD (figure 7.5) and XPS (figure 7.6) with increasing the zinc concentration in the material. From the XRD and XPS characterisation, it can be concluded that the PdZn alloy was saturated in zinc (60 at. % of Zn) on the PdZn(1:5)/TiO<sub>2</sub> catalyst, since further incorporation of zinc (PdZn(1:10)/TiO<sub>2</sub>) led to no PdZn peak enhancement.

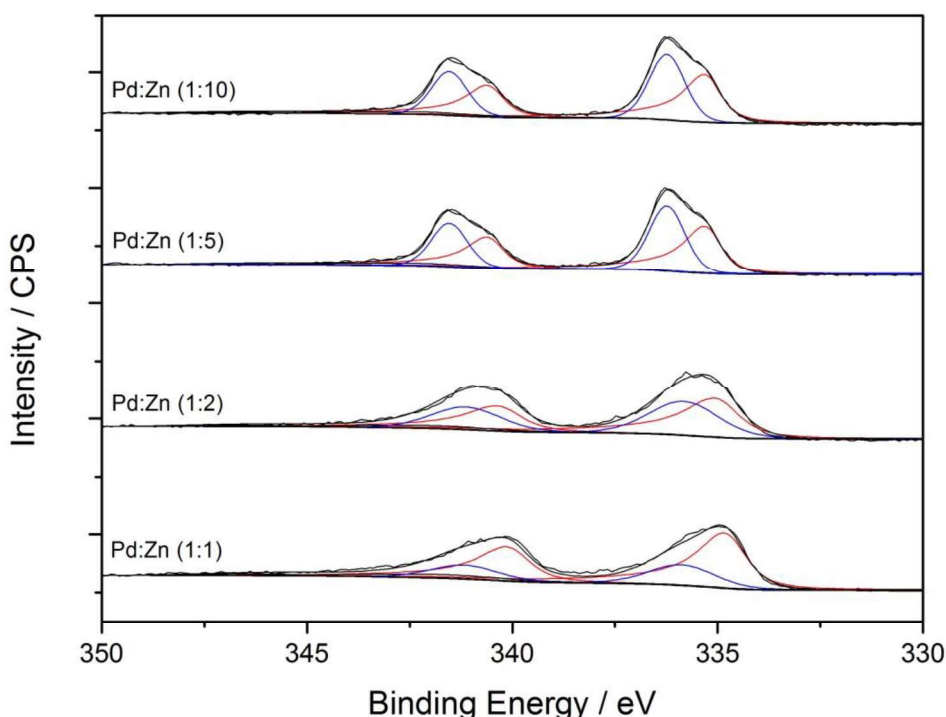


**Figure 7.6.** Pd(3d) XPS scan for 5% PdZn(1:1 to 1:10)/TiO<sub>2</sub> after annealing in static air (500 °C, 16 h) followed by reduction in 5% H<sub>2</sub>/Ar (400 °C, 1 h). Pd<sup>0</sup> and PdZn represented in red and blue fitting respectively.

Zn(2p) and Zn(LM<sub>2</sub>) orbitals were also analysed by XPS. The Zn(2p) core orbital is non-sensitive towards chemical changes in the zinc environment, even metallic zinc cannot be differentiate from its oxide using this orbital.<sup>(23, 24)</sup> For this reason, the remaining elements were calibrated towards the zinc 2p orbital at 1022 eV. As observed in figure 7.7a for the Zn(2p) orbital, apart from increased signal intensity, no change were detected with varying the zinc concentration. This might be expected from its low sensitivity towards chemical changes. On the other hand, Zn(LM<sub>2</sub>) is more sensitive to chemical changes. Metallic zinc has a major kinetic energy peak at 992 eV with a minor satellite contribution peak at 996 eV,<sup>(25)</sup> while these are shifted to 988 eV and 991 eV respectively for its oxide.<sup>(26)</sup> Surface metallic zinc is believed to re-oxidise to ZnO when exposed to air. The Zn(LM<sub>2</sub>) orbital for PdZn(1:1 to 1:10)/TiO<sub>2</sub> catalysts at 988 eV and 991 eV indicated the presence of ZnO as the main zinc component (figure 7.7b) albeit being pre-reduced at 400 °C in 5% H<sub>2</sub>. However, at higher Zn loadings: 5% PdZn(1:5)/TiO<sub>2</sub> and 5% PdZn(1:10)/TiO<sub>2</sub>, a perceptible shoulder appears at 995 eV. This shoulder can be assigned to formation of β-PdZn alloy or to the presence of oxygen vacancies within the ZnO lattice.<sup>(27)</sup> Reduction studies carried out on commercial Cu/ZnO/Al<sub>2</sub>O<sub>3</sub> catalyst and commercial ZnO showed that under reductive

treatment, the Cu-containing catalyst developed a shoulder in the Zn(LM<sub>2</sub>) orbital assigned to formation of the CuZn alloy whereas the Zn(LM<sub>2</sub>) for ZnO did not change during the reduction treatment.<sup>(28)</sup> XRD and Pd(3d) XPS characterisation therefore confirm the presence of  $\beta$ -PdZn, as the shoulder at 995 eV on the Zn(LM<sub>2</sub>) orbital can be assigned to this alloy.

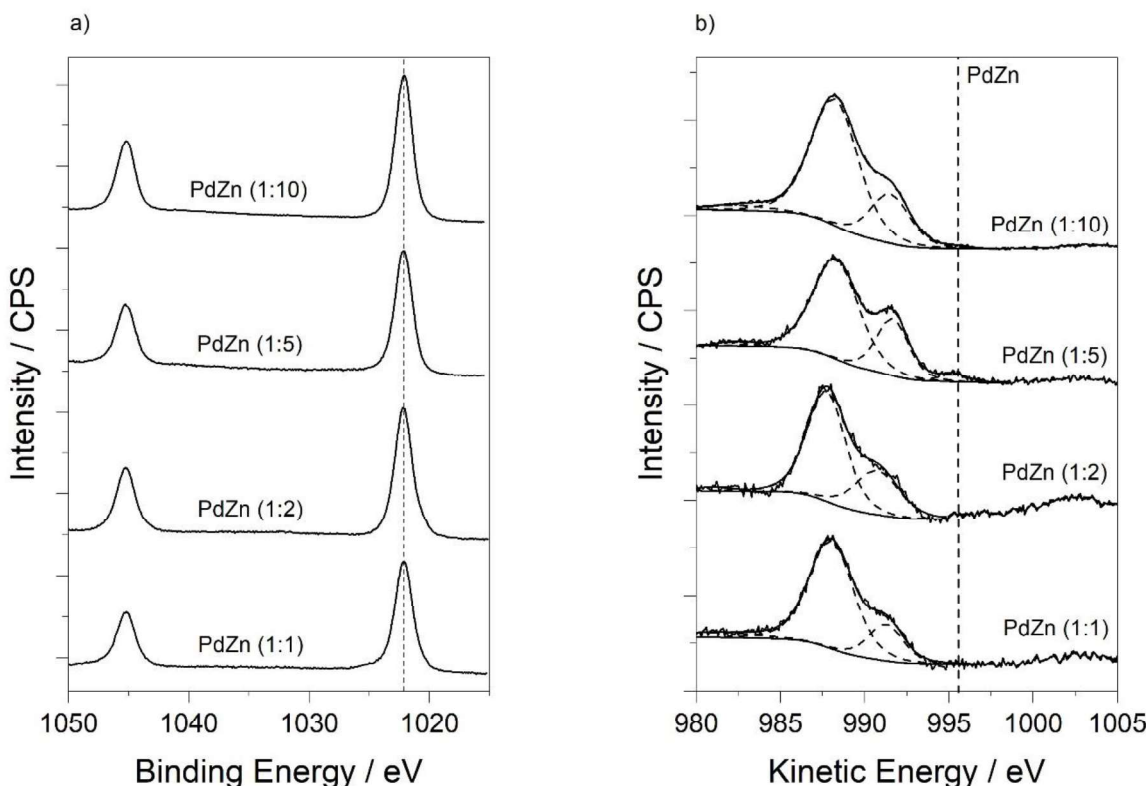


**Figure 7.7.** a) Zn(2p) and b) Zn(LM<sub>2</sub>) XPS characterisation for 5% PdZn(1:1 to 1:10)/TiO<sub>2</sub> catalysts after annealing in static air (500 °C, 16 h) and subsequent reduction in 5% H<sub>2</sub>/Ar (400 °C, 1 h).

Titanium and oxygen are the main components of the catalysts since TiO<sub>2</sub> (P25) was used as support. Thus, Ti(2p) and O(1s) orbitals were recorded as well. As expected from titania being a relatively inert support, no changes were observed in the Ti(2p) orbital (figure 7.8a).

A similar situation was observed in the O(1s) orbital, oxygen is present mainly as lattice oxide, TiO<sub>2</sub> and ZnO, by the peak at 530 eV. A less intense shoulder at 531.6 eV was also observed, this can be related to the presence of hydroxides or carbonates, formed during the decomposition of the acetylacetone ligand (figure 7.8b).

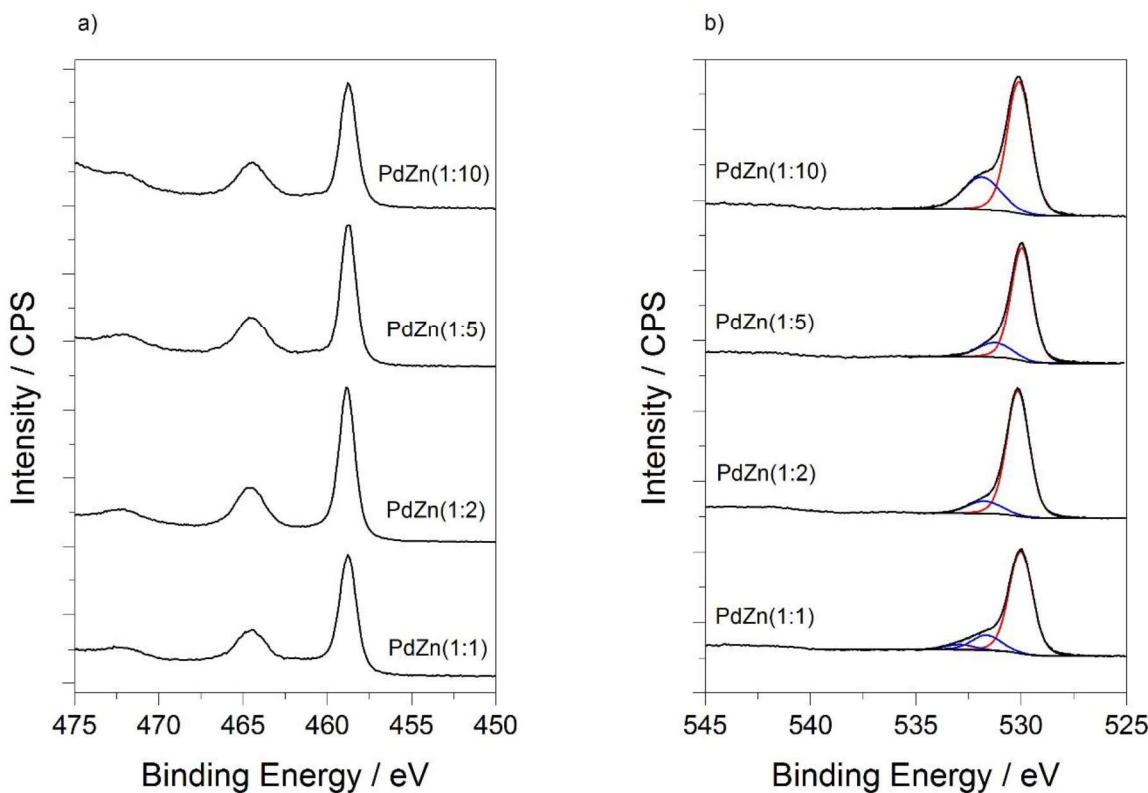


**Figure 7.8.** a) Ti(2p) and b) O(1s) XPS characterisation for 5% PdZn(1:1 to 1:10)/TiO<sub>2</sub> catalysts after annealing in static air (500 °C, 16 h) followed by reduction in 5% H<sub>2</sub>/Ar (400 °C, 1 h). Lattice oxygen (ZnO/TiO<sub>2</sub>) and hydroxides/carbonates are represented in a red and blue fitting respectively.

#### *Surface area measurement by BET*

The successful synthesis of PdZn after pre-reduction was confirmed by XRD and XPS. To follow surface area changes that can occur on TiO<sub>2</sub> after catalyst preparation, Zn and Pd impregnation, calcination (500 °C, 16 h) and reductive (400 °C, 1 h) heat treatment, BET analysis was performed. Commercial zinc oxide (Sigma Aldrich, 15 m<sup>2</sup>·g<sup>-1</sup>) has lower surface area compared to titania (Sigma Aldrich P25, 50 m<sup>2</sup>·g<sup>-1</sup>). As previously described, the palladium loading was 5 wt. % for all catalysts, while the Pd:Zn molar ratio changed between (1:1) and (1:10). Therefore, excess of zinc in the material is expected, in the form of ZnO as observed in the Zn(LM)<sub>2</sub> orbital, which can decrease the surface area of the material. Additionally, further decrease in the surface area might be expected from carbon contamination formed by the thermal decomposition of metal precursors, Pd(acac)<sub>2</sub> and Zn(acac)<sub>2</sub>.

Prior to surface area analysis, samples were degased under vacuum (130 °C, 3 h) in the BET tube. Measured surface areas are showed in table 7.1. As observed, the surface area of catalysts was not considerably affected by the addition of palladium and zinc or by the

consecutive heat treatments. Considering the deviation of approximately 10 % in BET measurements, no significant changes on the surface area were detected.

**Table 7.1.** Surface areas obtained by BET for 5% PdZn(1:1 to 1:10)/TiO<sub>2</sub> after calcination in air (500 °C, 16 h) and consecutive reductive heat treatment (400 °C, 1 h).

Material	BET surface area (m <sup>2</sup> /g)
TiO <sub>2</sub> P25	50 ± 5
PdZn (1:1)/TiO <sub>2</sub>	49 ± 5
PdZn (1:2)/TiO <sub>2</sub>	41 ± 4
PdZn (1:5)/TiO <sub>2</sub>	44 ± 4
PdZn (1:10)/TiO <sub>2</sub>	47 ± 5

#### *Transmission electron microscopy (TEM)*

The particle size of the active phase greatly influences the catalytic properties. Generally, smaller metal nanoparticles translate in enhanced catalyst's surface area and the number of active sites, higher activity is hence expected. To determine the PdZn particle size and its distribution after calcination in air (500 °C, 16 h) and consecutive reduction in 5% H<sub>2</sub>/Ar (400 °C, 1 h) catalysts were characterised by TEM.

TEM images are shown in image 7.1, regardless of the Pd:Zn molar ratio, homogeneous, small ( $\approx$ 4 nm) and well dispersed nanoparticles were observed throughout the support. The electron beam transmitted through the sample is greatly disturbed by Pd-containing nanoparticles as a result of its higher atomic mass compared to Ti, O or Zn, hence PdZn nanoparticles are observed darker than the support. ZnO was detected by XRD on catalyst with the highest zinc concentration: PdZn(1:5)/TiO<sub>2</sub> and PdZn(1:10)/TiO<sub>2</sub>. Therefore, it would be expected to observe agglomeration of ZnO particles by TEM. Nevertheless, the presence of ZnO could not be distinguished from TiO<sub>2</sub> or PdZn. Darker regions were observed but most probably corresponded to sample charging instead of to the presence of ZnO.

To compare accurately differences between 5% PdZn(1:1 to 1:10)/TiO<sub>2</sub> catalysts, particle size distribution histograms were obtained using image J software.<sup>(29)</sup> To minimise the error in the calculation of the particle size and its distribution a minimum of 100 particles were analysed for each catalyst. As shown in the particle size distribution histogram in figure 7.9, increasing the zinc concentration produced no significant changes in the particle size, since the standard deviation for each catalyst included the remaining catalyst's main sizes. For

instance, the PdZn particle size for 5% PdZn(1:1)/TiO<sub>2</sub> and 5% PdZn(1:10)/TiO<sub>2</sub> was 4.46 ± 1.61 nm and 3.95 ± 1.06 nm respectively.

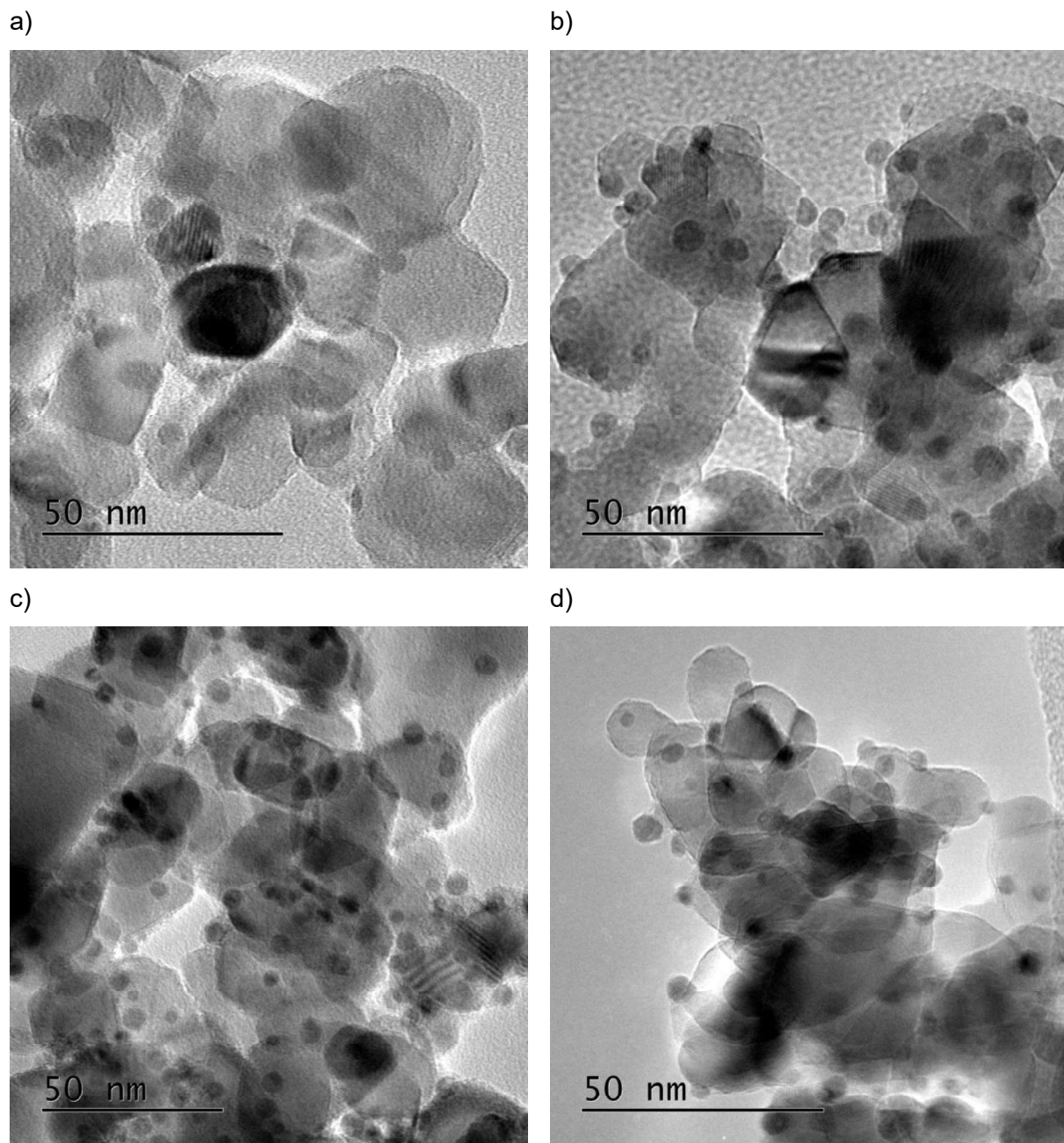


**Image 7.1.** TEM images obtained for 5% PdZn/TiO<sub>2</sub> catalysts with a Pd:Zn molar ratio of a) (1:1), b) (1:2), c) (1:5) and d) (1:10) after annealing in air (500 °C, 16 h) and subsequent reduction in 5% H<sub>2</sub>/Ar (400 °C, 1h).

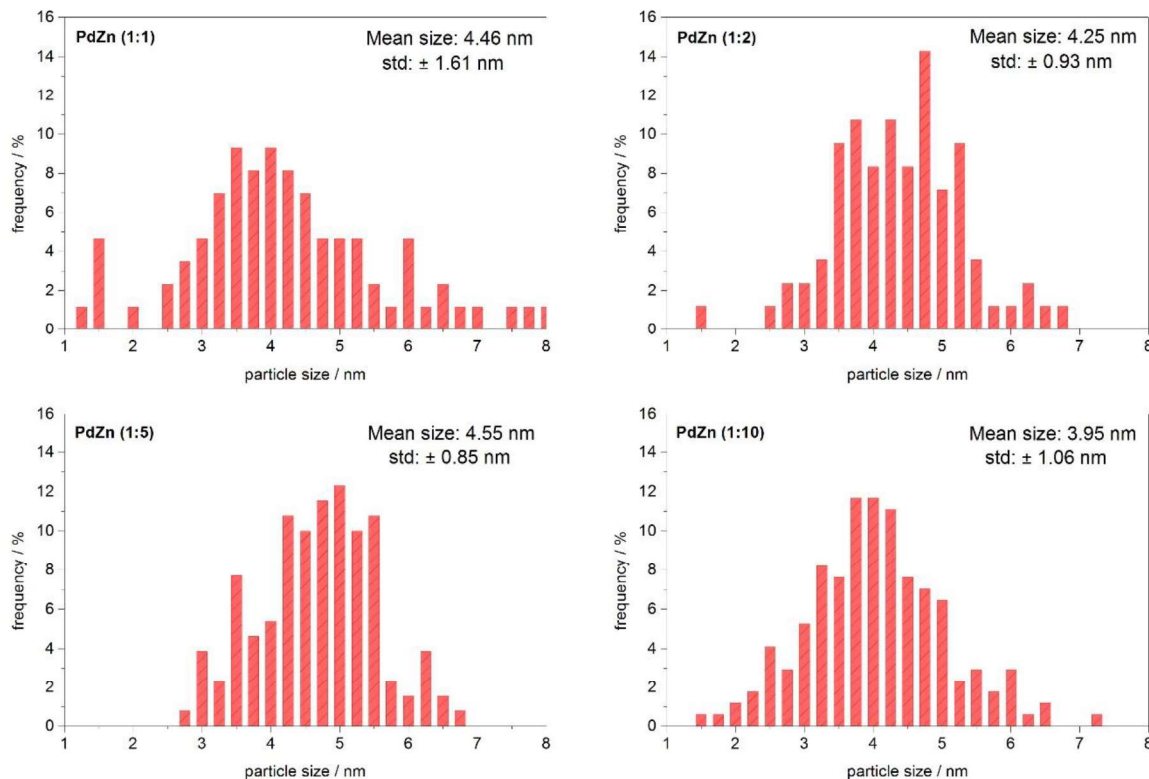


**Figure 7.9.** Particle size histogram obtained by TEM for PdZn(1:1 to 1:10)/TiO<sub>2</sub> catalysts after annealing in air (500 °C, 16 h) followed by reductive heat treatment in 5% H<sub>2</sub>/Ar (400 °C, 1h).

### 7.2.3 Catalyst activity.

Annealing in air (500 °C, 16 h) was necessary to remove the organic part from the organometallic precursor: Pd(acac)<sub>2</sub> and Zn(acac)<sub>2</sub>. As reported previously in literature for 5% Pd/ZnO catalyst prepared by CVI, if the catalyst was assessed towards the CO<sub>2</sub> hydrogenation (20 bar, 250 °C) without previous annealing but pre-reduced (pure H<sub>2</sub>, 30 ml·min<sup>-1</sup>, 400 °C, 1 h) a 97 % CO selectivity and 88 mmol·kg<sub>cat</sub><sup>-1</sup>·h<sup>-1</sup> methanol productivity was measured. However, annealing in air (500 °C, 16 h) prior to reaction led to the decrease in the CO selectivity to 68 % and the methanol productivity increase to 1070 mmol·kg<sub>cat</sub><sup>-1</sup>·h<sup>-1</sup>.<sup>(14)</sup>

The promoting effect of Zn on a Pd-based catalyst was also reported towards promoting the CO<sub>2</sub> hydrogenation (20 bar, 250 °C) selectivity towards methanol. The CO selectivity over 90 % observed for 5% Pd/TiO<sub>2</sub> and 5% Pd/Al<sub>2</sub>O<sub>3</sub> catalysts shifted towards methanol, (53 %, 1510 mmol<sub>MeOH</sub>·kg<sub>cat</sub><sup>-1</sup>·h<sup>-1</sup>) and (19 % 635 mmol<sub>MeOH</sub>·kg<sub>cat</sub><sup>-1</sup>·h<sup>-1</sup>) respectively, after the addition of ten equivalents of zinc.<sup>(14)</sup>

Prior to testing, catalysts were pelleted (10 ton, 600 µm - 425 µm mesh) and pre-reduced *in situ* in pure hydrogen (30 ml·min<sup>-1</sup>, 400 °C, 1 h).

CO<sub>2</sub> hydrogenation data (250 °C, 20 bar, 60 % H<sub>2</sub>, 20 % CO<sub>2</sub>, 20 % N<sub>2</sub>) obtain for 5% PdZn(1:1 to 1:10)/TiO<sub>2</sub> catalysts is presented in table 7.2, catalytic data obtained previously in the group for 5% Pd/TiO<sub>2</sub> prepared by CVI is also included for comparison.<sup>(14)</sup> In agreement with the literature, the 3.0 % methanol selectivity observed for Pd/TiO<sub>2</sub> increased to 16.7 % after the addition of one equivalent of zinc. Increasing further the Pd:Zn molar ratio, from (1:1) to (1:10), translated in no significant improvement in methanol selectivity. Nevertheless, the CO<sub>2</sub> conversion increased progressively from 7.3 % to 9.5 % with increasing the Pd:Zn molar ratio from (1:1) to (1:5). The further increase in the Pd:Zn molar ratio to (1:10) led to a decrease in the CO<sub>2</sub> conversion.

**Table 7.2.** CO<sub>2</sub> hydrogenation catalytic data for 5% PdZn(1:1 to 1:10)/TiO<sub>2</sub> catalysts (250 °C, 20 bar, 30 ml·min<sup>-1</sup>, 20 % CO<sub>2</sub>, 20 % N<sub>2</sub>, 60 % H<sub>2</sub>). Prior to reaction catalysts were annealed in air (500 °C, 16 h) and reduced *in situ* in hydrogen (400 °C, 1 h). Catalytic data corresponds to 3 hours of reaction.

Catalyst	CO <sub>2</sub> conv. %	CH <sub>3</sub> OH sel. %	CO sel. %	CH <sub>3</sub> OH prod. mmol Kg <sub>cat</sub> <sup>-1</sup> h <sup>-1</sup>
5% Pd/TiO <sub>2</sub>	6.8 ± 0.1	3.0 ± 0.1	97.0 ± 0.1	80.4 ± 2
5% PdZn(1:1)/TiO <sub>2</sub>	7.3 ± 0.3	16.7 ± 1.5	83.3 ± 1.5	610 ± 31
5% PdZn(1:2)/TiO <sub>2</sub>	9.1 ± 0.5	15.1 ± 1.0	84.9 ± 1.0	584 ± 47
5% PdZn(1:5)/TiO <sub>2</sub>	9.5 ± 0.8	16.7 ± 1.1	83.3 ± 1.1	711 ± 59
5% PdZn(1:10)/TiO <sub>2</sub>	7.1 ± 0.9	18.9 ± 1.5	81.1 ± 1.5	468 ± 87

Characterisation performed on 5% PdZn(1:1 to 1:10)/TiO<sub>2</sub> catalysts confirmed the PdZn alloy formation after pre-reduction in 5% H<sub>2</sub>/Ar (400 °C, 1 h). Increasing the Zn concentration led to an increase in the PdZn formation by XRD and XPS, which can explain the CO<sub>2</sub> conversion. However, the CO<sub>2</sub> conversion decreased for 5% PdZn(1:10)/TiO<sub>2</sub>, which can relate to the formation of ZnO, as observed by XRD. The excessive concentration of zinc can block active sites present in the material. Thus, the best methanol productivity (711 mmol<sub>MeOH</sub>·kg<sub>cat</sub><sup>-1</sup>·h<sup>-1</sup>) was observed for 5% PdZn(1:5)/TiO<sub>2</sub> catalyst.

### 7.3 Catalyst optimisation by high temperature pre-reduction.

#### 7.3.1 Reduction at 400 °C, 550 °C and 650 °C for the 5 % PdZn(1:5)/TiO<sub>2</sub> catalyst.

From the presented results, the best palladium to zinc molar ratio was 1:5. Since zinc was in a five-fold molar concentration compared to palladium, and the  $\beta$ -PdZn phase can accommodate an atomic zinc proportion between 40 % and 60 %, it can be expected that the pre-reduction of 5% PdZn (1:5)/TiO<sub>2</sub> at higher temperature could increase the zinc concentration in the alloy, which might improve the methanol selectivity. This was observed in the literature for 5% Pd/ZnO prepared by sol-immobilisation, where increasing pre-reduction temperature from 150 °C to 750 °C led to a progressive increase in the methanol selectivity from 48 % to 72 %, which was associated with the higher formation of  $\beta$ -PdZn alloy.<sup>(7)</sup>

To prove the hypothesis that higher pre-reduction temperature can translate in improved methanol selectivity, the 5% PdZn (1:5)/TiO<sub>2</sub> catalyst was pre-reduced in 5% H<sub>2</sub>/Ar at 550 °C and 650 °C for 1 h. Previous reports on 5% Pd/ZnO prepared by SIM showed, that although higher methanol selectivity occurred with increasing the reductive heat treatment temperature from 150 °C to 750 °C, the CO<sub>2</sub> conversion decreased after pre-reduction above 400 °C. This was assigned to the increased in the particle size observed after reduction at 400 °C and at 700 °C (3.2 nm and 25.3 nm respectively).<sup>(7)</sup> However, PdZn particle sintering with increasing pre-reduction temperature is expected to be less severe for 5% PdZn(1:5)/TiO<sub>2</sub> because of its better dispersion. Furthermore, strong metal-support interactions were reported for Pd and TiO<sub>2</sub> which might limit PdZn particle agglomeration.<sup>(30, 31)</sup> Hypothetically, reduction at higher temperature would increase the amount of zinc in the alloy, without considerably increasing the PdZn particle size, leading to higher selectivity towards methanol but without hampering CO<sub>2</sub> conversion.

#### *Catalyst characterisation*

As shown in figure 7.10, in addition to rutile and anatase TiO<sub>2</sub> reflections, after reducing heat treatment at 400 °C the formation of  $\beta$ -PdZn at 41.1° and 44.4° the presence of ZnO at 31.9° and 34.5° were observed in the XRD pattern. After pre-reduction in 5% H<sub>2</sub>/Ar at 550 °C, new peaks at 24.0°, 31.9° and 35.5° were detected. Since PdTi has been reported in the literature,<sup>(32)</sup> the first thought was to assign those new reflections to PdTi alloy formed via a similar mechanism as PdZn. However, the first PdTi reflection appears close to 40° and hence the presence of this crystallographic phase was discarded. Eventually, the new detected reflections were assigned to rhombohedral ZnTiO<sub>3</sub> (JCDs-26-1500).<sup>(33, 34)</sup> After reduction at 650 °C, these reflections intensified and sharpened as a result of higher

crystallinity and larger crystallite domains. Interestingly, ZnO reflections observed after pre-reduction at 400 °C and at 550 °C vanished, whilst PdZn peaks remained unchanged, indicating that just non-alloyed Zn was incorporated into the TiO<sub>2</sub> lattice. Increasing the pre-reduction temperature, from 400 °C to 550 °C and to 650 °C, led to progressive reduction in the BET surface area, from 44 m<sup>2</sup>·g<sup>-1</sup> to 39 m<sup>2</sup>·g<sup>-1</sup> and to 29 m<sup>2</sup>·g<sup>-1</sup> respectively. As it will be shown in the following section, the reduction in the surface area is assigned to TiO<sub>2</sub> transition to ZnTiO<sub>3</sub>, with respective surface area of 50 m<sup>2</sup>·g<sup>-1</sup> and 17 m<sup>2</sup>·g<sup>-1</sup>, and to the conversion of anatase TiO<sub>2</sub> to the denser rutile phase TiO<sub>2</sub>.

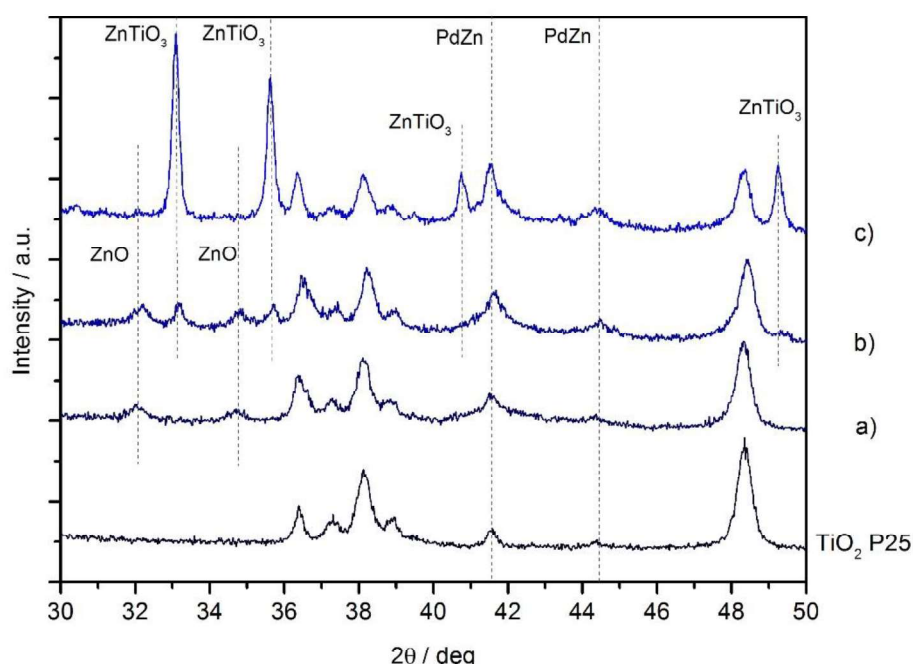


**Figure 7.10.** XRD patterns for 5% PdZn(1:5)/TiO<sub>2</sub> catalyst annealed in static air (500 °C, 16 h) followed by reduction in 5% H<sub>2</sub>/Ar at a) 400 °C, b) 550 °C and c) 650 °C. As received TiO<sub>2</sub> P25 (Sigma Aldrich) included for comparison.

Reduction above 400 °C showed the incorporation of ZnO into the TiO<sub>2</sub> lattice, forming ZnTiO<sub>3</sub> mixed oxide. From the XRD characterisation it is proposed that Zn within the PdZn remained in the alloy during reductive treatment at 650 °C, instead ZnTiO<sub>3</sub> is formed from non-alloyed Zn and TiO<sub>2</sub>. The  $\beta$ -PdZn reflections increased in intensity with increasing reductive heat treatment temperature, indicating a higher concentration of PdZn alloy or the formation of larger domains, which might increase the methanol selectivity. Counterproductively, the surface area decreased with pre-reduction temperature, which is expected to have a detrimental effect on the activity.

### Catalyst activity

For safety reasons 5% PdZn(1:5)/TiO<sub>2</sub> catalysts were pre-reduced in 5% H<sub>2</sub>/Ar at 400 °C, 550 °C and 650 °C in a separate furnace using a calcination boat prior to its transfer into the reaction tube. Because catalysts were in contact with air in its transfer to the reaction tube, which could lead to surface passivation, pre-reduction at 400 °C for 1 h was performed *in situ* (H<sub>2</sub>, 30 ml·min<sup>-1</sup>, 400 °C, 1 h) prior to reaction (250 °C, 20 bar, 30 ml·min<sup>-1</sup>, 60 % H<sub>2</sub>, 20 % CO<sub>2</sub>, 20 % N<sub>2</sub>).

Obtained catalytic data is summarised in table 7.3. The progressive decrease in the surface area, detected by BET, with increasing the reductive heat treatment temperature had no significant effect on the CO<sub>2</sub> conversion. In fact, CO<sub>2</sub> conversion increased from 9.5 % to 11.2 % after increasing the pre-reduction temperature from 400 °C to 550 °C, with improved methanol selectivity from 17 % to 22 %. Higher pre-reduction at 650 °C, however, seemed to decrease the CO<sub>2</sub> conversion and the methanol selectivity to 10.6 % and 16 % respectively, comparable to pre-reduction at 400 °C. Nevertheless, one paramount trend was observed. In the previous section methane, formed from the complete hydrogenation of CO<sub>2</sub>, was detected in the GC at trace levels for 5% PdZn(1:1 to 1:10)/TiO<sub>2</sub> catalysts at comparable productivities. Methane is a problematic by-product since it would increase the industrial production cost.<sup>(35)</sup> The formation of CO is not necessarily an inconvenient since the gas products can be easily re-cycled into the reactor, whereas the presence of methane would add an additional gas phase purification step.

After pre-reduction at 550 °C and at 650 °C, and simultaneously with the formation of ZnTiO<sub>3</sub>, methane selectivity decreased in one order of magnitude, close to the detection limit, compared to pre-reduction at 400 °C.

**Table 7.3.** CO<sub>2</sub> hydrogenation data over 5% PdZn(1:5)/TiO<sub>2</sub> catalyst annealed at 500 °C for 16 h in static air followed by *ex-situ* pre-reduced at 400 °C, 550 °C and 650 °C. Catalysts were pre-reduced in the reactor tube at 400 °C for 1 h in H<sub>2</sub>. Reaction conditions: 250 °C, 20 bar, 30 ml / min CO<sub>2</sub> (20%), H<sub>2</sub> (60%), N<sub>2</sub> (20%).

Reduction	Temp. / °C	CO <sub>2</sub> conv. / %	CH <sub>3</sub> OH sel. / %	CO sel. / %	CH <sub>4</sub> sel. / %
	400	9.5	16.7	83.3	0.02
	550	11.2	21.8	78.2	0.005
	650	10.6	16.3	83.7	0.002

### 7.3.2 Different Palladium loading and ZnTiO<sub>3</sub> phase formation effect.

As observed for the 5% PdZn(1:5)/TiO<sub>2</sub> prepared by CVI, the formation of ZnTiO<sub>3</sub> induced by reductive treatment above 400 °C considerably decreased CH<sub>4</sub> production. Minimising methane production is important for industrial applications, otherwise, a gas phase purification step must be added, which the concomitant economical increase in methanol production. Additionally, the production of CH<sub>4</sub> is accompanied by an extra consumption of H<sub>2</sub> compared to the production of methanol. Then, it is worth mentioning that the aim of this chapter is to store renewable energy, in the form of hydrogen, to facilitate the energy transition from finite resources. Additionally, the co-feed of CO and CO<sub>2</sub> is proved to enhance methanol yield in the commercial syngas route over Cu/Zn/Al<sub>2</sub>O<sub>3</sub> catalyst.<sup>(2, 36)</sup>

#### *Catalyst preparation and characterisation*

3 g of catalysts with a palladium loading of 1 wt. %, 2.5 wt. % and 5 wt. % and a Pd:Zn (1:5) molar ratio were prepared following the CVI procedure described previously. Catalysts were annealed in static air (500 °C, 16 h) followed by pre-reduction in 5% H<sub>2</sub>/Ar at 400 °C or 650 °C for 1 h. Catalysts with different palladium loading reduced at 400 °C were first compared by XRD in figure 7.11. No PdZn or ZnO reflection were detected for 1 % and 2.5 % PdZn(1:5)/TiO<sub>2</sub> catalysts. However, the β-PdZn peaks overlap with (111) and (201) rutile TiO<sub>2</sub> reflections at 41° and 44°, making the detection of PdZn challenging. However, the peak at 41° increased in intensity for the 5% PdZn(1:5)/TiO<sub>2</sub> catalyst, indicating the presence of PdZn. ZnO was also observed at 31.8°. Constant Pd:Zn molar ratio (1:5) translated in higher zinc concentration with increasing the palladium loading. This explains the detection of ZnO on the 5% PdZn(1:5)/TiO<sub>2</sub> catalysts but not on the 1% and 2.5% PdZn(1:5)/TiO<sub>2</sub>.

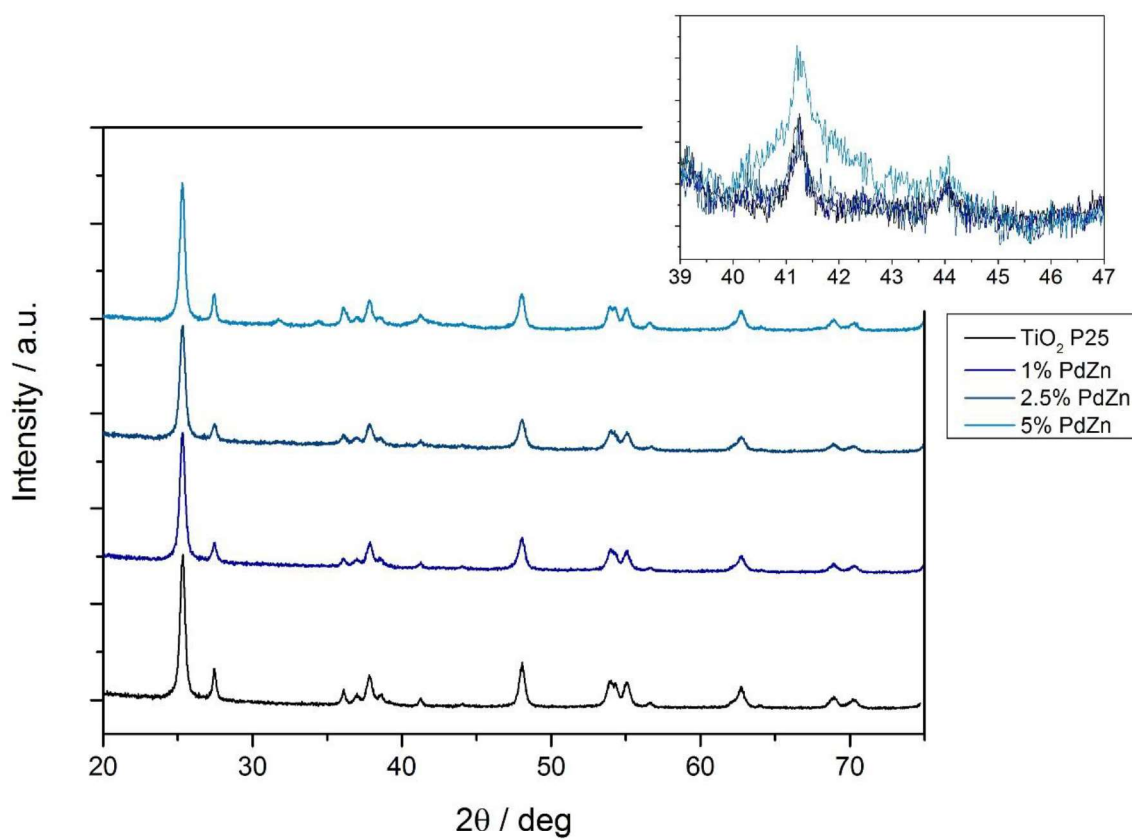


**Figure 7.11.** XRD patterns for PdZn(1:5)/TiO<sub>2</sub> catalysts with a 1 wt. %, 2.5 wt. % and 5 wt. % Pd loading after annealing in static air (500 °C, 16 h) followed by pre-reduction in 5% H<sub>2</sub>/Ar (400 °C, 1 h).

After reductive heat treatment at 650 °C, rhombohedral ZnTiO<sub>3</sub> was detected for 2.5 % and 5 % PdZn(1:5)/TiO<sub>2</sub> catalysts (figure 7.12). Increasing Pd loading, and hence Zn loading, led to an increase in the ZnTiO<sub>3</sub> peak intensity, indicating that more zinc was incorporated into the TiO<sub>2</sub> lattice. Additionally, the intensity of the PdZn alloy reflections at 41.4° and 44.1° intensified, indicating the formation of larger PdZn crystallites.

At a constant palladium loading, increasing the reductive heat treatment temperature resulted in an increase in the PdZn peaks intensity. On one hand this indicated the increase of PdZn alloy crystallite size; On the other, zinc incorporation to form ZnTiO<sub>3</sub> is restricted to non-alloyed zinc.

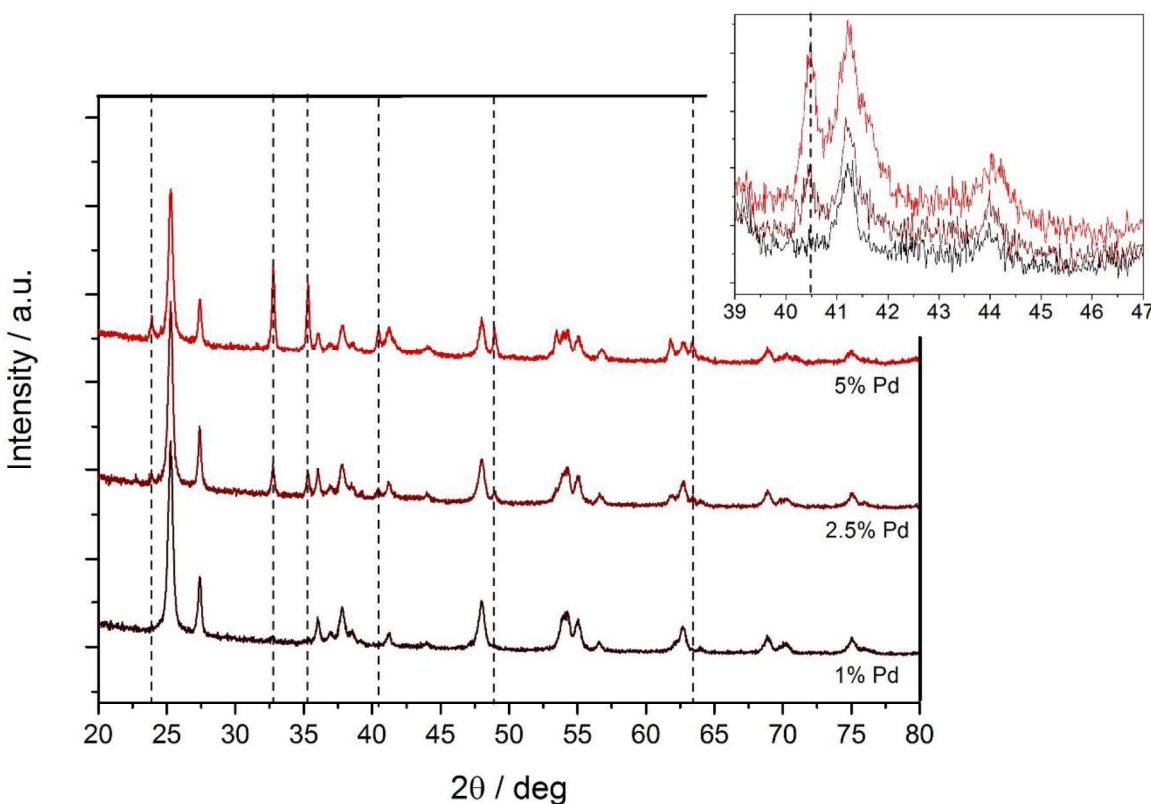


**Figure 7.12.** XRD patterns for 1%, 2.5% and 5% PdZn(1:5)/TiO<sub>2</sub> catalysts reduced at 650 °C in 5% H<sub>2</sub>/Ar. The position of rhombohedral ZnTiO<sub>3</sub> reflections are represented with dashed lines.

In order to detect the effect of phase transition after pre-reduction at 400 °C or 650 °C, the surface area was measured by BET (table 7.4). The surface area of TiO<sub>2</sub> (P25), 50 m<sup>2</sup>·g<sup>-1</sup>, was not altered after the impregnation of Pd and Zn by CVI, annealing in air (500 °C, 16 h) and pre-reduction in 5% H<sub>2</sub>/Ar (400 °C, 1 h). However, the surface area considerably decreased after pre-reduction at 650 °C for all catalysts, regardless of the palladium loading. One factor contributing to the reduction of the surface area after pre-reduction at 650 °C could be due to the anatase TiO<sub>2</sub> phase transformation to the denser rutile TiO<sub>2</sub>.<sup>(37)</sup> In order to confirm the TiO<sub>2</sub> phase transformation, the crystallite size TiO<sub>2</sub>, anatase and rutile, was determined through the Scherrer equation (Eq. 7.4).

$$\tau = \frac{K\lambda}{\beta \cos\theta} \quad \text{Eq. 7.4}$$

Where  $\tau$  is the crystallite size,  $\beta$  the reflection broadening at half maximum intensity,  $\theta$  is the reflection position,  $\lambda$  is the X-ray radiation wavelength used and  $K$  is a constant that depends on the crystallite shape.

As observed in table 7.4, no change in the anatase TiO<sub>2</sub> crystallite size was observed after pre-reduction at 650 °C compared to reductive heat treatment at 400 °C. Nevertheless, rutile TiO<sub>2</sub> crystallite size considerably increased, for all catalysts, after reduction at 650 °C. Another important phase transformation, taking place during reduction at 650 °C, is the ZnO incorporation into the TiO<sub>2</sub> lattice to form ZnTiO<sub>3</sub>. As observed by XRD, ZnTiO<sub>3</sub> reflections were not detected after reduction at 400 °C but unambiguously observed after reduction at 650 °C. As it will be shown later, the ZnTiO<sub>3</sub> surface area (15 m<sup>2</sup>·g<sup>-1</sup>) is considerably lower than that of TiO<sub>2</sub>.

**Table 7.4.** Surface area, analysed by BET, and crystallite size for anatase and rutile TiO<sub>2</sub>, measured using the Scherrer equation from XRD reflections, for 1%, 2.5% and 5% PdZn(1:5)/TiO<sub>2</sub> catalysts reduced at 400 °C and at 650 °C.

catalyst	Reduction Temperature / °C	BET Surface area / m <sup>2</sup> ·g <sup>-1</sup>	anatase / nm	Rutile / nm
1% PdZn/TiO <sub>2</sub>	400	49	25	25
	650	35	26	43
2.5% PdZn/TiO <sub>2</sub>	400	50	25	33
	650	40	28	51
5% PdZn/TiO <sub>2</sub>	400	44	27	32
	650	29	29	48

To determine if zinc incorporation into the PdZn alloy was further promoted after pre-reduction at 650 °C compared to pre-reduction at 400 °C catalysts were characterised by XPS.

Since reduction at 650 °C promoted formation of ZnTiO<sub>3</sub>, the Ti(2p) orbital was also analysed, as well as the Pd(3d), O(1s), Zn(2p) and Zn(LM<sub>2</sub>). As a standard procedure, elements were calibrated against the C(1s) at 284.8 eV. Carbon was still detected, even after annealing in air (500 °C, 16 h) followed by reduction in 5% H<sub>2</sub>/Ar (400 °C or 650 °C). However, when the XPS signals were calibrated against the carbon peak, the rest of elements (Ti, Pd, O and Zn) shifted without following a rational trend. For instance, the Pd(3d) orbital for 1% Pd catalyst shifted 0.3 eV towards lower binding energy after reduction at 650 °C compared to reduction at 400 °C, whilst for 2.5 % PdZn(1:5)/TiO<sub>2</sub> catalyst a 0.3 eV shift on the Pd(3d) orbital towards higher binding energy was observed (figure 7.13a). Another example is the 0.2 eV shift for the Ti(2p) orbital to lower binding energy for 1% PdZn(1:5)/TiO<sub>2</sub>, which can be explained by the formation of ZnTiO<sub>3</sub>, as reported for

SrTiO<sub>3</sub>.<sup>(38)</sup> However, it would be expected to observe this shift consistently with increasing the reductive heat treatment temperature, regardless of the palladium loading. Whereas for 2.5 % PdZn(1:5)/TiO<sub>2</sub> the opposite trend was observed, reduction at 650 °C led to a 0.4 eV shift toward higher binding energy compared to reduction at 400 °C (figure 7.13b). Similar trend was also observed for O(1s) and Zn(2p). Consequently, it was thought that the nature of the remaining carbon changed during reduction at 400 °C or 650 °C, and hence it is not suitable for peak calibration.

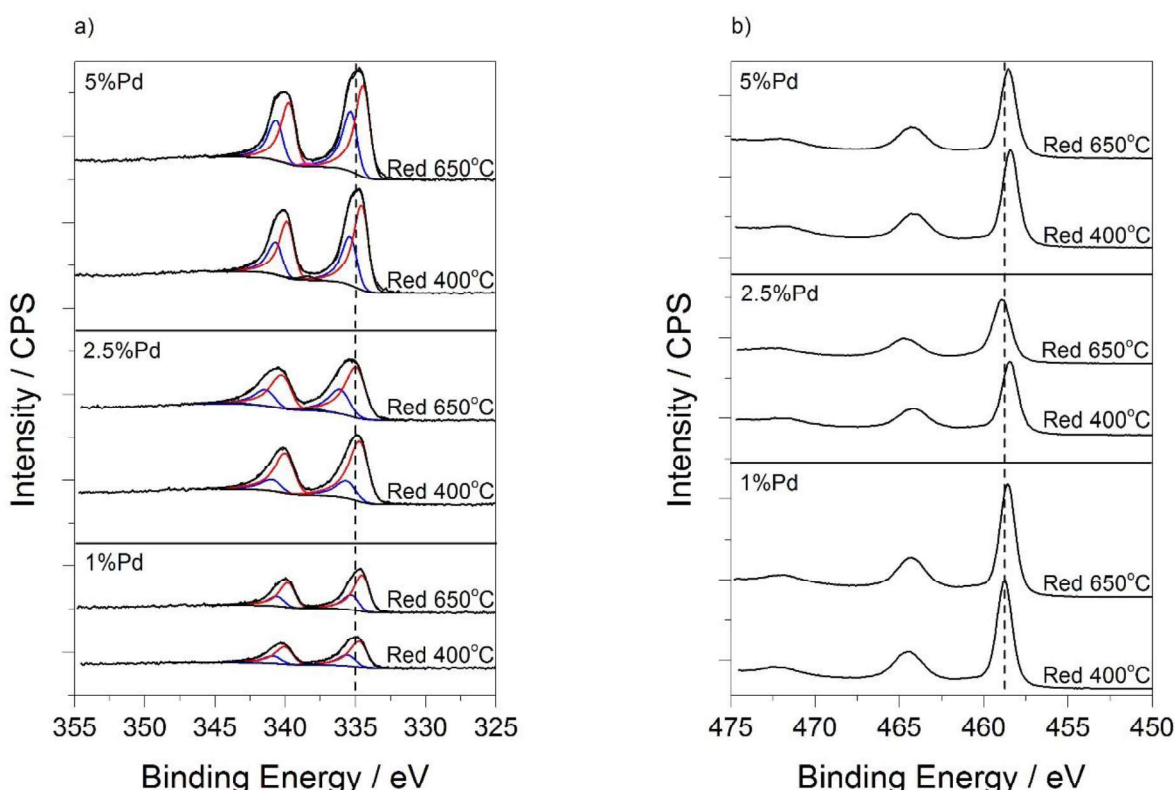


**Figure 7.13.** a) Pd(2p) and b) Ti(2p) for 1%, 2.5% and 5% PdZn(1:5)/TiO<sub>2</sub> catalysts after annealing in air (500 °C, 16 h) and subsequent reduction in 5% H<sub>2</sub>/Ar at 400 °C or 650 °C for 1 h.

Because the inconsistency among the different elements when calibrated to carbon, the XPS signal was calibrated to Ti(2p) at 458.6 eV instead.<sup>(39)</sup> This was thought to be a more satisfactory approach, since Ti is the main component in the material and its oxidation state is not expected to change when TiO<sub>2</sub> is converted to ZnTiO<sub>3</sub>.

A small palladium contribution in the Pd(2p) at 338 eV attributed to PdO was observed for all catalysts, this might be caused by re-oxidation of Pd, or PdZn, to PdO when in contact with air. As illustrated in figure 7.14, for 1% PdZn(1:5)/TiO<sub>2</sub> and 5% PdZn(1:5)/TiO<sub>2</sub> catalysts, no significant increase in the peak at 335.4 eV, assigned to the formation of PdZn, was observed after reducing 650 °C compared to 400 °C, indicating that further zinc

incorporation into the alloy was not achieved by increasing the pre-reduction temperature. Instead, zinc present in excess, non-alloyed, was incorporated into the TiO<sub>2</sub> lattice to form ZnTiO<sub>3</sub>, as indicated by XRD.

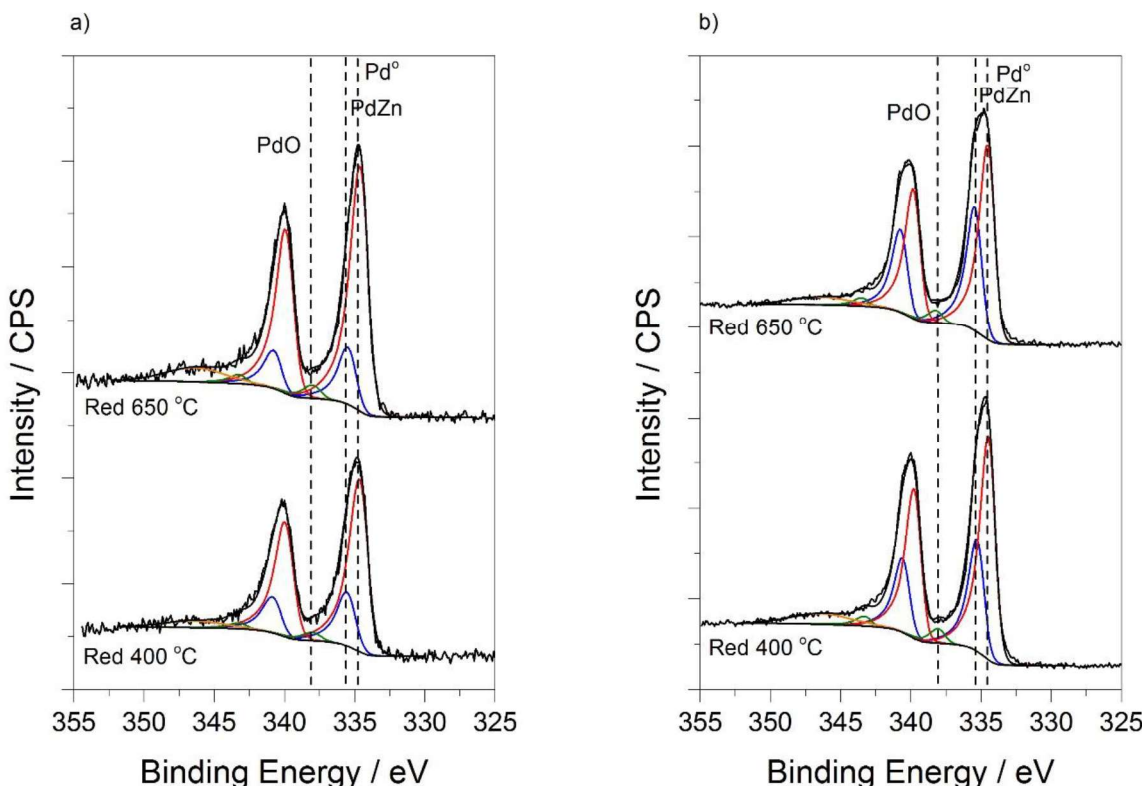


**Figure 7.14.** Pd(2p) orbital calibrated to Ti(2p) at 458.6 eV for a) 1% PdZn(1:5)/TiO<sub>2</sub> and b) 5% PdZn(1:5)/TiO<sub>2</sub> after annealing at 500 °C for 16 h in static air followed by reduction at 400 °C or 650 °C in 5% H<sub>2</sub>/Ar for 1 h. Red, blue and green fitting correspond to Pd<sup>0</sup>, PdZn and PdO respectively.

Zinc presented low sensitivity towards chemical changes by XPS. As a consequence, no conclusive information was obtained from the Zn(2p) or the Zn(LM<sub>2</sub>) orbitals (figure 7.15a). No changes in the zinc orbital were observed after increasing the reduction temperature from 400 °C to 650 °C. Zinc was present as its oxide, observed by the main peak at a kinetic energy of 988 eV with a less intense shoulder at 991 eV. However, a shoulder at 995 eV was observed, assigned to the formation of the PdZn alloy, for the 5% PdZn(1:5)/TiO<sub>2</sub>; no change in intensity was detected for this peak with increasing pre-reduction temperature. The absence of the PdZn peak at 995 for 1% and 2.5% PdZn(1:5)/TiO<sub>2</sub> catalysts does not mean that the alloy is not formed, since the presence of the alloy was confirmed by XRD and was observed on the Pd(2p) orbital.

Ti and O are the main components of catalysts since TiO<sub>2</sub> was used as support. No changes in the Ti(2p) orbital could be observed, since it was used for calibrating against the other

elements. Moreover, no significant changes were observed in the study of the O(1s) after reduction at 400 °C or at 650 °C (figure 7.15b and 7.15c respectively).

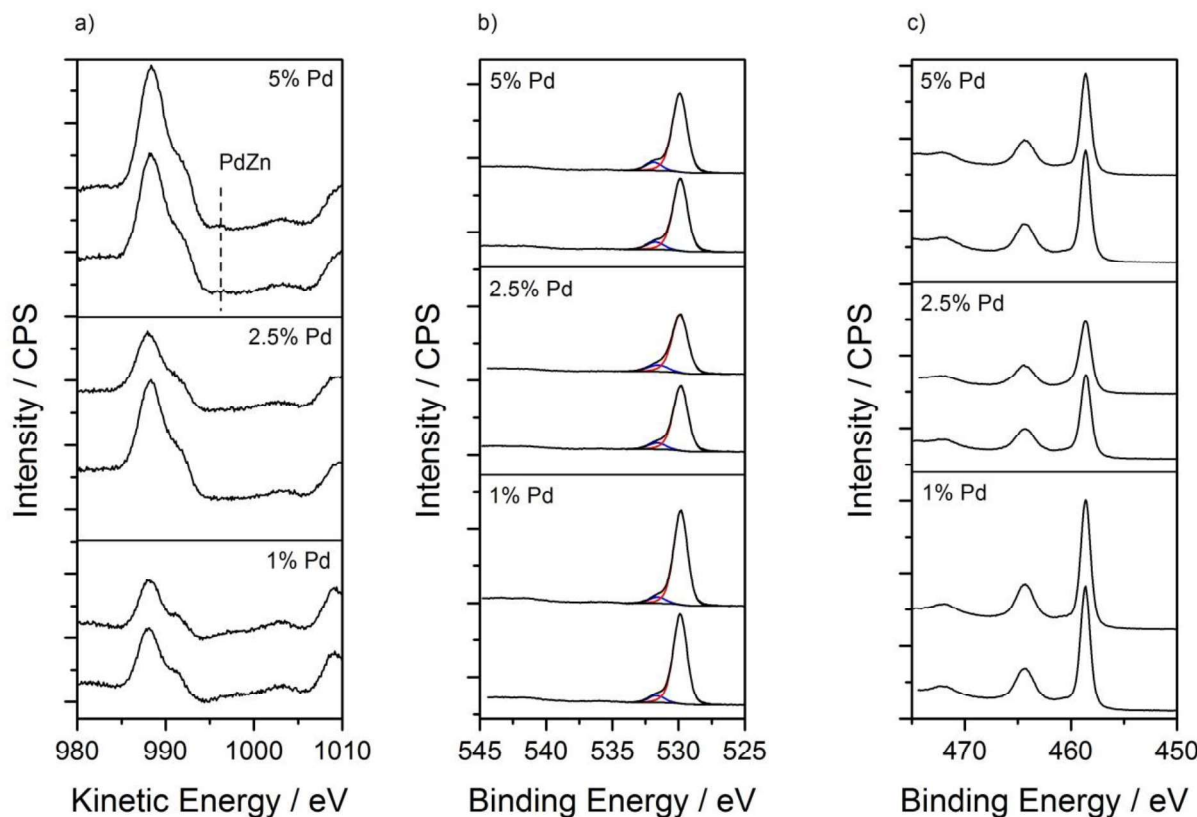


**Figure 7.15.** XPS a) Zn(LM<sub>2</sub>), b) O(1s) and c) Ti(2p) for 1% PdZn(1:5)/TiO<sub>2</sub>, 2.5% PdZn(1:5)/TiO<sub>2</sub> and 5% PdZn(1:5)/TiO<sub>2</sub> catalysts after annealing in air (500 °C, 16 h) followed by reduction in 5% H<sub>2</sub>/Ar at 400 °C or 650 °C for 1 h. Reduction at 650 °C is represented above reduction at 400 °C for each palladium concentration.

Pre-reduction at 400 °C or at 650 °C seemed to not produce detectable changes by XPS, however, XRD characterisation suggested larger crystallites after reduction at 650 °C compared to reduction at 400 °C for the 1%, 2.5% and 5% PdZn(1:5)/TiO<sub>2</sub> catalysts. This can be explained by particle sintering, but without changing its chemical nature *per se*.

In order to confirm the nanoparticle sintering after reduction at 650 °C, catalysts were analysed by TEM. As shown in image 7.2, for 1% PdZn(1:5)/TiO<sub>2</sub> and 5% PdZn(1:5)/TiO<sub>2</sub> catalysts reduced at 400 °C, lowering the palladium loading reduced the PdZn nanoparticles population. In order to obtain reliable histograms, at least 100 particles were counted. Because the number of particles counted on each catalyst differed, particle size distribution was presented as frequency instead of particle counts.

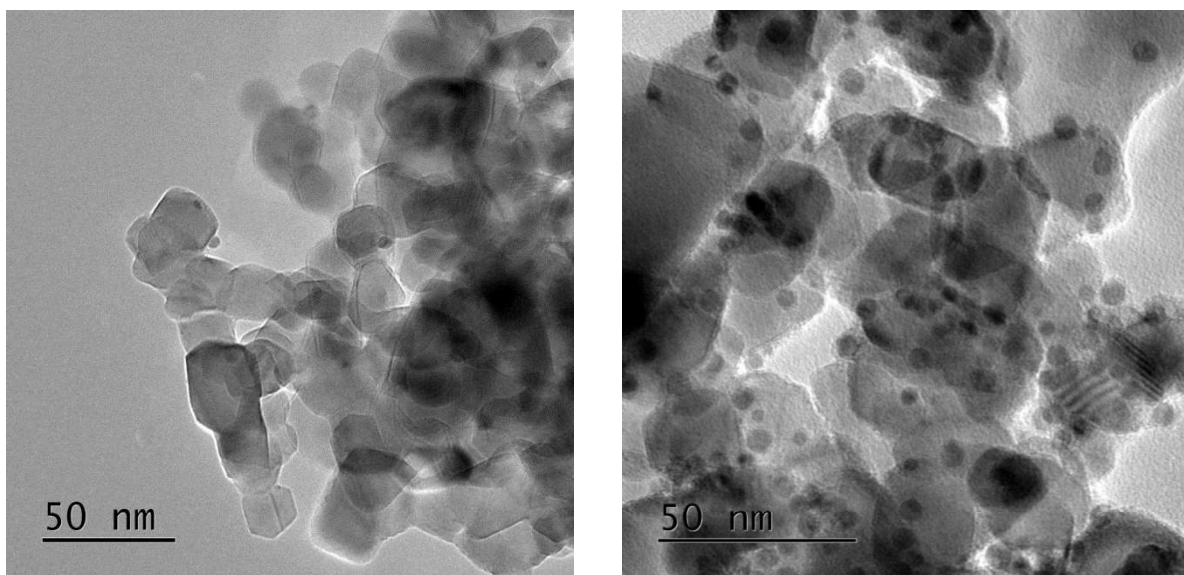


**Image 7.2.** On the left TEM image for 1% PdZn(1:5)/TiO<sub>2</sub> catalyst and on the right TEM image for 5% PdZn(1:5)/TiO<sub>2</sub> after annealing in air (500 °C, 16 h) and subsequent reduction in 5% H<sub>2</sub> / Ar (400 °C, 1 h).

The mean particle size, with its associated standard deviation, is tabulated in table 7.5. Pre-reduction treatment at the same temperature led to no significant changes in the PdZn particle size. For instance, after reduction at 400 °C the 1% PdZn(1:5)/TiO<sub>2</sub> catalyst's particle size ( $3.9 \text{ nm} \pm 1.2 \text{ nm}$ ) included the 5% PdZn(1:5)/TiO<sub>2</sub> measured particle size ( $4.6 \text{ nm} \pm 0.9 \text{ nm}$ ).

Nevertheless, at constant palladium loading, higher reduction temperature followed by an increased in the PdZn nanoparticle size and to broader size distribution, as shown on figure 7.15 for 5% PdZn(1:5)/TiO<sub>2</sub>. Particle size sintering is expected with increasing the heat treatment temperature, as a result of higher particle mobility. Moreover, since the temperature ramp was  $5 \text{ }^{\circ}\text{C}\cdot\text{min}^{-1}$ , regardless of the final pre-reduction temperature, materials reduced at 650 °C were at higher temperature for a longer period of time than those reduced at 400 °C, prolonging the time that metal atoms can migrate alongside the support.

**Table 7.5.** Particle size distribution and standard deviation for 1 wt. %, 2.5 wt. % and 5 wt. % PdZn(1:5)/TiO<sub>2</sub> catalysts annealed in air (500 °C, 16 h) followed by reduction at 400 °C or at 650 °C in 5% H<sub>2</sub>/Ar for 1 h.

Catalyst	Mean size / nm	Std ± nm
<b>1% PdZn/TiO<sub>2</sub> Red-400°C</b>	3.9	1.2
<b>1% PdZn/TiO<sub>2</sub> Red-650°C</b>	4.3	1.1
<b>2.5% PdZn/TiO<sub>2</sub> Red-400°C</b>	4.0	0.9
<b>2.5% PdZn/TiO<sub>2</sub> Red-650°C</b>	4.3	1.2
<b>5% PdZn/TiO<sub>2</sub> Red-400°C</b>	4.6	0.9
<b>5% PdZn/TiO<sub>2</sub> Red-650°C</b>	6.2	2.0

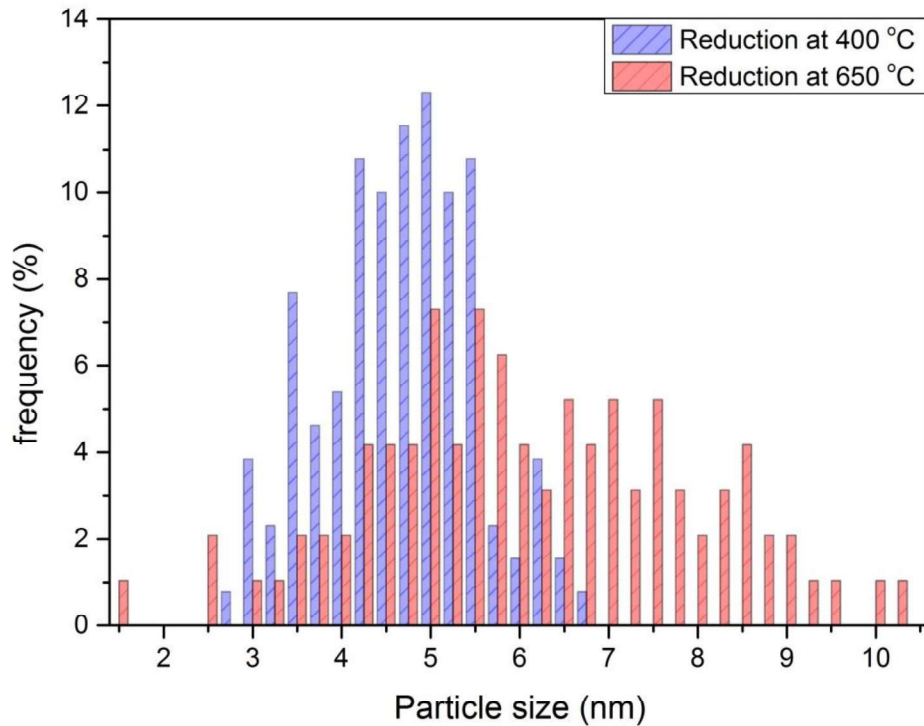


**Figure 7.16.** Particle size histogram for 5% PdZn(1:5)/TiO<sub>2</sub> after annealing in air (500 °C, 16 H) followed by reduction at 400 °C or at 650 °C in 5% H<sub>2</sub>/Ar.

### Catalyst activity

PdZn(1:5)/TiO<sub>2</sub> catalysts prepared by CVI with 1 wt %, 2.5 wt % and 5 wt % Pd loading were tested for the CO<sub>2</sub> hydrogenation (250 °C, 20 bar, 30 ml·min<sup>-1</sup>, 60 % H<sub>2</sub>, 20 % CO<sub>2</sub>, 20 % N<sub>2</sub>). Prior to reaction, catalysts were pre-reduced at either 400 °C or 650 °C in a tubular furnace (5% H<sub>2</sub>/Ar, 1 h). Reduction in a separate furnace was done to avoid reducing *in situ* at 650 °C under pure H<sub>2</sub>. Because the catalysts were exposed to air after the reduction treatment, while transferred inside the reactor tube, *in situ* pre-reduction (400 °C, 1 h, 30 ml·min<sup>-1</sup>, H<sub>2</sub>) was carried out prior to reaction. Catalytic data is presented in table 7.6. As expected, increasing palladium loading enhanced CO<sub>2</sub> conversion regardless of the pre-reduction temperature because of the higher population of PdZn nanoparticles in the catalysts as observed by TEM. After pre-reduction at 400 °C, 7.5 %, 10.9 % and 12.6 % CO<sub>2</sub> conversion was observed for 1 %, 2.5 % and 5 % of PdZn(1:5)/TiO<sub>2</sub> catalysts respectively. Whilst 5.3 %, 7.4 % and 11.2 % CO<sub>2</sub> conversion was observed after pre-reduction at 650 °C as the palladium loading increased from 1 wt. % to 5 wt. %.

At a constant palladium loading, a decrease in the CO<sub>2</sub> conversion was observed after increasing the pre-reduction temperature from 400 °C to 650 °C. For instance, the 1% PdZn(1:5)/TiO<sub>2</sub> catalyst showed a CO<sub>2</sub> conversion of 5.3 % after reduction at 650 °C compared to 7.5 % after reduction at 400 °C. Conversely, methanol selectivity improved from 14.6 % to 16.6 % and from 12.6 % to 19.8 % for 1% PdZn(1:5)/TiO<sub>2</sub> and 2.5% PdZn(1:5)/TiO<sub>2</sub> respectively with increasing the pre-reduction temperature.

For catalysts with 1 wt. % Pd and 2.5 wt. % Pd, the better selectivity towards methanol after reduction at 650 °C compensates for the decrease in activity, leading to enhanced methanol yield. Conversely, higher nanoparticle sintering observed by TEM after pre-reduction at 650 °C for the 5% PdZn(1:5)/TiO<sub>2</sub> can be responsible for the decrease in the methanol yield compared to pre-reduction at 400 °C, from 711 mmol·h<sup>-1</sup>·kg<sup>-1</sup> to 543 mmol·h<sup>-1</sup>·kg<sup>-1</sup> respectively. More importantly, the presence of methane observed after pre-reduction at 400 °C, regardless of the Pd loading, was hampered after increasing the reductive heat treatment temperature to 650 °C, with the simultaneous formation of rhombohedral ZnTiO<sub>3</sub>.

**Table 7.6.** CO<sub>2</sub> hydrogenation catalytic data (250 °C, 20 bar, 30 ml·min<sup>-1</sup>, 60 % H<sub>2</sub>, 20 % CO<sub>2</sub>, 20% N<sub>2</sub>) for 1%, 2.5% and 5% PdZn(1:5)/TiO<sub>2</sub> catalysts after annealing in static air (500 °C, 16 h) followed by pre-reduction in 55 H<sub>2</sub>/Ar at 400 °C or at 650 °C in a tubular furnace. Catalysts were pre-reduced in situ (400 °C, H<sub>2</sub>, 1 h). Presented catalytic data correspond to 4 h of reaction.

Catalyst	CO <sub>2</sub> conv. / %	CH <sub>3</sub> OH sel. / %	CO sel. / %	CH <sub>4</sub> sel. / %	MeOH yield / mmol·h <sup>-1</sup> ·kg <sup>-1</sup>
1% PdZn/TiO <sub>2</sub> red 400 °C	7.5 ± 1.1	14.6 ± 4.1	85.4 ± 4.1	0.02 ± 0.01	256 ± 74
1% PdZn/TiO <sub>2</sub> red 650 °C	5.3 ± 0.7	16.6 ± 2.1	83.4 ± 2.1	0.007 ± 0.005	338 ± 61
2.5% PdZn/TiO <sub>2</sub> red 400 °C	10.9 ± 0.4	12.6 ± 2.6	87.4 ± 2.6	0.02 ± 0.004	365 ± 91
2.5% PdZn/TiO <sub>2</sub> red 650 °C	7.4 ± 1.2	19.8 ± 5.2	83.4 ± 5.2	0.007 ± 0.001	454 ± 70
5% PdZn/TiO <sub>2</sub> red 400 °C	12.6 ± 0.8	16.7 ± 1.1	83.3 ± 1.1	0.02 ± 0.004	711 ± 59
5% PdZn/TiO <sub>2</sub> red 650 °C	11.2 ± 0.7	17.0 ± 3.7	83.0 ± 3.7	0.005 ± 0.001	543 ± 43

#### 7.4 PdZn alloy catalysts supported on ZnTiO<sub>3</sub>.

In the previous section it was observed that the non-alloyed zinc, remaining in the material as ZnO, was incorporated into the TiO<sub>2</sub> lattice after reduction at 650 °C to form rhombohedral ZnTiO<sub>3</sub>. This seemed to be associated with the considerable reduction in CH<sub>4</sub> productivity during the CO<sub>2</sub> hydrogenation (250 °C, 20 bar, 60 % H<sub>2</sub>, 20 % CO<sub>2</sub>, 20 % N<sub>2</sub>). Therefore, it can be hypothesised that the TiO<sub>2</sub>-PdZn interface acted as the active site for CH<sub>4</sub> formation, and thus altering the interface by transforming TiO<sub>2</sub> to ZnTiO<sub>3</sub> hampered methane production. Previous reports showed that the support largely affects the CO<sub>2</sub> hydrogenation product selectivity.<sup>(40, 41)</sup> In 1 %, 2.5 % and 5% PdZn(1:5)/TiO<sub>2</sub>, the amount of zinc in the material was limited by the palladium to zinc molar ratio. After reduction at 650 °C, it is possible that not all the TiO<sub>2</sub>-PdZn interface is altered and hence CH<sub>4</sub> formation is not completely suppressed. Therefore, the use of ZnTiO<sub>3</sub> as support instead of TiO<sub>2</sub> is desirable.

This section of the chapter focuses on the study of the TiO<sub>2</sub>-PdZn and ZnTiO<sub>3</sub>-PdZn interface with regards to the formation of CH<sub>4</sub>, in order to prove the postulated hypothesis

that methane is produced at the interface with titania and PdZn alloy. Two materials were prepared on ZnTiO<sub>3</sub> by CVI: One catalyst was designed to contain the TiO<sub>2</sub>-PdZn interface by impregnating Pd by CVI; While this interface was deliberately absent on the other by impregnating Pd and Zn simultaneously.

#### 7.4.1 ZnTiO<sub>3</sub> preparation and characterisation.

In order to form the rhombohedral ZnTiO<sub>3</sub> phase, a stoichiometric amount of Zn(acac)<sub>2</sub> was impregnated on to TiO<sub>2</sub> by CVI following the procedure described previously. The material was then annealed in static air at 500 °C for 16 h, followed by reduction at 650 °C for 3 h in 5 % H<sub>2</sub>/Ar to ensure complete TiO<sub>2</sub> to ZnTiO<sub>3</sub> phase transformation. Since zinc was present in high concentrations, it was considered that incomplete TiO<sub>2</sub> transformation to ZnTiO<sub>3</sub> might occur, with the concomitant ZnO formation. However, no ZnO or TiO<sub>2</sub> related reflections were observed by XRD (figure 7.17), indicating complete Zn incorporation into the TiO<sub>2</sub> lattice. This phase transformation led to an abrupt shrink in the surface area of the support from 50 m<sup>2</sup>·g<sup>-1</sup> for TiO<sub>2</sub> to 17 m<sup>2</sup>·g<sup>-1</sup> for ZnTiO<sub>3</sub>.

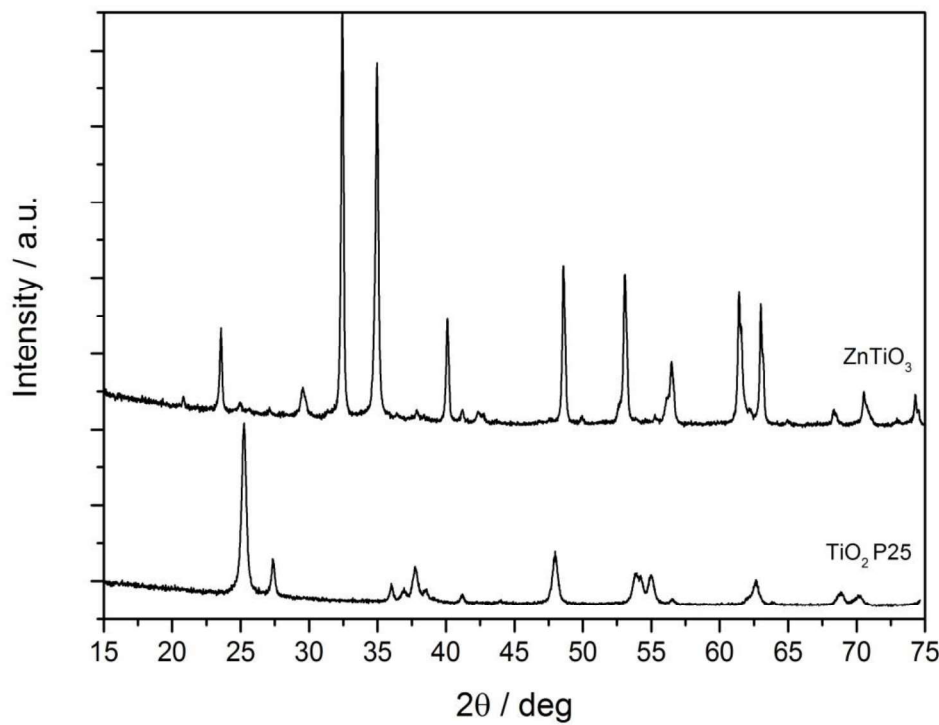


**Figure 7.17.** XRD pattern showing the TiO<sub>2</sub> P25 phase transition to rhombohedral ZnTiO<sub>3</sub> after impregnation with Zn(acac)<sub>2</sub>, annealing in static air (500 °C, 16 h) followed by reduction in 5% H<sub>2</sub>/Ar (650 °C, 3 h).

### 7.4.2 PdZn and Pd catalysts supported on ZnTiO<sub>3</sub>.

#### *Catalyst preparation*

Having successfully proved the complete conversion of TiO<sub>2</sub> to ZnTiO<sub>3</sub>, the impregnation of Pd and PdZn on ZnTiO<sub>3</sub> was carried out by CVI. Two catalysts with a 5 wt % palladium loading were prepared, 5% Pd/ZnTiO<sub>3</sub> and 5% PdZn/ZnTiO<sub>3</sub>. On 5% Pd/ZnTiO<sub>3</sub> just palladium was impregnated whereas on 5% PdZn/ZnTiO<sub>3</sub> Pd and Zn (with a molar ratio of 1 to 5) were added to the support. Both catalysts were annealed in air at 500 °C for 16 h followed by reduction at 400 °C for 1 h in 5% H<sub>2</sub>/Ar for comparison with the previously described 5% PdZn(1:5)/TiO<sub>2</sub> catalyst.

The surface area of TiO<sub>2</sub> decreased considerably after its transformation to ZnTiO<sub>3</sub> from 50 m<sup>2</sup>·g<sup>-1</sup> to 17 m<sup>2</sup>·g<sup>-1</sup> respectively. However no further reduction was observed after the impregnation of Pd and/or Zn by CVI.

#### *Catalyst characterisation*

##### *X-ray powder diffraction (XRD)*

5 % PdZn/ZnTiO<sub>3</sub> (figure 7.18a) and 5 % Pd/ZnTiO<sub>3</sub> (figure 7.18b) catalysts were analysed by XRD in order to confirm the PdZn alloy formation. Since palladium and zinc were impregnated on ZnTiO<sub>3</sub> on the 5% PdZn/TiO<sub>2</sub> catalyst, the presence of both metal oxides was expected after annealing in air. (100), (002) and (101) ZnO planes reflections were observed at 31.8°, 34.4° and 36.2° respectively while the presence of PdO was confirmed at 33.9°. ZnO reflections remained after pre-reduction at 400 °C for 1 h in 5% H<sub>2</sub>. Nevertheless, the PdO reflection disappeared with the simultaneous growth of the β-PdZn reflections at 41° and 44°. Contrary to what is observed with TiO<sub>2</sub> as support, the formation of the alloy can be unambiguously observed because ZnTiO<sub>3</sub> reflections do not overlap with the PdZn reflections.

For the 5 % Pd/ZnTiO<sub>3</sub> catalyst, where just palladium was impregnated on to the support, XRD showed a different trend. PdO at 33.9° was observed after annealing in air at 500 °C. Nevertheless, no ZnO reflections were observed in accordance with no zinc being impregnated on the support. Likewise, the PdO reflection vanished after reduction at 400 °C for 1 h in 5% H<sub>2</sub>/Ar followed by the concomitant formation of β-PdZn alloy at 44.3° and 44.1°. This indicates that the zinc present in the support is mobile and can migrate from the ZnTiO<sub>3</sub> structure to the Pd forming the PdZn alloy. This was also observed by the slight decrease in intensity for the ZnTiO<sub>3</sub> reflections compared with the annealed sample for the 5% Pd/ZnTiO<sub>3</sub> catalyst. This phase transformation implies that zinc neighbouring with palladium

is reduced to form the alloy and therefore leaving the ZnTiO<sub>3</sub> lattice which in turn must generate a TiO<sub>2</sub>-PdZn interface.

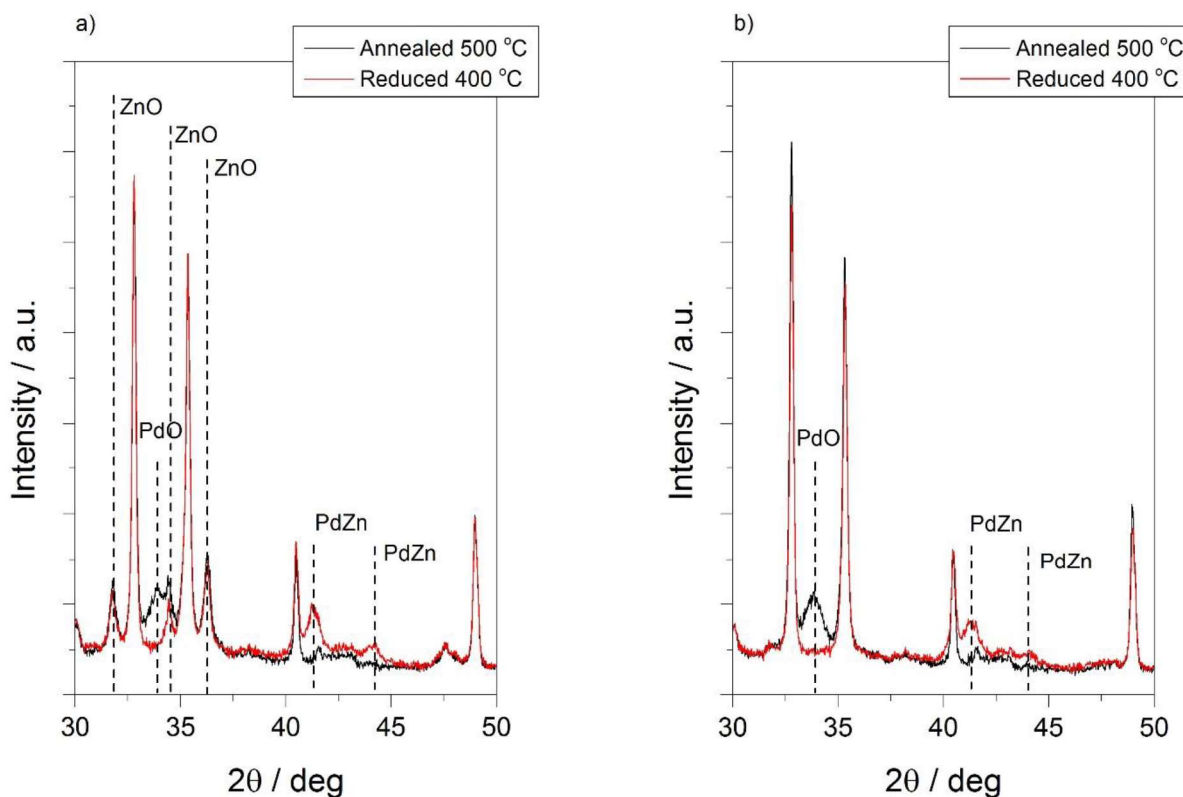


**Figure 7.18.** XRD pattern for a) 5% PdZn/ZnTiO<sub>3</sub> and b) 5% Pd/ZnTiO<sub>3</sub> catalysts after annealing in static air (500 °C, 16 h) followed by reduction in 5% H<sub>2</sub>/Ar (400 °C, 1 h). No labelled reflections correspond to rhombohedral ZnTiO<sub>3</sub> prepared previously and used as support.

#### *Transmission electron microscopy (TEM)*

The conversion of TiO<sub>2</sub> to ZnTiO<sub>3</sub> led to a considerable decrease in the surface area, from 50 m<sup>2</sup>·g<sup>-1</sup> to 17 m<sup>2</sup>·g<sup>-1</sup>. On high surface area support, nanoparticles are normally highly dispersed and as such agglomeration is hampered to some extent, whereas on low surface area supports higher particle agglomeration is expected. The 5% PdZn(1:5)/TiO<sub>2</sub> discussed in the previous section of the chapter showed a particle size of 4.55 ± 0.85 nm: in order to compare the particle dispersion and size on ZnTiO<sub>3</sub> TEM imaging was performed (image 7.3).

TEM analysis indicated that the impregnation of both metals simultaneously, Pd and Zn, led to smaller nanoparticles in comparison with the impregnation of just palladium on ZnTiO<sub>3</sub>. 4.68 ± 1.25 nm and 6.38 ± 2.03 nm particle size was measured for 5% PdZn/ZnTiO<sub>3</sub> and 5% Pd/ZnTiO<sub>3</sub> catalysts, respectively. It was noted that no change in the PdZn nanoparticle size

was observed when Pd and Zn were impregnated on TiO<sub>2</sub> or on ZnTiO<sub>3</sub>, regardless of the difference in the surface area between both supports.

Although rhombohedral ZnTiO<sub>3</sub> phase was confirmed as the main crystallographic phase by XRD, the corresponding crystallographic planes were not observed by TEM.

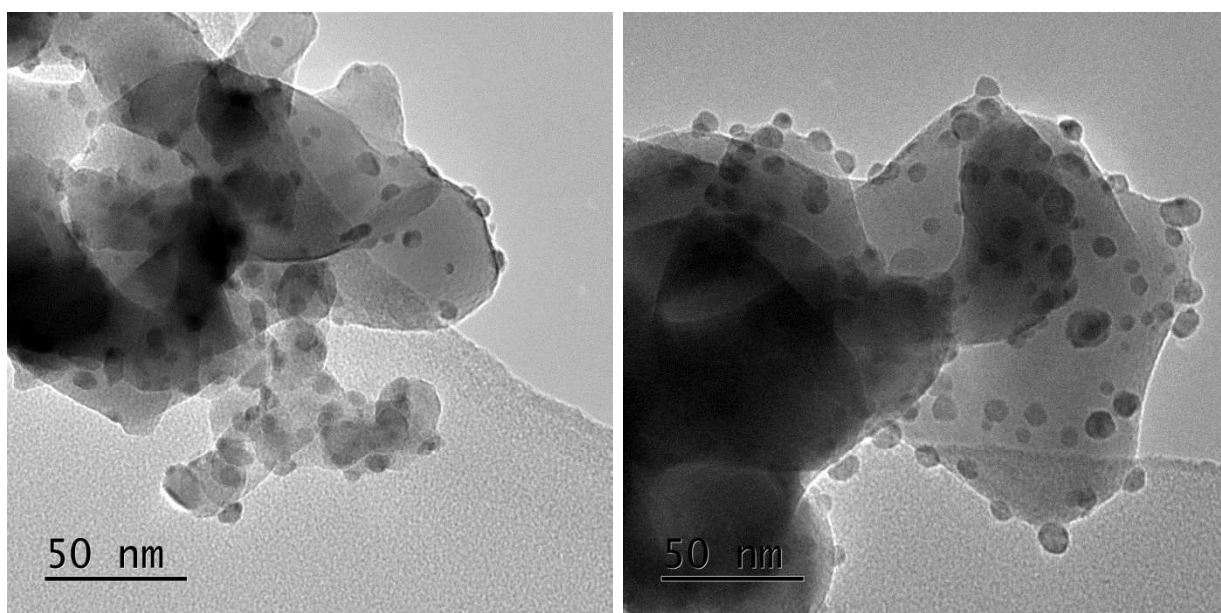


**Image 7.3.** TEM images for 5% PdZn/ZnTiO<sub>3</sub> (left) and 5% Pd/ZnTiO<sub>3</sub> (right) after annealing in static air (500 °C, 16 h) and subsequent reduction in 5% H<sub>2</sub>/Ar (400 °C, 1 h).

As illustrated in figure 7.19, the 5% Pd/ZnTiO<sub>3</sub> promoted not only the increase in the PdZn mean particulate size compared to 5% PdZn/ZnTiO<sub>3</sub> but also the particle size distribution broadened.

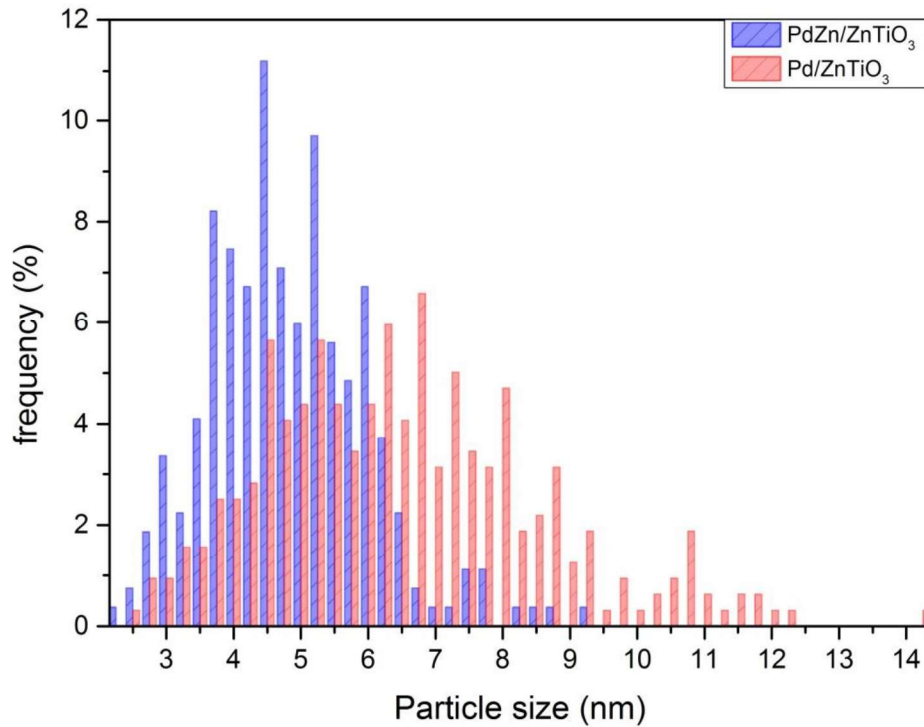


**Figure 7.19.** Particle size distribution obtained from TEM images for 5% PdZn/ZnTiO<sub>3</sub> and 5% Pd/ZnTiO<sub>3</sub> catalysts after annealing in static air (500 °C, 16 h) and subsequent reduction in 5% H<sub>2</sub>/Ar (400 °C, 1 h). A minimum of a 100 particles were counted in order to obtain the particle size histogram.

#### Catalytic activity

It was hypothesised that the PdZn-TiO<sub>2</sub> interface acted as the active site for CH<sub>4</sub> formation. To prove it, 5% PdZn/ZnTiO<sub>3</sub> and 5% Pd/ZnTiO<sub>3</sub> catalysts were prepared. XRD characterisation confirmed the presence of PdZn alloy on both catalysts after pre-reduction at 400 °C. Thus implying that lattice Zn from ZnTiO<sub>3</sub> migrated out of the structure forming the TiO<sub>2</sub>-PdZn alloy interface on the 5% Pd/ZnTiO<sub>3</sub> catalyst. Nevertheless, on the 5% PdZn/ZnTiO<sub>3</sub> catalyst zinc was in excess and the PdZn-TiO<sub>2</sub> interface is not expected to form. Therefore, according to the hypothesis that PdZn-TiO<sub>2</sub> interface acts as the active site for methane formation, it would be expected to observe CH<sub>4</sub> on Pd/TiO<sub>2</sub> and on Pd/ZnTiO<sub>3</sub> catalysts but not on PdZn/ZnTiO<sub>3</sub>.

Prior to reaction, catalyst were pelleted (10 ton, 600 µm - 425 µm mesh) and pre-reduced *in situ* in pure hydrogen (30 ml·min<sup>-1</sup>, 400 °C, 5 °C·min<sup>-1</sup>, 1 h). Catalytic data (150 °C to 275 °C, 20 bar, 30 ml·min<sup>-1</sup>, 60 % H<sub>2</sub>, 20 % CO<sub>2</sub>, 20 % N<sub>2</sub>) for 5% PdZn/TiO<sub>2</sub>, 5% PdZn/ZnTiO<sub>3</sub> and 5% Pd/ZnTiO<sub>3</sub> catalysts is presented in table 7.7.

The same catalytic trend (CO<sub>2</sub> conversion and CO and CH<sub>3</sub>OH selectivity) was observed with increasing the reaction temperature for all three studied catalysts. The CO<sub>2</sub> hydrogenation to methanol is an exothermic reaction and as expected from its thermodynamics it is favoured at lower temperature and high pressure.<sup>(2)</sup> Consequently, higher selectivity towards methanol was observed at lower reaction temperatures. At 150 °C the methanol selectivity was 88 %, 100 % and 79 % for PdZn/ZnTiO<sub>3</sub>, Pd/ZnTiO<sub>3</sub> and PdZn/TiO<sub>2</sub> respectively. However high selectivity was linked with poor CO<sub>2</sub> conversion: close to 1 %.

As expected, increasing the reaction temperature facilitated CO<sub>2</sub> activation. Leading to an increase in the CO<sub>2</sub> conversion: at 275 °C the CO<sub>2</sub> conversion was close to 15 % for all three catalysts. Nevertheless, this was accompanied by a progressive decrease in the methanol selectivity in favour of CO. When increasing the reaction temperature above 200 °C CO was the main product formed via the RWGS. And at 275 °C methanol selectivity dropped to 13 %, 16 % and 13 % for PdZn/ZnTiO<sub>3</sub>, Pd/ZnTiO<sub>3</sub> and PdZn/TiO<sub>2</sub> respectively.

**Table 7.7.** CO<sub>2</sub> hydrogenation catalytic data (20 bar, 60 % H<sub>2</sub>, 20 % CO<sub>2</sub>, 20 % N<sub>2</sub>, 30 ml·min<sup>-1</sup>, between 150 °C and 275 °C) for 5% PdZn(1:5)/TiO<sub>2</sub>, 5% PdZn(1:5)/ZnTiO<sub>3</sub> and 5% Pd/ZnTiO<sub>3</sub> catalysts after annealing in air (500 °C, 16 h) followed by reduction in pure H<sub>2</sub> (400 °C, 1 h). \*CH<sub>3</sub>OH and CO productivities are expressed as mmol·kg<sup>-1</sup>·h<sup>-1</sup>.

Catalyst	Reaction temperature	CO <sub>2</sub> conv. / %	CH <sub>3</sub> OH sel. / %	CO sel. / %	CH <sub>4</sub> sel. / %	CH <sub>3</sub> OH prod.*	CO prod.*
PdZn/ZnTiO <sub>3</sub>	150	1.0	87.6	12.4	0.000	249	25
	175	2.0	76.0	24.0	0.000	436	137
	200	4.3	58.6	41.4	0.001	599	423
	225	8.2	36.0	64.0	0.001	669	1196
	250	13.2	20.9	79.1	0.002	702	2683
	275	17.3	12.6	87.4	0.004	647	4540
Pd/ZnTiO <sub>3</sub>	150	0.3	100	0.0	0.000	81	0
	175	1.9	71.0	29.0	0.000	230	121
	200	3.2	57.0	43.0	0.000	465	302
	225	6.1	42.7	57.3	0.007	634	833
	250	8.9	25.6	74.4	0.015	661	1874
	275	14.4	15.5	84.5	0.021	630	3390
PdZn/TiO <sub>2</sub>	150	1.0	78.8	21.2	0.000	207	56
	175	2.3	69.6	30.4	0.000	357	156
	200	4.7	59.5	40.5	0.002	541	354
	225	6.9	32.5	67.5	0.010	592	1229
	250	12.0	20.0	80.0	0.020	631	2562
	275	16.6	12.8	87.2	0.022	644	4308

The larger PdZn alloy particle size observed by TEM for the Pd/ZnTiO<sub>3</sub> catalyst can be associated with the slightly lower CO<sub>2</sub> conversion compared to PdZn/ZnTiO<sub>3</sub> and PdZn/TiO<sub>2</sub> catalysts for the range of temperatures studied.

It is important to remember that the aim for supporting PdZn alloy catalysts on ZnTiO<sub>3</sub> rather than on TiO<sub>2</sub> was not to improve the CO<sub>2</sub> conversion or to enhance methanol selectivity, but to deter the undesired formation of methane. As hypothesised, catalysts with the presence of TiO<sub>2</sub>-PdZn interface, 5% PdZn/TiO<sub>2</sub> and 5% Pd/ZnTiO<sub>3</sub>, presented a CH<sub>4</sub> selectivity of approximately 0.02 % at 250 °C. Even though the selectivity towards methane seems insignificant it would lead to an increase in the production cost of methanol if applied in an industrial scale. Methane is a non-desired by-product, but unlike CO it would need to be purified in order to avoid its accumulation in the reactor. Conversely, on the 5% PdZn/ZnTiO<sub>3</sub> catalyst where the PdZn-TiO<sub>2</sub> interface was suppressed, the CH<sub>4</sub> detection dropped to noise levels.

Whilst the production of methanol is favoured at low temperature, high temperature is needed to activate the CO<sub>2</sub>. Increasing the reaction temperature was followed by a decrease in the methanol selectivity with the concomitant increase in the production of by-products. In figure 7.20, the methane productivity is plotted against the CO<sub>2</sub> conversion.

At lower CO<sub>2</sub> conversion of 6 %, corresponding to a reaction temperature of 200 °C, no CH<sub>4</sub> was detected for any of the catalysts studied. However, above this temperature methane productivity increased linearly with CO<sub>2</sub> conversion for catalysts with the PdZn-TiO<sub>2</sub> interface, 5% PdZn/TiO<sub>2</sub> and 5% Pd/ZnTiO<sub>3</sub>. Both catalysts presented a comparable methane formation profile, indicating that the active sites involved in CH<sub>4</sub> formation were probably present in similar concentrations. Conversely, methane formation was significantly reduced on 5% PdZn/ZnTiO<sub>3</sub>. As elucidated, the absence of the PdZn-TiO<sub>2</sub> interface can be related with the low methane yield observed on PdZn/ZnTiO<sub>3</sub> catalyst which fell within the reactor blank measurements at the same temperature.

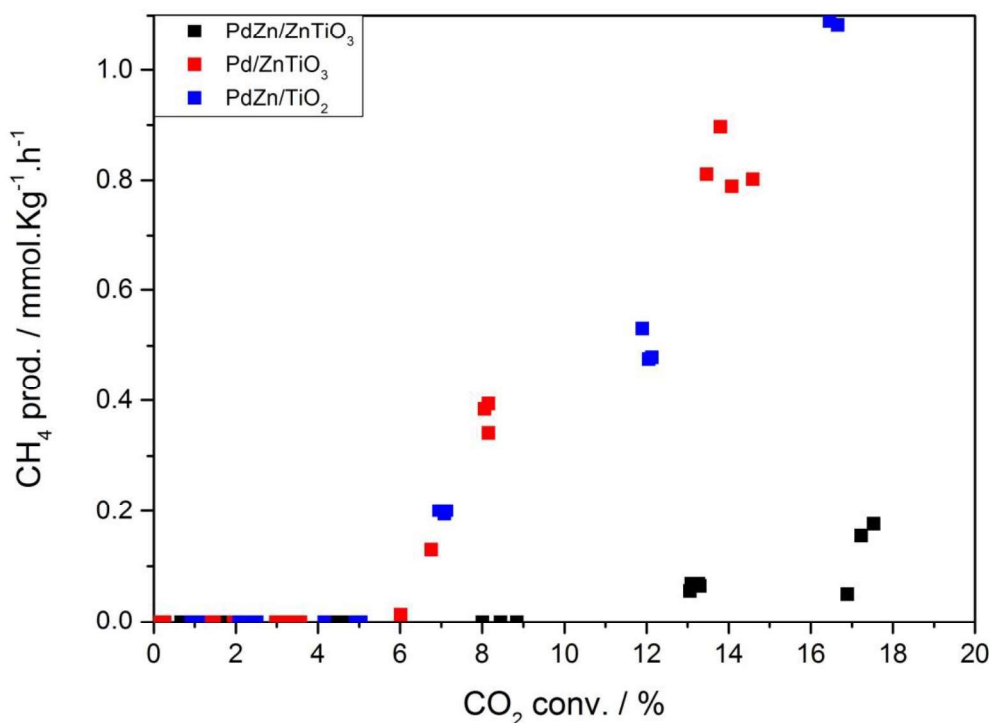


**Figure 7.20.** CH<sub>4</sub> productivity (20 bar, 60 % H<sub>2</sub>, 20 % CO<sub>2</sub>, 20 % N<sub>2</sub>, 30 ml·min<sup>-1</sup>, between 150 °C and 275 °C). compared to CO<sub>2</sub> conversion for 5% PdZn/ZnTiO<sub>3</sub>, 5% Pd/ZnTiO<sub>3</sub> and 5% PdZn/TiO<sub>2</sub> catalysts after annealing in air (500 °C, 16 h) followed by reduction in pure H<sub>2</sub> (400 °C, 1 h).

5% PdZn/ZnTiO<sub>3</sub>, 5% Pd/ZnTiO<sub>3</sub> and 5% PdZn/TiO<sub>2</sub> catalysts were tested at each temperature for 5 hours accounting to a total reaction time of 30 h. In this time frame no deactivation was observed. However, Cu-based catalysts for the production of methanol from syngas are required to perform at least for two years before regeneration and hence future work must focus on assessing the stability of PdZn prepared catalysts.

## 7.5 Conclusions.

In conclusion, it has been shown that by using chemical vapour impregnation (CVI) it is possible to synthesise well dispersed PdZn catalysts supported on TiO<sub>2</sub> and ZnTiO<sub>3</sub>, as confirmed by XRD and TEM. *In situ* XRD characterisation on 5% Pd/ZnO catalysts revealed that, upon reduction, metallic palladium is formed between 125 °C and 280 °C which then, by hydrogen spill over, reduced neighbouring zinc atoms to form the PdZn alloy phase at 350 °C.

Compared to Pd/TiO<sub>2</sub> catalysts, the stoichiometric incorporation of zinc shifted the product selectivity towards CH<sub>3</sub>OH from 3 % to 17 %. Varying the palladium to zinc molar ratio from 1:1 to 1:10 led to an increase in the PdZn phase formation on the Pd(3d) and Zn(LM<sub>2</sub>) by XPS. No significant improvement towards methanol selectivity was observed, whereas the CO<sub>2</sub> conversion progressively increased from 7.3 % to 9.5 % for the 1:5 Pd to Zn molar ratio. Further increases in the PdZn molar ratio to 1:10 led to a decrease in the CO<sub>2</sub> conversion to 7.1 %, indicating that an excess of zinc in the catalyst blocks active sites.

Increasing the reduction temperature from 400 °C to 650 °C in 5% H<sub>2</sub>/Ar showed no further zinc incorporation in the PdZn phase. Conversely, non-alloyed zinc formed rhombohedral ZnTiO<sub>3</sub> by reaction with TiO<sub>2</sub>. Surface area analysis by BET decreased after pre-reduction at 650 °C as a consequence of ZnTiO<sub>3</sub> phase formation, and the anatase to rutile TiO<sub>2</sub> phase transition. Pre-reduction treatment at 650 °C compared to 400 °C produced no particle growth by TEM for the 1% and 2.5 % PdZn(1:5)/TiO<sub>2</sub> catalysts. Nevertheless, methanol selectivity improved whilst CO<sub>2</sub> conversion decreased. Eventually the methanol yield increased after reduction at 650 °C compared to 400 °C. Meaningfully, the selectivity towards CH<sub>4</sub> decreased one order of magnitude after pre-reduction at 650 °C: this is attributed to the formation of the ZnTiO<sub>3</sub> phase.

It was hypothesised that the PdZn-TiO<sub>2</sub> interface acted as the active site for CH<sub>4</sub> formation. To prove this, 5% PdZn/ZnTiO<sub>3</sub> and 5% Pd/ZnTiO<sub>3</sub> catalysts were synthesised. After reduction at 400 °C the PdZn phase formed on both catalysts, as confirmed by XRD. This implied that the TiO<sub>2</sub>-PdZn phase was formed on the latter catalyst while it was absent in the 5% PdZn/ZnTiO<sub>3</sub>. Increasing the reaction temperature from 150 °C to 275 °C (20 bar) led to higher CO<sub>2</sub> conversion. However, selectivity shifted from CH<sub>3</sub>OH to CO with increasing temperature, with CO becoming the major product above 200 °C. A larger nanoparticle size for 5% Pd/ZnTiO<sub>3</sub> was related to comparably lower CO<sub>2</sub> conversion. To conclude, catalysts with the TiO<sub>2</sub>-PdZn interface (PdZn/TiO<sub>2</sub> and Pd/ZnTiO<sub>3</sub>) formed CH<sub>4</sub> at comparable rates whereas PdZn/ZnTiO<sub>3</sub> hampered CH<sub>4</sub> formation, confirming the postulated hypothesis.

---

## 7.6 Bibliography.

1. R. Schlögl, The Role of Chemistry in the Energy Challenge, *ChemSusChem*, **2010**, 3 (2), 209-222.
2. S. G. Jadhav, P. D. Vaidya, B. M. Bhanage, J. B. Joshi, Catalytic carbon dioxide hydrogenation to methanol: A review of recent studies, *Chemical Engineering Research and Design*, **2014**, 92 (11), 2557-2567.
3. W. J. Shen, M. Okumura, Y. Matsumura, M. Haruta, The influence of the support on the activity and selectivity of Pd in CO hydrogenation, *Applied Catalysis A: General*, **2001**, 213 (2), 225-232.
4. N. Iwasa, H. Suzuki, M. Terashita, M. Arai, N. Takezawa, Methanol synthesis from CO<sub>2</sub> under atmospheric pressure over supported Pd catalysts, *Catalysis letters*, **2004**, 96 (1-2), 75-78.
5. X. Wang, H. Shi, J. H. Kwak, J. Szanyi, Mechanism of CO<sub>2</sub> Hydrogenation on Pd/Al<sub>2</sub>O<sub>3</sub> Catalysts: Kinetics and Transient DRIFTS-MS Studies, *ACS Catal*, **2015**, 5, 6337–6349.
6. A. Ota, E. L. Kunkes, I. Kasatkin, E. Groppo, D. Ferri, B. Poceiro, R. M. Navarro Yerga, M. Behrens, Comparative study of hydrotalcite-derived supported Pd<sub>2</sub>Ga and PdZn intermetallic nanoparticles as methanol synthesis and methanol steam reforming catalysts, *Journal of Catalysis*, **2012**, 293, 27-38.
7. H. Bahruji, M. Bowker, G. J. Hutchings, N. Dimitratos, P. Wells, E. Gibson, W. Jones, C. Brookes, D. J. Morgan, G. Lalev, Pd/ZnO catalysts for direct CO<sub>2</sub> hydrogenation to methanol, *Journal of Catalysis*, **2016**, 343, 133-146.
8. J. Xu, X. Su, X. Liu, X. Pan, G. Pei, Y. Huang, X. Wang, T. Zhang, H. Geng, Methanol synthesis from CO<sub>2</sub> and H<sub>2</sub> over Pd/ZnO/Al<sub>2</sub>O<sub>3</sub>: Catalyst structure dependence of methanol selectivity, *Appl Catal, A*, **2016**, 514, 51-59.
9. X. L. Liang, X. Dong, G. D. Lin, H. B. Zhang, Carbon nanotube-supported Pd–ZnO catalyst for hydrogenation of CO<sub>2</sub> to methanol, *Applied Catalysis B: Environmental*, **2009**, 88 (3–4), 315-322.
10. H. Bahruji, M. Bowker, W. Jones, J. Hayward, J. Ruiz Esquius, D. J. Morgan G. J. Hutchings, PdZn catalysts for CO<sub>2</sub> hydrogenation to methanol using chemical vapour impregnation (CVI), *Faraday Discussions*, **2017**, 197, 309-324.
11. M. M. Forde, R. D. Armstrong, C. Hammond, Q. He, R. L. Jenkins, S. A. Kondrat, N. Dimitratos, J. A. Lopez-Sanchez, S. H. Taylor, D. Willock, C. J. Kiely, G. J. Hutchings, Partial Oxidation of Ethane to Oxygenates Using Fe- and Cu-Containing ZSM-5, *Journal of the American Chemical Society*, **2013**, 135 (30), 11087-11099.

12. M. M. Forde, R. D. Armstrong, R. McVicker, P. P. Wells, N. Dimitratos, Q. He, L. Lu, R. L. Jenkins, C. Hammond, J. A. Lopez-Sanchez, C. J. Kielyc, G. J. Hutchings, Light alkane oxidation using catalysts prepared by chemical vapour impregnation: tuning alcohol selectivity through catalyst pre-treatment, *Chemical Science*, **2014**, 5 (9), 3603-3616.
13. M. M. Forde, L. Kesavan, M. I. bin Saiman, Q. He, N. Dimitratos, J. A. Lopez-Sanchez, R. L. Jenkins, S. H. Taylor, C. J. Kiely, G. J. Hutchings, High Activity Redox Catalysts Synthesized by Chemical Vapor Impregnation, *ACS Nano*, **2014**, 8 (1), 957-969.
14. H. Bahruji, M. Bowker, W. Jones, J. Hayward, J. Ruiz Esquius, D. J. Morgan G. J. Hutchings, PdZn catalysts for CO<sub>2</sub> hydrogenation to methanol using chemical vapour impregnation (CVI), *Faraday Discussions*, **2017**, 197, 309-324.
15. N. Iwasa, S. Masuda, N. Ogawa, N. Takezawa, Steam reforming of methanol over Pd/ZnO: Effect of the formation of PdZn alloys upon the reaction, *Applied Catalysis A: General*, **1995**, 125 (1), 145-157.
16. M. W. Tew, H. Emerich, J. A. van Bokhoven, Formation and Characterization of PdZn Alloy: A Very Selective Catalyst for Alkyne Semihydrogenation, *J Phys Chem C*, **2011**, 115 (17), 8457-8465.
17. V. Lebarbier, R. Dagle, A. Datye, Y. Wang, The effect of PdZn particle size on reverse-water-gas-shift reaction, *Appl Catal, A*, **2010**, 379 (1-2), 3-6.
18. S. Shah, A. Qureshi, N. L. Singh, P. K. Kulriya, K. P. Singh, D. K. Avasthi, Structural and chemical modification of polymer composite by proton irradiation, *Surface and Coatings Technology*, **2009**, 203 (17), 2595-2599.
19. Z. Zsoldos, A. Sarkany, L. Guczi, XPS Evidence of Alloying in Pd/ZnO Catalysts, *Journal of Catalysis*, **1994**, 145 (1), 235-238.
20. P. S. Wehner, G. C. Tustin, B. L. Gustafson, XPS study of the reduction and reoxidation of ZnO-supported palladium, *Journal of Catalysis*, **1984**, 88 (1), 246-248.
21. J. A. Rodriguez, Interactions in Bimetallic Bonding: Electronic and Chemical Properties of PdZn Surfaces, *J Phys Chem*, **1994**, 98 (22), 5758-5764.
22. J. Vizdal, A. Kroupa, J. Popovic, A. Zemanova, The Experimental and Theoretical Study of Phase Equilibria in the Pd-Zn (-Sn) System, *Advanced Engineering Materials*, **2006**, 8 (3), 164-176.
23. M. L. Cubeiro, J. L. G. Fierro, Partial oxidation of methanol over supported palladium catalysts, *Applied Catalysis A: General*, **1998**, 168 (2), 307-322.

24. A. Bayer, K. Flechtner, R. Denecke, H. P. Steinrück, K. M. Neyman, N. Rösch, Electronic properties of thin Zn layers on Pd(111) during growth and alloying, *Surface Science*, **2006**, *600* (1), 78-94.
25. G. Deroubaix, P. Marcus, X-ray photoelectron spectroscopy analysis of copper and zinc oxides and sulphides, *Surface and Interface Analysis*, **1992**, *18* (1), 39-46.
26. W. Li, L. Fang, G. Qin, H. Ruan, H. Zhang, C. Kong, L. Ye, P. Zhang, F. Wu, Tunable zinc interstitial related defects in ZnMgO and ZnCdO films, *Journal of Applied Physics*, **2015**, *117* (14), 145301.
27. S. U. Awan, S. K. Hasanain, M. F. Bertino, G. H. Jaffari, Ferromagnetism in Li doped ZnO nanoparticles: The role of interstitial Li, *Journal of Applied Physics*, **2012**, *112* (10), 103924.
28. S. Kuld, C. Conradsen, P. G. Moses, I. Chorkendorff, J. Sehested, Quantification of Zinc Atoms in a Surface Alloy on Copper in an Industrial-Type Methanol Synthesis Catalyst, *Angewandte Chemie International Edition*, **2014**, *53* (23), 5941-5945.
29. Image Processing and Analysis in Java, ImageJ. [www.imagej.nih.gov](http://www.imagej.nih.gov)
30. K. V. Kovtunov, D. A. Barskiy, O. G. Salnikov, D. B. Burueva, A. K. Khudorozhkov, A. V. Bukhtiyarov, I. P. Prosvirin, E. Y. Gerasimov, V. I. Bukhtiyarov, I. V. Koptyug, Strong Metal-Support Interactions for Palladium Supported on TiO<sub>2</sub> Catalysts in the Heterogeneous Hydrogenation with Parahydrogen, *ChemCatChem*, **2015**, *7* (17), 2581-2584.
31. S. J. Tauster, S. C. Fung, R. T. K. Baker, J. A. Horsley, Strong Interactions in Supported-Metal Catalysts, *Science*, **1981**, *211* (4487), 1121.
32. Y. Liu, C. Xu, Nanoporous PdTl Alloys as Non-Platinum Oxygen-Reduction Reaction Electrocatalysts with Enhanced Activity and Durability, *ChemSusChem*, **2013**, *6* (1), 78-84.
33. Y. S. Chang, Y. H. Chang, I. G. Chen, G. J. Chen, Y. L. Chai, T. H. Fang, S. Wu, Synthesis, formation and characterization of ZnTiO<sub>3</sub> ceramics, *Ceramics International*, **2004**, *30* (8), 2183-2189.
34. A. Chaouchi, S. D'Astorg, S. Marinel, M. Aliouat, ZnTiO<sub>3</sub> ceramic sintered at low temperature with glass phase addition for LTCC applications, *Mater Chem Phys*, **2007**, *103* (1), 106-111.
35. A. B. Stiles, F. Chen, J. B. Harrison, X. Hu, D. A. Storm, H. X. Yang, Catalytic conversion of synthesis gas to methanol and other oxygenated products, *Industrial & Engineering Chemistry Research*, **1991**, *30* (5), 811-821.
36. M. Aresta, A. Dibenedetto, Utilisation of CO<sub>2</sub> as a chemical feedstock: opportunities and challenges, *Dalton Transactions*, **2007**, (28), 2975-2992.
37. N. R. C. Fernandes Machado, V. S. Santana, Influence of thermal treatment on the structure and photocatalytic activity of TiO<sub>2</sub> P25, *Catalysis Today*, **2005**, *107-108*, 595-601.

38. M. Oku, K. Wagatsuma, S. Kohiki, Ti 2p and Ti 3p X-ray photoelectron spectra for TiO<sub>2</sub>, SrTiO<sub>3</sub> and BaTiO<sub>3</sub>, *Physical Chemistry Chemical Physics*, **1999**, 1 (23), 5327-5331.
39. XPS simplified. [www.xpssimplified.com](http://www.xpssimplified.com), **2018**.
40. W. Wei, G. Jinlong, Methanation of carbon dioxide: an overview, *Frontiers of Chemical Science and Engineering*, **2011**, 5 (1), 2-10.
41. A. S. Malik, S. F. Zaman, A. A. Al-Zahrani, M. A. Daous, H. Driss, L. A. Petrov, Development of highly selective PdZn/CeO<sub>2</sub> and Ca-doped PdZn/CeO<sub>2</sub> catalysts for methanol synthesis from CO<sub>2</sub> hydrogenation, *Applied Catalysis A: General*, **2018**, 560, 42-53.

# Chapter 8

## Conclusions and future work

This thesis was divided into two different catalytic systems to explore the conversion of renewable energy to hydrogen via water splitting, splitting and the further conversion of hydrogen to methanol by its reaction with CO<sub>2</sub>.

The first catalytic system consisted on the preparation of IrO<sub>2</sub> materials as catalysts for the OER reaction in acid media. IrO<sub>2</sub> catalysts were prepared through a hydrothermal process. Apart from the simplicity of the materials preparation, this method is of particular interest because it avoids the use of heat treatment on dry samples, allowing for the synthesis of the amorphous iridium oxo-hydroxide phase that is known to be responsible for improved activity compared to crystalline rutile IrO<sub>2</sub>. The second catalytic system was focused on the optimisation of PdZn alloy catalysts supported on TiO<sub>2</sub>, prepared by chemical vapour impregnation (CVI), in order to enhance the metal distribution on the surface of the catalyst. CVI consists of a dry preparation technique that avoids contamination from the solvent or from metal precursors, producing highly dispersed metal catalysts. The following conclusions can be made from the research reported in this thesis.

### 8.1 Chapter 3

The aim of chapter 3 was to determine the effect of the base used during the synthesis of amorphous IrO<sub>2</sub> materials through a hydrothermal preparation. The corresponding carbonate and hydroxide bases from lithium, sodium and potassium were used during the synthesis. The amorphicity of the prepared IrO<sub>2</sub> catalysts was confirmed by XRD and Raman spectroscopy. Although, the use of conventional TEM microscopes showed crystalline IrO<sub>2</sub> due to electron beam damage, realistic TEM images were obtained using a low electron dose HR-TEM microscope. Ir(4f) XPS characterisation confirmed the presence of different iridium sites: Ir(IV) forming part of the oxide-like lattice and Ir(III) sites and/or iridium hydroxide at the surface. Macroscopic morphology is dependent on the cation present during the synthesis. The use of Li<sub>2</sub>CO<sub>3</sub> or LiOH led to sponge like morphology while flat surfaces were observed when K<sub>2</sub>CO<sub>3</sub> or KOH were used as a base. An intermediate morphology with flat surfaces and porous structures was obtained when Na<sub>2</sub>CO<sub>3</sub> or NaOH were used as a base. Improved surface area correlated with more porous morphologies: IrO<sub>2</sub> catalysts prepared with potassium bases had the lowest surface area while catalysts prepared with lithium bases showed the highest. Significantly, IrO<sub>2</sub>-Li<sub>2</sub>CO<sub>3</sub> had comparable surface area to

the state of the art  $\text{IrO}_2\cdot 2\text{H}_2\text{O}$ . Synthesised catalysts and commercial standards were tested towards OER in a three-electrode flow cell set up in 0.1 M  $\text{HClO}_4$ . Catalytic intrinsic activity and stability were determined by LSV (1.2  $V_{\text{RHE}}$  to 1.8  $V_{\text{RHE}}$  at  $5 \text{ mV}\cdot\text{s}^{-1}$ ) and CP ( $10 \text{ mA}\cdot\text{cm}^{-2}$ , 2h) respectively. The use of  $\text{Li}^+$  bases led to materials with improved catalytic activity and stability compared to other bases. In our reaction system,  $\text{IrO}_2\text{-LiOH}$  had comparable activity and stability to the commercial state of the art  $\text{IrO}_2\cdot 2\text{H}_2\text{O}$ . Whereas, the reaction overpotential, determined by LSV at a current density of  $10 \text{ mA}\cdot\text{cm}^{-2}$ , reduced by 33 mV on the  $\text{IrO}_2\text{-Li}_2\text{CO}_3$  compared to the commercial  $\text{IrO}_2\cdot 2\text{H}_2\text{O}$  catalyst with improved stability. Nevertheless, no correlations between activity or stability with physical or chemical features were found. This work stresses the detrimental effect of heat treatment in air, even at mild temperatures, on the catalytic activity towards OER which could be correlated with the loss of hydration as observed by TGA-MS measurements.

## Future work

It has been shown that the use of  $\text{Li}_2\text{CO}_3$  base during the hydrothermal synthesis of  $\text{IrO}_2$  led to a catalyst with improved activity and stability towards OER in acid media compared to commercial  $\text{IrO}_2$ . Nevertheless, the factor determining its improved performance was not determined. When using Na-containing or K-containing bases significant cation contamination (2 at %) was detected by SEM-EDX and hence it could be thought that lithium remained in the material, which could be acting as a dopant. It would be desirable to determine the doping/poisoning effect of different cations on  $\text{IrO}_2$  catalytic performance, specifically lithium.

### 8.2 Chapter 4

The aim of chapter 4 was to determine if the base used during the hydrothermal synthesis of supported  $\text{IrO}_2/\text{ATO}$  catalysts for the OER reaction was a determining parameter as observed for non-supported  $\text{IrO}_2$  materials. The iridium loading on ATO determined by SEM-EDX after preparation corresponded with the theoretical value, regardless of the base used, suggesting that the hydrothermal synthesis is a feasible methodology for the preparation of supported materials. However,  $\text{IrO}_2$  precipitates under the preparation conditions and it is feasible that the metal was not attached to the support. Indeed, it was found by TEM characterisation, although perceptible to electron beam damage, that a film of  $\text{IrO}_2$  was formed over the support when  $\text{Li}_2\text{CO}_3$  or  $\text{Na}_2\text{CO}_3$  were used as a base during the preparation, whereas not supported  $\text{IrO}_2$  agglomerates were formed when  $\text{K}_2\text{CO}_3$  was used. The lack of metal-support interaction observed for  $\text{IrO}_2/\text{ATO-K}_2\text{CO}_3$  accounted for the low activity and stability compared to the other materials. Normalising to the iridium loading on

the electrode, supported  $\text{IrO}_2/\text{ATO-Li}_2\text{CO}_3$  showed improved activity and stability than unsupported  $\text{IrO}_2\text{-Li}_2\text{CO}_3$ , which would be related with the higher iridium surface area. A thin layer of the support over the  $\text{IrO}_2$  was grown by performing heat treatments under reducing and oxidising conditions, in order to stabilise the catalytic activity. In correlation with what was observed for unsupported  $\text{IrO}_2\text{-Li}_2\text{CO}_3$  catalysts, annealing in air led to catalyst deactivation. The activity measured by LSV of supported  $\text{IrO}_2\text{-Li}_2\text{CO}_3/\text{ATO}$  catalyst increased by 24 mV (at  $10 \text{ mA}\cdot\text{cm}^2$ ) after annealing at  $300^\circ\text{C}$ . After reduction treatment at  $300^\circ\text{C}$ , the  $\text{IrO}_2$  film observed for the as prepared catalyst agglomerated, forming nanoparticles followed by the support growth over the metallic iridium, as observed by low dose electron HR-TEM. As a consequence, iridium active sites were blocked from water molecules, which would stop the OER reaction from proceeding. Hence, the optimisation of  $\text{IrO}_2$  catalysts by annealing should be avoided.

### Future work

The 83 mV rise in potential during chronopotentiometry ( $10 \text{ mA}\cdot\text{cm}^{-2}$  for 2 h) suggests that supported  $\text{IrO}_2/\text{ATO}$  could be further optimised. However, the optimisation should be sought by improving the preparation methodology (e.g., iridium loading,  $\text{IrCl}_3$  to  $\text{Li}_2\text{CO}_3$  molar ratio, solvent) rather than through heat treatment. In order to enhance the iridium-support interaction it would be interesting to induce the simultaneous precipitation of ATO and  $\text{IrO}_2$ .

### 8.3 Chapter 5

It was noticed that after annealing in air at  $500^\circ\text{C}$  to induce the crystallisation of amorphous  $\text{IrO}_2$  to rutile, the formation of a hollandite structure was detected among the common rutile phase, by XRD. The aim of chapter 5 was to report the synthesis of single-phase  $\text{Li}_x\text{IrO}_2$  hollandite with lithium as the cation host within the channel structure and to compare it to  $\text{IrO}_2$  rutile prepared by the same synthetic procedure towards OER. Under high lithium availability, the hollandite phase is preferentially formed after annealing in air at  $500^\circ\text{C}$ . Conversely, in the absence of lithium the common rutile phase was formed after annealing. It was found through XPS characterisation and by comparison with commercial rutile  $\text{IrO}_2$  that synthesised rutile  $\text{IrO}_2$  is formed mainly of Ir(IV) sites, with oxide oxygen comprising the principal contribution to the O(1s) peak. Nevertheless, crystalline  $\text{Li}_x\text{IrO}_2$  hollandite had a major contribution of hydroxide oxygen and a mixture of iridium species which, on the bases of previous literature on iridium-based hollandites, were assigned to the presence of Ir(IV) and Ir(III) sites. As expected from previous chapters, rutile  $\text{IrO}_2$  (which went through annealing at  $500^\circ\text{C}$ ) presented lower catalytic activity towards OER compared to as-prepared  $\text{IrO}_2\text{-Li}_2\text{CO}_3$ . As a consequence, Ir(IV) and Ir(III) sites present after annealing in the

hollandite structure, no catalyst deactivation compared to the fresh  $\text{IrO}_2\text{-Li}_2\text{CO}_3$  catalyst was observed.

## Future work

Apart from the crystallinity, no appreciable differences in the characterisation were observed between as-prepared  $\text{IrO}_2\text{-Li}_2\text{CO}_3$  and hollandite  $\text{IrO}_2$ . It would be useful to elongate the CP stability test for longer periods to emphasise differences between the catalysts. A plausible deactivation mechanism for amorphous  $\text{IrO}_2$  would be its crystallisation to the less active rutile phase. The formation of crystalline hollandite  $\text{IrO}_2$  could be a strategy to overcome deactivation due to phase changes. In order to investigate the stability issue, it would be interesting to determine the different deactivation mechanisms of hollandite catalysts. Channels along the hollandite structure can accommodate different cations: it would be also desirable to study the effect of varying the cation hosted in the structure.

### 8.4 Chapter 6

The aim of chapter 6 was to significantly reduce the amount of iridium on the electrode by diluting it with a non-noble metal, without compromising the activity or stability towards OER. Because only iridium is known to be stable towards dissolution under reaction conditions it was postulated that a core-shell catalyst design with iridium at the surface could fulfil this goal instead of a homogeneous distribution of both metals throughout the material. XPS characterisation confirmed the homogeneous distribution of iridium and the diluent agent used (Cu or Ni). On one hand the elemental XPS quantification agreed with the theoretical value and on the other the Ir(4f) peak shifted towards higher binding energy with the addition of Ni or Cu. Conversely, in a core-shell distribution, XPS quantification showed iridium enrichment compared to the nominal value indicating a larger presence of iridium at the surface, whilst the shifting of the Ir(4f) peak towards higher binding energy due to intermetallic interactions was not observed. The presence of Ni or Cu at the surface resulted in a severe increase in the overpotential measured by LSV compared to  $\text{IrO}_2\text{-Li}_2\text{CO}_3$  catalyst prepared in chapter 3. Additionally, even the catalyst with the lowest concentration of diluent,  $\text{Ir}_{0.8}\text{Ni}_{0.2}\text{O}_2$ , presented complete deactivation during CP ( $10 \text{ mA}\cdot\text{cm}^{-2}$ ) before 30 min. Nevertheless, no decrease in activity or stability was observed by LSV or CP respectively for the  $\text{Ir}_{0.5}\text{Ni}_{0.5}\text{O}_2$  catalyst synthesised with a core-shell approach. Therefore, the loading of iridium was halved by concentrating it at the surface of the catalysts and substituting inaccessible active sites with a diluent.

## Future work

It would be useful to further optimise the core-shell synthesis process. No characterisation on the core formation was performed. It would be interesting to determine, by cryogenic TEM, the core particle size distribution. The synthesis of homogeneous core particles would enable one to determine the minimum  $\text{IrO}_2$  thickness necessary on the shell to preserve the activity and stability compared to bulk  $\text{IrO}_2$ . This would correspond to the most efficient usage of iridium. Moreover, focusing on the synthesis of smaller core colloid particles would be a feasible way for improving iridium surface area.

### 8.5 Chapter 7

Finally, the aim of chapter 7 was to optimise the synthesis of PdZn alloy catalysts supported on  $\text{TiO}_2$  via chemical vapour impregnation (CVI) for direct  $\text{CO}_2$  hydrogenation to  $\text{CH}_3\text{OH}$ . The first parameter optimised was the palladium to zinc molar ratio at a constant palladium loading of 5 wt %. Catalysts with a Pd:Zn molar ratio from (1:1) to (1:10) were prepared by CVI and annealed in air at 500 °C for 16 h, followed by pre-reduction in 5%  $\text{H}_2/\text{Ar}$  to induce the PdZn alloy formation. Increasing the zinc molar proportion on the catalyst was followed by improved  $\text{CO}_2$  conversion and methanol selectivity. As reported in the literature, this could be correlated with a higher PdZn alloy formation, as observed by XPS. However, as observed for 5% PdZn(1:10)/ $\text{TiO}_2$ , the  $\text{CO}_2$  conversion dropped compared to the 5% PdZn(1:5)/ $\text{TiO}_2$  catalyst, indicating that a high excess of zinc can block active PdZn sites. The reduction temperature for forming the PdZn alloy on the PdZn(1:5)/ $\text{TiO}_2$  was increased from 400 °C to 650 °C with the aim of increasing the amount of zinc in the alloy, which can vary from 40 at. % to 60 at. %. Nevertheless, XRD showed that zinc was being incorporated into the  $\text{TiO}_2$  lattice forming  $\text{ZnTiO}_3$  as well as on the PdZn alloy. As expected, reduction at 650 °C instead of 400 °C followed by particle sintering correlated with the observed reduction in  $\text{CO}_2$  conversion, whereas the higher PdZn alloy formation observed by XRD led to improved methanol selectivity. This in turn accounted for the higher methanol productivity for the 1% PdZn(1:5)/ $\text{TiO}_2$  and 2.5 % PdZn(1:5)/ $\text{TiO}_2$  catalysts. The paramount benefit of pre-reducing at higher temperature was the detected reduction of the  $\text{CH}_4$  selectivity, by one order of magnitude. It was hypothesised that the PdZn- $\text{TiO}_2$  interphase was responsible for methane formation. To prove this, two model catalysts were synthesised (PdZn/ $\text{ZnTiO}_3$  and Pd/ $\text{ZnTiO}_3$ ). After pre-reduction at 400 °C, the PdZn alloy was confirmed by XRD on both catalysts. This implied that on the Pd/ $\text{ZnTiO}_3$  catalyst, the zinc migrated from the support to the palladium to form the alloy, forming a PdZn- $\text{TiO}_2$  interphase, whilst because of the Zn excess on the PdZn/ $\text{ZnTiO}_3$  catalyst no PdZn- $\text{TiO}_2$  interphase was formed. No significant catalytic differences, apart from the methane production, were observed between 5%

PdZn/TiO<sub>2</sub>, 5% PdZn/ZnTiO<sub>3</sub> and Pd/ZnTiO<sub>3</sub>. The catalysts with the PdZn-TiO<sub>2</sub> interphase produced CH<sub>4</sub> at comparable rates whereas the methane production dropped one order of magnitude on the 5% PdZn/ZnTiO<sub>3</sub> catalyst.

### Future work

It would be useful to further confirm the active sites responsible for CH<sub>4</sub> formation on the PdZn/TiO<sub>2</sub> systems by means of computational chemistry and in situ spectroscopy (e.g., ion scattering, Raman spectroscopy or diffuse reflectance FTIR). ZnTiO<sub>3</sub> is a low surface area support (15 m<sup>2</sup>·g<sup>-1</sup>), therefore it would be interesting to synthesise high surface area ZnTiO<sub>3</sub> to increase the PdZn alloy dispersion. In order for a catalyst to be significant for industry, it must remain active for several years: it would be interesting to study these materials for prolonged runs and under more severe temperature and pressure conditions. Moreover, copper catalysts are known to not be stable in the presence of water, so it would be important to study the effect of water on the PdZn alloy catalysts.

# Appendix I

## Name and formula

Reference code: 00-004-0477  
 Mineral name: Anatase, syn  
 Compound name: Titanium Oxide  
 Empirical formula: O<sub>2</sub>Ti  
 Chemical formula: TiO<sub>2</sub>

## Crystallographic parameters

Crystal system: Tetragonal  
 Space group: I41/amd  
 Space group number: 141  
 a (Å): 3.7830  
 b (Å): 3.7830  
 c (Å): 9.5100  
 Alpha (°): 90.0000  
 Beta (°): 90.0000  
 Gamma (°): 90.0000  
 Calculated density (g/cm<sup>3</sup>): 3.90  
 Volume of cell (10<sup>6</sup> pm<sup>3</sup>): 136.10  
 Z: 4.00  
 RIR: -

## Status, subfiles and quality

Status: Marked as deleted by ICDD  
 Subfiles:  
 Alloy, metal or intermetallic  
 Common Phase  
 Excipient  
 Forensic  
 Inorganic  
 Mineral  
 Pharmaceutical  
 Pigment/Dye  
 Quality: Indexed (I)

## Comments

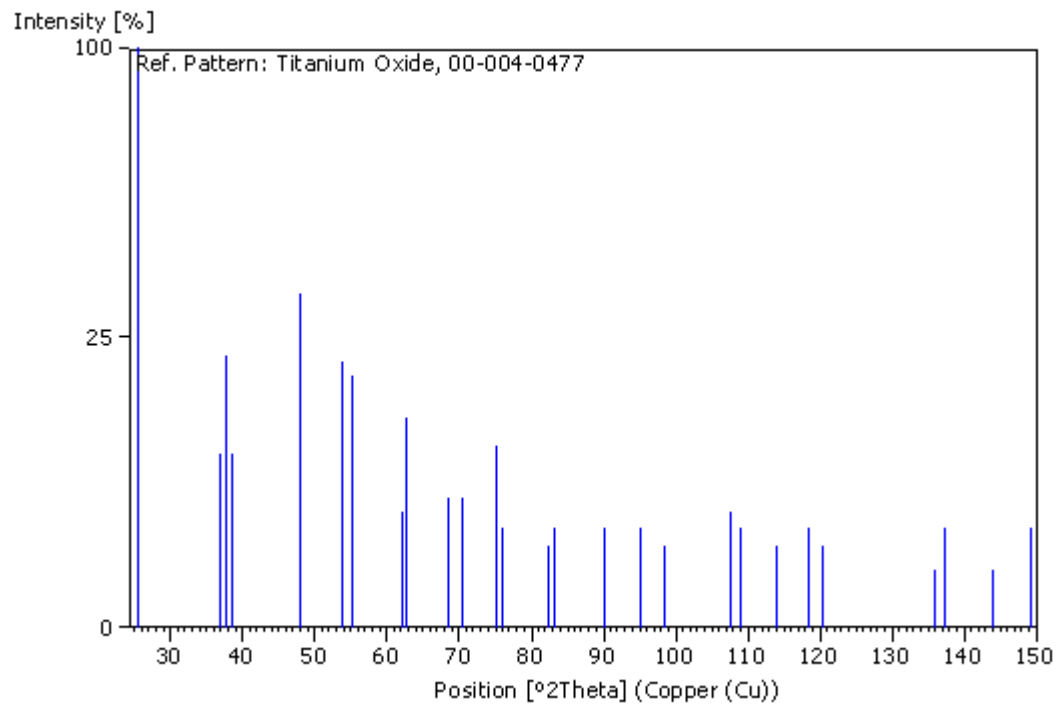
Creation Date: 9/1/1954  
 Modification Date: 1/1/1970  
 Warning: One or more lines are unindexed.

## References

Primary reference: Swanson, Tatge., *Private Communication*, (1950)

**Peak list**

No.	h	k	l	d [Å]	2Theta [deg]	I [%]
1	1	0	1	3.51000	25.354	100.0
2	1	0	3	2.43500	36.884	9.0
3	0	0	4	2.37900	37.785	22.0
4	1	1	2	2.33600	38.507	9.0
5	2	0	0	1.89100	48.077	33.0
6	1	0	5	1.69900	53.922	21.0
7	2	1	1	1.66500	55.116	19.0
8	2	1	3	1.49400	62.075	4.0
9	2	0	4	1.48000	62.728	13.0
10	1	1	6	1.36700	68.596	5.0
11	2	2	0	1.33700	70.359	5.0
12	2	1	5	1.26400	75.094	10.0
13	3	0	1	1.25000	76.084	3.0
14	3	0	3	1.17100	82.267	2.0
15	3	1	2	1.16090	83.140	3.0
16				1.08690	90.261	3.0
17	3	2	1	1.04330	95.179	3.0
18	1	0	9	1.01730	98.436	2.0
19	3	1	6	0.95500	107.530	4.0
20	4	0	0	0.94610	109.014	3.0
21	3	2	5	0.91890	113.919	2.0
22	1	1	10	0.89600	118.568	3.0
23	2	2	8	0.88770	120.396	2.0
24	3	2	7	0.83110	135.896	1.0
25	4	1	5	0.82680	137.391	3.0
26	3	0	9	0.81000	143.974	1.0
27				0.79900	149.193	3.0

**Stick Pattern**

**Name and formula**

Reference code:	01-075-8100
Compound name:	Antimony Tin Oxide
PDF index name:	Antimony Tin Oxide
Empirical formula:	O <sub>2</sub> Sb <sub>0.3</sub> Sn <sub>0.7</sub>
Chemical formula:	( Sn <sub>0.7</sub> Sb <sub>0.3</sub> ) O <sub>2</sub>

**Crystallographic parameters**

Crystal system:	Tetragonal
Space group:	P42/mnm
Space group number:	136
a (Å):	4.7358
b (Å):	4.7358
c (Å):	3.1857
Alpha (°):	90.0000
Beta (°):	90.0000
Gamma (°):	90.0000
Volume of cell (10 <sup>6</sup> pm <sup>3</sup> ):	71.45
Z:	2.00
RIR:	9.56

**Subfiles and quality**

Subfiles:	ICSD Pattern
	Inorganic
Quality:	Indexed (I)

**Comments**

ANX:	AX2
ICSD collection code:	155964
Creation Date:	9/1/2009
Modification Date:	9/1/2011
ANX:	AX2
Analysis:	O <sub>2</sub> Sb <sub>0.3</sub> Sn <sub>0.7</sub>
Formula from original source:	(Sn <sub>0.7</sub> Sb <sub>0.3</sub> ) O <sub>2</sub>
ICSD Collection Code:	155964
Calculated Pattern Original Remarks:	Sample prepared from Sb <sub>2</sub> O <sub>3</sub> . Sample contains also other phases (Sb, Sb <sub>2</sub> O <sub>4</sub> )
Minor Warning:	No R factors reported/abstracted
Wyckoff Sequence:	f a (P42/MNM)
Unit Cell Data Source:	Powder Diffraction.

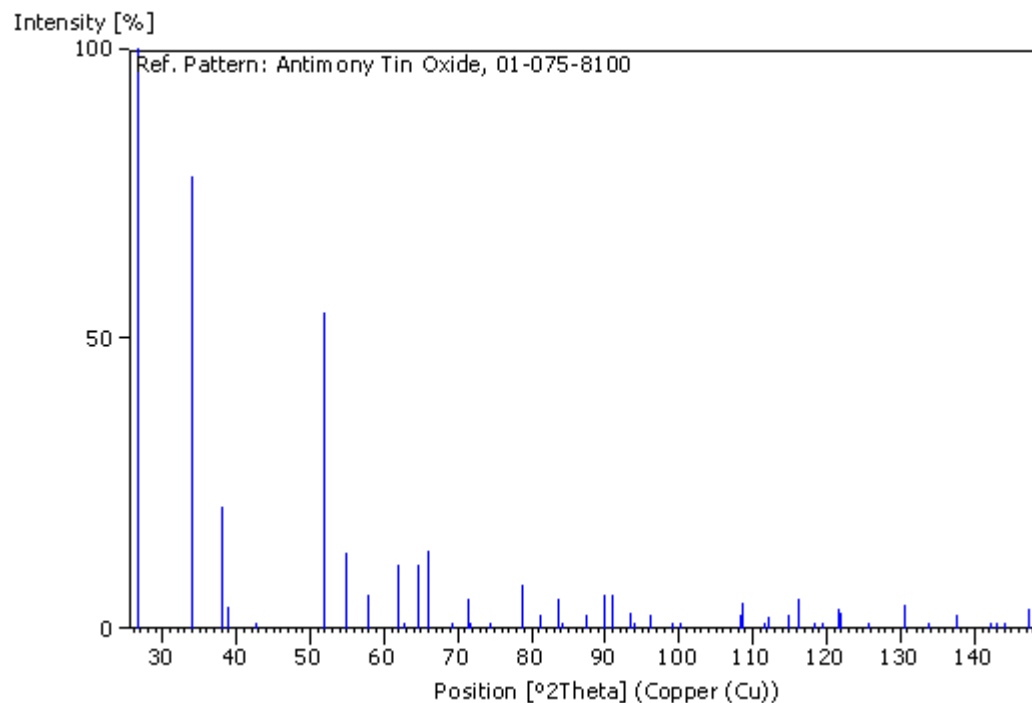
**References**

Primary reference:	<i>Calculated from ICSD using POWD-12++</i>
Structure:	Tena, M.A., Sorli, S., Llusar, M., Badenes, J.A., Fores, A., Monros, G., <i>Z. Anorg. Allg. Chem.</i> , <b>631</b> , 2188, (2005)

**Peak list**

No.	h	k	l	d [Å]	2Theta [deg]	I [%]
1	1	1	0	3.34870	26.598	100.0
2	1	0	1	2.64330	33.886	77.9
3	2	0	0	2.36790	37.969	21.0
4	1	1	1	2.30810	38.992	3.7
5	2	1	0	2.11790	42.656	1.1
6	2	1	1	1.76370	51.794	54.5
7	2	2	0	1.67440	54.780	13.0
8	0	0	2	1.59290	57.839	6.1
9	3	1	0	1.49760	61.909	11.1
10	2	2	1	1.48210	62.629	0.1
11	1	1	2	1.43840	64.759	11.1
12	3	0	1	1.41450	65.991	13.6
13	3	1	1	1.35530	69.272	0.2
14	2	0	2	1.32170	71.297	5.2
15	3	2	0	1.31350	71.811	0.1
16	2	1	2	1.27300	74.473	0.2
17	3	2	1	1.21430	78.745	7.7
18	4	0	0	1.18400	81.172	2.5
19	2	2	2	1.15410	83.741	5.0
20	4	1	0	1.14860	84.233	0.2
21	3	3	0	1.11620	87.278	2.3
22	3	1	2	1.09110	89.818	5.8
23	4	1	1	1.08050	90.944	6.0
24	4	2	0	1.05900	93.335	2.7
25	3	3	1	1.05340	93.983	0.1
26	1	0	3	1.03620	96.042	2.3
27	3	2	2	1.01340	98.949	0.1
28	1	1	3	1.01220	99.108	0.1
29	4	2	1	1.00490	100.089	0.1
30	4	0	2	0.95020	108.323	2.6
31	2	1	3	0.94930	108.474	4.5
32	4	1	2	0.93170	111.536	0.1
33	5	1	0	0.92880	112.064	2.1
34	3	3	2	0.91410	114.850	2.3
35	4	3	1	0.90790	116.085	5.0
36	2	2	3	0.89680	118.396	0.1
37	5	1	1	0.89170	119.505	0.1
38	4	2	2	0.88190	121.725	3.4
39	3	0	3	0.88110	121.912	2.5
40	3	1	3	0.86620	125.567	0.1
41	5	2	1	0.84770	130.651	4.0
42	4	4	0	0.83720	133.879	0.8
43	3	2	3	0.82580	137.749	2.4
44	4	3	2	0.81410	142.240	0.1
45	5	3	0	0.81220	143.032	1.1
46	4	4	1	0.80970	144.105	0.1
47	5	1	2	0.80230	147.527	3.3

## **Stick Pattern**



## **Name and formula**

Reference code: 00-022-1141  
 Mineral name: Zabuyelite, syn  
 Compound name: Lithium Carbonate  
 Empirical formula:  $\text{CLi}_2\text{O}_3$   
 Chemical formula:  $\text{Li}_2\text{CO}_3$

## **Crystallographic parameters**

Crystal system:	Monoclinic
Space group:	C2/c
Space group number:	15
a (Å):	8.3590
b (Å):	4.9767
c (Å):	6.1940
Alpha (°):	90.0000
Beta (°):	114.7200
Gamma (°):	90.0000
Calculated density (g/cm <sup>3</sup> ):	2.10
Volume of cell (10 <sup>6</sup> pm <sup>3</sup> ):	234.06
Z:	4.00
RIR:	0.90

## **Subfiles and quality**

Subfiles: Common Phase  
 Educational pattern  
 Forensic  
 Inorganic

Mineral  
NBS pattern  
Pharmaceutical  
Star (S)

Quality:

**Comments**

Color: Colorless  
 Creation Date: 9/1/1972  
 Modification Date: 1/1/1970  
 Additional Patterns: To replace 00-009-0359. See PDF 01-083-1454  
 Color: Colorless  
 Sample Source or Locality: Sample reagent grade from Baker and Adamson Allied Chemical and Dye Corp., New York, NY, USA  
 Structures: Natrite is the Na analogue  
 Temperature of Data Collection: Pattern taken at 298 K  
 Unit Cell Data Source: Powder Diffraction.

**References**

Primary reference: *Natl. Bur. Stand. (U. S. ) Monogr. 25, 8, 42, (1970)*

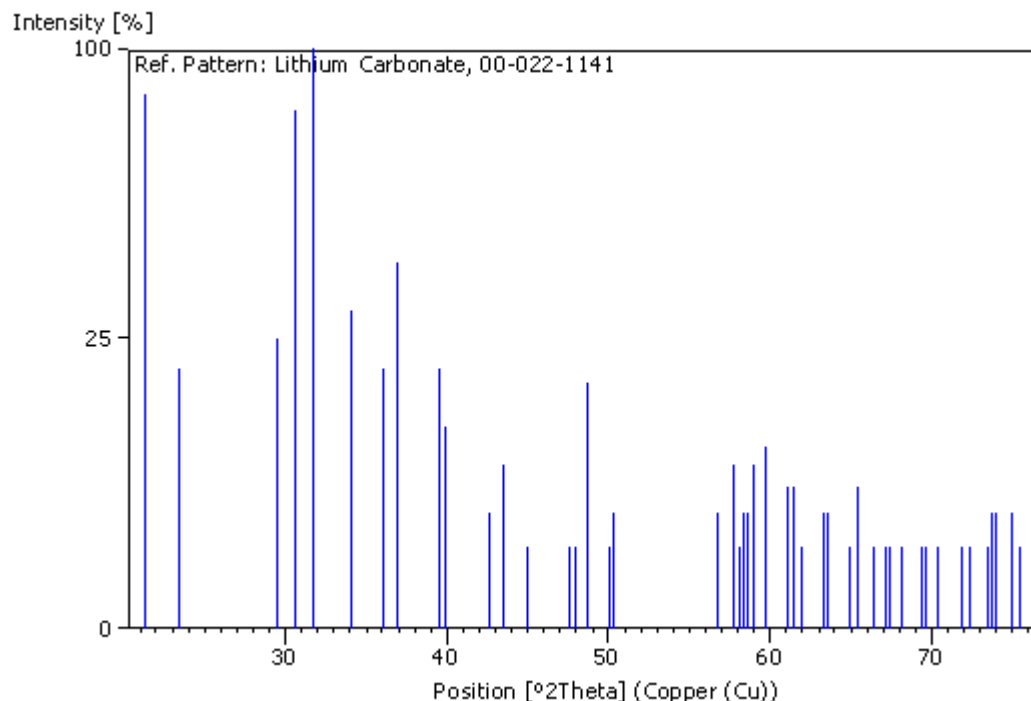
**Peak list**

No.	h	k	l	d [Å]	2Theta [deg]	I [%]
1	-1	1	0	4.16400	21.321	85.0
2	2	0	0	3.79700	23.410	20.0
3	1	1	1	3.02900	29.465	25.0
4	-2	0	2	2.91800	30.613	80.0
5	0	0	2	2.81200	31.797	100.0
6	-1	1	2	2.62700	34.102	30.0
7	0	2	0	2.48800	36.071	20.0
8	-3	1	1	2.43100	36.947	40.0
9	0	2	1	2.27600	39.564	20.0
10	3	1	0	2.25600	39.930	12.0
11	-2	2	1	2.11600	42.697	4.0
12	-2	2	0	2.08100	43.451	8.0
13	-4	0	2	2.01200	45.021	2.0
14	2	0	2	1.91000	47.569	2.0
15	-2	2	2	1.89300	48.023	2.0
16	3	1	1	1.86700	48.735	18.0
17	2	2	1	1.82050	50.064	2.0
18	-3	1	3	1.81210	50.312	4.0
19	1	3	0	1.62080	56.752	4.0
20	-1	3	1	1.59590	57.720	8.0
21	-2	2	3	1.58580	58.123	2.0
22	1	1	3	1.58040	58.341	4.0
23	-5	1	2	1.57230	58.671	4.0
24	-5	1	1	1.56520	58.963	8.0
25	-2	0	4	1.54690	59.731	10.0
26	2	2	2	1.51540	61.103	6.0
27	-4	2	0	1.50920	61.381	6.0
28	0	2	3	1.49800	61.891	2.0
29	-5	1	3	1.46690	63.353	4.0
30	-1	3	2	1.46220	63.580	4.0
31	-1	1	4	1.43600	64.881	2.0
32	-3	3	1	1.42500	65.444	6.0
33	0	0	4	1.40660	66.409	2.0
34	-6	0	2	1.39230	67.182	2.0

---

35	3	3	0	1.38790	67.423	2.0
36	-3	3	2	1.37540	68.119	2.0
37	1	3	2	1.35290	69.413	2.0
38	4	2	1	1.34970	69.601	2.0
39	4	0	2	1.33610	70.414	2.0
40	-2	2	4	1.31320	71.830	2.0
41	-5	1	4	1.30420	72.403	2.0
42	5	1	1	1.28720	73.515	2.0
43	-1	3	3	1.28420	73.715	4.0
44	3	3	1	1.28070	73.950	4.0
45	6	0	0	1.26550	74.990	4.0
46	-4	2	4	1.25860	75.473	2.0

### **Stick Pattern**



### **Name and formula**

Reference code: 00-005-0681  
 Mineral name: Palladium, syn  
 Compound name: Palladium  
 Empirical formula: Pd  
 Chemical formula: Pd

### **Crystallographic parameters**

Crystal system:	Cubic
Space group:	Fm-3m
Space group number:	225
a (Å):	3.8898
b (Å):	3.8898
c (Å):	3.8898
Alpha (°):	90.0000

---

Beta (°): 90.0000  
 Gamma (°): 90.0000  
 Volume of cell (10^6 pm^3): 58.85  
 Z: 4.00  
 RIR: -

### **Status, subfiles and quality**

Status:	Alternate Pattern
Subfiles:	Alloy, metal or intermetallic Common Phase Educational pattern Forensic Inorganic Mineral NBS pattern
Quality:	Star (S)

### **Comments**

Color:	Black
Creation Date:	9/1/1955
Modification Date:	1/1/1970
Additional Patterns:	See PDF 00-046-1043
Analysis:	Spectroscopic analysis shows <0.1% Ag, Si; <0.01% Ca, Cu, Mg, Pt; 0.0001% Pb
Color:	Black
Physical property:	Hydrogen storage materials
Sample Source or Locality:	Sample from Johnson Matthey Company, Ltd
Temperature of Data Collection:	Pattern taken at 299 K
Unit Cell Data Source:	Powder Diffraction.

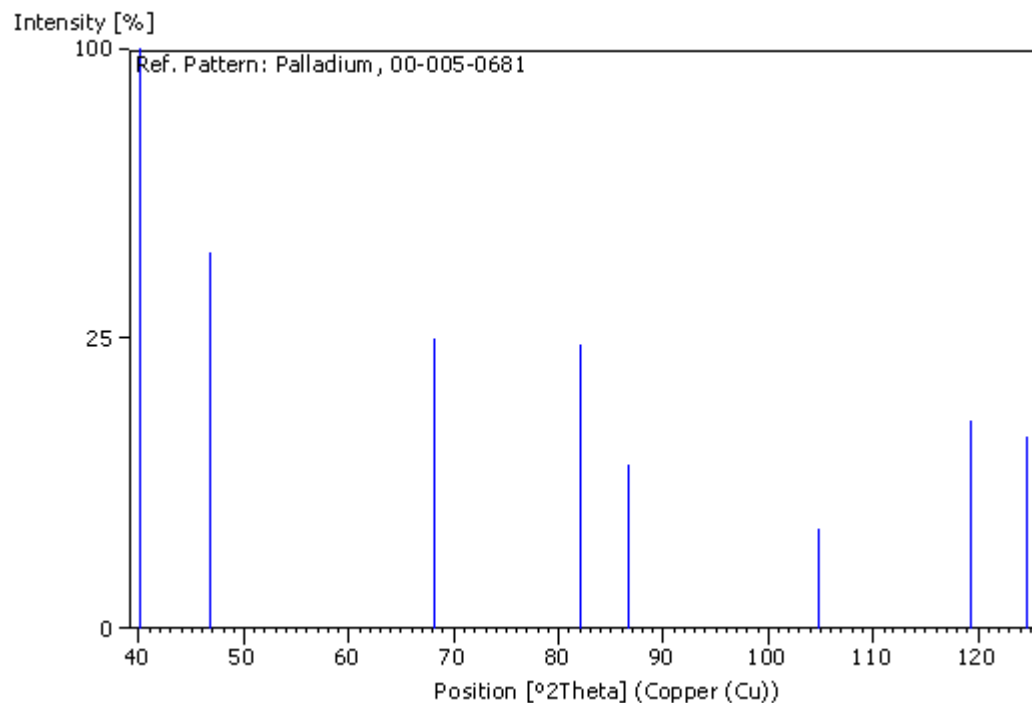
### **References**

Primary reference: Swanson, Tatge., *Natl. Bur. Stand. (U. S. ), Circ. 539, I, 21,* (1953)

### **Peak list**

No.	h	k	l	d [Å]	2Theta [deg]	I [%]
1	1	1	1	2.24600	40.115	100.0
2	2	0	0	1.94500	46.662	42.0
3	2	2	0	1.37600	68.085	25.0
4	3	1	1	1.17300	82.096	24.0
5	2	2	2	1.12320	86.598	8.0
6	4	0	0	0.97230	104.792	3.0
7	3	3	1	0.89240	119.351	13.0
8	4	2	0	0.86970	124.677	11.0

## **Stick Pattern**



## **Name and formula**

Reference code: 00-006-0515  
 Compound name: Palladium Oxide  
 Common name: palladinite  
 Empirical formula: OPd  
 Chemical formula: PdO

## **Crystallographic parameters**

Crystal system: Tetragonal  
 Space group: P42/mmc  
 Space group number: 131  
 a (Å): 3.0430  
 b (Å): 3.0430  
 c (Å): 5.3370  
 Alpha (°): 90.0000  
 Beta (°): 90.0000  
 Gamma (°): 90.0000  
 Calculated density (g/cm<sup>3</sup>): 8.24  
 Volume of cell (10<sup>6</sup> pm<sup>3</sup>): 49.42  
 Z: 2.00  
 RIR: -

## **Status, subfiles and quality**

Status: Alternate Pattern  
 Subfiles: Alloy, metal or intermetallic  
 Common Phase  
 Educational pattern  
 Inorganic

NBS pattern  
 Superconducting Material  
 Quality: Indexed (I)

### **Comments**

Color: Black  
 Creation Date: 9/1/1956  
 Modification Date: 1/1/1970  
 Additional Patterns:  
 Analysis: Validated by calculated pattern 00-043-1024. See PDF 00-041-1107  
 Spectrographic analysis: <0.1% Pt; <0.01% Fe, Si; <0.001% Ag,  
 Al, Ca, Cu, Mg, Pb. Color: Black. Sample Preparation: PdO formed  
 by heating metal at 600 C for 18 hours in air. Sample Source or  
 Locality: Pd metal from Bishop and Company. Temperature of Data  
 Collection: Pattern taken at 299 K. Warning: Lines with abs(delta  
 $2\Theta$ )>0.06 DEG. Unit Cell Data Source: Powder Diffraction.

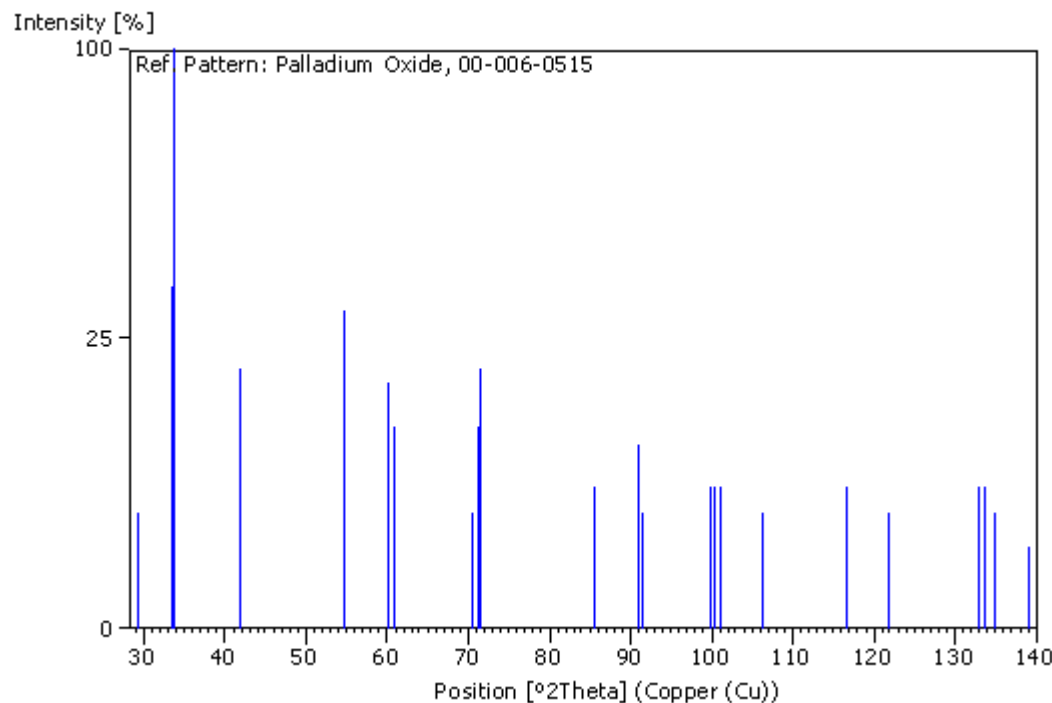
### **References**

Primary reference: Swanson et al., *Natl. Bur. Stand. (U. S. ), Circ. 539, IV, 27, (1955)*

### **Peak list**

No.	h	k	l	d [Å]	2Theta [deg]	I [%]
1	1	0	0	3.04600	29.297	4.0
2	0	0	2	2.66700	33.575	35.0
3	1	0	1	2.64400	33.876	100.0
4	1	1	0	2.15300	41.928	20.0
5	1	1	2	1.67400	54.794	30.0
6	1	0	3	1.53600	60.198	18.0
7	2	0	0	1.52200	60.810	12.0
8	0	0	4	1.33500	70.480	4.0
9	2	0	2	1.32200	71.278	12.0
10	2	1	1	1.31900	71.465	20.0
11	1	1	4	1.13340	85.630	6.0
12	2	1	3	1.08060	90.934	10.0
13	2	2	0	1.07610	91.422	4.0
14	1	0	5	1.00720	99.777	6.0
15	2	0	4	1.00350	100.280	6.0
16	2	2	2	0.99770	101.081	6.0
17	3	0	1	0.99660	101.235	4.0
18	3	1	0	0.96230	106.352	4.0
19	3	1	2	0.90530	116.615	6.0
20	3	0	3	0.88120	121.889	4.0
21	2	1	5	0.84000	132.990	6.0
22	2	2	4	0.83770	133.718	6.0
23	3	2	1	0.83380	134.989	4.0
24	1	1	6	0.82190	139.179	2.0

## **Stick Pattern**



## **Name and formula**

Reference code: 01-072-2936  
 Compound name: Palladium Zinc  
 Empirical formula: PdZn  
 Chemical formula: PdZn

## **Crystallographic parameters**

Crystal system:	Tetragonal
Space group:	P4/mmm
Space group number:	123
a (Å):	2.8990
b (Å):	2.8990
c (Å):	3.3460
Alpha (°):	90.0000
Beta (°):	90.0000
Gamma (°):	90.0000
Volume of cell (10^6 pm^3):	28.12
Z:	1.00
RIR:	12.67

## **Subfiles and quality**

Subfiles:	Alloy, metal or intermetallic ICSD Pattern
	Inorganic
Quality:	Indexed (I)

## **Comments**

ANX: NO  
 ICSD collection code: 105752  
 Creation Date: 9/1/2006  
 Modification Date: 9/1/2011  
 ANX: NO  
 Analysis: Pd1 Zn1  
 Formula from original source: Pd Zn  
 ICSD Collection Code: 105752  
 Calculated Pattern Original Remarks: Composition: Pd.96 Zn1.04. Minor Warning: No e.s.d reported/abstracted on the cell dimension. No R factors reported/abstracted. Wyckoff Sequence: d a(P4/MMM). Unit Cell Data Source: Powder Diffraction.

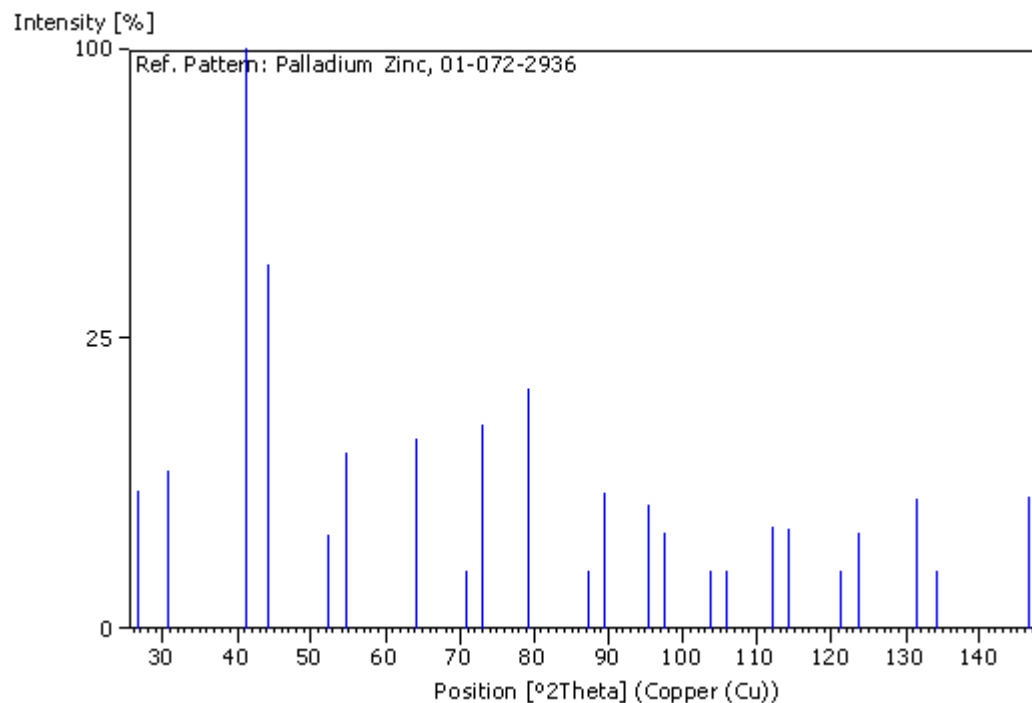
## **References**

Primary reference: *Calculated from ICSD using POWD-12++*  
 Structure: Bittner, H., Nowotny, H., *Monatsh. Chem.*, **81**, 679, (1950)

## **Peak list**

No.	h	k	l	d [Å]	2Theta [deg]	I [%]
1	0	0	1	3.34600	26.619	5.6
2	1	0	0	2.89900	30.819	7.5
3	1	0	1	2.19100	41.167	100.0
4	1	1	0	2.04990	44.144	39.2
5	1	1	1	1.74800	52.294	2.7
6	0	0	2	1.67300	54.830	9.1
7	1	0	2	1.44950	64.204	10.7
8	2	0	0	1.44950	64.204	10.7
9	2	0	1	1.33010	70.779	0.9
10	2	1	0	1.29610	72.929	12.4
11	1	1	2	1.29610	72.929	12.4
12	2	1	1	1.20890	79.165	17.2
13	0	0	3	1.11530	87.366	0.1
14	2	0	2	1.09550	89.360	5.5
15	1	0	3	1.04100	95.456	4.5
16	2	2	0	1.02500	97.443	2.8
17	2	1	2	1.02500	97.443	2.8
18	2	2	1	0.98000	103.630	0.6
19	1	1	3	0.98000	103.630	0.6
20	3	0	0	0.96630	105.720	0.2
21	3	0	1	0.92840	112.137	3.1
22	3	1	0	0.91670	114.343	3.0
23	3	1	1	0.88420	121.193	0.8
24	2	0	3	0.88420	121.193	0.8
25	2	2	2	0.87400	123.611	2.7
26	2	1	3	0.84550	131.304	5.0
27	0	0	4	0.83650	134.104	0.8
28	3	0	2	0.83650	134.104	0.8
29	1	0	4	0.80400	146.705	5.1
30	3	1	2	0.80400	146.705	5.1

## **Stick Pattern**



## **Name and formula**

Reference code:	00-015-0870
Compound name:	Iridium Oxide
Empirical formula:	$\text{IrO}_2$
Chemical formula:	$\text{IrO}_2$

## **Crystallographic parameters**

Crystal system:	Tetragonal
Space group:	P42/mnm
Space group number:	136
a (Å):	4.4983
b (Å):	4.4983
c (Å):	3.1544
Alpha (°):	90.0000
Beta (°):	90.0000
Gamma (°):	90.0000
Calculated density (g/cm <sup>3</sup> ):	11.66
Volume of cell (10 <sup>6</sup> pm <sup>3</sup> ):	63.83
Z:	2.00
RIR:	7.90

## **Subfiles and quality**

Subfiles:	Alloy, metal or intermetallic Inorganic NBS pattern
Quality:	Star (S)

**Comments**

Color: Black  
 Creation Date: 9/1/1965  
 Modification Date: 1/1/1970  
 Additional Patterns: Validated by calculated pattern 00-043-1019  
 Analysis: Spectroscopic analysis: 0.01 to 0.1% each of Na, Pb and Pt. Color: Black. Sample Preparation: It was heated in an evacuated sealed Vycor tube for 6 hours at 900 C. Sample Source or Locality: Sample was obtained from K&K Laboratories, Inc., Jamaica, New York, USA. Temperature of Data Collection: Pattern taken at 298 K. Unit Cell Data Source: Powder Diffraction.

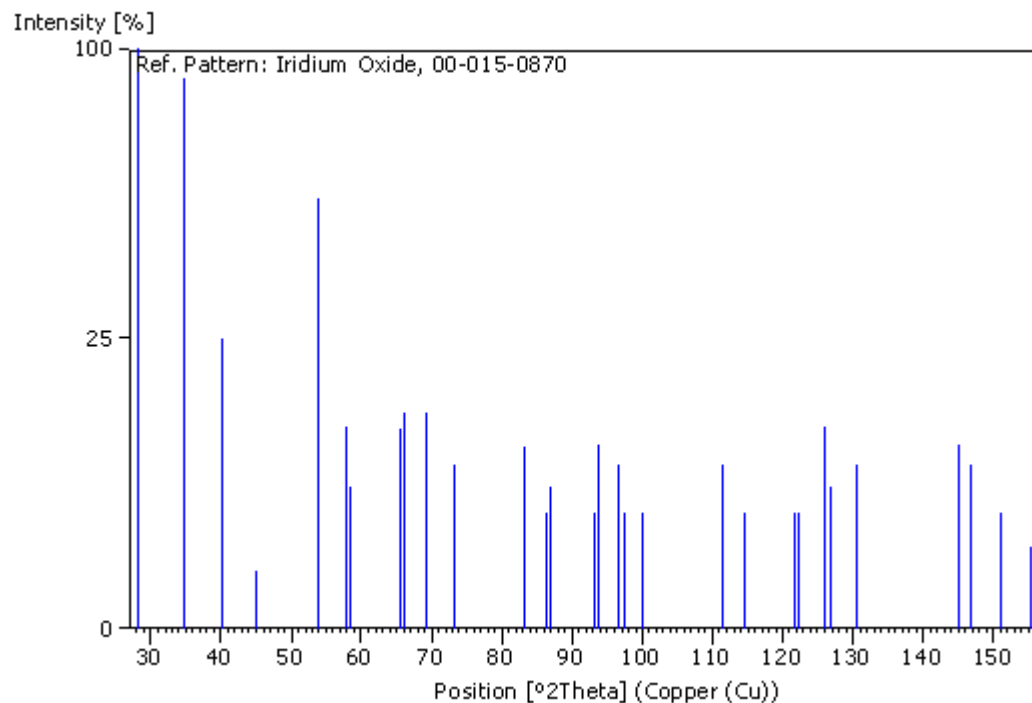
**References**

Primary reference: *Natl. Bur. Stand. (U. S. ) Monogr. 25, 4, 19, (1965)*

**Peak list**

No.	h	k	l	d [Å]	2Theta [deg]	I [%]
1	1	1	0	3.17800	28.055	100.0
2	1	0	1	2.58200	34.715	90.0
3	2	0	0	2.24880	40.063	25.0
4	2	1	0	2.01190	45.023	1.0
5	2	1	1	1.69600	54.025	55.0
6	2	2	0	1.59030	57.943	12.0
7	0	0	2	1.57710	58.475	6.0
8	3	1	0	1.42270	65.563	12.0
9	1	1	2	1.41330	66.054	14.0
10	3	0	1	1.35420	69.336	14.0
11	2	0	2	1.29140	73.237	8.0
12	3	2	1	1.16040	83.184	10.0
13	4	0	0	1.12470	86.455	4.0
14	2	2	2	1.11990	86.917	6.0
15	3	3	0	1.06020	93.198	4.0
16	3	1	2	1.05630	93.646	10.0
17	4	1	1	1.03100	96.686	8.0
18	1	0	3	1.02400	97.571	4.0
19	4	2	0	1.00580	99.967	4.0
20	2	1	3	0.93180	111.518	8.0
21	4	0	2	0.91570	114.537	4.0
22	5	1	0	0.88220	121.655	4.0
23	3	3	2	0.87990	122.194	4.0
24	4	3	1	0.86520	125.826	12.0
25	3	0	3	0.86090	126.956	6.0
26	4	2	2	0.84800	130.563	8.0
27	5	2	1	0.80750	145.082	10.0
28	3	2	3	0.80400	146.705	8.0
29	4	4	0	0.79530	151.192	4.0
30	0	0	4	0.78860	155.265	2.0

## **Stick Pattern**



## **Name and formula**

Reference code:	00-004-0551
Mineral name:	Rutile
Compound name:	Titanium Oxide
Empirical formula:	O <sub>2</sub> Ti
Chemical formula:	TiO <sub>2</sub>

## **Crystallographic parameters**

Crystal system:	Tetragonal
Space group:	P42/mnm
Space group number:	136
a (Å):	4.5940
b (Å):	4.5940
c (Å):	2.9580
Alpha (°):	90.0000
Beta (°):	90.0000
Gamma (°):	90.0000
Calculated density (g/cm <sup>3</sup> ):	4.25
Volume of cell (10 <sup>6</sup> pm <sup>3</sup> ):	62.43
RIR:	-

## **Status, subfiles and quality**

Status:	Marked as deleted by ICDD
Subfiles:	Alloy, metal or intermetallic Common Phase Excipient

Forensic  
 Inorganic  
 Mineral  
 Pharmaceutical  
 Pigment/Dye  
 Quality: Indexed (I)

### **Comments**

Creation Date: 9/1/1954  
 Modification Date: 1/1/1970  
 Warning: Lines with abs(delta 2Theta)>0.06 DEG.

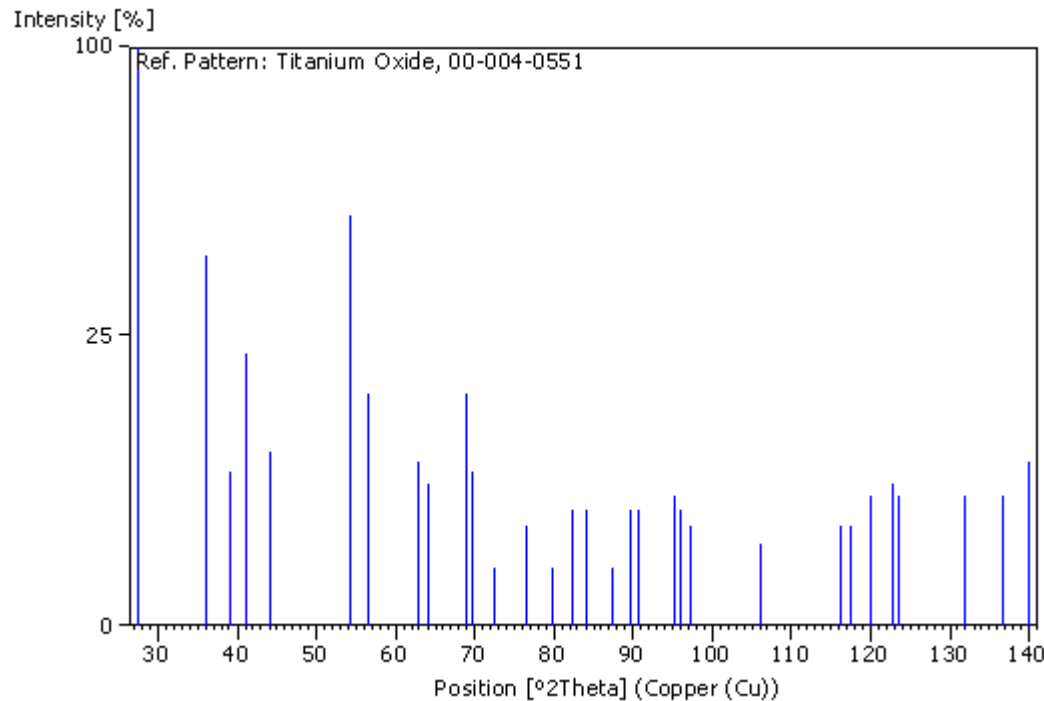
### **References**

Primary reference: Swanson, Tatge, JC Fel. Reports, NBS., *Private Communication*, (1950)

### **Peak list**

No.	h	k	l	d [Å]	2Theta [deg]	I [%]
1	1	1	0	3.24500	27.464	100.0
2	1	0	1	2.48900	36.056	41.0
3	2	0	0	2.29700	39.188	7.0
4	1	1	1	2.18800	41.226	22.0
5	2	1	0	2.05400	44.052	9.0
6	2	1	1	1.68700	54.337	50.0
7	2	2	0	1.62400	56.631	16.0
8	0	0	2	1.48000	62.728	8.0
9	3	1	0	1.45300	64.030	6.0
10	3	0	1	1.36000	68.999	16.0
11	1	1	2	1.34700	69.761	7.0
12	3	1	1	1.30500	72.352	1.0
13	2	0	2	1.24300	76.590	3.0
14	2	1	2	1.20000	79.870	1.0
15	3	2	1	1.17000	82.352	4.0
16	4	0	0	1.14850	84.242	4.0
17	4	1	0	1.11400	87.494	1.0
18	2	2	2	1.09330	89.589	4.0
19	3	3	0	1.08270	90.708	4.0
20	4	1	1	1.04240	95.287	5.0
21	3	1	2	1.03610	96.054	4.0
22	4	2	0	1.02730	97.151	3.0
23	1	0	3	0.96420	106.050	2.0
24	4	0	2	0.90710	116.247	3.0
25	5	1	0	0.90070	117.569	3.0
26	2	1	3	0.88920	120.059	5.0
27	5	0	1	0.87730	122.812	6.0
28	3	3	2	0.87390	123.636	5.0
29	4	2	2	0.84370	131.847	5.0
30	3	0	3	0.82900	136.618	5.0
31	5	2	1	0.81960	140.052	8.0

## **Stick Pattern**



## **Name and formula**

Reference code:	00-005-0664
Mineral name:	Zincite, syn
Compound name:	Zinc Oxide
Common name:	zinc white, chinese white
Empirical formula:	OZn
Chemical formula:	ZnO

## **Crystallographic parameters**

Crystal system:	Hexagonal
Space group:	P63mc
Space group number:	186
a (Å):	3.2490
b (Å):	3.2490
c (Å):	5.2050
Alpha (°):	90.0000
Beta (°):	90.0000
Gamma (°):	120.0000
Calculated density (g/cm^3):	5.68
Measured density (g/cm^3):	5.66
Volume of cell (10^6 pm^3):	47.58
Z:	2.00
RIR:	4.50

## **Status, subfiles and quality**

---

Status:	Alternate Pattern
Subfiles:	Alloy, metal or intermetallic
	Common Phase
	Excipient
	Forensic
	Inorganic
	Mineral
	NBS pattern
	Pharmaceutical
	Pigment/Dye
Quality:	Indexed (I)

## **Comments**

Color: Orange-yellow, dark red  
 Creation Date: 9/1/1955  
 Modification Date: 1/1/1970  
 Additional Patterns: See PDF 00-036-1451  
 Analysis: Spectroscopic analysis: <0.001% each of Mg, Si and Ca. Color: Orange-yellow, dark red. Melting Point: 1943(10) K. Reflectance: Opaque mineral optical data on specimen from Sterling Hill, New Jersey, USA: R3R%=11.8, Disp.=Std. Sample Source or Locality: Sample from New Jersey Zinc Company, Sterling Hill, New Jersey, USA. Temperature of Data Collection: Pattern taken at 299 K. Vickers Hardness Number: VHN100=190-219. Warning: Lines with  $\text{abs}(\Delta 2\text{Theta}) > 0.06$  DEG. Unit Cell Data Source: Powder Diffraction.

## **References**

Primary reference: Swanson, Fuyat., *Natl. Bur. Stand. (U. S. ), Circ. 539, 2, 25,* (1953)  
 Optical data: *Dana's System of Mineralogy, 7th Ed., 1,* 504

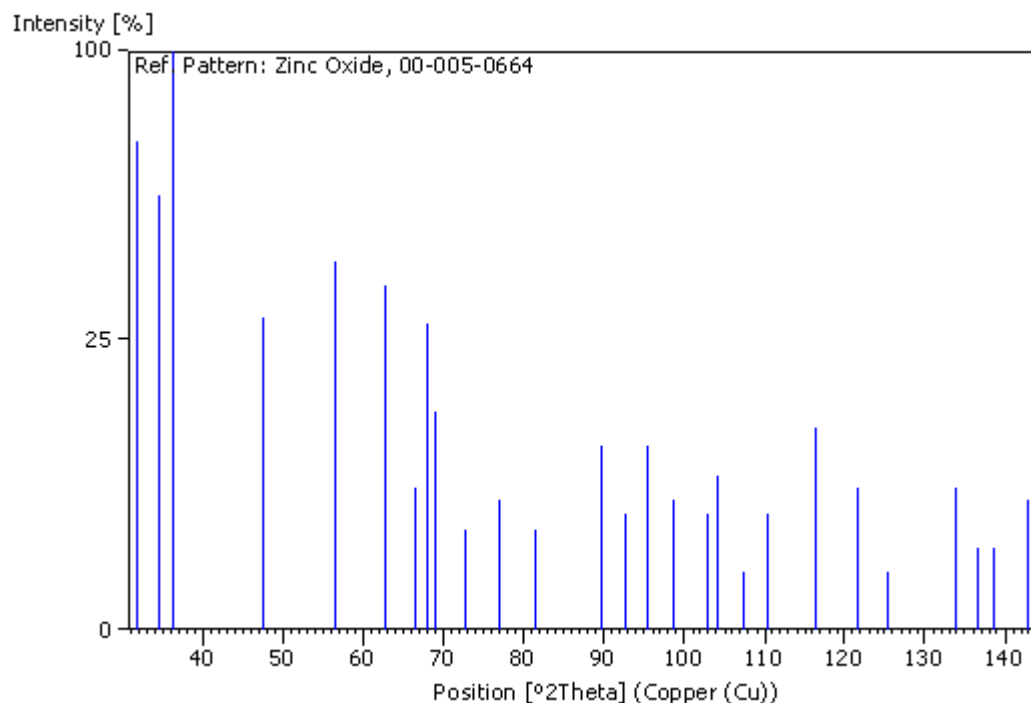
## **Peak list**

No.	h	k	l	d [Å]	2Theta [deg]	I [%]
1	1	0	0	2.81600	31.751	71.0
2	0	0	2	2.60200	34.440	56.0
3	1	0	1	2.47600	36.252	100.0
4	1	0	2	1.91100	47.543	29.0
5	1	1	0	1.62600	56.555	40.0
6	1	0	3	1.47700	62.870	35.0
7	2	0	0	1.40700	66.388	6.0
8	1	1	2	1.37900	67.917	28.0
9	2	0	1	1.35900	69.057	14.0
10	0	0	4	1.30100	72.610	3.0
11	2	0	2	1.23800	76.956	5.0
12	1	0	4	1.18120	81.405	3.0
13	2	0	3	1.09290	89.630	10.0
14	2	1	0	1.06390	92.777	4.0
15	2	1	1	1.04220	95.311	10.0
16	1	1	4	1.01580	98.632	5.0
17	2	1	2	0.98480	102.923	4.0
18	1	0	5	0.97640	104.169	7.0
19	2	0	4	0.95550	107.448	1.0
20	3	0	0	0.93820	110.378	4.0
21	2	1	3	0.90690	116.288	12.0
22	3	0	2	0.88260	121.562	6.0

---

23	0	0	6	0.86750	125.234	1.0
24	2	0	5	0.83690	133.975	6.0
25	1	0	6	0.82900	136.618	2.0
26	2	1	4	0.82370	138.511	2.0
27	2	2	0	0.81250	142.905	5.0

### **Stick Pattern**



### **Name and formula**

Reference code: 00-026-1500  
 Mineral name: Ecadrewsite, syn  
 PDF index name: Zinc Titanium Oxide  
 Empirical formula:  $O_3TiZn$   
 Chemical formula:  $ZnTiO_3$

### **Crystallographic parameters**

Crystal system:	Rhombohedral
Space group:	R-3
Space group number:	148
a (Å):	5.0787
b (Å):	5.0787
c (Å):	13.9270
Alpha (°):	90.0000
Beta (°):	90.0000
Gamma (°):	120.0000
Calculated density (g/cm^3):	5.16
Volume of cell (10^6 pm^3):	311.10
Z:	6.00
RIR:	2.50

**Subfiles and Quality**

Subfiles:	Inorganic Mineral Corrosion Common Phase NBS pattern
Quality:	Star (S)

**Comments**

Color:	Colorless.
General comments:	Because of the presence of small amounts of "Ti O <sub>2</sub> " and "Zn <sub>2</sub> Ti O <sub>4</sub> " the intensities may have slight errors.
Sample preparation:	Prepared by heating an equimolar mixture of "Zn ( N O <sub>3</sub> ) <sub>2</sub> " and "Ti O <sub>2</sub> " (anatase) for two weeks at 900 C with remixings and reheatings.
Additional pattern:	To replace 00-025-0671. See PDF 01-085-0547.
Unit cell data source:	Powder Diffraction.
Temperature:	Pattern taken at 298 K.

**References**

Primary reference: *Natl. Bur. Stand. (U.S.) Monogr. 25, 13, 49, (1976)*

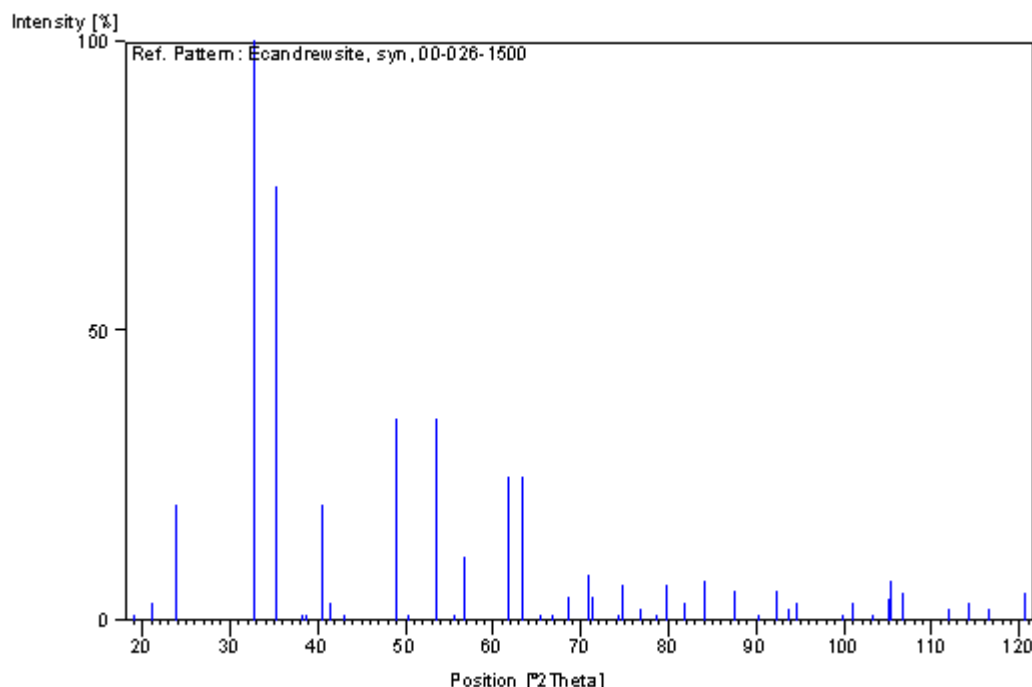
**Peak list**

No.	h	k	l	d [Å]	2Theta [deg]	I [%]
1	0	0	3	4.63000	19.154	1.0
2	1	0	1	4.19100	21.182	3.0
3	0	1	2	3.71700	23.921	20.0
4	1	0	4	2.72900	32.791	100.0
5	1	1	0	2.54000	35.308	75.0
6	0	1	5	2.35500	38.185	1.0
7	0	0	6	2.32100	38.766	1.0
8	1	1	3	2.22800	40.453	20.0
9	0	2	1	2.17300	41.524	3.0
10	2	0	2	2.09700	43.103	1.0
11	0	2	4	1.86000	48.930	35.0
12	1	0	7	1.81300	50.286	1.0
13	1	1	6	1.71300	53.446	35.0
14	2	1	1	1.65100	55.623	1.0
15	0	1	8	1.61900	56.821	11.0
16	2	1	4	1.50000	61.799	25.0
17	3	0	0	1.46600	63.396	25.0
18	1	2	5	1.42800	65.289	1.0
19	3	0	3	1.39900	66.817	1.0
20	2	0	8	1.36500	68.710	4.0
21	1	0	10	1.32760	70.932	8.0
22	1	1	9	1.32180	71.291	4.0
23	2	1	7	1.27600	74.268	1.0
24	2	2	0	1.26960	74.706	6.0
25	3	0	6	1.23960	76.838	2.0
26	0	1	11	1.21660	78.567	1.0
27	1	2	8	1.20200	79.710	6.0
28	0	2	10	1.17660	81.791	3.0
29	1	3	4	1.15120	84.000	7.0
30	2	2	6	1.11390	87.503	5.0

---

31	0	4	2	1.08620	90.335	1.0
32	2	1	10	1.06740	92.383	5.0
33	1	1	12	1.05580	93.704	2.0
34	4	0	4	1.04850	94.558	3.0
35	1	2	11	1.00690	99.818	1.0
36	3	1	8	0.99900	100.900	3.0
37	2	2	9	0.98160	103.393	1.0
38	0	1	14	0.97020	105.114	4.0
39	3	2	4	0.96920	105.269	7.0
40	4	1	0	0.95990	106.735	5.0
41	0	4	8	0.92960	111.918	2.0
42	1	3	10	0.91750	114.188	3.0
43	2	0	14	0.90640	116.390	2.0
44	4	1	6	0.88680	120.599	5.0

### Stick Pattern



### Name and formula

Reference code: 00-039-0190  
 PDF index name: Zinc Titanium Oxide  
 Empirical formula: O<sub>3</sub>TiZn  
 Chemical formula: ZnTiO<sub>3</sub>

### Crystallographic parameters

Crystal system:	Cubic
a (Å):	8.4080
b (Å):	8.4080
c (Å):	8.4080
Alpha (°):	90.0000
Beta (°):	90.0000

---

Gamma (°): 90.0000  
 Volume of cell (10^6 pm^3): 594.40  
 RIR: -

### Subfiles and Quality

Subfiles: Inorganic  
 Corrosion  
 Quality: Star (S)

### Comments

Additional pattern: To replace 00-013-0471.

### References

Primary reference: Yamaguchi, O., Morimi, M., Kawabata, H., Shimizu, K., *J. Am. Ceram. Soc.*, **70**, C97, (1987)

### Peak list

No.	h	k	l	d [Å]	2Theta [deg]	I [%]
1	1	1	0	5.95000	14.877	8.0
2	2	1	0	3.76000	23.643	7.0
3	2	1	1	3.43000	25.956	6.0
4	2	2	0	2.97300	30.033	45.0
5	3	0	0	2.80300	31.902	1.0
6	3	1	0	2.65900	33.679	2.0
7	3	1	1	2.53500	35.380	100.0
8	3	2	0	2.33200	38.576	2.0
9	4	0	0	2.10200	42.995	9.0
10	3	3	1	1.92900	47.072	2.0
11	4	2	1	1.83500	49.642	3.0
12	4	2	2	1.71600	53.345	15.0
13	5	1	0	1.64900	55.697	1.0
14	5	1	1	1.61800	56.860	28.0
15	5	2	0	1.56100	59.137	2.0
16	5	2	1	1.53500	60.242	3.0
17	4	4	0	1.48600	62.446	34.0

**Stick Pattern**

